

Wiesław Ostachowicz  
Malcolm McGugan  
Jens-Uwe Schröder-Hilrichs  
Marcin Luczak  
*Editors*

# MARE-WINT

New Materials and Reliability in  
Offshore Wind Turbine Technology



MARE-WINT



Wiesław Ostachowicz • Malcolm McGugan •  
Jens-Uwe Schröder-Hinrichs • Marcin Luczak  
Editors

# MARE-WINT

New Materials and Reliability in Offshore  
Wind Turbine Technology



*Editors*

Wiesław Ostachowicz  
Mechanics of Intelligent Structures  
Polish Academy of Sciences (IFFM)  
Gdansk, Poland

Malcolm McGugan  
Department of Wind Energy  
Technical University of Denmark  
Roskilde, Denmark

Jens-Uwe Schröder-Hinrichs  
Maritime Risk and System Safety  
(MaRiSa)  
World Maritime University  
Malmö, Sweden

Marcin Luczak  
Institute of Fluid-Flow Machinery  
Polish Academy of Sciences (IFFM)  
Gdansk, Poland

ISBN 978-3-319-39094-9

ISBN 978-3-319-39095-6 (eBook)

DOI 10.1007/978-3-319-39095-6

Library of Congress Control Number: 2016950528

© The Editor(s) (if applicable) and The Author(s) 2016. This book is published open access.

**Open Access** This book is distributed under the terms of the Creative Commons Attribution-NonCommercial 4.0 International License (<http://creativecommons.org/licenses/by-nc/4.0/>), which permits any noncommercial use, duplication, adaptation, distribution, and reproduction in any medium or format, as long as you give appropriate credit to the original author(s) and the source, provide a link to the Creative Commons license and indicate if changes were made.

The images or other third party material in this book are included in the work's Creative Commons license, unless indicated otherwise in the credit line; if such material is not included in the work's Creative Commons license and the respective action is not permitted by statutory regulation, users will need to obtain permission from the license holder to duplicate, adapt, or reproduce the material.

This work is subject to copyright. All commercial rights are reserved by the Publisher, whether the whole or part of the material is concerned, specifically the rights of translation, reprinting, reuse of illustrations, recitation, broadcasting, reproduction on microfilms or in any other physical way, and transmission or information storage and retrieval, electronic adaptation, computer software, or by similar or dissimilar methodology now known or hereafter developed.

The use of general descriptive names, registered names, trademarks, service marks, etc. in this publication does not imply, even in the absence of a specific statement, that such names are exempt from the relevant protective laws and regulations and therefore free for general use.

The publisher, the authors and the editors are safe to assume that the advice and information in this book are believed to be true and accurate at the date of publication. Neither the publisher nor the authors or the editors give a warranty, express or implied, with respect to the material contained herein or for any errors or omissions that may have been made.

Printed on acid-free paper

This Springer imprint is published by Springer Nature  
The registered company is Springer International Publishing AG Switzerland

# Acknowledgements

## The European Commission

The editors would like to start by thanking the European Commission for their Marie Skłodowska-Curie actions (MSCA). The current research and publication was primarily made possible through funding under the MSCA project FP7-PEOPLE-20120 ITN 309395 “MARE-WINT” (new MAterials and REliability in offshore WINd Turbines technology).

## *About MSCA*

The Marie Skłodowska-Curie actions (MSCA) provide grants at all stages of researchers’ careers, from doctoral candidates to highly experienced researchers, and encourage transnational, intersectoral and interdisciplinary mobility. For research institutions (universities, research centres and companies), MSCA offer the possibility to host talented foreign researchers and create strategic partnerships with leading institutions. The idea is to equip researchers with the necessary skills for a successful career, be it in the public or the private sector.

The MSCA are open to all domains of research and innovation, from basic research up to market take-up and innovation services. Research and innovation fields are chosen freely by the applicants (individuals and/or organisations) in a fully bottom-up manner. International mobility is prerequisite under all Marie Skłodowska-Curie actions. There are no restrictions in terms of research field, nationality or age.

Endowing researchers with new skills and a wider range of competencies, while offering them attractive working conditions, is a crucial aspect of the MSCA. In addition to mobility between countries, the MSCA also seek to break the real and perceived barriers between academic and other sectors, especially business.

## ***About ITN***

The doctoral training is covered under the action Innovative Training Networks (ITN). This high-quality joint research and doctoral training is delivered by international networks that bring together universities, research centres and non-academic organisations (companies, NGOs, charities, etc.) across Europe and beyond.

ITN can take one of three forms:

- European Training Networks (ETN): Joint research training, involving a minimum of three partners from in and outside academia (business, museum, NGO, etc.).
- European Industrial Doctorates (EID): Joint doctoral training delivered by at least one academic partner entitled to award doctoral degrees and at least one partner from outside academia, primarily enterprise. Each participating researcher is enrolled in a doctoral programme and is jointly supervised by supervisors from the academic and non-academic sector, where they spend at least 50% of their time. The aim is to broaden the career perspective of the PhD candidate upon completion of the training.
- European Joint Doctorates (EJD): A minimum of three academic organisations form a network with the aim of delivering joint, double or multiple degrees. Joint supervision of the research fellow and a joint governance structure are mandatory. The participation of additional organisations from anywhere in the world, including from the non-academic sector, is encouraged.

During their ITN training, researchers will develop key transferable skills common to all fields, such as entrepreneurship, management and financing of research activities and programmes, management of intellectual property rights, ethical aspects and communication.

In all cases, the recruited researchers are fully funded by the Marie Skłodowska-Curie actions, with an attractive living and mobility allowance. The host organisations receive a contribution to the research and training costs of the recruited researcher and apply good employment practices in line with the European Charter for Researchers and the European Code of Conduct for the Recruitment of Researchers (European Commission 2016a).

The Marie Skłodowska-Curie actions support PhD candidates by financing organisations which subsequently recruit candidates to the training programmes. Therefore PhD candidates do not apply to the commission for the funding of their posts. Instead, they apply directly on the European Researchers Mobility portal EURAXESS (European Commission 2016b).

## The External Contributors

In addition to the research conducted under MARE-WINT and MSCA, several fellows collaborated with other researchers, funded under different schemes. On behalf of all authors, the editors would like to thank these external collaborators; individual acknowledgements are present in the various chapters.

The editors would also like to thank all external contributors who were not directly involved in MARE-WINT but contributed through workshops and subsequent special chapters for the current book. Their knowledge, expertise and time were very greatly appreciated. In particular, the editors would like to thank:

- Gregor Giebel and Charlotte Bay Hasager, who provided Chap. 19
- Johan Finsteen Gjørdvad and Morten Dallov Ibsen, who authored Chap. 22
- Justine Beauson and Povl Brøndsted, who presented Chap. 23

## The MARE-WINT Fellows and Project Partners

The editors would especially like to thank all the fellows whose hard work led to the excellent research that is present in this book; the editors also extend their gratitude to the various supervisors and colleagues, who guided the fellows and helped them achieve their aims in the relevant research fields.

## References

European Commission (2016a) The European Charter for Researchers. <http://ec.europa.eu/euraxess/index.cfm/rights/europeanCharter>. Accessed 06 Apr 2016

European Commission (2016b) EURAXESS Researchers in Motion. <http://ec.europa.eu/euraxess/index.cfm/jobs/index>. Accessed 06 Apr 2016



# Contents

<b>1</b>	<b>Introduction</b> .....	1
	Raza Ali Mehdi, Wiesław Ostachowicz, and Marcin Luczak	
<b>Part I Wind Turbine Blades</b>		
<b>2</b>	<b>Design of Wind Turbine Blades</b> .....	13
	Malcolm McGugan	
<b>3</b>	<b>Damage Sensing in Blades</b> .....	25
	Borja Hernandez Crespo	
<b>4</b>	<b>Fibre Bragg Grating as a Multi-Stage Structure Health Monitoring Sensor</b> .....	53
	Gilmar Ferreira Pereira	
<b>5</b>	<b>Analysis and Design of Bend-Twist Coupled Wind Turbine Blades</b> .....	67
	Alexander R. Stäblein	
<b>6</b>	<b>Improvement of Wind Turbine Blade Performance by Means of Rod Vortex Generators</b> .....	81
	Javier Martinez, Pawel Flaszynski, Piotr Doerffer, and Oskar Szulc	
<b>7</b>	<b>Trailing and Leading Edge Flaps for Load Alleviation and Structure Control</b> .....	103
	Vladimir Leble and George N. Barakos	
<b>Part II Enabling Technologies for Drivetrain and Gearbox Analysis</b>		
<b>8</b>	<b>OWT Drivetrain &amp; Gearbox Simulation and Testing</b> .....	117
	Simone Manzato and Bert Plummers	

<b>9</b>	<b>Dynamic Behavior of Bearings on Offshore Wind Turbine Gearboxes</b> .....	123
	Rubén Cerdá, Bart Blockmans, Jakob Fiszer, Tommaso Tamarozzi, Bert Pluymers, and Wim Desmet	
<b>10</b>	<b>Experimental Characterization of Wind Turbine Gearbox in Operation</b> .....	147
	Emilio Di Lorenzo and Simone Manzato	
<b>Part III Tower &amp; Support Structure</b>		
<b>11</b>	<b>An Overview of Analysis and Design of Offshore Wind Turbines</b> ....	169
	Torgeir Moan and Tomasz Bugalski	
<b>12</b>	<b>Dynamic Response Analysis of Floating Wind Turbines with Emphasis on Vertical Axis Rotors</b> .....	173
	Zhengshun Cheng, Torgeir Moan, and Zhen Gao	
<b>13</b>	<b>Bottom Fixed Substructure Analysis, Model Testing and Design for Harsh Environment</b> .....	193
	Duje Veic, Marek Kraskowski, and Tomasz Bugalski	
<b>14</b>	<b>Detection of Damage in Metallic Structures for Offshore Applications</b> .....	213
	Rohan Soman, Paweł Malinowski, and Wiesław Ostachowicz	
<b>Part IV Reliability &amp; Preventive Maintenance of Offshore Wind Turbines</b>		
<b>15</b>	<b>Reliability and Preventive Maintenance</b> .....	235
	Itamar Esdras Martínez García, Alejandro Sánchez Sánchez, and Stefano Barbati	
<b>Part V CFD Analysis of a Complete Offshore Wind Turbine</b>		
<b>16</b>	<b>An Overview of the CFD Analyses in the MARE-WINT Project</b> .....	275
	George N. Barakos	
<b>17</b>	<b>CFD Investigation of a Complete Floating Offshore Wind Turbine</b> .....	277
	Vladimir Leble and George N. Barakos	
<b>18</b>	<b>CFD Study of DTU 10 MW RWT Aeroelasticity and Rotor-Tower Interactions</b> .....	309
	Sergio González Horcas, François Debrabandere, Benoît Tartinville, Charles Hirsch, and Grégory Coussement	

**Part VI Offshore Wind Farm Design**

**19 An Overview of Offshore Wind Farm Design** ..... 337  
 Gregor Giebel and Charlotte Bay Hasager

**20 Large Eddy Simulation of Wind Farm Aerodynamics  
 with Energy-Conserving Schemes** ..... 347  
 Dhruv Mehta

**21 A Theoretical Risk Management Framework for Vessels  
 Operating Near Offshore Wind Farms**..... 359  
 Raza Ali Mehdi and Jens-Uwe Schröder-Hinrichs

**Part VII Offshore Wind Decommissioning**

**22 ODIN-WIND: An Overview of the Decommissioning  
 Process for Offshore Wind Turbines** ..... 403  
 Johan Finsteen Gjørdvad and Morten Dallov Ibsen

**23 Wind Turbine Blades: An End of Life Perspective** ..... 421  
 Justine Beauson and Povl Brøndsted



# Chapter 1

## Introduction

Raza Ali Mehdi, Wiesław Ostachowicz, and Marcin Luczak

**Abstract** The current chapter provides an overview of the offshore wind industry, followed by an introduction to the MARE-WINT project. We discuss the important role that MARE-WINT has fulfilled in reducing the cost of offshore wind energy, by improving the reliability, and operation and maintenance strategies of various wind turbine components. Lastly, we present an overview of the current book for the readers.

### 1.1 The Emergent Offshore Wind Industry

Wind is one of the most plentiful and widely available natural resources available on our planet. For centuries, mankind has harvested the power of the wind for applications such as maritime and agriculture. Most of the world was explored on the back of wind-powered ships, and it was truly wind that made globalisation and exploration possible.

With society becoming increasingly mindful of the impacts of fossil fuels, renewable energy is on the rise, and the harvesting of wind to generate electricity is becoming increasingly common. To enable this to happen, wind turbines have been installed all over the globe. A vast majority of these wind turbines have been installed on land and are referred to as onshore wind turbines. Statistics by the Global Wind Energy Council (GWEC) indicate that only around 3 % of global electricity is currently generated by wind power—but this number is on the rise.

---

R.A. Mehdi (✉)

Maritime Risk and System Safety (MaRiSa) Research Group, World Maritime University,  
Fiskehamngatan 1, 21118 Malmö, Sweden  
e-mail: [rm@wmu.se](mailto:rm@wmu.se)

W. Ostachowicz

Mechanics of Intelligent Structures Department, Institute of Fluid Flow Machinery, Polish  
Academy of Sciences, ul. Fiszerza 14, 80-231 Gdańsk, Poland  
e-mail: [wieslaw@imp.gda.pl](mailto:wieslaw@imp.gda.pl)

M. Luczak

Aerodynamics Department, Institute of Fluid Flow Machinery, Polish Academy of Sciences  
(IFFM), ul. Fiszerza 14, 80-231 Gdańsk, Poland  
e-mail: [marcin.luczak@imp.gda.pl](mailto:marcin.luczak@imp.gda.pl)

The International Energy Agency (IEA) expects that by the year 2035, 25 % of the electricity generation will be fulfilled by renewable sources, and that wind energy will have a major role to play.

### 1.1.1 The Benefits of Wind Energy

The popularity of wind energy arises from the simple fact that it is, by and large, cost effective, environmentally friendly and socially popular amongst a majority of the populace. A common method of assessing the cost-effectiveness of an energy source is through a parameter called Levelized Cost of Energy (LCOE), which is essentially a ratio between two parameters: the *total lifetime costs* and the *total electricity produced over the lifetime*. Siemens (2014) calculated the LCOE of various electricity generation sources to be as follows:

As Table 1.1 shows, the LCOE of onshore wind is reasonably close to the LCOE of commonly used fossil fuels. However, the LCOE alone does not often provide the complete picture.

A more comprehensive measure, as provided by Siemens (2014) is the so-called Society's Cost of Energy (SCOE). The SCOE takes into consideration further factors such as number of jobs created by energy source, subsidies, transmission costs, variability costs, geopolitical risk impact, and environmental impact. The predicted SCOE in the year 2025 for various electricity generation sources is shown in Table 1.2.

As shown in Table 1.2, it is expected that onshore and offshore wind will be the two most viable sources of energy in the near future. In fact, this phenomenon is already manifesting—statistics indicate the benefits from wind energy to be

**Table 1.1** LCOE in 2013 for various electricity generation sources

Source of electricity generation	LCOE (€/MWh)
Nuclear	79
Coal	63
Gas	60
Photovoltaics	145
Onshore wind	81
Offshore wind	140

Source: Siemens (2014)

**Table 1.2** SCOE in 2025 for various electricity generation sources

Source of electricity generation	SCOE (€/MWh)
Nuclear	107
Coal	110
Gas	89
Photovoltaics	78
Onshore wind	60
Offshore wind	61

Source: Siemens (2014)

significant. As an example of the social benefits of wind energy, GWEC estimates that more than 600,000 people are employed by the wind industry—a number that is likely to rise to more than 2,000,000 by 2030. In terms of a positive environmental impact, wind energy helped to avoid more than 608 million tonnes of carbon dioxide emissions in 2014 alone. GWEC also estimate that wind farms generate between 17 and 39 times more power than they consume—compared to 16 times for nuclear and 11 times for coal plants (GWEC 2016).

### ***1.1.2 The Challenges of Going Offshore***

The continued increase in wind energy is not without its challenges. Offshore wind, in particular, still has some way to go before it can meet the LCOE and SCOE cost expectations. This raises the question—why go offshore at all?

The growth of offshore wind is primarily due to better, more consistent wind resource available on open seas. Combined with limited land space, and the fact that onshore turbines may be less socially acceptable, this makes offshore wind very appealing.

On the other hand, going offshore presents novel challenges—currently, there are limitations in deep-water installation technology, and the harsher environment is not ideal for the reliability, maintainability and availability of offshore wind turbines. Furthermore, offshore wind farms (OWFs) need to be situated in locations where simultaneously, the wind resource *and* the transmission-to-shore options are optimum. Often times, these locations may be in conflict with national, regional or international marine spatial plans, and other sectors such as fisheries and shipping may take precedence in these areas.

There is, thus, a clear need to improve the viability and feasibility of OWFs, and to make offshore turbines closely competitive to their onshore counterparts—and indeed other sources of energy. To fulfil this gap, organizations like the European Commission have encouraged and funded research projects such as MARE-WINT.

## **1.2 An Introduction to the MARE-WINT Project**

The aim of the MARE-WINT (new MAterials & REliability in offshore Wind Turbine Technology) project was to reduce cost of energy, and increase the energy output, by improving reliability of wind turbines and their components and optimizing operation and maintenance (O&M) strategies. Thus, the project contributed towards making wind energy more competitive. The outcomes of the project are particularly evident and relevant for the offshore sector, where O&M represents a high percentage of total costs.

An offshore wind turbine (OWT) is a complex energy conversion fluid flow machine with coupled hydro-aero-mechanical issues. To design, build, and operate

a reliable OWT, knowledge from disciplines like mechanical engineering, material science, metrology, fluid mechanics, condition monitoring, and computer simulation needs to be combined. The MARE-WINT network brought together specific partners' capabilities and know-how to realize tailored training trajectories, focusing on an increased reliability OWT design.

MARE-WINT achieved the overall aim by providing training in the context of doctoral programmes for 15 researchers, in multi-disciplinary areas related to future generations of Offshore Wind Turbines (OWT). An emphasis was placed on issues that may have a major impact on the mechanical loading of OWT and which were not sufficiently addressed at the initiation of the project. One of the strengths of MARE-WINT has been the validation of various numerical, analytical and empirical models through experimental data. This has allowed novel concepts such as floating 10 MW wind turbines to be thoroughly investigated, to better prepare the industry for the challenges of tomorrow.

### **1.3 An Overview of the Current Research**

To get a better insight of the outstanding work done by the fellows in the MARE-WINT project—as presented in this book—it is firstly important to understand the components, design process and operation of a typical wind turbine.

#### ***1.3.1 The Components of a Wind Turbine***

Wind turbines are aero-mechanical devices that convert the rotational movement of a rotor into electrical energy. In order for wind turbines to function, there needs to be wind flowing past them. Wind on Earth is created as a result of the uneven heating of our atmosphere, the irregularities of the Earth's surface, and the actual rotation of our planet. As wind flows past a turbine, it generates a lifting force on the blades of a wind turbine—which are connected to a rotor. The lifting force on the blades creates a rotational movement on the rotor. This rotational movement is transferred, via a shaft and gearbox, to a generator where it is converted into electrical energy. The components of a turbine are shown in Fig. 1.1.

#### ***1.3.2 Designing a Wind Turbine***

Within the MARE-WINT project, several researchers worked in the context of the 10 MW reference turbine developed by the Technical University of Denmark (DTU), and described by Bak et al. (2013); the parameters are shown in Table 1.3.

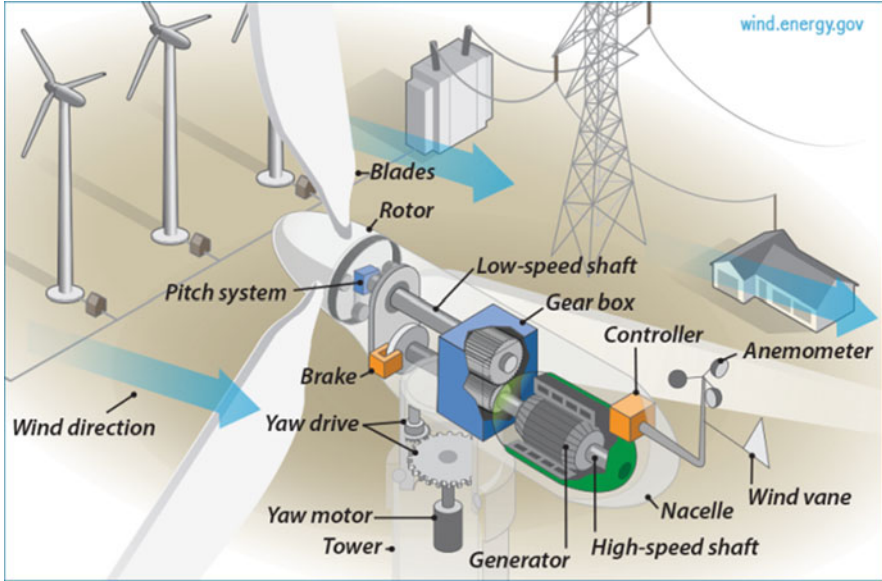


**Fig. 1.1** Wind turbine components. *Source:* wind.energy.gov; copyright: public domain

**Table 1.3** Properties of the 10 MW DTU reference wind turbine

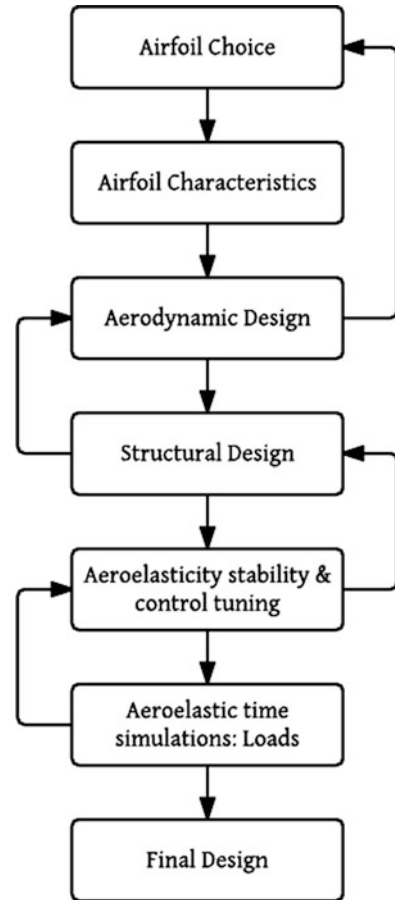
Parameter	Value
Rating	10 MW
Rotor orientation, configuration	Upwind, three blades
Control	Variable speed, collective pitch
Drivetrain	Medium speed, multiple stage gearbox
Rotor, hub diameter	178.3 m, 5.6 m
Cut-in, rated, cut-out wind speed	4 m/s, 11.4 m/s, 25 m/s
Cut-in, rated rotor speed	6 RPM, 9.6 RPM
Rated tip speed	90 m/s
Overhang, shaft tilt, pre-cone	7.07 m, 5°, 2.5°
Pre-bend	3 m
Rotor mass	229 tons (each blade ~41 tons)
Nacelle mass	446 tons
Tower mass	605 tons

Source: Bak et al. (2013)

To design and develop this 10 MW reference turbine, the Bak et al. (2013) applied the method shown in Fig. 1.2.

Figure 1.2 has a heavy emphasis on aerodynamics and structural mechanic and is, in fact, only a simplified version of a much more sophisticated process. Typically, as shown in Fig. 1.2, the starting point for a wind turbine concept is the design of the blades. The size (primarily, the length) of the blades directly determines the capacity

**Fig. 1.2** Method for developing the 10 MW reference wind turbine. Adapted from Bak et al. (2013)



of the turbine. As a rule of thumb, the larger the diameter, the greater the power output of the turbine. Of course, principals of aerodynamics govern the efficiency of the wind turbine. On a very basic level, the Betz law means that theoretically only around 59.3 % (16/27) of the kinetic energy from wind can actually be captured—no matter how large the rotor size is; furthermore, being a mechanical device, there are further inefficiencies in the system, which means that only around 75–80 % of the 59.3 % theoretical cap is actually achieved. In order to make wind turbines more reliable and efficient, these inefficiencies need to be minimized as much as possible. Therefore, the design of blades is crucial. Blades must be aerodynamically efficient, whilst at the same time being structurally sound enough to bear all the mechanical and aerodynamic loads. Balancing the aerodynamic and structural parameters is becoming increasingly challenging as wind turbines get larger and more sophisticated.

The blades are connected to a rotor, which in turn is connected to a shaft, which goes through a gearbox into the generator. The shaft and gearbox must be able to

tolerate the mechanical loads in an often harsh environment, and be able to transmit the rotational movement as efficiently as possible. If the drivetrain and gearbox are unable to handle the loads from the blade and rotor, the blades design may have to be changed; alternatively, the gearbox and drivetrain would be updated. The research in this area, too, is critical as offshore turbines get more complex.

The blade and the nacelle (housing the gearbox and generator, amongst other components) assembly must be supported on an adequate tower structure, which in turn needs to be mounted or tethered on the sea-bed through an appropriate sub-structure. Depending on the design requirements and factors such as the turbine location, optimizing the tower and sub-structure can be a substantial task. The tower and sub-structure must not only cope with aerodynamic and mechanical loading (particularly from the blades, rotor and nacelle), but also bear its own load and various hydrodynamic loads. As with the research conducted for the blades and the gearbox, optimizing the tower and support structure for larger, more complex turbines is a unique challenge.

Once all the components are in place and assembled, the overall reliability of the turbine and all its sub-systems must be assessed. Furthermore, maintenance strategies must be optimized in order to reduce the costs associated with offshore wind. If it is unfeasible to maintain a wind farm in a cost effective manner, the design or maintenance strategy may have to be adapted.

To ensure that a turbine is reliable and efficient, it is also important to analyse the complete system. This is generally done using combined fluid and structural analysis methods, to ensure that the components complement each other, and are able to tolerate design loads without failures occurring.

A wind turbine on its own is often not the end goal—it needs to be integrated into a wind farm. In order to do so, one must analyse the aerodynamic effects of wake turbulence from each individual turbine over the entire proposed wind farm area. This helps to determine the efficiency of various turbines in different layouts. The layout of a wind farm is not only driven by aerodynamic factors; factors such as seabed conditions, grid connection locations, hydrography and bathymetry must also be taken into account. Furthermore, wind resource in an area must be considered. Equally important is the consideration of potential ‘conflict’ or ‘overlap’ areas—which may be reserved for marine, environmental, or other purposes. The layout of any wind farm can also have an impact on the navigational safety of passing vessels; in turn, vessel accidents in the area may damage wind turbines, or cause a wind farm shutdown, leading to reduced reliability. Wind turbine towers may have to be designed to be ‘collision-friendly’ to ships (BSH 2015). A potential conflict with other marine and maritime activities may cause a wind farm application to be denied, or at the very least, the layout may have to be changed.

Wind turbines are designed to last around 25 years. Once their lifetime has been fulfilled, the turbines need to be decommissioned. This is a fairly novel research area, as most offshore turbines are *just* now entering their end-of-life cycle. Despite this, the decommissioning is an important phase to consider when assessing LCOE, as it can have a significant impact on the parameter. It may even be the case that a wind farm is approved or denied permission based on its decommissioning plan.

### 1.3.3 *MARE-WINT's Contribution to the Offshore Wind Industry*

In the MARE-WINT project, the focus was not solely on the *design* of a wind turbine; rather, the fellows also focused on developing tools to analyse and improve the reliability and efficiency of various wind turbine components. The best way to highlight the contributions of the MARE-WINT project is by summarizing the content of the present book, which more or less covers the topic areas identified in Sect. 1.3.2:

- Part I of this book focuses on blade design, and tools to improve analysis and reliability of wind turbine blades. This research ranges from damage sensing to the analysis of bend-twist coupling of blades—and even a study into rod-vortex generators to minimize aerodynamic noise on the blade. Part I also describes the ‘Smart-Blade’ strategy used in the current work.
- Part II focuses on analysing and improving the reliability of these components. The research described in this part of the book can allow turbine engineers to assess the adequacy of the drivetrain and gearbox sub-systems.
- Part III presents tools that can be used to study, analyse and improve the reliability and design of the tower and substructure. Researchers performed a thorough fluid–structure interaction analysis of different wind turbine concepts—floating, horizontal axis, and vertical axis, and determined the feasibility and viability of each, compared to the others. Researchers also conducted numerical and experimental studies focusing on hydrodynamic loads on various sub-structures and towers. Lastly, a tool for structural health monitoring, to provide an improved method of assessing turbine tower damage is also presented.
- Part IV discusses tools, methods strategies which can be used to analyse and improve reliability and preventive maintenance of offshore wind turbines.
- Part V of the current book presents novel research in this area of complete offshore wind turbine analysis. It describes relevant tools and models to assess the fluid–structure interactions in a complex system like an offshore turbine.
- Part VI covers the crucial area of wind farm design. Topics including aerodynamic simulations over wind farms, maritime risk assessment are covered. The EERA-DTOC tool for designing wind farm clusters is also presented.
- Part VII of this book covers original decommissioning tools and strategies, both from an industry and research perspective.

Several topics are not explicitly covered in this book, as they have been sufficiently addressed in other published works. The spatial planning and approval of wind farms, for instance, has been the focus of the SEANERGY project (EWEA et al. 2012). Similarly, the environmental impacts of wind farms have been covered by Koeller et al. (2006). The installation process of OWFs is also not explicitly covered in this current work, although it is briefly discussed in Chap. 22, in the context of the decommissioning phase of offshore turbines. Aside from these aforementioned areas, the book comprehensively covers all topics from design to decommissioning of OWFs.



### 1.3.4 Contributions from External Authors

The majority of the content in this book has been generated from original research conducted within the MARE-WINT project. Some research topics, however, were not explicitly researched within the project; instead, subject matter experts were invited to speak to the fellows during various training workshops. Some of these experts were also invited to provide specific chapters for the book.

- Gregor Giebel and Charlotte Bay Hasager provided Chap. 19.
- Johan Finsteen Gjørdvad and Morten Dallov Ibsen authored Chap. 22.
- Justine Beauson and Povl Brøndsted presented Chap. 23.

This book has been authored for everyone interested in advanced topics related to offshore wind energy. It provides a unique perspective—both academic and industrial—on novel research topics that will shape the future of the offshore wind industry. On behalf of all the editors and authors, we wish you a very pleasant and insightful reading!

**Open Access** This chapter is distributed under the terms of the Creative Commons Attribution-NonCommercial 4.0 International License (<http://creativecommons.org/licenses/by-nc/4.0/>), which permits any noncommercial use, duplication, adaptation, distribution and reproduction in any medium or format, as long as you give appropriate credit to the original author(s) and the source, provide a link to the Creative Commons license and indicate if changes were made.

The images or other third party material in this chapter are included in the work's Creative Commons license, unless indicated otherwise in the credit line; if such material is not included in the work's Creative Commons license and the respective action is not permitted by statutory regulation, users will need to obtain permission from the license holder to duplicate, adapt or reproduce the material.

## References

- Bak C, Zahle F, Bitsche R et al (2013) The DTU 10-MW reference wind turbine. In: DTU orbit—the research information system. Available via Technical University of Denmark. [http://orbit.dtu.dk/files/55645274/The\\_DTU\\_10MW\\_Reference\\_Turbine\\_Christian\\_Bak.pdf](http://orbit.dtu.dk/files/55645274/The_DTU_10MW_Reference_Turbine_Christian_Bak.pdf). Accessed 6 Apr 2016
- BSH (2015) Minimum requirements concerning the constructive design of offshore structures within the Exclusive Economic Zone (EEZ). Available via BSH. <http://www.bsh.de/en/Products/Books/Standard/7005-15.pdf>. Accessed 6 Apr 2016
- EWEA, ECN, 3E et al (2012) Delivering offshore electricity to the EU: spatial planning of offshore renewable energies and electricity grid infrastructures in an integrated EU maritime policy; SEANERGY 2020 Final Project Report. In: Intelligent Energy Europe. Available via European Commission. <http://ec.europa.eu/energy/intelligent/projects/en/printpdf/projects/seanergy-2020>. Accessed 6 Apr 2016
- GWEC (2016) Wind in numbers. <http://www.gwec.net/global-figures/wind-in-numbers/>. Accessed 6 Apr 2016
- Koeller J, Koepfel J, Peters W (eds) (2006) Offshore wind energy: research on environmental impacts. Springer, New York
- Siemens AG (2014) A macro-economic viewpoint: what is the real cost of offshore wind? Available via Siemens AG. <http://www.energy.siemens.com/hq/pool/hq/power-generation/renewables/wind-power/SCOE/Infoblatt-what-is-the-real-cost-of-offshore.pdf>. Accessed 6 Apr 2016

**Part I**  
**Wind Turbine Blades**

# Chapter 2

## Design of Wind Turbine Blades

Malcolm McGugan

**Abstract** In this section the research program framework for European PhD network MARE-WINT is presented, particularly the technology development work focussing on reliability/maintenance and the models describing multi-body fluid structure interaction for the Rotor Blade structure. In order to give a context for the effort undertaken by the individual researchers this section gives a general background for Wind Turbine blades identifying the trends and issues of importance for these structures as well as concepts for “smarter” blades that address these issues.

### 2.1 Rotor Blades as a Common Research Topic

In order to meet its objective of strengthening the fundamental scientific work within the multi-disciplinary engineering field of hydro-aero-mechanical coupling in the wind energy conversion process, the MARE-WINT project was organised as five cross-linked work packages in a common research programme. The first three research work packages focus on the major structural components of the Offshore Wind Turbine; Blade, Drive train, and Support structure. In addition to these independent structure based work packages, there were two consolidating technology based work packages focussing on Reliability and Predictive maintenance, and Fluid–Structure interaction. In this way the goal of integrating multiple disciplines was to be achieved. This concept is visualised in Fig. 2.1 where the three vertical, structure-based Work Packages, are connected by the two horizontal technology-based Work Packages.

Work Package 1 is the focus of this chapter and concerns the challenges for offshore wind turbines with regard to the rotor blades, as well as proposing an innovative response to address these. Within the network two researchers were allocated within Work Package 1; Gilmar Pereira, based at the Technical University of Denmark (DTU) and Vladimir Leble, based initially at the University of Liverpool, and later at the University of Glasgow. In addition three researchers in the network allocated within Work Packages 4 and 5 conducted work at the nexus

---

M. McGugan (✉)  
Department of Wind Energy, Technical University of Denmark (DTU), DTU Risø Campus,  
Frederiksborgvej 399, 4000 Roskilde, Denmark  
e-mail: [mamc@dtu.dk](mailto:mamc@dtu.dk)

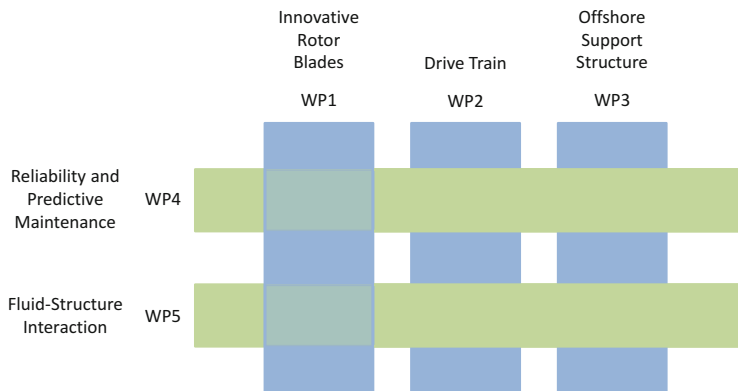


**Fig. 2.1** Diagram showing the cross-linked MARE-WINT Work Packages

between their technology area and the blade structure. Borja Hernandez Crespo, based at The Welding Institute in Cambridge, worked on Reliability and Predictive Maintenance for the blades, and Alexander Stäblein worked with wind turbine blade Fluid–Structure Interaction models at DTU Wind Energy, as Javier Martinez Suarez did at the Institute of Fluid-Flow Machinery in the Polish Academy of Sciences.

In Work Package 1 the structural and fluid dynamic investigations on the rotor blade are approached by numerical and experimental methods. Within the work package individual projects were developed, the first considering the behaviour of the composite material (particularly when in damaged condition) within the blade structure and the use of embedded sensors to detect this behaviour, and the second describing structural behaviour and rotor performance in Computational Fluid Dynamics models, including the use of leading and trailing edge flaps to modify this.

These activities cross-link with the combinatory horizontal work packages (4 and 5) by providing, among other things, structural health information to the reliability and predictive maintenance work package, and input to the fluid–structure interaction models developed for the entire turbine.

In Work Package 4 the prime consideration is the economic efficiency of an offshore wind farm as depending upon the individual turbines availability and reliability. For the blades this involves the study of the various damages observed in service, and understanding their root causes and criticality with respect to operational lifetime. Detecting damages that initiate and propagate during service is not straightforward and developing inspection technologies alongside remote sensing systems is a key part of the future optimisation in this area.

In Work Package 5 the structural description of the various Offshore Wind Turbine components are combined with flow models in a fluid–structure interaction description of the complete system. The key task involves identifying and integrating the various aero/hydro loadings and their effect on the structural responses, particularly any coupled effects. Of the three researchers in Work Package 5,

two worked specifically on the complex blade structure. The areas of interest here include the use of twist-coupled aeroelastic blades to achieve structural load reduction at high wind loads, and the development of flow control technology for advanced blades.

In order to provide a common platform for the different Work Packages, a reference model was agreed as one of the first deliverables within the project. Described by Bak et al. (2013), the DTU 10 MW reference wind turbine was developed by DTU Wind Energy together with Vestas Wind Systems as part of a collaborative research intended to create the design basis for the next generation of wind turbines. As such it is an ideal, publically available reference for MARE-WINT to work on the optimisation of large offshore wind installations; and indeed many of the inputs within this chapter use this shared reference.

## 2.2 General Background for WT Blades

Access to affordable, reliable, sustainable and modern energy is one of the 2030 targets for the United Nations (UN 2016). This requires a substantial increase in the share of renewable energy within the global energy mix, and wind is a prominent part of the solution if the world is to achieve such a target. The potential for offshore wind energy is enormous with industry projections in Europe showing an increase from 5 GW in 2012 to 150 GW in 2030 (European Wind Energy Association, Fig. 2.2 (EWEA 2016)). By moving to offshore sites the Industry can establish larger wind farms with turbines of a size that would not be easily accepted onshore where land use is at a premium. In addition to this, the quality of the wind resource is greatly improved away from the effect of land contours, forests, and so on.

However, moving such a large portion of the industrial production capacity offshore is a major challenge. The environment offshore can be extreme and requires a more robust and durable design for all components, access is expensive for establishing and maintaining production offshore, and support structure designs for deep water sites are yet to be proven commercially. At the European Wind Energy Association conference in 2014, the delegates were warned that without a reduction in energy costs corresponding to at least 40 %, offshore wind could not persist in the current energy market beyond 2020 (EWEA 2014). While costs for onshore wind are already competitive, targeting a reduction in the cost of energy offshore was vital if the ambitious political and industrial targets are to be achieved. It was further observed that initial offshore developments were based on technology from the offshore oil and gas supply chain which is driven by a need to maximise production, rather than by cost reduction. The solution agreed was for a more focussed investment in research and development that produces innovations in logistics, transport and operation.

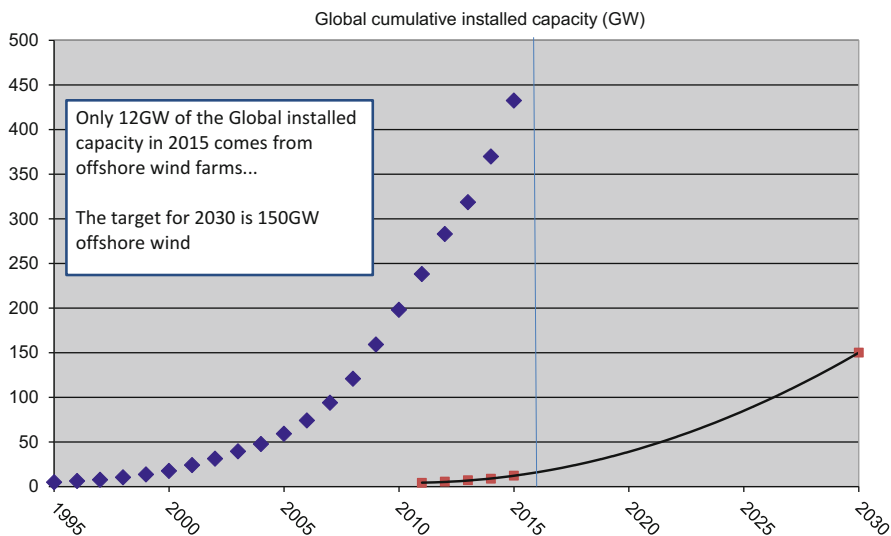


**Fig. 2.2** Growth in Wind Energy capacity from 1995 to 2015 (data available on [www.gwec.net](http://www.gwec.net))

**Table 2.1** Comparison example between commercial turbines developed by Vestas in 2000 and 2015

Year	Manufacturer (rotor diameter)	Effect	Tip height
2000	Vestas Wind Systems V52	2.5 MW	70 m
2014	Vestas Wind Systems V164	8.0 MW	222 m

One of the most eye-catching developments in the wind energy industry over the last 15 years has been the increase in the size of the turbines being manufactured with new turbine designs consistently providing larger turbines with higher power ratings, as shown in Table 2.1.

As the rotors become larger, the industry has relied on improvements in blade structural design, manufacturing processes and material properties in order to meet the requirements for ever longer blades that remain light-weight, strong and stiff. It can be argued that the blades present the most challenging materials, design and engineering problems being a complex, anisotropic material in an aerodynamic structure that is subjected to continuous dynamic loadings of a combined and non-uniform nature over long periods of time. These operational requirements and conditions lead to materials that must exhibit a high stiffness, a low density, and long fatigue life.

Material performance criteria therefore identify fibre reinforced polymer composites as the prime candidate for rotor blades. Here the stiff fibres (usually glass, sometimes carbon) are aligned in the primary load directions within a cured matrix of resin (usually thermosetting polyester or epoxy). The processing technology for such material (whether pre-preg, resin infusion, or wet layup) involves considering the material properties, design approach and manufacturing process as an integrated

issue as already at this stage the characteristics of the material (and hence the behaviour of the final structure) are determined. For example, in longer rotor blades the reinforcing (stiffening) fibres must be aligned along the length of the blade, but with sufficient understanding of the out-of-plane properties and weak laminate interfaces and bond lines so as not to generate problems with durability when the complex combined loads are encountered.

Blade design combines a relatively thin shelled aerodynamic profile supported by a longitudinal beam or webs which carry the bulk of the structural load. The blades are heavier at the root section and taper towards the tip to match the load distribution in a cantilever beam structure and maintain the allowed material strain levels. Industry demands have spurred improvements in design with an optimised aerodynamic profile, relative reduction in weight for longer blades and integrated bend-twist coupling into the structural response.

For much more on material and structure requirements for wind turbine blades see Brøndsted and Nijssen (2013).

The design philosophy for rotor blades (as with all fibre reinforced polymer structures) began with large safety factors and addressing simple issues of linear elastic behaviour. With time, as knowledge about the materials, structural behaviour and manufacturing approaches increased (coupled with the pressure to make more daring multi-MW designs) it became possible to adopt more advanced structural design approaches. The development in light weight structure design is nicely illustrated in a general way by Braga et al. (2014) and here we see that an implementation of “smart” structure technology is the anticipated innovation to supersede the current state of the art not only for offshore wind turbine blades, but also in other industries where polymer composites are utilised.

Recent trends in the wind energy industry can be summarized as follows:

- A rapid increase in the level of installed capacity world-wide
- An increase in the physical size (dimensions) of the structures
- An increase in the size (number of multi-MW turbines) of individual wind farms
- A tendency to place these wind farms offshore
- Higher industry requirements for reliability, safety and easy maintenance
- A strong focus on a reduction in the cost per “unit” of energy produced
- New materials, designs, and production methods continuously adopted

### 2.3 Innovative Blade Concept

As the most effective way to increase the power produced per turbine is to make each turbine bigger, we now have an industry that manufactures extremely large rotor blades using low-cost fibre composite material and low-cost manufacturing methods. A consequence of the components in a wind turbine blade being so large (in some companies almost the entire structure is manufactured in one piece via resin infusion of dry laminate layers), is that there is little scope for improving the

performance of a finished blade by rejecting parts that do not meet very high quality standards. This is because the low-cost manufacturing approach demanded by the industry makes manufacturing a “perfect” blade challenging, and parts thus rejected would be too costly to simply discard.

Instead the situation is that each blade has a unique set of “variations” (we might call then defects) from the intended “perfect” design; these are then more or less mitigated with repair technology before leaving the factory. And in operation the specific load profile will also vary for each turbine. Without detailed information about the distribution of structural/material defects and repairs present, combined with detailed loading and response history for each blade, it will be impossible to make accurate predictions about the lifetime performance of these blades individually; only a generalised probability analysis is possible. And prescribing regular manual inspection is neither an economical nor technically efficient solution to control the health of the structures as for large offshore farms this would be both costly and difficult.

Having an isolated understanding of the individual stages in the wind turbine blade operational life, such as manufacturing, operational, emergency situations, repairing, etc., is therefore not enough to achieve a smart wind turbine blade concept. Rather knowledge of how each stage interconnects with the processor and successor, and the impact of a change in any of the properties to the individual wind turbine blades operational life is required. The traditional Mono-Stage design and methodology, as shown in Fig. 2.3, is no longer applicable to match this requirement; especially as blades become larger, more complex and expensive to manufacture, more information feedback is required to maximise their lifetime and improve processes.

Thus, methods to measure and evaluate structural integrity and operational parameters through all the wind turbine blade life stages need to be implemented from the design stage (McGugan et al. 2015).

The smart blade design and methodology is shown in Fig. 2.4. The presence of sensors integrated in the structure since manufacture will provide feedback at each stage of the structure life time. For example, if during an extreme load a change in

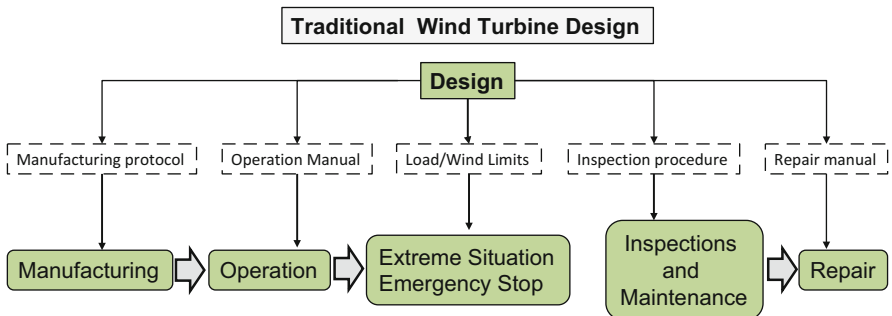


Fig. 2.3 Life stages of a wind turbine blade: traditional design methodology



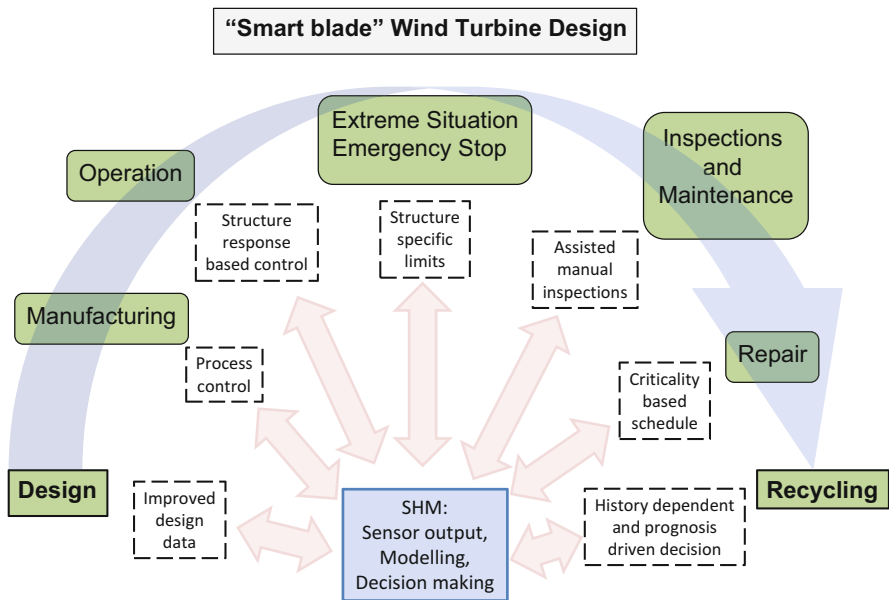


Fig. 2.4 Life stages of a wind turbine blade: “smart-blade” design methodology

the material stiffness is detected, caused by delamination or a crack in the adhesive joint, the wind turbine operation limit can be decreased based on this information. This will enable the structure to operate safely until the next repair action, continue to generate energy, and minimise monetary losses.

Structural Health Monitoring is a well-known engineering area concerned with assessing the current state of a specific asset in order to ensure proper performance. It has the perspective to function both as an automated (and remote) maintenance and inspection process, as well as a “smart” structure feedback allowing activation and response based on condition and environment.

The novel approach proposed is thus that blades are allowed to contain defects and develop stable damage under operation as under the current “passive” damage tolerant design philosophy. But the implementation of structural feedback from the embedded sensors and active response is combined with improved damage tolerant materials and design methods in order to expand the current design philosophy and include SHM and applied fracture mechanics from the initial concept. This allows a design that ensures any defects present cannot develop into unstable damage that leads to blade failure. Furthermore, a full life-time perspective is given that enables a holistic optimisation of the structural resources.

## 2.4 Operational Concept

Many industrial sectors share similar ambitions regarding polymer composite structural materials, structural diagnosis, and development of prognostic approaches. However each one differs in how they intend to exploit the new technology and apply the new developments. The different expectations and priorities across the sectors will influence the entire design, processing, and maintenance line. For example, the aerospace sector can be characterised by polymer composite structures that are high cost material and high value structures, whereas the wind energy sector considers the rotor blades as low cost material and high value structure.

In practice this means that a common “toolkit” of deliverables and work areas exist for defining a physics-based polymer composite structural component life analysis that can be investigated by researchers and industry across different sectors. However from this “open-source” framework, sector specific implementations will then be developed.

The upper part of Fig. 2.5 shows the concept of a blade structure operational lifetime being “consumed” during its’ use in a more or less controlled and progressive manner throughout the planned service life. The usage depends on a loading input which is monitored and understood and in some cases controlled (active management) to a greater or lesser extent.

This control could be in the form of a simple measurement of wind speeds and a calculation of the resulting aerodynamic loads on the structure which provide a “cut off” wind speed above which the turbine should not be permitted run (in part to avoid overload situations). Progressively more advanced turbine control systems can include passive bend-twist blade designs, an active control of pitch and leading/trailing edge settings combined with turbine specific in-flow measurements

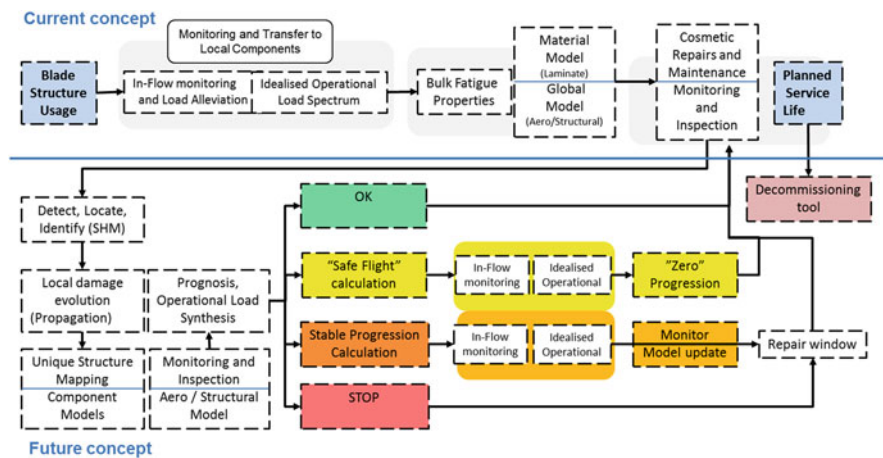


Fig. 2.5 Health Management Concept for future Innovative Rotor Blades

to allow for load alleviation from tower shadow effects, shear loads, turbulence, and so on. The degree of structure control available will define the quality of the load spectra applied and specify the risk of stochastic peak loads that can progress (or initiate) damage. The greater the degree of control, the more availability a damaged structure can exhibit. The availability of a distributed in-situ load monitoring capability will enhance aerodynamic load control options.

Moreover, combining Structural Health Monitoring with other inspection technology will detect and characterise localised damage for each structure, generating a “damage map” for each wind turbine blade with local and global damage models communicating to define critical (and sub-critical) failure criteria. A prognosis tool based on the local forecast of operation can propose the suitable structural sustainment action:

- an unaltered operation (exploiting the passive/designed damage tolerance capability of the material/structure)
- a modification of the structure control settings to limit load conditions that risk progressing damage (a “safe flight” operation)
- an operation of the structure that will allow a progression of damage but in a stable regime allowing repair to be scheduled for the next available maintenance period
- or an immediate stop pending critical repair

In all cases the target for the individual structures is to meet the planned service life whereupon “problem” structures can be decommissioned and the remainder assessed for the feasibility of an extended operational lifetime. The updated database of structural integrity information generated by this process improves the decision making regarding which structures can be safely licensed for continued operation and those that need to go to refit, resale, or recycling.

## **2.5 Research and Development Work Supporting the Concept**

The work carried out by the MARE-WINT researchers associated with Work Package 1 supports the implementation of this new operating concept for wind turbine blades across a broad area of material and structural advances. Each area of research and development is a valuable and acknowledged area of technology in and of itself and includes failure and damage mechanics, new sensing techniques, load spectra monitoring, characterisation of structural damages, data acquisition and analysis, handling environmental effects and other sources of uncertainties, residual properties prognosis, and the assessment of various maintenance and damage mitigation actions. The challenge for the adoption of innovative blade concepts is to combine the many fields into a multi-disciplinary technology within the minds of the next generation of designers and engineers.

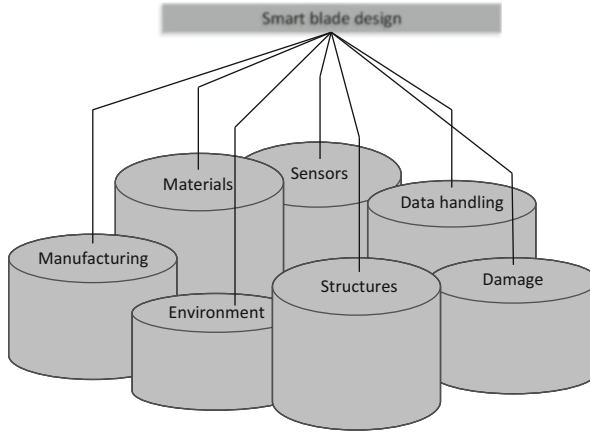


**Fig. 2.6** Independent technology platforms supporting a “Smart” blade design concept

This idea of a set of independent technology platforms that can be combined to support a specific “smart” design concept is illustrated in Fig. 2.6. Note that the names of the technology platforms are illustrative only and far from exhaustive.

In Chap. 3 the topic of damage in composite materials and structural failures in the blades is discussed. In conjunction with the deepening understanding of the causes and effects of these, technology developments are also underway to provide remote sensing solutions and release the pressure on manual inspection procedure. Monitoring this degradation of structural material via manual Non-Destructive Inspection (NDI) during the service lifetime is an expensive, hazardous, and inefficient proposal for offshore wind farms. Therefore, integrating various robust and inexpensive remote sensing technologies and developing them to detect the most common and/or most critical of in-service failures is a clear target for research groups. The demands for improved material performance to achieve the structural designs for extremely long multi-Megawatt blades has propelled research in composite material fabrication, minimising imperfections and improving understanding of the behaviour especially in damaged condition. Crack propagation sensing techniques using embedded fibre optics are described in Chap. 4 and these offer a tool for optimising structural bondlines, and the remote monitoring of known damages (active damage tolerance).

In Chap. 5 the potential for blade design tailored to twist upon deflection and thus enjoy a passive load reduction capacity is explored; and the analysis and design of such blades that can safely exploit this effect at regions along their length whilst maintaining required structural stiffness is proposed. In Chap. 6 the development of flow control devices is described as designers seek to optimise performance for the rotor and researchers deepen the understanding of complex flow control cases. And in Chap. 7 the modelling of active flaps on the leading and trailing edges of the blades is described suggesting that a localised effect on the load distribution can

be effected in-service, possibly eliminating adverse effects caused by tower shadow without generating any additional pitching moment.

Each area of research contains innovative aspects involving new approaches that improve on existing blade design procedures in a sustaining manner. Improving the sensor implementation via more robust and price competitive systems, better analysis tools, a deeper understanding of material and structural behaviour and degradation processes, ameliorating flow control devices, and providing assessment of designs for passive and active load alleviation.

These are all advances that are welcomed by an industry working to reduce Cost of Energy for offshore wind farms in the short term. However the greatest advance possible comes from a disruptive implementation of the new technology in a fully realised concept for structural sustainment. This essentially establishes a new relationship between the owner and their assets. This concept involves using permanent on-board health monitoring systems within a holistic management/control approach. It is a complex and multi-disciplinary field that has not been (and in fact cannot be) addressed by advancements in research alone.

Its realisation faces numerous training and research challenges; the main training challenge is the lack of young research scientists and engineers possessing the skills, research experience, and multi-disciplinary background required for undertaking the demanding research tasks of integrating, supporting and maintaining the innovative holistic structural health management systems and to propel their application in wind energy and other industries. The main research challenge is to focus and coordinate research in the previously mentioned fields to address technical voids which hinder the integration of the envisioned holistic approach. Training networks like MARE-WINT are successful in overcoming such challenges.

**Open Access** This chapter is distributed under the terms of the Creative Commons Attribution-NonCommercial 4.0 International License (<http://creativecommons.org/licenses/by-nc/4.0/>), which permits any noncommercial use, duplication, adaptation, distribution and reproduction in any medium or format, as long as you give appropriate credit to the original author(s) and the source, provide a link to the Creative Commons license and indicate if changes were made.

The images or other third party material in this chapter are included in the work's Creative Commons license, unless indicated otherwise in the credit line; if such material is not included in the work's Creative Commons license and the respective action is not permitted by statutory regulation, users will need to obtain permission from the license holder to duplicate, adapt or reproduce the material.

## References

- Bak C, Zahle F, Bitsche R et al (2013) The DTU 10-MW Reference Wind Turbine. In: DTU Orbit – The Research Information System. Available via Technical University of Denmark. [http://orbit.dtu.dk/files/55645274/The\\_DTU\\_10MW\\_Reference\\_Turbine\\_Christian\\_Bak.pdf](http://orbit.dtu.dk/files/55645274/The_DTU_10MW_Reference_Turbine_Christian_Bak.pdf). Accessed 06 Apr 2016
- Braga DFO, Tavares SMO, da Silva LFM et al (2014) Advanced design for lightweight structures: review and prospects. *Prog Aerosp Sci* 69:29–39. doi:[10.1016/j.paerosci.2014.03.003](https://doi.org/10.1016/j.paerosci.2014.03.003)

- Brøndsted P, Nijssen R (eds) (2013) *Advances in wind turbine blade design and materials*, 1st edn. Woodhead Publishing, Cambridge
- EWEA (2014) EWEA 2014, Recharge news, Day 3. Available via <http://www.ewea.org/annual2014/wp-content/uploads/RechargeDaily03.pdf>. Accessed 06 Apr 2016
- EWEA (2016) European Wind Energy Association. <http://www.ewea.org/>. Accessed 06 Apr 2016
- McGugan M, Pereira GF, Sørensen BF, Toftegaard HL, Branner K (2015) Damage tolerance and structural monitoring for wind turbine blades. *Phil Trans R Soc A*. doi:10.1098/rsta.2014.0077
- UN (2016) United Nations Department of Economic and Social Affairs. <https://sustainabledevelopment.un.org/topics/energy>. Accessed 06 Apr 2016

# Chapter 3

## Damage Sensing in Blades

**Borja Hernandez Crespo**

**Abstract** This chapter is divided into three parts; the problem, possible solutions and the chosen option to address the problem, which is my PhD topic within the project MAREWINT. So firstly, the chapter presents an overview of the typical damages that a wind turbine blade can suffer during its life operation. Then, a review of different Structural Health Monitoring (SHM) techniques which are currently being investigated for wind turbine blades is presented. Finally, the chapter provides the state-of-the-art of Guided Wave Technology in composite materials; where different aspects of this SHM technique are explained in more detail.

### 3.1 Introduction

Wind energy is an important renewable energy source which has gained high relevance during the last decades. Different countries have released plans to invest in wind energy in the future years; such as the USA that will generate 20% of the country's electricity from wind power by 2030 or Denmark that have set the targets of producing 50% of the power from the wind by 2020 and also of making Denmark completely free of dependence on fossil fuels by 2050. So, the use of wind power is not expected to decrease within the next decade (Márquez et al. 2012). The trend is to manufacture bigger wind turbines and deploy them offshore. These new wind turbines have around 6 MW power output, 120-metre height tower and 80-metre long blades. They are designed to be operating in rough conditions in difficult-to-reach areas. Therefore, the deployment of Structural Health Monitoring (SHM) techniques becomes essential in order to assess remotely the integrity of the structure. The advantages of using these techniques are many (Schulz and Sundaresan 2006), such as reducing expensive costs for periodic inspections of turbines which are hard to reach, prevention of unnecessary replacement of components based on time of use, or minimizing down time and frequency of sudden breakdowns.

---

B. Hernandez Crespo (✉)  
TWI Limited, Granta Park, Great Abington, Cambridge CB21 6AL, UK,  
e-mail: [borja.hernandez@twi.co.uk](mailto:borja.hernandez@twi.co.uk)

## 3.2 Structural Damages in Wind Turbine Blades

Wind turbine blades are composed by composite materials, mainly glass fibre, carbon fibre, balsa wood or foam, in order to improve efficiency by increasing the strength-weight ratio. The structure can be represented as a rectangular beam formed by the upper and lower spar caps and by two vertical shear webs, providing bending stiffness and torsional rigidity in order to withstand all the loads applied on the blade. The aerodynamic shape is given by two shells joint to the spars at both sides. Highly-toughness adhesive is used to bond both shells to each other at the leading and trailing edges, and also to join the shear webs to the spar caps. The outside of the blade is covered by a gel coat to be protected from ultraviolet degradation and water penetration. Typically in offshore wind turbine blades, the spar caps are formed by a thick laminate of glass fibre or glass/carbon hybrids, while the shells and the shear webs are sandwich panels composed by glass fibre skins and a thick foam or balsa wood core.

All those structures are susceptible to be damaged since they are continuously in operation under cycle loads in harsh environments. Structural damages, such as debonding or delamination, can be potentially generated in a number of ways.

- Leading Edge Erosion: It is a damage produced by abrasive airborne particles which impact and erode the leading edge, especially affects the region close to the tip where the velocity is higher. This erosion modifies the aerodynamic shape of the blade reducing the aerodynamic efficiency and hence, the power production. It also creates delaminations along the leading edge (Sareen et al. 2014).
- Lightning: The blades are the most vulnerable parts of the wind turbine to be impacted by a lightning. Currently, all blades have in place a lightning protection system to reduce as much as possible the damages generated by the impact, since otherwise the blade could be destroyed. Although it is common to have damages and cracks around the point of lightning attraction (Cotton et al. 2001).
- Icing: It is the accumulation of ice on the surface of the blade due to the combination of particular climate conditions and low temperature climate (Cattin 2012). Several problems can be caused by icing, such as the complete stop of the wind turbine due to highly severe icing, the disruption of aerodynamics with a reduction in energy generation or the increased fatigue due to imbalance loads caused by the ice mass resulting in a shortening of the structure lifetime (Homola 2005).
- Fatigue loads: Wind turbines are designed to be in continuous operation an average of 20 years. During this time, blades are permanently withstanding cycle loads which could lead in the creation of incipient damages due to fatigue mechanisms and then consequently their propagation till the collapse of the entire structure.

The different types of damages that a wind turbine blade can suffer during operation are reviewed in (Debel 2004) as follows. In Fig. 3.1, they are represented for further clarifications.



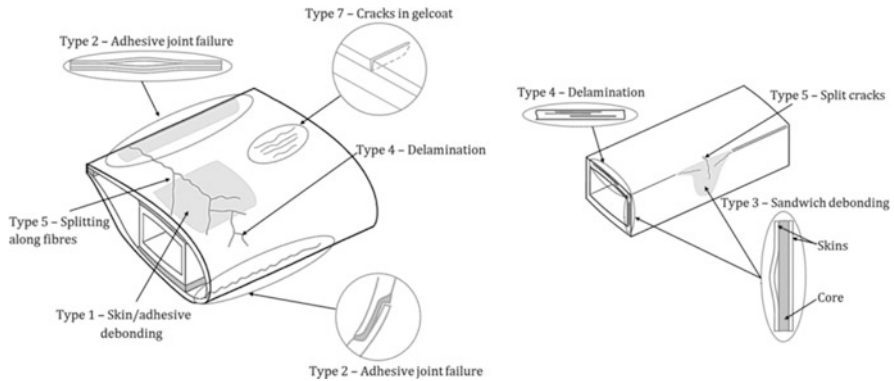


**Fig. 3.1** Sketch of the different types of damage that can occur in a wind turbine blade (Sørensen et al. 2004)

- Type 1: Damage formation and growth in the adhesive layer joining skin and main spar flanges (skin/adhesive debonding and/or main spar/adhesive layer debonding)
- Type 2: Damage formation and growth in the adhesive layer joining the up- and downwind skins along leading and/or trailing edges (adhesive joint failure between skins)
- Type 3: Damage formation and growth at the interface between face and core in sandwich panels in skins and main spar web (sandwich panel face/core debonding)
- Type 4: Internal damage formation and growth in laminates in skin and/or main spar flanges, under a tensile or compression load (delamination driven by a tensional or a buckling load)
- Type 5: Splitting and fracture of separate fibres in laminates of the skin and main spar (fibre failure in tension; laminate failure in compression)
- Type 6: Buckling of the skin due to damage formation and growth in the bond between skin and main spar under compressive load (skin/adhesive debonding induced by buckling, a specific type 1 case)
- Type 7: Formation and growth of cracks in the gel-coat; debonding of the gel-coat from the skin (gel-coat cracking and gel-coat/skin debonding).

Ciang et al. (2008) also presented the most likely locations of the blade where damages can appear, which are at 30–35% and 70% of the blade length from the root, the root of the blade, the maximum chord area, and the upper spar cap/flange of the spar.

### 3.3 SHM on Wind Turbine Blades

The value of the blades is around the 15–20% of the total costs of the wind turbine (Li et al. 2015a, b), thus the blades are critical parts that need to be monitored in order to ensure the cost-efficiency of the entire structure and its integrity. Currently, the blade assessment is based on costly periodic manned inspections. The techniques used are visual inspections and manual tapping tests, which require highly experienced experts. These techniques are not able to detect internal damages at early stages, so different NDT and SHM techniques have come out to fill this gap. In the following, current SHM techniques applied to wind turbine blades are presented.

#### 3.3.1 Modal Analysis

This technique is based on the analysis of the dynamic response of the wind turbine blade during operation. The modal parameters extracted from the structure, such as frequencies and modal shapes, are directly related to the physical properties of the blade, such as mass and stiffness. Therefore, the analysis of modal parameters will detect variations in the physical properties, such as stiffness reduction caused by incipient damages or mass increasing caused by icing. In order to apply this technique, it is required to induce an excitation over the structure. Ideally for a SHM application, it would be preferred to use an ambient energy during the normal operation of the wind turbine, such as the blade vibrations caused by the wind turbulence which has been proved that excites a wide range of blade modes (Yang et al. 2014; Requeson et al. 2015). Other excitation sources used in this analysis are external shakers or embedded actuators which usually provide better results since a well-distributed excitation is created over the entire structure and also a flat spectrum is generated in the desired frequency range. To monitor the modal responses accelerometers, piezoelectric transducers and strain gauges are used.

Damage identification method is commonly based on the comparison between an undamaged and a damaged state. Simple analyses using the eigenfrequencies are valid for controlled laboratory tests, but under more realistic conditions these methods are unable to detect damages, since the modal property variations caused by them are the same order as the ones created by the environmental effects and noise contamination (Salawu 1997). Therefore, sophisticated and robust methods, such as continuous wavelet transformation, have to be used along with modal analysis in order to be deployed as a SHM application (Ulriksen et al. 2014).

Figure 3.2 depicts a modal measurement setup. The advantages of Modal Analysis are that it is a mature technology widely used for gearbox and bearing faults, feasible, well-proven and low cost. The disadvantages are small sensitivity (detection of relatively big damages), so there is a necessity to have a fine measurement density (more sensors) and the impossibility to install sensors close

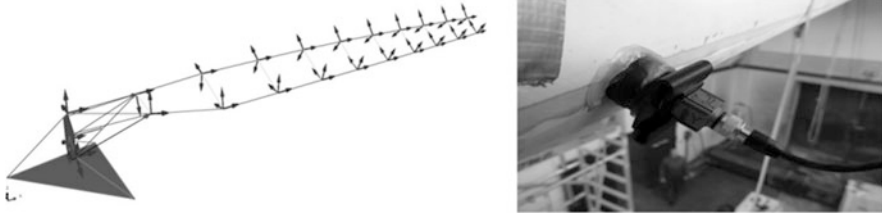


**Fig. 3.2** Modal measurement system setup for SSP 34 m blade: (a) accelerometer location and orientation; and (b) utilized accelerometers (Brüel & Kjær Type 4524-B) mounted on a swivel base (Brüel & Kjær UA-1473) (Ulriksen et al. 2014)

to the tip due to the small section since they should be placed inside the blade for SHM applications.

### 3.3.2 Fibre Optics

Optical fibres are cylindrical dielectric waveguides designed to propagate the light along its length. The core of the fibre has a refractive index slightly higher than the core cladding, so when the light confined in the core reaches the cladding/core interface with an angle greater than the critical angle (Snell's law); the light is reflected back to the core enabling its propagation along the fibre (Ostachowicz and Güemes 2013). The light may leak out when the optical fibre is bent with sharp radius; decreasing the optical power transmitted. This principle is used as a damage detection technique, called microbending fibre, where two solid corrugated parts bend the fibre, so relative displacement between both parts will cause sharper or flatter bends (decreasing or increasing the transmitted optical power) enabling the local monitoring of the structure. Optical fibres can be used to measure different type of properties, such as strain, temperature, loads or vibrations.

In wind energy applications, they have been mainly used as strain sensors. Two different measurement techniques have been utilized to monitor the strain in wind turbine blades, Fibre Bragg Gratings (FBGs) and distributed sensing. FBGs are local sensors with high sensitivity and reliability, allowing the possibility to multiplex several FBG sensors in a single optical fibre. In recent years, most of the investigations about fibre optic applications have been related to FBGs due to the variety of advantages that they offer (Choi et al. 2012; Glavind et al. 2013; Kim et al. 2013, 2014). FBGs are periodic variations in the refractive index of the core of the optical fibre. These refractive index variations are equally spaced a distance,  $\Lambda_0$ , and they behave like multiple mirrors which reflect a very narrow wavelength window,  $\lambda_B$ , of the light spectrum transmitted along the fibre, following this equation, Eq. (3.1):

$$\lambda_B = 2\bar{n}_e\Lambda_0 \quad (3.1)$$

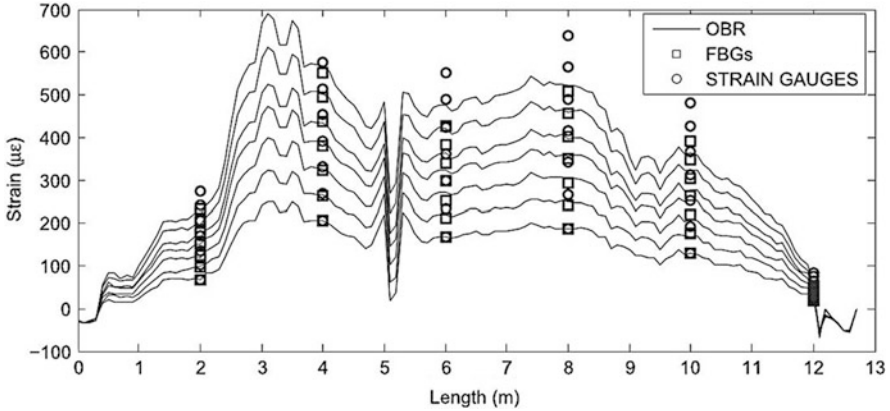


**Fig. 3.3** Example of strain profiles for seven load magnitudes along the blade length gathered with the OBR (distributed sensing), the FBGs and the strain gauges. Sensors located at intrados, trailing edge. Results for a Wind Turbine Blade test in flapwise configuration, pressure side to suction side (PTS) (Sierra-Pérez et al. 2016)

where  $\bar{n}_e$  is the average refractive index. Therefore, when the FBG is attached to a structure and it is strained or affected by changing temperature, the distance between the periodic variations changes, so the reflected wavelength shifts linearly enabling the monitoring of the local strain or temperature. In (Sierra-Pérez et al. 2016), a comparison between strain gauges and FBGs is studied for wind turbine applications, see Fig. 3.3. Both present similar detection capabilities and sensitivities, but FBGs offer comparative advantages, such as electromagnetic immunity, possibility to be embedded into composites or longest life. So, thinking in a future SHM application for wind turbine blades, FBGs would be more suitable than strain gauges. The other measurement method is the distributed sensing, where the entire length of the fibre works as a sensor. Several sensing methods have been used to provide distributed sensing; being the most used the Optical Frequency Domain Reflectometry (OFDR) based on the Rayleigh scatter. This Rayleigh backscattering component is caused by changes in density or composition along the fibre, so by controlling the slope of the decaying intensity curve, it is possible to identify breaks and heterogeneities along the fibre (Sundaresan et al. 2001). This technique can be used to measure the strain and the temperature with high resolution (better than  $1 \mu\epsilon$  and  $0.1^\circ\text{C}$ ) (Sierra-Pérez et al. 2016), and also with a high spatial resolution along the fibre, in the order of millimetres. Strain measurements in wind turbine blades have been performed in recent investigations (Pedrazzani et al. 2012; Niezrecki et al. 2014; Sierra-Pérez et al. 2016) with good results, but this technique is almost limited to static tests because the acquired light power is too low, so several test repetitions are needed to increase the Signal to Noise Ratio (SNR).

The advantages of Fibre Optics are its high sensitivity, small size (may be embedded in composites), low weight, immunity to electromagnetic interferences

and electrical noise, fatigue resistance and wide operation temperature range. The disadvantages are its fragility, highly costly equipment and bulky equipment.

### 3.3.3 Guided Wave Technology

Guided waves (GW) are ultrasonic elastic waves that propagate in finite solid media. The technique is based on the analysis of guided waves which have propagated along the structure. Piezoelectric transducers are attached on the structure and excited by a signal generator with a predefined input signal, usually an  $n$ -cycle sinusoidal pulse with a Hanning window centred at a specific frequency. The transducers convert the electrical input into mechanical strain which enables the generation of the wave into the structure. The waves propagate along the structure passing through/interacting with defects, such as delamination, debonding, cracks or thickness reduction due to corrosion. This interaction makes the wave change during its propagation enabling the identification of damage. The waves can be acquired by the same transducer, in a Pulse-Echo configuration, where the damage is detected by the echoes reflected backwards when the wave passes through the defect; or acquired by another transducer, in a Pitch-Catch configuration where the damage is detected due to changes in amplitude, phase or time of flight (TOF) of the acquired wave modes. The great advantage is that GW technology inspects wide areas from a small number of points, in contrast to the others techniques which are locally, like conventional ultrasonic testing, see Fig. 3.4.

Commercially, GW technology has been successfully applied for inspection of pipelines in the oil & gas industry (Mudge and Harrison 2001). This inspection is able to scan tens of metres from one position and detect wall thickness variations caused by corrosion. In wind turbines where the structure is composed by different materials, such as glass fibre, carbon fibre or balsa; the complexity of the wave propagation increases hindering the application of GW. In recent years, there have

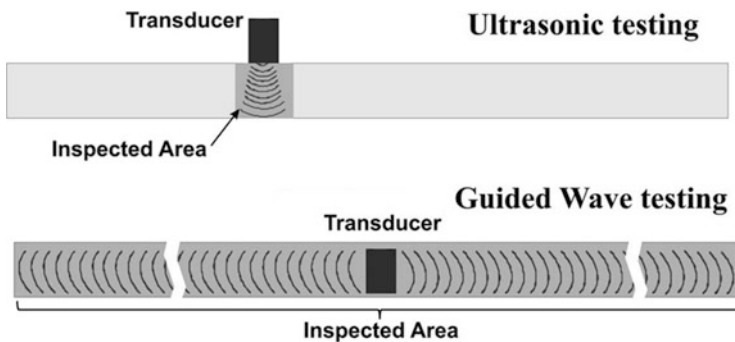


Fig. 3.4 Comparison of the inspected area between ultrasonic testing and GW testing

been many investigations studying the utilization of GW technology on wind turbine blades for damage detection (Claytor et al. 2010; Taylor et al. 2012, 2013a, b; Zak et al. 2012; Song et al. 2013; Li et al. 2015a, b). It has been demonstrated that GW are capable to detect composite damages (Su et al. 2002; Hay et al. 2003; Discalea et al. 2007; Sohn et al. 2011), such as delamination, debonding or fibre cracking; and also to locate the damages analysing the TOF of the wave modes. One issue for GW application in blades is the wave attenuation, since the amplitude of the wave decreases rapidly during its propagation in this type of materials allowing the inspection within a limited area. Investigations about ice detection and ice removal in wind turbine blades have been also carried using GW technology (Habibi et al. 2015; Shoja Chaeikar et al. 2015). The use of GW for composite materials is still in development, but it is seen as a promising technique for the future.

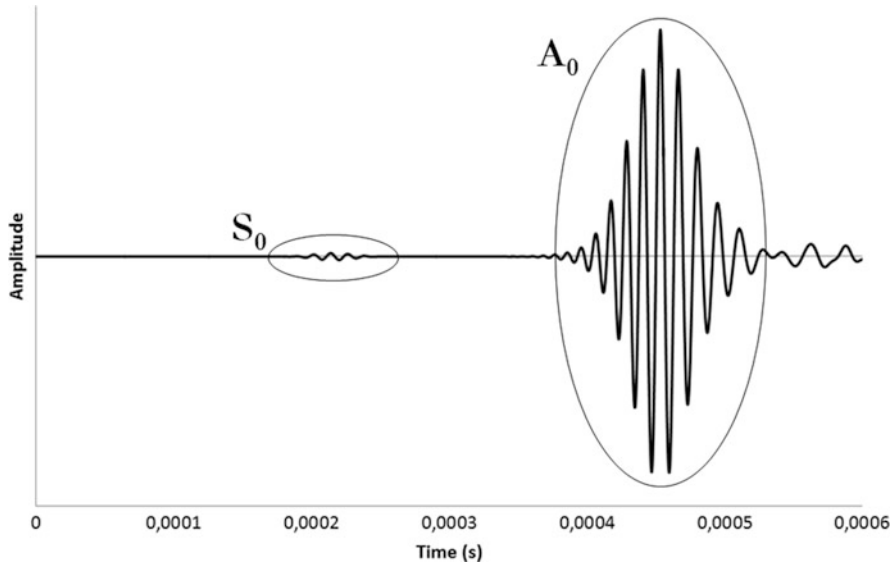
Another important improvement that is needed for the implementation of this technology in wind energy is the reliability. Wind turbine operators are usually reticent to install extra equipment in their turbines after investing a great deal of money. Therefore, more robust and reliable systems (transducers and equipment) are required in order to deploy this technology in wind turbine blades. Investigations in self-diagnosis of transducers during operation have been carried out by Taylor et al. (2013c), where they proposed a technique to analyse the impedance of the transducer in order to distinguish between structural damage and transducer malfunction, avoiding false positives in damage detection.

Figure 3.5 depicts a signal that can be acquired through the application of Guided Wave Technology in an aluminium plate. The advantages of Guided Wave Technology are that it is able to detect external and internal damages at early stages, it is capable to inspect large areas from a few locations, it is cost-effective and the transducers are small. The disadvantages are its improvable reliability and its bulky equipment.

### 3.3.4 *Acoustic Emission*

Acoustic Emission (AE) technique is based on the acquisition of transient elastic waves generated from a rapid release of energy caused by a damage or deformation (Pao et al. 1979). This wave generation can be produced by various phenomena such as cracks, rubbing, deformation, leakage, etc. The most detectable AE signals take place when plastic deformation is caused in the material or when it is loaded near its yield stress (NDT 2016). These phenomena create elastic waves which propagate in the material. The AE sensors, usually made of piezoelectric material, convert the strain caused by the elastic waves into electrical energy enabling the processing and signal analysis.

AE waves are comprised in a broad frequency range between 100 kHz and 1 MHz (Li and He 2012); conversely the waves in a lower frequency range are called vibration. The most common signal processing technique is to extract



**Fig. 3.5** Example of a signal acquired in a “pitch-catch” configuration in an aluminium plate. The two fundamental wave modes are highlighted, symmetric  $S_0$  and antisymmetric  $A_0$  modes

features from the time-domain signal due to its simplicity. However, more advanced signal processing techniques, such as wavelet transform, pattern recognition or classification methods, are needed in order to assess in a better manner the integrity of the structure (Chacon et al. 2015). This technique has been used in rotating machines and metallic structures, such as tanks or bridges with good results (Rauscher 2004; Nair and Cai 2010; Chacon et al. 2014). In wind turbine blades, AE has been applied in different investigations where it has been able to detect typical composite damages such as delamination or debonding (Han et al. 2014; Zhou et al. 2015). However, due to the high frequency content of the AE signals, attenuation is a major obstacle for this technique, especially in composite materials. Consequently, early stage damages where the amplitude signal is low will not be detectable, unless the sensors are placed close to the damage. Other disadvantages are that it is expensive and it generates large datasets due to the high sampling rate. Figure 3.6 shows an example of an acoustic emission signal.

### 3.3.5 Thermography

Thermal imaging technique is based on the measurement of the heat on the surface of the inspected structure in order to detect internal defects by observing temperature differences. The basic idea is that the thermal diffusivity will change if irregularities

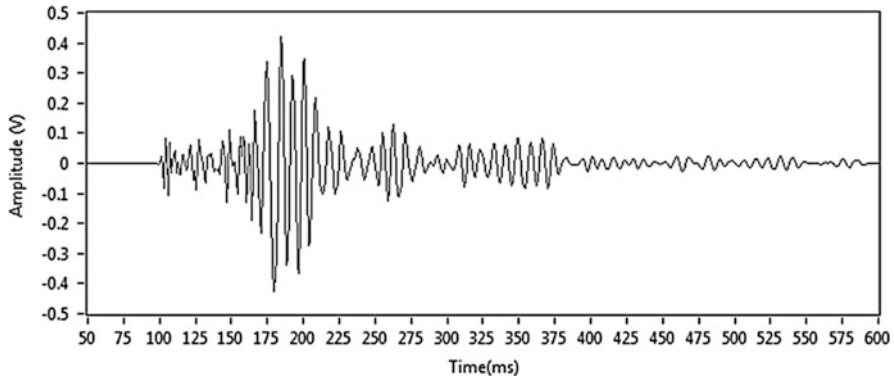


**Fig. 3.6** Example of an AE signal

are present in the material, so temperature differences will be observable externally. There are two approaches to apply this technique, passive and active. The passive method is utilized when the materials to inspect have different temperature in comparison to the ambient temperature. And the active method is when external excitation, such as heat lamps, is used to apply thermal energy into the specimen making more clearly the temperature differences.

Two big concerns with this technique are the limitation of amount of thermal energy applied on the surface of the structure, and the difficulty to apply thermal energy over large surfaces in a uniform manner (Manohar 2012). The former is caused by the application of too much energy to the surface in order to generate sufficient contrast to detect deeper defects which may cause permanent damages. The latter is due to non-uniform heating (unwilling temperature differences) which could cause erroneous results and the reduction of the accuracy of the technique. This limitation makes quite difficult its applicability in wind turbine blades during operation. Further investigations are needed to overcome this problem and gain sensitivity to spatial and temporal variations (Manohar 2012).

The advantages of Thermography are that it is a non-contact technique, no baseline is needed and it has a full-field defect imaging capability enabling a rapid structural evaluation. The disadvantages are that it is very difficult to be applied in-service and the equipment is highly costly.

### 3.4 Guided Wave Technology in Composites

Guided wave (GW) technology is a growing Non Destructive Testing (NDT) technique in order to inspect and monitor the health of structures. The advantages of this technique are the capacity to scan an area of several metres from few locations and to make the inspection to structures in-service. This allows the system



potentially capable to be permanently installed on the structure enabling it to be monitored continuously. Guided Wave technology has been widely applied in metallic structures in order to inspect pipes, plates, rails (Alleyne and Cawley 1992a; Alleyne and Cawley 1992b; Cawley et al. 2003; Hayashi et al. 2003; Rose et al. 2004). During the 1990s, significant research was focused on pipe inspection (Ditri and Rose 1992; Alleyne et al. 1998; Lowe et al. 1998), because there was a need to assess in a rapid manner the integrity of hundreds of kilometres of pipelines in the oil & gas, nuclear and chemical industries. As a result of these investigations, guided wave commercial devices were released to service these industries (Mudge and Harrison 2001) which are able to inspect tens of metres from one position and detect wall thickness variations caused by corrosion.

In addition to metallic structure inspection, composite inspection using guided waves has been investigated in the recent years (Cawley 1994; Monkhouse et al. 1997; Su et al. 2002; Han et al. 2006; Lissenden and Rose 2008; Giurgiutiu and Santoni-Bottai 2011; Castaings et al. 2012; Rose 2012; Torkamani et al. 2014; Baid et al. 2015; Rekatsinas et al. 2015; Zhong et al. 2015). Much interest has arisen in this topic due to the increasing implementation of composite materials in the aerospace and wind energy industries and the necessity to inspect and monitor large composite structures, such as wings or wind turbine blades, in a cost-effective and rapid way. Moreover, composite materials, especially carbon fibre-epoxy due to its high Young's modulus and high strength to low weight ratio, are commonly used as structural parts like the spar in wings and blades. It is essential the inspection of those members to assure the integrity of the entire structure. Composite materials can be easily damaged when impacted, presenting damages such as delamination or matrix cracking which are difficult to detect in a visual based inspection. Currently, conventional ultrasonic inspection is widely used as the preferred NDT technique for composite structures (Kapadia 2012). This technique is able to detect the most common composite damages (delamination, debonding, porosity), but dependence on manual inspection of parts with difficult accessibility and the slowness of the inspection are obstacles, as well as the interruption of the operation of the entire structure means that an automatic inspection is also desirable. Guided wave technology provides an alternative solution for an in-service assessment of the integrity of the structure which can be deployed automatically. Damage detectability in composites using guided waves has been proved in many scientific publications (Hayashi and Kawashima 2002; Su et al. 2002; Hay et al. 2003; Paget et al. 2003; Sohn et al. 2004; Su and Ye 2004; Park et al. 2005; Discalea et al. 2007; Su et al. 2007; Diamanti and Soutis 2010; Gao et al. 2010; Ramadas et al. 2011; Sohn et al. 2011; Yeum et al. 2012; Torkamani et al. 2014). The anisotropic nature of composites due to the different ply-orientations produces a directional dependence of the wave propagation properties in terms of velocity and wave directionality (Rose 2012) which increases the difficulty of the data analysis. Also the complex designs of in-service composite structures, such as wind turbine blades, which are composed of different materials, e.g. carbon fibre, glass fibre, balsa or honeycomb hinder the implementation of this technique commercially, since it is difficult to

extract relevant information from the complex signals. So, many investigations and great progress are being carried out to overcome these issues.

### 3.4.1 Fundamentals of Guided Waves

Guided waves are elastic waves that propagate in solid plates. The main characteristics of this kind of waves are that the phase velocity and group velocity are not necessarily the same and they can vary according to the frequency, which is called dispersion. Depending on the boundary conditions of the medium where the wave is propagating through, different guided wave modes can be obtained (Rose 2014). In the case of thin plate-like structure (Fig. 3.7) with free upper and lower surfaces, Lamb waves will propagate within both surfaces, established as boundaries, guiding the propagation of the waves. The governing equation of guided wave motion is Navier's equation, Eq. (3.2) (Rose 2014):

$$\mu \cdot \frac{\partial^2 u_i}{\partial x_j^2} + (\lambda + \mu) \cdot \frac{\partial^2 u_j}{\partial x_j \partial x_i} + \rho \cdot f_i = \rho \cdot \frac{\partial^2 u_i}{\partial t^2} \quad (i, j = 1, 2, 3) \quad (3.2)$$

where  $u_i$  is the displacement in the  $x_i$  direction,  $f_i$  is the body force which is assumed to be zero,  $\rho$  is the density and  $\lambda$  and  $\mu$  are the Lamé constants. By using the method of potentials, this second order partial differential equation can be decomposed into two uncoupled parts through Helmholtz decomposition, details in (Rose 2014).

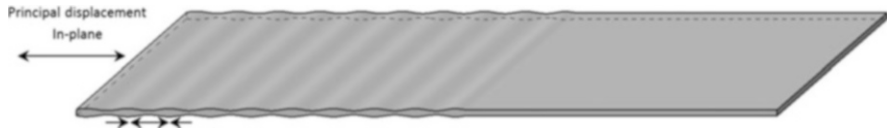
Finally, Eq's. (3.3a) and (3.3b) are obtained that, together with the displacement equations, it is possible to calculate the motion of the guided waves in an isotropic and homogeneous plate-like structure (Rose 2014):

$$\frac{\tan(qh)}{\tan(ph)} = -\frac{4k^2qp}{(k^2 - q^2)^2} \quad \text{for symmetric modes} \quad (3.3a)$$

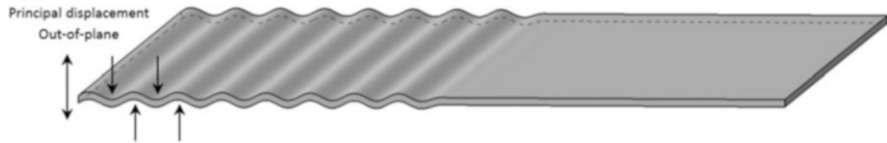
$$\frac{\tan(qh)}{\tan(ph)} = -\frac{(k^2 - q^2)^2}{4k^2qp} \quad \text{for antisymmetric modes} \quad (3.3b)$$



Fig. 3.7 Coordinates for thin plate-like structure



**Fig. 3.8** Symmetric mode of propagation



**Fig. 3.9** Antisymmetric mode of propagation



**Fig. 3.10** Shear mode of propagation

As it is shown in Eq's. (3.3a) and (3.3b), the solution of guided wave propagation presents a symmetric ( $S_i$ ) and an antisymmetric ( $A_i$ ) solution, consequently there will exist in the same plate two different modes of propagation one symmetric and one antisymmetric with respect to the middle plane along the thickness. Both wave motions are represented in Figs. 3.8 and 3.9 respectively.

Another wave motion related to guided waves is the shear horizontal (SH) wave mode where the particles displace transversally to the propagation direction, see Fig. 3.10. This mode presents advantages in comparison to  $S_i$  and  $A_i$  in terms of dispersion and attenuation, since the fundamental shear mode is non-dispersive so has less energy attenuation during its propagation (Rose 2014). Because of the non-dispersive nature of shear mode, the wave energy in the direction of propagation does not spread during its propagation, so the energy remains concentrated in the transmitting pulse enabling the wave to achieve longer distances. Also, the in-plane particle displacement of SH wave mode reduces the interaction with the surrounding media (Petcher et al. 2014). So, the wave energy transmitted remains inside the host material minimizing the energy leakage. These advantages are particularly important when a structure which is subsea, buried or with heavy coatings has to be inspected, or when longer distances are needed to reach in order to inspect areas where the accessibility is limited or prohibitive.

Regarding the attenuation, it may be divided in absorption, scattering and leakage (Wilcox et al. 2001). The first attenuation mechanism is due to the material damping of the host material which converts the wave energy into heat. The second one is produced when part of the wave energy is transmitted or reflected in other directions

than the original one. This scattering is mainly produced by defects or irregularities in the way of the wave which reflect part of the wave energy in other directions. This mechanism enables the identification of damages by guided wave technology inspection. And the third one is produced by the energy leakage which is the wave energy transmitted to the surrounding media. This energy transmission depends on the acoustic impedance compatibility between the surrounding material and the host material, the smaller the acoustic impedance mismatch the larger the energy is transmitted to the surrounding media. This energy leakage is commonly negligible for air, but it becomes more influential when coatings, paints or high damping materials are applied on the surface, or even more when the structure is subsea or buried, where the energy loss is highly significant (Wilcox et al. 2001).

### 3.4.1.1 Phase Velocity and Group Velocity

Generally, the velocity of guided waves can be described by the phase velocity and the group velocity. These two velocities measure different features of the wave, where phase velocity is the velocity related to the frequency,  $f$ , and wavelength,  $\lambda$ ,  $v_p = \lambda \cdot f$ , which is the speed at which any fixed phase of the cycle is displaced. And group velocity is defined as the speed with which the information or energy of the wave propagates through the media. In other words, the speed at which the whole wave packet propagates.

The propagation velocity of the guided waves, in most of the cases, is frequency-dependent. It is different at different frequencies, so consequently frequency components of the same wave packet will travel at different velocities distorting the original input signal along its propagation. This phenomenon is called dispersion, which will be explained further on. A graphic example is shown in Fig. 3.11.

A consequence of this dispersion is that phase velocity is different to group velocity. In terms of angular frequency,  $\omega = 2\pi f$ , and wavenumber,  $k = 2\pi/\lambda$ , phase velocity and group velocity can be expressed as Eq's. (3.4a) and (3.4b):

$$v_p = \frac{\omega}{k} \quad (3.4a)$$

$$v_g = \frac{d\omega}{dk} \quad (3.4b)$$

### 3.4.1.2 Dispersion Curves

The relationship between velocity and frequency can be plotted in graphs called "dispersion curves", where the variation of different wave mode velocities is shown along the frequency. In Fig. 3.12, dispersion curves of phase velocity and group velocity are represented against the frequency for symmetric and antisymmetric modes of a 3-mm thick aluminium plate.

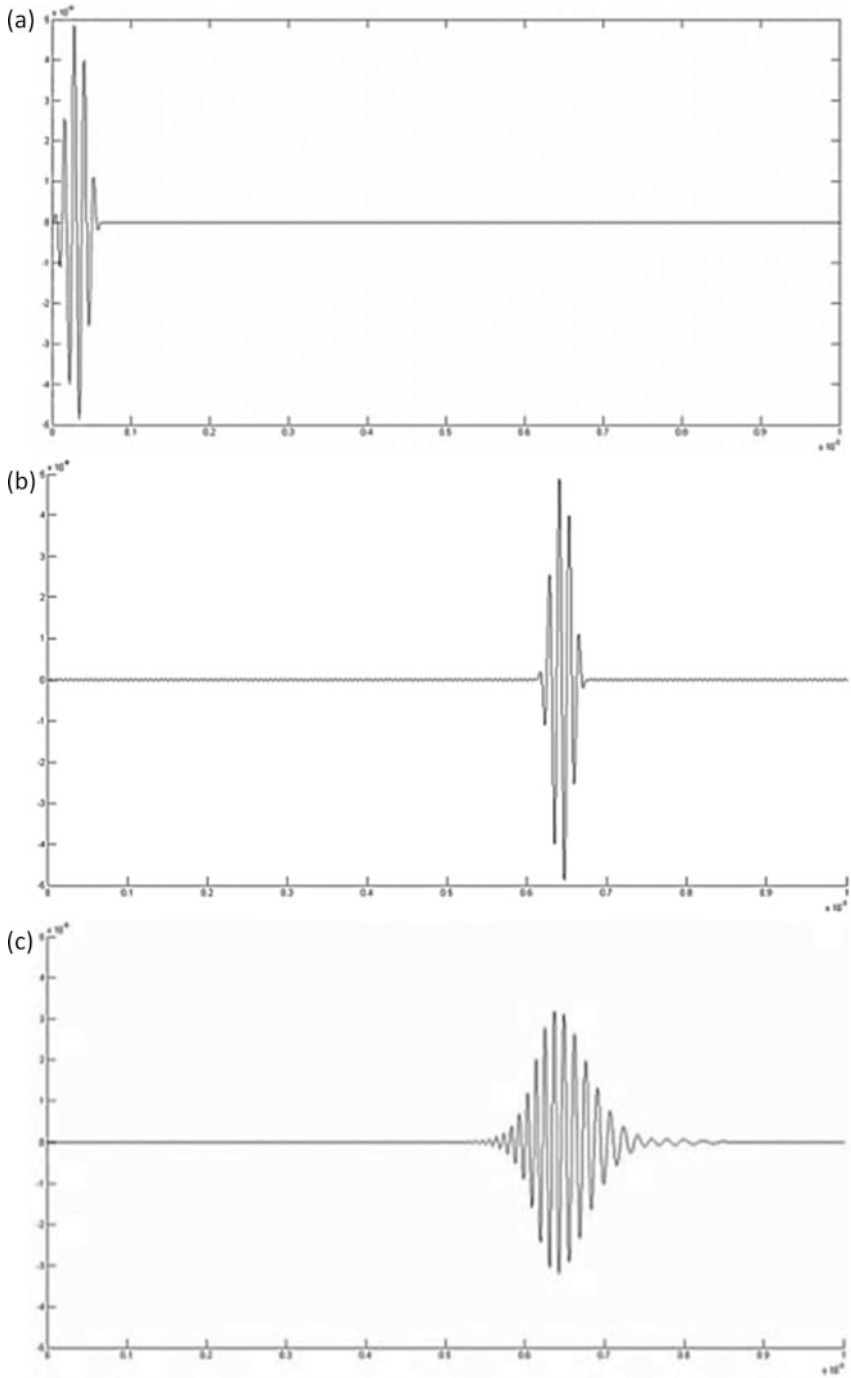


**Fig. 3.11** Example of dispersion. (a) Input signal. (b) Non-dispersive wave. (c) Dispersive wave

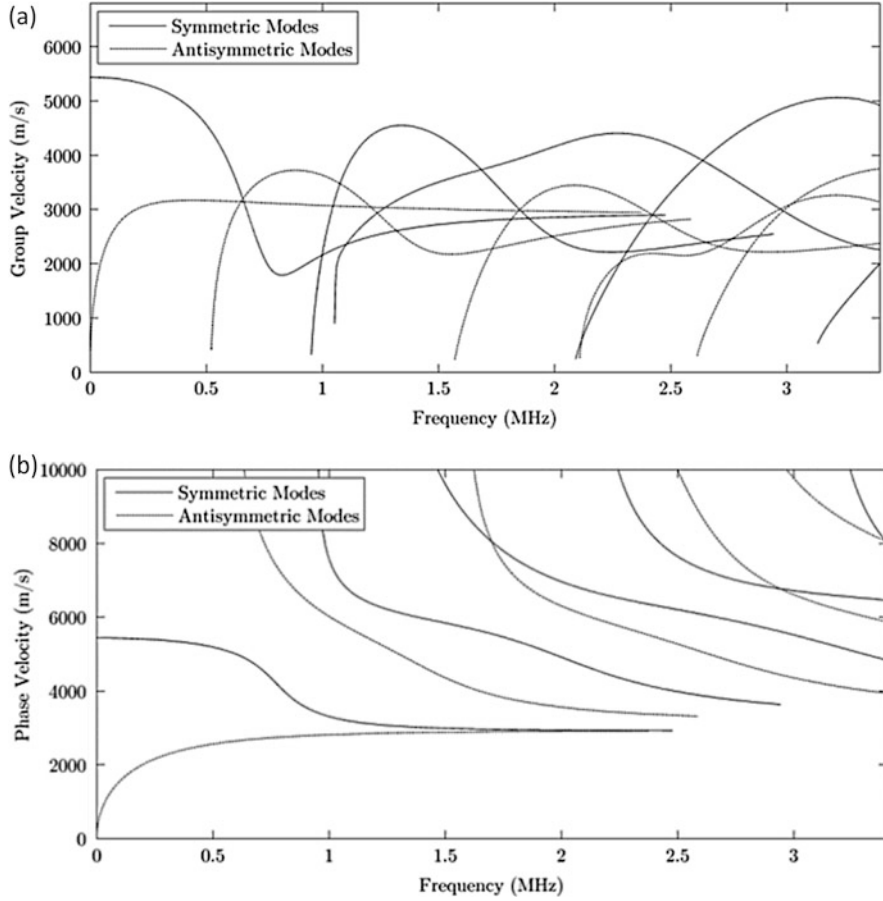


**Fig. 3.12** Dispersion Curves of a 3-mm thick aluminium plate. (a) Phase velocity against frequency. (b) Group velocity against frequency. Extracted from Disperse Software (Pavlakovic et al. 1997)

The dispersion equations of Lamb waves for plate-like isotropic structures are (Rose 2014):

$$\frac{\tan(qh)}{q} + \frac{4k^2p \tan(ph)}{(k^2 - q^2)^2} = 0 \quad \text{for symmetric modes} \quad (3.5a)$$

$$q \tan(qh) + \frac{(k^2 - q^2)^2 \tan(ph)}{4k^2p} = 0 \quad \text{for antisymmetric modes} \quad (3.5b)$$

$$p^2 = \frac{\omega^2}{c_L^2} - k^2, \quad q^2 = \frac{\omega^2}{c_T^2} - k^2 \quad \text{and} \quad k = \frac{2\pi}{\lambda_{\text{wave}}} \quad (3.5c)$$

where  $h$  is the plate half thickness,  $k$  is the wavenumber,  $c_L$  is the longitudinal velocity,  $c_T$  is the transverse velocity,  $\omega$  is the wave angular frequency and  $\lambda_{\text{wave}}$  is the wavelength. At each frequency, the wavenumber is modified in order to find the roots of the Eq's. (3.5a) and (3.5b) (Su and Ye 2009). The dispersion curves can be plotted by joining the roots of the different wave modes. These curves are highly important to guided wave damage detection in order to predict the time of arrival, to excite desired modes, to design phased arrays and generally to deploy any guided wave application.

Due to the utilization of finite number of cycles in a pulse to interrogate the structure in guided wave inspection, this technique is especially affected by dispersion. This is because short pulses contain broadband frequency ranges centred at the transmitting frequency, so more different frequency components are involved in the travelling wave packet distorting the acquired signal to a higher extent, instead of using a narrowband input signal. Consequently, when guided waves propagate long distances, very distorted and attenuated signals are acquired for dispersive wave modes. Many of the investigations related to dispersion compensation are based on time reversal, in which the excitation signal is modified in order to concentrate the wave packet energy at a certain distance. Wilcox (2003) also proposed dispersion compensation based on a signal processing methodology, in which the dispersion effect is removed by replacing the time domain signal into a distance domain signal. Very accurate data of the dispersion curves of the studied wave modes is required, as the proposed methodology is very sensitive to small variations.

### 3.4.2 Guided Waves in Composites

Composites are characterised by their multi-layered structure, in contrast to metallic materials which are a continuous media with no interfaces. Composites are commonly used in aerospace or wind energy industry, such as carbon fibre/epoxy or glass fibre/epoxy laminates, and constituted by a number of layers orientated at different directions. These layers are formed by fibres and resins. The high anisotropy of the fibres confers to the laminate anisotropic nature, which depends on the stacking sequence of the plies (Nadella et al. 2010). Therefore, a laminate can be highly anisotropic if all the fibres are oriented in the same direction or it can be weakly anisotropic if the fibres are equally oriented in all directions. This anisotropy makes the wave velocity dependent to the angle of propagation, so this angular dependency will be more significant for highly anisotropic composites, unlike the weakly anisotropic laminates which will have a velocity profile similar to the one of an isotropic material (Karmazin et al. 2011).

Another important consequence of the wave propagation in composites is the absence of pure modes of propagation. In isotropic materials Lamb waves have displacements in  $x$  and  $z$  directions and the shear horizontal only in  $y$  direction but in anisotropic materials guided waves have displacements in the

three directions (Rose 2012). For example, symmetric modes  $S_i$  have displacements in the propagating direction ( $x$  axis) and in the out-of-plane direction ( $z$  axis) but in composites small displacements in the perpendicular direction ( $y$  axis) will be induced as well. Consequently, another way to designate these non-pure modes was established. The modes which have their main displacement component in the direction of the wave propagation are called quasi-symmetric  $qS_i$ , the modes which have the main displacement component in the out-of-plane direction are called quasi-antisymmetric  $qA_i$ , and the modes with the main displacement component perpendicular to the wave propagation and parallel to the surface are called quasi-shear horizontal  $qSH_i$  (Karmazin et al. 2013). Hereafter called symmetric  $S_i$ , antisymmetric  $A_i$  and shear horizontal  $SH_i$  modes for simplicity reasons. The attenuation is another factor to have in mind for guided wave propagation in composites, since it gets significant at higher frequencies, due to the viscoelastic behaviour of the resin which damps the wave energy and also because of the scattering caused by the fibres (Wang and Yuan 2007).

For the dispersion curves creation, it is necessary to make a distinction between isotropic or anisotropic materials. Since for isotropic materials the wave velocity depends only on the magnitude of the wave vector  $k = |\mathbf{k}|$ , which is the wavenumber. But for anisotropic materials, it is required to consider the magnitude and also the direction of the wave vector. This distinction expands the previous definition of the phase velocity for anisotropic materials in order to involve in the equation the direction of the wave vector, which can be expressed as Eq. (3.6) (Wang and Yuan 2007):

$$\mathbf{c}_p = \left(\frac{\omega}{k}\right) \left(\frac{\mathbf{k}}{|\mathbf{k}|}\right) = \left(\frac{\omega}{k^2}\right) \mathbf{k} \quad (3.6)$$

where  $\omega$  is the angular frequency and  $\mathbf{k}$  the wave vector. A new concept that was not indicated before for isotropic materials is the slowness. Mathematically, it is defined as the inverse velocity and it is given by Eq. (3.7):

$$\mathbf{s} = \frac{\mathbf{k}}{\omega} \quad (3.7)$$

Note that the wave vector direction is always normal to the wave front of constant phase, so the phase velocity and the slowness always have the same direction as the wave vector. In order to calculate the group velocity, the wave vector direction has to be taken into consideration as well. So from the group velocity Eq. (3.4b) presented before, the group velocity can be defined as Eq. (3.8) (Wang and Yuan 2007; Karmazin et al. 2013):

$$\mathbf{c}_g = \frac{d\omega(k, \theta)}{d\mathbf{k}} = \nabla_{\omega}(k, \theta) = \frac{\partial\omega}{\partial k} \mathbf{e}_k + \frac{1}{k} \frac{\partial\omega}{\partial\theta} \mathbf{e}_\theta \quad (3.8)$$

where  $\mathbf{e}_k$  is the unit vector in the radial direction and  $\mathbf{e}_\theta$  is the unit vector in the angular direction. The group velocity in Cartesian coordinates can be calculated



using a transformation matrix, Eq. (3.9):

$$\begin{Bmatrix} c_{gx} \\ c_{gy} \end{Bmatrix} = \begin{bmatrix} \cos \theta & -\sin \theta \\ \sin \theta & \cos \theta \end{bmatrix} \begin{Bmatrix} \frac{\partial \omega}{\partial k} \\ \frac{1}{k} \frac{\partial \omega}{\partial \theta} \end{Bmatrix} \quad (3.9)$$

So the magnitude of the group velocity is given by Eq. (3.10):

$$c_g = \sqrt{c_{gx}^2 + c_{gy}^2} \quad (3.10)$$

And the angle of the group velocity direction is given by Eq. (3.11):

$$\theta_g = \tan^{-1} \frac{c_{gy}}{c_{gx}} \quad (3.11)$$

The difference between the wave vector angle and the group velocity angle is known as the skew angle,  $\varphi_{\text{skew}} = \theta - \theta_g$ . A different way to calculate the skew angle from the complex Poynting vector is described in (Rose 2012). The equation of the Poynting vector is Eq. (3.12):

$$\mathbf{P} = -\frac{\tilde{\mathbf{v}} \cdot \boldsymbol{\sigma}_M}{2} \quad (3.12)$$

where  $\tilde{\mathbf{v}}$  is the conjugate of particle velocity vector and  $\boldsymbol{\sigma}_M$  is the stress tensor as shown in Eq. (3.13):

$$\boldsymbol{\sigma}_M = \begin{bmatrix} \sigma_{kk} & \sigma_{k\theta} & \sigma_{kz} \\ \sigma_{\theta k} & \sigma_{\theta\theta} & \sigma_{\theta z} \\ \sigma_{zk} & \sigma_{z\theta} & \sigma_{zz} \end{bmatrix} \quad (3.13)$$

The integral of the Poynting vector across the thickness in a specific direction yields the power flow density in this chosen direction. Therefore in the case of plane waves, it is possible to determine the skew angle with Eq. (3.12) by calculating the power flow density in the wave vector direction  $P_k$ , and in the perpendicular direction (angular direction)  $P_\theta$ . For anisotropic materials,  $P_\theta$  is nonzero for certain wave modes. Hence, this component introduces a wave skew effect, which can be calculated by Eq. (3.14):

$$\varphi_{\text{skew}} = \tan^{-1} \left( \frac{\int P_\theta dz}{\int P_k dz} \right) \quad (3.14)$$

This is not the case for isotropic materials, where the component  $P_\theta$  will be equal to zero as there is no angular dependency of the velocities. So the skew angle will be zero and the wave vector and group velocity will have the same direction.

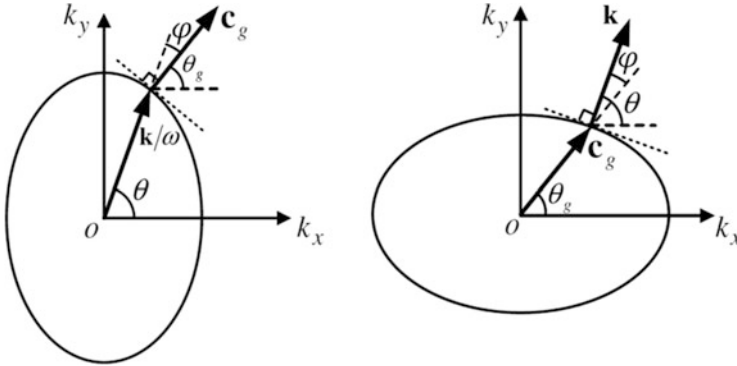


**Fig. 3.13** Relationship between wave vector and group velocity vector. (a) Slowness curve. (b) Group velocity wave front (Wang and Yuan 2007)

Geometrically, the wave vector can be related to the group velocity, see Fig. 3.13. The normal direction of group velocity wave front is the direction of the wave vector; vice versa, the normal direction of the slowness curve is the group velocity direction. Figure 3.13 also depicts the skew angle  $\varphi$ , in which the different directions of the group,  $\theta_g$ , and phase velocities,  $\theta$ , are clearly shown.

### 3.4.2.1 Simulation

The simulation of guided waves is an essential step for the understanding of the wave propagation in multi-layered structures and is also useful for validating new damage detection techniques or new transducer arrays. The wide range of different layups makes the experimental analysis of each one individually impracticable; therefore the simulation is used to investigate different materials or layups in an efficient manner. In guided wave analysis of composites, the hypothesis of considering each layer isotropic across the thickness is commonly adopted; each ply is a homogeneous orthotropic layer. This assumption is based on the fact that the wavelengths of the propagating guided waves are substantially longer than the characteristic size of the cross section of the fibres (Tauchert and Guzelsu 1972; Wang and Yuan 2007). In Tauchert and Guzelsu (1972), it is shown that the scattering produced by the fibres of each layer occurs when the wavelength is of the same order of the diameter of the fibres for longitudinal modes, and 40 times the order of the diameter for flexural modes.

The dispersion properties of composite materials and the analysis of the 3D propagation of guided waves are being commonly studied by numerical or analytical methods. Different techniques have been proposed, such as traditional Finite Element Method (FEM) (Lissenden et al. 2009; Song et al. 2009; Ricci et al. 2014), semianalytical finite element method (SAFE) (Hayashi et al. 2003; Deng and Yang 2011; Rose 2014), finite differences (Saenger and Bohlen 2004; Moczo et al.

2007) or applying the elasticity theory using the global matrix and transfer matrix (Wang and Yuan 2007; Karmazin et al. 2011, 2013). Finite Element Methods have limitations due to the available computational resources, since for high frequencies a very fine discretization, both temporal and spatial, is necessary to comply with the Nyquist theorem and to ensure a minimum number of elements per wavelength in order to replicate the wave. This problem is overcome with the use of SAFE, where the waveguide is only discretized in a cross section of the structure, reducing considerably the computational load. In the literature the analytical methods have been established as a good approach for the analysis of guided waves in composites, but they are more susceptible to miss roots of the dispersion equations and distort the results.

The wave mode displacements depending on the angle of propagation and the stacking sequence of the composite have been described in many publications (Rhee et al. 2007; Wang and Yuan 2007; Karmazin et al. 2011, 2013). For instance, it has been shown that the propagation in unidirectional laminates has a preferential direction along the fibre direction. In the case of cross-ply laminates  $0^\circ/90^\circ$ , the simulations show that there are two preferential directions  $0^\circ$  and  $90^\circ$  and it is also noticeable that for the angles in between the wave propagation is at  $45^\circ$  direction, see Fig. 3.14. For quasi-isotropic laminates, the wave front profile is very similar to the isotropic materials; the wave velocity has very small variations with the angle. In Karmazin et al. (2013), the authors analysed the wave propagation in a cross ply laminate using the analytical method of Green's matrix in a frequency-wavenumber domain. In this work, they concluded that the symmetric mode depends strongly on the wave propagation direction in high anisotropic laminates, in contrast to the antisymmetric modes which weakly depend on the propagation angle, as can be

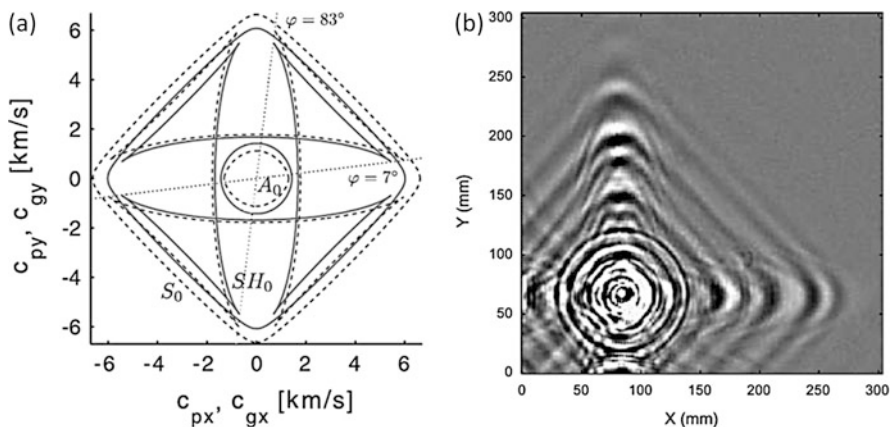


**Fig. 3.14** Representation of the group velocity wave front in a cross-ply laminate by two different methods. (a) An analytical method using the Fourier Transform of Green's matrix. *Solid line* (Karmazin et al. 2013). (b) An experimental technique using scanning air-coupled ultrasonic transducers (SAUT) (Michaels et al. 2011)

seen in Fig. 3.14. Another important observation in Fig. 3.14 is the shape of the wave front in the shear horizontal mode, which is caused when the curvature of the slowness shifts from convex to concave shape. This effect is well-known in the analysis of bulk waves in anisotropic solids (Wang and Yuan 2007). It is called the phenomenon of energy focusing. Note that near the angles of  $7^\circ$  and  $83^\circ$ , there is a concentration of energy.

In the example shown in Fig. 3.14a, the shear horizontal mode presents several group velocity values—particularly, it presents one, two or three different group velocities for the same direction. Therefore, in these particular multi-valued directions usually called caustics (Karmazin et al. 2013), three pulses of the same wave mode will propagate at different velocities.

### 3.4.2.2 Damage Detection

In composite materials, the most common damage is the delamination between plies caused by impacts or cyclic loads. This mode of failure consists in the separation of layers which leads to significant loss of strength. Typically, the flaws created inside the laminate by impacts are not visible to the naked eye, therefore guided wave inspection in composite is highly recommended since the wave modes propagate along the structure sweeping the entire thickness. Internal damages will interact with the propagating wave modes, inducing changes in its propagation pattern. The wave modes will be affected by the delamination in different ways depending on its mode of vibration. In the literature (Grondel et al. 2002; Su et al. 2007; Hu et al. 2008; Ramadas et al. 2009; Rekatsinas et al. 2015), the three fundamental wave modes  $S_0$ ,  $A_0$  and  $SH_0$  are the most studied and the most commonly used in order to interrogate a structure. The symmetric mode is chosen at low frequencies, below 200 kHz, because they are less dispersive so the shape of the pulse does not spread along the propagation direction which eases the post-analysis and reduce the complexity of the acquired signals. In addition, the symmetric mode has less attenuation since its displacement is an in-plane motion and the carried energy remains inside the structure avoiding scattering. The  $S_0$  mode also has more sensitivity to delaminations than the  $A_0$  mode (Wang and Yuan 2007). Nevertheless, the  $A_0$  mode has more resolution in order to detect smaller flaws, since the wavelength of the  $A_0$  mode is shorter than the others and the size defect detectability is commonly established at the same order of the wavelength of the propagating mode. The passing through of wave modes across a delamination produces a split in energy creating a new mode of propagation. This wave mechanism is called mode conversion and it also occurs when the wave reaches the edge of a plate, so new wave modes are created and reflected backwards. Mode conversion in delaminations has been studied in several investigations in order to take advantage of these changes and use them to detect and locate these defects (Su et al. 2007; Hu et al. 2008; Ramadas et al. 2009). Hu et al. (2008) analysed numerically the propagation of the  $S_0$  mode through a delamination. When the  $S_0$  mode enters in the delamination, a small amount of the energy of  $S_0$  (almost undetectable) is reflected backwards and most of

it is transmitted forward, but also mode conversion is produced, so a new  $A_0$  mode is reflected and a new  $A_0$  mode is transmitted. The same mechanism occurs when the wave mode moves out of the delamination, the  $S_0$  and a new  $A_0$  are transmitted forward and a reflected  $S_0$  and a new  $A_0$  are transmitted backwards. In this case the reflected  $S_0$  mode has a greater amount of energy which enables the detection of the delamination in a pulse-echo configuration. So, in the publication, they are able to locate the end of the delamination calculating the propagating distance with the dispersion curves but they cannot determine the extent of the delamination which is highly important. Other detection techniques are based on a pitch-catch configuration, where the acquired signal is usually compared to a baseline signal from an undamaged condition. These techniques analyse the incoming wave packets and study their phase, amplitude and time of arrival establishing a damage index in order to compare different damage states (Giurgiutiu and Santoni-Bottai 2011; Torkamani et al. 2014). The use of this technique on its own is quite limited since only the path between transmitter and receiver is inspected. Thus, a network of transducers covering the structure has been performed by many researchers (Zhao et al. 2007; Lissenden and Rose 2008; Ng and Veidt 2009) in order to interrogate in a pitch-catch configuration the entire structure. With this technique, the system is able to map the inspected area by analysing all the paths between transducers. The paths affected by damages are highlighted facilitating the visual localization of the damage. Another interesting technique is to apply a data processing algorithm to a wave field image acquired by a laser vibrometer system (Michaels et al. 2011; Sohn et al. 2011; Rogge and Leckey 2013). In (Michaels et al. 2011), the authors use a signal processing technique in order to remove specific wave modes from the images in order to reveal low amplitude reflections from damages masked by high amplitude wave modes. To do this, the images are transformed to a frequency-wavenumber plane using the 2D Fourier Transform. In this domain, the different propagating wave modes are easily recognisable, so by applying a filter it is possible to remove a specific wave mode, and subsequently perform the inverse Fourier Transform to get the images without this mode. The disadvantage of this technique is that it is not applicable to in-service structures, since the equipment to get the images is very sensitive to external vibrations so the acquisition has to be performed in very controlled conditions. Wavelet Transform is another signal processing technique widely used in guided wave technology, mainly in a pitch-catch configuration (Kessler et al. 2002; Yan and Yam 2002; Paget et al. 2003). In composite materials, it has been proved that it provides good detectability results.

Another important damage in composites that has been studied in the literature is the debonding, which is the separation between the shell and the core in a sandwich structure or between two parts joined by adhesive or co-curing. This kind of damage is structurally of great importance, since the debonding of a stiffener from the shell in a wing or the shear web from the spar in a wind turbine blade can cause a great loss of stiffness and a possible collapse of the entire structure. Investigations of this type of damage with guided waves follow a similar approach to the delamination detection. Since most of the studies are based on a transducer network in order to map the bonding area and locate the debonding by analysing the paths between

transducers (Lissenden et al. 2009; Mustapha et al. 2012; Song et al. 2012; Ricci et al. 2014).

**Open Access** This chapter is distributed under the terms of the Creative Commons Attribution-NonCommercial 4.0 International License (<http://creativecommons.org/licenses/by-nc/4.0/>), which permits any noncommercial use, duplication, adaptation, distribution and reproduction in any medium or format, as long as you give appropriate credit to the original author(s) and the source, provide a link to the Creative Commons license and indicate if changes were made.

The images or other third party material in this chapter are included in the work's Creative Commons license, unless indicated otherwise in the credit line; if such material is not included in the work's Creative Commons license and the respective action is not permitted by statutory regulation, users will need to obtain permission from the license holder to duplicate, adapt or reproduce the material.

## References

- Alleyne DN, Cawley P (1992a) Optimization of Lamb wave inspection techniques. *NDT&E Int* 25:11–22
- Alleyne DN, Cawley P (1992b) The interaction of Lamb waves with defects. *IEEE Trans Ultrason Ferroelectr* 39:381–397
- Alleyne DN, Lowe M, Cawley P (1998) The reflection of guided waves from circumferential notches in pipes. *J Appl Mech* 65:635–641. doi:10.1115/1.2789105
- Baid H, Schaal C, Samajder H et al (2015) Dispersion of Lamb waves in a honeycomb composite sandwich panel. *Ultrasonics* 56:409–416
- Castaigns M, Singh D, Viot P (2012) Sizing of impact damages in composite materials using ultrasonic guided waves. *NDT&E Int* 46:22–31
- Cattin R (2012) Icing of wind turbines: Vindforsk projects, a survey of the development and research needs. In Reports. ELFORSK. Available via ELFORSK. [http://elforsk.se/Rapporter/?download=report&rid=12\\_13\\_](http://elforsk.se/Rapporter/?download=report&rid=12_13_). Accessed 06 Apr 2016
- Cawley P (1994) The rapid non-destructive inspection of large composite structures. *Composites* 25:351–357
- Cawley P, Lowe M, Alleyne D et al (2003) Practical long range guided wave inspection applications to pipes and rail. *Mater Eval* 61:66–74
- Ciang CC, Lee J-R, Bang H-J (2008) Structural health monitoring for a wind turbine system: a review of damage detection methods. *Meas Sci Technol* 19(12):2001
- Clayton TN, Ammerman CN, Park G et al (2010) Structural damage identification in wind turbine blades using piezoelectric active sensing with ultrasonic validation. In Publications. Los Alamos National Laboratory. Available via LANL. <http://permalink.lanl.gov/object/tr?what=info:lanl-repo/lareport/LA-UR-10-00416>. Accessed 06 Apr 2016
- Cotton I, Jenkins N, Pandiaraj K (2001) Lightning protection for wind turbine blades and bearings. *Wind Energy* 4:23–37
- Chacon JLF, Andicoberry EA, Kappatos V et al (2014) Shaft angular misalignment detection using acoustic emission. *Appl Acoust* 85:12–22
- Chacon JLF, Kappatos V, Balachandran W et al (2015) A novel approach for incipient defect detection in rolling bearings using acoustic emission technique. *Appl Acoust* 89:88–100
- Choi K-S, Huh Y-H, Kwon I-B et al (2012) A tip deflection calculation method for a wind turbine blade using temperature compensated FBG sensors. *Smart Mater Struct* 21:025008
- Debel C (2004) Identification of damage types in wind turbine blades tested to failure. In: Somers MAJ (ed) *Materialeopførsel og skadesanalyse*. DMS, Lyngby, pp 123–127

- Deng Q, Yang Z (2011) Propagation of guided waves in bonded composite structures with tapered adhesive layer. *Appl Math Model* 35:5369–5381
- Diamanti K, Soutis C (2010) Structural health monitoring techniques for aircraft composite structures. *Prog Aerosp Sci* 46:342–352
- Discalea FL, Matt H, Bartoli I et al (2007) Health monitoring of UAV wing skin-to-spar joints using guided waves and macro fiber composite transducers. *J Intell Mater Syst Struct* 18:373–388
- Ditri JJ, Rose JL (1992) Excitation of guided elastic wave modes in hollow cylinders by applied surface tractions. *J Appl Phys* 72:2589–2597
- Gao H, Ali S, Lopez B (2010) Efficient detection of delamination in multilayered structures using ultrasonic guided wave EMATs. *NDT&E Int* 43:316–322
- Giurgiutiu V, Santoni-Bottai G (2011) Structural health monitoring of composite structures with piezoelectric-wafer active sensors. *AIAA J* 49:565–581
- Glavind L, Olesen IS, Skipper BF et al (2013) Fiber-optical grating sensors for wind turbine blades: a review. *Opt Eng* 52:030901
- Grondel S, Paget C, Delebarre C et al (2002) Design of optimal configuration for generating A0 Lamb mode in a composite plate using piezoceramic transducers. *J Acoust Soc Am* 112:84–90
- Habibi H, Cheng L, Zheng H et al (2015) A dual de-icing system for wind turbine blades combining high-power ultrasonic guided waves and low-frequency forced vibrations. *Renew Energy* 83:859–870
- Han B-H, Yoon D-J, Huh Y-H et al (2014) Damage assessment of wind turbine blade under static loading test using acoustic emission. *J Intell Mater Syst Struct* 25:621–630
- Han J, Kim C-G, Kim J-Y (2006) The propagation of Lamb waves in a laminated composite plate with a variable stepped thickness. *Compos Struct* 76:388–396
- Hay TR, Wei L, Rose JL et al (2003) Rapid inspection of composite skin-honeycomb core structures with ultrasonic guided waves. *J Compos Mater* 37:929–939
- Hayashi T, Kawashima K (2002) Multiple reflections of Lamb waves at a delamination. *Ultrasonics* 40:193–197
- Hayashi T, Song W-J, Rose JL (2003) Guided wave dispersion curves for a bar with an arbitrary cross-section, a rod and rail example. *Ultrasonics* 41:175–183
- Homola M (2005) Impacts and causes of icing on wind turbines. Available via Høgskolen i Narvik. <http://ansatte.hin.no/mch/documents/Wind%20energy%20BSR-Impacts%20and%20causes%20of%20icing%20on%20wind%20turbines.pdf>. Accessed 06 Apr 2016
- Hu N, Shimomukai T, Yan C et al (2008) Identification of delamination position in cross-ply laminated composite beams using S0 Lamb mode. *Compos Sci Technol* 68:1548–1554
- Kapadia A (2012) Best practice guide: non-destructive testing of composite materials. Composites UK. Available via National Composites Network. <https://compositesuk.co.uk/system/files/documents/ndtocomposites.pdf>. Accessed 06 Apr 2016
- Karmazin A, Kirillova E, Seemann W et al (2011) Investigation of Lamb elastic waves in anisotropic multilayered composites applying the Green's matrix. *Ultrasonics* 51:17–28
- Karmazin A, Kirillova E, Seemann W et al (2013) A study of time harmonic guided Lamb waves and their caustics in composite plates. *Ultrasonics* 53:283–293
- Kessler SS, Spearing SM, Atalla MJ et al (2002) Damage detection in composite materials using frequency response methods. *Compos Part B Eng* 33:87–95
- Kim H-I, Han J-H, Bang H-J (2014) Real-time deformed shape estimation of a wind turbine blade using distributed fiber Bragg grating sensors. *Wind Energy* 17:1455–1467
- Kim S-W, Kang W-R, Jeong M-S et al (2013) Deflection estimation of a wind turbine blade using FBG sensors embedded in the blade bonding line. *Smart Mater Struct* 22:125004
- Li D, Ho S-CM, Song G et al (2015a) A review of damage detection methods for wind turbine blades. *Smart Mater Struct* 24:033001
- Li R, He D (2012) Rotational machine health monitoring and fault detection using EMD-based acoustic emission feature quantification. *IEEE Trans Instrum Meas* 61:990–1001
- Li X, Yang Z, Zhang H et al (2015b) Crack growth sparse pursuit for wind turbine blade. *Smart Mater Struct* 24:015002



- Lissenden C, Puthillath P, Rose J (2009) Guided wave feature identification for monitoring structural damage in joints between composite laminates. *Mater Forum* 33:279–285
- Lissenden CJ, Rose JL (2008) Structural health monitoring of composite laminates through ultrasonic guided wave beam forming. In: Abstracts of the RTO Applied Vehicle Technology Panel (AVT) symposium, NATO, Montreal, 13–16 Oct 2008
- Lowe MJ, Alleyne DN, Cawley P (1998) Defect detection in pipes using guided waves. *Ultrasonics* 36:147–154
- Manohar A (2012) Quantitative nondestructive testing using infrared thermography. Dissertation, University of California
- Márquez FPG, Tobias AM, Pérez JMP et al (2012) Condition monitoring of wind turbines: techniques and methods. *Renew Energy* 46:169–178
- Michaels TE, Michaels JE, Ruzzene M (2011) Frequency-wavenumber domain analysis of guided wavefields. *Ultrasonics* 51:452–466
- Moczo P, Robertsson JO, Eisner L (2007) The finite-difference time-domain method for modeling of seismic wave propagation. *Adv Geophys* 48:421–516
- Monkhouse R, Wilcox P, Cawley P (1997) Flexible interdigital PVDF transducers for the generation of Lamb waves in structures. *Ultrasonics* 35:489–498
- Mudge P, Harrison J (2001) TELETEST guided wave technology—case histories. Paper presented at nondestructive testing. In: 1st Middle East conference and exhibition, Bahrain, 24–26 September 2001
- Mustapha S, Ye L, Wang D et al (2012) Debonding detection in composite sandwich structures based on guided waves. *AIAA J* 50:1697–1706
- Nadella KS, Salas KI, Cesnik CES (2010) Characterization of guided-wave propagation in composite plates. In Kundu T (ed) Proceedings of the SPIE 7650, health monitoring of structural and biological systems, California, 2010
- Nair A, Cai C (2010) Acoustic emission monitoring of bridges: review and case studies. *Eng Struct* 32:1704–1714
- NDT Resource Center (2016) Theory - AE sources. [https://www.nde-ed.org/EducationResources/CommunityCollege/Other%20Methods/AE/AE\\_Theory-Sources.htm](https://www.nde-ed.org/EducationResources/CommunityCollege/Other%20Methods/AE/AE_Theory-Sources.htm). Accessed 25 Jan 2016
- Ng CT, Veidt M (2009) A Lamb-wave-based technique for damage detection in composite laminates. *Smart Mater Struct* 18:074006
- Niezrecki C, Avitabile P, Chen J et al (2014) Inspection and monitoring of wind turbine blade-embedded wave defects during fatigue testing. *Struct Health Monit* 13(6):629–643
- Ostachowicz W, Güemes A (eds) (2013) New trends in structural health monitoring. Springer, Berlin
- Paget CA, Grondel S, Levin K et al (2003) Damage assessment in composites by Lamb waves and wavelet coefficients. *Smart Mater Struct* 12:393
- Pao Y-H, Gajewski RR, Ceranoglu AN (1979) Acoustic emission and transient waves in an elastic plate. *J Acoust Soc Am* 65:96–105
- Park G, Rutherford AC, Wait JR et al (2005) High-frequency response functions for composite plate monitoring with ultrasonic validation. *AIAA J* 43:2431–2437
- Pavlovic B, Lowe M, Alleyne D et al (1997) Disperse: a general purpose program for creating dispersion curves. In: Thompson DO, Chimenti DE (eds) Review of progress in quantitative nondestructive evaluation, vol 16. Springer, Heidelberg, p 185
- Pedrazzani JR, Castellucci M, Sang AK et al (2012) Fiber optic distributed strain sensing used to investigate the strain fields in a wind turbine blade and in a test coupon with open holes. In: Proceedings of the SAMPE technical conference, Charleston, 22–24 Oct 2012
- Petcher P, Burrows SE, Dixon S (2014) Shear horizontal (SH) ultrasound wave propagation around smooth corners. *Ultrasonics* 54:997–1004
- Ramadas C, Balasubramaniam K, Joshi M et al (2009) Interaction of the primary anti-symmetric Lamb mode (Ao) with symmetric delaminations: numerical and experimental studies. *Smart Mater Struct* 18:085011
- Ramadas C, Padiyar J, Balasubramaniam K et al (2011) Lamb wave based ultrasonic imaging of interface delamination in a composite T-joint. *NDT&E Int* 44:523–530



- Rauscher F (2004) Defect detection by acoustic emission examination of metallic pressure vessels. *J Acoust Em* 22:49–58
- Rekatsinas C, Nastos C, Theodosiou T et al (2015) A time-domain high-order spectral finite element for the simulation of symmetric and anti-symmetric guided waves in laminated composite strips. *Wave Motion* 53:1–19
- Requeson OR, Tcherniak D, Larsen GC (2015) Comparative study of OMA applied to experimental and simulated data from an operating Vestas V27 wind turbine. In: Abstracts of the international operational modal analysis conference, Gijón, 12–14 May 2015
- Rhee S-H, Lee J-K, Lee J-J (2007) The group velocity variation of lamb wave in fiber reinforced composite plate. *Ultrasonics* 47:55–63
- Ricci F, Mal AK, Monaco E et al (2014) Guided waves in layered plate with delaminations. In: Abstracts of the EWSHM-7th European workshop on structural health monitoring, Nantes, 8–11 July 2014
- Rogge MD, Leckey CA (2013) Characterization of impact damage in composite laminates using guided wavefield imaging and local wavenumber domain analysis. *Ultrasonics* 53:1217–1226
- Rose JL (2012) Health monitoring of composite structures using guided waves. In: The Defense Technical Information Center. Available via DTIC. <http://www.dtic.mil/cgi-bin/GetTRDoc?Location=U2&doc=GetTRDoc.pdf&AD=ADA563790> Accessed 06 Apr 2016
- Rose JL (2014) *Ultrasonic guided waves in solid media*. Cambridge University Press, New York
- Rose JL, Avioli MJ, Mudge P et al (2004) Guided wave inspection potential of defects in rail. *NDT&E Int* 37:153–161
- Saenger EH, Bohlen T (2004) Finite-difference modeling of viscoelastic and anisotropic wave propagation using the rotated staggered grid. *Geophysics* 69:583–591
- Salawu O (1997) Detection of structural damage through changes in frequency: a review. *Eng Struct* 19:718–723
- Sareen A, Sapre CA, Selig MS (2014) Effects of leading edge erosion on wind turbine blade performance. *Wind Energy* 17:1531–1542
- Schulz M, Sundaresan M (2006) Smart sensor system for structural condition monitoring of wind turbines. In: National Renewable Energy Laboratory Documents. Available via NREL. <http://www.nrel.gov/docs/fy06osti/40089.pdf>. Accessed 06 Apr 2016
- Shoja Chaeikar S, Berbyuk V, Boström A (2015) Investigating the application of guided wave propagation for ice detection on composite materials. In: Boltež M, Slavič J, Wiercigroch M (eds) Proceedings of the international conference on engineering vibration, Ljubljana, 2015
- Sierra-Pérez J, Torres-Arredondo MA, Güemes A (2016) Damage and nonlinearities detection in wind turbine blades based on strain field pattern recognition. FBGs, OBR and strain gauges comparison. *Compos Struct* 135:156–166
- Sohn H, Dutta D, Yang J et al (2011) Delamination detection in composites through guided wave field image processing. *Compos Sci Technol* 71:1250–1256
- Sohn H, Park G, Wait JR et al (2004) Wavelet-based active sensing for delamination detection in composite structures. *Smart Mater Struct* 13:153
- Song F, Huang G, Hu G (2012) Online guided wave-based debonding detection in honeycomb sandwich structures. *AIAA J* 50:284–293
- Song F, Huang G, Hudson K (2009) Guided wave propagation in honeycomb sandwich structures using a piezoelectric actuator/sensor system. *Smart Mater Struct* 18:125007
- Song G, Li H, Gajic B et al (2013) Wind turbine blade health monitoring with piezoceramic-based wireless sensor network. *Int J Smart Nano Mater* 4:150–166
- Sørensen BF, Jørgensen E, Debel CP et al (2004) Improved design of large wind turbine blade of fibre composites based on studies of scale effects (Phase 1). Summary report. In: DTU Orbit - The Research Information System Publications. Available via DTU Orbit. [http://orbit.dtu.dk/fedora/objects/orbit:90493/datastreams/file\\_7702048/content](http://orbit.dtu.dk/fedora/objects/orbit:90493/datastreams/file_7702048/content). Accessed 06 Apr 2016
- Su Z, Yang C, Pan N et al (2007) Assessment of delamination in composite beams using shear horizontal (SH) wave mode. *Compos Sci Technol* 67:244–251
- Su Z, Ye L (2004) Lamb wave-based quantitative identification of delamination in CF/EP composite structures using artificial neural algorithm. *Compos Struct* 66:627–637

- Su Z, Ye L (2009) Identification of damage using lamb waves: from fundamentals to applications. Springer, Heidelberg
- Su Z, Ye L, Bu X (2002) A damage identification technique for CF/EP composite laminates using distributed piezoelectric transducers. *Compos Struct* 57:465–471
- Sundaesan M, Pai P, Ghoshal A et al (2001) Methods of distributed sensing for health monitoring of composite material structures. *Compos Part A Appl Sci Manuf* 32:1357–1374
- Tauchert TR, Guzelsu A (1972) An experimental study of dispersion of stress waves in a fiber-reinforced composite. *J Appl Mech-T ASME* 39:98–102. doi:10.1115/1.3422677
- Taylor SG, Farinholt KM, Jeong H et al (2012) Wind turbine blade fatigue tests: lessons learned and application to SHM system development. In: The 6th European workshop on structural health monitoring – EWSHM. Available via NDT Net. <http://www.ndt.net/article/ewshm2012/papers/we2b4.pdf>. Accessed 06 Apr 2015
- Taylor SG, Farinholt K, Choi M (2013a) Incipient crack detection in a composite wind turbine rotor blade. *J Intell Mater Syst Struct* 25(5):613–620. doi:10.1177/1045389X13510788
- Taylor SG, Park G, Farinholt KM et al (2013b) Fatigue crack detection performance comparison in a composite wind turbine rotor blade. *Struct Health Monit* 12:252–262
- Taylor SG, Park G, Farinholt KM et al (2013c) Diagnostics for piezoelectric transducers under cyclic loads deployed for structural health monitoring applications. *Smart Mater Struct* 22:025024
- Torkamani S, Roy S, Barkey ME et al (2014) A novel damage index for damage identification using guided waves with application in laminated composites. *Smart Mater Struct* 23:095015
- Ulriksen MD, Tcherniak D, Kirkegaard PH et al (2014) Operational modal analysis and wavelet transformation for damage identification in wind turbine blades. In: The 7th European workshop on structural health monitoring – EWSHM. Available via NDT Net. <http://www.ndt.net/article/ewshm2014/papers/0210.pdf>. Accessed 06 Apr 2016
- Wang L, Yuan F (2007) Group velocity and characteristic wave curves of Lamb waves in composites: modeling and experiments. *Compos Sci Technol* 67:1370–1384
- Wilcox P, Lowe M, Cawley P (2001) Mode and transducer selection for long range Lamb wave inspection. *J Intell Mater Syst Struct* 12:553–565
- Wilcox PD (2003) A rapid signal processing technique to remove the effect of dispersion from guided wave signals. *IEEE Trans Ultrason Ferroelectr* 50:419–427
- Yan Y, Yam L (2002) Online detection of crack damage in composite plates using embedded piezoelectric actuators/sensors and wavelet analysis. *Compos Struct* 58:29–38
- Yang S, Tcherniak D, Allen MS (2014) Modal analysis of rotating wind turbine using multiblade coordinate transformation and harmonic power spectrum. In: De Clerck J (ed) Topics in modal analysis I: Proceedings of the 32nd IMAC, a conference and exposition on structural dynamics, Brescia, July 2012. Conference proceedings of the society for experimental mechanics series, vol 7. Springer, Heidelberg
- Yeum CM, Sohn H, Ihn JB et al (2012) Instantaneous delamination detection in a composite plate using a dual piezoelectric transducer network. *Compos Struct* 94:3490–3499
- Zak A, Krawczuk M, Ostachowicz W (2012) Spectral finite element method for propagation of guided elastic waves in wind turbine blades for SHM purposes. In: The 6th European workshop on structural health monitoring – EWSHM. Available via NDT Net. <http://www.ndt.net/article/ewshm2012/papers/tu2d2.pdf>. Accessed 06 Apr 2016
- Zhao X, Gao H, Zhang G et al (2007) Active health monitoring of an aircraft wing with embedded piezoelectric sensor/actuator network: I. Defect detection, localization and growth monitoring. *Smart Mater Struct* 16(4):1208–1217
- Zhong C, Croxford A, Wilcox P (2015) Remote inspection system for impact damage in large composite structure. *P Roy Soc Lond A Mat*. doi:10.1098/rspa.2014.0631
- Zhou W, Li Y, Li Z et al (2015) Interlaminar shear properties and acoustic emission monitoring of the delaminated composites for wind turbine blades. In: Shen G, Wu Z, Zhang J (eds) Advances in acoustic emission technology, vol 158, Springer proceedings in physics. Springer, Heidelberg, pp 557–566

# Chapter 4

## Fibre Bragg Grating as a Multi-Stage Structure Health Monitoring Sensor

Gilmar Ferreira Pereira

**Abstract** There is a clear need to implement models and measurement systems through the entire life of the wind turbine blade. In this chapter will be presented some work conducted to implement optical fibres as a multi-stage sensor, capable to measure different structural properties, and link them with all the different life stages and support a better design of the wind turbine blades. The characteristics and functionality of fibre Bragg grating sensors are briefly introduced. Their application as multi-stage structure health monitoring sensors for polymer laminate composite is then described. At the manufacturing stage, where the sensors can measure several parameters of infusion and curing, sensor feedback can help control the process, avoid residual strain, and contribute to the product certification; and then in operation where cracks can be detected and monitored. Experimental mechanical testing involving crack growth and fibre Bragg sensing is described that highlights the response from the fibre optic which will correctly detect the presence and growth of damage. Models to implement these results in a damage detection system for a wind turbine blade can then be developed.

### 4.1 Fibre Bragg Grating Sensors

Fibre Bragg grating (FBG) sensors are the most commonly used type of sensors in the fibre optic field. An FBG sensor can be embedded in the Fibre reinforced polymer material (main material of the wind turbine blade), without compromising its structural resistance. This is due to the FBG reduced size, with a diameter of 125  $\mu\text{m}$  it is virtual non-intrusive to the material. Also, FBG sensors present other interesting features, such high resolution, multiplexing capability, immunity to electro-magnetic fields, chemical inertness and long term stability.

A FBG is formed by a permanent periodic modulation of the refractive index along a section of an optical fibre, by exposing the optical fibre to an interference pattern of intense ultra-violet light. The photosensitivity of the silica exposed to the

---

G.F. Pereira (✉)

Department of Wind Energy, Technical University of Denmark (DTU), DTU Risø Campus,  
Frederiksborgvej 399, 4000 Roskilde, Denmark  
e-mail: [gilmar.fepe@gmail.com](mailto:gilmar.fepe@gmail.com)

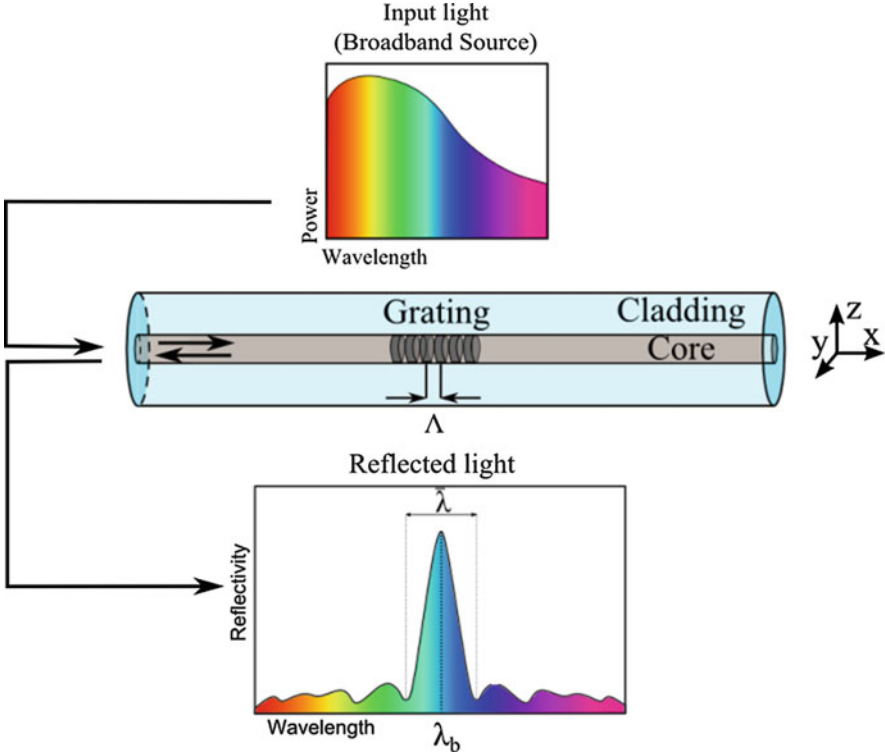


**Fig. 4.1** Fibre Bragg grating: strongest mode coupling at the Bragg wavelength

ultra-violet light is increased, so that when light propagates through the periodically alternating regions of higher and lower refractive index within the fibre, it is reflected by successive, coherent scattering from the index variations. When the reflection from a crest in the index modulation is in phase with the next one, it is generated the maximum mode coupling or reflection. The strongest mode coupling occurs at the Bragg wavelength,  $\lambda_b$ , as shown in Fig. 4.1. The wavelength  $\lambda_b$ , is described by the Bragg condition:

$$\lambda_b = 2n_{\text{eff}}\Lambda \quad (4.1)$$

where  $n_{\text{eff}}$  is the mean effective refractive index at the location of the grating and  $\Lambda$  is the constant nominal period of the refractive index modulation (Hill and Meltz 1997).

The bandwidth  $\bar{\lambda}$  (distance between the two first minima) is given by:

$$\frac{\bar{\lambda}}{\lambda_b} = \frac{1}{n_{\text{eff}}} \sqrt{(\zeta \delta n_{\text{eff}})^2 + \left(\frac{\lambda_b}{L}\right)^2} \quad (4.2)$$

where  $L$  is the gauge length,  $\overline{\delta n_{eff}}$  is the mean induced change in  $n_{eff}$  and  $\zeta$  is the amplitude of the induced index change (Peters et al. 2001). An external load or temperature variation will change the effective index of refraction and/or the period of modulation; this will create a shift of the wavelength reflected peak from its original value.

## 4.2 Manufacturing Stage: Residual Stress Induced by Resin Shrinkage and Curing Process Control

The FBG sensors are an excellent choice to monitor the curing process of wind turbine blades, where their capability of surveying the curing process is combined with their capability to monitor strain and other features over the structure lifetime. Because the FBG sensor small size that makes them virtually non-intrusive to the structure, they can be embedded in the composite layers from the first manufacturing step.

This embedded sensor will monitor several parameters of the curing process: temperature of the resin, which enables a retro-feedback of temperature to the process controller; residual stress that are a big issue in the fatigue performance of the composite; resin flow, by measuring the position of dry spots in the laminate; etc. Additionally, the FBG sensor can be used as part of the process certification, by giving information about the curing profile of the structure, the residual stress, the load history during manufacturing, transport and installation.

### 4.2.1 Embedded FBG Response to Strain and Temperature Variation

Assuming a perfect strain transfer between an embedded FBG sensor and the host material, the wavelength shift,  $\Delta\lambda_b$ , under variation of strain in the longitudinal direction of the fibre optic,  $\varepsilon_1$ , and temperature,  $\Delta T$ , is given by Eq (4.3):

$$\frac{\Delta\lambda_b}{\lambda_b} = (1-p_e) \varepsilon_1 + [(1-p_e) (\alpha_s - \alpha_f) + \xi] \Delta T \quad (4.3)$$

The parameter  $p_e$  is the optical fibre photo-elastic coefficients,  $\alpha_s$  and  $\alpha_f$  are the thermal expansion coefficient of the host material and the optical fibre, respectively, and  $\xi$  is the thermos-optic coefficient (Magne et al. 1997). Figure 4.2 depicts a typical Fibre Bragg grating response.

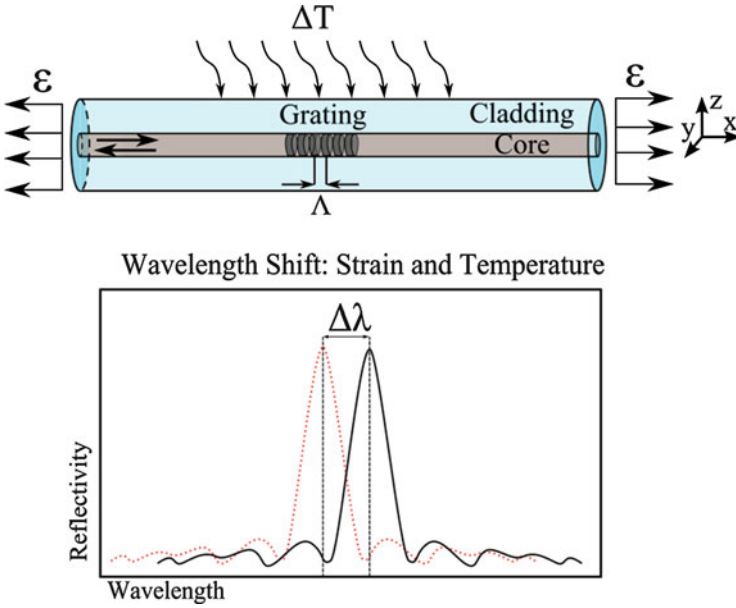


Fig. 4.2 Fibre Bragg grating response: strain and temperature variation

### 4.2.2 Residual Stress Measurement

Curing cycles are often defined on the basis of experience and economical aspects, missing the opportunity to improve curing cycles and blades, by understanding the physic-chemical process. Reducing the reaction time by increasing the temperature leads to a decrease in production time and consequent lower production cost. But this can lead to residual stress induced by the curing process, which causes worst mechanical properties and reduces the fatigue life of the structure. Equation (4.3) was rewritten to measure the residual stress caused by the material shrinkage:

$$\epsilon_{\text{shrinkage}} = \frac{\frac{\Delta\lambda_b}{\lambda_b} - \xi \Delta T}{1 - p_e} + \alpha_f \Delta T \tag{4.4}$$

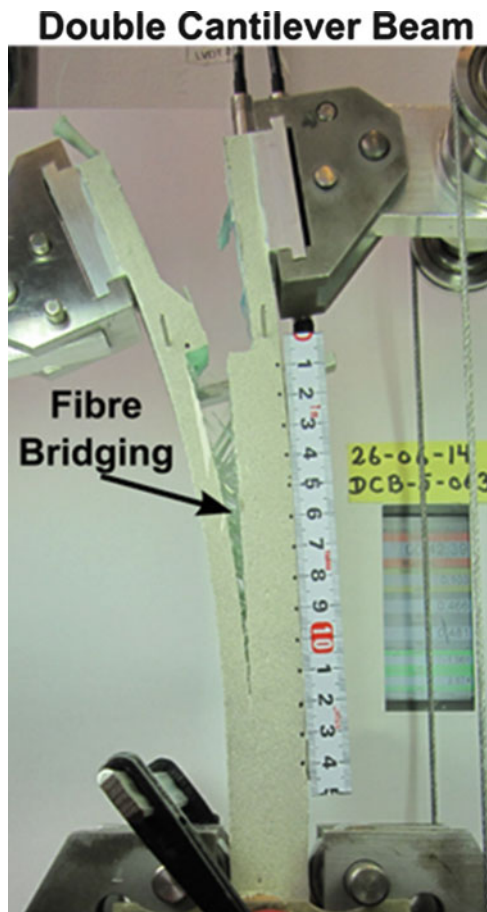
By measuring the temperature in the resin using a thermocouple, it is possible to decouple the temperature-strain cross sensitivity of the FGB and calculates the epoxy shrinkage.

### 4.3 Operation Stage: Crack Growth Detection by Embedded FBG Sensors

Often in fibre reinforced polymers (FRP), delamination is accompanied by the formation of a crack bridging zone, where intact fibres connect the crack faces behind the crack tip, as shown in Fig. 4.3. Thus, the energy required for the crack to propagate is higher than required to initiate. The relationships between the crack bridging stresses and the crack opening displacement (bridging laws) are used to describe the effect of fibres on the crack propagation (Sørensen 2010). The cracking in homogeneous isotropic materials usually occurs under pure Mode I (opening loading) but in weak planes or along interfaces, like in composite materials cracking, occurs under a combination of Modes (Shear and opening loading).

In order to detect delamination/crack in FRP materials the sensor/monitoring system need to track specific fracture features that only appear in the vicinities of the

**Fig. 4.3** Fibre bridging during delamination of a DCB specimen



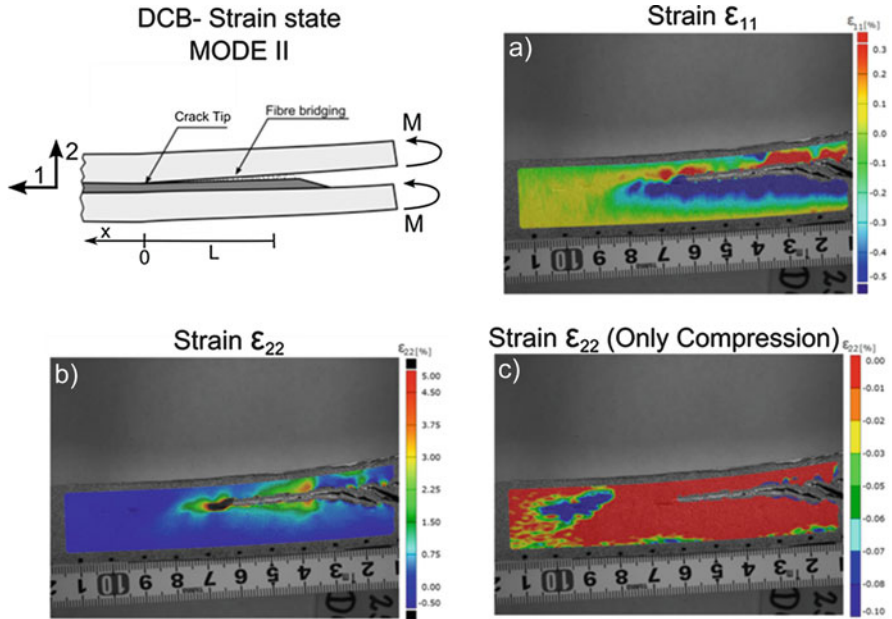


**Fig. 4.4** Strain distribution at the crack tip during Mode II fracture (Pereira et al. 2015)

crack, independent of geometry and loading conditions. Thus, to link these fracture features with the measured parameters, the strain distribution around a crack tip during delamination was analysed using Digital Image Correlation (DIC), as shown in Fig. 4.4 (Pereira et al. 2015). The DIC technique is a non-contact optical method that, by tracking changes in a random pattern on the specimen, can correlate it with deformation/strain of the material.

It is possible to divide the strain distribution in two distinct contributions: crack tip singularity/material damage and fibre bridging. Near the crack tip, the stress field closely approaches the singular stress field of linear elastic fracture mechanics. This means that the stress tends to infinity and has a fast variation (high gradient). Also, with the progression of the crack the material/structure losses stiffness increasing the strain, here it is possible to observe higher values of strain  $\epsilon_{11}$  at the crack faces, as showed in Fig. 4.4a. In the fibre bridging zone ( $L < x < 0$ ), a positive strain  $\epsilon_{22}$  was observed, due to the forces transferred by the fibre that are connecting the two crack faces, as shown in Fig. 4.4c. These forces are balanced by a compression stress that appears ahead of the crack tip ( $x > 0$ ), which creates a negative strain  $\epsilon_{22}$ , shown in Fig. 4.4c as a blue area.



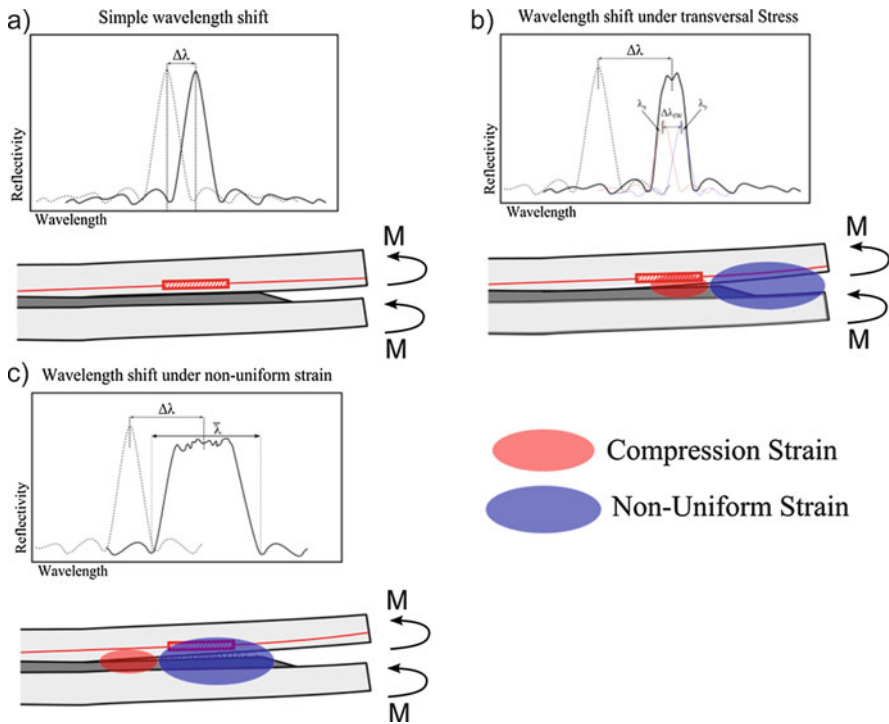


Fig. 4.5 Stages of the FBG response under a crack growth event

### 4.3.1 Crack/Delamination Detection by Embedded Fibre Bragg Gratings

As measured using DIC technique, during a crack/delamination event different fracture features will be present near the crack tip. Being able to identify and measure these specific phenomena with a FBG sensor is the key factor to correctly determine the presence of damage and its growth.

The three different stages of the FBG responses under a crack growth event are presented in Fig. 4.5. First, before the crack reaches the proximity of the grating (Fig. 4.5a), the material will build-up strain, that will create a uniform wavelength shift in the FBG reflected peak. Next, a compression field is formed ahead of the crack tip due to the formation of a crack bridging zone (Fig. 4.5b). When this compression field reaches the grating area it creates a peak splitting of the FBG response. Then, when the grating is near the influence of the crack singularity (Fig. 4.5c), a non-uniform strain field will also modify the shape of the reflected peak. After the crack passes the FBG sensor, the shape of the reflected peak will go back to the original shape, and the sensor response will again be a simple wavelength shift, because at this stage only uniform strains will be present at the FBG.

### 4.3.1.1 Embedded FBG Response: Strain

As mentioned before, the FBG response to strain and temperature variation can be described by Eq. (4.3). However, during crack growth the temperature variation can be neglected. The wavelength shift  $\Delta\lambda_b$  (Fig. 4.5a) is given by (4.5):

$$\frac{\Delta\lambda_b}{\lambda_b} = (1-p_e) \varepsilon_1 \quad (4.5)$$

### 4.3.1.2 Embedded FBG Response: Transverse Stress

The compression field formed ahead of the crack tip will reach the grating area, which will create a peak split of the FBG reflected signal (Fig. 4.5b). This peak split phenomenon is due to a birefringent effect, which can be defined as the change of the refractive index  $n_{eff}$  in the two directions  $n_{effy}$  and  $n_{effz}$ , when the grating is subjected to a transverse force (Sørensen et al. 2007; Jülich and Roths 2010). The increase in the width of the reflected peak,  $\Delta\lambda_{wv}$ , is given by Eq. (4.6):

$$\Delta\lambda_{wv} = 2\Lambda \left| \Delta n_{effy} - \Delta n_{effz} \right| = \frac{\Lambda n_0^3}{E_f} [(1-\nu_f) p_{12} - (1 + \nu_f) p_{11}] \left| \sigma_y - \sigma_z \right| \quad (4.6)$$

where  $\sigma_{y,z}$  is the transverse stress,  $E_f$  is the elastic modulus of the optical fibre,  $\nu_f$  is the Poisson's ration,  $n_0$  is the initial refractive index,  $p_{11}$  and  $p_{12}$  are the photo-elastic coefficients of the optical fibre.

### 4.3.1.3 Embedded FBG Response: Non-Uniform Strain

A non-uniform strain changes the periodicity of the grating pattern along the sensor length, modifying the grating pattern configuration from "uniform" to "chirped". As demonstrated by Peters et al. (2001), in a uniform grating the applied strain will induce a change in both grating period and the mean index. These two effects can be superimposed by applying an effective strain of " $(1 - p_e) \varepsilon_1(x)$ ". Then it is possible to rewrite the grating period as:

$$\Lambda(x) = \Lambda_0 [1 + (1-p_e) \varepsilon_x(x)] \quad (4.7)$$

where  $\Lambda_0$  is the grating period with zero strain. The non-uniform strain effect can be approximated by using the maximum and minimum strain values along the grating. So, the maximum grating period  $\Lambda_{max}$  and minimum  $\Lambda_{min}$  can be calculated using the Eq. (4.1). Thus, an approximated increase of the width of the reflected peak due to a non-uniform strain,  $\bar{\lambda}$ , is given by combining Eqs. (4.7) and (4.1):

$$\bar{\lambda} = 2n_{eff} [\Lambda_{max} - \Lambda_{min}] \quad (4.8)$$

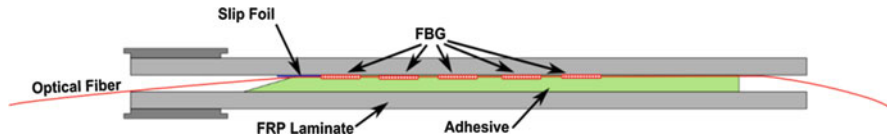


Fig. 4.6 DCB specimen geometry and FBG sensor array configuration

### 4.3.2 *Delamination Detection in Fibre Reinforced Polymer Specimen Using Embedded FBG Sensor: Material and Testing Procedure*

To validate the crack detection technique double cantilever beam (DCB) specimens were tested in a fracture testing machine, developed by Sørensen (2010). The DCB specimens were loaded with different combination of moments, giving different type of fracture modes that simulates different crack/delamination cases. The DCB specimens were manufactured using two FRP material arms, made of unidirectional and triaxial glass fibre layers (SAERTEX UD and TRIAX), with a layup stacking of : [90/+45/-45/04/04/+45/-45/90], glued by a commercial epoxy structural adhesive (Epikote MGS BPR 135G/Epikote MGS BPH137G). A thin slip foil was placed in the edge of the structural adhesive, to act as a pre-crack and ease crack initiation.

An array of 5 uncoated single mode (SM) FBG sensors, each with a length of 10 mm, was embedded in the interface of the composite material with the structural adhesive. The gratings array were spaced by 10 mm from each other, and the first grating was positioned 10 mm from the edge of the adhesive. In Fig. 4.6, the DCB specimen and FBG sensor array configuration is presented. The sensors were connected to an Optical Spectral Analyser (OSA) FS2200—Industrial BraggMETER from FiberSensingTM.

#### 4.3.2.1 **Experimental Results**

In Figs. 4.7 and 4.8, the strain distribution on the surface of the DCB specimen (left pictures) and the FBG sensor output (right picture), before and during the propagation of the crack/delamination are shown. Before the crack starts to propagate in the material, it is observed a build-up of strain caused by the increase of load. Once the crack start to grow, a compression field is formed ahead the crack tip due to the formation of a crack bridging zone. This compression stress area can be observed in Fig. 4.7 (in the top left image, the DIC measurement is shown as a blue spot). At the same time, a decrease in the material compliance due to the growth of the crack causes a rapid local increase of strain, creating a gradient of strain near the crack tip (non-uniform strain), which can be observed in Fig. 4.8 (the bottom left image depicts the DIC measurement).

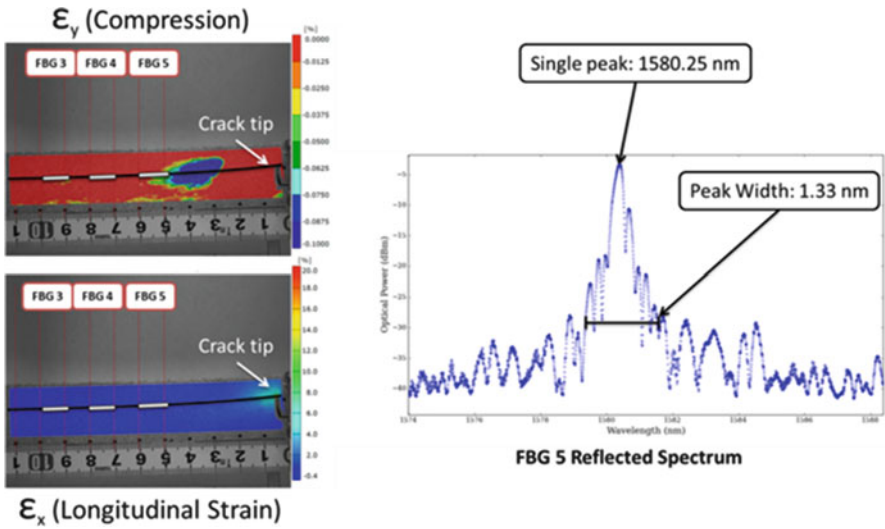


Fig. 4.7 FBG sensor output and DIC measurement before crack growth

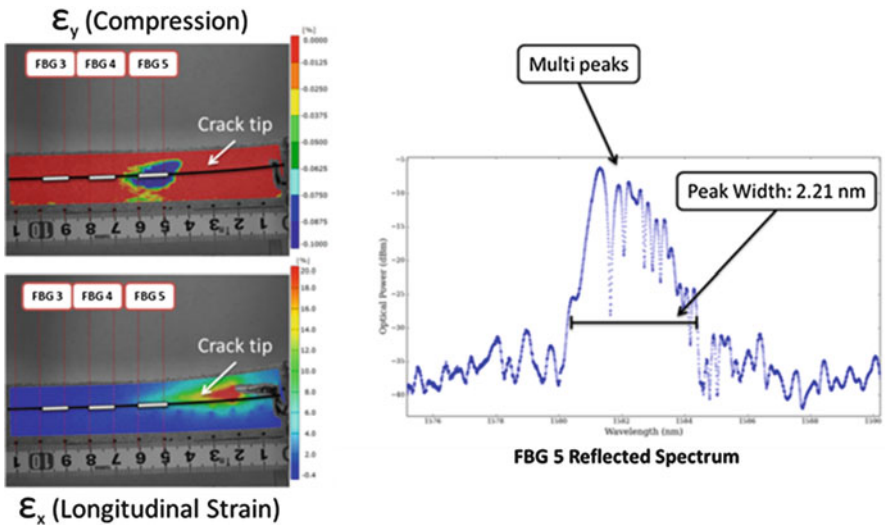


Fig. 4.8 FBG sensor output and DIC measurement during crack growth

The wavelength shift and peak width at  $-30$  dBm, computed from the output of the FBG array in three different loading conditions, it is presented in Fig. 4.9. The different colours plotted correspond to each Bragg grating in the sensor array. The FBG5 (Orange colour line) is the grating located closest to adhesive edge and the FBG1 (Black colour line) is the grating more distant. The crack growth in the order: FBG 5  $\rightarrow$  4  $\rightarrow$  3  $\rightarrow$  2  $\rightarrow$  1. The wavelength shift is dependent on the loading

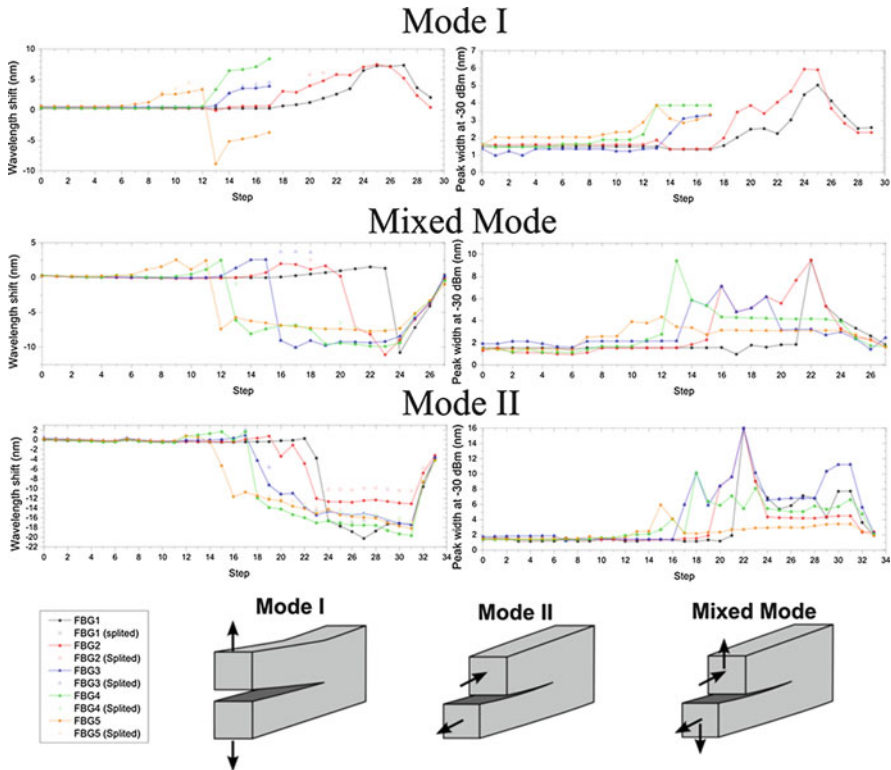


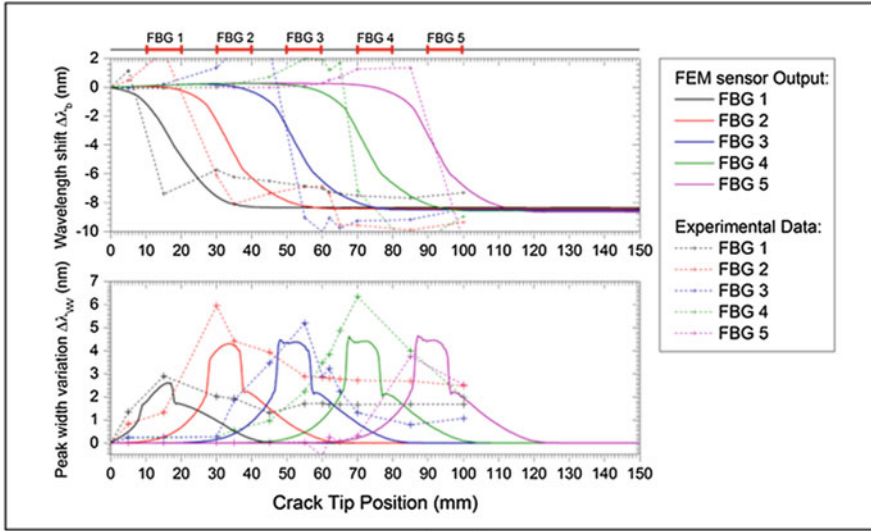
Fig. 4.9 Sensor array output during crack growth



type, but the increase in the width of the peak is related to the presence of the crack (Birefringent effect and non-uniform strain). Using this information it is possible to track the crack by measure an abrupt variation of the wavelength and/or increase in the width of the reflected peak.

### 4.4 Application of the FBG Crack Detection Method

By using this method it becomes possible to extract two types of information from the sensor: one type dependent of the loading and geometry,  $\epsilon_{zz}$ , which give information about the global strain/loading state of the structure; The other type,  $\epsilon_{zz}(z)$  and  $\sigma_{x,y}$ , independent and only affected by the proximity of a crack.

To demonstrate the applicability of this technique to other structures or materials, this monitoring method was implemented in a Finite Element Method (FEM) Model of the DCB specimen, which simulates the response of the FBG sensor during the process of the crack growth, as shown in Fig. 4.10.



**FBG Measurement**  **Model Prediction** 

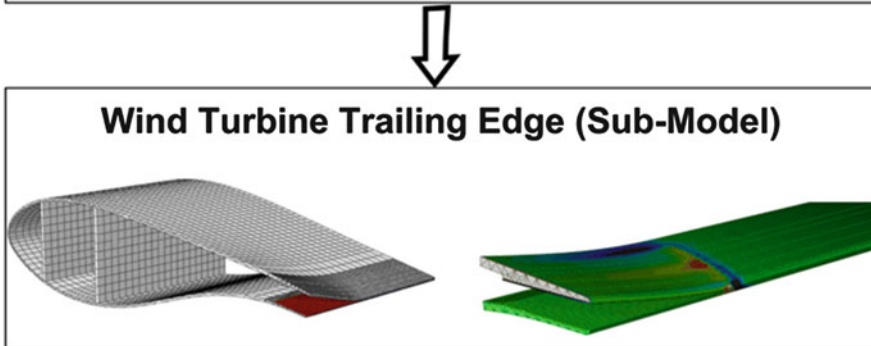
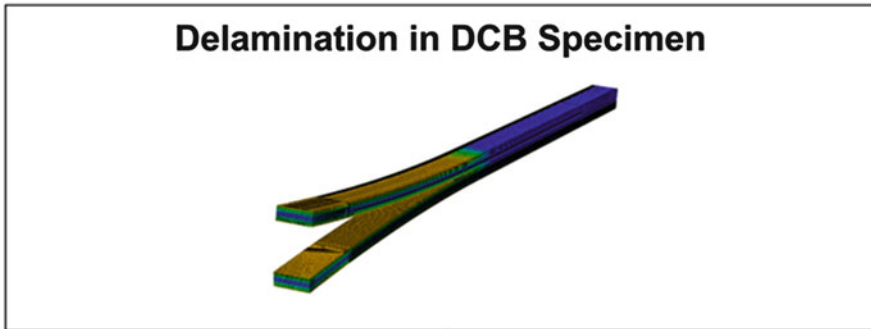


**Fig. 4.10** Application of the FBG crack detection method in a DCB specimen and Wind Turbine trailing edge

## 4.5 Fibre Bragg Grating as a Multi-Stage Structure Health Monitoring Sensor: Published Work

A compiled list of select references pertaining to Fibre Bragg grating sensors and their role in the monitoring structure health at multiple stages:

- Pereira G, Mikkelsen LP, McGugan M (forthcoming) Crack Detection in Fibre Reinforced Plastic Structures Using Embedded Fibre Bragg Grating Sensors: Theory, Model Development and Experimental Validation. Plos One
- Pereira G, Mikkelsen LP, McGugan M (forthcoming) Fibre Bragg Grating Sensor Signal Post-Processing Algorithm: Crack Growth Monitoring in Fibre Reinforced Plastic Structures. Springer Proc Phys
- Pereira G, Mikkelsen LP, McGugan M (2014) Damage tolerant design: failure and crack propagation in composites. In: Abstracts of the 10th EAWW PhD Seminar on Wind Energy in Europe. European Academy of Wind Energy, Orléans, 28–31 Oct 2014
- Pereira G, Mikkelsen LP, McGugan M (2014). FEM model of Embedded Fibre Bragg Grating Sensor Response: Crack Growing Detection. In: Abstracts of the NAFEMS NORDIC – Simulation Verification and Validation (V&V): A Key Enabler for Virtual Product Development, NAFEMS, Copenhagen, 3–4 November 2014
- Pereira G, Mikkelsen LP, McGugan M (2015) Crack Growth Monitoring by Embedded Optical Fibre Bragg Grating Sensors. In: Abstracts of the 3rd International Conference on Photonics, Optics and Laser Technology, Berlin, 13–15 March 2015
- Pereira G, Mikkelsen LP, McGugan M (2015) Embedded Fibre Bragg Grating Sensor Response Model: Crack Growing Detection in Fibre Reinforced Plastic Materials. In: DAMAS 2015. 11th International Conference on Damage Assessment of Structures, Ghent, August 2015. Journal of Physics: Conference Series, Vol 628. Institute of Physics, Temple Back, p 012115. doi:[10.1088/1742-6596/628/1/012115](https://doi.org/10.1088/1742-6596/628/1/012115)
- Pereira G, Mikkelsen LP, McGugan M (2015), Structural Health Monitoring Method for Wind Turbine Trailing Edge: Crack Growth Detection Using Fibre Bragg Grating Sensor Embedded in Composite Materials. Paper presented at the 20th International Conference on Composite Materials, ICCM20, Copenhagen, 19–24 July 2015

**Open Access** This chapter is distributed under the terms of the Creative Commons Attribution-NonCommercial 4.0 International License (<http://creativecommons.org/licenses/by-nc/4.0/>), which permits any noncommercial use, duplication, adaptation, distribution and reproduction in any medium or format, as long as you give appropriate credit to the original author(s) and the source, provide a link to the Creative Commons license and indicate if changes were made.

The images or other third party material in this chapter are included in the work's Creative Commons license, unless indicated otherwise in the credit line; if such material is not included in the work's Creative Commons license and the respective action is not permitted by statutory

regulation, users will need to obtain permission from the license holder to duplicate, adapt or reproduce the material.

## References

- Hill KO, Meltz G (1997) Fiber Bragg grating technology fundamentals and overview. *J Lightwave Technol* 15(8):1263–1276
- Jülich F, Roths J (2010) Comparison of transverse load sensitivities of fibre Bragg gratings in different types of optical fibres. In: Berghmans F, Mignani AG, van Hoof CA (eds) *Optical sensing and detection*. SPIE, Brussels, May 2010. SPIE proceedings, vol 7726. SPIE, Washington. doi:[10.1117/12.854019](https://doi.org/10.1117/12.854019)
- Magne S, Rougeault S, Vilela M et al (1997) State-of-strain evaluation with fiber Bragg grating rosettes: application to discrimination between strain and temperature effects in fiber sensors. *Appl Optics* 36:9437–9447. doi:[10.1364/AO.36.009437](https://doi.org/10.1364/AO.36.009437)
- Pereira G, Mikkelsen LP, McGugan M (2015) Embedded fibre Bragg grating sensor response model: crack growing detection in fibre reinforced plastic materials, 2015 In: DAMAS 2015. 11th International conference on damage assessment of structures, Ghent, August 2015. *Journal of Physics: Conference Series*, Vol 628. Institute of Physics, Temple Back, p 012115. doi:[10.1088/1742-6596/628/1/012115](https://doi.org/10.1088/1742-6596/628/1/012115)
- Peters K, Studer M, Botsis J et al (2001) Embedded optical fiber Bragg grating sensor in a nonuniform strain field: measurements and simulations. *Exp Mech* 41(1):19–28
- Sørensen L (2010) Cohesive laws for assessment of materials failure: Theory, experimental methods and application. Dissertation, Technical University of Denmark
- Sørensen L, Botsis J, Gmür T et al (2007) Delamination detection and characterisation of bridging tractions using long FBG optical sensors. *Compos Part A Appl Sci Manuf* 38(10):2087–2096



# Chapter 5

## Analysis and Design of Bend-Twist Coupled Wind Turbine Blades

Alexander R. Ståblein

**Abstract** Bend-twist coupling allows wind turbine blades to self-alleviate sudden inflow changes, as in gusty or turbulent conditions, resulting in reduced ultimate and fatigue loads. If the coupling is introduced by changing the fibre direction of the anisotropic blade material, the assumptions of classical beam theory are not necessarily valid. This chapter reviews the effects of anisotropic material on the structural response of beams and identifies those relevant for wind turbine blade analysis. A framework suitable for the structural analysis of wind turbine blades is proposed and guidance for the design of bend-twist coupled blades is given.

### 5.1 Introduction

Bend-twist coupling (BTC) is used to improve the aeroelastic response of wind turbine blades. As the name suggests, BTC creates a coupling between bending and twist of the blade. The coupling links the aerodynamic forces, which induce bending in the blade, with the twist of the blade. The twist of the blade in turn changes the angle of attack and thereby the aerodynamic forces. This feedback loop, when twisting towards a lower angle of attack, enables the blade to self-alleviate sudden inflow changes, as in gusty or turbulent conditions, leading to a reduction in ultimate and fatigue loads. The aeroelastic response of a bend-twist coupled blade section is illustrated in Fig. 5.1. When subjected to a sudden increase in inflow velocity  $\Delta W$  the lift force increases and the blade deflects until the elastic forces  $\Delta F$  are in equilibrium with the increased lift  $\Delta L$  at deflection  $\Delta u$ , shown in the middle of the figure. For a blade section twisting to feather as shown on the left, the angle of attack reduces by  $\Delta\alpha$ . A lower angle of attack results in a reduced lift increase  $\Delta L - \rho W^2 c\pi \Delta\alpha$  and smaller blade deflections  $\Delta u_f < \Delta u$  are required to obtain force equilibrium. For a blade section twisting to stall as shown on the right, the angle of attack increases and with it the lift force  $\Delta L + \rho W^2 c\pi \Delta\alpha$  resulting in larger deflections  $\Delta u_s > \Delta u$  to obtain equilibrium. As BTC intends to reduce the

---

A.R. Ståblein (✉)  
Department of Wind Energy, Technical University of Denmark (DTU), DTU Risø Campus,  
Frederiksborgvej 399, 4000 Roskilde, Denmark  
e-mail: [alsta@dtu.dk](mailto:alsta@dtu.dk)

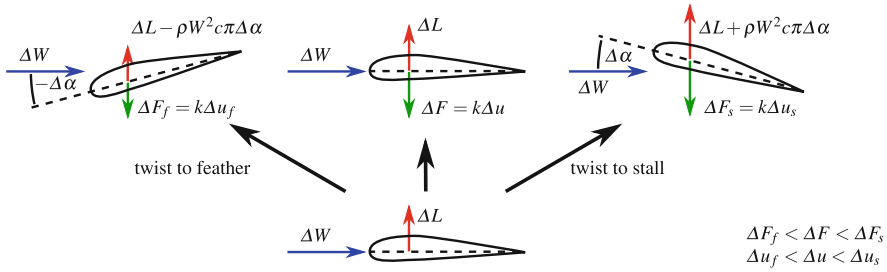


**Fig. 5.1** Aeroelastic response to a sudden change in inflow velocity  $\Delta W$  of a bend-twist to feather coupled (*left*), uncoupled (*middle*) and bend-twist to stall coupled (*right*) blade section

aerodynamic loads on the blade, the coupling is designed to twist towards a lower angle of attack (twist to feather) for modern, pitch regulated wind turbines.

BTC can be achieved by either sweeping the planform of the blade (geometric coupling) which induces additional torsion when the blade is loaded, or by changing the fibre direction of the blade material (material coupling) in the spar caps and/or skin of the blade. The change in fibre direction results in coupling of the normal and shear stresses on lamina level which can be used to induce bend-twist coupling in the cross-section of the beam. The effects resulting from this anisotropic material behaviour are not representable with conventional Euler-Bernoulli or Timoshenko beam theory. This chapter reviews the effects of anisotropic material on the structural response of beams and identifies those relevant for wind turbine blade analysis. A framework suitable for the structural analysis of wind turbine blades is subsequently proposed. The cross-sectional properties of anisotropic beams are discussed and related to classical beam properties. And a Timoshenko beam element for fully coupled cross-sectional stiffness matrices is presented. The next section provides guidance on the design of bend-twist coupled blades and presents a pre-twisting procedure to reduce the power loss associated with coupled blades. To maintain stiffness (e.g. for tower clearance), the blade regions where coupling is most efficiently applied are also identified.

## 5.2 Analysis of Anisotropic Beams

The analysis of fibre-reinforced polymer (FRP) beams is complex due to the anisotropic properties of the composite material. FRP usually consists of glass or carbon fibres that are embedded in a polymer matrix. Due to the different material properties of fibres and matrix, the longitudinal and transverse stiffness of a FRP ply can differ by several orders of magnitude. A considerable amount of papers have been published on the analysis of anisotropic composite beams. Reviews of those literature is provided by e.g. Hodges (1990b) and Jung et al. (1999). This section provides an overview of the behaviour of composite beams and identifies the

effects that are relevant for wind turbine blade analysis. A framework suitable for the analysis of wind turbine blades is proposed, consisting of cross-section analysis, beam element and co-rotational formulation. The cross-sectional properties of an anisotropic beam are discussed and related to classical beam properties, elastic and shear centre and principle axes. Finally, a Timoshenko beam element for anisotropic beams is presented.

### ***5.2.1 Structural Properties of Anisotropic Beams***

Euler-Bernoulli is considered the most fundamental beam formulation. It allows for bending about the two principle axes of the cross-section and extension along the beam axis. It assumes that the cross-section plane remains plane after deformation (i.e. no warping) and perpendicular to the elastic axis of the beam (no shear deformation). The Euler-Bernoulli theory is deemed valid for the static analysis of long, slender beams and the dynamic analysis of lower modes.

#### **5.2.1.1 Shear Deformations**

The beam formulation by Timoshenko (1921) allows for transverse shear deformations by dropping the assumption of a cross-section plane that is perpendicular to the beam axis. The ‘plane sections remain plane’ assumption is maintained. The Timoshenko formulation gives better results for short, stocky beams and the dynamic analysis of higher modes where the wavelength approaches the thickness of the beam. For composite beams, Chandra and Chopra (1992) separate the shear effect into two categories: a direct effect due to the shear stiffness of the section (i.e. Timoshenko) and an effect via shear-related coupling. Smith and Chopra (1991) and Jung et al. (1999) suggest that transverse shear deformations cannot be neglected in composite beams, particularly when coupling is present. Smith and Chopra report that bending-shear coupling reduces the effective bending stiffness of a strongly coupled box-beam by more than 30%. Volovoi et al. (2001) on the other hand claim that correct deformations can also be obtained with an Euler-Bernoulli formulation if shear deformations are considered correctly when calculating the cross-sectional stiffness. However, in an earlier publication (Rehfield et al. 1990) one of the authors concludes that the direct shear flexibility term may not be negligible and that bending-shear coupling must be present in any general-purpose analysis of composite beams. Cortínez and Piovan (2002) suggest that the shear effect is more important for composite than for isotropic beams due to the high ratio between the longitudinal and transverse modulus of elasticity. Their results show that the shear deformations have a significant effect even on the first frequency of a slender uncoupled composite beam.

### 5.2.1.2 Torsional Warping

The Euler-Bernoulli and Timoshenko beam theories can be extended by St. Venant's torsion. St. Venant's torsion theory assumes that out-of-plane warping is unrestrained and therefore does not cause axial stress in the section. The free warping assumption is deemed valid for closed sections where torsional warping contributes little to the normal stresses or when warping is unrestrained by e.g. supports. Vlasov's torsion theory allows to restrain the torsional warping by introducing an additional degree of freedom along the beam. The restrained warping can cause significant stresses in the beam direction, in particular for open cross-sections (i.e. I-beams). Chandra and Chopra (1992) show that constrained warping has a stronger influence on the torsional stiffness of composite I-beams than isotropic I-beams. For the closed cross-section beams in their study the constrained warping effect is not important. Rehfield et al. (1990) relate the effect of restrained warping to the decay length which can be split into a material and a geometric part. The geometric part is mainly influenced by the slenderness of the beam. The material part depends on the axial and transverse stiffness and on how much they are coupled. Rehfield et al. (1990) conclude that an additional variable for warping would be important for certain laminated structures. The work of Smith and Chopra (1991) suggests that restrained warping along the beam can have a significant influence on coupled composite beams with closed sections. However, they assume that locally restrained warping is negligible for 'very slender' beams. The results of Cortínez and Piovan (2002) show that torsional warping has a great influence on the vibration and stability behaviour of open sections but it is negligible for closed sections.

### 5.2.1.3 General Warping

So far, the effects of out-of-plane warping due to transverse shear and in-plane warping have not been considered. Attempts to include those in an analytical solution are made by Smith and Chopra (1991) who introduce the concept of zero net in-plane forces and moments into the constitutive relations of the cross-section. Their results show that load deflection for an anti-symmetric box beam is altered by 30–100 % if in-plane warping is not accounted for. A general approach to calculate the properties of arbitrary cross-sections of anisotropic material is proposed by Giavotto et al. (1983). The formulation invokes the virtual work per unit beam length to obtain a linear system of second-order differential equations with constant coefficients that have a homogeneous and particular solution. The particular (or central) solution is used to determine a  $6 \times 6$  cross-section stiffness matrix while the homogeneous (or extremity) solution, which is related to warping, is generally ignored. Hodges (1990b) suggests to use the homogeneous solutions to introduce additional degrees of freedom to account for restrained warping at the end of the blade. Another general approach for calculating the cross-section stiffness matrix is proposed by Cesnik and Hodges (1997). The formulation is based on the variational-asymptotic method by Berdichevskii (1979).

#### 5.2.1.4 Superelements

An approach that avoids some of the conjectures of beam analysis is the use of superelements by static condensation. The concept originated from aerospace engineering in the early 1960s (Guyan 1965). Superelements are created by reducing the structural degrees of freedom (static condensation) of a higher fidelity model, often comprised of shell and/or solid elements. While the process of static condensation is reasonably straightforward, due attention must be given to the interpolation function if the many degrees of freedom of a beam cross-section are to be reduced to a single node to obtain beam like elements.

#### 5.2.1.5 Large Displacements

Using non-linear finite element methods, various approaches exist to model a beam undergoing large displacements. Bathe and Bolourchi (1979) present an updated and a total Lagrangian degenerate beam formulation. Variational formulations, where the beam strains are derived from internal virtual work, are proposed by e.g. Simo and Vu-Quoc (1986) and Cardona and Geradin (1988). A further approach is the co-rotational formulation (Crisfield 1990; Battini and Pacoste 2002) that separates rigid body motions from local deformations. The separation is achieved by introducing a local coordinate frame that follows the rigid body motions of the element. Within the local frame (at element level) small displacements and strains are assumed. The method therefore allows to use existing elements (or superelements), which are not able to represent large displacements, in a geometrical non-linear analysis. The co-rotational approach is not restricted to beam elements but also applicable to shell and continuous elements.

The above beam formulations generally assume isotropic material properties. For the large displacement analysis of anisotropic beams, the theory of Giavotto et al. (1983) is extended by Borri and Merlini (1986) to allow for finite strains. Hodges (1990a) presents a mixed variational formulation for the large displacement analysis of anisotropic beams. Kim et al. (2013) present a beam element assuming polynomial shape functions of arbitrary order where the shape function coefficients are eliminated by minimizing the elastic energy of the beam. The element by Stäblein and Hansen (2016) is an extension of a Timoshenko beam element by Bazoune et al. (2003) to allow for the analysis of anisotropic cross-sectional properties. The formulations by Kim et al. (2013) and Stäblein and Hansen (2016) assume small displacements and are intended for the application in a co-rotational or multibody formulation.

#### 5.2.1.6 Wind Turbine Blade Analysis

Wind turbine blades are made of anisotropic material and have a closed cross-section. Previous research indicates that the analysis of blades should therefore consider shear deformations and general warping as those effects have a

considerable influence on the response of anisotropic beams. Restrained warping is less important for closed cross-sections, which also applies for anisotropic beams, and can therefore be neglected. Wind turbine blades are subjected to large displacements ( $w/l = 0.14$  for the DTU 10 MW Reference Wind Turbine (DTU 10 MW RWT) (Bak et al. 2013)) and rotations, geometrical non-linear effects should therefore be considered in the analysis. A suitable framework for the analysis of wind turbine blades could be comprised of a cross-section analysis that considers general warping and the coupling effects from the anisotropic material (Giavotto et al. 1983; Borri and Merlini 1986), and a beam element formulation which allows for anisotropic cross-sectional properties and large displacements, either through its formulation (Borri and Merlini 1986; Hodges 1990a) or by embedding it in a co-rotational or multibody formulation (Kim et al. 2013; Stablein and Hansen 2016).

### 5.2.2 Anisotropic Cross-Sectional Properties

The analysis framework for wind turbine blades proposed above comprises the calculation of anisotropic cross-sectional properties. Those properties are usually expressed in a  $6 \times 6$  cross-sectional stiffness matrix, the entries of which are briefly discussed below.

A Cartesian coordinate system as shown in Fig. 5.2 is assumed for the cross-section. The beam axis  $x$  is normal to the cross-sectional plane which is defined by axes  $y$  and  $z$ . Displacements and rotations are denoted  $u_i$  and  $\theta_i$ , and forces and moments are  $F_i$  and  $M_i$ . The indices  $i \in \{x, y, z\}$  are used to indicate the direction or rotation axis. By introducing the cross-sectional stiffness matrix

$$\mathbf{K}_{cs} = \begin{bmatrix} K_{11} & K_{12} & K_{13} & K_{14} & K_{15} & K_{16} \\ & K_{22} & K_{23} & K_{24} & K_{25} & K_{26} \\ & & K_{33} & K_{34} & K_{35} & K_{36} \\ & & & K_{44} & K_{45} & K_{46} \\ \text{sym.} & & & & K_{55} & K_{56} \\ & & & & & K_{66} \end{bmatrix}, \quad (5.1)$$

the beam strain vector

$$\boldsymbol{\varepsilon} = \{u'_x, u'_y - \theta_z, u'_z + \theta_y, \theta'_x, \theta'_y, \theta'_z\}^T, \quad (5.2)$$

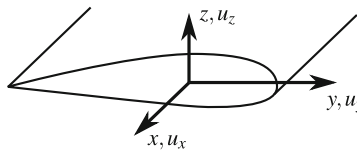


Fig. 5.2 Coordinate system of blade cross-section

where  $u_i$  and  $\theta_i$  are the displacements and rotations of the beam axis and  $( )'$  are derivatives with respect to  $x$ , and the vector of the cross-sectional forces and moments

$$\mathbf{F} = \{F_x, F_y, F_z, M_x, M_y, M_z\}^T, \quad (5.3)$$

the cross-sectional constitutive relation can be written as

$$\mathbf{K}_{cs}\mathbf{e} = \mathbf{F}. \quad (5.4)$$

For an isotropic and symmetric beam the diagonal entries  $K_{jj}$  for  $j \in \{1, \dots, 6\}$  of the cross-sectional stiffness matrix represent the classical beam properties

$$\begin{aligned} K_{11} &= EA & K_{44} &= GJ \\ K_{22} &= k_y GA & K_{55} &= EI_y \\ K_{33} &= k_z GA & K_{66} &= EI_z \end{aligned} \quad (5.5)$$

where  $E$  and  $G$  are elastic and shear modulus of the material,  $A$  is the area,  $I_y$  and  $I_z$  are the second moments of area, and  $J$  is the torsion constant of the cross-section. The Timoshenko shear coefficients are  $k_y$  and  $k_z$ . Entries  $K_{15}$  and  $K_{16}$  of the cross-sectional stiffness matrix are related to the elastic centre  $(y_e, z_e)$  which is defined as the point through which the normal force does not induce bending:

$$y_e = -\frac{K_{16}}{K_{11}}, \quad z_e = \frac{K_{15}}{K_{11}} \quad (5.6)$$

Entries  $K_{24}$  and  $K_{34}$  of the cross-sectional stiffness matrix are related to the shear centre  $(y_s, z_s)$  which is defined as the point through which the shear force resultant does not induce twist:

$$y_s = \frac{K_{34}}{K_{33}}, \quad z_s = -\frac{K_{24}}{K_{22}} \quad (5.7)$$

Entry  $K_{56}$  of the stiffness matrix is related to the angle  $\beta$  between the current axes and the principle axes which are defined as the axes where the moments of area are maximum and minimum and the product moment of area is zero. To obtain the angle  $\beta$  between the current axes and the principle axes, one of the eigenvectors  $\mathbf{v} = \{v_1, v_2\}^T$  of the sub-matrix  $\begin{bmatrix} K_{55} & K_{56} \\ K_{56} & K_{66} \end{bmatrix}$  has to be determined. The angle  $\beta$  is then obtained from:

$$\beta = \arctan\left(\frac{v_2}{v_1}\right) \quad (5.8)$$

Entries  $K_{45}$  and  $K_{46}$  are associated with bend-twist coupling. Lobitz and Veers (1998) propose a coupling coefficient  $\gamma$  as a measure of bend-twist coupling:

$$K_{45/46} = \gamma \sqrt{K_{44}K_{55/66}}, \quad -1 < \gamma < 1 \quad (5.9)$$

The theoretical limit of  $|\gamma| < 1$  results from the requirement of a positive definite stiffness matrix. In a realistic setting values up to 0.2–0.4 are deemed achievable for wind turbine blades (Capellaro and Kuhn, 2010; Fedorov and Berggren, 2014).

The remaining entries are  $K_{23}$  which is related to coupling between the shear forces and is usually non-zero for anisotropic beams. Entries  $K_{12}$  and  $K_{13}$ , which should be expected non-zero if bend-twist coupling is present. And  $K_{14}$  which is related to extension-twist coupling. Extension-twist coupling will most probably also cause  $K_{25}$ ,  $K_{26}$ ,  $K_{35}$  and  $K_{36}$  to be non-zero.

### 5.2.3 Timoshenko Beam Element with Anisotropic Cross-Sectional Properties

The anisotropic cross-sectional properties discussed in the previous section require a beam element formulation that accounts for all possible couplings between the cross-sectional forces. One such formulation is the two-noded, three-dimensional Timoshenko beam element proposed by Stablein and Hansen (2016). The element is an extension of the formulation by Bazoune et al. (2003) to account for fully coupled cross-sectional properties.

The origin of the element coordinate frame is assumed at the first node of the element. The  $x$  axis points towards the second node and axes  $y$  and  $z$  define the cross-sectional plane of the beam as shown in Fig. 5.2. The lateral displacements along the beam axis  $u_x$ , and in the cross-sectional plane  $u_y$  and  $u_z$  are expressed as functions of the coordinate  $x$  along the beam length  $L$ . A first order polynomial is assumed for  $u_x$  and third order polynomials are assumed for  $u_y$  and  $u_z$ :

$$u_x(x) = c_1x + c_2 \quad (5.10)$$

$$u_y(x) = c_3x^3 + c_4x^2 + c_5x + c_6 \quad (5.11)$$

$$u_z(x) = c_7x^3 + c_8x^2 + c_9x + c_{10} \quad (5.12)$$

The torsional displacements are expressed by a first order polynomial:

$$\theta_x(x) = c_{11}x + c_{12} \quad (5.13)$$

Timoshenko's assumption that the curvature of the beam equals the slope plus a contribution from shear deformation is used to define the rotational displacements



$\theta_y$  and  $\theta_z$  around the beams cross-sectional axes:

$$\theta_y(x) = -u'_z + c_{13} \quad (5.14)$$

$$\theta_z(x) = u'_y - c_{14} \quad (5.15)$$

In the equations above  $c_k$  for  $k \in \{1, \dots, 14\}$  are shape function coefficients. The 14 coefficients are eliminated by introducing two equilibrium equations of the shear force and bending moment relationship:

$$M'_y - F_z = 0, \quad M'_z + F_y = 0 \quad (5.16)$$

and 12 compatibility conditions (6 nodal displacements + 6 nodal rotations) at the element boundaries  $x = 0, L$ . With the displacements and rotations along the element determined, the elastic energy of the beam is calculated from:

$$V = \frac{1}{2} \int_0^L \boldsymbol{\varepsilon}^T \mathbf{K}_{cs} \boldsymbol{\varepsilon} dx \quad (5.17)$$

The element stiffness  $\mathbf{K}_{el}$  is finally obtained by creating the Hessian of the elastic energy  $V$  with respect to the nodal degrees of freedom. The matrix notation of the beam element for implementation in a finite element code is presented in the original publication (Ståblein and Hansen 2016). A Python implementation of the beam element in a three-dimensional co-rotational formulation is available on Git Hub. [https://github.com/alxrs/eccomas\\_2016.git](https://github.com/alxrs/eccomas_2016.git)

### 5.3 Design of Bend-Twist Coupled Blades

Bend-twist coupling intends to reduce the fatigue load of wind turbine blades. Fatigue load alleviation between 10 and 20 % have been observed in previous studies (Lobitz and Veers 2003; Verelst and Larsen 2010). While the load reduction is desired, bend-twist coupling is also associated with a reduction in energy production (Lobitz and Laino 1999; Verelst and Larsen 2010; Bottasso et al. 2013). The reduced energy yield is associated with a no longer optimal twist distribution along the blade. The twist distribution is typically designed to maximize power at a specific tip-speed ratio. For bend-twist coupled blades, however, the twist distribution depends on the bending in the blade which increases with the thrust between cut-in and rated wind speed. Figure 5.3 shows the power and thrust of the DTU 10 MW RWT (Bak et al. 2013) over its operational range. The thrust increases nearly linearly between cut-in at 4 m/s and rated at 12 m/s. With the twist distribution dependant on wind speed it

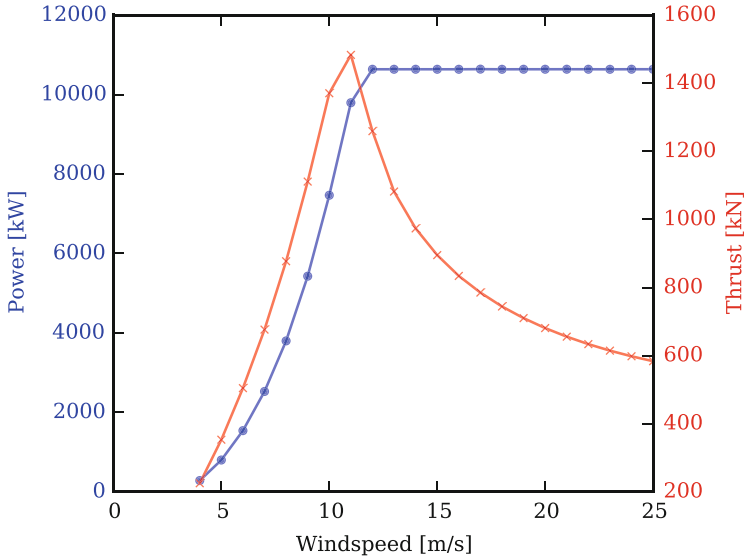


**Fig. 5.3** Power and thrust curve of the DTU 10 MW RWT over the operational range

is no longer possible to design the blade for a specific tip-speed ratio. There are two approaches to deal with the non-optimal twist:

- (1) Determine the optimal blade twist distribution for a tip-speed ratio (as for uncoupled blades). Choose a reference wind speed at which the twist distribution of the coupled blade should be optimal. Determine the pre-twist of the undeformed blade to match the optimal twist distribution under the aerodynamic load at reference speed.

The procedure ensures that the twist is optimal for the reference speed. Away from the reference speed the twist distribution will deteriorate. However, the blade can be pitched to improve the energy yield in those regions. The reference speed for pre-twisting is chosen to maximize annual energy production which depends on the wind speed distribution of the site. A pre-twisting procedure for linear blade deflections is proposed by Lobitz and Veers (2003) and extended to non-linear blade deflections by Stablein et al. (2016). The latter show that pre-twisting significantly reduces the power loss in annual energy production of the DTU 10 MW RWT.

- (2) Optimize the twist, and probably also the chord, distribution of the coupled blade for a given wind speed distribution. The tip-speed ratio might also be considered an optimization variable. To the authors knowledge there has not been a study that pursued this approach.

In the following, the pre-twist procedure presented by Stablein et al. (2016) is revisited. As a constant coupling coefficient is applied along the length of the blade,

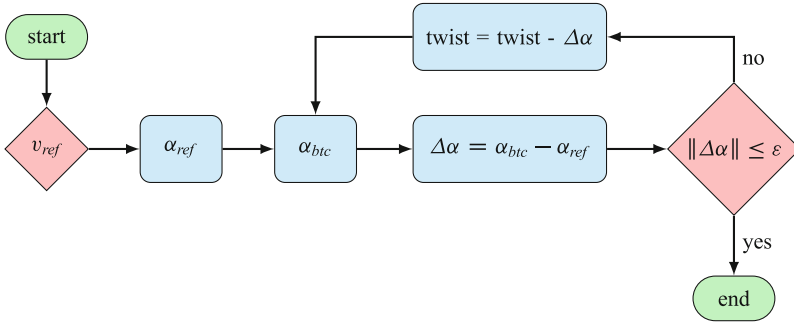
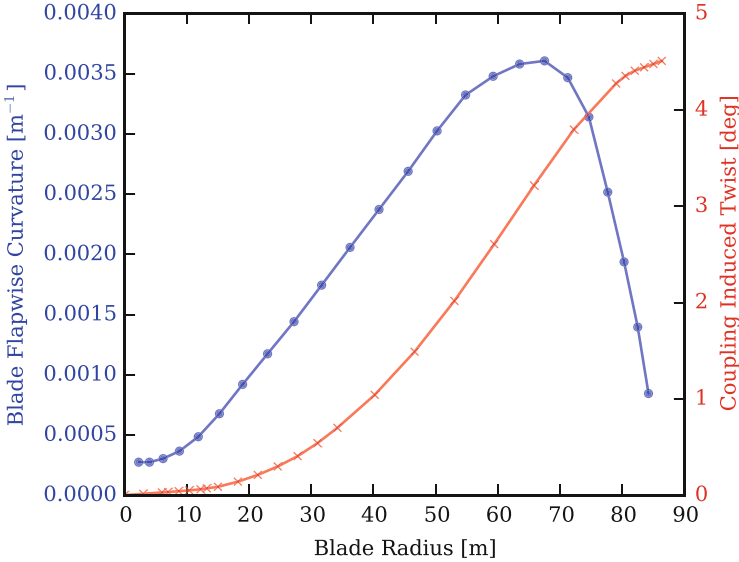


Fig. 5.4 Flowchart of the pre-twisting procedure presented by Stablein et al. (2016)

the resulting pre-twist distribution provides a good indication of the blade regions where coupling is most efficient.

### 5.3.1 Pre-Twisting Procedure

Pre-twisting adjusts the structural twist of a coupled blade in an iterative procedure to provide the same angle of attack along the blade as the uncoupled blade for a given reference wind speed. The first step is to calculate the steady state angle of attack along the uncoupled  $\alpha_{ref}$  and coupled blade  $\alpha_{btc}$  at the reference wind speed  $v_{ref}$ . The angle of attack is chosen as a reference as it results in the same aerodynamic state, irrespective of the blade twist which is not uniquely defined for large displacements and rotations. The difference between the angles of attack  $\Delta\alpha$  is then imposed on the coupled blade as a pre-twist. Both steps are repeated until the angle of attack along the uncoupled and coupled blade are identical at the reference speed. A flowchart of the procedure is shown in Fig. 5.4. The power curve is further improved by recalculating the optimal pitch angle over the operational range of the turbine. Pre-twisting results in an identical angle of attack along the blade at the reference wind speed  $v_{ref}$ . Below the reference speed, the thrust on the blade is lower which results in reduced bending and consequently less coupling induced twist. The blade therefore has a higher angle of attack slope along the blade as the blade twists towards stall. In this region, it is important to consider the angle of attack limit when determining the optimal pitch angle in order to avoid flow separation. Above the reference speed, where thrust is larger, the coupling will result in a lower angle of attack slope along the blade as the blade twists towards feather.



**Fig. 5.5** Blade flapwise curvature and coupling induced twist at 8 m/s wind speed (Stablein et al. 2016)

### 5.3.2 Coupling Distribution

If bend-twist coupling is introduced by utilising the anisotropic properties of the blade material, the change in fibre direction in the spar caps and/or skin of the blade results in a reduced bending stiffness. Previous studies (Fedorov and Berggreen 2014) have shown that coupling reduces the bending stiffness of the blade by 30–35 % when no material is added. As the tower clearance of the blade tip is often a governing design criteria a loss in stiffness is undesirable and it is advisable to introduce the coupling only in blade regions where it is most efficient. Figure 5.5 shows the coupling induced twist and the flapwise curvature at 8 m/s reference speed for the DTU 10MW RWT with a constant flap-twist to feather coupling coefficient of 0.2 along the blade. It can be seen that the curvature correlates with the slope of the induced twist. The relationship can also be shown by reducing the cross-sectional constitutive relation (5.4) to flapwise moment and torsion. Assuming torsion to be zero, a linear relationship between curvature and twist rate can be established:

$$\begin{bmatrix} K_{44} & K_{45} \\ K_{45} & K_{55} \end{bmatrix} \begin{Bmatrix} \theta'_x \\ -u''_z \end{Bmatrix} = \begin{Bmatrix} 0 \\ M_y \end{Bmatrix} \Rightarrow \theta'_x = \frac{K_{45}}{K_{44}} u''_z \quad (5.18)$$

Returning to Fig. 5.5, the curvature-twist relationship shows that, for the DTU 10MW RWT, coupling is most efficient in the outer half of the blade. A similar

observation is also made by Bottasso et al. (2013) who show that partially coupled blades exhibit a similar load alleviation performance as fully coupled blades.

## 5.4 Summary

Bend-twist coupling is a proven technique to reduce the fatigue loads of wind turbine blades. If the coupling is introduced by changing the fibre direction of the anisotropic blade material, it is important to account for the effects the material has on the structural response of the blade. Previous research indicates that shear deformations, general warping and the geometric non-linearity from large displacements need to be considered. An analysis framework that includes all those effects, consisting of cross-section analysis, beam element and co-rotational formulation, has been presented in this chapter. When designing bend-twist coupled blades, pre-twisting can be used to reduce the power loss associated with the coupling. To maintain blade stiffness for tower clearance while utilizing the load alleviation potential of coupled blades, the coupling should only be introduced in regions with high curvature as this is where it is most efficient.

**Open Access** This chapter is distributed under the terms of the Creative Commons Attribution-NonCommercial 4.0 International License (<http://creativecommons.org/licenses/by-nc/4.0/>), which permits any noncommercial use, duplication, adaptation, distribution and reproduction in any medium or format, as long as you give appropriate credit to the original author(s) and the source, provide a link to the Creative Commons license and indicate if changes were made.

The images or other third party material in this chapter are included in the work's Creative Commons license, unless indicated otherwise in the credit line; if such material is not included in the work's Creative Commons license and the respective action is not permitted by statutory regulation, users will need to obtain permission from the license holder to duplicate, adapt or reproduce the material.

## References

- Bak C, Zahle F, Bitsche R, et al (2013) The DTU 10-MW reference wind turbine. In: DTU orbit - the research information system. Available via Technical University of Denmark. [http://orbit.dtu.dk/files/55645274/The\\_DTU\\_10MW\\_Reference\\_Turbine\\_Christian\\_Bak.pdf](http://orbit.dtu.dk/files/55645274/The_DTU_10MW_Reference_Turbine_Christian_Bak.pdf). Accessed 08 Apr 2016
- Bathe KJ, Bolourchi S (1979) Large displacement analysis of three-dimensional beam structures. *Int J Numer Methods Eng* 14(7):961–986
- Battini JM, Pacoste C (2002) Co-rotational beam elements with warping effects in instability problems. *Comput Method Appl M* 191(17):1755–1789
- Bazoune A, Khulief YA, Stephen NG (2003) Shape functions of three-dimensional Timoshenko beam element. *J Sound Vib* 259(2):473–480
- Berdichevskii VL (1979) Variational-asymptotic method of constructing a theory of shells. *J Appl Math Mech* 43(4):711–736
- Borri M, Merlini T (1986) A large displacement formulation for anisotropic beam analysis. *Meccanica* 21(1):30–37

- Bottasso CL, Campagnolo F, Croce A, Tibaldi C (2013) Optimization-based study of bend-twist coupled rotor blades for passive and integrated passive/active load alleviation. *Wind Energy* 16(8):1149–1166
- Capellaro M, Kühn M (2010) Boundaries of bend twist coupling. In: Voutsinas S (ed) *Torque 2010: the science of making torque from wind*. Crete, 2010
- Cardona A, Geradin M (1988) A beam finite element non-linear theory with finite rotations. *Int J Numer Methods Eng* 26(11):2403–2438
- Cesnik CES, Hodges DH (1997) VABS: a new concept for composite rotor blade cross-sectional modeling. *J Am Helicopter Soc* 42(1):27–38
- Chandra R, Chopra I (1992) Structural response of composite beams and blades with elastic couplings. *Compos Eng* 2(5–7):347–374, wOS:A1992HZ76200006
- Cortínez VH, Piovan MT (2002) Vibration and buckling of composite thin-walled beams with shear deformability. *J Sound Vib* 258(4):701–723
- Crisfield MA (1990) A consistent co-rotational formulation for non-linear, three-dimensional, beam-elements. *Comput Method Appl M* 81(2):131–150
- Fedorov V, Berggreen C (2014) Bend-twist coupling potential of wind turbine blades. *J Phys Conf Ser* 524:012035
- Giavotto V, Borri M, Mantegazza P, Ghiringhelli GL, Carmaschi V, Maffioli GC, Mussi F (1983) Anisotropic beam theory and applications. *Comput Struct* 16(1):403–413
- Guyan RJ (1965) Reduction of stiffness and mass matrices. *AIAA J* 3(2):380–380
- Hodges DH (1990a) A mixed variational formulation based on exact intrinsic equations for dynamics of moving beams. *Int J Solids Struct* 26(11):1253–1273
- Hodges DH (1990b) Review of composite rotor blade modeling. *AIAA J* 28(3):561–565
- Jung SN, Nagaraj VT, Chopra I (1999) Assessment of composite rotor blade modeling techniques. *J Am Helicopter Soc* 44(3):188–205
- Kim T, Hansen AM, Branner K (2013) Development of an anisotropic beam finite element for composite wind turbine blades in multibody system. *Renew Energ* 59:172–183
- Lobitz DW, Laino DJ (1999) Load mitigation with twist-coupled HAWT blades. In: *ASME/AIAA wind energy symposium*, Reno, NV, pp 124–134
- Lobitz DW, Veers PS (1998) Aeroelastic behavior of twist-coupled HAWT blades. In: *ASME/AIAA wind energy symposium*, Reno, NV, pp 75–83
- Lobitz DW, Veers PS (2003) Load mitigation with bending/twist-coupled blades on rotors using modern control strategies. *Wind Energy* 6(2):105–117
- Rehfield LW, Atilgan AR, Hodges DH (1990) Nonclassical behavior of thin-walled composite beams with closed cross sections. *J Am Helicopter Soc* 35(2):42–50
- Simo J, Vu-Quoc L (1986) A three-dimensional finite-strain rod model. Part II: computational aspects. *Comput Method Appl M* 58:79–116
- Smith EC, Chopra I (1991) Formulation and evaluation of an analytical model for composite box-beams. *J Am Helicopter Soc* 36(3):23–35
- Stäblein AR, Hansen MH (2016) Timoshenko beam element with anisotropic cross-sectional properties. In: *VII European congress on computational methods in applied sciences and engineering (ECCOMAS 2016)*, Crete Island
- Stäblein AR, Tibaldi C, Hansen MH (2016) Using pretwist to reduce power loss of bend-twist coupled blades. In: *34th wind energy symposium*, p 1010
- Timoshenko SP (1921) On the correction for shear of the differential equation for transverse vibrations of prismatic bars. *Philos Mag* 41(245):744–746
- Verelst DR, Larsen TJ (2010) Load Consequences when sweeping blades - a case study of a 5 MW pitch controlled wind turbine. *Tech. Rep. Risø-R-1724(EN)*, Risø National Laboratory for Sustainable Energy
- Volovoi VV, Hodges DH, Cesnik CES, Popescu B (2001) Assessment of beam modeling methods for rotor blade applications. *Math Comput Modell* 33(10–11):1099–1112

# Chapter 6

## Improvement of Wind Turbine Blade Performance by Means of Rod Vortex Generators

Javier Martinez, Pawel Flaszynski, Piotr Doerffer, and Oskar Szulc

**Abstract** Wind turbines are complex energy conversion fluid-flow machines which entail coupled aero-mechanical issues. From an aero-acoustical point of view, wind turbine blades present two main problems: first, a reduced aerodynamic performance due to flow separation, and second, the level of noise emissions. Flow separation appears on the blade as a result of high angles of attack causing a decrease in the aerodynamic efficiency. In this chapter, the application of rod vortex generators (RVGs) to control and decrease the flow separation—by the creation of streamwise vorticity on the blade—is presented. The NREL Phase VI wind turbine rotor and the S809 airfoil are used as reference cases. The validation of NREL Phase VI model rotor against experimental data is found to be satisfactory. A study into the effects of RVGs' chordwise location and spanwise distance is presented for selected cases and a range of inflow conditions. It is shown that the proposed RVGs lead to an improvement of the aerodynamic performance, and can be successfully applied by the wind energy industry.

### 6.1 Introduction

The wind energy sector has experienced rapid growth in the last few decades. The developments in the materials science, engineering and allied fields have ushered in turbines of increasing sizes; turbines with rotor diameters of up to 160 m (Vestas V164 8 MW) have been developed, and the current trend of increasing sizes is expected to continue in the future (Bak et al. 2012).

The increasing sizes of wind turbines pose new challenges for engineers. One particular challenge is that large rotor dimensions result in non-uniform inflow conditions along the blade span—which leads to increased flow separation even after the application of traditional flow control approaches. As a consequence of

---

J. Martinez (✉) • P. Flaszynski • P. Doerffer • O. Szulc  
Aerodynamics Department, Institute of Fluid Flow Machinery, Polish Academy of Sciences,  
ul. Fiszerza 14, 80-231 Gdańsk, Poland  
e-mail: [javier.martinez@imp.gda.pl](mailto:javier.martinez@imp.gda.pl); [pawel.flaszynski@imp.gda.pl](mailto:pawel.flaszynski@imp.gda.pl); [piotr.doerffer@imp.gda.pl](mailto:piotr.doerffer@imp.gda.pl);  
[oskar.szulc@imp.gda.pl](mailto:oskar.szulc@imp.gda.pl)

the boundary layer separation, the air flow on the blade is detached leading to increased aerodynamic losses and noise generation (Wagner et al. 2012). In order to reduce the flow separation, different flow control devices have been developed and implemented on the blades during the last few decades (Van Dam et al. 2008). Several flow control devices, such as trailing edge flaps, microtabs, microflaps, plasma actuators, active flexible walls or vortex generators, have been proposed in literature (Van Dam et al. 2007, 2008; Andersen et al. 2010; Johnson et al. 2010; Nelson et al. 2008; Gao et al. 2015). Of these, the current chapter focuses on vortex generators.

Vortex generators (VGs) are located in the boundary layer in order to create a streamwise vorticity, which influences the transport of momentum in the direction normal to the wall. The fluid with higher momentum transported to the near wall zone energizes the boundary layer. This leads to increased shear stresses and higher resistance to the adverse pressure gradient effect which results in reduction or even complete removal of the separation.

The first VG investigations were conducted by Taylor (1947) in the late 1940s. These initial devices, of height ( $h$ ) higher or equal to the boundary layer ( $\delta$ ), were called vane vortex generators (VVGs). During the 1950s, air jet vortex generators (AJVGs) were developed. It was found that they could be considered as an effective alternative to traditional VGs for separation reduction (Wallis and Stuart 1962). In the 1980s, Taylor's VGs were replaced by smaller devices, with the introduction of low profile VGs ( $h/\delta < 0.65$ ) (Rao and Kariya 1988); these devices generate lower disturbance and flow non-uniformity outside boundary layer in comparison with the classical vanes as they are submerged inside the boundary layer. As an effect, the drag is lower and the effectiveness of the flow control method can be higher. However, these devices generally need to be located closer to the critical zone than classical vanes due to faster decaying streamwise vorticity (Lin 2002).

In the last few decades VGs have been widely researched and new concepts of non-solid VGs—such as synthetic jets or pulsed jets (Lin 2002; Wiltse and Glezer 1993; Amitay et al. 1998; McManus et al. 1994; Kostas et al. 2007)—have been proposed. It has been demonstrated that active VGs provide similar benefits as passive VGs, but with a major added advantage: when they are not functional, there is no increment in the parasitic drag (Paul et al. 2013). Despite the clear benefits of active VGs, different configurations of vane-type VGs are still a commonly implemented solution on wind turbine blades.

This chapter focuses on the investigation and application of a new type of VG, called Rod Vortex Generator (RVG) (Doerffer et al. 2009), on wind turbine blades. Optimized RVGs have demonstrated a capability to generate similar streamwise vortex intensity as the one generated by the AJVGs (Tejero et al. 2015). Furthermore, RVGs do not require complex installation, as is the case with AJVGs. In contrast to the traditional vane-type VGs, RVGs can be combined with Micro-Electro-Mechanical Systems (MEMS) technology, thus allowing for activation during the system operation if the conditions require its application.

RVGs can be defined by five parameters: diameter ( $D$ ), height ( $h$ ), skew angle ( $\theta$ ), pitch angle ( $\alpha$ ) and spacing ( $W$ ), as shown in Fig. 6.1. The first four parameters



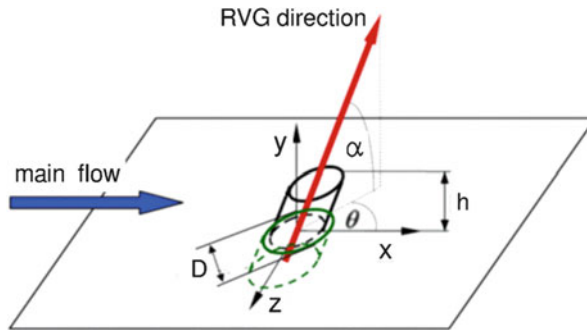


**Fig. 6.1** Rod vortex generator configuration

define the geometry and orientation of the rod, while the spacing ( $W$ ) refers to the spanwise distance between rods. The orientation angles ( $\theta$  and  $\alpha$ ) are optimized to obtain the maximum streamwise vorticity. The rod diameter and the height are proportional to the boundary layer thickness. The chordwise location of the RVG along the blade ( $x_{RVG}/c$ ) is also a crucial parameter which has to be taken into account.

The application of RVGs on wind turbine blades, as a flow control device to improve aerodynamic performance, is analysed for the NREL Phase VI wind turbine rotor. The NREL turbine was selected because of the large amount of experimental data available (Hand et al. 2001) and the detailed geometry description (Lindenburg 2003) which is highly advantageous for the validation step.

## 6.2 Flow Solver

The numerical investigations have been carried out by means of FINE<sup>TM</sup>/Turbo Numeca. The compressible, mass-weighted RANS equations are solved adopting a preconditioning scheme (Hakimi 1997; Choi and Merkle 1993). A full multigrid technique is applied in order to increase the convergence rate. Spatial discretization is based on a cell centred control volume approach, and a 2nd order central difference scheme with scalar artificial dissipation formulated by Jameson (1991) is applied. The results presented in this chapter are obtained for turbulence models (Spalart and Allmaras 1992),  $k-\omega$  SST (Menter 1994) and Explicit Algebraic Reynolds Stress Model (EARSM) (Menter et al. 2012). A perfect gas model is employed for closure of the system of differential equations. The dynamic viscosity is calculated using the Sutherland's law (Sutherland 1893).

## 6.3 The NREL Phase VI Wind Turbine Rotor

### 6.3.1 Experimental Set-Up

The computational model is validated by the comparison of numerical simulations results with the experimental data available in the National Renewable Energy Laboratory (NREL) database for the Unsteady Aerodynamics Experiment Phase VI (Hand et al. 2001). The geometry of the investigated configuration is shown in Fig. 6.2.

The two-bladed rotor was located in the 24.4 m  $\times$  36.6 m NASA Ames Wind Tunnel and tested under several different inflow conditions, with velocities ranging from 0 to 25 m/s. The stall regulated rotor was equipped with two linearly tapered, non-linearly twisted blades of radius  $R = 5.209$  m with rounded tip caps (Lindenburger 2003). The tapered region of the blades starts at  $r/R = 0.25$  with a chord length  $c = 0.737$  m, and ends at the tip,  $c = 0.357$  m. The non-linearly twisted blade, defined with respect to the  $r/R = 0.75$  section and considered positive towards feather, varies from  $20.05^\circ$  at  $r/R = 0.25$  to  $-1.82^\circ$  at tip.

During the sequence S of the experimental campaign (Hand et al. 2001), the blade tip pitch angle was set to  $3^\circ$  with respect to the rotor plane, the rotational speed to 72 rpm, and the cone angle to  $0^\circ$ . Static pressure measurements were obtained at five spanwise locations ( $r/R = 0.3, 0.466, 0.633, 0.80$  and  $0.95$ ). Yaw angles were varied from 0 to  $180^\circ$ , but only the results from the  $0^\circ$  yaw angle case were harnessed for validation purposes. In the present work, only wind speeds of 5, 7, 10 and 13 m/s are considered. Table 6.1 summarizes the operational conditions for the computed cases (Hand et al. 2001; Sørensen and Michelsen 2000).

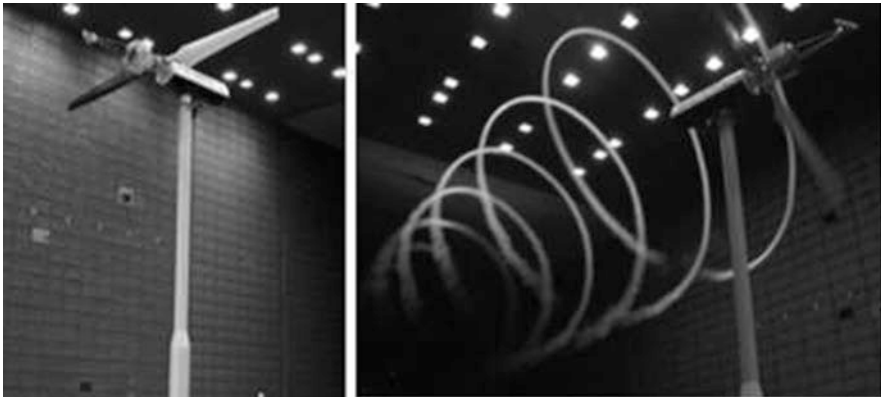
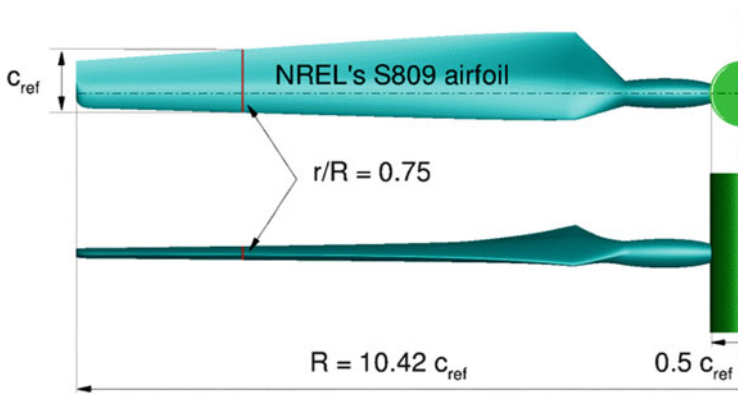


Fig. 6.2 NREL Phase VI wind turbine at NASA Ames (Lindenburger 2003)

**Table 6.1** NREL Phase VI operating conditions

Wind speed [m/s]	Density ( $\rho$ ) [kg/m <sup>3</sup> ]	RPM	Temperature [K]
5.0	1.243	71.7	284.25
7.0	1.246	71.9	284.25
10.0	1.246	72.1	284.15
13.1	1.227	72.1	286.85

**Fig. 6.3** NREL Phase VI rotor model

### 6.3.2 Numerical Modelling

A numerical model is created for the NREL Phase VI rotor. The section  $r/R = 0.75$  was taken as the reference section, and the local chord was set to unit ( $c_{ref} = 1$ ). The blade radius to reference chord length ratio ( $AR \approx 10.42$ ) was kept constant in comparison with the full scale model. Thus the blade radius was rescaled to  $R = AR \cdot c_{ref}$ . The pitch and sectional twists were not affected by the process. The nacelle was modelled as a cylinder with radius  $0.5 \cdot c_{ref}$  (Fig. 6.3) (Martinez et al. 2015a).

The rotational periodicity of the flow allows the use of a computational domain defined by a half of cylinder with a single blade in the middle. Farfield boundary conditions are applied at the outer cylinder, located at a distance of 3 blade radius ( $R$ ) from the rotor axis. The inlet and outlet are located at a distance equal to  $3 \cdot R$  from the rotor plane. At the inlet, a uniform velocity distribution in normal direction to the rotor plane is applied, while at the outlet, atmospheric static pressure is imposed. The blade is defined as a non-slip wall, while at the cylindrical surface (hub) an Euler wall (no shear stress at the wall) condition is applied. This enables one to save resources and computational time (Fig. 6.4).

The computational domain consists of 8.8 million cells distributed amongst 76 hexahedral full-matching connection blocks. The structured grid is of C type in the crosswise direction, and H type in the spanwise and freestream directions, as shown

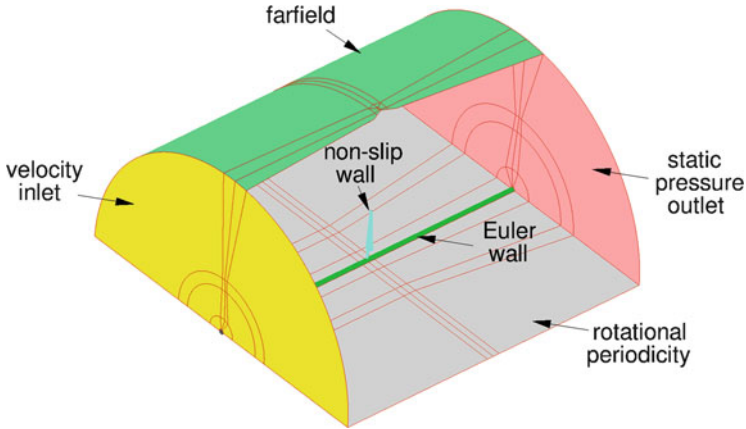


Fig. 6.4 NREL Phase VI rotor computational domain and boundary conditions

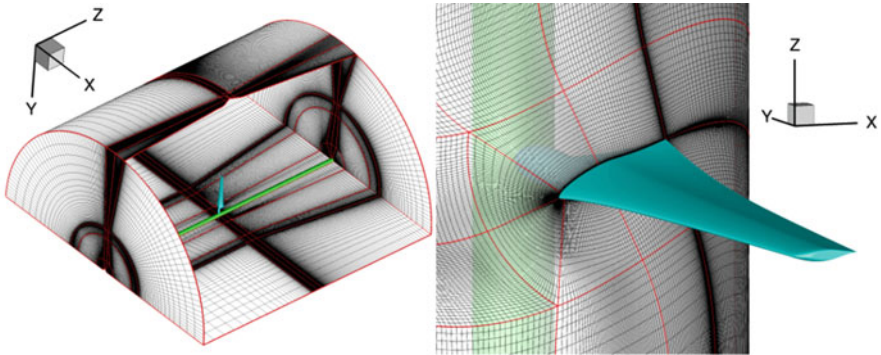


Fig. 6.5 NREL Phase VI rotor C-H-H grid

in Fig. 6.5. The blade surface is discretized by 294 nodes around the airfoil and 91 nodes in the spanwise direction. The non-dimensional distance of the first cell layer close to the wall is of the order of  $y^+ \sim 1$ .

### 6.3.3 Numerical Results

The numerical simulations for the NREL wind turbine rotor show good agreement with measurements of the total thrust and torque. The only difference noted is for a wind speed 10 m/s (Fig. 6.6), where torque is over-predicted (Martinez et al. 2015b).

It is shown in Fig. 6.6 that the predictions obtained by means of 2-equation  $k-\omega$  SST and EARSM models are almost identical. One has to emphasize that in case of

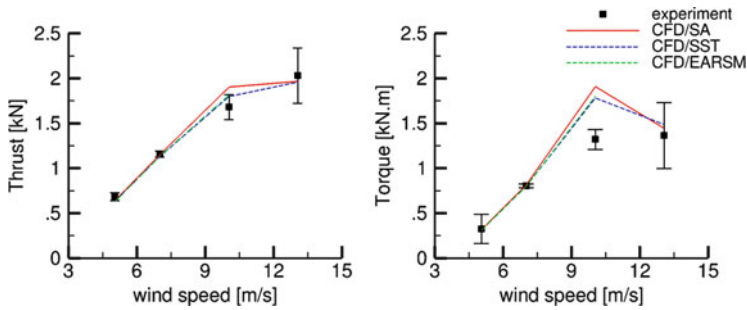


Fig. 6.6 Integrated thrust (left) and torque (right) for NREL Phase VI rotor

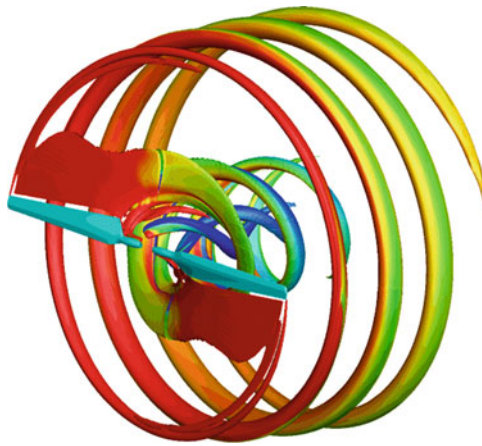


Fig. 6.7 NREL Phase VI rotor aerodynamic wake at 5 m/s

thrust measurements, computed values are within the measurement accuracy. The discrepancy is higher for the SA model.

A Q-criterion (coloured by the vorticity magnitude) visualization of the rotor wake (Fig. 6.7) was extracted from the numerical solution for an inflow wind velocity of 5 m/s, and the one equation Spalart-Allmaras turbulence model. The rotor wake created by wind turbines is closely related to the amount of energy extracted from the wind, and its prediction is of primary importance in the assessment of performance and power. An example of the wake prediction by numerical model, described in more details in Martinez et al. (2015a, b), is shown in Fig. 6.7.

For validation purposes a more detailed analysis of the flow properties (particularly, flow attachment state and local blade loading) is needed. The blade surface streamlines and friction coefficient  $c_f$  provide information of utmost importance regarding the flow attachment state and developed flow patterns. The blade loading analysis is given by the sectional chordwise pressure coefficient  $c_p$ , and spanwise

normal  $c_N$  and tangential  $c_T$  force coefficients distributions. The friction coefficient  $c_f$  is defined as:

$$c_f = \frac{\mu \frac{du_s}{dn}}{0.5\rho U_\infty^2} \tag{6.1}$$

where  $u_s$  is the component of cross sectional velocity tangential to the surface,  $n$  is the direction normal to the blade surface,  $U_\infty$  the cross sectional reference velocity,  $\mu$  the freestream viscosity and  $\rho$  the density.

The friction coefficient  $c_f$  along with velocity streamlines are shown in Fig. 6.8 for the 4 wind speeds ranging from 5 to 13 m/s. Contours for  $c_f$ , obtained only from the Spalart-Allmaras turbulence model, are shown. Analogous behavior is observed in case of the two equation turbulence models.

It is observed that in the case of 5 and 7 m/s wind speeds, the flow stays fully attached—except for the inner section, where the cylindrical shape (close to root) induces local separation. At 10 m/s, according to the SA model prediction, the previous local separation moves towards the outer span of blade until  $r/R = 0.95$ . The plot for the wind speed of 13 m/s reveals that the flow is completely detached on the suction side, except for a very narrow region at the blade tip. Further increasing of the wind speed causes the detached flow area to increase.

An example of pressure coefficient distributions  $c_p$  located at four blade cross sections ( $r/R = 0.30, 0.466, 0.80$  and  $0.95$ ) and the non-dimensional force coefficient  $c_N$  are compared to the experimental data in the Figs. 6.8 and 6.9 for wind

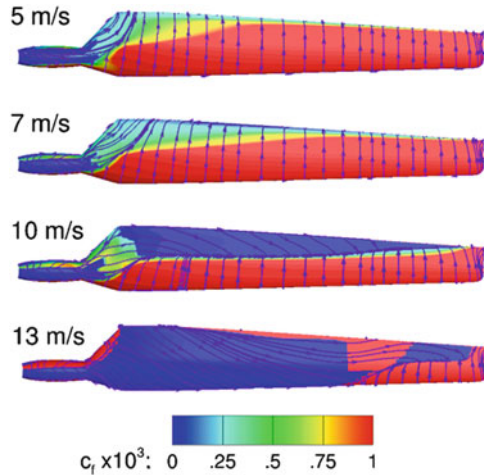


**Fig. 6.8** Skin friction coefficient  $c_f$  and surface streamlines (suction side)

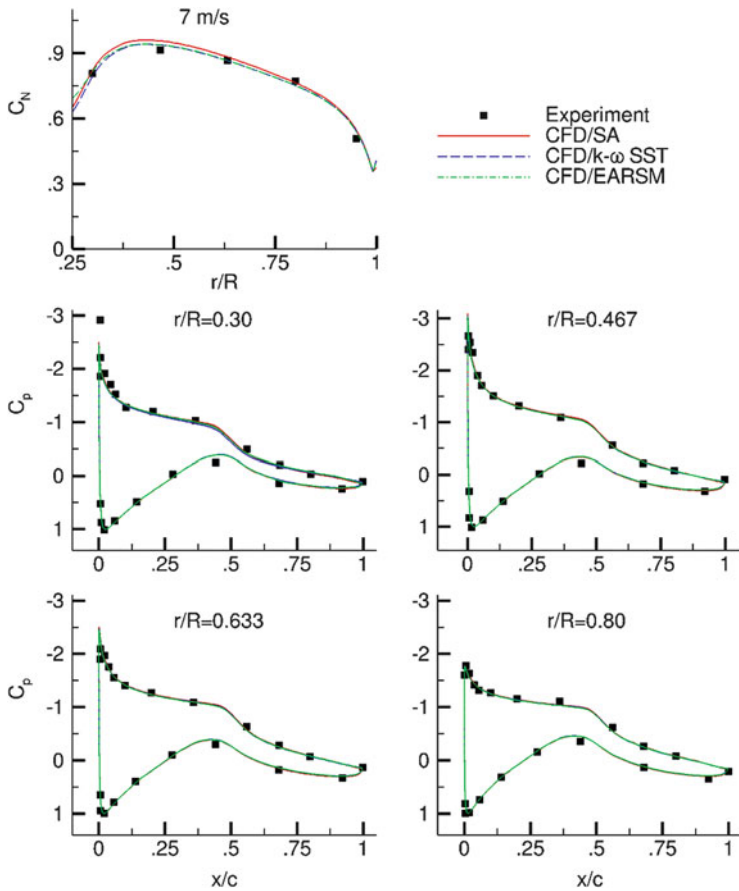


**Fig. 6.9** Pressure coefficient  $c_p$  and normal force  $c_N$  distributions at 7 m/s

speeds of 7 and 10 m/s, respectively. The sectional normal force coefficient  $c_N$  distributions predictions were obtained by the integration of the  $c_p$  distributions along each one of the 100 cross sections employed. Figure 6.9 shows an exemplary agreement with the experimental data. A slight difference among models is observed at the 30 % cross section.

As the wind speed increases to 10 m/s the prediction of SA model fails to reproduce the normal force coefficient distribution, although the  $k-\omega$  SST and EARSM models predictions are still close to the experimental data (Fig. 6.10). The 10 m/s case shows important discrepancies between the  $c_p$  distribution predicted and the experimental data for the 46.6 % span section. The experimental data seems to show a local separation at this section, which is not predicted by numerical simulations, while a reasonably good agreement with the experimental data is obtained in the remaining sections.

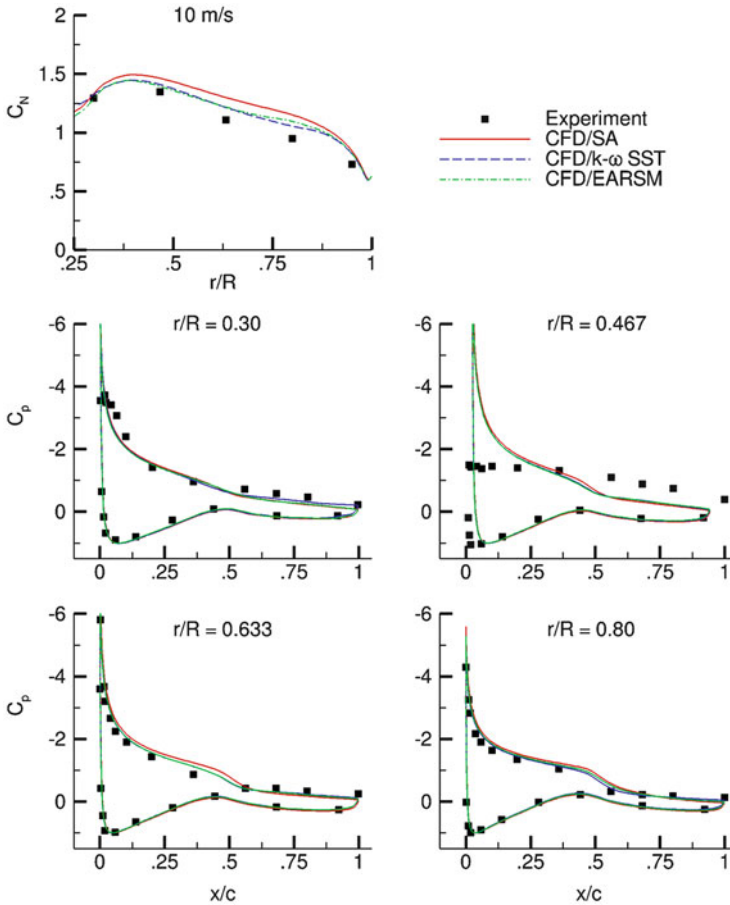


Fig. 6.10 Pressure coefficient  $c_p$  and normal force distributions  $c_N$  at 10 m/s

Disregarding the 46.6% span section, a reasonably good agreement between experimental and numerically predicted  $c_p$  distributions has been shown for the turbine operating at wind speeds ranging from 5 to 13 m/s (see Martinez et al. 2015a). Consequently, a flow structure similar to the displayed in Fig. 6.8 is expected to have been developed during the experimental campaign.

The optimum tip speed ratio is close to 5.4 (wind speed 7 m/s) (Martinez et al. 2015a, b); thus, as the wind speed increases beyond the optimum, the flow separation comes out on the blade, affecting the rotor performance. It influences the rising flow structure complexity, and causes difficulties with the prediction accuracy of the solver. The area of detached flow in the 10 m/s case is quite susceptible of being decreased by means of rod vortex generator, thus improving the aerodynamic



performance and delaying the separation as the wind speed increases. When the flow on the blade is totally detached, however, the application of RVGs is not expected to bring significant (if any) aerodynamic improvement. Besides, modern horizontal axis wind turbine rotors equipped with individual pitch control are more likely to operate with partially flow-separated blades, than in a strong stall situation. Thus the 10 m/s case is chosen as a reference for a flow control study in wind turbines.

## 6.4 The S809 Aerofoil (Clean Case)

The NREL Phase VI rotor blades employ the 21% thickness S809 aerofoil. For this reason a validation study is performed for this aerofoil. Designed for wind turbines applications using the Eppler code (Eppler and Somers 1980), a short ramp of adverse pressure is present on the upper surface of this profile, downstream of the mid-chord. It promotes an efficient laminar to turbulent transition, followed by a low drag concave pressure recovery region (Somers 1997).

The S809 aerofoil was tested in the Ohio State University (OSU) and Delft University of Technology (DUT) facilities and experimental data is available for several angles of attack (Somers 1997) and Reynolds numbers (Ramsay et al. 1995). The validation against experimental data was performed for a Reynolds number of  $1 \cdot 10^6$  to ensure that the analysis was representative of the studied flow around the NREL Phase VI blade.

The aerofoil surface was modelled as a non-slip wall. A C type grid was used, and the farfield was located at 40 chords from the aerofoil. The total computational cells amount to 0.3 million, distributed into 13 blocks. The S809 aerofoil surface is defined by  $737 \times 145$  nodes in the wrap-around and normal directions, respectively (Fig. 6.11).

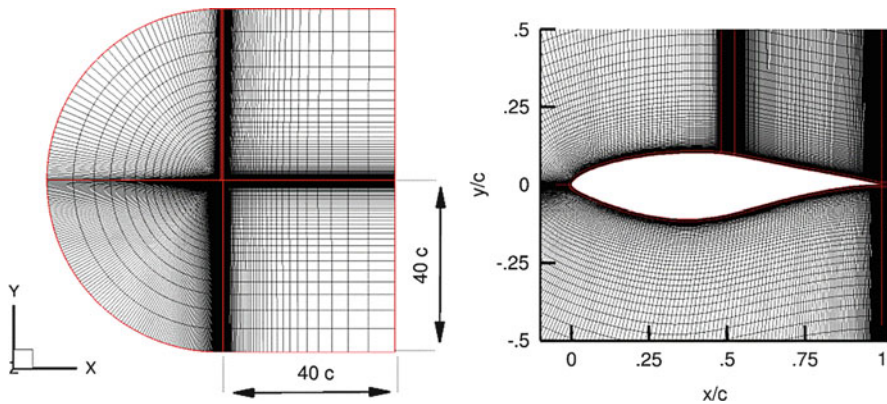


Fig. 6.11 C type grid around the S809 aerofoil

Numerical RANS simulations were performed with and without a transition model. The  $\gamma - Re_{\theta}$  transition model is used. This model is based on two transport equations, one for intermittency,  $\gamma$ , and the second one for the transition momentum thickness Reynolds number,  $Re_{\theta}$ . For simulations performed without the transition model, the flow is assumed to be fully turbulent and the one equation Spalart-Allmaras and the two equation  $k-\omega$  SST and EARSM models were employed. The gamma Reynolds theta transitional model ( $\gamma - Re_{\theta}$ ) is adopted together with the  $k-\omega$  SST and the EARSM turbulent models. Additionally, a Hakimi preconditioning scheme is applied for all the simulations.

Figure 6.12 depicts the evolution of lift  $c_l$  and drag  $c_d$  coefficients with respect the angle of attack. It is apparent that numerical models have a good ability to predict the lift for moderate angles of attack, but overestimate the value for larger angles. Considering the drag prediction, the turbulence models including transition effect have proven to have a better prediction capability.

Comparisons between the predicted pressure coefficient  $c_p$  distribution along the aerofoil and experimental data are shown in Fig. 6.13. Two selected angles of attacks, 4.1 and 13.3°, are compared. A pressure overestimation is given on the suction side by the SA model for the 13.3° angle of attack, while the other two fully turbulent models provide a good agreement. For the 4.1° angle of attack, both transition models are able to predict accurately the laminar separation bubble located just aft of the mid-chord on the suction side of the aerofoil.

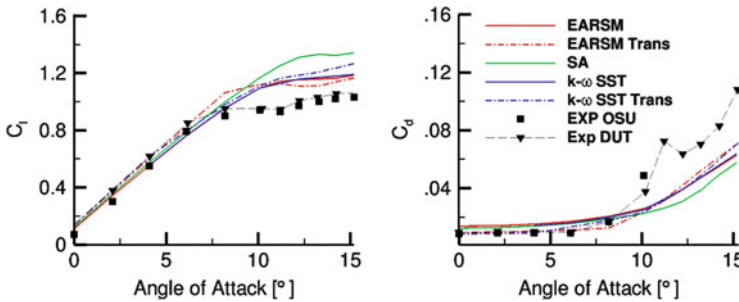


Fig. 6.12 Lift  $c_l$  and drag  $c_d$  coefficients versus angle of attack for S809 aerofoil

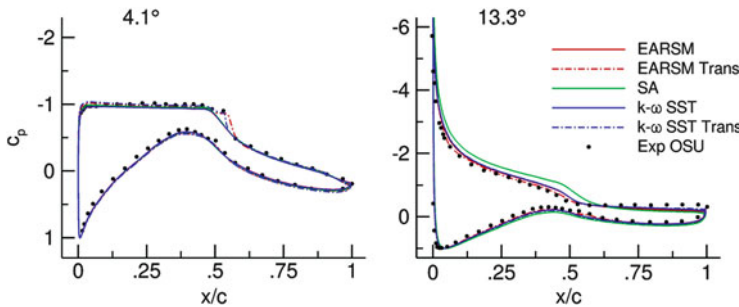


Fig. 6.13 Pressure coefficient  $c_p$  distributions for S809 aerofoil

The better prediction obtained with the 2 equation turbulent models compared to the 1 equation SA model, makes the former more adequate for the analysis of the complex flow structure developed inside the boundary layer when flow control devices are applied. Simulations for RVGs applied on blade are computationally demanding and only one turbulence model is selected for the further analysis.

The nonlinear constitutive relations of the EARSM model are capable of reproducing the anisotropy of the stress distribution—which is a very important feature beyond the possibilities of linear eddy viscosity turbulence models (SA,  $k-\omega$  SST)—and makes this model even more suitable for the RVG implementation study.

## 6.5 The S809 Aerofoil (Flow Control Case)

### 6.5.1 Basic Configuration

Once the numerical methods have been favourably validated against experimental data for the NREL Phase VI wind turbine rotor and the S809 profile, the obtained results can be employed to the rod vortex generators design and optimization. In particular, the numerical predictions for the S809 aerofoil given by the fully turbulent EARSM model are employed for the dimensioning of the RVGs ( $h$ ,  $D$ ) and for the optimization of their chordwise location ( $x_{RVG}/c$ ) and spanwise distribution ( $W$ ). Table 6.2 summarizes the parameters of the basic RVG configuration.

Four flow cases are taken into consideration for flow control investigations. All of them are selected for high inflow angles: 11.2, 12.2, 13.3 and 13.9°, with the separation onset located at  $x/c = 0.88$ , 0.65, 0.55 and 0.53, respectively. As the angle of attack increases the separation moves upstream to the mid-chord in the case of the highest loading considered.

The case of the 13.9° inflow angle, where the most severe flow conditions exist, is taken as the reference and the rods are initially located slightly upstream of the separation onset ( $x_{RVG}/c = 0.50$ ).

Boundary layer thickness is estimated based on the comparison of simulated velocity  $v$  and ideal velocity  $v_{id}$  profiles normal to the wall at a certain location.

**Table 6.2** Parametric values for RVG

Parameter	Value
Pitch angle, $\theta$ [°]	45
Skew angle, $\alpha$ [°]	30
Height, $h/\delta$ [-]	0.36
Diameter, $D/\delta$ [-]	0.20
Spacing, $W/D$ [-]	10

The ideal velocity profile can be obtained from the isentropic relation given in Eq. (6.2) for a constant total pressure  $P_0$  (the value outside of the boundary layer):

$$v_{id} = \left[ \left( \left( \frac{P_0}{P} \right)^{\frac{\gamma-1}{\gamma}} - 1 \right) 2C_p T \right]^{1/2} \quad (6.2)$$

The boundary layer thickness,  $\delta$ , is defined as the distance normal to the wall at which  $v = 0.99 \cdot v_{id}$ . In Eq. (6.2),  $T$  is static temperature and  $P$  is static pressure. Coefficient  $C_p$  is the heat capacity of the gas at constant pressure and  $\gamma$  the heat capacity ratio. The boundary layer thickness  $\delta$  at the rod location for the reference case  $13.9^\circ$  amounts to  $\delta \approx 0.0216 \cdot c$  and RVGs are scaled according to parameters established in Table 6.2.

Due to the small spacing among rods ( $W \approx 0.043 \cdot c$ ) a large amount of them would be needed to cover the entire spanwise length of the experimental models employed by Somers (1997) and Ramsay et al. (1995). Besides, a large grid clustering is needed in the vicinities and downstream of the rod location in order to properly capture the development of streamwise vorticity. Additionally, the complexity of the model to be solved increases rapidly, and the computational resources needed for the full 3D configuration would be far beyond the available resources. Therefore, the 3D computational domain was limited to a slice of the original experimental model, inside which a single rod was placed and the periodic boundary conditions were applied in the spanwise direction, at lateral surfaces. The RVGs and aerofoil surface were modelled as walls (Fig. 6.14). The proximities of the RVG are resolved by means of a butterfly mesh topology.

The computational domain was divided into a total of 29 blocks. Full non matching boundary (FNMB) connections were applied, so the final number of mesh cells is  $3.3 \times 10^6$ . The NMB connections were applied at an approximate distance of  $0.13 \cdot c$  from the aerofoil wall (Fig. 6.14).

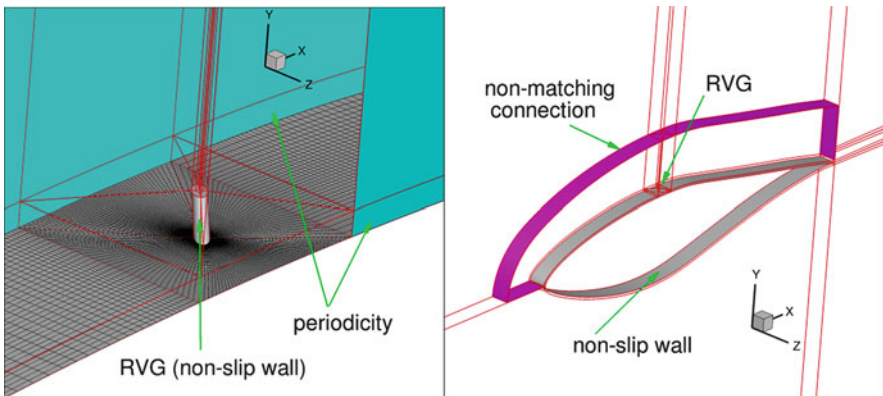


**Fig. 6.14** Topology and boundary conditions for flow control case

In order to avoid the influence of grid nodes distribution in the streamwise direction for the case with and without RVG, the mesh employed for both cases is the same apart from the blocks with the RVG presence. Thus, the S809 aerofoil surface is defined by  $737 \times 145 \times 33$  nodes in the wrap-around, normal and spanwise directions, respectively.

Lift  $c_l$  and drag  $c_d$  coefficients as a function of the angle of attack, obtained numerically for both cases (with and without RVG), are compared in Fig. 6.15. It is shown that for the selected flow cases the application of RVGs provides not only a higher lift force, but also leads to slight reduction of drag. The maximum improvement is observed for an angle of attack of  $12.2^\circ$ , where the lift coefficient  $c_l$  is increased by 5.2% with respect to the clean case and drag is reduced by 1.2% ( $\Delta c_l = 5.2\%$ ,  $\Delta c_d = -1.2\%$ ).

It is important to notice that the RVGs dimensions and spacing are kept constant at the defined location while the increasing inflow angle influences on boundary layer development, so the boundary layer thickness  $\delta$  is not the same for all cases. Thus, for an angle of attack of  $11.2^\circ$  the ratio RVGs height to boundary layer thickness is approximately  $h/\delta \approx 0.47$  ( $\delta \approx 0.0165 \cdot c$ ) and for  $12.2^\circ$ ,  $h/\delta \approx 0.42$  ( $\delta \approx 0.0185 \cdot c$ ), thus verifying the low profile VGs condition ( $h/\delta < 0.65$ ) defined by Rao and Kariya (1988).

### 6.5.2 RVGs Chordwise Location

RVGs were initially located slightly upstream of the separation onset for an angle of attack of  $13.9^\circ$ , at the chordwise position  $x_{RVG}/c = 0.50$ , and designed according to the local boundary layer height using the parametric values summarized in Table 6.2. Notwithstanding the aerodynamic performance improvement obtained by implementing the RVGs at this location, it is prudent to conduct a study of the chordwise location effect on the devices' effectiveness. The flow control devices should be neither positioned too close to the separation (not enough space to develop vortical structures), nor too far away (vorticity diffusion). Four additional

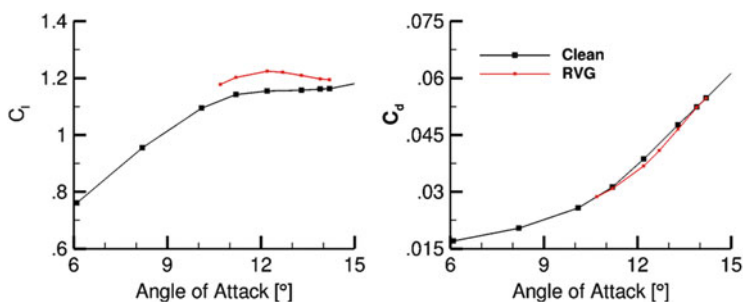


Fig. 6.15 Lift  $c_l$  and drag  $c_d$  coefficients vs angle of attack for clean and flow control cases

chordwise locations ( $x_{RVG}/c = 0.35, 0.40, 0.45$  and  $0.55$ ) were considered and rods dimensioned in relation to the local boundary layer height at each one of the four chordwise locations for a  $13.9^\circ$  inflow angle. The spacing between rods ( $W$ ) was kept the same as for the initial configuration. The number of grid nodes and spacing was also preserved—except in the region of the device location, where the refinement is adjusted in order to diminish the grid influence.

A comparison was done for four angles of attack  $11.2, 12.2, 13.3$  and  $13.9^\circ$ . As mentioned above, increasing the inflow angle from  $11.2$  to  $13.9^\circ$  enforces earlier separation, so flow control devices should be located further upstream in order to improve aerofoil performance.

Lift  $c_l$  and drag  $c_d$  variations for the considered RVG locations and inflow angles, in respect to the case without flow control, are shown in Fig. 6.16. The values indicate configurations for which the positive or negative effect is obtained. It can be observed that a lift increase is obtained for all locations and inflow angles, except for the angle of attack  $13.9^\circ$  and  $x_{RVG}/c = 0.55$ , where RVG is located inside the separation bubble. A reduction of drag is obtained for certain rods locations and angles of attack. However, the configuration of maximum lift increase corresponds with the area of drag reduction, leading to aerodynamic improvement.

When the angle of attack is  $11.2^\circ$ , the maximum lift is for RVGs located at  $x_{RVG}/c = 0.55$ . The lift decreases as these are moved closer to the leading edge. Simultaneously, as the RVG location is moved upstream, the drag increases. This means that even if the higher vorticity is created by the RVG located further upstream, the streamwise vortices would dissipate faster than if they were located closer to separation.

A similar effect to the one analysed above is obtained for an inflow angle of  $12.2^\circ$ . The maximum improvement in aerodynamic performance by the implementation of flow control devices is obtained for  $x_{RVG}/c = 0.50$ .

As the angle of attack increases to  $13.3^\circ$  the separation line moves to  $x/c = 0.55$  and the optimum RVG placement is at the mid-chord. Further upstream locations provide smaller increases in lift (vortices are more dissipated) and higher drag. For

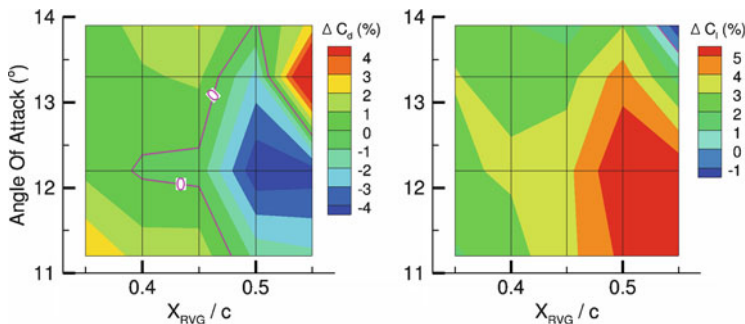


**Fig. 6.16** Effect of RVGs chordwise location  $x_{RVG}/c$  on  $c_l$  and  $c_d$  coefficients

$x_{RVG}/c = 0.55$ , the lack of distance to the separation onset impedes the development of the vortex structure and results in a high drag penalty.

Further increasing of the angle of attack up to  $13.9^\circ$ , leads to a more modest profit with the RVG inclusion. The RVGs located at  $x_{RVG}/c = 0.55$  show a negative effect on the aerodynamic performance—which is expected since the devices are located inside the region of detached flow (separation onset is at  $x/c = 0.53$ ). At this inflow angle only RVGs located at mid-chord provide a drag reduction.

Based on the contour map analysis, one can conclude that for the selected spanwise distance,  $W \approx 0.043 \cdot c$ , the optimum RVG location is at mid-chord,  $x_{RVG}/c = 0.50$ .

### 6.5.3 RVGs Spanwise Separation

Experimental investigations were conducted to assess the effectiveness of RVGs by varying different parameters; based on the results of these experimental investigations, it was found that the most effective spanwise distance ( $W$ ) to rod diameter ( $D$ ) ratio is equal to 10. Consequently, this spanwise distance was used together with the other parameters summarized in Table 6.2 for the initial RVG design. However, due to another flow conditions investigated in the presented chapter, the four RVG spacing scenarios ( $W/D = 7.5, 10, 15$  and  $20$ ) are analysed in order to determine a possible influence on separation. The remaining parameters are kept unchanged. Grid influence was minimised by keeping the same number of nodes—except in the spanwise direction, where the number of cells was adjusted according to the increased spanwise distance.

In Fig. 6.17, contour maps of skin friction coefficient  $c_f$  on the suction side of the S809 aerofoil, at the angle of attack  $11.2^\circ$ , are shown. The case without RVG is shown at the top; below, the cases for rising RVG spanwise distance are compared. The skin friction provides information on the shear stresses distribution and the presence of separation. Additionally, streamlines displayed on top of the skin friction contours allow one to assess the development of flow patterns on the aerofoil. In the presented flow control cases, RVGs were located at the optimum chordwise position previously identified (Sect. 6.5.2):  $x_{RVG}/c = 0.50$ .

It is clearly visible in Fig. 6.17 that skin friction along the chord increases downstream of the RVGs' location and it is higher than in the case of “uncontrolled” flow. Narrow regions of lower friction are present in the zones between rods. This structure is originated by the streamwise vortices. The convected vortices transport momentum from the outer region of the boundary layer to the layer closer to the wall on one vortex side, while lifting the boundary layer on the opposite one.

Assuming a spanwise distance equal to 10 rod diameters (reference configuration), the region of detached flow existing in the clean case vanishes and shrunken backflow zones appear between RVGs at around 75 % of the chord. It is also clearly visible that a spanwise velocity component is generated by the RVGs, rooted in the spanwise migration of the created vortices.



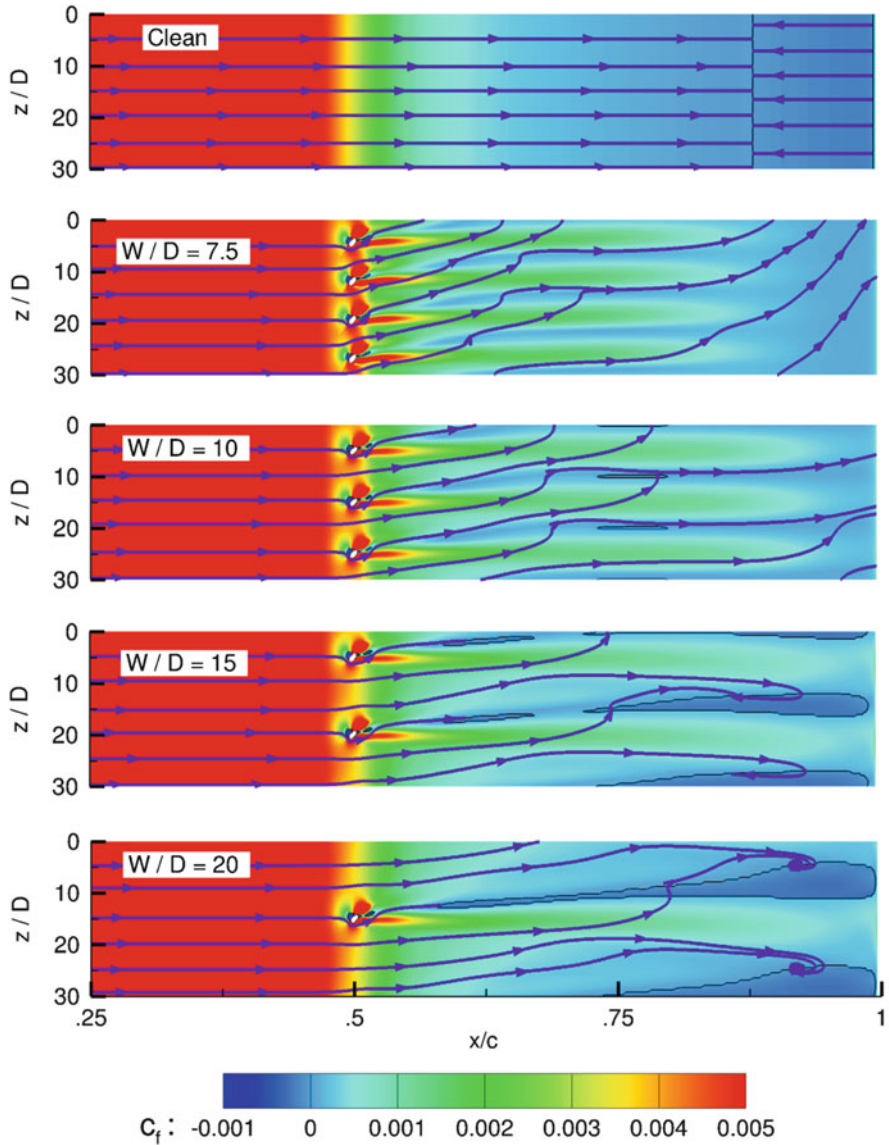


**Fig. 6.17** Skin friction coefficient  $c_f$  and surface streamlines for different RVGs spanwise distance  $W/D$

When the distance is decreased to 7.5 diameters, the small separation bubbles between streamwise vortices vanished and no detached flow is noticed. Notwithstanding this fact, the skin friction contour map reveals that the penetration of the streamwise vorticity has been shortened in comparison with the reference configuration ( $10 \cdot D$ ). Consequently, a possible interaction of streamwise vortices



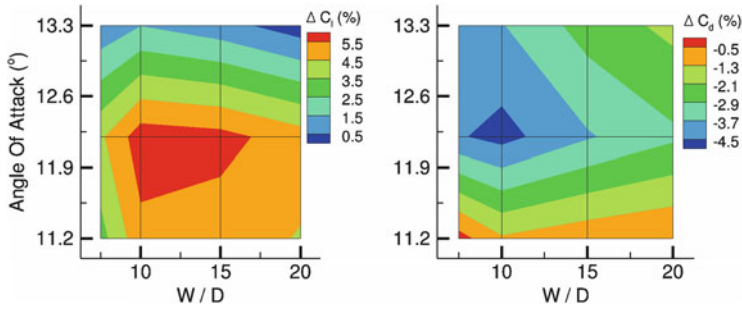


**Fig. 6.18** Effect of RVGs spanwise separation  $W/D$  in  $c_l$  and  $c_d$  coefficients

appeared in the flow for a distance  $7.5 \cdot D$  which could decrease the RVG effectiveness.

As the separation between rods increases from the reference to 15 diameters, the length and width of the backflow bubbles located between rods also increases. The separation onset is moved upstream to 70 % of the chord. Furthermore, for this RVG configuration, the trailing edge separation was only partially eliminated and the elongated regions of detached flow in the proximities of the trailing edge still exist. For a further rods spacing increase to  $20 \cdot D$ , one can observe that the previously described backflow bubbles have merged into a long recirculation region. In any case, the global separated area is still lower compared to a case without RVG.

In Fig. 6.18, the contourmaps of lift  $c_l$  and drag  $c_d$  variations with respect to the clean case for RVGs at chordwise location  $x_{RVG}/c = 0.5$  are presented. It is clearly shown that for an angle of attack of  $11.2^\circ$  a separation of 7.5 rod diameters provides the minimum drag reduction and lift increase, which strengthen the previous hypothesis of interaction between streamwise vortices. Spanwise distances of  $10 \cdot D$  and  $15 \cdot D$  provide the highest increases of lift coefficient for all angles of attack. However, the implementation of a spanwise distance  $10 \cdot D$  allows for further decrease of the drag in the studied angles of attack. At  $13.3^\circ$  the separation has moves upstream to  $x/c = 0.55$  and the decay of maximum streamwise vorticity in chordwise direction is more intensive than for lower angles of attack. Nevertheless, aerodynamic improvement obtained by means of implemented RVG is still positive, although the global extremum is found for  $W = 10 \cdot D$ .

## 6.6 Conclusions

The numerical simulations carried out for NREL Phase VI rotor configurations indicated a good agreement of obtained results with experimental data. This validated the model, and proved its capability to predict aerodynamic performance. Hence, the validated model was used to investigate rod vortex generators as a means of improving aerodynamic performance. The effect of RVGs and generated

streamwise vortices on the separation reduction was analysed on a S809 aerofoil. Numerical simulations for a blade section defined by the S809 aerofoil were also validated by experimental data, and the results were considered as the reference case for the flow control analysis. A study was conducted to analyse the effect of varying the location and spanwise direction of rod vortex generators: the subsequent numerical results confirmed the effectiveness of RVGs as a means of flow separation reduction and increasing aerodynamic performance.

**Acknowledgments** The authors would like to acknowledge the European Commission for their research grant under the project FP7-PEOPLE-2012-ITN 309395 “MARE-WINT” (new MAterials and REliability in offshore WINDd Turbines technology). The research was supported in part by the PL-Grid Infrastructure and TASK Supercomputing Centre in Gdansk.

**Open Access** This chapter is distributed under the terms of the Creative Commons Attribution-NonCommercial 4.0 International License (<http://creativecommons.org/licenses/by-nc/4.0/>), which permits any noncommercial use, duplication, adaptation, distribution and reproduction in any medium or format, as long as you give appropriate credit to the original author(s) and the source, provide a link to the Creative Commons license and indicate if changes were made.

The images or other third party material in this chapter are included in the work's Creative Commons license, unless indicated otherwise in the credit line; if such material is not included in the work's Creative Commons license and the respective action is not permitted by statutory regulation, users will need to obtain permission from the license holder to duplicate, adapt or reproduce the material.

## References

- Amitay M, Smith BL, Glezer A (1998) Aerodynamic flow control using synthetic jet technology. In: Abstracts of the 36th AIAA aerospace sciences meeting exhibit, Reno, 12–15 January 1998
- Andersen PB, Henriksen L, Gaunaa M et al (2010) Deformable trailing edge flaps for modern megawatt wind turbine controllers using strain gauge sensors. *Wind Energy* 13:193–206
- Bak C, Bitsche R, Yde A et al (2012) Light rotor: the 10-MW reference wind turbine. Paper presented at the EWEA 2012 – European wind energy conference and exhibition, Copenhagen, 16–19 April 2012
- Choi YH, Merkle CL (1993) The application of preconditioning in viscous flows. *J Comput Phys* 105(2):207–223
- Doerffer P, Flaszyski P, Szwaba R (2009) Rod patent. Poland patent PL38968
- Eppler R, Somers DM (1980) A computer program for the design and analysis of low-speed airfoils. In: NASA Technical Reports. Available via NASA Technical Reports Server (NTRS) <http://hdl.handle.net/2060/19810005410>. Accessed 07 Apr 2016
- Gao L, Zhang H, Liu Y et al (2015) Effects of vortex generators on a blunt trailing-edge airfoil for wind turbines. *Renew Energ* 76:303–311
- Hakimi N (1997) Preconditioning methods for time dependent Navier-Stokes equations: application to environmental and low speed flows. Dissertation, Vrije Universiteit
- Hand MM, Simms DA, Fingersh L et al (2001) Unsteady aerodynamics experiment phase VI: wind tunnel test configurations and available data campaigns: NREL/TP-500-29955. In: National Renewable Energy Laboratory (NREL) Publications. Available via NREL. <http://www.nrel.gov/docs/fy02osti/29955.pdf>. Accessed 06 Apr 2016

- Jameson A (1991) Time dependent calculations using multigrid, with applications to unsteady flows past airfoils and wings. In: Abstracts of the 10th computational fluid dynamics conference, fluid dynamics and co-located conferences, AIAA, Honolulu, 24–26 June 1991
- Johnson SJ, Baker JP, Van Dam CP et al (2010) An overview of active load control techniques for wind turbines with an emphasis on microtabs. *Wind Energy* 13:239–253
- Kostas J, Foucaut JM, Stanislas M (2007) The flow structure produced by pulsed-jet vortex generators in a turbulent boundary layer in an adverse pressure gradient. *Flow Turbul Combust* 78:331–363
- Lin JC (2002) Review of research on low-profile vortex generators to control boundary-layer separation. *Prog Aerosp Sci* 38:389–420
- Lindenburg C (2003) Investigation into rotor blade aerodynamics: analysis of the stationary measurements on the UAE phase-VI rotor in the NASA-AMES wind tunnel ECN-C-03-025. In: Energy Research Centre of the Netherlands (ECN) Publications. Available via ECN. <https://www.ecn.nl/publications/PdfFetch.aspx?nr=ECN-C--03-025>. Accessed 07 Apr 2016
- Martinez J, Doerffer P, Szulc O et al (2015a) Aerodynamic analysis of wind turbine rotor blades. *Task Q* 19(2):129–140
- Martinez J, Doerffer P, Szulc O (2015b) CFD validated technique for prediction of aerodynamic characteristics on horizontal axis wind energy turbines. Poster presented at the Offshore 2015 Conference, The European Wind Energy Association, Copenhagen, 10–12 March 2015
- McManus K, Legner HH, Davis SJ (1994) Pulsed vortex generator jets for active control of flow separation. In: Abstracts of the fluid dynamics conference, AIAA, Colorado Springs, 20–23 June 1994
- Menter FR (1994) Two-equation eddy-viscosity turbulence models for engineering applications. *AIAA J* 32(8):1598–1605
- Menter FR, Garbaruk AV, Egorov Y (2012) Explicit algebraic Reynolds stress models for anisotropic wall-bounded flows. *Prog Flight Phys* 3:89–104
- Nelson RC, Corke TC, Othman H (2008) A smart wind turbine blade using distributed plasma actuators for improved performance. In: Abstracts of the 46th AIAA aerospace sciences meeting and exhibit, Reno, 7–10 January 2008
- Paul AR, Joshi S, Jindal A et al (2013). Comparison active-passive: experimental studies of active and passive flow control techniques applied in a twin air-intake. *Sci World J*. doi:10.1155/2013/523759
- Ramsay RR, Hoffman MJ, Gregorek GM (1995) Effects of grit roughness and pitch oscillations on the S809 airfoil NREL/TP-442-7817. In: National Renewable Energy Laboratory Reports. Available via NREL. [https://wind.nrel.gov/airfoils/OSU\\_data/reports/3x5/s809.pdf](https://wind.nrel.gov/airfoils/OSU_data/reports/3x5/s809.pdf). Accessed 07 Apr 2016
- Rao DM, Kariya TT (1988) Boundary-layer submerged vortex generators for separation control—an exploratory study. In: Abstracts of the 1st national fluid dynamics conference, AIAA, Cincinnati, 25–28 July 1988
- Somers DM (1997) Design and experimental results for the S809 airfoil NREL/SR-440-6918. NREL Report: In: National Renewable Energy Laboratory Reports. Available via NREL. [www.nrel.gov/docs/legosti/old/6918.pdf](http://www.nrel.gov/docs/legosti/old/6918.pdf). Accessed 07 Apr 2016
- Sørensen NN, Michelsen JA (2000) NREL/NWTC aerodynamics code blind comparison. In: Abstracts of the 2 science panel meeting, NREL Boulder, Colorado, 5–6 December 2000
- Spalart PR, Allmaras SR (1992) A one-equation turbulence model for aerodynamic flows. In: Abstracts of the 30th AIAA aerospace sciences meeting and exhibit, AIAA, Reno, 6–9 January 1992
- Sutherland W (1893) LII. The viscosity of gases and molecular force. *Philos Mag Ser 5* 36(223):507–531
- Taylor HD (1947) The elimination of diffuser separation by vortex generators. United Aircraft Corporation Research Department Report No. R-4012-3
- Tejero F, Doerffer P, Szulc O (2015) Shock wave induced flow separation control by air-jet and rod vortex generators. *Task Q* 19(2):167–180

- van Dam CP, Chow R, Zayas JR et al (2007) Computational investigations of small deploying tabs and flaps for aerodynamic load control. *J Phys Conf Ser*. doi:[10.1088/1742-6596/75/1/012027](https://doi.org/10.1088/1742-6596/75/1/012027)
- van Dam CP, Berg DE, Johnson SJ (2008) Active load control techniques for wind turbines. In: Department of Energy Scientific and Technical Information (OSTI). Available via OSTI. <http://www.osti.gov/scitech/servlets/purl/943932>. Accessed 07 Apr 2016
- Wagner S, Bareiss R, Guidati G (eds) (2012) *Wind turbine noise*. Springer, Berlin
- Wallis RA, Stuart CM (1962) On the control of shock induced boundary layer separation with discrete air jets. In: National Advisory Committee for Aeronautics (NACA) Archives. Available via NACA. <http://naca.central.cranfield.ac.uk/reports/arc/cp/0595.pdf>. Accessed 07 Apr 2016
- Wiltse JM, Glezer A (1993) Manipulation of free shear flows using piezoelectric actuators. *J Fluid Mech* 249:261–285

# Chapter 7

## Trailing and Leading Edge Flaps for Load Alleviation and Structure Control

Vladimir Leble and George N. Barakos

**Abstract** This chapter presents the results of numerical computations for a 10-MW wind turbine rotor equipped with the trailing and leading edge flaps. The aerodynamic loads on the rotor are computed using the Helicopter Multi-Block flow solver. The method solves the Navier-Stokes equations in integral form using the arbitrary Lagrangian-Eulerian formulation for time-dependent domains with moving boundaries. The trailing edge flap was located at 75%R, and the leading edge flap was located at 60%R, where R is the radius of the blade. The chapter is divided in the description of employed numerical methods, mesh convergence study, and the cases with trailing and leading edge flaps. Also, the chapter defines flap geometry, deformation and frequency of motion. The blade structure was assumed rigid for all presented cases. The comparison of the flap performance is conducted using non-dimensional parameters, and conclusions are drawn at the end of the chapter.

### 7.1 Numerical Methods

The HMB3 code is a 3D multi-block structured solver for the 3D Navier-Stokes equations. HMB3 solves the Navier-Stokes equations in integral form using the arbitrary Lagrangian-Eulerian formulation for time-dependent domains with moving boundaries. The solver uses a cell-centred finite volume approach combined with an implicit dual-time method. Osher's upwind scheme (Osher and Chakravarthy 1983) is used to resolve the convective fluxes, and MUSCL (Van Leer 1979) variable extrapolation is used to provide formally third-order accuracy on uniform grids. Central differencing (CD) spatial discretisation is used for the viscous terms. The non-linear system of equations that is generated as a result of the linearization is solved by integration in pseudo-time using a first-order backward difference method based on Jameson's pseudo-time integration approach (Jameson 1991). A Generalised Conjugate Gradient (GCG) method is then used (Eisenstat et al. 1983)

---

V. Leble • G.N. Barakos (✉)  
Division of Aerospace Sciences, School of Engineering, University of Glasgow, James Watt  
South Building, Glasgow G12 8QQ, UK  
e-mail: [v.leble.1@research.gla.ac.uk](mailto:v.leble.1@research.gla.ac.uk); [George.Barakos@glasgow.ac.uk](mailto:George.Barakos@glasgow.ac.uk)

in conjunction with a Block Incomplete Lower-Upper (BILU) factorisation as a preconditioner. The HMB3 solver has a library of turbulence closures including several one- and two- equation models. Turbulence simulation is also possible using either the Large-Eddy or the Detached-Eddy simulation approach (Spalart et al. 1997). The solver was designed with parallel execution in mind and the MPI library along with a load-balancing algorithm are used to this end. The flow solver can be used in serial or parallel fashion for large-scale problems. Depending on the purposes of the simulations, steady and unsteady wind turbine CFD simulations can be performed in HMB3 using single or full rotor meshes generated using the ICEM-Hexa tool. Rigid or elastic blades can be simulated using static or dynamic computations. HMB3 allows for sliding meshes to simulate rotor-tower interaction (Steijl and Barakos 2008). Alternatively, overset grids can be used (Jarkowski et al. 2013). To account for low-speed flows, the Low-Mach Roe scheme (LM-Roe) developed by (Rieper 2011) is employed for wind turbine cases (Carrión et al. 2013).

The HMB3 CFD solver has so far been validated for several wind turbine cases, including the NREL Annex XX experiments (Gómez-Iradi et al. 2009), where the effect of the blades passing in front of the tower was captured. The pressure and PIV data of the MEXICO project (Carrión et al. 2014) have also been used for validation, where the wake was resolved on a fine mesh capable to capture and preserve the vortices downstream the rotor, which enabled the prediction of the onset of wake instabilities (Carrión et al. 2015).

A new flap deflection algorithm was implemented in HMB3 to allow for arbitrary flap motion. The algorithm is based on the surface interpolation, where the mean, maximum, and minimum flap deflections are defined by separate surfaces. Then, the linear interpolation is employed for each point on the surface between the mean and deflected shape of the flap. The motion of the flap can be a complex function of time i.e. not a simple function like  $\sin(\omega t)$  or  $\cos(\omega t)$ . In this case the motion is described by a Fourier series of arbitrary number of harmonics. It must be noted here, that since only mean and maximum surfaces are known to the solver, the interpolation tends to shrink the flap slightly. To understand this behaviour, consider a 2D rod-like flap shown in Fig. 7.1. As can be seen, the linear interpolation tends to shrink the flap, but the effect is not pronounced for relatively small angles of deflection.

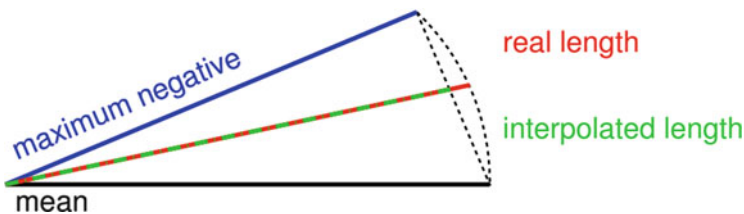


**Fig. 7.1** Schematic of the trailing edge flap, showing mean and maximum negative deflections, and real and interpolated length of the flap during motion

The computational mesh is updated at each time step after the deformation of the surface. The Trans-Finite Interpolation (TFI), described by Dubuc et al. (2000), is applied to the blocks attached to the deformed surface. The TFI interpolates the block face deformation from the edge deformations and then the full block deformation from the deformation of the block faces. The grid deformation uses a weighted approach to interpolate a face/block from the boundary vertices/surfaces respectively. The weight depends on the curvilinear coordinate divided by the length of the curve.

## 7.2 Numerical Parameters

This work employed the DTU 10 MW reference wind turbine design of Bak et al. (2013). For all presented cases, the density of air was assumed to be  $\rho = 1.225 \text{ kg/m}^3$ , the dynamic viscosity of the air was  $\mu = 1.8 \times 10^{-5} \text{ N s/m}^2$ , and the speed of sound was 340 m/s. Further, a fully turbulent flow was assumed with free-stream level of turbulence of 2.6 % and uniform inflow velocity distribution was set across the inflow boundary. The k- $\omega$  SST turbulence model was employed for all tests, unless otherwise stated. The  $y^+$  parameter was estimated based on the flat-plate boundary layer theory. For given Reynolds number, inflow velocity  $U_\infty$ , density  $\rho$ , dynamic viscosity  $\mu$  and cord length  $c$  the  $y^+$  parameter was computed in the following steps:

- 1 Estimate the skin friction coefficient from Schlichting's correlation:

$$C_f = [2 \cdot \log_{10}(Re) - 0.65]^{-2.3} \quad (7.1)$$

- 2 Obtain the wall shear stress from the definition of  $C_f$ :

$$\tau_w = C_f \cdot 0.5 \cdot \rho \cdot U_\infty^2 \quad (7.2)$$

- 3 Compute the friction velocity from:

$$U_* = \sqrt{\tau_w / \rho} \quad (7.3)$$

- 4 Compute the  $y^+$  parameter from the definition, where  $y$  is the employed spacing next to the wall:

$$y^+ = y \cdot \rho \cdot U_* / \mu \quad (7.4)$$

For the presented cases with trailing and leading edge flaps, the inflow wind speed was set to 11.4 m/s, and the rotational speed of the rotor was set to 9.6 rpm, giving a tip speed ratio of 7.83.

### 7.3 Mesh Convergence Study

The mesh convergence study was performed before various test cases were computed to find the required density of the mesh and cell distribution in the vicinity of the blade surface. Only 70 % of the blade was modelled for this study—from 0.3R to 1R, where R is the radius of the blade. The flow around the blade was considered to be periodic in space and time. This allowed the use of the HMB3 “hover” formulation described by Steijl et al. (2006). The formulation includes a combination of mesh motion and additional source terms in the Navier-Stokes equations. The spinner was approximated with a long cylinder running parallel to the flow along the computational domain. The free-stream was kept to the level of turbulence of 2.6 %, and the  $k-\omega$  turbulence model was employed. The conditions selected for the mesh convergence study are presented in Table 7.1. The domain size and boundaries are shown in Fig. 7.2, and the results of the mesh convergence study are presented in Fig. 7.3. This study showed that a mesh density between 3 and 5 M cells per blade is sufficient to obtain mesh independent solutions.

**Table 7.1** Computational conditions for the mesh convergence study

Parameter	Value
$U_{wind}$	11 m/s
$U_{tip}$	82.437 m/s
RPM	8.836
$Re_{tip}$	$34.817^\circ \times 10^6$
$M_{tip} = U_{tip}/U_{sound}$	0.243
$\lambda$	7.494
Pitch angle	$0^\circ$

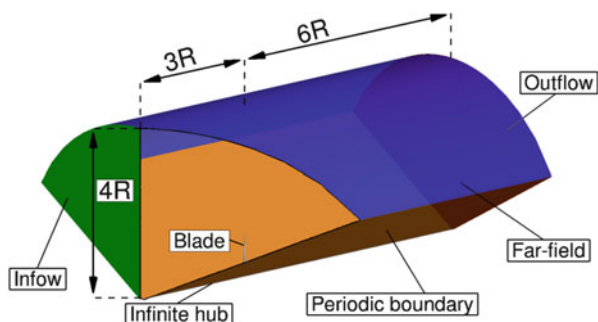


**Fig. 7.2** Computational domain for mesh convergence study with employed boundary conditions. Part of the domain removed to expose the blade



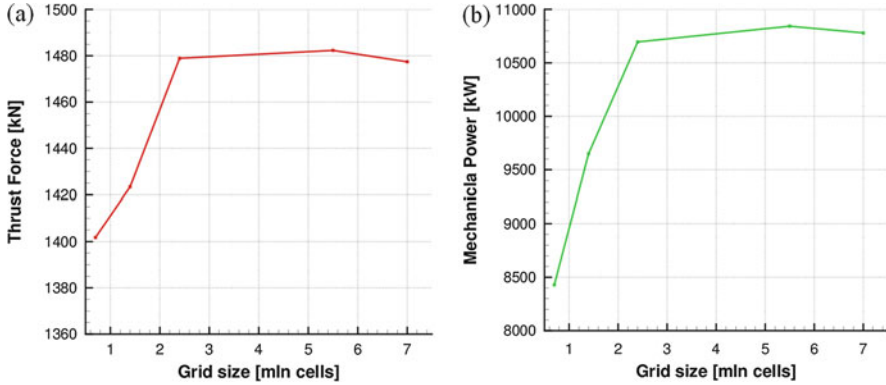


Fig. 7.3 Thrust force (a) and mechanical power (b) as function of computational grid density

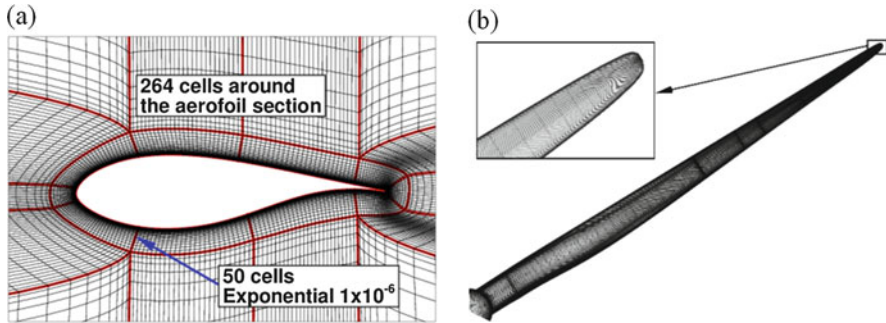
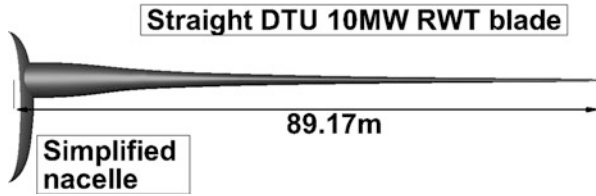


Fig. 7.4 Slices through the mesh near the surface of the blade (a); and surface grids (b) for the 9.2 M cell grid

## 7.4 Computational Grid

Based on the mesh study, a fine mesh consisting of 9.2 M points was constructed and included the necessary refinement to allow for the flaps. The computational domain had the same dimensions as for the grid convergence study shown in Fig. 7.2. The grid included the complete DTU 10 MW RWT blade in a straight configuration (no pre-bending or pre-coning), and employed an O-grid topology around the airfoil sections, as shown in Fig. 7.4a. The first cell wall distance was  $10^{-6}c$ , where  $c = 6.206 \text{ m}$  is a maximum chord of the blade. The  $y^+$  parameter for this grid at rated conditions was 0.2. Figure 7.4b shows the surface grid on the blade for the 9.2 M cells grid.

The blade was modelled in a straight configuration with a simplified nacelle, as shown in Fig. 7.5. The simplified nacelle shape was obtained by rotating the hub of the rotor by  $180^\circ$ .



**Fig. 7.5** Shape of the DTU 10 MW RWT blade with simplified nacelle as employed for the 9.2 M cells mesh

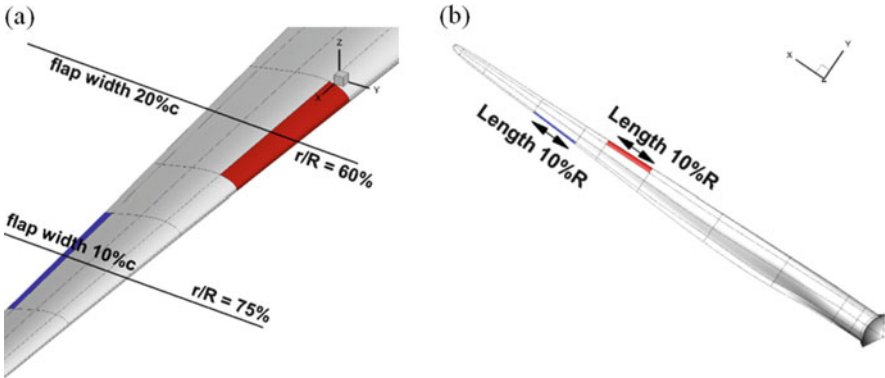


**Fig. 7.6** The location and dimensions of the trailing and leading edge flaps. (a) Location and width of the flaps. (b) Length of the flaps

## 7.5 Definition of the Flaps

The DTU 10-MW RWT blade was equipped with leading and trailing edge flaps. The leading edge (LE) flap was located at 60%*R* station, and the trailing edge (TE) flap was located at 75%*R*. The length of each flap was 10%*R*, but the width of the TE flap was 10% of the local chord, whereas the width of the LE flap was 20% of the local chord, as shown in Fig. 7.6a, b. The choice of the TE flap width was made under the understanding that flaps will be used for load control and elevation. For the LE flap, it was assumed that its operation is similar but less efficient to that of the TE flap. The width in this case is increased to 20% so as to allow larger control surface and a smooth transition of the surface slope.

The deformation of the flaps was defined with respect to the mean line of the aerofoils as indicated in Fig. 7.7. The deformation of the mean line was defined by the shape function  $\eta(\xi) = \alpha\xi^2(3 - \xi)/2$ , where  $\xi \in [0, 1]$  and depends on the location of the deformed point  $x$ , and  $\alpha$  is providing the maximum deflection for given time instance. For the trailing edge flap  $\xi^{TE} = (x/c - x_0^{TE}) / (1 - x_0^{TE})$ , and for the leading edge flap  $\xi^{LE} = (x_0^{LE} - x/c) / (x_0^{LE})$ , where  $x_0^{TE}$  and  $x_0^{LE}$  are the  $x/c$  locations of the hinge point for the trailing and leading edge flap, respectively; and

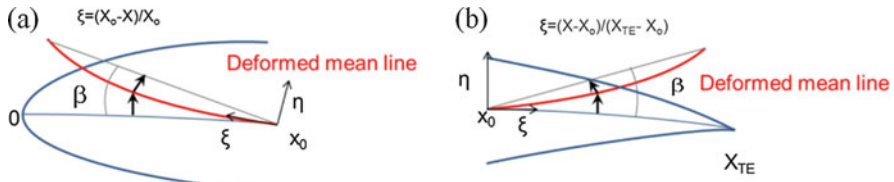


Fig. 7.7 Definition conditions for the LE (a) and TE (b) flap deformation

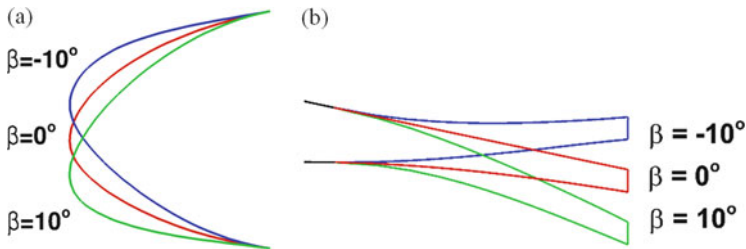


Fig. 7.8 Definition of the positive and negative deflection for the LE (a) and TE (b) flap

$c$  is the local chord. From the equation for the shape function it follows that  $\eta(\xi) \in [0, \alpha]$ . In principle,  $\alpha \equiv \alpha(t) = \alpha_m \sin(\omega t)$ , where  $\alpha_m$  is the maximum value of deflection determined by the maximum deflection angle  $\beta$ . Here, the maximum deflection was obtained as  $\alpha_m^{TE} = (1 - x_0^{TE}) \tan(\beta)$  and  $\alpha_m^{LE} = (x_0^{LE}) \tan(\beta)$  for trailing and leading edge flap, respectively. By denoting the point at which the flap starts with  $x_0$ , the process to compute flap deflection is as follows: For each point  $x > x_0$ , define  $\xi = \xi(x)$  based on the length along the chord line; compute point displacement  $\alpha$  based on the maximum deflection angle  $\beta$  and time  $t$ ; compute shape function  $\eta(\xi)$ ; apply shape function and obtain deformed flap shape.

The flaps were deflected from  $-10^\circ$  to  $10^\circ$  with the shape and notation presented in Fig. 7.8. The frequency of flap motion was set to 0.96 Hz, or six times per revolution.

## 7.6 Results for the TE Flap

Span-wise load distributions for the DTU 10-MW reference wind turbine equipped with the trailing edge flap are shown in Fig. 7.9. The flap oscillates at frequency 0.96 Hz—six times per revolution. The length of each section in radial direction used in pressure integration is  $\Delta r = 2.15m$ .

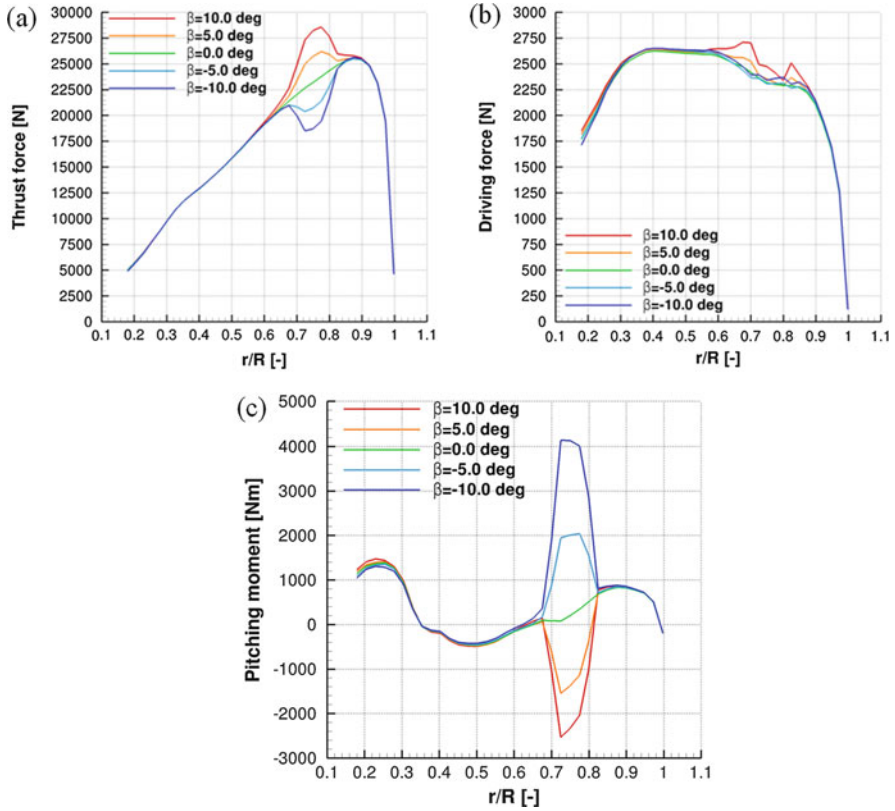


**Fig. 7.9** Spanwise distribution of thrust force (a), driving force (b) and pitching moment (c) for DTU blade equipped with TE flap. Flap motion frequency  $f = 0.96$  Hz (6 times per revolution)

## 7.7 Results for the LE Flap

Span-wise load distributions for the DTU 10-MW reference wind turbine equipped with the leading edge flap are shown in Fig. 7.10. Flap oscillates at frequency 0.96 Hz—six times per revolution. The length of each section in radial direction used in pressure integration is  $\Delta r = 2.15m$ .

## 7.8 Comparison of the Performance

In order to conduct a meaningful comparison of the performance of both flaps the non-dimensional coefficients were used. This was chosen, since flaps are located at different radial positions and have different inflow conditions. For this, the normal

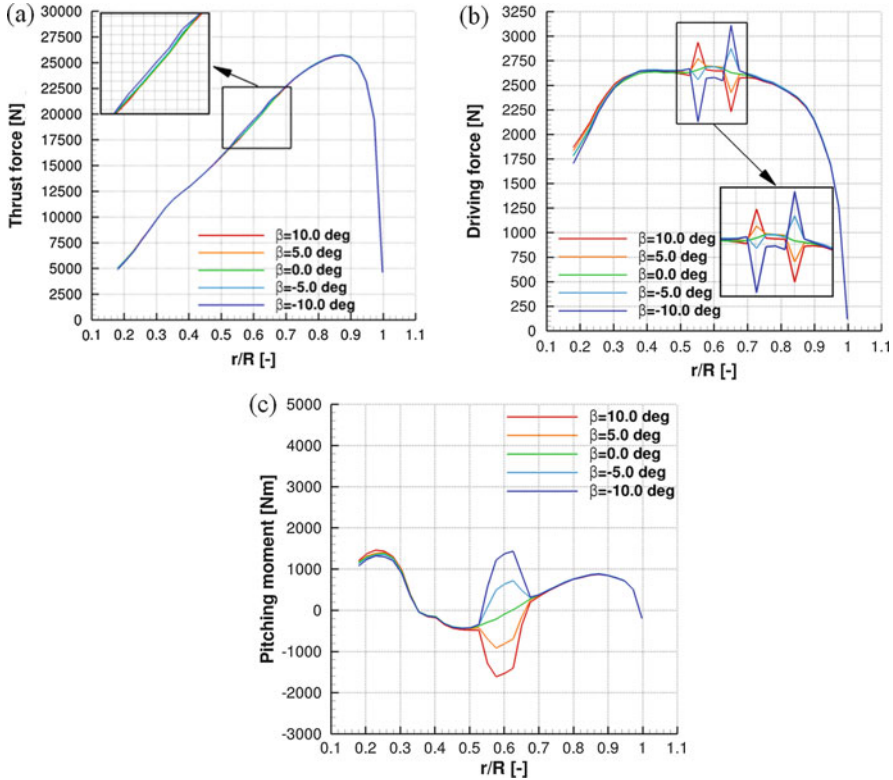


**Fig. 7.10** Spanwise distribution of thrust force (a), driving force (b) and pitching moment (c) for DTU blade equipped with LE flap. Flap motion frequency  $f = 0.96$  Hz (6 times per revolution)

force coefficient ( $C_N$ ), tangential force coefficient ( $C_T$ ) and pitching moment coefficient ( $C_M$ ) were computed. First, the thrust and driving forces were projected on the normal and tangential directions using local geometrical pitch angle  $\alpha$  as:

$$F_N = T_F \cdot \cos(\alpha) + D_F \cdot \sin(\alpha) \quad (7.5)$$

$$F_T = D_F \cdot \cos(\alpha) - T_F \cdot \sin(\alpha) \quad (7.6)$$

The thrust ( $T_F$ ) and driving ( $D_F$ ) forces are defined in Fig. 7.11, and were obtained from the surface pressure integration in the middle of the flap with the length of the section in radial direction  $\Delta r = 2.15m$ . Note, that the geometrical pitch angle  $\alpha$  is defined in Bak et al. (2013), and is constant i.e. it does not change

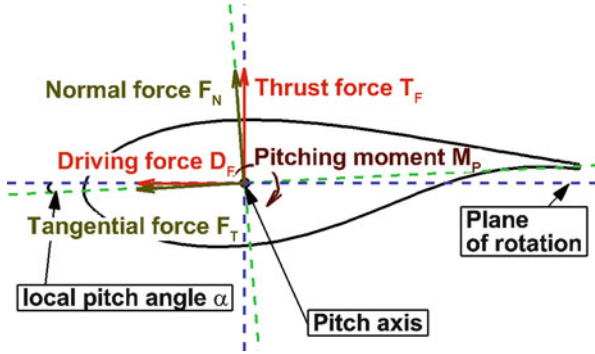


**Fig. 7.11** Definition of the normal force, tangential force and pitching moment. Quantities shown in the directions defined as positive

with the flap angle  $\beta$ . Then, the forces and moment were non-dimensionalized as:

$$CN = \frac{F_N}{0.5\rho U^2 A} \quad (7.7)$$

$$CT = \frac{F_T}{0.5\rho U^2 A} \quad (7.8)$$

$$CM = \frac{M_P}{0.5\rho U^2 A c} \quad (7.9)$$

where  $U$  and  $A$  are the geometrical local inflow velocity and the local platform area, respectively. The inflow velocity is defined as:

$$U^2 = (\Omega r)^2 + U_{wind}^2 \quad (7.10)$$

and the platform area is defined as:

$$A = \Delta r \cdot c \quad (7.11)$$

where  $c$  is the local chord in the middle of the flap.

The obtained coefficients for both flaps as functions of the flap angle  $\beta$  are compared in Fig. 7.12. As can be seen, the trailing edge flap significantly modifies all three non-dimensional coefficients. On the other hand, leading edge flap has the most pronounced effect on the pitching moment coefficient, and almost negligible (as compared to the TE flap) influence on the normal force coefficient. Further, the relative change and slope of the pitching moment coefficient is higher for the trailing edge flap. Finally, both flaps can change the tangential force coefficient, but the TE flap has higher hysteresis loop, as compared to the results for the LE flap.

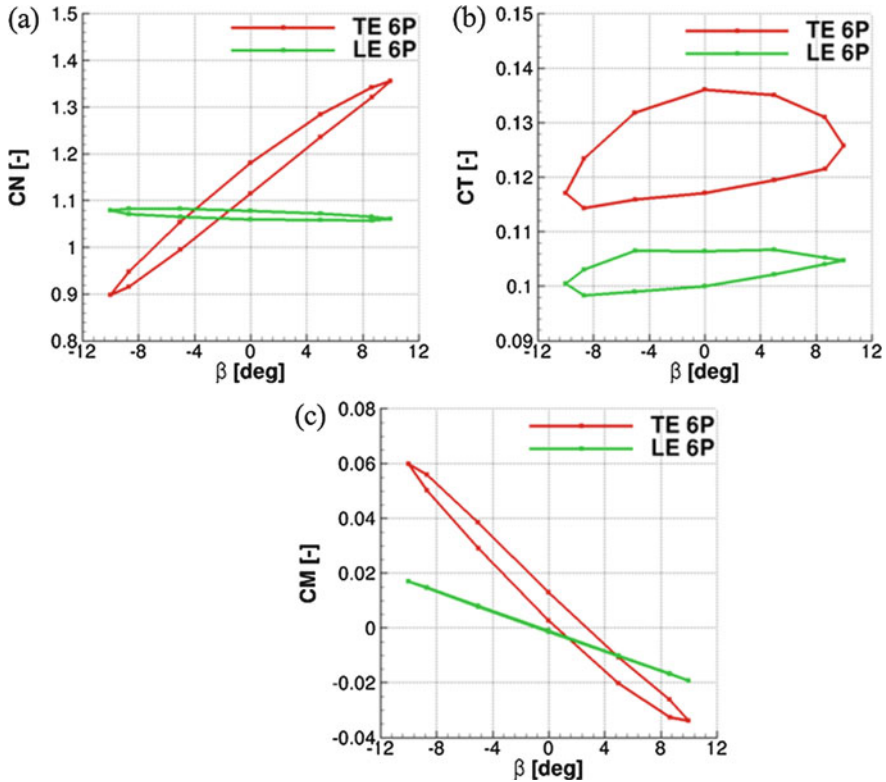


**Fig. 7.12** Comparison of the performance of TE and LE flaps based on the non-dimensional coefficients as function of flap deflection angle. (a) Normal force coefficient. (b) Tangential force coefficient. (c) Pitching moment coefficient

## 7.9 Summary

The results showed a significant, but localized effect of the flap deflection on the distribution of the loads. The trailing edge flap can modify both thrust force and pitching moment, whereas trailing edge flap mostly affects the pitching moment. That suggests, that trailing edge flaps can be used to locally change aerodynamic loads on the blades, possibly eliminating the adverse effect of the blade passing in front of the tower. On the other hand the leading edge flap can be used to counter the additional pitching moment created by the deflection of the trailing edge flap.

**Acknowledgments** Results were obtained using the EPSRC funded ARCHIE-WeSt High Performance Computer ([www.archie-west.ac.uk](http://www.archie-west.ac.uk)). EPSRC grant no. EP/K000586/1.

**Open Access** This chapter is distributed under the terms of the Creative Commons Attribution-NonCommercial 4.0 International License (<http://creativecommons.org/licenses/by-nc/4.0/>), which permits any noncommercial use, duplication, adaptation, distribution and reproduction in any medium or format, as long as you give appropriate credit to the original author(s) and the source, provide a link to the Creative Commons license and indicate if changes were made.

The images or other third party material in this chapter are included in the work's Creative Commons license, unless indicated otherwise in the credit line; if such material is not included in the work's Creative Commons license and the respective action is not permitted by statutory regulation, users will need to obtain permission from the license holder to duplicate, adapt or reproduce the material.

## References

- Bak C, Zahle F, Bitsche R et al (2013) The DTU 10-MW reference wind turbine. In: DTU Orbit – The Research Information System. Available via Technical University of Denmark. [http://orbit.dtu.dk/files/55645274/The\\_DTU\\_10MW\\_Reference\\_Turbine\\_Christian\\_Bak.pdf](http://orbit.dtu.dk/files/55645274/The_DTU_10MW_Reference_Turbine_Christian_Bak.pdf). Accessed 06 Apr 2016
- Carrión M, Woodgate M, Steijl et al (2013) Implementation of all-Mach Roe-type schemes in fully implicit CFD solvers – demonstration for wind turbine flows. *Int J Numer Methods Fluids* 73(8):693–728. doi:10.1002/fld.3818
- Carrión M, Steijl R, Woodgate M et al (2014) Computational fluid dynamics analysis of the wake behind the MEXICO rotor in axial flow conditions. *Wind Energy* 18:1025–1045. doi:10.1002/we.1745
- Carrión M, Woodgate M, Steijl R et al (2015) Understanding wind-turbine wake breakdown using computational fluid dynamics. *AIAA J* 53(3):588–602. doi:10.2514/1.J053196
- Dubuc L, Cantariti F, Woodgate M et al (2000) A grid deformation technique for unsteady flow computations. *Int J Numer Methods Fluids* 32(3):285–311
- Eisenstat S, Elman H, Schultz M (1983) Variational iterative methods for nonsymmetric systems of linear equations. *Siam J Numer Anal* 20:345–357. doi:10.1137/0720023
- Gómez-Iradi S, Steijl R, Barakos G (2009) Development and validation of a CFD technique for the aerodynamic analysis of HAWT. *J Sol Energy Eng*. doi:10.1115/1.3139144
- Jameson A (1991) Time dependent calculations using multigrid, with applications to unsteady flows past airfoils and wings. In Abstracts of the 10th computational fluid dynamics conference, fluid dynamics and co-located conferences, AIAA, Honolulu, 24–26 June 1991
- Jarkowski M, Woodgate M, Barakos G et al (2013) Towards consistent hybrid overset mesh methods for rotorcraft CFD. *Int J Numer Methods Fluids* 74(8):543–576. doi:10.1002/fld.3861
- Osher S, Chakravarthy S (1983) Upwind schemes and boundary conditions with applications to Euler equations in general geometries. *J Comput Phys* 50:447–481. doi:10.1016/0021-9991(83)90106-7
- Rieber F (2011) A low-Mach number fix for Roe's approximate Riemann solver. *J Comput Phys* 230(13):5263–5287. doi:10.1016/j.jcp.2011.03.025
- Spalart P, Jou W, Strelets M et al (1997) Comments on the feasibility of LES for wings, and on a hybrid RANS/LES approach. In: Liu C, Liu Z (eds) Proceedings of the first AFOSR international conference on DNS/LES, Louisiana, 1997
- Steijl R, Barakos G (2008) Sliding mesh algorithm for CFD analysis of helicopter rotor-fuselage aerodynamics. *Int J Numer Methods Fluids* 58:527–549. doi:10.1002/fld.1757
- Steijl R, Barakos G, Badcock K (2006) A framework for CFD analysis of helicopter rotors in hover and forward flight. *Int J Numer Methods Fluids* 51(18):819–847. doi:10.1002/fld.1086
- Van Leer B (1979) Towards the ultimate conservative difference scheme, a second order sequel to Godunov's method. *J Comput Phys* 32:101–136



**Part II**  
**Enabling Technologies for Drivetrain**  
**and Gearbox Analysis**

# Chapter 8

## OWT Drivetrain & Gearbox Simulation and Testing

Simone Manzato and Bert Pluymers

**Abstract** As wind turbines continue to grow in size and offshore installations become more and more attractive for investors, the design of reliable drivetrains and gearboxes is becoming very critical. One key element is represented by the challenging environmental conditions, which are significantly different and harsher than those experienced by onshore machines. Additionally, a deeper understanding of the operational loads and the effects of combined aero—and hydrodynamic forces on the drivetrain is essential to ensure the wind turbines can be guaranteed for the expected lifetime. These problems result in increased research efforts towards improving the capabilities and the use of simulation tools to better understand the complex drivetrain dynamic behavior. In parallel, advances in experimental techniques are also sought, as a way of deriving reliable information for model verification and validation, and to get a deeper insight in the structure operational response.

### 8.1 Simulation and Testing in Drivetrain and Gearbox Design

The drivetrain and the gearbox in particular continue to play a key role in the wind turbine industry. According to a report published online by OffshoreWIND.biz (2014), the global gearbox market increased from approximately \$1.9 billion in 2006 to \$4.0 in 2013, thanks in particular to the significant increase in installed power worldwide. However, direct-drive solutions are attracting more and more the interest of the manufacturers and it is expected that the market share of the two solutions (displayed in Fig. 8.1) will soon be balanced.

---

S. Manzato (✉)

Siemens Industry Software (SISW), Interleuvenlaan 68, 3001 Leuven, Belgium  
e-mail: [simone.manzato@siemens.com](mailto:simone.manzato@siemens.com)

B. Pluymers

Department of Mechanical Engineering, KU Leuven, Celestijnenlaan 300c, 3001 Leuven, Belgium  
e-mail: [bert.pluymers@kuleuven.be](mailto:bert.pluymers@kuleuven.be)

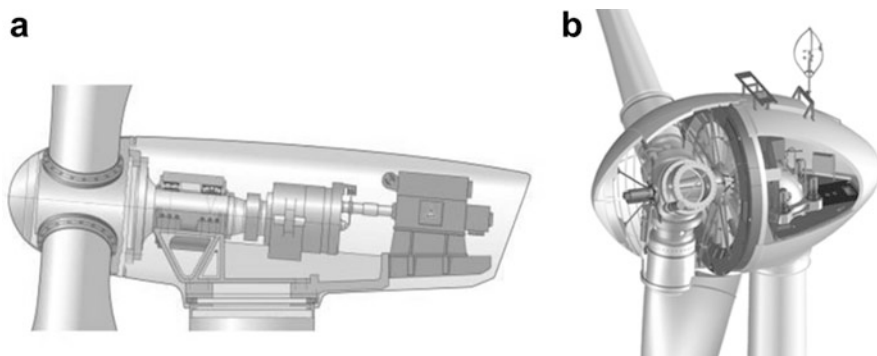


**Fig. 8.1** Typical turbine driveline configurations. (a) Gearbox and (b) Direct-drive generator

Gearboxes typically have the advantage of requiring smaller initial investments, but because of the number of rotating parts, gear pairs and bearings, reliability is typically an issue. On the other hand, direct-drive machines require a bigger investment related to the development and construction of big permanent magnet generators but have typically lower operation and maintenance costs. To guarantee the effectiveness and competitiveness of the gearbox solution, significant improvements in the design phase are required to better understand the mechanisms leading to gearbox failures. This can only be achieved by developing more accurate, reliable and efficient numerical models, able to replicate not only the global load transfer paths across the driveline but also the local load transfer mechanisms.

More advanced design tools are not only motivated by the call for reliability, but also by other technological drivers which makes the role of the drivetrain more and more critical. As extensively discussed by Helsen et al. (2012), turbine manufacturers are aiming at developing ever bigger machines, with the objective of maximizing the power produced by each individual machine. This trend, over the past 30 years, is shown in Fig. 8.2: bigger and longer blades installed on higher turbines will give access to higher wind speeds and consequently increase the generated power. However, this also poses critical design challenges. Bigger wind turbines and corresponding bigger blades impose higher loads on the turbine components, and in particular the drivetrains, and these loads cannot be considered quasi-static as in the majority of industrial applications. These loads represent a combination of aerodynamic loads at variable wind speeds, gravitational loads and corresponding bending moments, inertial loads due to acceleration, centrifugal and gyroscopic effects, generator torque loads and loads introduced by control actions such as blade pitching, starting up, emergency braking and yawing. Besides, driveline is also subjected to transient phenomena related to sudden wind gusts or electrical grid malfunctioning which generates heavy loads on all rotating components, and in particular on gears and bearing. These effects contribute to non-torque loading, where vertical, horizontal and axial loads are applied on the gears and bearings. Neglecting these effects in design phase is one of the causes of premature failure of gearboxes components, in particular bearings and gears.

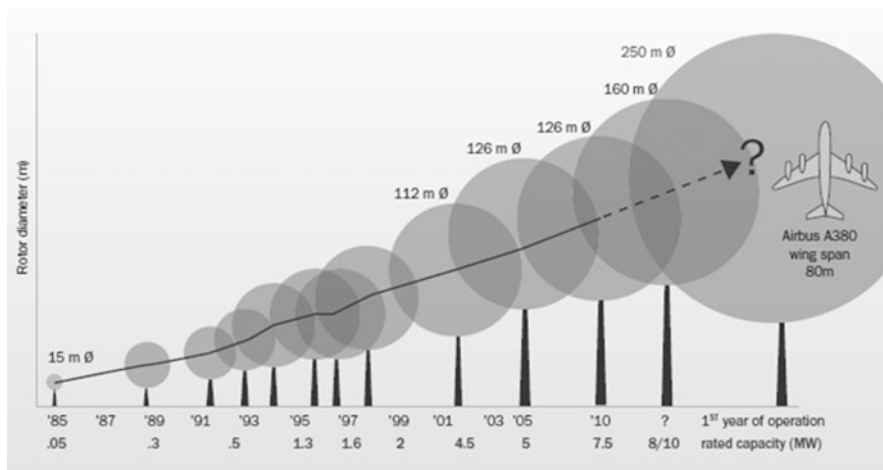


Fig. 8.2 Wind turbine upscaling trend over the past 30 years (Source: FP6 Upwind project, 2011)

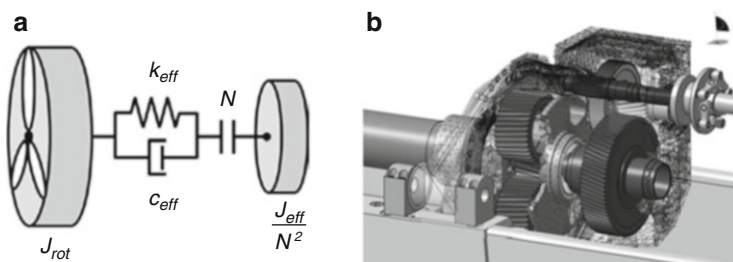


Fig. 8.3 Modelling approaches for wind turbine gearboxes. (a) two DOFs torsional model from Girsang et al. (2013), (b) flexible MBS model of the NREL GRC gearbox

Over the past decade, gearbox manufacturers have recognized the limitations related to common design approaches and started integrating more and more numerical tools to validate innovative designs. This paradigm shift represents the foundation of the work by Peeters (2006), where the limitations in traditional design codes for wind turbine design were identified. The work reviews state-of-the-art design tools for wind turbine drivetrain in the early 2000 and introduces a new modelling approach for the simulation of more detailed drivetrain loads relying on the flexible Multibody Simulation (MBS) approach. Two of the discussed modelling approaches, going from two to thousands of degrees of freedom, are shown in Fig. 8.3. The work focused on the importance of modelling the internal dynamics in the gearbox and the complex interaction between the different subcomponents to be able to correctly estimate the operational loads and consequently include this information in the design phase.

The conclusion of Peeters (2006) paved the way for further developments and optimization in the modelling strategies of gearboxes. In the work of Helsen (2012)

efficient simulation strategies have been investigated to understand the interaction of the turbine transients with the dynamic excitation within the drivetrain originating from the meshing gears and the full drivetrain structural behavior. The importance of modelling dynamic flexibility of internal gearbox components such as the ring wheel and the planet carrier(s) has also been investigated. Advanced model order reduction techniques based on static mode switching (Tamarozzi et al. 2013) have been applied to accurately simulate a 3D gear contact problem. The results show that the method is able to keep the same level of accuracy of fully non-linear simulation models while drastically reducing the computational resources. Finally, the recent work of Vanhollebeke (2015) demonstrated the possibility to use very accurate flexible MBS models of gearbox and to integrate them in the design phase not only to accurately predict loads but also to efficiently analyze possible NVH problems such as tonalities and vibrations.

Within the MAREWINT project, specific activities were conducted to follow up on these findings and complement the existing work with focus on two specific aspects. Chapter 9 focuses on a review of advanced modelling techniques for bearing and the optimal integration of these models in a flexible multibody simulation environment. In Chap. 10, recent advances on the experimental characterization of gearboxes in operations are presented. Being able to identify an operational model of the gearbox under different loading conditions will provide valuable inputs for validation of global gearbox models and verification of design assumptions.

**Open Access** This chapter is distributed under the terms of the Creative Commons Attribution-NonCommercial 4.0 International License (<http://creativecommons.org/licenses/by-nc/4.0/>), which permits any noncommercial use, duplication, adaptation, distribution and reproduction in any medium or format, as long as you give appropriate credit to the original author(s) and the source, provide a link to the Creative Commons license and indicate if changes were made.

The images or other third party material in this chapter are included in the work's Creative Commons license, unless indicated otherwise in the credit line; if such material is not included in the work's Creative Commons license and the respective action is not permitted by statutory regulation, users will need to obtain permission from the license holder to duplicate, adapt or reproduce the material.

## References

- Girsang IP, Dhupia JS, Muljadi E et al (2013) Gearbox and drivetrain models to study dynamic effects of modern wind turbines. Paper presented at the IEEE energy conversion congress and exposition Denver, 15–19 September 2013
- Helsen J (2012) The dynamics of high power density gear units with focus on the wind turbine application. Dissertation, KU Leuven
- Helsen J, Vanhollebeke F, Vandepitte D et al (2012) Some trends and challenges in wind turbine upscaling. In: Abstracts of the ISMA 2012, international conference on noise and vibration engineering, Leuven, 17–19 September 2012
- OffshoreWIND.biz (2014) Report on Wind Turbine Gearbox and Direct-Drive Systems out now. <http://www.offshorewind.biz/2014/09/19/report-on-wind-turbine-gearbox-and-direct-drive-systems-out-now/>. Accessed 19 Jan 2016

- Peeters J (2006) Simulation of dynamic drive train loads in a wind turbine. Dissertation, KU Leuven
- Tamarozzi T, Ziegler P, Eberhard P et al (2013) Static modes switching in gear contact simulation. *Mech Mach Theory* 62:69–106. doi:[10.1016/j.mechmachtheory.2013.01.006](https://doi.org/10.1016/j.mechmachtheory.2013.01.006)
- Vanhollebeke F (2015) Dynamic analysis of a wind turbine gearbox: towards prediction of mechanical tonalities. Dissertation, KU Leuven

# Chapter 9

## Dynamic Behavior of Bearings on Offshore Wind Turbine Gearboxes

Rubén Cerdá, Bart Blockmans, Jakob Fiszer, Tommaso Tamarozzi, Bert Pluymers, and Wim Desmet

**Abstract** Gearbox failure is among the highest causes of downtime in a wind turbine, causing a significant loss to the wind energy sector, especially in the complex offshore environment. Quite often, the cause of these gearbox and drivetrain errors, as well as other undesired noise and vibrations issues, is premature bearing failure. Therefore, developing more efficient and reliable bearing models and simulation methods that can accurately predict the nonlinear dynamic loads already in the design phase is still crucial. Without claims of completeness, a few important items to be considered when analyzing bearings and a state-of-the-art review for bearing modelling approaches (from analytical lumped parameter models to complex flexible multibody simulations) will be discussed in this chapter. Furthermore, some recent modelling developments and the problem of integrating these bearing models with similar advanced gear models into flexible multibody simulations at full-scale wind turbine drivetrain level will be addressed.

### 9.1 Introduction

Improving the reliability of wind turbines (WT) is an essential component in the bid to minimize the cost of energy (COE) from wind, especially for offshore wind turbines because of the difficulties associated with access for maintenance. Unfortunately, many drivetrains are suffering premature bearing failures. These bearing failures are very costly, particularly given the long downtime incurred per failure. Numerous studies have been undertaken to obtain the distribution of failures by assembly in WTs. Gearbox and generator failure rates remain unacceptably high. Furthermore, the downtime for these failures is amongst the highest of all WT assemblies. Often the entire gearbox or generator needs to be replaced, which requires the deployment of a large crane. These cranes are costly and may take days or weeks to deploy. Offshore, it is not unusual for rough weather to prevent access

---

R. Cerdá (✉) • B. Blockmans • J. Fiszer • T. Tamarozzi • B. Pluymers • W. Desmet  
Department of Mechanical Engineering, KU Leuven, Celestijnenlaan 300c, 3001 Leuven, Belgium  
e-mail: [ruben.cerda@kuleuven.be](mailto:ruben.cerda@kuleuven.be); [bart.blockmans@kuleuven.be](mailto:bart.blockmans@kuleuven.be); [jakob.fiszer@kuleuven.be](mailto:jakob.fiszer@kuleuven.be);  
[tommaso.tamarozzi@kuleuven.be](mailto:tommaso.tamarozzi@kuleuven.be); [bert.pluymers@kuleuven.be](mailto:bert.pluymers@kuleuven.be); [wim.desmet@kuleuven.be](mailto:wim.desmet@kuleuven.be)

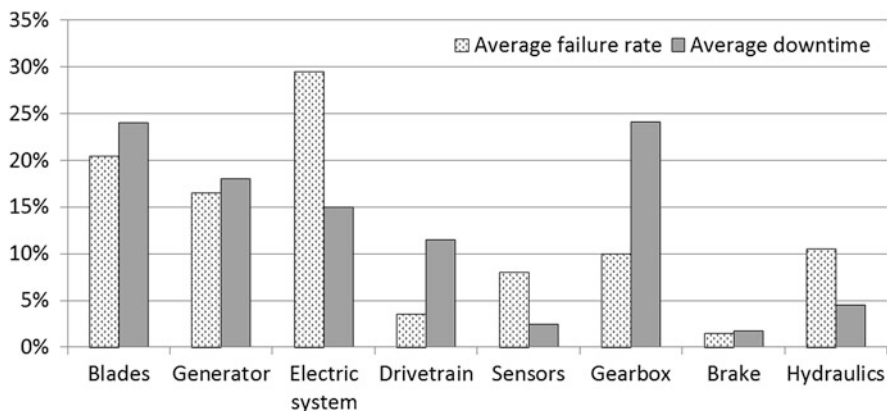


**Fig. 9.1** Distribution of failures and downtime by assembly in WT (adapted from EWEA 2011)

for operation and maintenance for weeks at a time. Figure 9.1 shows the average failure rate and the incurred average downtime by assembly, based on the work presented in EWEA (2011).

Moreover, Chen and Alewine (2010) published the findings of a survey of over 800 failed WT generators, which showed that the dominant source in multi-megawatt WT generators is the bearing. Despite this evidence, and although the unique operational conditions of the bearings resulting from widely varying wind loads and high vibration levels are well known, the root causes of these failure data are not completely known. There is, therefore, a need to search for more accurate and trustworthy component-level models and to undertake full dynamic multibody simulations at WT drivetrain system level.

Mechanical transmissions have been continuously attracting the interest of researchers and engineers, who dedicated consistent resources and efforts since the second half of the past century to investigate the multiple and interconnected phenomena that are typical in transmission dynamics. However, despite extensive studies in the last decades, system-level dynamics for the whole mechanical transmission is gaining a game-changer role and requires a deeper understanding and a more detailed knowledge to allow designers to address at the same time efficiency, durability and noise predictions and optimization.

Current simulation techniques rely on the assumption that the components are rigid, or adopt linearized modal reductions, which are applicable for the shafts and the housing but introduce significant approximations for the other components since they do not allow modelling the nonlinear dynamic contact interactions involved in the gear meshing and in the bearings with sufficient accuracy if a lumped-parameters approach is used.

Due to the highlighted reasons, the design of a WT drivetrain that is optimized from the dynamic point of view at a system level can be achieved only by establishing a simulation methodology that is capable of capturing, in a multi-discipline



integrated, detailed yet computationally efficient way, all those phenomena that are relevant for the non-linear dynamic behavior of the system.

## 9.2 Bearings for Wind Turbine Applications

Besides gears, bearings are the other main sub-system in every mechanical transmission. Due to the great variety of bearing types, the scope of this section is narrowed down to rolling-element bearings (also known as rolling or roller bearings). This type of bearing is one of the most used in mechanical applications, playing a crucial and effective role across various industries such as automotive or wind turbines.

In this section, some of the main phenomena affecting bearings, with a specific focus on wind turbine applications, are discussed.

### 9.2.1 Rolling-Element Bearings: Basic Concepts

The term “rolling” is collectively used for all forms of bearings that utilize the rolling action of balls or rollers to minimize the friction from a constrained motion of one body relative to another. Most bearings provide a close relative position of two loaded components yet allow a rotational motion between them. Special types only allow a linear motion in the direction of a stationary shaft (e.g. linear guides). A combination of both degrees of freedom is also possible. Various types of rolling elements are available to achieve this constrained motion. They can be categorized into five standard shapes: ball bearing, cylindrical bearing, tapered bearing, needle bearing and barrel bearing; each suitable for a different application.

A common rolling element bearing typically consists of an inner and an outer ring and a number of rolling elements which form the connection between the rings. The rolling elements are often guided by a cage to ensure uniform distribution and to prevent mutual contact. To prevent axial motion of the elements, both the inner and outer ring of most ball bearings include a gap called groove or raceway. Besides constraining the axial motion, the raceways also store the lubrication, which is necessary in order to reduce the friction and wear in the rolling contacts. A seal is also implemented to contain the lubricant and protect the raceway from dirt.

A more extensive version of this brief introduction to the nomenclature of rolling bearings can be found in Harris and Kotzalas (2006) and Wensing (1998).

The need to reduce vibrations of rotating machinery has stimulated researchers for many years to analyze the dynamic behavior of rolling element bearings. As the bearings are in the transmission path of vibrations between the shaft and bearing housing, they play a key role in the resulting vibrations. They determine for instance the machine’s critical speeds and the forces acting on the different components. Subsequently, they influence the noise emanating from the machine and component

stresses and wear. Some of the main phenomena that affect the non-linear dynamic behavior of the bearings are discussed in the following subsections.

### 9.2.2 Contact Mechanics

When two elastic solids contact under a load  $w$ , a contact area develops. In many engineering applications such as rolling element bearings and gears, the contact area is small and the resulting pressure is high. The local deformation and stresses can be determined from analytical formulas, based on the theory of elasticity and derived by Hertz. Hertz's contact model is based on the following assumptions (Wensing 1998):

- The material deformation is elastic.
- The load is directed normally to the contacting surfaces, such that surface shear stresses can be neglected.
- The dimensions of the contact area are small compared to the radii of curvature of the contacting bodies.
- The effect of surface roughness is negligible.

For a point contact in ball bearings, an elliptical shape of the contact area is assumed. Figure 9.2 shows the contact geometry (Jacobs 2014). The rolling element load  $w$  is oriented in the  $x$ -direction, the rolling direction equals the  $y$ -direction and the bearing's rotation axis is oriented in the  $z$ -direction. The contact is characterized by its radii of curvature in two principal planes, perpendicular to each other. The first principal plane ( $xz$ -plane) contains the bearing's rotation axis and a rolling element center. The semi-major axis of the elliptical contact  $a$  is located in this plane. The

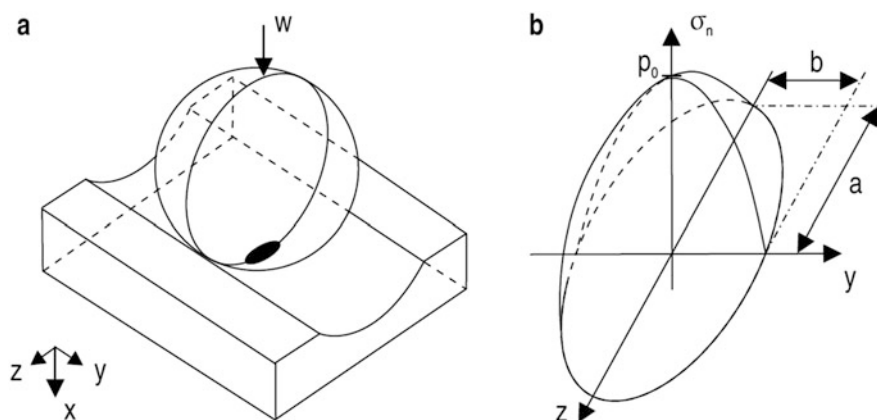


**Fig. 9.2** (a) Elliptical contact area in *black* and in (b) the corresponding surface stress distribution (Jacobs 2014)

second principal plane (xy-plane) is perpendicular to the rotation axis and contains a rolling element center. The semi-minor axis of the elliptical contact  $b$  is located in this plane.

The contact problem is reduced to the problem of a paraboloid shaped surface approaching a flat surface. The normal stress is distributed over the contact area in the form of a semi ellipsoid, as shown in Fig. 9.2b. The maximum normal stress at the surface  $p_0$  occurs at the geometrical center of the contact area and thus amounts to 1.5 times the evenly distributed pressure:

$$p_0 = 1.5 \frac{w}{A} \quad (9.1)$$

where the contact surface area  $A$  is given by:

$$A = \pi \cdot a \cdot b \quad (9.2)$$

with  $a$  and  $b$  being the semi-major and semi-minor axis of the elliptical contact.

This maximum stress is also called maximum Hertzian contact pressure. The normal stress  $\sigma_n$  at all other points within the contact area is given by:

$$\sigma_n = p_0 \left( 1 - \left( \frac{z}{a} \right)^2 - \left( \frac{y}{b} \right)^2 \right)^{1/2} \quad (9.3)$$

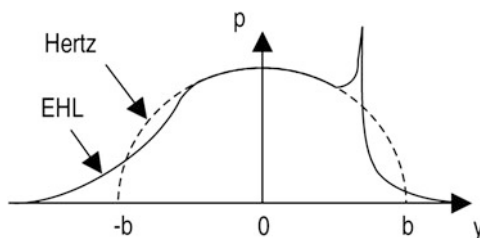
Beside the surface stresses caused by a concentrated force applied perpendicular to the surface, rolling contacts of ball bearings also have subsurface stresses. The principal stresses occurring below the center of the contact area were calculated by Jones (1946). Based on Mohr's circle, the maximum shear stress is derived as well. Due to friction between the rolling elements and raceways, tangential forces are introduced on the surface. The effect of the resulting surface shear stress on the subsurface stresses was analyzed by Zwirlein and Schlicht (1980).

### 9.2.3 Influence of the Lubricant Film

The first realistic model which provided an approximate solution for the lubricant film thickness was proposed by Grubin (1949). It was found that the combination of three effects is instrumental to the lubrication mechanism: hydrodynamic lubrication, elastic deformation of the metal surfaces and the increase in viscosity of oil under extreme pressures. It was shown theoretically that under the condition of intense contact stress, a lubricating oil film can be formed. This elasto-hydrodynamic lubrication (EHL) film is very thin (0.1–1  $\mu\text{m}$ ), but separates the interacting surfaces.

In a stationary contact between a ball and raceway, the pressure distribution is ellipsoidal according to the classical Hertzian theory (Fig. 9.2b). The pressure field

**Fig. 9.3** Pressure distribution considering the EHL film (Jacobs 2014)



changes when the lubricant is dragged into the contact with a mean velocity. An EHL film is generated, which modifies the pressure distribution at the entry and exit regions of the contact. Figure 9.3 (Jacobs 2014) shows the pressure distribution along the minor axis of the elliptical contact.

Due to the strong interaction between the EHL film and the deformation of the contacting surfaces, the lubricant film affects the stiffness and damping characteristics of the bearing.

One of the most up-to-date analyses of the stiffness and damping evaluation for elasto-hydrodynamic contacts is based on the assessment of the dynamic response through a full dynamic simulation of the contact forces. It was first published by Wijnant (1998) and later extended by Wensing (1998) and Nonato and Cavalca (2012). Owing to the formation of a lubricant film, an increasing stiffness of each contact in comparison to a dry contact is observed. Also, the effective internal bearing clearance is reduced. The formation of a lubricant film consequently leads to an increased bearing stiffness.

Experimental studies analyze the variations of the bearing dynamics for different values of the load, speed and lubricant's viscosity. Dietl et al. (2000) measure the damping capabilities of two rolling element bearings supporting a rigid shaft. Mitsuya et al. (1998) investigate the damping characteristics of a single deep groove ball bearing. A higher damping of the lubricated bearing in comparison to a dry bearing is observed in each publication. The difficulty of performing sufficiently accurate measurements and the multitude of parameters influencing the results (type of bearings, radial and axial preload, speed, loose/interference fits of the bearing seats, lubricant properties, temperature, etc.) is emphasized in most of these publications.

### 9.2.4 Durability

Rolling elements bearing failure is one of the foremost causes of breakdown in rotating machinery (Li et al. 1999). Bearings fail prematurely in service due to phenomena like contamination, poor lubrication, poor fits, misalignments, etc. The main contributors to the decrease in the durability of a rolling bearing are the behavior of the lubricant film during strong external excitation and the damage of

the raceway surfaces due to the external dynamic loads that can be applied to the bearing for a long period of time.

**Common Fatigue Failure Modes** Every rolling element bearing rotating under load above the endurance strength limit has a definite fatigue life. The bearing approaches the end of its life when the rolling surfaces are damaged by rolling contact fatigue (RCF). Two mechanisms of fatigue damage initiation can be distinguished (Muro and Tsushima 1970):

- *The subsurface failure mode:* In many applications, the lubrication of the rolling contacts is adequate and the friction between the rolling elements and raceways is negligible. The von Mises equivalent stress reaches its maximum at a point below the surface. The stress can locally exceed the yield strength of the bearing steel (between 1400 and 1800 MPa) such that plastic deformation occurs. During cyclic loading, residual stresses build up and minute cracks are formed below the surface. This is often observed in the region of material inhomogeneities, where the stresses are maximal. The subsurface cracks eventually progress towards the surface. Surface material can break loose such that deep spalls are formed. During the remaining bearing lifetime, the damage spreads rapidly since torn-off particles are rolled over causing local overloading. A detrimentally preloaded bearing, for instance due to poor fits or misalignment, fails prematurely due to RCF initiated below the surface.
- *The surface failure mode:* Ceramic or metallic foreign solid particles contaminate the lubricant in the contacts. The solid particles originate for instance from the grinding process of the bearing and/or its surrounding structure (carbide cluster). Due to over-rolling during the bearing operation, indentations on the raceway surfaces are formed. The Hertzian micro-contacts between the surfaces and the solid particles are subjected to cyclic loading. This results in increasing residual stresses near the surface up to a depth related to the size distribution of the indentations. Strain hardening by severe plastic deformation leads to material embrittlement and subsequent crack initiation on the surface. Further failure development produces shallow V-shaped pits which are originally only several micrometers deep. The pits are formed behind the indentations. Chips of surface material flake off causing accelerated wear. While a small amount of wear is natural and unavoidable in most bearing arrangements, inadequate sealing and defective lubrication lead to severe wear. The bearing fails prematurely due to RCF initiated at the surface.

**Lifetime Calculation** Accurate prediction of the lifetime of rolling element bearings is a crucial step towards a reliable design of many rotating machines. The general lifetime calculations are based on the assumption that the rolling surfaces flake sooner or later due to RCF initiated below the surface (subsurface failure mode). According to the classical fatigue theory, the first cracks usually emanate from inhomogeneities in the material, such as microscopically small inclusions or metallurgical dislocations. In recent years, inhomogeneities in the bearing material became less important as a cause of fatigue damage, owing to the

constant improvement of the material cleanliness. Today, most cracks emanate from indentations caused by solid particles (surface failure mode). The inhomogeneities are randomly distributed in the material and vary in size and type. The solid particles may enter rolling contact areas at an earlier or later time. With identical bearings and operating conditions, fatigue damage therefore occurs after different periods of operation. Brandlein et al. (1999) describe a series of lifetime tests. Thirty bearings of the same batch are loaded in the same way till failure. Differences in lifetime up to a factor 20 are observed.

The wide scatter of running times explains the impossibility to accurately predict the lifetime of an individual bearing. Predictions can only be made for a large group of nominally identical bearings stressed in the same manner. The rating life  $L_{10}$  is defined as the running time at which 10 % of the bearings have failed. The ISO 281 standard gives the general equation for lifetime calculations, used for bearing dimensioning (ISO 2007):

$$L_{10} = \left( \frac{C}{P} \right)^p \quad (9.4)$$

where  $P$  is the equivalent dynamic load which takes into account both the radial and axial bearing load. The dynamic load rating  $C$  corresponds to a pure radial constant load at which the  $L_{10}$  life equals one million revolutions. The exponent  $p$  equals 3 for ball bearings. The rating life  $L_{10}$  is expressed in million revolutions.

When a bearing is not stressed beyond its endurance strength limit and the operating conditions meet certain prerequisites with regard to the lubricant film thickness and cleanliness of the lubricating gap, it does not fail. Also, the bearing life not only depends on the load. Other influences, such as the lubrication condition, have a significant effect. These aspects are not taken into account by Eq. (9.4). However, the equation remains the basis of bearing dimensioning and the starting point for adjusted calculation methods. Since the 1970s, empirical factors are added to the equation, considering the endurance strength limit, the lubrication condition, etc. In many bearing arrangements, the load and rotational speed change either randomly or according to a work cycle. An equivalent dynamic load is then calculated based on a series of individual loads and speeds of a certain duration  $q_i$ . This calculation is derived from the Palmgren-Miner rule of variable amplitude loading in the classical fatigue theory. With the rotational speed  $n_i$  when the load  $P_i$  is acting on the bearing and the mean rotational speed  $n_m$ , the equivalent dynamic load equals:

$$P = \left( \frac{\sum_{i=1}^k n_i q_i P_i^p}{n_m} \right)^{1/p} \quad (9.5)$$

**Effect of External Dynamic Loads** For bearings subjected to highly varying loads, recent research emphasizes a strong reduction of the actual bearing lifetime w.r.t. the calculated bearing lifetime. The influence of external dynamic loads on the lifetime of bearings is elaborately analyzed by Gegner (2011), and Nierlich and Gegner (2011). Cylindrical roller bearings are tested under high dynamic load using a novel bearing test rig. Due to axial vibrations, asperities of the contacting bodies experience strong sliding motion. Material aging is shifted towards the surface. This type of damage is not covered by the classical bearing lifetime calculations. Reductions of the actual  $L_{10}$  bearing life of 80 % w.r.t. the calculated lifetime are estimated.

### 9.2.5 Non Torque Loading

Non-torque loads include pitching moments caused by the rotor weight and tower shadow, wind-induced moments, moments caused by the controller, thrust, etc. Guo et al. (2014) and Park et al. (2013) have investigated the effects of non-torque loads, gravity and bearing clearance in the load-sharing and planetary loads of a three-point suspension wind turbine drivetrain. Non-torque loads affect gear and bearing loads and planetary gear load sharing. It is present on all the different drivetrain configurations: 3-point suspension (Fig. 9.4), 2-point suspension and on integrated gearboxes.

An analytical formulation was developed and a 3D dynamic drivetrain model that included mesh stiffness variation, tooth modifications and gearbox housing flexibility was built (Guo et al. 2014).

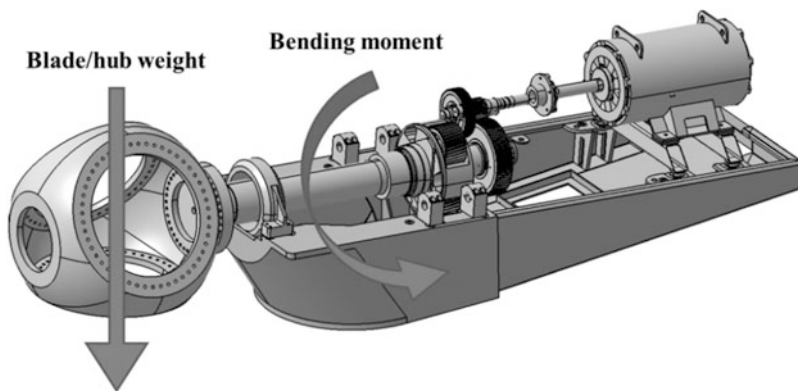


**Fig. 9.4** Non-torque loadings and their effects on a typical 3-point suspension drivetrain

The shaft pitching moment causes unequal load sharing between the upwind and downwind planet bearings, which can lead to abnormal tooth contact (consisting of tooth-edge loading, partial contact loss and reversing contact). These conditions can result in tooth failure modes such as micro-pitting. At low-input torque, the effects of non-torque loads on the gearbox internal loads were dominant. In this condition, the planet bearings are at risk of skidding and the gear teeth are at risk of contact loss, also leading to reduced gearbox life. The planetary load-sharing factor increased with bearing clearance. With carrier bearing-clearance, the shaft pitching moment was transmitted into the gear meshes and planet bearings. Optimizing the carrier-bearing clearance reduced the gearbox sensitivity to non-torque loads.

### 9.3 Numerical Modelling of Bearings

Modelling and simulation methods provide an increasingly accurate approach for predicting the dynamic performance of mechanical systems. The bearing models evolved from analytical formulations of a nonlinear spring to complex flexible multibody simulations. An overview of these modelling approaches is given in Sect. 9.3.1, while the technical details of the various approaches are discussed in Sects. 9.3.2–9.3.4.

#### 9.3.1 Overview of State-of-the-Art Bearing Models

A bearing is a mechanical component that constraints the relative motion between two bodies by allowing relative rotation about one axis and constraining relative motion along the other coordinates (i.e. two relative rotations and three relative translational displacements). Due to the finite stiffness of a mechanical bearing and the presence of clearance, however, relative motion along the constrained coordinates can occur in practice when the bearing deforms or moves through its clearance. As such, a mechanical bearing can be viewed as a multi-dimensional spring with non-linear (state-dependent) stiffness constants. In this representation, the non-linearity of the spring is caused by clearance, the varying number of rolling elements in contact and the nonlinear nature of these contact interactions (see Sect. 9.2.2).

The representation of a mechanical bearing as a multi-dimensional spring has proven to be a productive ground for modelling bearings in modal analyses of multibody systems (Peeters 2006; Helsen 2012). As such analyses are typically conducted at a (or a sequence of) predefined operating point(s) of the multibody system, the non-linear bearing can be linearized and represented by a three-dimensional linear spring. This spring is mathematically described by a constant symmetric 6-by-6 stiffness matrix (typically provided by the bearing manufacturer), which represents the relationship between the relative motion of the bearing's inner



and outer rings and the resulting bearing forces. However, as this representation is only valid at a specific operating point, it cannot be used for time domain simulations when the nonlinear bearing stiffness and/or internal bearing dynamics are expected to play an important role in explaining the overall system behavior. In the latter case, non-linear bearing models should be used.

A first distinction in non-linear bearing modelling is based on the dimensionality of the problem: if only in-plane motion is considered, two-dimensional bearing models are to be used. These models allow relative rotation about the axis perpendicular to the plane, while constraining translational motion in the plane (note that for modal analyses, a linearized 2D bearing model represented by a 3-by-3 stiffness matrix usually suffices). Three-dimensional bearing models are used when general motion is considered; in this case two relative rotations and three relative translations are constrained by the bearing model. Two-dimensional bearing models are discussed in Sect. 9.3.2, whereas three-dimensional models are discussed in Sect. 9.3.3.

A second distinction is based on the level of complexity and detail included in the flexibility description of the bearing. In Sects. 9.3.2–9.3.3, it is assumed that the (elastic) deformation of the bearing is confined to the contact zones within the bearing (i.e. the areas over which contact takes place between the rolling elements and the inner and outer raceways). Under this assumption, Hertzian contact theory (cf. Sect. 9.2.2) suffices to describe the elastic deformation of the bearing and to compute bearing stiffness. While the assumption of localized deformation is reasonable in a wide range of applications as far as the (generally compact and solid) rolling elements are concerned, this might not be the case for the bearing's inner and/or outer rings, especially when they are integrated with the bearing's flexible supporting structure (e.g. gearbox housing). In that case, Hertzian contact theory only describes the local contribution to the overall bearing deformation, whereas more advanced methods are required to describe the global (or 'bulk') bearing deformation. Such methods are described in Sect. 9.3.4.

Further distinctions of the various bearing models are based on the following aspects:

- **Type of bearing:** typically, a distinction is made between ball bearings (point contact between rolling elements and raceways) and roller bearings (line contact between rolling elements and raceways), because of the different mathematical tools required to model the contact interactions.
- Inclusion of **dynamic effects** such as centrifugal, gyroscopic and inertial effects: these effects can either be taken into account quasi-statically (excluding inertial effects) or by assigning a dynamic degree of freedom to each rolling element in the bearing model. In quasi-static bearing models the solution to a set of nonlinear algebraic equilibrium equations is generally required, while in dynamic models the solution is obtained through integration of the differential equations of motion of the bearing elements. Obviously, the importance of dynamic effects increases as the bearing's cage velocity increases.

- Inclusion of the influence of **elasto-hydrodynamic lubrication (EHL)**: lubrication reduces friction and wear in the contact interactions between rolling elements and raceways. The stiffness and damping properties of the EHL film play an important role in the transfer of mechanical vibrations through the bearing, and should therefore be taken into account when investigating internal bearing dynamics. As damping in the EHL film is mainly attributed to viscous losses in the lubricant (Wensing 1998), the damping behavior of the lubricant is typically taken into account by adding a linear viscous damper in parallel with the nonlinear contact stiffness spring. Wijnant (1998) obtained an analytical expression for the EHL damping constant in ball bearings by solving (for various parameters) the structural and fluid equations governing the transient behavior of a single EHL contact in which an initially equilibrated rolling element is slightly lifted from its equilibrium position and subsequently released. Similar analyses have been conducted for roller bearings (Qian 2013). Furthermore, the stiffness of a fully-developed lubricant film generally is several orders of magnitude larger than the Hertzian contact stiffness and therefore its contribution to the flexibility of the contact zone can be neglected.
- Inclusion of the **cage**: the rolling elements are usually held in an angularly spaced relationship by a cage or separator, which is generally constructed using materials that are relatively soft as compared to the rolling element and ring materials. A properly designed cage is often crucial for the bearing to withstand misalignment loads, and can therefore play an important role in establishing equilibrium of the bearing components. Cage modelling varies from (implicitly defined) geometric constraint relations to the inclusion of flexible cage representations including contact modelling of the interactions between cage and rolling elements.
- Inclusion of the influence of **friction**: friction in a bearing is made up of several components, including rolling friction, sliding friction of both the rolling elements and the cage, fluid friction and seal friction. These components lead to (motion-resisting) frictional forces and moments in the bearing that can modify the equilibrium conditions in the bearing. Friction energy is converted to heat, which is mostly dissipated by the (preferably recirculating) lubricant. Friction in particular plays a role in cylindrical and tapered roller bearings, where sliding contact between the roller ends and ring flanges can result in considerable frictional forces.

In the subsequent sections, the focus will be on dry (i.e. non-lubricated) frictionless contact between the rolling elements and raceways. One of the main complexities in developing a non-linear bearing model is determining the mutual approach between a rolling element and a raceway, which generally requires a thorough geometrical analysis of the bearing. Once an expression for the mutual approach is obtained, its derivative with respect to time can be computed relatively easily (if not analytically, then using finite differencing) and this information can potentially be used to include the effect of EHL damping in the model by including a linear viscous damper. Finally, frictional forces are assumed to only slightly alter the load distribution across the rolling elements and will therefore not be considered in

the present work (the interested reader is referred to Gupta (2012) for the inclusion of frictional forces and moments in the bearing model).

### 9.3.2 Two-Dimensional Bearing Models

2D bearing models are typically used when investigating the global dynamical behavior of a planar multibody system (or one that can be idealized as such), or when the axial forces and misalignment torques (i.e. torques about the in-plane axes) in the bearing are negligible. Most two-dimensional bearing models in literature are based on (all of) the following assumptions:

- The rolling elements and inner and outer rings have motions in the plane of the bearing only;
- All deformations occur according to the Hertzian theory of elasticity, plastic deformations are neglected, and there is no bulk deformation of the bearing's components;
- The cage ensures a constant angular separation between rolling elements, hence there is no interaction between the rolling elements;
- There is no slipping of the rolling elements as they roll over the raceways;
- The bearings are assumed to operate under isothermal conditions such that thermal effects like the expansion of rolling elements and raceways and the change of lubricant viscosity can be neglected.

The assumptions of two-dimensional bearing modelling most naturally apply to bearings that are characterized by point contacts, such as ball bearings. Nevertheless, two-dimensional models have been used to model roller bearings as well, with only minor changes to the mathematical framework, as discussed below.

One of the distinguishing features of the various planar bearing models is the way the contact interactions and the inertial properties of the rolling elements are modelled. In a static bearing model (Fig. 9.5a), each rolling element (and the contact

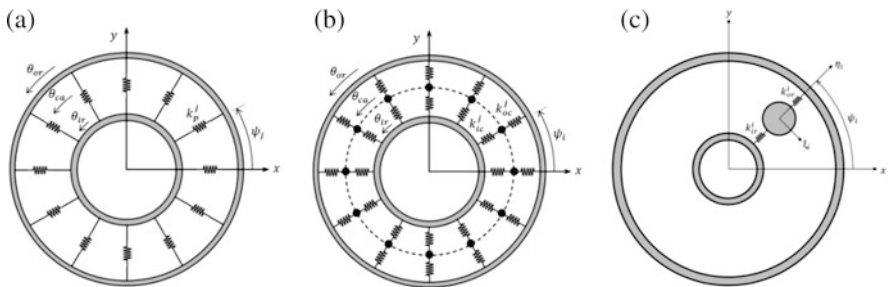


**Fig. 9.5** 2D bearing models: (a) static bearing model, (b) quasi-static bearing model, (c) dynamic bearing model

interactions it has with both the inner and outer raceways) is represented by a single non-linear spring having zero stiffness when the spring is stretched. In this case, all dynamic effects that are due to the motion of the rolling elements (i.e. inertial and centrifugal forces) are neglected. Centrifugal effects are taken into account by the quasi-static bearing model (Fig. 9.5b) where each contact interaction is represented by a non-linear spring (i.e. two springs in series for each rolling element), and a centrifugal force proportional to the cage's angular velocity is applied at the interconnection between the two springs. This force acts to increase the clearance between the inner raceway and the rolling elements, and therefore alters the contact forces applied to the respective raceways (which are equal in magnitude in the case of the static bearing model). In addition to the series arrangement of non-linear springs, the dynamic bearing model (Fig. 9.5c) takes into account the mass of each rolling element and adds one degree of freedom per rolling element to the bearing's equations of motion. The latter are typically obtained by substituting the bearing's kinetic and potential energies into Lagrange's equation of motion, and need to be integrated in time simultaneously with the equations governing the dynamic behavior of the remainder of the multibody system.

Irrespective of the type of bearing model that is used, one critical aspect of modelling bearings, both in planar and spatial modelling, is the computation of the contact stiffness of the interaction between a rolling element and a raceway. The contact stiffness appears in the load-displacement relationship of the contact interaction, which has the form of the power law  $Q = K_c \delta^p$ , where  $Q$  is the contact load,  $K_c$  is the contact stiffness,  $\delta$  is the mutual approach between rolling element and raceway, and  $p$  is the exponent—the latter is equal to 3/2 for point contacts according to Hertz's theory and is usually taken to be 10/9 in the case of line contact (de Mul et al. 1989b). The contact stiffness  $K_c$  depends on the contact geometry (radii of curvature of the contact surfaces) and the material properties (Young's modulus and Poisson's coefficient), and closed-form expressions are readily available in e.g. Harris and Kotzalas (2006). Because of the different geometries of the inner and outer raceways, the raceways typically have different contact stiffnesses.

Technical details on the mathematical derivation and implementation of two-dimensional bearing models are readily available in literature. Static bearing models including the effects of non-linear contact stiffness, varying number of rolling elements in contact and radial clearance were used in Abbes et al. (2011), Kappaganthu and Nataraj (2011), and Xu and Li (2012) to study the dynamic behavior of respectively a pair of helical gears supported by ball bearings, a rotor-bearing system and a slider-crank including a ball bearing joint. The inclusion of centrifugal effects in quasi-static bearing models is discussed in Hamrock and Anderson (1983), which includes a comprehensive overview of bearing modelling and all related aspects. Furthermore, an investigation of the influence of centrifugal effects is included in Liew et al. (2001). Dynamical two-dimensional ball bearing models were used in Harsha (2005) and Dougdag et al. (2012) to investigate the influence of bearing defects on system dynamics. Leblanc et al. (2009) developed

a dynamical two-dimensional roller bearing including the influence of EHL and contact interactions with the cage.

### 9.3.3 *Three-Dimensional Bearing Models*

3D bearing models offer far greater insight into the internal bearing dynamics than their two-dimensional counterparts. They are typically used when the dynamic performance of the bearings are at the heart of the investigation, or when a three-dimensional bearing representation is necessary to accurately grasp the global system behavior, e.g. when axial forces and/or misalignment torques are expected to play an important role. While compared to the overall computational cost of general multibody systems the three-dimensional bearing models are not significantly less efficient than the 2D models, the numerical implementation of these models is often considerably more involved. Due to the fundamental differences in the nature of the contact interactions (point vs. line contact), different mathematical models are typically used to model ball and roller bearings.

#### 9.3.3.1 **Ball Bearings**

In the case of point contacts, all internal bearing forces and moments originate from simple Hertzian point contact interactions (between rolling elements and raceways) that are described by the same load-displacement relationship given in Sect. 9.3.2. The complexity of three-dimensional ball bearing models is therefore solely related to the rather complex geometry and kinematics of three-dimensional ball bearings.

The first to investigate three-dimensional ball bearing models in a systematic way was Jones (1960). He formulated a quasi-static three-dimensional ball bearing model that included the influence of centrifugal forces and gyroscopic moments. The model consists of five nonlinear, simultaneous equilibrium equations (corresponding to the five coordinates that are constrained by the bearing, cf. Sect. 9.3.1) that need to be linearized and solved iteratively by the Newton-Raphson method. The complexity of the model lies mainly in determining the internal bearing forces and moments, which are expressed w.r.t. a reference frame that is aligned with the shaft (or bearing inner ring), leading to rather cumbersome expressions, especially when the influence of quadratic velocity terms is included.

In response to the complexity of the Jones model, Gupta (2012) developed a dynamical ball bearing model (in which each ball bearing was assigned with a number of degrees of freedom), arguing that despite the increased computing effort in obtaining a solution (through integration of the equations of motion), the dynamic model provides a significant reduction in the overall design costs of the model (as the influence of centrifugal and gyroscopic effects follows naturally from the bearing's equation of motion). Furthermore, the dynamic model is free of the typical convergence problems that are associated with solving equilibrium solutions

in quasi-static bearing models, and therefore are better suited for including lubricant behavior (Gupta 2012).

Another simplification of the model of Jones was provided by de Mul et al. (1989a), who developed a quasi-static bearing model in five degrees of freedom and including centrifugal forces. The formulation of the model is less cumbersome than the model of Jones and lends itself better for computer implementation. Assuming no circumferential motion of the rolling element at equilibrium, the equilibrium equations for each roller element are formulated in a plane (two translations and one rotation) at the rolling element level, and are then transformed to the central bearing reference frame through a 3-by-5 transformation matrix. The mutual approach between rolling element and raceway is obtained through a comparatively simple two-dimensional geometric analysis, and closed-form expressions for the bearing's global stiffness matrix are provided.

### 9.3.3.2 Roller Bearings

The classical Hertzian theory is usually not valid for roller contact. This can be either because of the dimension of the contact area that exceeds the assumption of Hertz, due to noncircular contact profiles, or due to high loads making the contact ellipse being truncated at the end of the rollers. These types of problems are referred to as non-Hertzian contact problems and there is, unfortunately, no exact and explicit relationship available for expressing the load as a function of the deflection. Many authors, such as Lundberg and Sjövall (1958), Palmgren (1959), and Young and Budynas (2002), have addressed these types of problems based on half-space theory and experiments to find an, often implicit, relationship between the load and the deformation. These relationships are often found in idealized contact situations (e.g. no misalignments, close to half-space conditions) and sometimes even profiled roller geometries.

More recently, numerical techniques are adopted to account e.g. for misaligned rollers. Some authors numerically integrate the Boussinesq's half-space theory to iteratively obtain the required solution (Reusner 1977; Andréason 1973). Others apply more simple techniques (Harris and Kotzalas 2006; Andréason 1973), however less accurate, for computational reasons in case that multiple contacts need to be solved simultaneously. In the so-called slicing technique, the contact length is sliced into a number of laminae. Each slice is given a fraction of the total roller stiffness, which is often based on some of the above mentioned load-deflection relations. A distinction can be made in whether each slice is treated separately, and thus having no effect on the deflection of adjacent slices, or treated in a combined way, and thus having a mutual influence. In the former case, pressure concentrations cannot be taken into account. Nevertheless, the problem is less expensive to solve. In the other case, where the deflection of one slices depends on the deflection of other slices, iterative procedures are required. Teutsch and Sauer (2004) propose a method in which the optimum between accuracy and efficiency is searched for.

The modelling of 3D roller bearings is conceptually similar to ball bearings; the mutual approach between the contacting bodies has to be found such that the load-deflection relation can be applied and the contact forces computed. As mentioned above, the slicing technique is often used to discretize the roller into a set of laminae. Consequently, the mutual approach of each slice to the bearing raceway should be determined by a (kinematic) model.

As for ball bearings, many authors have provided various levels of complexity. Gupta (2012) followed his own approach for ball bearings and assigned again degrees-of-freedom to the rollers. The slicing technique is adopted to compute the roller contact forces. In models such as those of de Mul et al. (1989b) and Andréason (1973), among many others, the equilibrium equations are again determined in a two-dimensional plane at rolling element level and include the centrifugal and gyroscopic forces in a quasi-static way. de Mul et al. (1989b) refer next to the slicing technique also to a more sophisticated technique to model non-Hertzian contact in a general way that was presented in de Mul et al. (1986).

To end this section, it should be noted that rollers are profiled by the bearing manufacturers, in order to optimize the stress distribution over the rollers for a particular loading condition and to avoid high edge stresses that can substantially exceed the computed stresses in case of separately treated slices. The knowledge of the profile, as for the geometry of the raceways and rolling elements in bearings, is key for an accurate prediction of the contact stresses and the stiffness of a bearing.

### 9.3.4 Bearings with Distributed Flexibility

The above listed solutions pertain to bearings that have rigidly supported rings. The considered deflections are the local Hertzian deformations and are based on the assumptions presented in 9.2.2. In some applications, however, the influence of the supporting structure's and ring's flexibility can be decisive for the bearing's behavior as it might affect, for instance, the load distribution over the rolling elements. Consequently, the global (or bulk) deformations such as the bending of the bearing housing cannot always be neglected.

An obvious way to tackle this modelling problem is to use the *Finite Element* (FE) method to include and combine both the local nonlinear contact deflections and the global flexibility of the ring and supporting structure. In addition, the influence of e.g. materials, manufacturing errors, lubrication, and cage effects has been investigated by adding those effects to (nonlinear) FE codes. A brief overview of such codes is given in Qian (2013). Although these (nonlinear) FE approaches have proven their value for many high technology applications, they suffer from some severe disadvantages for drivetrain modelling. First, since the contact interaction (or mutual approach) between the rolling elements and the raceways can generally not be sought purely analytically as for the techniques listed in the previous sections, some standard contact detection algorithms are obliged to search for contact in all possible contact elements. This process is often the most time-consuming process



in dynamic contact simulations. It should however be mentioned that, generally, the known (undeformed) geometry can in fact be exploited to reduce the number of possible contact elements for a specific rolling element. A second disadvantage is that one has to rely on FE models with a highly refined mesh at the contact zone and thus a large number of nodes in order to capture the nonlinear behavior of the Hertzian contact with a reasonable accuracy. The resulting models have therefore an extremely high number of *degrees-of-freedom* (DOFs). For time-domain analyses of gearboxes and drivetrains, where it is not uncommon to have multiple bearings and gears, these models result in unacceptable simulation times.

Model order reduction schemes can be introduced to lower the dimensionality of the problem to alleviate above mentioned computational burden with a minimal loss of accuracy. However, traditional model order reduction techniques typically become inefficient for models with time-varying load locations, as is the case for the moving rolling elements in a bearing. In fact, to obtain a favorable accuracy on displacement and stress levels one has to include so-called static modes for each of the interacting nodes in the reduction space, as it is likely that almost every node positioned on the raceway of the bearing can be loaded by the rolling elements. This action might result in a poor reduction in terms of DOFs.

To deal with the latter problem, some advanced model order reduction techniques have been developed to accurately simulate problems with time-varying load locations, such as gears and bearings. A statically complete procedure is provided by the *Static Modes Switching* (SMS) method (Heirman et al. 2011), which has been applied to the gear contact problem in Tamarozzi et al. (2013). SMS makes use of a discontinuously changing reduction basis, of minimal dimension, by taking advantage of the fact that each time step only a few out of many interface DOFs are loaded simultaneously. The technique has been modified in Tamarozzi et al. (2014) to obtain a continuously time-varying reduction space by use of a parametric relationship describing the location of externally applied moving loads, further referred to as *Static Mode Sliding* (SMS<sup>2</sup>). It has been shown that the price to pay for the very compact reduction basis is the evaluation of some extra terms in the equations of motion. This model order reduction strategy is later extended and applied for the simulation and prediction of the behavior of an indirect dynamic bearing force measurement setup (Fiszer et al. 2015b) and for efficient time-simulation of gear pairs (Blockmans et al. 2015). In Blockmans et al. (2015), the performance of the novel technique is demonstrated by simulating a dynamic gear contact problem and comparing results against traditional model reduction techniques as well as commercial nonlinear finite element software.

Although the computational burden is alleviated by use of the model order reduction techniques, a highly refined mesh at the contact zone is still required to capture the nonlinear behavior of the Hertzian contact. The latter retains the need for a large number of so-called static modes to be computed in a pre-processing step, despite the fact that only few are active at a certain moment in time during the simulation.



Some authors have proposed to combine analytic solutions with the FE method, (Wensing 1998; Andersson and Vedmar 2003; Vijayakar 1991; Fiszer et al. 2015a), thereby eliminating the need for highly refined meshes at the contact zone. The main advantage of such a semi-analytic strategy lies in the accurate contact description that combines the nonlinear effects present at the contacting interface with a standard FE formulation in those regions in which nonlinear effects are not prominent. Therefore, coarser FE meshes can be used; these meshes should only accurately represent the more global bulk deformation.

In the semi-analytic strategy presented by Wensing (1998), the total deformation is separated in the bulk deformation, represented by a reduced order model, and the nonlinear local Hertzian deflections at the contact zone. The multitude of static shape vectors is replaced by a comparatively small set of global constraint modes to capture the effect of the bulk flexibility of the rings, supporting structure and the mounting conditions on the behavior of the bearings. The global constraint modes are determined by use of Chebyshev polynomials, which are also utilized as contact geometry. These analytic surfaces are then used to determine the mutual approach between the ring and the rolling element to compute the contact forces based on Hertzian contact theory.

The approach presented in Fiszer et al. (2015a) offers an equivalent semi-analytic strategy. Nevertheless, the global constraint modes, that are used to reduce the FE model representing the bulk deformation, are replaced by global attachment modes. The latter allows for a one-to-one relation between the contact load and the static mode, such that a parametric relationship describing the contact location can be defined and the efficient model reduction technique SMS<sup>2</sup> becomes applicable. In addition, the Chebyshev polynomials that represent smooth interacting raceways are replaced by NURBS or B-spline surfaces. It is shown in Fiszer et al. (2015b) that by selecting an appropriate basis for the B-splines, the interacting surface can be composed by a linear combination of the control points, using the modal participation factors (or reduced elastic coordinates) of the affected mode shapes during simulations. These offline computed B-splines or NURBS are therefore referred to as NURBS-modes.

## 9.4 Conclusions: Towards Unified Wind Turbine Gearbox Models

Sections 9.2 and 9.3 underlined some key aspects regarding the behavior and the modelling of wind turbine drivetrains with a specific focus on bearings. It goes without saying that another major component that needs to be accurately simulated within drivetrains, are gears. Helical stages and planetary helical stages are mostly of relevance in this framework. Similarly to bearings, gears are also complex components in which accurate geometry, material properties and lubrication play an important role. They can also be simulated with different levels of complexity

ranging from analytical models and lumped parameter models (Özgüven and Houser 1988; Cai and Hayashi 1994; Kuang and Yang 1992; Vexlex 2012; Kahraman 1993; Eritenel and Parker 2012; Kahraman 1994; Lin and Parker 1999; Andersson and Vedmar 2003) up to fully flexible non-linear contact simulations (Tamarozzi et al. 2013; Blockmans et al. 2015; Ziegler et al. 2006; Parker et al. 2000). The literature about gear modelling and analysis is as rich as the one for bearings and it is out of the scope of this chapter to provide a detailed review.

While the modelling of single components can be interesting for troubleshooting of localized problems in a wind turbine gearbox, these are seldom enough to draw conclusions regarding the behavior of the full drivetrain. In order to benefit from the different levels of complexity in which gears and bearings can be represented, there is a strong need for coupling them to system-level simulation tools such as e.g. multibody and flexible multibody models. Multibody simulation is an established technology that is aimed to investigate the dynamic behavior of systems of interconnected bodies. Within this type of models it is possible to connect different body representations (e.g. rigid or flexible) by making use of idealized joints or force elements that can represent localized stiffness and damping with different levels of complexity. Examples of wind turbine drivetrains modelled through multibody simulation can be found in Helsen (2012) and Vanhollebeke (2015).

Multibody models with idealized joints or constraints form a set of highly non-linear Differential Algebraic Equations (DAE). For relatively simple systems with mainly rigid bodies, computational strategies exist to perform dynamic transient simulations in a relatively short time-frame. Depending on the phenomena that need to be investigated, bearings and gears models can be included in multibody models with different levels of complexity. In order to achieve drivetrain models that are of wide applicability and address different design questions some research effort still needs to be focused on several open topics as e.g.:

- *Scalability of different model complexities* for bearings and gears to be included in system level simulation. In particular bearings and gears can be idealized in different ways but all the different model types should be able to interact with their surrounding environment. Depending on the model complexity adopted for the different components, these interactions can happen at localized or distributed interfaces. As an example, a gear or a bearing can be modelled in three dimensions as a  $6 \times 6$  stiffness matrix that interacts with shafts and housing through forces and torques acting at localized interface points. On the other extreme, flexible gear models and bearings interact with their surrounding structure through distributed FE interface nodes. The inherently different interface behavior of the modelling strategies makes it difficult to create a single drivetrain model that is scalable for different levels of complexity depending on the target use. The inclusion of 3D modelling capabilities within natively 1D environments such as Matlab Simulink, SISW Imagine, Lab Amesim, Dymola, etc. . . . could potentially alleviate these difficulties and is topic of current research.

- Advanced drivetrain models including e.g. flexible housing deformation, contact mechanics models for gears and bearings, spline connection models, etc. . . . can easily become computationally cumbersome. Modern linear and non-linear model order reduction techniques are one of the main research fields from which wind turbine drivetrain modelling could benefit.

Sections 9.1–9.3 summarized a few key focal points regarding drivetrain modelling in a wind turbine context with specific focus on state-of-the-art of bearing modelling. The discussion should not be considered as exhaustive but underlines a few important items to be considered when analyzing and simulating drivetrains. The improvements of components modelling methods (e.g. bearing and gears) and scalable inclusion in system-level simulation tools for accurate and affordable drivetrain analysis remain (partially) open challenges where further research efforts needs to be focused.

**Acknowledgements** The authors would like to gratefully acknowledge the European Commission for their support of the MAREWINT research project (GA 309395). Additionally, the IWT Flanders within the OPTIWIND project and the Research Fund KU Leuven for the IDO\_WIND project are kindly acknowledged for their support.

**Open Access** This chapter is distributed under the terms of the Creative Commons Attribution-NonCommercial 4.0 International License (<http://creativecommons.org/licenses/by-nc/4.0/>), which permits any noncommercial use, duplication, adaptation, distribution and reproduction in any medium or format, as long as you give appropriate credit to the original author(s) and the source, provide a link to the Creative Commons license and indicate if changes were made.

The images or other third party material in this chapter are included in the work's Creative Commons license, unless indicated otherwise in the credit line; if such material is not included in the work's Creative Commons license and the respective action is not permitted by statutory regulation, users will need to obtain permission from the license holder to duplicate, adapt or reproduce the material.

## References

- Abbes MS, Hentati T, Maatar M et al (2011) Dynamic analysis of helical gears supported by rolling elements bearings. *J Theor Appl Mech* 41(1):33–50
- Andréason S (1973) Load distribution in a taper roller bearing arrangement considering misalignment. *Tribology* 6(3):84–92. doi:[10.1016/0041-2678\(73\)90241-8](https://doi.org/10.1016/0041-2678(73)90241-8)
- Andersson A, Vedmar L (2003) A dynamic model to determine vibrations in involute helical gears. *J Sound Vib* 260(2):195–212
- Blockmans B, Tamarozzi T, Naets F et al (2015) A nonlinear parametric model reduction method for efficient gear contact simulations. *Int J Numer Methods Eng* 102(5):1162–1191
- Brandlein J, Eschmann P, Hasbargen L et al (1999) *Ball and roller bearings: theory, design and application*. Wiley, Chichester
- Cai Y, Hayashi T (1994) The linear approximated equation of vibration of a pair of spur gears (theory and experiment). *J Mech Des* 116(2):558–564
- Chen W, Alewine K (2010) Wind turbine generator failure modes analysis and occurrence. Paper presented at the Wind Power, Dallas, 24–26 May 2010

- de Mul JM, Kalker JJ, Fredriksson B (1986) The contact between arbitrarily curved bodies of finite dimensions. *J Tribol* 108(1):140–148
- de Mul JM, Vree JM, Maas DA (1989a) Equilibrium and associated load distribution in ball and roller bearings loaded in five degrees of freedom while neglecting friction – part I: general theory and application to ball bearings. *J Tribol* 111(1):142–148
- de Mul JM, Vree JM, Maas DA (1989b) Equilibrium and associated load distribution in ball and roller bearings loaded in five degrees of freedom while neglecting friction – part II: application to roller bearings & experimental verification. *J Tribol* 111(1):149–155
- Dietl P, Wensing J, van Nijen G (2000) Rolling bearing damping for dynamic analysis of multibody systems: experimental and theoretical results. *Proc Inst Mech Eng K J Multi-Body Dyn* 214:33–43
- Dougdag M, Ouali M, Boucherit H et al (2012) An experimental testing of a simplified model of a ball bearing: stiffness calculation and defect simulation. *Meccanica* 47(2):335–354
- Eritenel T, Parker RG (2012) Three-dimensional nonlinear vibration of gear pairs. *J Sound Vib* 331(15):3628–3648
- EWEA (2011) Upwind: design limits and solutions for very large wind turbines. In: European Wind Energy Association Wind Energy Association Reports. Available via EWEA. [http://www.ewea.org/fileadmin/files/library/publications/reports/UpWind\\_Report.pdf](http://www.ewea.org/fileadmin/files/library/publications/reports/UpWind_Report.pdf). Accessed 08 Apr 2016
- Fiszer J, Tamarozzi T, Desmet W (2015a) A semi-analytic strategy for the system-level modelling of flexibly supported ball bearings. *Meccanica*. doi:10.1007/s11012-015-0318-6
- Fiszer J, Tamarozzi T, Blockmans B et al (2015b) A time-dependent parametric model order reduction technique for modelling indirect bearing force measurements. *Mech Mach Theory* 83:152–174
- Gegner J (2011) Tribological Aspects of Rolling Bearing Failures. In: Kuo CH (ed) *Tribology – lubricants and lubrication*. InTech, Rijeka, pp 33–94
- Grubin A (1949) Fundamentals of the hydrodynamic theory of lubrication of heavily loaded cylindrical surfaces. In: Ketova KhF (ed) *Symposium on Investigation of the Contact of Machine Components*, Moscow, 1949, Central Scientific Research Institute for Technology and Mechanical Engineering, vol 30. TsNIITMASH, Moscow, p 115
- Guo Y, Keller J, LaCava W (2014) Planetary gear load sharing of wind turbine drivetrains subjected to non-torque loads. *Wind Energy* 18(4):757–768
- Gupta PK (2012) *Advanced dynamics of rolling elements*. Springer, New York
- Hamrock BJ, Anderson WJ (1983) *Rolling-element bearings*. NASA Reference Publication 1105. National Aeronautics and Space Administration Publications. Available via NASA NTRS. <http://ntrs.nasa.gov/archive/nasa/casi.ntrs.nasa.gov/19830018943.pdf>. Accessed 08 Apr 2016
- Harris TA, Kotzalas M (2006) *Advanced concepts of bearing technology: rolling bearings analysis*. Taylor and Francis, New York
- Harsha SP (2005) Non-linear dynamic response of a balanced rotor supported on rolling element bearings. *Mech Syst Signal Process* 19(3):551–578
- Heirman GHK, Tamarozzi T, Desmet W (2011) Static modes switching for more efficient flexible multibody simulation. *Int J Numer Methods Eng* 87(11):1025–1045
- Helsen J (2012) *The dynamics of high power density gear units with focus on the wind turbine application*. Dissertation, KU Leuven
- ISO (2007) *ISO 281:2007 Rolling bearings – dynamic load ratings and rating life*. ISO, Geneva
- Jacobs W (2014) *Experimental analysis of the dynamic characteristics and lubricant film of a ball bearing under combined static and dynamic load*. Dissertation, KU Leuven
- Jones AB (1946) *New departure engineering data; analysis of stresses and deflections*. Bristol Conn, New Departure, Division General Motors Corp, Chicago
- Jones AB (1960) A general theory for elastically constrained ball and radial roller bearings under arbitrary load and speed conditions. *J Basic Eng* 82(2):309–320
- Kahraman A (1993) Effect of axial vibrations on the dynamics of a helical gear pair. *J Vib Acoust* 115(1):33–39
- Kahraman A (1994) Planetary gear train dynamics. *J Mech Design* 116(3):713–720

- Kappaganthu K, Nataraj C (2011) Nonlinear modeling and analysis of a rolling element bearing with a clearance. *Commun Nonlinear Sci* 16(10):4134–4145
- Kuang JH, Yang YT (1992) An estimate of mesh stiffness and load sharing ratio of a spur gear pair. In: The 1992 ASME design technical conferences – 6th international power transmission and gearing conference, Scottsdale, September 1992. *Advancing Power Transmission into the 21st Century*, vol 1. ASME, New York, p 1
- Leblanc A, Nelias D, Defaye C (2009) Nonlinear dynamic analysis of cylindrical roller bearing with flexible rings. *J Sound Vib* 325(1):145–160
- Li Y, Billington S, Kurfess C et al (1999) Adaptive prognostics for rolling element bearing condition. *Mech Syst Signal Process* 13(1):103–113
- Liew A, Feng NS, Hahn EJ (2001) Transient rotordynamic modeling of rolling element bearing systems. In: Abstracts of the ASME Turbo Expo 2001: Power for Land, Sea, and Air, American Society of Mechanical Engineers, New Orleans, 4–7 June 2001
- Lin J, Parker RG (1999) Analytical characterization of the unique properties of planetary gear free vibration. *J Vib Acoust* 121(3):316–321
- Lundberg G, Sjövall H (1958) Stress and deformation in elastic contacts. Institution of Theory of Elasticity and Strength of Materials, Gothenburg
- Mitsuya Y, Sawai H, Shimizu M, Aono Y (1998) Damping in vibration transfer through deepgroove ball bearing. *J Tribol* 120:413–420
- Muro H, Tsushima N (1970) Microstructural, microhardness and residual stress changes due to rolling contact. *Wear* 15:309–330
- Nierlich W, Gegner J (2011) Material response bearing testing under vibration loading. In: Beswick J (ed) *Selected Technical Papers STP 1548 Bearing Steel Technologies*. Ninth International Symposium on Bearing Steel Technologies, November 2011. *Advances in Rolling Contact Fatigue Strength Testing and Related Substitute Technologies*, vol 9. ASTM, New York
- Nonato F, Cavalca K (2012) Local linear approximation for the stiffness characteristics of elasto-hydrodynamic point contacts. In: Abstracts of the 10th international conference on vibrations in rotating machinery, IMechE, London, 11–13 Sep 2012
- Özgülven HN, Houser DR (1988) Mathematical models used in gear dynamics—a review. *J Sound Vib* 121(3):383–411
- Palmgren A (1959) *Ball and roller bearing engineering*. SH Burbank, Philadelphia
- Park YJ, Lee GH, Song JS, Nam YY (2013) Characteristic analysis of wind turbine gearbox considering non-torque loading. *J Mech Des* 135(4):044501–044508. doi:10.1115/1.4023590
- Parker RG, Agashe V, Vijayakar SM (2000) Dynamic response of a planetary gear system using a finite element/contact mechanics model. *J Mech Des* 122(3):304–310
- Peeters J (2006) *Simulation of dynamic drive train loads in a wind turbine*. Dissertation, KU Leuven
- Qian W (2013) *Dynamic simulation of cylindrical roller bearings*. Dissertation, RWTH Aachen University
- Reusner H (1977) *Druckflächenbelastung und Oberflächenverschiebung im Wälzkontakt von Rotationskörpern*. Dissertation TH Karlsruhe
- Tamarozzi T, Ziegler P, Eberhard P et al (2013) Static modes switching in gear contact simulation. *Mech Mach Theory* 62:69–106. doi:10.1016/j.mechmachtheory.2013.01.006
- Tamarozzi T, Heirman GH, Desmet W (2014) An on-line time dependent parametric model order reduction scheme with focus on dynamic stress recovery. *Comput Methods Appl Mech Eng* 268:336–358
- Teutsch R, Sauer B (2004) An alternative slicing technique to consider pressure concentrations in non-Hertzian line contacts. *J Tribol* 126(3):436–442
- Vanhollebeke F (2015) *Dynamic analysis of a wind turbine gearbox: towards prediction of mechanical tonalities*. Dissertation, KU Leuven
- Velex P (2012) *On the modelling of spur and helical gear dynamic behaviour*. Cornell University Library: Classical Physics. Available via arXiv. <http://arxiv.org/pdf/1204.2636v1> preprint arXiv:1204.2636. Accessed 07 Apr 2016

- Vijayakar S (1991) A combined surface integral and finite element solution for a three-dimensional contact problem. *Int J Numer Methods Eng* 31(3):525–545
- Wensing J (1998) On the dynamics of ball bearings. Dissertation, University of Twente
- Wijnant Y (1998) Contact dynamics in the field of elasto-hydrodynamic lubrication. Dissertation, University of Twente
- Xu LX, Li YG (2012) An approach for calculating the dynamic load of deep groove ball bearing joints in planar multibody systems. *Nonlinear Dyn* 70(3):2145–2161
- Young WC, Budynas RG (2002) *Roark's formulas for stress and strain*, vol 7. McGraw-Hill, New York
- Ziegler P, Eberhard P, Schweizer B (2006) Simulation of impacts in geartrains using different approaches. *Arch Appl Mech* 76:537–548
- Zwirlein O, Schlicht H (1980) Werkstoffanstrengung bei Wälzbeanspruchung - Einfluss von Reibung und Eigenspannungen. *Werkstofftechnik* 1:11–14

# Chapter 10

## Experimental Characterization of Wind Turbine Gearbox in Operation

**Emilio Di Lorenzo and Simone Manzato**

**Abstract** The gearbox is one of the key subsystems in a geared wind turbine, as it must transfer the power from the low speed shaft connected to the rotor to the high speed shaft connected to the generator. As turbines become larger, more power can be generated, but consequently gearboxes with higher load capacity need to be designed. Gaining a deep knowledge into gearbox dynamics becomes of fundamental importance and more and more accurate and detailed noise and vibration measurements are demanded. When dealing with a machine in operating conditions with several rotating components and, in particular with a multi-stage transmission system, components are introduced in the signal that make the application of standard techniques such as Operational Modal Analysis (OMA) very difficult and in some cases almost impossible. For this reason, new techniques to tackle with these conditions have been investigated, such as Order Based Modal Analysis (OBMA). As suggested by its own name, this technique is a combination of Order Tracking and Operational Modal Analysis. On one hand, OMA is based upon the calculation of auto- and cross-powers and it works very well for most cases. On the other hand, OBMA is based upon the extracted orders during run-up or coast-down. During such events, the orders are sweeping through a certain frequency band which is useful for characterizing the dynamic behavior of the rotating structures.

### 10.1 Introduction and Motivation

The current approach in industry is to qualitatively measure the vibrations generated by the dominant excitation sources as well as the overall sound power levels, so that the machine performance can be certified according to standards and/or customer specifications. However, as mentioned, by following this approach only qualitative information can be obtained and the root causes of high vibration levels or acoustic tonalities cannot be understood. Also, analyzing these data requires a lot of user-interaction, as each peak need to be independently analyzed. Experimental modal analysis techniques (Heylen et al. 2013) aim at identifying a system characteristic

---

E. Di Lorenzo (✉) • S. Manzato  
Siemens Industry Software (SISW), Interleuvenlaan 68, 3001 Leuven, Belgium  
e-mail: [emilio.dilorenzo@siemens.com](mailto:emilio.dilorenzo@siemens.com); [simone.manzato@siemens.com](mailto:simone.manzato@siemens.com)

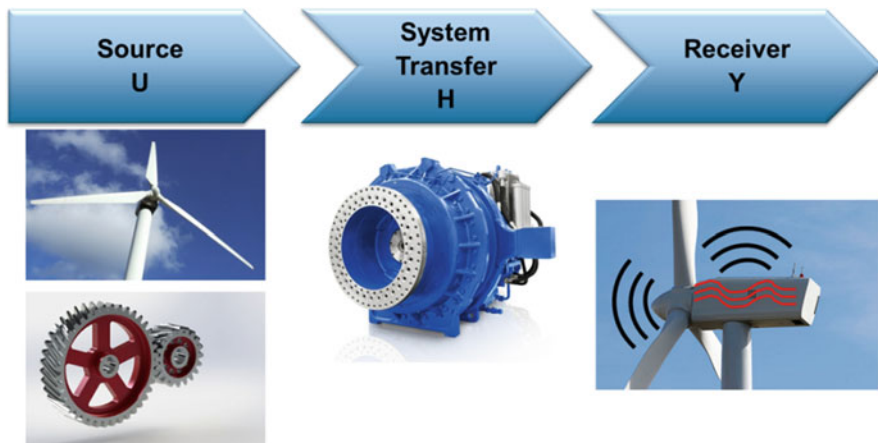


**Fig. 10.1** The Source-Transfer-Receiver approach applied to a wind turbine gearbox

model based on input/output dynamic measurements. By identifying the origin of each of the phenomena of interest, it is possible to understand where corrective action should be applied increase the system NVH performances. Additionally, the identification of a system characteristic model will allow designer to compare experimental and numerical models using similar quantities. This approach will objectively quantify the agreement between the design assumptions and the behavior of the real structure.

The method is based on the so-called Source-Transfer-Receiver approach, as shown in Fig. 10.1 for a wind turbine gearbox. Experimental Modal Analysis relies on measurements of the system response at the receiver (i.e. acceleration) due to the measured inputs at the sources (typically forces) to identify a System Transfer function which represent the dynamics of the system itself. Modal Analysis will try to represent the information in the measured system transfer as natural frequencies, damping ratios and mode shapes. During operations, however, measuring the forces into the system can be practically impossible (for a gearbox, these are the loads transmitted from the whole turbine via the main shaft and the gearbox supports as well as the internal gear contact forces). Methods have been developed to overcome this limitation and thus allow to identify the modal properties of a system also in operating conditions, provided some assumption on the forces acting on the systems are verified (Peeters et al. 2007; Carne and James 2010). However, the main forces acting on a gearbox during operations appear at discrete frequencies multiple of the fundamental rotational speed. As one of the assumptions of Operational Modal Analysis is on the broadband spectrum of the forces, it is clear that identifying a modal model during stationary conditions is practically unfeasible for a gearbox, where the harmonic density is such that barely any mode is visible (Manzato et al. 2013).



However, during transient operations such as run ups and run downs, the rotational speed, and consequently its harmonics, is varying during the measurement. The different orders are then sweeping in a frequency band which is related to the minimum and maximum rotational speeds. As it happens during a sine sweep test, whenever one of these orders crosses a resonance, the response will increase accordingly. Orders can then be considered as representative of the system transfer (Fig. 10.1) and modal parameters identification techniques can be applied. The method was first introduced few years ago as Order based Modal Analysis (Janssens et al. 2006) and was further developed and validated recently. In this section, the concept of the method will be reviewed, with particular focus on the techniques required to extract orders that can be successfully used for modal analysis. Moreover, it will be positioned against standard Operational Modal Analysis techniques, showing the clear advantages in identifying reliable modal models of operating rotating machines and in particular for the wind turbine gearbox case.

As already discussed, the identification of operational modal model will allow not only to characterize the dynamic response of a structure in operating conditions, but will also provide means of validating, and subsequently updating, global numerical models developed with Multi Body and Finite Element tools, as demonstrated in Goris et al. (2013).

## 10.2 Order Tracking Techniques

Order tracking is the analysis of frequency components whose frequency is related to the rotational frequency of the operating machine. If the machine is running in non-stationary conditions, then the frequency components will be time varying and some more information are needed in order to perform the analysis. The additional information are in the form of tachometer signals measured on reference shafts of the machine. Several methods have been employed to digitally track orders which results from rotating components in noise and vibration problems (Blough 1998). In order to allow the computation of the exact frequency for the orders of interest, an accurate tachometer signal is needed for all the methods discussed in this section:

- Time domain sampling Fast Fourier Transform (FFT) order tracking;
- Angle domain computed order tracking;
- Time Variant Discrete Fourier Transform (TVDFFT);
- Vold-Kalman (VK) filter based order tracking.

### 10.2.1 Time Domain Sampling-Based Fast Fourier Transform Order Tracking

The simplest digital order tracking techniques are based on the FFT on time domain data. These methods require time domain data sampled with a constant  $\Delta t$  (Fig. 10.2). The method performs a sliding FFT on time domain data and calculates the average rpm over which the transform is performed. This averaged rpm is then used for estimating the frequency of the orders of interest for each estimated spectra. Finally, the amplitude and the phase of the order are extracted from the FFT spectra. The order itself will not always fall on a single spectral line, so normally multiple spectral lines are summed. The FFT kernels are given in Eqs. (10.1) and (10.2), where  $x(n\Delta t)$  is the  $n$ th discrete data sample,  $f_m$  is the frequency of the sine/cosine terms and  $a_m$  and  $b_m$  are the estimated Fourier coefficients:

$$a_m = \frac{1}{N} \sum_{n=1}^N x(n\Delta t) \cos(2\pi f_m n\Delta t) \quad (10.1)$$

$$b_m = \frac{1}{N} \sum_{n=1}^N x(n\Delta t) \sin(2\pi f_m n\Delta t) \quad (10.2)$$

The main advantage of this method is its computational efficiency. However, an important limitation is the constant time over which the transform is performed, regardless of the rpm of the machine. Additionally, it is assumed that all the sinusoidal functions are constant in amplitude over the time that the transform is performed. A leakage error is also present as orders are estimated by using an FFT based approach and a Hanning window is typically applied in order to reduce this effect.

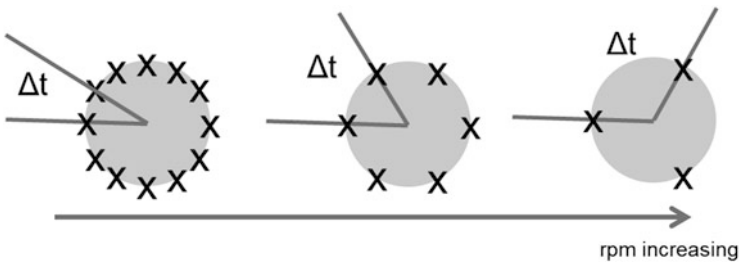


Fig. 10.2 Time domain sampling based FFT order tracking representation

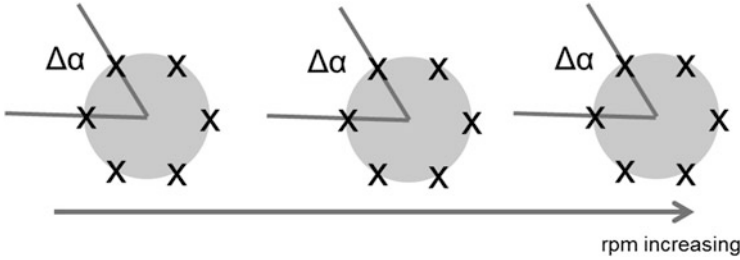


Fig. 10.3 Angle domain order tracking representation

### 10.2.2 Angle Domain Resampling Order Tracking

A very well-known order tracking method which is widely used in commercial software is based on angular resampling. Data are acquired with a uniform  $\Delta t$  and then resampled to the angle domain through the use of an adaptive digital resampling algorithm. The final result of the technique is that uniform  $\Delta t$  data become uniformly spaced angle data (Fig. 10.3). Estimates of amplitude and phase of the orders are obtained by processing these data with a Discrete Fourier Transform (DFT) instead of a FFT for computational flexibility in performing the transform without being restricted to a power of two number of samples.

In order to perform the transformation from time domain data to angle domain data, a reference signal has to be selected to define the instant of time in which the uniform angular intervals have been spaced. Typically, this signal is considered to be the tachometer signal measured on a reference shaft of the operating machine. The kernels of the Fourier transform are reformulated as shown in Eqs. (10.3) and (10.4), where  $o_m$  is the order which is being analyzed:

$$a_m = \frac{1}{N} \sum_{n=1}^N x(n\Delta\theta) \cos(2\pi o_m n\Delta\theta) \quad (10.3)$$

$$b_m = \frac{1}{N} \sum_{n=1}^N x(n\Delta\theta) \sin(2\pi o_m n\Delta\theta) \quad (10.4)$$

The advantages of the resampling based order tracking are leakage free estimates of orders which fall on spectral lines as well as an order resolution which is constant in terms of width. On the other hand, also this method has several restrictions. Orders may only be tracked with reference to one rotating shaft and it is very difficult to distinguish among order which cross one another. Another limitation is due to the finite defined order resolution which makes very difficult the analysis of orders which do not fall on a spectral line.

### 10.2.3 Time Varying Discrete Fourier Transform (TVDFFT)

The Time Variant Discrete Fourier Transform (TVDFFT) method gives results very similar to the resampling based order tracking, but with less computational efforts. It is based on a Fourier transform kernel whose frequency varies with time and it does not require the transformation from the time to the angle domain (Blough et al. 1997). The TVDFFT is based on kernels in which the sine and cosine functions have unity amplitude and an instantaneous frequency matching that of the tracked order at each instant in time, as shown in Eqs. (10.5) and (10.6):

$$a_m = \frac{1}{N} \sum_{n=1}^N x(n\Delta\theta) \cos \left( 2\pi \int_0^{n\Delta t} (o_m * \Delta t * rpm/60) dt \right) \quad (10.5)$$

$$b_m = \frac{1}{N} \sum_{n=1}^N x(n\Delta\theta) \sin \left( 2\pi \int_0^{n\Delta t} (o_m * \Delta t * rpm/60) dt \right) \quad (10.6)$$

The formulation can be extended in order to separate close or crossing orders through a secondary calculation. There can be a leakage error using the TVDFFT with constant  $\Delta t$  sampled data because it is not guaranteed that the integer revolution values required for a constant order bandwidth analysis will fall on a  $\Delta t$ . If it is not the case, it will lead to a leakage error by performing the transformation over a non-integer number of revolutions. This error can be reduced by oversampling the data to finer  $\Delta t$ . The method retains most of the advantages of the resampling based order tracking and it can be implemented in a very efficient manner without having the computational load and complexity of the transformation from the time domain to the angle domain.

### 10.2.4 Vold-Kalman (VK) Filter-Based Order Tracking

Vold and Leuridan (1993) introduced an algorithm for high resolution, slew rate independent order tracking based on the concepts of Kalman filtering. The Vold-Kalman (VK) algorithm allows tracking multiple orders at the same time and it is able to decouple close and crossing orders. This method extracts the time history of the order as well as the estimate of the amplitude and the phase of the same order.

As the Kalman filter is based on the process and measurement equations, the VK filter is based on the structural and data equations. The structural equation describes the mathematical characteristics of the order to be extracted. It relies on information from the tachometer signal and represents a sine wave whose frequency and amplitude are constant over three consecutive points. To account for deviations

from a perfect sine wave over the considered time samples, a non-homogeneity term  $\varepsilon(n)$  is introduced on the right-hand side of Eq. (10.7):

$$x(n) - 2 \cos(\omega\Delta t)x(n-1) + x(n-2) = \varepsilon(n) \quad (10.7)$$

where  $x(n)$  represents the  $n$ th discrete time sample and  $\omega$  the instantaneous frequency of the sine wave. The second equation of the VK method is the so called data Eq. (10.8) and describes the relationship between the order  $x(n)$  and the measured data  $y(n)$ . Normally the measured data are a combination of all orders generated in the machine plus a random noise component. This random noise, as well as the non-tracked orders, are then combined into the signal  $\eta(n)$ :

$$y(n) = x(n) + \eta(n) \quad (10.8)$$

A weighted solution is obtained by introducing the Harmonic Confidence Factor (HCF)  $r$ . This value determines the tracking characteristic of the filter and is calculated according to Eq. (10.9) as the ration between the standard deviations of the structure and data equations:

$$r(n) = \frac{s_\varepsilon(n)}{s_\eta(n)} \quad (10.9)$$

Choosing large values of  $r$  leads to a highly selective filtering in the frequency domain; on the contrary, small values will decrease the frequency resolution while obtaining faster convergence. By applying the ratio as a weighting function and combining the two previous equations, the system in Eq. (10.10) is obtained:

$$\begin{bmatrix} 1 & -2 \cos(\omega\Delta t) & 1 \\ 0 & 0 & r(n) \end{bmatrix} \begin{bmatrix} x(n-2) \\ x(n-1) \\ x(n) \end{bmatrix} = \begin{bmatrix} \varepsilon(n) \\ r(n)y(n) - \eta(n) \end{bmatrix} \quad (10.10)$$

Applying Eq. (10.10) to all observed time samples will give a global system of over-determined equations for the desired waveform  $x(n)$  that can be easily solved with standard least square techniques. For the specific case of order tracking, the filtered waveform is most conveniently described in terms of amplitude and phase with respect to a reference channel such as the tachometer.

### 10.3 Order-Based Modal Analysis

Operational Modal Analysis (OMA) algorithms, such as Operational Polymax (Peeters et al. 2007), allow the identification of the modal parameters of a structure by taking into account only operational measurements. However, when applied to data acquired during transient phenomena, such as run ups and coast down, data

need to be carefully interpreted. Input data for the modal parameter identification process are auto and cross spectra calculated from the complete time histories and assuming the excitation can be considered broad-band white noise. However, when spectra are calculated on run up data of rotating machineries, sharp peaks appears at fixed intervals. These peaks relate to the so-called “end-of-order” effect and originate from order components suddenly stopping at the maximum rpm. When using this spectra in standard OMA, they will be erroneously identified as physical poles from the algorithm; additional, they can hamper the accuracy in the estimation of modes at nearby frequencies.

The idea of performing OMA on tracked orders instead of considering the spectra arose because, during a run-up or run-down test, the measured response are mainly caused by the rotational excitation. In this formulation, the run-up or run-down is then considered as a multi-sine sweep excitation in the frequency band of interest. The excitation force acting on the structure is considered to be equivalent to that of a rotating mass with increasing (or decreasing) frequency, which can be represented as two correlated perpendicular forces of equal amplitude and in quadrature (90° phase difference). The measured structural response can then be represented in the frequency domain as shown in Eq. (10.11) where the terms  $F$  relate to the forces while the  $H$  indicate the corresponding columns in the transfer function matrix:

$$Y(\omega) = H_{(:,fx)}(\omega) F_x(\omega) + H_{(:,fy)}(\omega) F_y(\omega) \quad (10.11)$$

Taking into account the relation between the two perpendicular rotating forces and considering only the positive frequency axis, Eq. (10.12) is obtained:

$$Y(\omega) \propto \omega_0^2 \left( H_{(:,fx)}(\omega) - jH_{(:,fy)}(\omega) \right) \delta(\omega - \omega_0) \quad (10.12)$$

where  $\omega_0$  is the rotation speed. This equation shows that the measured output is proportional to the squared rotation speed and to a complex combination of two structural FRFs related to  $x$  and  $y$  excitation. In general, a structural FRF can be modally decomposed as shown in Eq. (10.13):

$$H_{(:,\bullet)}(\omega) = V(j\omega I - \Lambda)^{-1} L_{\bullet} + \frac{1}{\omega^2} LR_{\bullet} + UR_{\bullet} \quad (10.13)$$

where  $LR$  and  $UR$  are the real-valued lower and upper residuals which are used for modeling the influences of the modes outside of the considered frequency band.  $V$ ,  $\Lambda$  and  $L$  are the mode shape matrix, the diagonal matrix containing the complex poles and the modal participation factors. Equations (10.11) and (10.13) show that modal analysis can be applied to displacement orders taking into account that:

- Displacement orders are proportional to the squared rotation speed and, as a consequence, acceleration orders are proportional to the forth power of the same rotation speed. The main difference is that in the classical modal analysis the acceleration FRFs are proportional to the squared frequency axis.

- Upper and lower residuals are complex, while in classical modal analysis they are real.
- Participation factors are complex both in classical and order based modal analysis.

Methods such as Operational Polymax and Operational Polymax Plus are robust against these observations and they can be employed for estimating the modal parameters in case of rotating machineries by looking at the orders rather than at the spectra.

## 10.4 Dynamic Characterization of Operational Gearboxes

With the main objectives of characterizing the gearbox dynamic response in different operating conditions and obtaining experimental data for model validation and updating, a measurement campaign took place on the 13.2 MW dynamic test rig at ZF Wind Power in Lommel, Belgium (Fig. 10.4). Using this test rig, gearboxes can be tested under representative loading condition using parameterized load cases that can be programmed into the test rig controller. In this case, the following scenarios were tested:

- Shaker sine sweep during standstill and in stationary operating conditions at 1200 rpms.
- Stationary operating conditions at 1200 and 800 rpms.
- Run up from 200 to 1500 rpms with a speed of 5 rpms/s.
- The operational measurements were all repeated under different torque loading (33 %, 66 % and 100 % of nominal torque).

As shown in Fig. 10.4 (right) an extensive grid of 250 points on both the gearboxes and the test rig was measured using tri-axial accelerometers. To measure all points, the whole test schedule was repeated 7 times moving the available sensors to cover the whole grid. To ensure the data from the different dataset could be

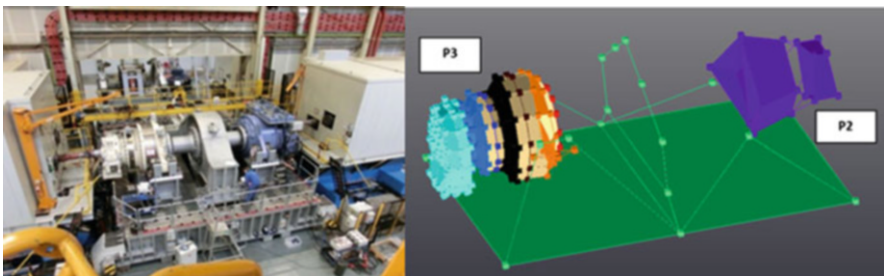


**Fig. 10.4** Test-rig configuration (*left*); markers identifying the measurement points on the test-rig (*right*)

compared, a set of 7 single axis accelerometers was always kept in the same positions. 3 optical sensors (zebra tape + laser) were respectively installed on the Low Speed Shaft and at the High Speed Shaft of each of the two gearboxes in the test rig.

With the objective of comparing the modal parameters obtained in different operating conditions, data measured during shaker excitation with the gearbox in standstill conditions have been analysed. After computing Frequency Response Functions, standard Experimental Modal Analysis methods were applied and a set of reference modal parameters obtained (Manzato et al. 2015). A similar processing was also performed on the data collected applying the sine sweep via the shaker during stationary operations. However, although some of the modes could still be identified, it was concluded that the shaker were not powerful enough to sufficiently excite the structure and ensure a reliable modal estimation.

Response data acquired during acceleration measurement were also acquired and the signature of the gearbox during operation at constant speed is shown in Fig. 10.5.

All vertical lines in the time-frequency diagram represent highly excited harmonics of the fundamental rotational speed and they can all be related to rotational speed of the shafts of the different stages as well as to the gear meshing frequencies. As the response is dominated by narrow and closely spaced harmonic components, standard Operational Modal Analysis cannot be applied. As a consequence, to understand the response, only Operational Deflection Shapes can be analysed, but, as mentioned, it will be impossible to understand whether the high response at the receiver is due to the system or the source (Fig. 10.1). Of course one could compare the harmonic frequency with the natural frequencies identified by applying shaker excitation in stationary conditions. However, as the boundary conditions

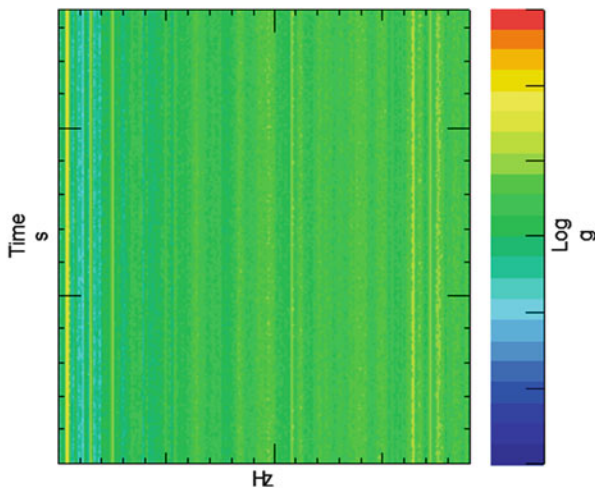


**Fig. 10.5** Signature of the gearbox on the test rig during stationary operations



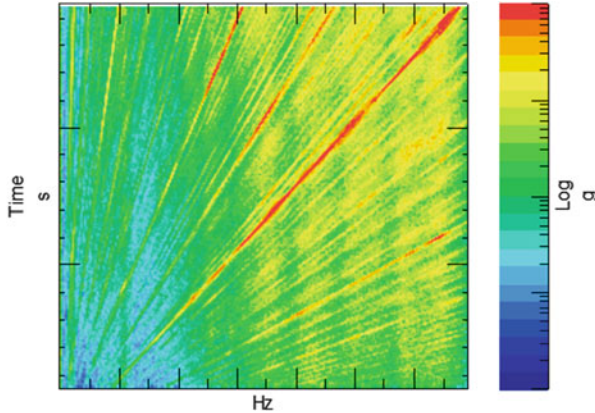


**Fig. 10.6** Signature of the gearbox on the test rig during a run-up at 5 rpm/s

between standstill and operational conditions are significantly different, erroneous conclusion might be derived.

The signature obtained during a run up is significantly different and is shown in Fig. 10.6. In this case, the different orders vary in frequency and the resulting excitation is similar to that of a multi-sine sweep. As will be explained in the next sections, both Operational and Order-based Modal Analysis can be applied to these data to extract the modal parameters.

#### 10.4.1 *Operational Modal Analysis*

Operational Modal Analysis requires as input data acceleration auto and cross-spectra calculated using the complete time history. The results can then be considered as an average over time of the frequency response shown in Fig. 10.5. By combining the response at the different orders, the resulting spectra can be considered as the response to a “flat” broadband excitation, thus complying with the OMA assumption. The resulting spectra are shown in Fig. 10.7. Although the spectrum shown is suitable for OMA processing, the results might be wrongly interpreted if the data are not carefully analysed.

A comparison of the two graphs reveals that some of the peaks in the spectrum (and in particular the sharpest ones) originate from order components suddenly stopping at the maximum rpms. Cursors were added to the pictures at frequencies that were identified as poles of the gearbox by classical OMA. Moreover, as the two gearboxes on the test rig were slightly different prototypes, they rotate at slightly different speeds, resulting on a doubling of these “end-of-order” related poles. This is the main weakness of this method: not only the real poles are identified, but also the so-called “end-of-order” related poles which are physically not present

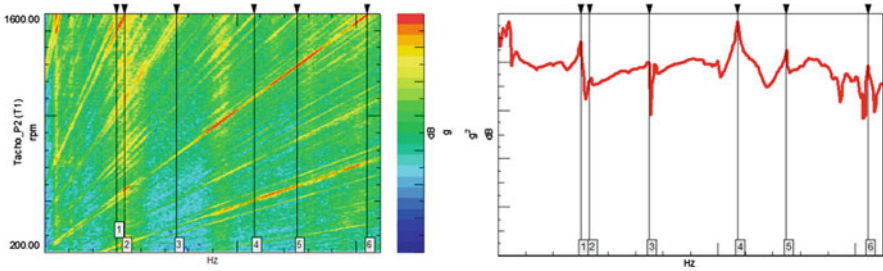


**Fig. 10.7** RPM-frequency spectrogram of the gearbox run up and corresponding spectrum

in the system and are purely processing artifact. The four identified frequencies correspond to some of the main order components ending at that frequency. The estimated modal model is consequently not correct because it considers them as poles of the system. While these poles could be ignored a-posteriori, in cases where many orders are present (such as this one) they can also affect the estimation of close modes, thus reducing the confidence in the identified model.

### 10.4.2 Order-Based Modal Analysis

The conclusions from Sect. 10.4.1 motivated the development of a new method able to reliably identify a modal model of a rotating machine during operation. Instead of applying modal parameter identification on the spectra, the concept is to identify the dominant orders in the response and then use them to extract the modal parameters in the frequency band of interest. The process to perform Order-based Modal Analysis is displayed in Fig. 10.8. The first two steps pre-process the tacho data to remove spikes that could be present in the signal and make it smoother. Once the tacho is corrected, order tracking can be applied using one of the techniques discussed in Sect. 10.2 and the orders of interest extracted. On each of these orders operational modal identification can then be applied and the modal parameters from the different orders combined to obtain the modal response in the frequency band of interest.

As an example, Fig. 10.9 compares the cross-power spectrum and the 1st order of the high speed gear stage order (1st gear mesh frequency of the High Speed Stage) for the same channel over the same frequency bandwidth. The order is estimated using two of the techniques presented in Sect. 10.2, namely the Time varying Discrete Fourier Transform (TVDFFT) and the Vold-Kalman filter (VK). It can be observed that, while the cross spectrum on the left spans the complete frequency band, the order only starts from a higher minimum frequency. To span the full bandwidth, different orders need to be extracted and the modes identified.

Applying the classical OMA processing (see Sect. 10.4.1) and using the Operational Polymax algorithm, 13 modes are identified in the frequency band between 80 and 400 Hz. The same processing was repeated for different load levels to

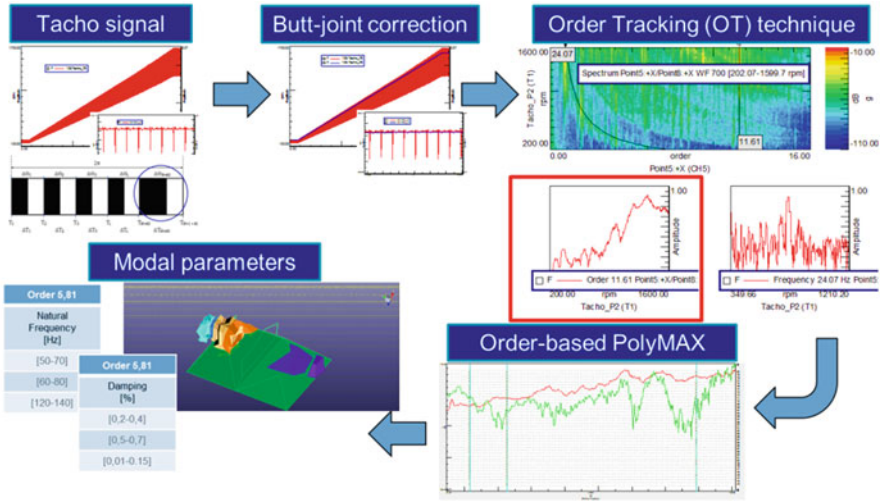


Fig. 10.8 Order-based Modal Analysis process overview

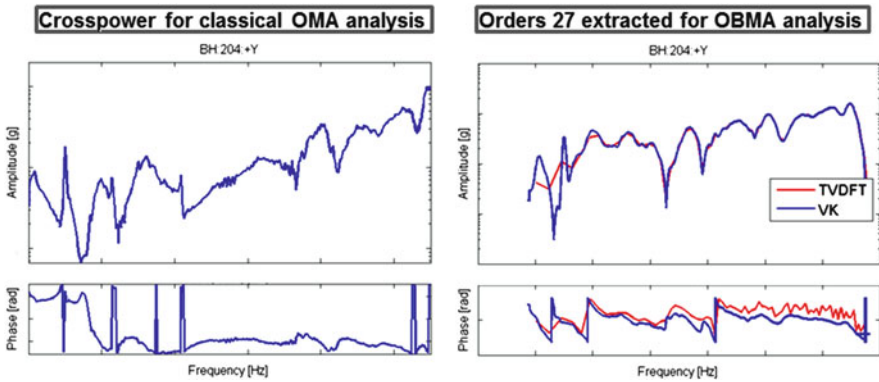
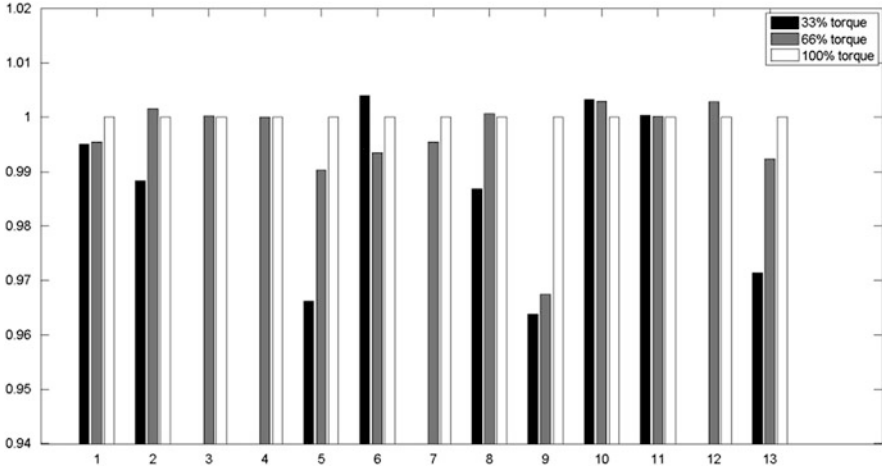


Fig. 10.9 Crosspower for classical OMA analysis (left) and 1st high speed gear stage order extracted by using two different order tracking techniques for OBMA analysis (right)

investigate possible system non-linearities resulting in variations of modal parameters. The results are summarized in Fig. 10.10, where the relative variations of the natural frequencies for the 3 cases (using as reference load case the one with 100% load) are displayed. The general trend from the results shows an increase of the natural frequencies with the torque value. Generally, almost all modes are consistently identified in the 3 load cases, but it should be noted that the majority of them actually represent “end-of-order” poles.

By first extracting the orders with the TVDFT and VK tracking algorithms from the same time data and then using these orders for OBMA, the results shown in Figs. 10.11 and 10.12 are obtained.



**Fig. 10.10** Operational Modal Analysis results on run up data—relative variation of natural frequencies with torque level

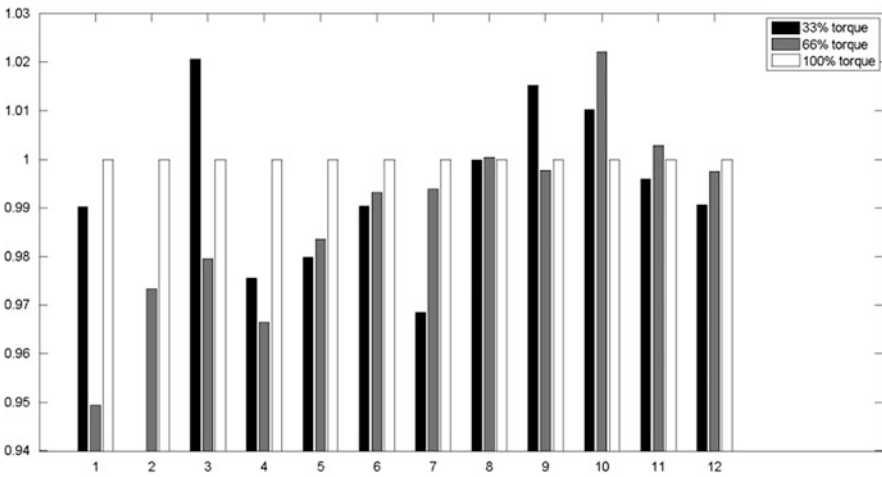


**Fig. 10.11** Order-based Modal Analysis with TVDFT order tracking—relative variation of natural frequencies with torque level

From the displayed results it is immediately clear that OBMA on the VK tracked orders is the process which identifies the highest number of modes. One way of validating the identification results is to compare the measured order with the one computed using the modal parameters in the parameterization of the system transfer presented in Eq. (10.13). The synthesized models from OBMA using the two selected order tracking techniques are shown in Fig. 10.13. In the mid-high frequency band, the identified modal models are able to accurately replicate the measured order. However, at lower frequencies, where the number

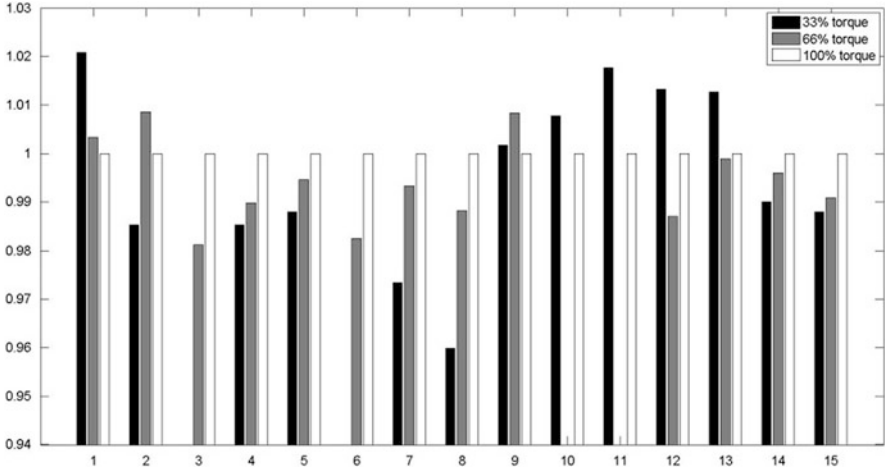


**Fig. 10.12** Order-based Modal Analysis with VK order tracking—relative variation of natural frequencies with torque level

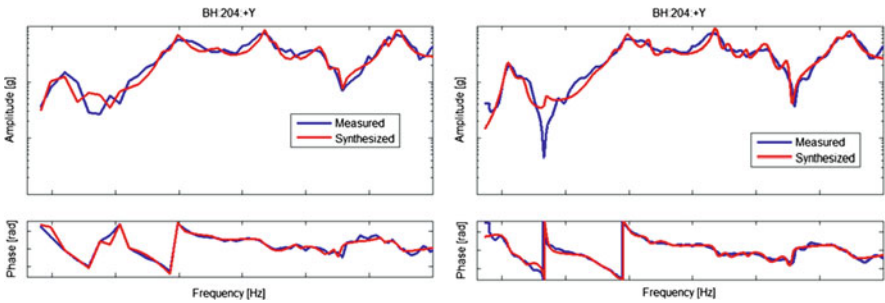


**Fig. 10.13** Measured vs. synthesized orders by using OBMA with TVDFT (*left*) and VK (*right*) order tracking

of available samples for the order estimation is typically smaller, VK as expected performs significantly better. By applying OMA on the data, the results displayed in Fig. 10.14 are obtained. The difference between the measured and synthesized curve is now immediately evident and the identified model is thus not able to represent the true measured response. Also, the majority of the identified peaks appear very sharp and they correspond to end-of-order poles.

Finally, a further comparison between the different methods can be performed by computing the Modal Assurance Criterion (MAC) between mode sets. The results for different combinations of mode sets are displayed in Fig. 10.15: values of MAC equal to 1 (Red) mean two modes are perfectly correlated, while a MAC of 0 (Blue) means the two vector are perfectly orthogonal.

The displayed results focus on the results obtained for the 100% load cases using the three different discussed methods. Only few modes are found to be similar

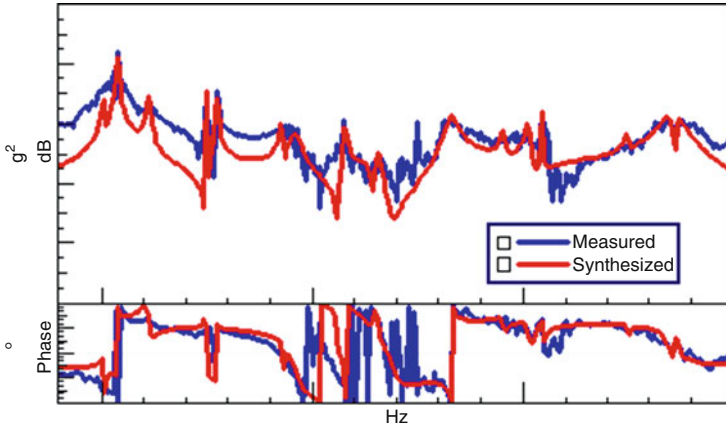


**Fig. 10.14** Measured vs. synthesized crosspower spectra using classical OMA

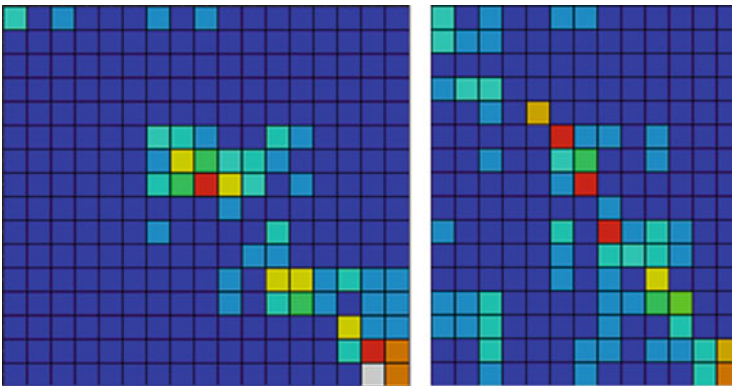


**Fig. 10.15** MAC comparisons. *Left*: OMA vs. OBMA-VK; *right*: OBMA-TVDFDFT vs. OBMA-VK

between OMA and OBMA and this is related to the high number of end-of-order poles identified. By comparing the results obtained using the two order tracking techniques, a discrete correlation is found for the modes in the mid-high frequency range. As expected from the results displayed also in Fig. 10.12, at lower frequencies the predicted orders differ significantly, thus a difference in the extracted modes is also expected.

Table 10.1 summarizes the differences between the analyzing order tracking techniques by analyzing:

- the input parameters the user has to define.
- the computational effort required for the estimation.

**Table 10.1** Critical assessment of the different analyzed order tracking techniques

Order tracking technique	Advantages & drawbacks
Angle Domain Order Tracking	Suitable for real-time processing Equidistant order lines Huge number of parameters to be set Great sensitivity of the resulting order on the settings Very noisy phase Modal parameter estimation is not reliable
Time Variant Discrete Fourier Transform	1 parameter to be set (number of rotation per order line) Computationally efficient Post-calculation to separate close and crossing orders Non equidistant order lines Low resolution at low frequency Phase smoothness depends strongly on the number of rotation per order line Difficult to fit higher frequency
Vold-Kalman Filter Order Tracking	2 parameters to be set (filter bandwidth and number of poles in the filter) Very high order resolution (number of lines equal to the number of acquired samples) Very good quality of the fit Beat free extraction of close and crossing orders Tracking capabilities are independent of the slew rate Non equidistant order lines Computationally demanding

The performed comparison also includes standard Angle-domain resampling order tracking. Although the results are not discussed here, the method is one of those most employed in industry and implemented in commercial solutions.

Figures 10.16 and 10.17 show the comparison between the same mode obtained by applying the OMA and OBMA techniques. In Manzato et al. (2015), the same results were also compared with the modes identified with shaker excitation. In terms of natural frequencies, the different techniques correlate very well.

On the other hand, damping values are more scattered, which is however expected with operational data. However, when comparing mode shapes using the Modal Assurance criterion, very poor correlation is observed although the shapes graphically compare. These results can be however be expected by taking into account the number of measurement points, the measurement and processing noise and uncertainties as well as the small inconsistencies between the different runs where the setup was changed.

Thus, at least when these conditions apply, it is envisaged to validate the analysis only qualitatively by comparing the mode shapes rather than performing a quantitative analysis based on the MAC.



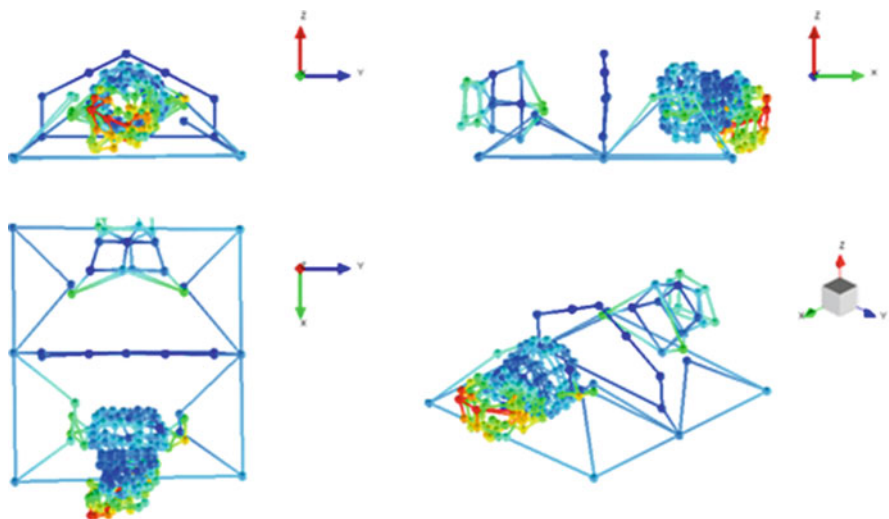


Fig. 10.16 OMA results—Deformed shape of mode #9

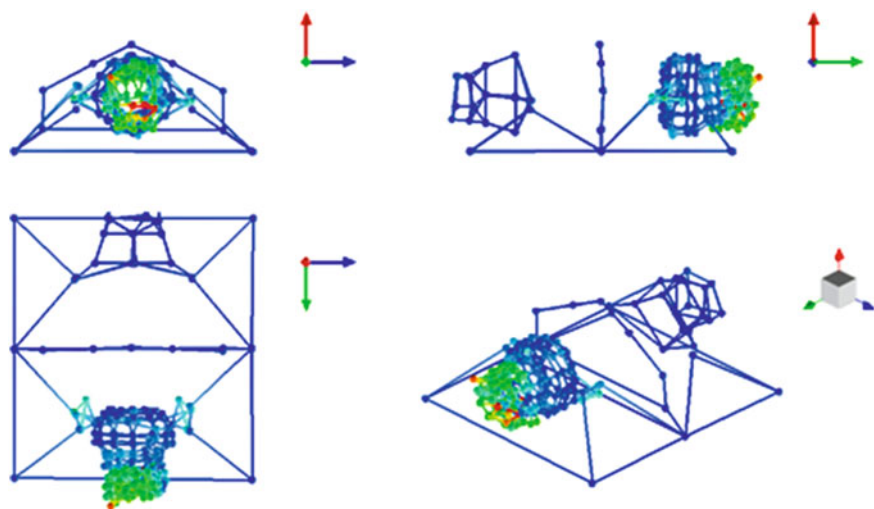


Fig. 10.17 OBMA-VK results—Deformed shape of mode #9

## 10.5 Conclusions

When analysing the dynamic response of rotating machines in operating conditions, the techniques developed to perform operational modal analysis don't hold. After clearly demonstrating that these methods don't provide reliable results both during



stationary and transient condition, a novel method is introduced, which is able to extract an operational modal model from run-up or run-down experiments.

Order-Based Modal Analysis (OBMA) relies on extracting high quality order from the throughput time data that can be then used for modal parameter identification using classical operational modal analysis algorithm. The advantages over classical Operational Deflection Shape (ODS) that also rely on order extraction are the possibility to clearly identify which part of the response can be associate to the system dynamics, which to the input forces and which to a combination of both. Moreover, damping information for each of the modes can be extracted and closely separated modes, as soon as the order resolution allows it, can be distinguished.

However, the use of an accurate phase reference signal is mandatory to obtain a reliable modal model and because of this an accurate tacho measurement is even more critical than in standard ODS analysis. Also, by using more advanced order tracking techniques, although sometimes computationally demanding, can lead to significant improvement of the results.

OBMA has demonstrated to be suitable for operational processing and to give very good results. The method was significantly improved and the two new methods (TVDFFT and VK) showed much improved results compared to older implementations. The extra effort compared to calculate the ODS are limited, although the Vold-Kalman order tracking is computationally more demanding and the quality of the tacho signal should be high enough to allow a reliable processing of the data. The results of the proposed approach were used in Vanhollebeke et al. (2015) to validate the operational response of the analysed gearbox predicted using a flexible multibody model.

**Acknowledgments** The authors would link to kindly acknowledge Frederik Vanhollebeke, Sonja Goris and Joris Peeters of ZF Wind Power for the possibility of using the data acquired on the gearbox test rig to carry out this research. Additionally, the authors kindly acknowledge the Institute for Promotion of Innovation through Science and Technology in Flanders, Belgium (IWT Vlandereen) for the O&O grant ALARM in which the aforementioned experimental campaign was performed. The ALARM project was furthermore supported by an Eureka label in the framework of international co-operations.

**Open Access** This chapter is distributed under the terms of the Creative Commons Attribution-NonCommercial 4.0 International License (<http://creativecommons.org/licenses/by-nc/4.0/>), which permits any noncommercial use, duplication, adaptation, distribution and reproduction in any medium or format, as long as you give appropriate credit to the original author(s) and the source, provide a link to the Creative Commons license and indicate if changes were made.

The images or other third party material in this chapter are included in the work's Creative Commons license, unless indicated otherwise in the credit line; if such material is not included in the work's Creative Commons license and the respective action is not permitted by statutory regulation, users will need to obtain permission from the license holder to duplicate, adapt or reproduce the material.

## References

- Blough J (1998) Improving the analysis of operating data on rotating automotive components. Dissertation, University of Cincinnati
- Blough J, Brown DL, Vold H (1997) The time variant discrete fourier transform as an order tracking method. In: Publications: Technical Paper Number 972006. Society of Automotive Engineers. Available via SAE. <http://papers.sae.org/972006/>. Accessed 08 Apr 2016
- Carne TG, James GH III (2010) The inception of OMA in the development of modal testing for wind turbines. *Mech Syst Signal Pr* 24:1213–1226
- Goris S, Vanhollebeke F, Ribbentrop A et al (2013) A validated virtual prototyping approach for avoiding wind turbine tonalities. Paper presented at the 5th international conference on wind turbine noise, INCE-Europe, Denver, 28–30 August 2013
- Heylen W, Lammens S, Sas P (2013) Modal analysis theory and testing. KU Leuven, Belgium
- Janssens K, Kollar Z, Peeters B et al (2006) Order-based resonance identification using operational Polymax. In: Abstracts of the IMAC-XXIV: conference and exposition on structural dynamics – looking forwards: technologies for IMAC, Society for Experimental Mechanics, St. Louis, 30 January–02 February 2006
- Manzato S, White JR, LeBlanc B et al (2013) Advanced identification techniques for operational wind turbine data. In: Allemang R, De Clerck J, Niezrecki C et al (eds) Topics in modal analysis volume 7: proceedings of the 31st IMAC, a conference on structural dynamics, 2013. Conference Proceedings of the Society for Experimental Mechanics Series, Springer, New York
- Manzato S, Di Lorenzo E, Medici A et al (2015) Order-based modal analysis versus standard techniques to extract modal parameters of operational wind turbine gearboxes. In: Mains M (ed) Topics in modal analysis volume 10: proceedings of the 33rd IMAC, a conference and exposition on structural dynamics, 2015. Conference Proceedings of the Society for Experimental Mechanics Series, Springer, New York
- Peeters B, Van der Auweraer H, Vanhollebeke F et al (2007) Operational modal analysis for estimating the dynamic properties of a stadium structure during a football game. *Shock Vib* 11:395–409
- Vanhollebeke F, Peeters P, Helsen J et al (2015) Large scale validation of a flexible multibody wind turbine gearbox model. *J Comput Nonlinear Dynam*. doi:10.1115/1.4028600
- Vold H, Leuridan J (1993) High resolution order tracking at extreme slew rates, using Kalman tracking filters. In: Publications: Technical Paper Number 931288. Society of Automotive Engineers. Available via SAE. <http://papers.sae.org/931288/>. Accessed 08 Apr 2016

**Part III**  
**Tower & Support Structure**

# Chapter 11

## An Overview of Analysis and Design of Offshore Wind Turbines

Torgeir Moan and Tomasz Bugalski

**Abstract** Offshore wind provides an important source of renewable energy and new opportunities for marine technology. Various fixed and floating concepts have been proposed for offshore wind application. Offshore wind turbines (OWTs) with a monopile support structure fixed to the sea bed in shallow water, have already been industrialized, while fixed turbines in deeper water are emerging. Floating wind turbines are still at an early stage of development. The works presented in this chapter deal with selected recent developments of wind turbine concepts, design criteria and methods for integrated dynamic analysis. Besides design, topics such as inspection, monitoring, maintenance and repair during operation are also briefly addressed.

### 11.1 Introduction

An increased focus on renewable energy is needed in view of the climate challenges. Globally, there is a significant potential for offshore wind energy. Wind power is produced offshore by wind turbines that consist of a rotor, a drivetrain and an electric generator, supported on a tower and a bottom fixed or floating structure. The rotor can have a horizontal or vertical axis. While the horizontal axis turbines currently dominate the commercial market, vertical axis turbines provide advantages that especially could reduce the costs of floating turbines. The drivetrain is commonly a mechanical transmission with a gear but a hydraulic transmission or direct drive is also an alternative. For traditional wind turbines with gear transmissions, the gearbox is among the most expensive components.

---

T. Moan

Department of Marine Technology, Centre for Ships & Ocean Structures (CeSOS)/Centre for Autonomous Marine Operations & Systems (AMOS), Norwegian University of Science and Technology (NTNU), 7491 Trondheim, Norway  
e-mail: [torgeir.moan@ntnu.no](mailto:torgeir.moan@ntnu.no)

T. Bugalski (✉)

Centrum Techniki Okrętowej S.A. (Ship Design and Research Centre S.A.), ul. Szczecińska 65, 80-392 Gdańsk, Poland  
e-mail: [tomasz.bugalski@cto.gda.pl](mailto:tomasz.bugalski@cto.gda.pl)

Up until now, fixed foundations, such as monopile, gravity-base and tripod, are used in offshore wind farms in relatively shallow waters, i.e. 10–30 m depths. Jacket-type wind turbines have been installed in water depths up to 45 m and will play an important role in the near-future development. In deeper water, beyond 80 m, it may be more cost work effective to exploit wind resource by using floating wind turbines. This is because the foundation cost of a fixed wind turbine will increase significantly when the water depth increases, while the cost of a floater is less sensitive to the water depth.

The development of floating wind turbines is still at an early stage and further studies are required to demonstrate which of the concepts is the best one for certain site conditions, such as water depth and met ocean conditions. This not only requires due considerations of the support structure, but also of the rotor and drivetrain as wind turbines are tightly coupled systems where the different subsystems interact.

Fixed bottom wind turbines are usually designed as a de-coupled system. Hydrodynamic loads in deep water or intermediate water depth where wave profiles are not too steep, are well described by linear wave theory. As wave height increases and water depth decreases, the wave crest tends to become more narrow and steep, whereas the wave trough becomes long and flat. This happens as the wave starts to ‘sense’ the bottom. The nonlinearity of a wave increases with the wave steepness. Weakly non-linear undisturbed waves are in general well understood and for regular waves higher order perturbation solutions exist. Near the point of breaking, waves become highly nonlinear, and at the point of breaking release a high amount of energy; such events can have a significant impact on the loading on offshore wind turbines.

Spar-type floating wind turbines are suited for deep water due to their draft; Statoil plans to install five 6 MW spar turbines in 100 m water depth in Scotland.

So far semi-submersible wind turbines have been based on three columns connected by braces. Typically they are designed to support one central turbine or 1–3 turbines located on the top of columns. Clearly, if more than one turbines are installed on one platform, a weather-vaning mooring system will be needed to reduce the aerodynamic wake inter-action between them.

Alternative designs without braces have also been proposed. Current single 5 MW turbine concepts show a large scatter of displacement—between 4500 and 14,000 tons.

Tension-leg concepts normally require a displacement larger than a semi-submersible to ensure the necessary pretension of the tendons and hence the performance that implies limited heave, pitch and roll motions. The main challenge in tension-leg design is to satisfy the ‘no slack’ and limited maximum tension criteria for the tendons with a minimum displacement.

## 11.2 Research Activities in the MARE-WINT Project

Two types of large floating wind turbines are feasible for offshore applications—floating horizontal axis wind turbines (HAWTs) and floating vertical axis wind turbines (VAWTs). VAWTs have the potential to reduce the cost of energy, compared

to HAWTs. Chapter 12 thus deals with the integrated modeling and dynamic response analysis of typical floating VAWT concepts. A fully coupled aero-hydro-servo-elastic method is presented for numerical modeling and dynamic response analysis of floating wind turbine systems. In addition, comparative studies of floating HAWTs and VAWTs are performed.

Chapter 13 deals with hydrodynamic loads on a tripod substructure in relatively shallow water. It provides a brief review of existing analytical and empirical formulations and presents results of a numerical study, considering weak non-linear waves. Open-source codes were used in the simulation of breaking wave, with a focus on impulse forces.

The last chapter in this part (Chap. 14) deals with the use of condition monitoring (CM) and structural health monitoring (SHM) on the turbine tower. SHM allows early detection of damage and aids with maintenance planning, which reduces the cost. The SHM needs to be low cost, suitable for continuous measurement, insensitive to measurement noise, loading conditions and the ambient condition changes. While most efforts on CM and SHM of wind turbines are focused on the drivetrain, and to some extent on the blades, the purpose of this work has been to investigate the applicability of SHM for the tower.

In Chap. 14, a novel SHM technique, using the change in the location of the tower's Neutral Axis (NA) as a damage sensitive feature, is proposed. The method uses the Kalman Filter for the estimation of the NA location based on the measured strains along two mutually perpendicular axes. A decision based data fusion technique then allows the isolation of the damage. The use of NA as a damage sensitive feature allows the methodology to be insensitive to the ambient loading conditions, while the use of Kalman Filter allows temperature compensation and the robustness to the presence of measurement noise. The study has been carried out on the simulated finite element (FE) model of the wind turbine tower and indicates that bi-axial NA tracking based on data fusion is indeed necessary and at the same time is sensitive to damage. The proposed methodology is then validated using real strain data from the Nordtank NTK 500/41 wind turbine. Based on the results presented, it is concluded that a change in NA is indeed a robust damage indicator insensitive to ambient condition changes, and the applied loads.

**Open Access** This chapter is distributed under the terms of the Creative Commons Attribution-NonCommercial 4.0 International License (<http://creativecommons.org/licenses/by-nc/4.0/>), which permits any noncommercial use, duplication, adaptation, distribution and reproduction in any medium or format, as long as you give appropriate credit to the original author(s) and the source, provide a link to the Creative Commons license and indicate if changes were made.

The images or other third party material in this chapter are included in the work's Creative Commons license, unless indicated otherwise in the credit line; if such material is not included in the work's Creative Commons license and the respective action is not permitted by statutory regulation, users will need to obtain permission from the license holder to duplicate, adapt or reproduce the material.

# Chapter 12

## Dynamic Response Analysis of Floating Wind Turbines with Emphasis on Vertical Axis Rotors

Zhengshun Cheng, Torgeir Moan, and Zhen Gao

**Abstract** Large floating wind turbines are feasible for offshore application. Due to the commercial success onshore and nearshore, floating horizontal axis wind turbines (HAWTs) are now being widely studied. However, floating vertical axis wind turbines (VAWTs) have an excellent potential in the cost of energy reduction compared with floating HAWTs. This paper deals with the integrated modeling and dynamic response analysis of typical floating VAWT concepts. A fully coupled aero-hydro-servo-elastic method is presented for numerical modeling and dynamic response analysis of floating wind turbine systems. Considering a two-bladed 5 MW Darrieus rotor, the dynamic response characteristics of typical floating VAWT concepts are studied. In addition, comparative studies of floating HAWTs and VAWTs are performed.

### 12.1 Introduction

During the 1970s and 1980s, a large amount of efforts was devoted to develop VAWTs, particularly in the United States and Canada. However, the VAWTs gradually lost the competition with the horizontal axis wind turbines (HAWTs) due to low efficiency and fatigue problems within the bearings and blades. In recent years, offshore wind farms are moving towards deeper waters where floating wind turbines are required in countries such as the Japan, Norway and United States. Due to the commercial success onshore and nearshore, floating HAWTs are now being widely studied and prototypes have been developed and tested, such as the Hywind demo in Norway, the WindFloat demo in Portugal and the floating wind turbines off the Fukushima coast of northeast Japan.

The interest in the development of VAWTs for offshore application has also been resurging. Compared with floating HAWTs, floating VAWTs have lower centers of gravity, are independent of wind direction, can provide reduced machine complexity and have the potential of achieving more than 20% cost of energy reductions

---

Z. Cheng (✉) • T. Moan • Z. Gao

Department of Marine Technology, Centre for Ships & Ocean Structures (CeSOS)/Centre for Autonomous Marine Operations & Systems (AMOS), Norwegian University of Science and Technology (NTNU), 7491 Trondheim, Norway

e-mail: [zhengshun.cheng@ntnu.no](mailto:zhengshun.cheng@ntnu.no); [torgeir.moan@ntnu.no](mailto:torgeir.moan@ntnu.no); [zhen.gao@ntnu.no](mailto:zhen.gao@ntnu.no)

(Paquette and Barone 2012). Moreover, floating platforms can help to mitigate the fatigue damage suffered by the onshore VAWTs (Wang et al. 2016). In addition, floating VAWTs are more suitable for deploying as wind farms than floating HAWTs (Dabiri 2011). Thus, more and more efforts are devoted to the development of floating VAWTs.

In order to assess the technical feasibility of floating VAWTs, a numerical simulation tool is required to conduct the fully coupled aero-hydro-servo-elastic analysis. To date the available simulation tools that can model the floating VAWTs in a fully-coupled way are limited, but are emerging, such as the FloVAWT code by Cranfield University (Collu et al. 2013), the OWENS toolkit by Sandia National Laboratories (Brian et al. 2013), the HAWC2 by DTU Wind Energy (Larsen and Madsen 2013), the SIMO-RIFLEX-DMS (Wang et al. 2013) and SIMO-RIFLEX-AC (Cheng et al. 2016b) code by NTNU. Among these codes, the aerodynamic loads are mainly computed using the double multi-streamtube (DMS) model (Paraschivoiu 2002) or actuator cylinder (AC) flow model (Madsen 1982), which are capable of predicting the aerodynamic loads accurate at a small computational cost. These two models are validated using experimental data by Wang et al. (2015b) and Cheng et al. (2016a). Code-to-code comparisons between these codes were also conducted to verify each code, such as the comparison of FloVAWT and SIMO-RIFLEX-DMS by Borg et al. (2014c), and the comparison of three codes SIMO-RIFLEX-DMS, SIMO-RIFLEX-AC and HAWC2 by Cheng et al. (2016b).

Considerable efforts have been made to study the floating VAWTs by many researchers using the aforementioned codes. Using the code HAWC2, Paulsen et al. (2013) performed a design optimization of the proposed DeepWind concept. An improved design has been obtained with an optimized blade profile with less weight and higher stiffness than the 1st baseline design. Based on the code FloVAWT, Borg et al. (2014a, b) presented a review on the dynamic modeling of floating VAWTs, used a wave energy converter as a motion suppression device for floating wind turbines (Borg et al. 2013) and further performed a comparison on the dynamics of floating VAWTs with three different floating support structures (Borg and Collu 2014). A floating VAWT concept with a 5 MW Darrieus rotor mounted on a semi-submersible was proposed by Wang et al. (2013) and fully coupled aero-hydro-servo-elastic simulations were carried out with emphasis on stochastic dynamic responses (Wang et al. 2016), effects of second order difference-frequency forces and wind-wave misalignment (Wang et al. 2015a), and emergency shutdown process with consideration of faults (Wang et al. 2014a).

In this study, dynamic response characteristics of typical floating VAWTs are addressed. The development and verification of fully coupled numerical simulation tools SIMO-RIFLEX-DMS and SIMO-RIFLEX-AC are presented. Using a two-bladed 5 MW Darrieus rotor, dynamic responses of three floating VAWT concepts (Cheng et al. 2015a, 2015c) are studied by fully coupled nonlinear time domain simulations. In addition, comparative studies of the dynamic responses of floating HAWTs with the NREL 5 MW wind turbine (Jonkman et al. 2009) and VAWTs with the 5 MW Darrieus rotor (Vita 2011) are also performed to assess the merits and disadvantages of each concept.



## 12.2 Typical Floating VAWT Concepts

Currently several floating VAWT concepts have been proposed, including the DeepWind (Vita 2011), VertiWind (Cahay et al. 2011) and floating tilted axis (Akimoto et al. 2011) concepts. They are comprised of a vertical axis rotor, a floater and a mooring system. The rotor can be straight-bladed H-type rotor, curve-bladed Darrieus rotor, helical-bladed rotor and V-type rotor, while the floater could be a spar, semi-submersible or TLP.

Herein three floating support structures were studied: namely a spar, a semi-submersible and a TLP, as depicted in Fig. 12.1 and listed in Table 12.2. The concepts were used to support a 5 MW Darrieus rotor, which is the baseline design developed in the DeepWind project (Vita 2011). The rotor is comprised of two blades and one rotating tower that spans from the top to the bottom that is connected to the generator. Main specifications of this rotor are summarized in Table 12.1. The generator considered here was assumed to be placed at the tower base, and the generator mass was incorporated in the platform hull mass.

The concepts were originally designed to support the NREL 5 MW wind turbine (Jonkman et al. 2009). The concepts were considered in the water depth where they were designed, ranging from 150 m for the TLP, 200 m for the semi to 320 m for the spar. Here reasonable modifications were made on each platform to support the 5 MW Darrieus rotor, such as adjusting the ballast of the spar and the semi, and the tendon pretension of the TLP. For each platform, the draft and displacement were maintained the same as the original one. Details regarding the adjustment can refer to Cheng et al. (2015c). Properties related to the three floating VAWT systems are given in Table 12.2. The natural periods of rigid body motions for the floating

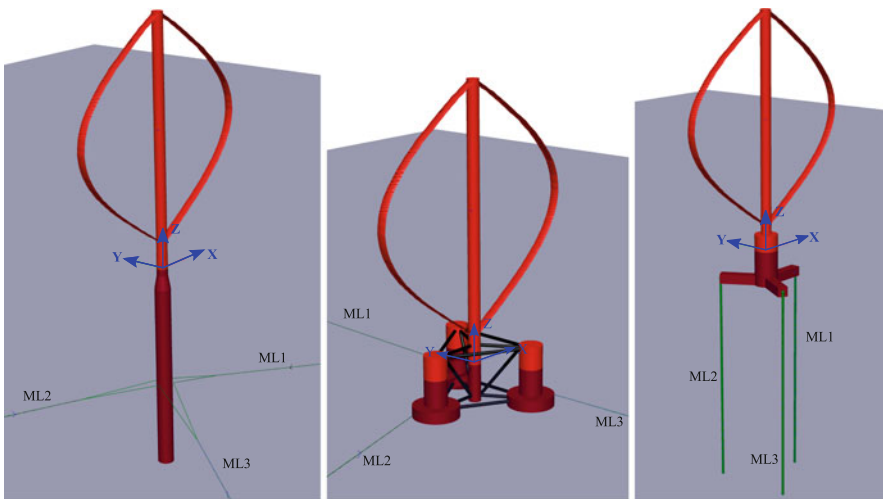


**Fig. 12.1** Three floating VAWT concepts: spar, semi-submersible and TLP

**Table 12.1** Specifications of the Darrieus 5 MW wind turbine

	Darrieus rotor
Rated power [MW]	5
Rotor radius [m]	63.74
Rotor height, root-to-root [m]	129.56
Chord length [m]	7.45
Cut-in, rated, cut-out wind speed [m/s]	5, 14, 25
Rated rotor rotational speed [rpm]	5.26
Total mass, including rotor, shaft and tower [kg]	754,226
Location of overall center of mass [m]	(0, 0, 75.6)

**Table 12.2** Properties of the three floating wind turbine systems

Floater	Spar	Semi-submersible	TLP
Water depth [m]	320	200	150
Draft [m]	120	20	22
Diameter at mean water line [m]	6.5	12.0/6.5	14.0
Platform mass, including ballast & generator [ton]	7308.3	13353.7	2771.9
Center of mass for platform [m]	(0, 0, -89.76)	(0, 0, -15.38)	(0, 0, -13.42)
Buoyancy in undisplaced position [kN]	80,710	139,816	56,804
Center of buoyancy [m]	(0, 0, -62.07)	(0, 0, -13.15)	(0, 0, -14.20)
Surge/Sway natural period [s]	130.8	114.0	45.3
Heave natural period [s]	27.3	17.1	0.6
Roll/Pitch natural period [s]	34.5	31.0	4.5/4.9
Yaw natural period [s]	8.5	79.7	19.3

systems were estimated by conducting free decay tests using numerical simulations (Cheng et al. 2015c).

Since the difference in mass between the 5 MW Darrieus rotor and the NREL 5 MW wind turbine was small compared to the displacements of these three concepts, it was assumed that such modifications would not alter the hydrostatic performance of each platform significantly, which was verified by the following simulations. After these modifications, these substructures supporting the 5 MW Darrieus rotor may not be optimal from an economical point of view, but they are sufficient to demonstrate the inherent motion and structural response characteristics of each concept.

### 12.3 Integrated Modeling of a Floating VAWT System

A floating wind turbine system is usually comprised of a rotor harvesting wind energy, a floater supporting the rotor and a mooring system keeping the floater in position. To evaluate its performance, a fully coupled aero-hydro-servo-elastic

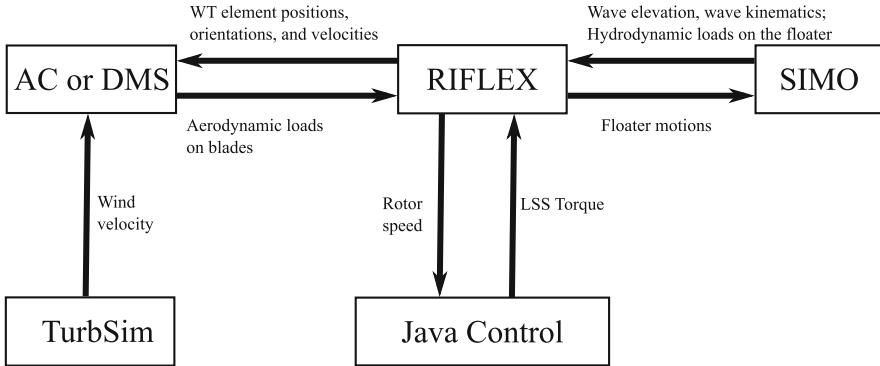


**Fig. 12.2** Overview of the fully coupled aero-hydro-servo-elastic codes SIMO-RIFLEX-DMS and SIMO-RIFLEX-AC

simulation tool is required to carry out the time domain simulations similar as those used for analysis of floating HAWTs. This coupled code should account for the aerodynamics, hydrodynamics, structural dynamics, controller dynamics and mooring line dynamics. Currently, two fully coupled codes, namely SIMO-RIFLEX-DMS and SIMO-RIFLEX-AC, are developed in NTNU to conduct such fully integrated modeling and analysis for floating VAWTs. These two codes are based on the codes SIMO (MARINTEK 2012b) and RIFLEX (MARINTEK 2012a), which are originally developed and are now widely used in the offshore oil & gas industry. The SIMO-RIFLEX wind turbine module has previously been verified (Luxcey et al. 2011; Ormberg et al. 2011).

As illustrated in Fig. 12.2, each coupled code integrates three computer codes, including the SIMO (MARINTEK 2012b), RIFLEX (MARINTEK 2012a) and an aerodynamic module. SIMO computes the hydrodynamic forces and moments on the floater; RIFLEX represents the blades, tower, shaft and mooring lines as nonlinear flexible finite elements and provides the links to an external controller and an aerodynamic module. Obviously, the significant difference between these two codes lies in the method used to compute the aerodynamic loads. Detailed discussions about the related aerodynamic theories are demonstrated in Sect. 12.3.1. In addition, the external controller based on two different control strategies is written in Java. In this way, each of these two fully coupled codes can provide a comprehensive aero-hydro-servo-elastic simulation tool with well-known aerodynamic module, sophisticated hydrodynamic model, stable nonlinear finite element solver, and user-defined controller.

In each fully coupled code, the blades, shaft, tower and mooring lines are modeled as nonlinear flexible finite elements while the floater is considered as a rigid body. Detailed structural model for each component and the corresponding external load models are illustrated in Fig. 12.3. The aerodynamic force is computed in the aerodynamic module as distributed lift and drag forces along the blade and then transferred from the rotor to the generator. The first- and second-order

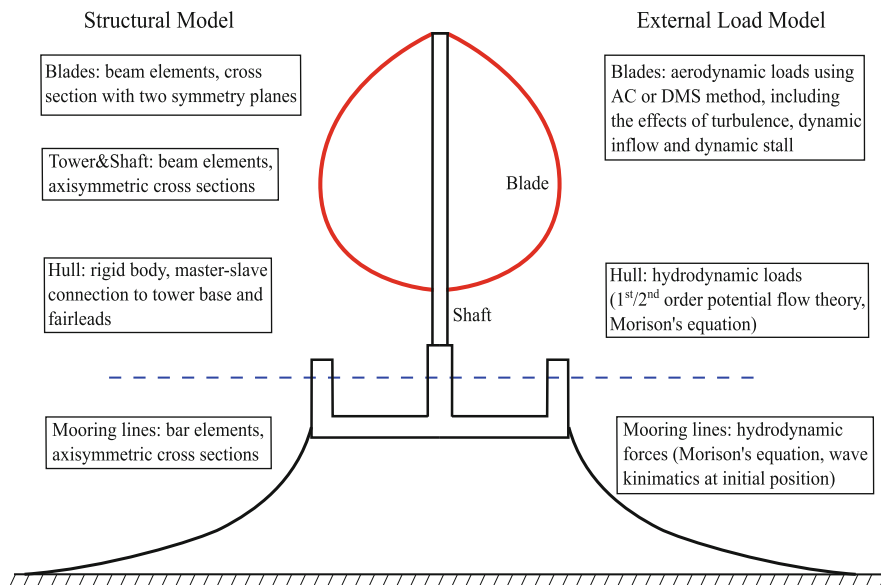


Fig. 12.3 The structural model and external force model of a floating VAWT (Cheng et al. 2016b)

wave excitation forces on the floater are pre-generated in SIMO, while the viscous drag forces on the floater are updated. At each time step, the dynamic equilibrium equations of the rotor, platform and mooring lines are solved in RIFLEX and the rotor rotational speed is regulated through the external controller. Then the platform motions are transferred to SIMO to update the viscous drag forces on the floater, while the positions, velocities and accelerations of the blade elements are transferred to the aerodynamic module to update the aerodynamic loads.

### 12.3.1 Aerodynamics

Among the aerodynamic models for VAWTs, the Double Multiple-Streamtube (DMS) model (Paraschivoiu 2002) and Actuator Cylinder (AC) flow method (Madsen 1982) are two favorable methods that are suitable for fully coupled modeling and analysis for floating VAWTs. Based on these two methods, two aerodynamic codes are developed for fully coupled modeling and analysis of floating VAWTs by Wang et al. (2015b) and Cheng et al. (2016a), respectively.

The DMS method is based on the conservation of mass and momentum in a quasi-steady flow. It assumes that the rotor is vertically divided into a series of adjacent streamtubes, within which a pair of actuator disks are used to represent the turbine. Then the forces on the rotor blades are equated to the change in the streamwise momentum through the turbine, so as to calculate the axial induction

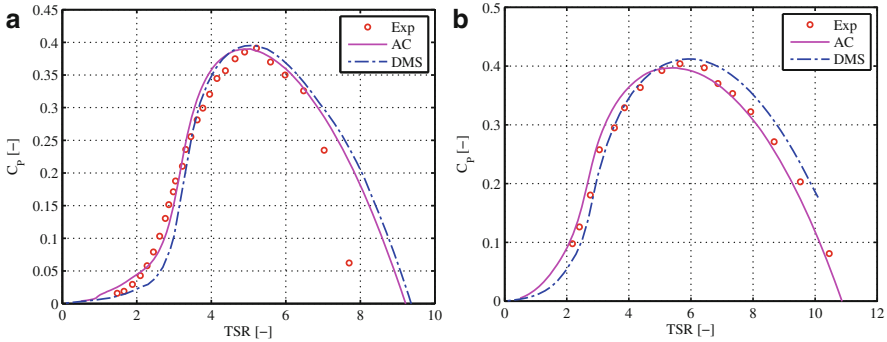


**Fig. 12.4** Comparison of power coefficient curve between simulation model and experimental data. (a) The 3-bladed Sandia 5 m Darrieus rotor at rotational speed of 150 rpm, (b) the 2-bladed Sandia 17 m Darrieus rotor at rotational speed of 50.6 rpm

factor. The DMS model implemented by Wang et al. (2013) accounts for the effect of variation in the Reynolds number and incorporates the effect of dynamic stall using the Beddoes-Leishman dynamic stall model. It is validated by comparison with experimental results of the Sandia 5 m and 17 m Darrieus rotors, as shown in Fig. 12.4.

The AC method is a 2D quasi-steady flow model developed by Madsen (1982). The model extends the actuator disc concept to an actuator surface coinciding with the swept area of the 2D VAWT. In the AC model, the normal and tangential forces resulting from the blade forces are applied on the flow as volume force perpendicular and tangential to the rotor plane, respectively. The induced velocities are thus related to the volume force based on the continuity equation and Euler equation. The induced velocity includes a linear part and a nonlinear part; the linear part can be computed analytically given the normal and tangential loads. However, it's to some extent time-consuming to compute the nonlinear solution directly. A simple correction is therefore introduced to make the final solution in better agreement with the fully nonlinear solution. The developed AC model (Cheng et al. 2016a) is verified by comparison with other numerical models and experimental data, as demonstrated in Fig. 12.4. The AC model implemented in Cheng et al. (2016b) includes the effects of wind shear and turbulence, and dynamic inflow. The effect of dynamic stall is also incorporated using the Beddoes-Leishman dynamic stall model.

### 12.3.2 Hydrodynamics

The hydrodynamic loads are computed using a combination of the potential flow theory and Morison's equation. For large volume structures, the added mass, radiation damping and first order wave forces were obtained from a potential flow model

and applied in the time domain using the convolution technique (Faltinsen 1995). When the second-order wave force becomes important for structures with natural frequencies that either very low or near twice the wave frequency, the second-order potential flow theory is applied to account for the mean drift, difference-frequency and sum-frequency wave forces using the Newman approximation or quadratic transfer function (QTF). Regarding the slender structures where the diameter  $D$  is small compared to the wavelength  $\lambda$  (roughly,  $D/\lambda < 1/5$ ), the Morison equation is applied to calculate the inertial load and viscous drag load (Faltinsen 1995). In addition, viscous forces on large volume structures can also be incorporated through the Morison's equation by considering only the quadratic viscous drag term.

### 12.3.3 Structural Dynamics

In the structural model, the blades are modeled as flexible beam elements with two symmetric planes to differ the flapwise stiffness and edgewise stiffness. The tower and shaft are modeled as axisymmetric beam elements while the mooring lines are considered as nonlinear bar element, as shown in Fig. 12.3. A flexible joint is used to connect the rotating part and non-rotating part within the shaft. The electric torque from the generator is also applied at this joint to regulate the rotor rotational speed according to the prescribed control strategy. Moreover, master–slave connections are applied to integrate the motions between the tower base and fairleads.

In RIFLEX, the dynamic equilibrium equations can be solved in the time domain using the Newmark- $\beta$  numerical integration ( $\beta = 0.256$ ,  $\gamma = 0.505$ ). Structural damping is included through global proportional Rayleigh damping terms for all beam elements.

### 12.3.4 Control System

Considering a typical floating VAWT that operates at a fixed blade pitch angle, a generator torque controller can be used to regulate the rotational speed (Cheng et al. 2016b). The controller aims to minimize the error between the measured and filtered rotational speed  $\Omega_{\text{mea}}$  and the reference rotational speed  $\Omega_{\text{ref}}$  by adjusting the generator torque through a PI control algorithm.

For a typical floating VAWT system the relationship between the reference rotational speed and the wind speed is demonstrated in Fig. 12.5 (Cheng et al. 2016b). According to the operating conditions, it can be divided into three regions, as highlighted in Fig. 12.5. In region I where wind speeds ranges from  $V_{\text{in}}$  to  $V_{\Omega N}$ , the rotor operates at the optimal tip speed ratio so as to achieve the highest power coefficient. In region II, the rotor operates at a moderate tip speed ratio and holds the rotational speed constant at the rated one. The control targets in region I and II aim to maximize the power capture and at the same time keep the rotational speed

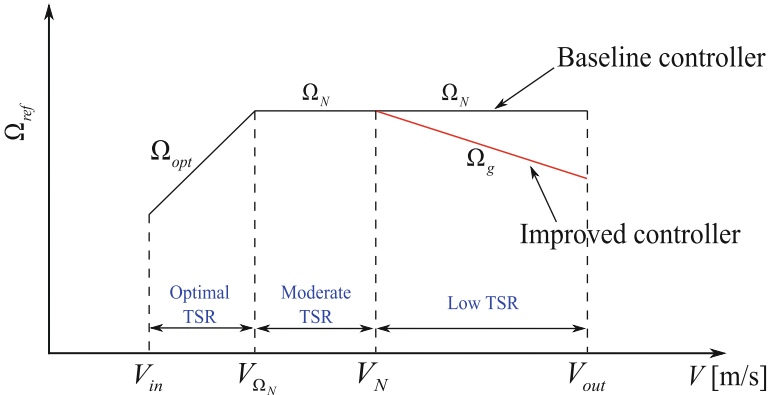


**Fig. 12.5** The relationship between the reference rotor rotational speed and the wind speed for the baseline and improved controllers.  $V_{in}$ ,  $V_N$  and  $V_{out}$  are the cut-in, rated, and cut-out wind speed, respectively;  $V_{\Omega_N}$  is the wind speed for the rated rotational speed;  $\Omega_N$  is the rated rotational speed;  $\Omega_{opt}$  is the optimal rotational speed that can maximize the power capture;  $\Omega_g$  is the rotational speed that can hold the mean generator power approximately constant (Cheng et al. 2016b)

not larger than the rated one. However, the control targets in region III shift to limit the aerodynamic loads acting on the rotor by limiting the rotational speed. In this case, the rotor rotates at relatively low tip speed ratios and two control strategies, as illustrated in Fig. 12.5, are considered here.

Based on these two control strategies, two controllers were developed, namely i.e. the baseline controller and improved controller. This baseline controller is capable of maximizing the power capture for wind speeds below  $V_{\Omega_N}$  and maintaining the rotational speed for wind speeds above  $V_{\Omega_N}$ , while the improved controller aims to maximize the power capture for wind speeds below  $V_N$  and maintain the power capture approximately constant for the above rated wind speeds.

Both the baseline and improved controllers were implemented in the fully coupled codes. Figure 12.6 shows the mean generator power and thrust of a 5 MW Darrieus rotor with different controllers. Above the rated wind speed, the improved controller successfully maintains the mean generator power approximately constant. Detailed information on the discrepancies between these two controllers is provided by Cheng et al. (2016b, 2016c).

### 12.3.5 Verification of the Fully Coupled Codes

The code SIMO-RIFLEX-DMS is developed by Wang et al. (2013) and verified by validating each module separately; the code SIMO-RIFLEX-AC is developed by Cheng et al. (2016b) and verified by a series of comparisons with the codes SIMO-RIFLEX-DMS and HAWC2. Considering an equivalent landbased 5 MW Darrieus rotor, these three codes are verified with each other by comparing the thrust, side force and aerodynamic torque in steady wind conditions, as shown in Figs. 12.7

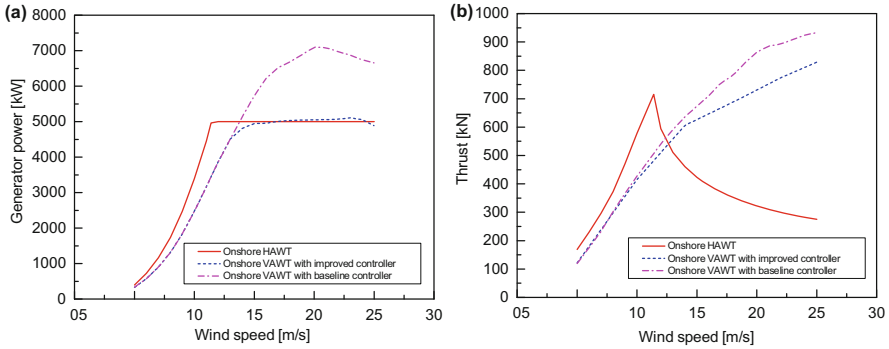


**Fig. 12.6** Steady-state mean generator power and thrust of the onshore HAWT and VAWT with different control strategies (Cheng et al. 2016c)

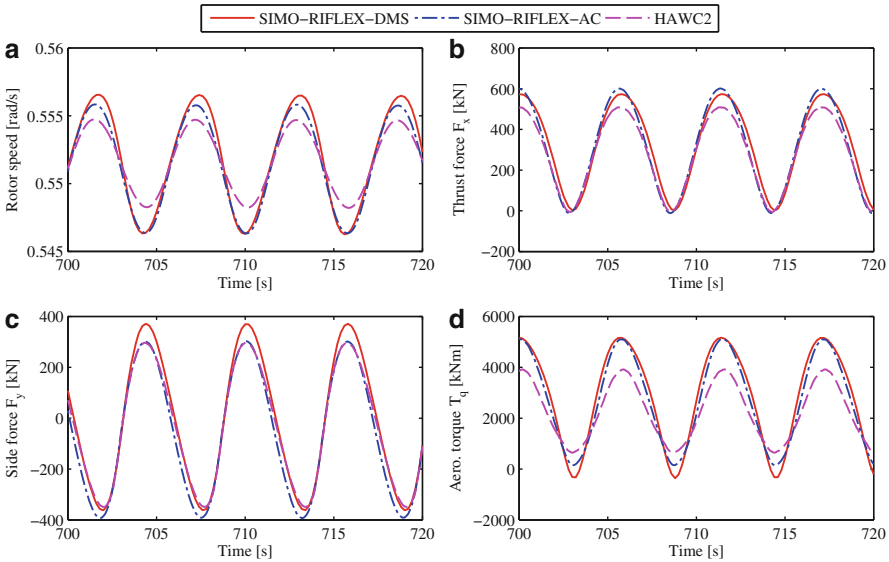


**Fig. 12.7** Comparison of the rotational speed, thrust, side force and aerodynamic torque of the landbased VAWT using three codes without considering the effect of dynamic stall in the steady wind case with a wind speed of 8 m/s (Cheng et al. 2016b)

and 12.8. The load cases shown in these two figures correspond to a tip speed ratio of 4.39 and 2.51, which locate in region I and II as illustrated in Fig. 12.5, respectively. Here the effect of dynamic stall is not included since these three codes use different dynamic stall models. The developed codes SIMO-RIFLEX-DMS and SIMO-RIFLEX-AC are accurate enough in predicting the aerodynamic loads for landbased VAWTs. Essential differences among these three codes are also revealed and presented by Cheng et al. (2016b).



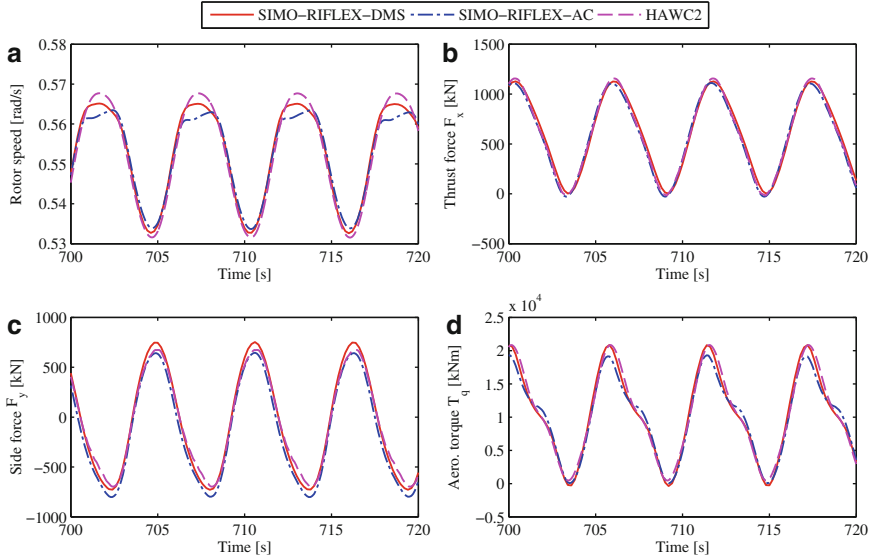


**Fig. 12.8** Comparison of the rotational speed, thrust, side force and aerodynamic torque of the landbased VAWT using three codes without considering the effect of dynamic stall in the steady wind case with a wind speed of 14 m/s (Cheng et al. 2016b)

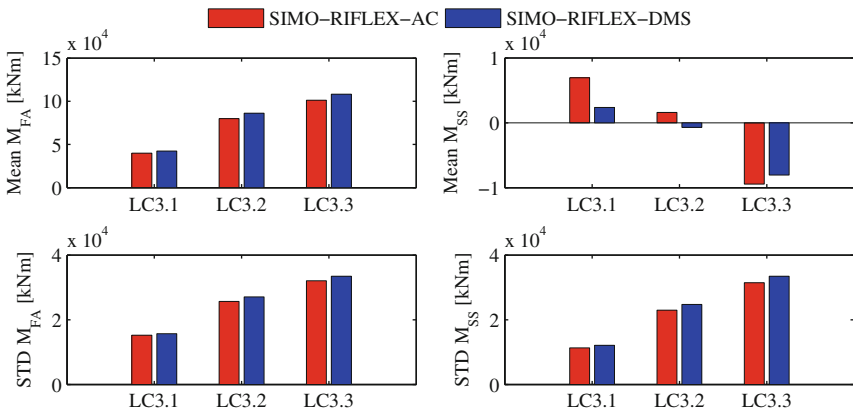


**Fig. 12.9** Mean values and standard deviations of tower base fore-aft bending moment  $M_{FA}$  and side-side bending moment  $M_{SS}$  of the semi VAWT simulated using SIMO-RIFLEX-AC and SIMO-RIFLEX-DMS. The load cases are described by Cheng et al. (2016b)

In addition, the semi VAWT described in Sect. 12.2 is used to verify the capability of the codes SIMO-RIFLEX-DMS and SIMO-RIFLEX-AC in modeling and dynamic analysis of floating VAWTs. Figure 12.9 demonstrates the mean value and standard deviation of the tower base fore-aft and side-side bending moment for

the semi VAWT. It is found that the code SIMO-RIFLEX-AC can to some extent predict more accurate dynamic responses than the code SIMO-RIFLEX-DMS.

## 12.4 Dynamic Response Characteristics of Three Floating VAWTs

The stochastic dynamic responses of the three floating VAWT concepts (Cheng et al. 2015c), as described in Sect. 12.2, are studied under the turbulent wind and irregular wave conditions, including the generator power production, global platform motion, tower base fore-aft and side-side bending moments and tensions in mooring lines. The baseline controller is used during the simulations. Detailed descriptions of load cases used can be found in Cheng et al. (2015c). It should be noted that the stochastic dynamic responses in this section are calculated using the code SIMO-RIFLEX-DMS, and the results are plotted with the mean wind speed as the variable in the abscissa axis for simplicity.

Figure 12.10 shows the mean values of the generator power production of the three floating VAWT concepts. The error bar indicates the standard deviation from the mean value. It can be observed that the mean generator powers increase as the wind speed increases. At rated wind speed of 14 m/s, the mean generator powers slightly exceed the rated power of 5 MW, since the Beddoes-Leishman dynamic stall model is included in the DMS model. The rotor considered can achieve a rated power of 5 MW when excluding the dynamic stall effect. In addition, the mean

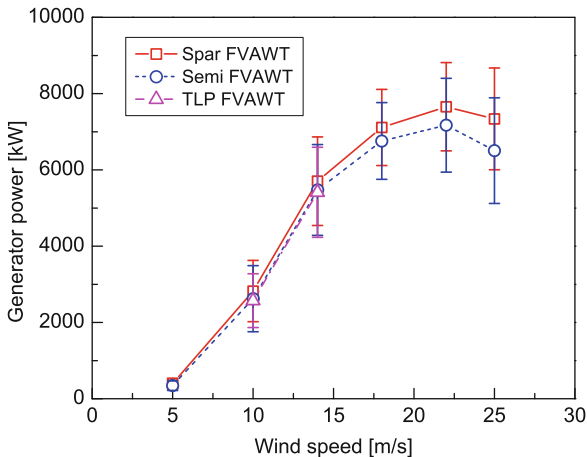


**Fig. 12.10** Mean power production for the three floating VAWT concepts with error bar indicating the standard deviation from the mean value in the turbulent wind and irregular wave load cases. The load cases are indicated using mean wind speed in the abscissa axis. Results of the TLP VAWT are only given in load cases with wind speeds of 10 and 14 m/s (Cheng et al. 2015c)

generator power of the three floating VAWT concepts is very close to each other, except at high wind speeds where the mean generator power of the semi VAWT begins to differ from that of the spar VAWT. The difference results from the different rotational speed and increases as the wind speed increases. The different rotational speeds for the three concepts are due to the implemented controller. The controller regulates the rotational speed by adjusting the generator torque, but fails to keep the rotational speed at above rated wind speed exactly constant. The variations of the generator power for the three floating VAWT concepts are very close to each other as well.

The global platform motions of the three floating VAWT concepts present significant differences. The mean values of platform motions increase as the wind speed increases, since the mean values are mainly wind-induced. For each load case, the spar VAWT suffers the considerable larger platform motions in surge and pitch. But the standard deviations of the spar VAWT and semi VAWT in pitch motions are very close to each other. Regarding the yaw motion, the mean yaw motions of the three floating VAWT concepts are fairly close. However, the standard deviation of the yaw motion of the semi VAWT is relatively larger than that of the spar VAWT, this is due to the resonant yaw motions excited by the turbulent wind.

Characteristic structural responses for the three floating VAWT concepts are also of great interest. Here both the tower base fore-aft bending moment  $M_{FA}$  and side-side bending moment  $M_{SS}$  are chosen as the primary structural performance parameters. The tower base was assumed to be located below the bearings between the rotating shaft and the drive train shaft. Since the aerodynamic loads of each blade varies with the azimuthal angle, not only  $M_{FA}$  but also  $M_{SS}$  have great variations, which is quite different from the horizontal axis wind turbine. These variations of bending moments can cause large stress fluctuations, thus leading to great fatigue damage. Figure 12.11 compares the power spectra of  $M_{FA}$  and  $M_{SS}$  under the turbulent wind and irregular wave condition. The turbulent winds excite the certain low-frequency response of  $M_{FA}$ , but the wind-induced response is much smaller than the 2P response in both  $M_{FA}$  and  $M_{SS}$ . Furthermore, since the taut tendons cannot absorb the 2P aerodynamic excitations for the TLP VAWT, the 2P responses in  $M_{FA}$  and  $M_{SS}$  of the spar VAWT and semi VAWT are much smaller than that of the TLP VAWT, which implies that the catenary mooring system can greatly mitigate the 2P effects on structural dynamic responses. Eigen-frequency analysis has been carried out for this rotor and states that the natural frequencies of the first and second tower base bending modes are far away from the 1P and 2P excitations (Wang et al. 2013). As a consequence, the standard deviations of  $M_{FA}$  and  $M_{SS}$  for the spar VAWT and the semi VAWT are smaller than those of the TLP VAWT.

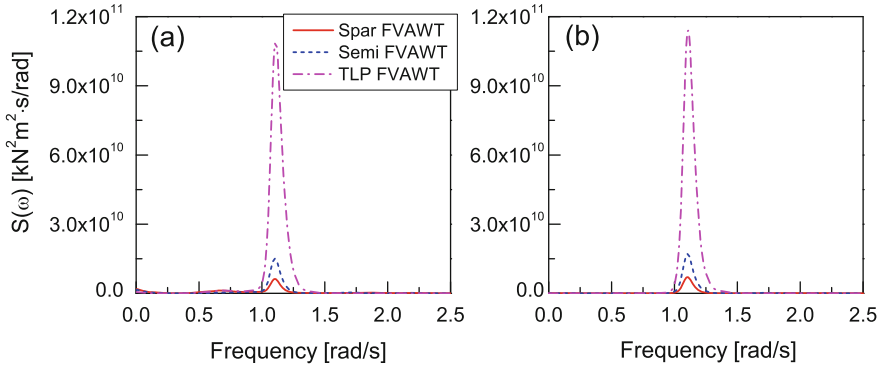


**Fig. 12.11** Power spectra of tower base (a) fore-aft bending moment and (b) side-side bending moment for the three floating VAWT concepts in turbulent wind and irregular wave condition with  $U_w = 14$  m/s,  $H_s = 3.62$  m,  $T_p = 10.29$  s

## 12.5 Comparative Study of Floating HAWTs and VAWTs

In this section, comparative studies on the dynamic responses of floating HAWTs and VAWTs are briefly discussed. The rotors considered are the NREL 5 MW wind turbine (Jonkman et al. 2009) and the 5 MW Darrieus rotor (Vita 2011). The code SIMO-RIFLEX-DMS and SIMO-RIFLEX-AeroDyn are used to conduct the fully coupled analysis for the floating VAWTs and HAWTs, respectively.

### 12.5.1 Semi HAWT vs. Semi VAWT

Wang et al. (2014b) studied the dynamics of the semi-type HAWT and VAWT with the OC4 semi-submersible supporting the NREL 5 MW wind turbine (Jonkman et al. 2009) and the 5 MW Darrieus rotor (Vita 2011). Regarding the semi VAWT, the baseline controller described in Sect. 12.3.4 was adopted in the simulations. Thus the generator power production of the semi VAWT exceeds 5 MW and is much larger than that of the semi HAWT above the rated wind speed. Other details with respect to the floating wind turbine systems and load cases can be found in Wang et al. (2014b).

The effect of 2P frequency on the structural responses, for instance the tower base bending moment, was identified for the semi VAWT. Moreover, power spectral analysis shows that the 2P response dominates the tower base fore-aft and side-side bending moment. Regarding the platform motions, the semi HAWT and VAWT have very close mean values and standard deviations in the pitch motion at low wind speeds. Power spectral analysis also reveals that the pitch motion of the semi VAWT has a smaller pitch resonant response and wave frequency response as well as a significantly notable 2P response, as demonstrated in Fig. 12.12.

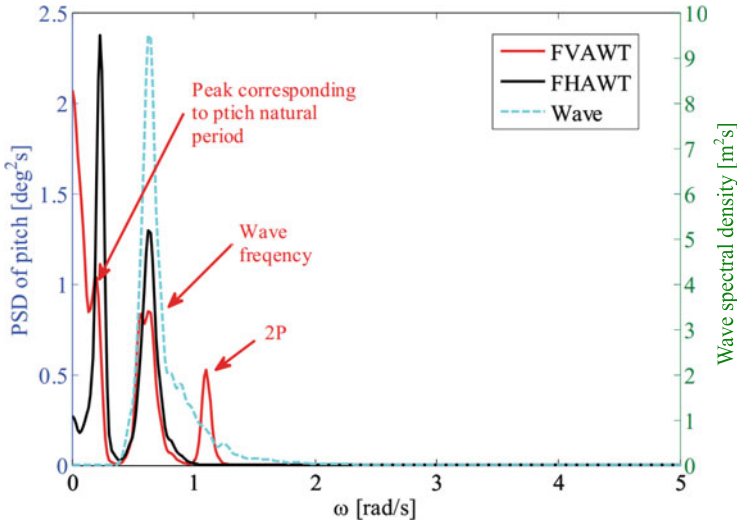


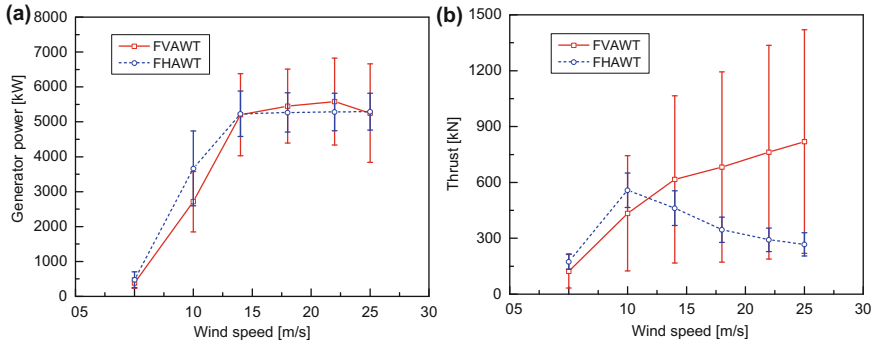
**Fig. 12.12** Power spectra of the pitch motion of the semi HAWT and VAWT in turbulent wind and irregular wave condition with  $U_w = 14$  m/s,  $H_s = 3.62$  m,  $T_p = 10.29$  s

### 12.5.2 Spar HAWT vs. Spar VAWT

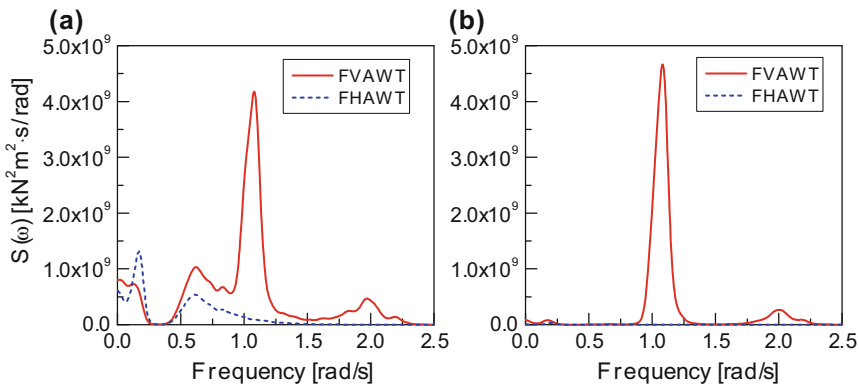
Comparative study of floating HAWTs and VAWTs was further extended to the spar-type concepts by Cheng et al. (2015b, 2016c). The OC3 spar buoy was used to support the aforementioned two rotors. Cheng et al. (2015b) conducted the comparative study using the baseline control strategy for the spar VAWT. To make the comparative study more reasonable, an improved control strategy was employed, as described in Sect. 12.3.4 (Cheng et al. 2016c). A series of numerical simulations were carried out under the turbulent wind and irregular wave conditions.

Figure 12.13 shows the mean values and standard deviations of the generator power and thrust for the spar HAWT and VAWT. The response curves are plotted using the mean values with the error bar showing one standard deviation from the mean value. At wind speeds above 14 m/s, the mean generator powers of the spar HAWT and VAWT are very close to the rated power of 5 MW. However, the standard deviation of the generator power of the spar VAWT is approximately twice of that of the spar HAWT. For wind speeds below 14 m/s, the mean generator power of the spar HAWT is always much greater than that of the spar VAWT due to the higher power coefficient.

The spar HAWT and VAWT also differ in the platform motions due to the different aerodynamic loads and control strategies. For both the spar HAWT and VAWT, the trends in the mean values of the surge, heave and pitch are very similar to those of the mean thrust acting on the rotors, since the mean values of the platform motions are mainly related to wind thrust force. The mean values of the sway, roll



**Fig. 12.13** Mean values and standard deviations of (a) generator power and (b) thrust for the spar type HAWT and VAWT under turbulent wind conditions. The error bar indicates the standard deviation



**Fig. 12.14** Power spectra of the tower base (a) fore-aft bending moment and (b) side-side bending moment for the spar HAWT and VAWT in turbulent wind and irregular wave condition with  $U_w = 14 \text{ m/s}$ ,  $H_s = 3.62 \text{ m}$ ,  $T_p = 10.29 \text{ s}$

and yaw motions of the spar HAWT are very small, because the aerodynamic lateral force and yaw moment are small due to symmetry. However, the spar VAWT has much larger mean values in sway, roll and yaw motions, especially at high wind speed.

The structural responses of the spar HAWT and VAWT illustrate significant differences as well. Figure 12.14 shows the power spectra of the tower base fore-aft and side-side bending moment for the spar HAWT and VAWT in turbulent wind and irregular wave condition with  $U_w = 14 \text{ m/s}$ ,  $H_s = 3.62 \text{ m}$ ,  $T_p = 10.29 \text{ s}$ . Obviously the response corresponding to the 2P frequency is considerably dominating in the tower base fore-aft and side-side bending moments for the spar VAWT. Moreover, the tower base fore-aft bending moment for the spar VAWT also includes prominent low-frequency turbulent wind induced response and wave frequency response. With respect to the spar HAWT, the tower base fore-aft bending moment consists of

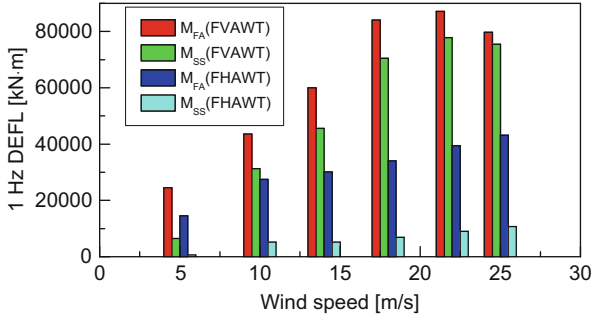


**Fig. 12.15** 1 Hz damage equivalent fatigue loads (DEFLs) of the tower base fore-aft bending moment ( $M_{FA}$ ) and side-side bending moment ( $M_{SS}$ ) for the spar HAWT and VAWT

significant low-frequency turbulent wind induced response, pitch resonant response and wave frequency response. The pitch resonant response mainly results from the relatively large platform pitch motion. In addition, the tower base of the spar HAWT is mainly affected by the fore-aft bending moment, while the side-to-side bending moment can be neglected.

The tower base of the spar VAWT will suffer relatively larger fatigue damage than that of the spar HAWT, as shown in Fig. 12.15. A Matlab-based computer program MLife developed by NREL (Hayman 2012) is used to estimate the short-term damage equivalent fatigue loads (DEFLs). The DEFL of the fore-aft bending moment for the spar VAWT above the rated wind speed is approximately twice that of the spar HAWT. Moreover, the DEFL of the side-side bending moment for the spar VAWT is more than six times greater than that of the spar HAWT.

## 12.6 Conclusions

This paper deals with the integrated modeling methodology for a floating vertical axis wind turbine (VAWT) system and reveals the dynamic response characteristics of representative floating VAWTs.

Firstly two fully coupled simulation tools, namely SIMO-RIFLEX-DMS and SIMO-RIFLEX-AC, are briefly introduced so as to assess the dynamic performance of typical floating VAWT concepts. These two simulation tools are based on the double multi-streamtube (DMS) method and actuator cylinder (AC) flow method, respectively. Moreover, they are capable of accounting for the turbulent inflow, aerodynamics, hydrodynamics, structural elasticity and controller dynamics. Validations of the aerodynamic module using experimental data and verifications of the fully coupled tools using a series of code-to-code comparisons are also presented.

The dynamic responses of three floating VAWT concepts are then studied. A spar, semi-submersible and TLP floater is used to support a two-bladed Darrieus rotor, respectively. Stochastic dynamic response analysis reveals that 2P effects resulting from the 2P aerodynamic loads are prominent in the dynamic responses of these concepts. Due to the compliant catenary mooring systems, the spar and the semi-submersible can help to mitigate the 2P effects on structural loads and mooring line tensions as compared to the TLP concept, at the cost of larger platform motions. The TLP is not a good substructure for vertical axis wind turbine unless the cyclic variation of aerodynamic loads is significantly reduced.

Comparative studies on the dynamics of floating VAWTs and HAWTs are also demonstrated. Due to different aerodynamic load characteristics and control strategies, the spar VAWT results in larger mean tower base bending moments and mooring line tensions above the rated wind speed. Because significant 2P aerodynamic loads act on the spar VAWT, the generator power, tower base bending moments and delta line tensions show prominent 2P variation. Consequently the spar VAWT suffers severe fatigue damage at the tower bottom. The semi VAWT shows significant 2P variations in structural responses as well.

**Acknowledgments** The authors would like to acknowledge the financial support from the EU FP7 project MARE WINT (project NO. 309395) and Research Council of Norway through the Centre for Ships and Ocean Structures (CeSOS) and Centre for Autonomous Marine Operations and Systems (AMOS) at the Department of Marine Technology, Norwegian University of Science and Technology (NTNU), Trondheim, Norway. The first author would also thank Dr. Kai Wang from Aker Solutions for his valuable comments and discussions.

**Open Access** This chapter is distributed under the terms of the Creative Commons Attribution-NonCommercial 4.0 International License (<http://creativecommons.org/licenses/by-nc/4.0/>), which permits any noncommercial use, duplication, adaptation, distribution and reproduction in any medium or format, as long as you give appropriate credit to the original author(s) and the source, provide a link to the Creative Commons license and indicate if changes were made.

The images or other third party material in this chapter are included in the work's Creative Commons license, unless indicated otherwise in the credit line; if such material is not included in the work's Creative Commons license and the respective action is not permitted by statutory regulation, users will need to obtain permission from the license holder to duplicate, adapt or reproduce the material.

## References

- Akimoto H, Tanaka K, Uzawa K (2011) Floating axis wind turbines for offshore power generation—a conceptual study. *Environ Res Lett* 6(4):044017. doi:10.1088/1748-9326/6/4/044017
- Borg M, Collu M (2014) A comparison on the dynamics of a floating vertical axis wind turbine on three different floating support structures. *Energy Procedia* 53:268–279. doi:10.1016/j.egypro.2014.07.236
- Borg M, Collu M, Brennan FP (2013) Use of a wave energy converter as a motion suppression device for floating wind turbines. *Energy Procedia* 35:223–233. doi:10.1016/j.egypro.2013.07.175



- Borg M, Collu M, Kolios A (2014a) Offshore floating vertical axis wind turbines, dynamics modelling state of the art. Part II: mooring line and structural dynamics. *Renew Sustain Energy Rev*. doi:10.1016/j.rser.2014.07.122
- Borg M, Shires A, Collu M (2014b) Offshore floating vertical axis wind turbines, dynamics modelling state of the art. Part I: aerodynamics. *Renew Sustain Energy Rev*. doi:10.1016/j.rser.2014.07.096
- Borg M, Wang K, Collu M et al (2014c) A comparison of two coupled model of dynamics for offshore floating vertical axis wind turbines (VAWT). Paper presented at the 33rd international conference on ocean, offshore and arctic engineering, ASME, San Francisco, 8–13 June 2014
- Cahay M, Luquiau E, Smadja C (2011) Use of a vertical wind turbine in an offshore floating wind farm. Paper presented at the offshore technology conference, Houston, 2–5 May 2011
- Cheng Z, Wang K, Gao Z et al (2015a) Dynamic modelling and analysis of three floating wind turbine concepts with vertical axis rotor. In: Chung JS, Vorpahl F, Hong SY et al (eds) *The proceedings of the 25th (2015) international ocean and polar engineering conference*, Kona, June 2015. ISOPE, California, p 415
- Cheng Z, Wang K, Gao Z et al (2015b) Comparative study of spar type floating horizontal and vertical axis wind turbines subjected to constant winds. Paper presented at the Offshore 2015. European Wind Energy Association, Copenhagen, 10–12 March 2015
- Cheng Z, Wang K, Gao Z, Moan T (2015c) Dynamic response analysis of three floating wind turbine concepts with a two-bladed Darrieus rotor. *J Ocean Wind Energy* 2(4):213–222. doi:10.17736/jowe.2015.jcr33
- Cheng Z, Madsen HA, Gao Z et al (2016a) Aerodynamic modeling of floating vertical axis wind turbines using the actuator cylinder method. Submitted to *Energy Procedia*
- Cheng Z, Madsen HA, Gao Z, Moan T (2016b) A fully coupled method for numerical modeling and dynamic analysis of floating vertical axis wind turbines. Submitted to *Renewable Energy*
- Cheng Z, Wang K, Gao Z, Moan T (2016c) A comparative study on dynamic responses of spar-type floating horizontal and vertical axis wind turbines. *Wind Energy* (accepted)
- Collu M, Borg M, Shires A et al (2013) FloVAWT: progress on the development of a coupled model of dynamics for floating offshore vertical axis wind turbines. Paper presented at the 32nd international conference on ocean, offshore and arctic engineering, ASME, Nantes, 9–14 June 2013
- Dabiri JO (2011) Potential order-of-magnitude enhancement of wind farm power density via counter-rotating vertical-axis wind turbine arrays. *J Renew Sustain Energy* 3(4):043–104. doi:10.1063/1.3608170
- Faltinsen OM (1995) *Sea loads on ships and offshore structures*. Cambridge University Press, Cambridge
- Hayman G (2012) Mlife theory manual for version 1.00. In: National Renewable Energy Laboratory National Wind Technology Center (NWTCC) Information Portal. Available via NWTCC. [https://nwtcc.nrel.gov/system/files/MLife\\_Theory.pdf](https://nwtcc.nrel.gov/system/files/MLife_Theory.pdf). Accessed 09 Apr 2016
- Jonkman JM, Butterfield S, Musial W et al (2009) Definition of a 5-mw reference wind turbine for offshore system development: Tech. Rep. NREL/TP-500-38060. In: NREL publications. Available via NREL. <http://www.nrel.gov/docs/fy09osti/38060.pdf>. Accessed 09 Apr 2016
- Larsen TJ, Madsen HA (2013) On the way to reliable aeroelastic load simulation on VAWT's. Paper presented at the European Wind Energy Conference and Exhibition (EWEA), Austria, 4–7 February 2013
- Luxey N, Ormberg H, Passano E (2011) Global analysis of a floating wind turbine using an aero-hydro-elastic numerical model: Part 2: benchmark study. Paper presented at the ASME 2011, 30th international conference on ocean, offshore and arctic engineering, Rotterdam, 19–24 June 2011
- Madsen HA (1982) The actuator cylinder: a flow model for vertical axis wind turbines. Technical Report, Institute of Industrial Constructions and Energy Technology, Aalborg University Centre, Aalborg
- MARINTEK (2012a) RIFLEX theory manual, version 4.0. Norwegian Marine Technology Research Institute, Trondheim

- MARINTEK (2012b) SIMO theory manual version 4.0. Norwegian Marine Technology Research Institute, Trondheim
- Ormberg H, Passano E, Luxcey N (2011) Global analysis of a floating wind turbine using an aero-hydro-elastic model: Part 1 code development and case study. Paper presented at the ASME 2011, 30th international conference on ocean, offshore and arctic engineering, Rotterdam, 19–24 June 2011
- Owens B, Hurtado JE, Paquette JA et al (2013) Aeroelastic modeling of large off-shore vertical-axis wind turbines: development of the offshore wind energy simulation toolkit. Paper presented at the 54th AIAA/ASME/ASCE/AHS/ASC structures, structural dynamics and materials co-located conferences, Boston, 8–11 April 2016
- Paquette J, Barone M (2012) Innovative offshore vertical-axis wind turbine rotor project. Paper presented at the EWEA 2012 annual event, Copenhagen, 16–19 April 2012
- Paraschivoiu I (2002) Wind turbine design: with emphasis on Darrieus concept. Polytechnic International Press, Montreal
- Paulsen US, Madsen HA, Hattel JH et al (2013) Design optimization of a 5 mw floating offshore vertical-axis wind turbine. *Energy Procedia* 35:22–32. doi:[10.1016/j.egypro.2013.07.155](https://doi.org/10.1016/j.egypro.2013.07.155)
- Vita L (2011) Offshore floating vertical axis wind turbines with rotating platform. Dissertation, Technical University of Denmark
- Wang K, Moan T, Hansen MOL (2013) A method for modeling of floating vertical axis wind turbine. Paper presented at the 32nd international conference on ocean, offshore and arctic engineering, ASME, Nantes, 9–14 June 2013
- Wang K, Hansen MOL, Moan T (2014a) Dynamic analysis of a floating vertical axis wind turbine under emergency shutdown using hydrodynamic brake. *Energy Procedia* 53:56–69
- Wang K, Luan C, Moan T et al (2014b) Comparative study of a FVAWT and a FHAWT with a semi-submersible floater. In: Chung JS, Vorpahl F, Hong SY et al (eds) The proceedings of the 24th (2014) international ocean and polar engineering conference, Busan, June 2014. ISOPE, California, p 302
- Wang K, Cheng Z, Moan T et al (2015a) Effect of difference-frequency forces on the dynamics of a semi-submersible type FVAWT in misaligned wave-wind condition. In: Chung JS, Vorpahl F, Hong SY et al (eds) The proceedings of the 25th (2015) international ocean and polar engineering conference, Kona, June 2015. ISOPE, California, p 517
- Wang K, Hansen MOL, Moan T (2015b) Model improvements for evaluating the effect of tower tilting on the aerodynamics of a vertical axis wind turbine. *Wind Energy* 18:91–110. doi:[10.1002/we.1685](https://doi.org/10.1002/we.1685)
- Wang K, Moan T, Hansen MOL (2016) Stochastic dynamic response analysis of a floating vertical-axis wind turbine with a semi-submersible floater. *Wind Energy*. doi:[10.1002/we.1955](https://doi.org/10.1002/we.1955)

# Chapter 13

## Bottom Fixed Substructure Analysis, Model Testing and Design for Harsh Environment

Duje Veic, Marek Kraskowski, and Tomasz Bugalski

**Abstract** The aim of this chapter is to study the various hydrodynamic loads important for the design process of offshore wind turbines foundations. A numerical study on weakly non-linear waves was conducted, using the commercial code StarCCM++. Open-source codes OpenFoam and OceanWave3D were used for the simulation of breaking waves. Existing analytical and empirical formulations, and the results and conclusions from the current numerical study are presented.

### 13.1 Introduction

The main objective of this study is load analysis on fixed bottom support structures of offshore wind turbines suitable for shallow waters and transitional depths (up to 60 m). Usually, hydrodynamic loads cause lower impact on the tower deflection than the wind loads, however for some conditions hydrodynamic loads excite the structure more severely. Hydrodynamic loads are subject of the study in this research, with the primary focus on impulse forces from the breaking waves.

Quantitative data collection from model tests in the AQUILO<sup>1</sup> project is used for the study on wave propagation and wave loads in the numerical wave tank, by using commercial code StarCCM++. Furthermore, empirical solutions from the Morison equation (Morison et al. 1950) are compared with experimental data as well. Experiments were conducted on support structures installed in the intermediate water depths ( $d = 40\text{--}60$  m).

---

<sup>1</sup>AQUILO—Development of the selection method of the offshore wind turbine support structure for Polish maritime areas, project cofounded by NCBiR; [www.morceko-aquilo.pl](http://www.morceko-aquilo.pl)

D. Veic (✉) • M. Kraskowski • T. Bugalski  
Centrum Techniki Okrętowej S.A. (Ship Design and Research Centre S.A.), ul. Szczecińska 65,  
80-392 Gdańsk, Poland  
e-mail: [dujeveic@gmail.com](mailto:dujeveic@gmail.com); [marek.kraskowski@cto.gda.pl](mailto:marek.kraskowski@cto.gda.pl); [tomasz.bugalski@cto.gda.pl](mailto:tomasz.bugalski@cto.gda.pl)

Collaboration with Deltares/Delft within the framework of WiFi<sup>2</sup>, allowed for an insight into comprehensive experimental data for validation of numerical open-source codes—OpenFoam and OceanWave3D. Experiments were conducted on a monopile structure installed in relatively shallow water ( $d = 30$  m). A series of impulse loadings from breaking waves were observed. It is expected that more comprehensive results will be published after completion of the research. In this chapter, a part of the numerical study is presented.

In short, the purpose of this paper is to present the types of hydrodynamic loads important for the design process of offshore wind turbines foundations, to give a note on existing analytical and empirical formulations and to present results and conclusions from the numerical study.

## 13.2 Determination of Design Wave

Regular wave profiles in deep water, or intermediate water depth that is not too steep, follow a sinusoidal shape and are well described by linear wave theory. As wave height increases and water depth decreases the wave crest tends to become more narrow and steep, whereas the wave trough becomes long and flat. This happens as the wave starts to sense the bottom. Nonlinearity of wave increases with increased steepness of the wave. Weakly non-linear, undisturbed waves are in general well understood, and higher order perturbation solutions—such as Stokes 3rd, Stokes 5th, and fully non-linear stream function theories—exist for regular waves.

Figure 13.1 shows regions of recommended wave theories. Near the point of breaking, a wave becomes highly nonlinear, and at the point of breaking releases a high amount of energy; such events can have a significant contribution on the loading of offshore wind turbines.

Sea states are approximated by wave spectra. The Pierson-Moskowitz (Pierson and Moskowitz 1964) and JONSWAP spectrum are commonly used in practice. Generally, the point of interest is the maximum wave elevation in a 3 h storm duration which may occur once in 50-years. Within that duration, the maximum expected wave height can be estimated as  $H_{\max} = 1.86H_s$  (DNV 2014), where  $H_s$  is significant wave height.

Marked positions on Fig. 13.1 correspond to representative cases from experiments in the AQUILO and WiFi projects. Figure 13.2 presents comparison between experimentally observed wave elevation just before wave breaking and theoretical estimations.

---

<sup>2</sup>WiFi—joint industry project, Wave Impact on Fixed turbines; secondment at Deltares/Delft.

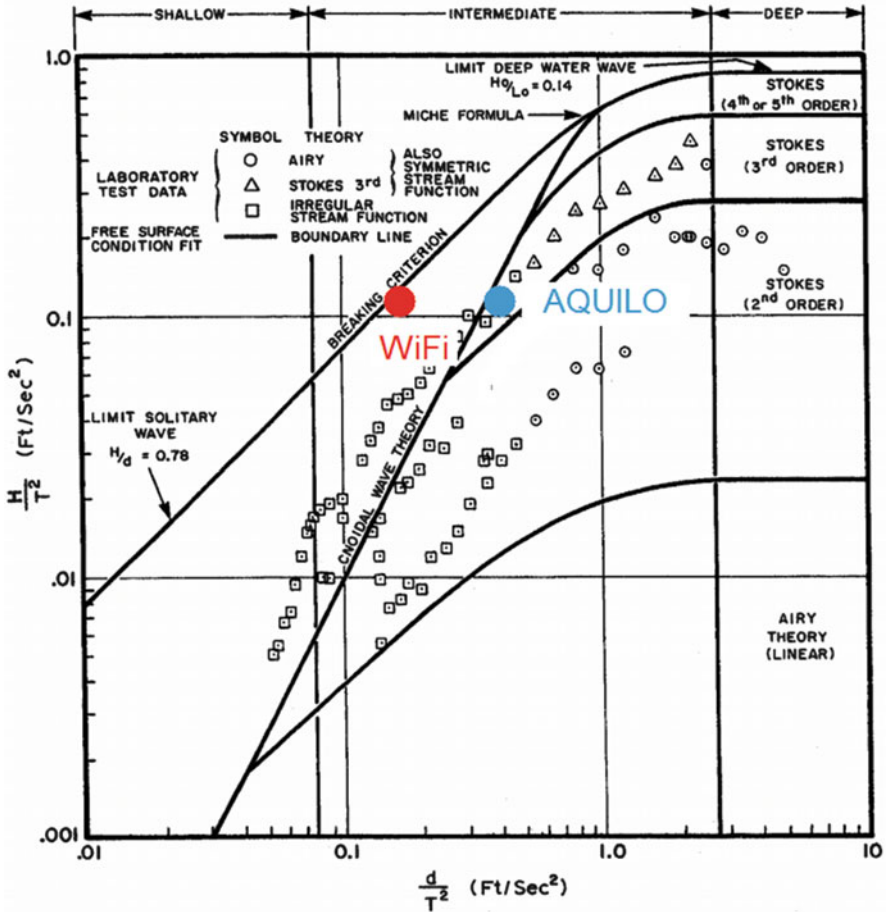


Fig. 13.1 Recommended wave theories (Source: DNV 2014)

### 13.3 Hydrodynamic Loads

The rotor thrust reaction to wind loads acts on a larger lever arm than loads from the waves. Usually, hydrodynamic loads cause a smaller impact on the tower deflection than wind loads. Wind loads are a dominant source of fatigue loading; however in cases when wind and waves are misaligned, there is no influence of aerodynamic damping, and fatigue from hydrodynamic loads has to be taken into consideration as well.

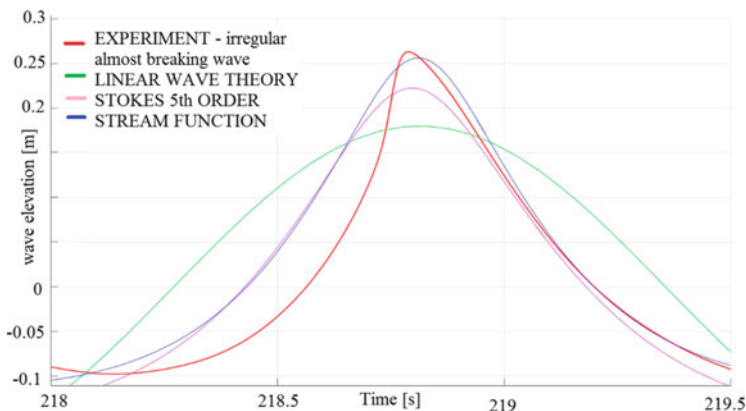


Fig. 13.2 Wave elevation time trace; comparison experiment-theories

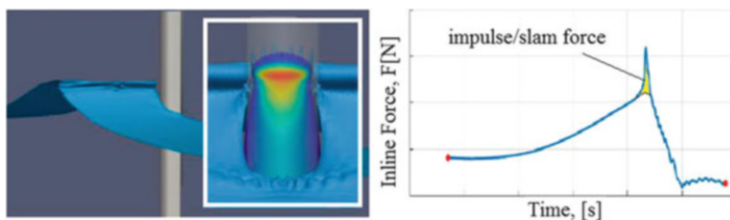


Fig. 13.3 Breaking wave impact (slam) force

Typical design drivers for foundations of offshore wind turbines are impact forces from very steep and breaking waves (Fig. 13.3), which can be expected at sites where monopile support structures are usually installed (in up to 30 m water depth).

The extreme and fatigue response stresses depend strongly on the dynamic behavior of the wind turbine structure. When harmonics of the wave frequency coincide with the natural frequency of the structure, the resonance of the structure may result in an amplification of the response. The foundations of fixed bottom wind turbines are designed such that the natural frequency of the structure is out of the range of wave spectrum frequencies. However, higher harmonics of wave excitation can excite structures in resonance and thus amplify the total response. In literature, the phenomena of “ringing” and “springing” are associated with higher harmonic excitations from the incident wave (Faltinsen 1993).

## 13.4 Analytical and Empirical Formulations

### 13.4.1 Morison Equation

The Morison equation (Morison et al. 1950) is by far the most used equation for computing wave loads on slender structures such as jackets and monopiles. The inline force on a slender body is estimated from fluid velocities and accelerations. The Morison equation is a sum of two terms; one being an empirical drag term proportional to the fluid velocity squared, and the other being an inertia term, derived from potential flow theory, proportional to the fluid acceleration. The Morison equation is defined as follows:

$$F = \frac{1}{2} C_d \rho D |U| U + C_m \rho A |\dot{U}| \quad (13.1)$$

The empirical force coefficients  $C_m$  and  $C_d$  in the Morison's equation are determined from 2D experiments. In general, the drag and inertia coefficients are functions of the Reynolds number, the Keulegan-Carpenter number, the relative roughness, and the ratio between waves and current. The Morison equation which is based on a stream function wave theory predicts the loadings of weakly non-linear waves with good accuracy.

### 13.4.2 Higher Harmonic Forces

An amplification of the structural response can be expected when higher harmonics of non-linear waves coincide with the 1st structural natural frequency. The “Ringing” phenomenon is usually associated with third harmonic excitations from incident waves. The reason why the third harmonic force and “ringing” responses are often associated is that  $f_{\text{tower}}/3$  is close to typical peak frequencies of storm waves (Paulsen 2013). When a “ringing” phenomenon is expected, it has to be considered in the design process of wind turbine foundations (DNV 2014).

A comprehensive literature review and a study on higher harmonic loads can be found in the work of (Paulsen 2013). Paulsen (2013) studied higher harmonic loads numerically and compared the obtained results with third order perturbation theories from Faltinsen (1993) and Malenica and Molin (1995). The study by Paulsen (2013) also compared results with the Morison equation with an additional term proposed by Rainey (1989).

### 13.4.3 Impulse (Slam) Forces from Breaking Waves

Plunging wave breakers can excite the structure most violently. For the calculation of the impact forces on slender structures, an additional part in the Morison equation is introduced:

$$F = F_{Morison} + F_{slam} = F_{inertia} + F_{drag} + F_{slam} \tag{13.2}$$

where  $F_{slam}[N]$  is the slam force, defined as the integration of inline impact force,  $f_i[N/m]$ , over the area of the impact (Fig. 13.4):

$$F_{slam} = \int_0^{area} f_i = \eta_b \lambda' * f_i \tag{13.3}$$

$$F_{slam} = \eta_b \lambda * f_i; \text{ rectangular force distribution} \tag{13.4a}$$

$$F_{slam} = 0.5 \eta_b \lambda * f_i; \text{ triangular force distribution} \tag{13.4b}$$

The parameter which indicates how much of the wave crest ( $\eta_b[m]$ ) is active in the impulse force is defined as the “curling factor” ( $\lambda$ ).

The line impact force is generally defined as:

$$f_i = C_s(t) \rho R C_b^2 \tag{13.5}$$

where  $C_s$  is defined as the “slamming coefficient”.

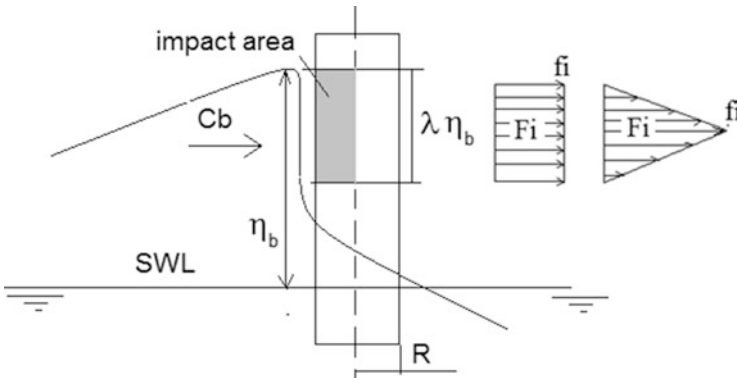


Fig. 13.4 Breaking wave parameters



Studies on impact forces from breaking waves are usually compared with one of the first studies on wave entry problems done by Von Karman (1929) and Wagner (1932). They studied impact forces for a case when an infinitely long falling cylinder hits a calm water surface. The cylinder was approximated as a flat plate. Von Karman (1929) considered the momentum conservation during the impact as:

$$f_i = d(m_h V) / dt \quad (13.6)$$

where  $m_h = 0.5\pi\rho c^2$  is the added mass below the flat plate.

Wagner (1932) considered the velocity potential around a flat plate as:

$$\phi = -V\sqrt{c(t)^2 - x^2} \quad (13.7)$$

and by estimating  $c(t) = 2\sqrt{VtR}$ , he solved temporal part of the Bernoulli's equation. Wagner (1932) also explained the so-called "pile-up" effect, which is the deformation of the water free surface around the plate. Due to this "pile-up effect", the immersion of the cylinder occurs earlier. As a result, the duration of the impact decreases and the maximum impact force increases. Thus, the force calculated by applying Wagner's theory is estimated as twice the line force calculated by von Karman's theory (Table 13.1). Both theories are time independent and present only a maximum line force.

For the calculation of impact forces due to plunging wave breakers on offshore wind turbines, a reference is usually made to the model developed by Wienke and Oumeraci (2005). The theoretical description of their model is based on Wagner's (1932) 2D-model; to account for the temporal development of the impact they compute the non-linear velocity term in Bernoulli's equation.

Comprehensive experimental studies have been conducted to study impact forces of breaking waves. High fluctuations and scattering from the point of view of local

**Table 13.1** Overview on wave impact studies

Author	Max inline force ( $\rho Rc^2$ )		Max press ( $\rho c^2$ )	
von Karman (1929)	$\pi$	T		
Wagner (1932)	$2\pi$	T		
Goda et al. (1966)	$\pi$	T		
Sawaragi and Nochino (1984)	$3\pi$	E		
Tanimoto et al. (1987)	$1.1\pi$ – $1.8\pi$	E		
Zhou et al. (1991)			4–13	E
Chaplin (1993)	$2\pi$ – $4\pi$	E		
Chan et al. (1995)			16–47	E
Wienke and Oumeraci (2005)	$2\pi$	T	40	E
Ros (2011)	$1.1\pi$ – $1.4\pi$	E		
Hildebrandt and Schlurmann (2012)	$0.8\pi$ – $1.1\pi$	N	4–12.5	E

*T* theory, *E* experiment, *N* numerical

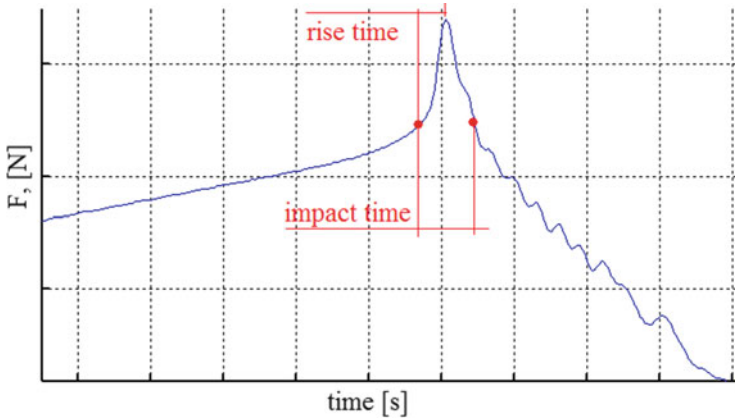


**Fig. 13.5** Force signal

line forces and local pressures are observed. Table 13.1 gives an overview on wave impact studies.

The nature of impulsive forces is characterized by very short durations, and the resulting structural responses are sensitive to dynamic analysis; hence, both the intensity and the time history of impact (slamming) forces are important design parameters. The total impact duration and the “rising time”, are both important parameters for dynamic structure analysis (Fig. 13.5).

### 13.5 Numerical Analysis

The Navier–Stokes equations can be solved in combination with volume of fluid (VOF) surface capturing scheme. For an incompressible two phase flow, conservation of mass and momentum in an Eulerian frame of reference, is given by:

$$\nabla \cdot \mathbf{u} = 0 \quad (13.8)$$

$$\frac{\partial}{\partial t} \rho \mathbf{u} + \rho (\nabla \mathbf{u}) \mathbf{u} = -\nabla p^* - (\mathbf{g} \cdot \mathbf{x}) \nabla \rho + \nabla \rho (\boldsymbol{\mu} \nabla \mathbf{u}) \quad (13.9)$$

where  $\mathbf{u} = (u, v, w)$  is the instantaneous velocity in Cartesian coordinates,  $\rho$  is the density,  $p^*$  is the pressure in excess of the hydrostatic pressure,  $\mathbf{g}$  is the acceleration due to gravity,  $\mathbf{x}$  is the Cartesian coordinate vector,  $\boldsymbol{\mu}$  is the dynamic molecular viscosity.

The free surface separating the air and water phase is captured using a VOF surface capturing scheme, which solves the following equation for the water volume fraction ( $\alpha$ ):

$$\frac{\partial \alpha}{\partial t} + \nabla \cdot \mathbf{u} \alpha + \nabla \cdot \mathbf{u}_r \alpha (1 - \alpha) = 0 \quad (13.10)$$

In Eq. (13.10),  $\mathbf{u}_r$  is a relative velocity (Berberović et al. 2009), which helps to retain a sharp interface, and the term  $\alpha (1 - \alpha)$  vanishes everywhere except at the interface. The marker function is 1 when the computational cell is filled with water, and 0 when it is empty; in the free surface zone, the marker function will have a value in the interval  $\alpha \in [0; 1]$  indicating the volume fraction of water and air respectively. The fluid density and viscosity is assumed continuous and differentiable in the entire domain, and the following linear weighting of the fluid properties is adopted:

$$\rho = \alpha \rho_w + (1 - \alpha) \rho_a; \quad \mu = \alpha \mu_w + (1 - \alpha) \mu_a \quad (13.11)$$

In Eq. (13.9), the sub-indices w and a refer to water and air respectively.

### 13.5.1 *Star CCM++*

Numerical analyses within the framework of the AQUILO project were done by using the commercial CFD package StarCCM++. Sensitivity analyses on the regular wave propagation in the numerical domain were also conducted. The inlet boundary condition in the computations is based on the free surface elevation and the velocity components are calculated according to desired wave, using the corresponding wave theory. Wave theories up to the Stokes 5th order theory are implemented in the StarCCM++ package. Waves examined in the scope of the AQUILO can be described as a weakly non-linear and they are well estimated by the Stokes 5th order regular wave theory (Fig. 13.1). The sensitivity of mesh parameters, time step, discretization method and turbulence model was investigated. It was ensured that the reflections from the boundaries were neutralized. The following conclusions were drawn:

- The domain should be refined in the free surface zone (around 25 cells per wave height and 115 cells per wave length); the aspect ratio should be  $dx/dz \leq 4$  (Fig. 13.6)
- Second order time discretization should be used with at least five iterations per time step; in the equation for volume fraction of water, the convection flux was discretized using a special high-resolution interface-capturing (HRIC) scheme which is designed to keep the interface sharp. To use the HRIC scheme propagation, the wave should be less than half a cell per time step

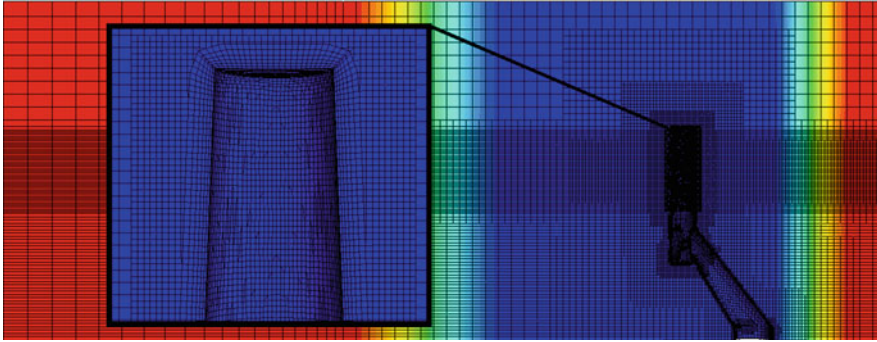


**Fig. 13.6** Part of the numerical domain domain, grid refinement

- $k-\varepsilon$  turbulence models introduce significant generation of eddy viscosity at the free surface interface; significant numerical diffusion was observed. After wave propagation of few wave lengths, wave height was reduced up to the 20% compared with the initialized wave height.
- Better results were obtained by using an inviscid model. After wave propagation of 20 wave lengths, the wave height was reduced up to the 6% compared to the initialized wave height
- The structure under analysis must not be placed too close to the inlet boundary because of the reflected waves that propagate upstream toward the inlet boundary and changing inlet values.
- In a case where the linear wave propagating in the numerical tank is influenced by the sea bed, the obtained wave height at the position of interest was around 20% lower than theoretically expected.
- It was found that the propagation of a wave, influenced by the sea bed, suffers from significant damping. It is suggested that parameters of initialised wave be close to the characteristics of the specific wave of interest.

As waves under the consideration in the AQUILO project are well approximated by Stokes 5th order theory (which is also implemented in the StarCCM++), a “forcing” technique for the further analysis. In the “forcing” technique, the idea is to have free zone around the structure of the interest while, in the rest of the domain, solutions are forced towards theoretical solutions (Fig. 13.7). At each time step, if the solution differs from the theoretical solution it is “forced” towards theoretical solution by assuming an additional source in the transport equation. The additional term in the transport equation is defined as:

$$b_{\phi} = -\lambda (\phi - \phi^*) \quad (13.12)$$

where  $\lambda$  is forcing coefficient;  $\phi$  is the solution of the transport equation at the given CV centroid; and  $\phi^*$  is the value towards which the solution is forced. This technique is used with very large values of  $\lambda$ , when the solution needs to be fixed

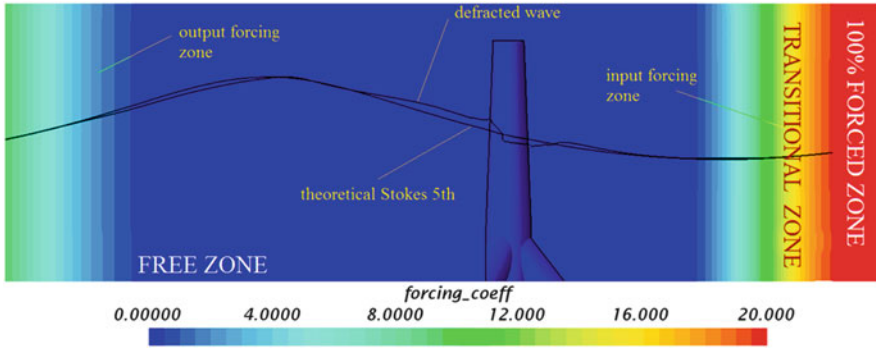


Fig. 13.7 “Forcing” technique

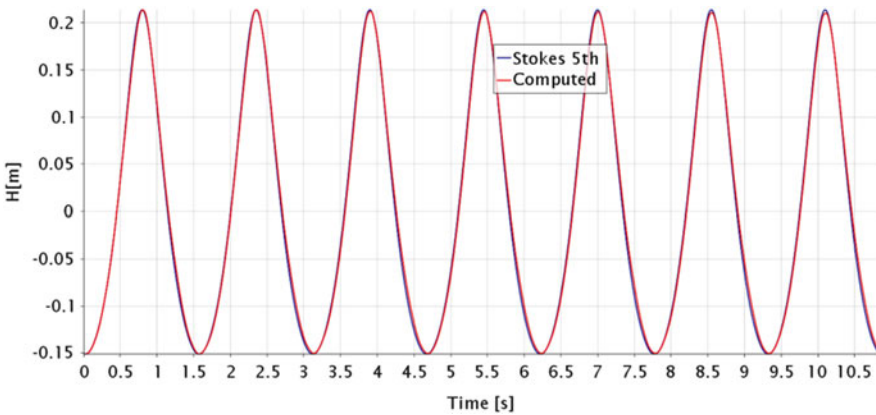


Fig. 13.8 Comparison between theoretical and computational results

to a certain value—after which then the remaining parts of the discretized equation become negligible.

In this technique, waves that are reflected off the structure and propagate upstream towards inlet boundary can be reduced and their influence on results can be eliminated; additionally, the necessary wave damping towards the outlet can be achieved more progressively, and the domain size can be reduced so that the speed of computation is increased.

An almost perfect comparison between the theoretical and numerical computations is presented in Fig. 13.8. As the Stokes 5th order wave theory is the highest wave theory implemented in STAR CCM++, theoretical solutions from other sources need to be employed for an analysis of steeper, strongly non-linear waves.

### 13.5.2 *OceanWave3D: OpenFoam*

To correctly predict the nonlinearity of the incident waves, bathymetry changes have to be taken into account as soon as the wave starts to get influenced by the bottom. To simulate the propagation of a wave with a strong influence of the sea bed (very steep, near breaking or breaking waves) the computation domain should be very long—however, the solution would be significantly influenced by numerical diffusion. To reduce the influence of numerical diffusion, and to reduce the time of the computation, one can solve the Navier–Stokes/VOF equations *in* a very small “inner” region of interest, while wave propagation *up to* the “inner” region of interest is solved by existing wave theories. A fully non-linear domain decomposed solver is presented by Paulsen et al. (2014). The fully non-linear potential flow solver is combined with a fully non-linear Navier–Stokes/VOF solver via generalized coupling zones of arbitrary shape.

To generate fully nonlinear boundary conditions for the Navier–Stokes/VOF solver, the potential flow solver “OceanWave3D” developed by Engsig-Karup et al. (2009) is applied. The model solves the three dimensional (3D) Laplace problem in Cartesian coordinates while satisfying the dynamic and kinematic boundary conditions. The equations evolve in time using a classic fourth order, five step Runge–Kutta method. The Laplace equation is solved in a  $\sigma$ -transformed domain using higher order finite differences for numerical efficiency and accuracy. Figure 13.9 depicts a comparison between the irregular wave elevation signal from the OceanWave3D solver, and the same signal measured in the WiFi project for a piston type wave maker.

The Navier–Stokes/VOF governing equations are solved using an open-source computational fluid dynamics toolbox, OpenFoam®. The equations are discretized using a finite volume approximation with a collocated variable arrangement on generally unstructured grids. For the current investigation, OpenFoam® version 2.3.0 is combined with the open-source wave generation toolbox, waves2Foam.

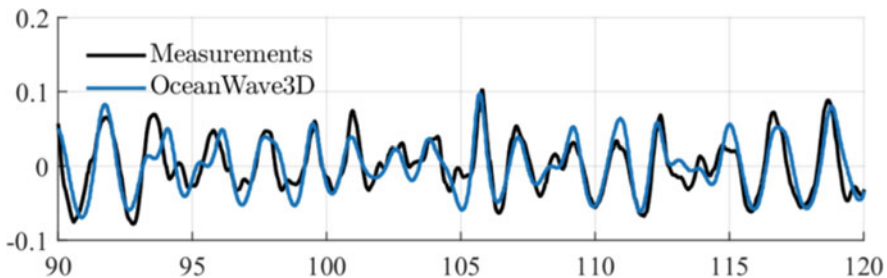


**Fig. 13.9** Comparison of irregular wave elevation, experiment vs. OceanWave3D

## 13.6 Results

### 13.6.1 Stokes 5th Order

Experimental analyses were conducted within the framework of the AQUILO project on four types of support structures: monopile, gravity based, tripod with pile foundation, and gravity tripod structure (Fig. 13.10). Predictions of wave loads are realized with theoretical JONSWAP energy spectra for a potential 50-year storm condition in the Baltic Sea. Global forces and moments on the structures were measured. The geometries do not represent any existing structures, and were designed for purposes of the AQUILO project, by taking into account typical shapes of existing structures and also the feasibility of manufacturing the physical models.

Due to limitations of the wave maker operability, the depth of the towing tank does not correspond to the design water depths (in a full scale case, the design water depth for a tripod structure is 60 m, while in CTO facilities, the minimum achievable water depth was 120 m). The location of the model relative to the free surface is then adjusted by using an additional support structure mounted to the bottom of the towing tank (Fig. 13.11). Obviously, the difference in water depth results in an incorrect modelling of the wave kinematics. The proposed method of model tests is a necessary compromise resulting from the limitations of the testing facility. In order to minimize the vertical motion of water particles in the vicinity of the foundations, a circular flat plate was mounted below the model (Fig. 13.11).

As a part of this study, experimental results on tripod gravity structure were compared with results from the Morison equation and numerical computations. Waves which excite the structure with the maximum inline force were taken into the

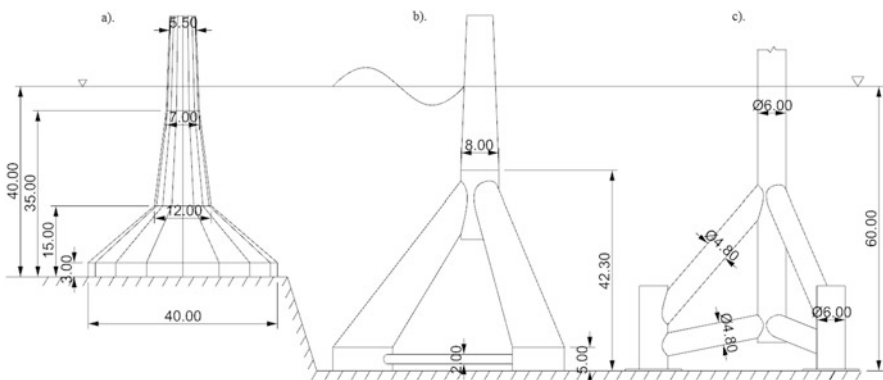
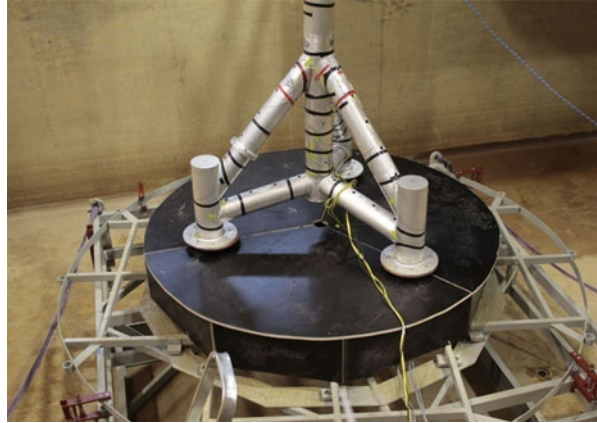
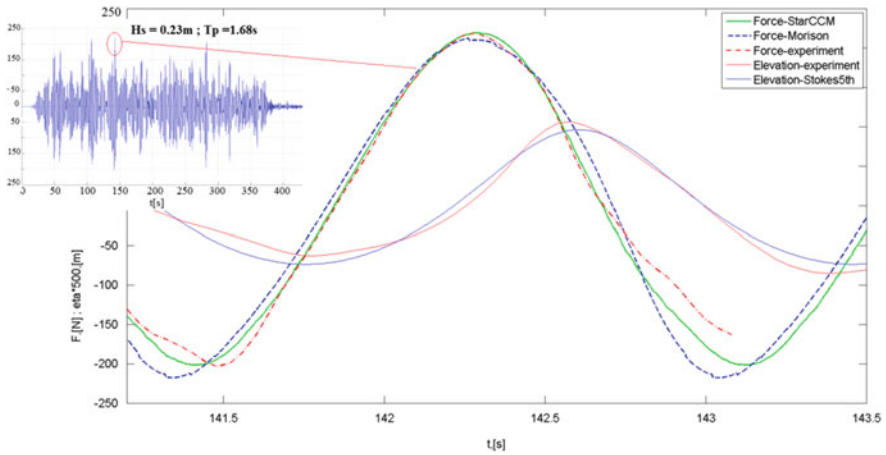


Fig. 13.10 Types of support structures analyzed in the AQUILO project





**Fig. 13.11** Installation in the towing tank



**Fig. 13.12** Comparison of inline force; experiment; Morison; Star CCM++

consideration. Drag and inertia coefficients were estimated as  $C_d = 1.8$  and  $C_m = 2$ , respectively. The numerical analysis was done with StarCCM++ code, by using the “forcing” technique and an inviscid model. The inviscid model is found to be suitable when the separation of the flow is not expected—i.e.—when the Keulegan-Carpenter number is low ( $KC < 5$ ) (Faltinsen et al. 1995). A good agreement was observed, as shown in Fig. 13.12.

A local wave breaking was observed during the experimental analysis on the monopile structure equipped with an ice breaking cone (Fig. 13.13). The results of the numerical computation done by StarCCM++ are compared with experimental



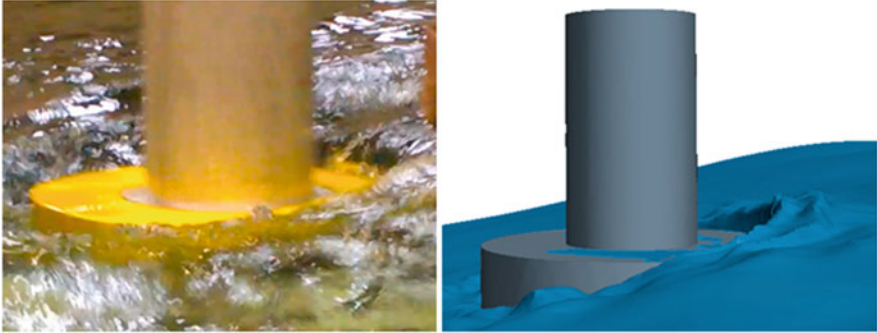


**Fig. 13.13** Monopilestructure equipped with ice-breaking cone; experiment vs Star CCM++

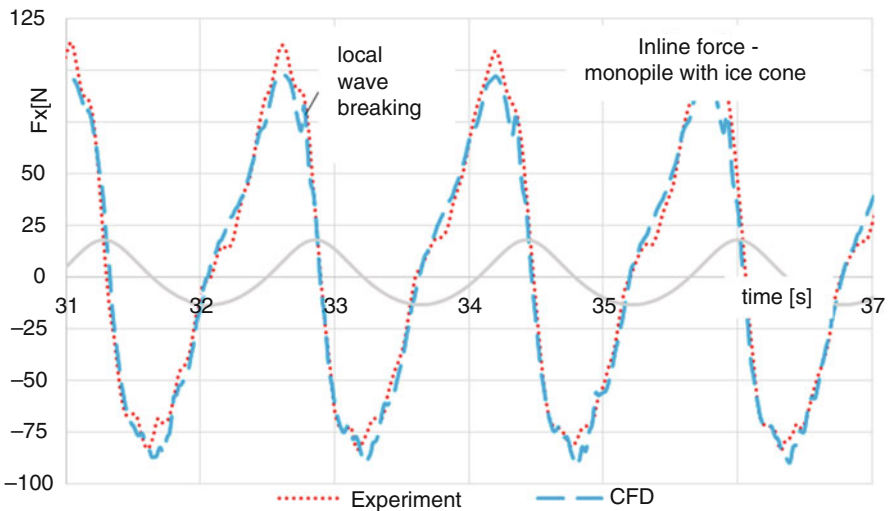


**Fig. 13.14** Inline force on monopile equipped with the ice breaking cone; comparison experiment-Star CCM++

measurements for the most violent regular wave which can be simulated in the CTO facilities. The comparison results are shown in Fig. 13.14. Because of experimental limitations, the maximum expected wave height could not be simulated ( $H_{max} \approx 1.86H_s$ ); thus, another numerical simulation was computed on the maximum expected wave height (Fig. 13.15). An impulse peak force caused by the local breaking of wave on the ice breaking cone is clearly visible: the total force increased by approximately 30 % due to the breaking wave.

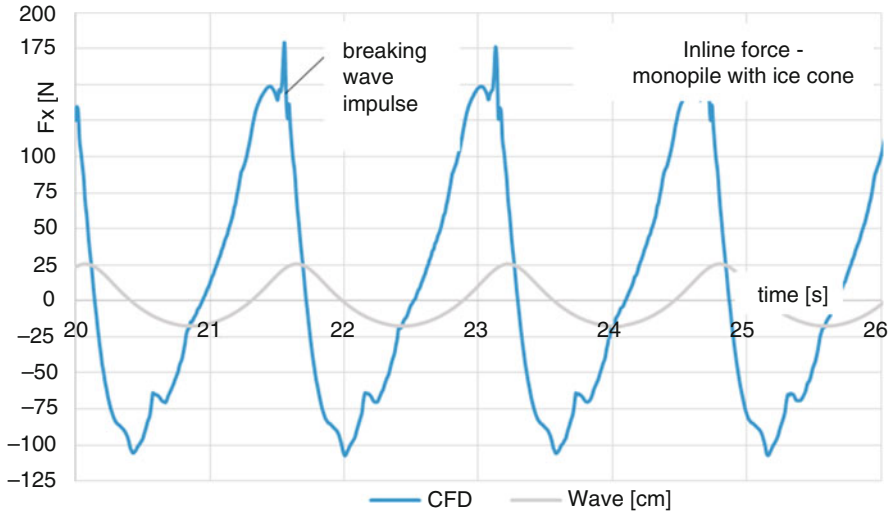


Fig. 13.15 Inline force on monopile equipped with the ice breaking cone; Star CCM++

### 13.6.2 Breaking Wave

Experimental analyses were conducted within the frame work of the WiFi project on a rigid monopile excited by irregular waves; the waves were estimated using the theoretical JONSWAP energy spectra for an expected 50-year storm condition. A series of impulse forces from breaking waves were observed. The total forces and pressures were measured. Numerical analyses were also conducted by OceanWave3D-OpenFoam interaction, and a good agreement between the measurements and computations was observed (Fig. 13.16).

The examined waves start breaking just before the front of structure, as shown in Fig. 13.17a, b. The pressure field presented in Fig. 13.17c is relative to the stagnation pressure—which is water density ( $\rho = 1000 \text{ kg/m}^3$ ) multiplied by the squared wave celerity ( $c = 2.2 \text{ m/s}$ ). The maximum computed pressure peak is  $1.5\rho c^2$ . The maximum line force ( $f_i$ ) is calculated as an integration of the pressure field around the circumference of the cylinder (around  $40^\circ$ ) and corresponds to the slamming coefficient value  $C_s = 1.8$ . The values of maximum local pressure and slamming coefficient are lower than any values shown in Table 13.1.

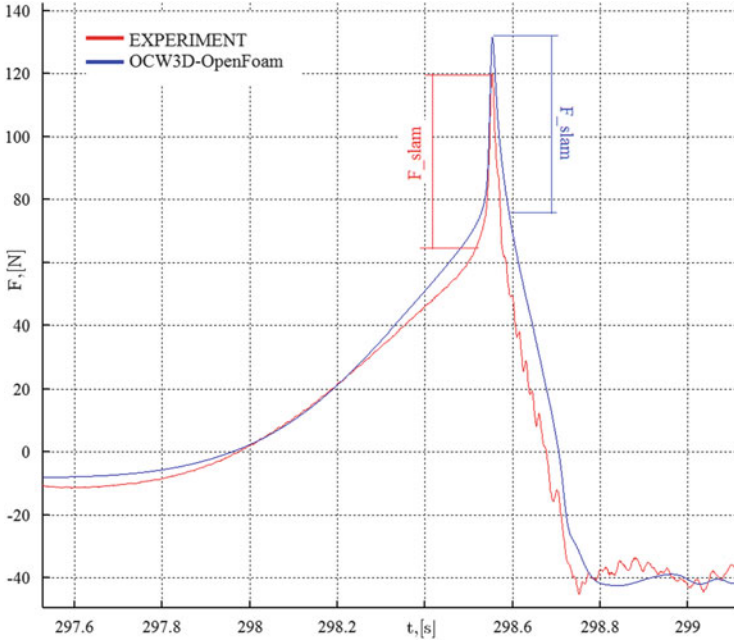


Fig. 13.16 Comparison of inline force; experiments-OceanWave3D & OpenFoam

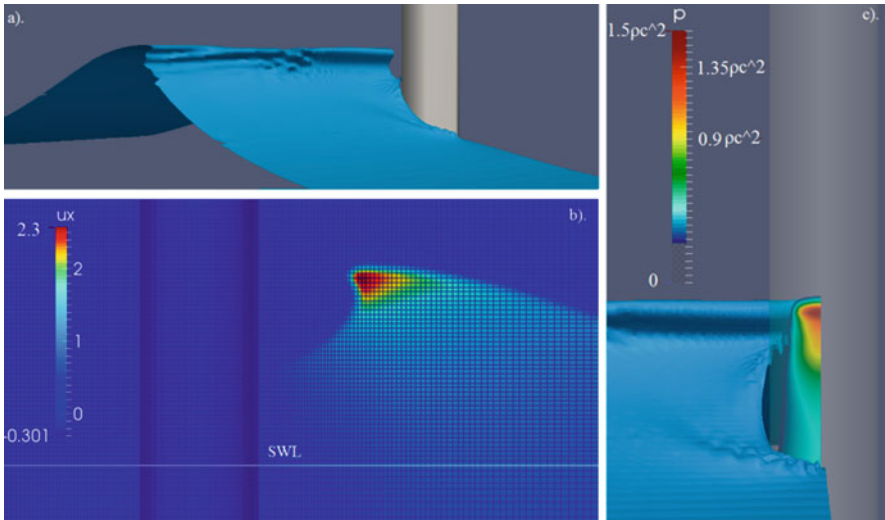


Fig. 13.17 Results from numerical analysis; OceanWave3D&OpenFoam

## 13.7 Conclusions

A series of computations for hydrodynamic forces on fixed bottom support structures for offshore wind turbines have been carried out. It can be conclusively stated that the Morison equation is an adequate and fast engineering tool for the estimation of inline forces on the slender structures installed in relatively deep water, where strongly non-linear waves are not expected. CFD tools are important for studies related to local flow around the structure, wave run-ups, higher harmonic forces, and impact forces from waves.

It is also noted that simulations of wave propagation (analyses with StarCCM++) suffer from artificial numerical diffusion, especially when  $k$ - $\varepsilon$  turbulence models are included in the computations. CFD simulations are too expensive and diffusive for simulation of undisturbed wave propagation—which can instead be computed with the potential wave tools, such as OceanWave3D.

An OpenFoam-OceanWave3D interaction was used to simulate breaking waves on a monopile support structure. A very good agreement between measurements and computations was obtained. The maximum obtained peak pressure was  $1.5\rho c^2$  and the maximum slamming coefficient ( $C_s$ ) was 1.8, which is quite low compared to the results of studies presented in Table 13.1.

**Acknowledgments** The presented work was realized within the framework of AQUILO project (PBS1/A6/8/2012), co-funded by The National Centre for Research and Development and MareWint project under research area FP7-PEOPLE-2012-ITN Marie-Curie Action : “Initial Training Networks”. Secondment in Deltares was realized under the framework of the joint industry project WiFi (Wave Impacts on Fixed Turbines).

**Open Access** This chapter is distributed under the terms of the Creative Commons Attribution-NonCommercial 4.0 International License (<http://creativecommons.org/licenses/by-nc/4.0/>), which permits any noncommercial use, duplication, adaptation, distribution and reproduction in any medium or format, as long as you give appropriate credit to the original author(s) and the source, provide a link to the Creative Commons license and indicate if changes were made.

The images or other third party material in this chapter are included in the work’s Creative Commons license, unless indicated otherwise in the credit line; if such material is not included in the work’s Creative Commons license and the respective action is not permitted by statutory regulation, users will need to obtain permission from the license holder to duplicate, adapt or reproduce the material.

## References

- Berberović E, van Hinsberg N, Jakirlić S, Roisman I, Tropea C (2009) Drop impact onto a liquid layer of finite thickness: dynamics of the cavity evolution. *Phys Rev E* 79(3)
- Chan ES, Cheong HF, Tan BC (1995) Laboratory study of plunging wave impacts on vertical cylinders. *Coast Eng* 25:87–107. doi:10.1016/0378-3839(94)00042-V
- Chaplin JR (1993) *Breaking wave forces on a vertical cylinder*. HMSO, London
- DNV (2014) *Design of offshore wind turbine structures*. Offshore Standard DNV-OS-J101
- Engsig-Karup AP, Bingham HB, Lindberg O (2009) An efficient flexible-order model for 3D nonlinear water waves. *J Comput Phys* 228:2100–2118

- Faltinsen OM (1993) Sea loads on ships and offshore structures. Cambridge University Press, Cambridge
- Faltinsen OM, Newman JN, Vinje T (1995) Nonlinear wave loads on a slender vertical cylinder. *J Fluid Mech* 289:179–198
- Goda Y, Haranaka S, Kitahata M (1966) Study of impulsive breaking wave forces on piles. In: Reports and technical notes. Port and Airport Research Institute (PARI). Available via PARI. <http://www.pari.go.jp/search-pdf/vol005-no06.pdf>. Accessed 10 Apr 2016
- Hildebrandt A, Schlurmann T (2012) Breaking wave kinematics, local pressures, and forces on a tripod support structure. In: Lynett P, Smith JM (eds) 33rd conference on coastal engineering 2012, Santander, July 2012
- Malenica Š, Molin B (1995) Third-harmonic wave diffraction by a vertical cylinder. *J Fluid Mech* 302:203–229
- Morison JR, Johnson JW, Schaaf SA (1950) The force exerted by surface waves on piles. *J Pet Technol* 5:149–154
- Paulsen BT (2013) Efficient computations of wave loads on offshore structures. Dissertation, Technical University of Denmark
- Paulsen BT, Henrik B, Bingam HB (2014) An efficient domain decomposition strategy for wave loads on surface piercing circular cylinders. *Coast Eng* 86:57–76
- Pierson WJ, Moskowitz L (1964) A proposed spectral form for fully developed wind seas based on the similarity theory of S. A. Kitaigorodskii. *J Geophys Res* 69(24):5181–5190
- Rainey RCT (1989) A new equation for calculating wave loads on offshore structures. *J Fluid Mech* 204:295–324
- Ros X (2011) Impact forces on a vertical pile from plunging breaking waves. Dissertation, Norwegian University of Science and Technology
- Sawaragi T, Nochino M (1984) Impact forces of nearly breaking waves on a vertical circular cylinder. *Coast Eng Jpn* 27:249–263
- Tanimoto K, Takahashi S, Kaneko T et al (1987) Impulsive breaking wave forces on an inclined pile exerted by random waves. In: Edge BL (ed) 20th international conference on coastal engineering, Taipei, November 1986. Coastal Engineering 1986 Proceedings, vol 20. American Society of Civil Engineers, Reston, p 2282
- von Karman TH (1929) The impact on seaplane floats during landing. In: National Advisory Committee for Aeronautics (NACA)—Technical Notes NACA-TN-321. Available via NTRS. <http://hdl.handle.net/2060/19930081174>. Accessed 10 Apr 2016
- Wagner H (1932) Über Stoß- und Gleitvorgänge an der Oberfläche von Flüssigkeiten. *Z Angew Math Mech* 12(4):193–215
- Wienke J, Oumeraci H (2005) Breaking wave impact force on a vertical and inclined slender pile—theoretical and large-scale model investigations. *Coast Eng* 2(5):435–462
- Zhou D, Chan ES, Melville WK (1991) Wave impact pressures on vertical cylinders. *Appl Ocean Res* 13(5):220–234

# Chapter 14

## Detection of Damage in Metallic Structures for Offshore Applications

Rohan Soman, Paweł Malinowski, and Wiesław Ostachowicz

**Abstract** Wind energy is seen as one of the most promising solutions to man's ever increasing demands of a clean source of energy. However, a major drawback of the wind energy is the high initial cost for setting up and maintenance. This makes the energy more expensive than the conventional energy sources like fossil fuels and nuclear and hence it has not been widely accepted. Thus, there is a concerted effort to reduce the cost of energy production. This can be achieved by increasing the lifetime of the wind turbines; reducing maintenance costs and ensuring low downtime of the turbine. The lifetime may be increased by ensuring a more robust design while the maintenance cost and the downtime of the equipment may be lowered through the use of condition monitoring (CM) and structural health monitoring (SHM). SHM allows early detection of damage and allows maintenance planning which becomes more important in the off-shore industry where the cost of unscheduled maintenance are high due to the need of specialized equipment. Also, maintenance planning can allow us to avoid unnecessary downtime, hence increasing the availability of the system. In wind turbine structures, tower damage is the third most common damage in wind turbines. Thus, this work concentrates on SHM of a wind turbine tower. A decision level data fusion based on bi-axial tracking of change in Neutral Axis (NA) position is proposed. A discrete Kalman Filter (KF) is employed for the estimation of the NA in the presence of measurement noise from the strain sensors. The KF allows data fusion from the strain sensors and the yaw mechanism for the accurate estimation of the NA. Any change in the NA position may be used as an indicator for the presence and location of the damage. The ratio of the change in the NA along two perpendicular axes is taken and used for the localization. The study has been carried out on the simulated finite element (FE) model of the wind turbine tower and indicates that bi-axial NA tracking based on data fusion is indeed necessary and at the same time is sensitive to damage. The proposed methodology is then validated on real strain data from the Nordtank NTK 500/41 wind turbine. Based on the results presented, the change in NA is indeed a robust damage indicator insensitive to ambient condition changes, and the applied loads.

---

R. Soman (✉) • P. Malinowski • W. Ostachowicz  
Mechanics of Intelligent Structures Department, Institute of Fluid Flow Machinery, Polish  
Academy of Sciences, ul. Fiszerza 14, 80-231 Gdańsk, Poland  
e-mail: [rsoman@imp.gda.pl](mailto:rsoman@imp.gda.pl); [pawel.malinowski@imp.gda.pl](mailto:pawel.malinowski@imp.gda.pl); [wieslaw@imp.gda.pl](mailto:wieslaw@imp.gda.pl)

## 14.1 Introduction

The main hindrance for more widespread deployment of the wind turbines is the high initial cost for setting up of wind farms and its subsequent maintenance. These high initial costs make the energy more expensive than the conventional energy sources. The cost of generation being the biggest drawback of wind energy, there is a concerted effort to reduce it. This can be achieved by increasing the life-time of the wind turbines; reducing maintenance costs and ensuring high availability. The lifetime may be increased by ensuring a more robust design while the maintenance cost may be lowered and the high availability ensured through the use of condition monitoring (CM) and structural health monitoring (SHM) (Cho et al. 2010). SHM allows early detection of damage and allows maintenance planning which reduces the cost (Doebeling et al. 1998). Furthermore, it can allow us to avoid unnecessary downtime, hence increasing the availability of the system.

The SHM needs to be low cost, and suitable for continuous monitoring. These techniques are based on the concept that, the change in mechanical properties of the structure will be captured by a change in its dynamic characteristics (Adewuyi et al. 2009). The SHM process involves the observation of a system over time using periodically sampled dynamic response measurements from an array of sensors, followed by the extraction of damage-sensitive features from these measurements, and the statistical analysis of these features to determine the current state of the system's health. The SHM process requires use of sensors for data collection, filters for data cleansing, and central data processing units for feature extraction and post processing.

SHM has been a field of active research in the aerospace and offshore industry for several decades and many methods have been proposed and investigated. These methods have been able to detect and locate damage in a laboratory environment under controlled conditions. However when these methods were implemented for field validations or in real structures, the results obtained were not up to the desired level. The discrepancy between the expected and the measured results are mainly attributed to the uncertainty in the measurement environment with respect to noise, temperature and excitation mechanism for the structure. Hence there is a search for an SHM system which is able to detect damage in working conditions, and is robust enough to changes in ambient conditions and excitation. Furthermore, the method should be able to detect small levels of damage.

The lack of a standard method for designing an SHM system which will enable us to perform accurate damage detection is the primary motivation of this research.

## 14.2 Methodology Overview

The scope of the research is SHM of Tower Structures through the measurement of the strain in the tower subject to in-service loading. The methodology is explained here.

### 14.2.1 Neutral Axis

The primary function of the tower structure is to support the hub, and the nacelle of the wind turbine. The nacelle and the hub are axial loads which are eccentrically loaded on the tower. This eccentric loading gives rise to axial compressive loads as well as bending loads as shown in Fig. 14.1. The axial compression is uniform over the entire cross section while the bending loads will be tensile at one end and compressive at the other. Furthermore, the tower experiences wind loads which result in bending strains in the tower. The axial strains are given by Eq. (14.1):

$$\epsilon_{axial} = \frac{F}{EA} \tag{14.1}$$

where,  $\epsilon_{axial}$  is the longitudinal strain in bending,  $F$  is the net axial force due to the nacelle, hub and other wind turbine components,  $E$  is the Young’s modulus and  $A$  is the area of the cross section. Equation (14.2) gives the bending

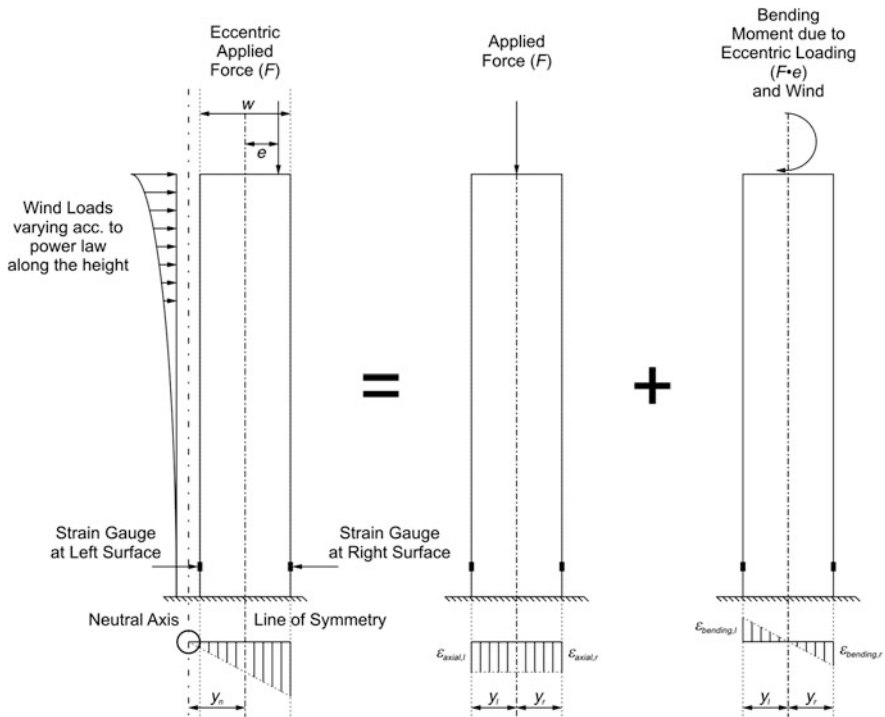


Fig. 14.1 Flexural strain distribution over the cross-section subject to eccentric loading (Soman et al. 2014b)



strains:

$$\varepsilon_{bending} = \frac{M_b y}{EI} \quad (14.2)$$

where,  $\varepsilon_{bending}$  is the longitudinal strain in bending,  $M_b$  is the net bending moment at the cross section due to wind loading and eccentricity, and  $I$  is the area moment of inertia,  $y$  is the distance from the NA to the location of the sensor (Xia et al. 2012).

Thus, one surface of the tower experiences, a combination of two axial compressions, (right side, Fig. 14.1) while the other end experiences a combination of compressive load due to the weight and tensile load due to the bending (left side, Fig. 14.1). The net strains on the right and left surface in Fig. 14.1 are given by Eq. (14.3) (Soman et al. 2015b):

$$\varepsilon_{r/l} = -\varepsilon_{axial} \pm \varepsilon_{bending} \quad (14.3)$$

If the line connecting the two strain levels is extended, there will be a point where the strain experienced will be zero, which is identified as the NA point. The NA of the section is a function of the flexural rigidity of the structure, and does not depend on the applied bending loads, thus by, measuring the strains at the opposite edges of the beam, the NA can be located, which in turn may be used as an indicator of the damage. Figure 14.1 explains the abbreviations used and the concept. The NA can thus be estimated based on the strain measurements. This point may be found out by linear extrapolation, and is given by Eq. (14.4) (Soman et al. 2015b):

$$L = \frac{(\varepsilon_{bending} - \varepsilon_{axial}) \cdot w}{2 \cdot \varepsilon_{bending}} = \frac{\varepsilon_l \cdot w}{(\varepsilon_l - \varepsilon_r)} \quad (14.4)$$

where,  $L$  is the NA Location. It should be noted that the dimensions of the NA location are that of distance, so this metric may be represented as a dimensionless quantity given by Eq. (14.5) (Soman et al. 2015b):

$$NAE = \frac{L}{w} \quad (14.5)$$

The NAE can be made at each time instant based on measured strains at that instance using Eq. (14.5). This approach is termed as direct estimation in further sections, or they can be estimated based on the previous estimates and updated at each time instant using the new measurements using KF which is explained in detail in the later section.

### 14.2.2 Damage Sensitive Feature

As mentioned, in earlier section, the NA location is independent of the loading conditions, and depends only on the condition of the structure. Thus the % change in the NAE is taken as the damage sensitive feature and is given by Eq. (14.6) (Soman et al. 2015a):

$$\Delta NAE = \frac{NAE_{healthy} - NAE_{monitored}}{NAE_{healthy}} \times 100\% \quad (14.6)$$

The  $NAE_{healthy}$  is developed at the time of the installation of sensors when the structure is known to be in healthy condition.  $NAE_{monitored}$  is the estimate at every time step. If the % change exceeds a certain threshold, an alarm is raised indicating damage. This threshold is based on sensitivity studies and the tradeoff between the probability of false positive and false negative detections.

### 14.2.3 Bi-Axial NA tracking

The aim of the SHM system is accurate Level II damage detection. In order to locate the damage, one needs the coordinates of the damage location along the x; y; z axes. The sensor placement at diametrically opposite locations along the tower, as shown in Fig. 14.1, if extended by placing an array of sensors in a line along the tower, can locate the damage along the altitude (z axis). In order to detect the location along the circumference of the tower, we need to perform bi-axial neutral axis tracking. The sensor pairs are placed along mutually perpendicular axes to map the x and y coordinates of damage location. In the polar coordinates, this location can be detected by the angle alone. By the mutually perpendicular sensor placement, the damage can be observed in the form of the sine and the cosine component. The change along x axis is given by the cosine component while along the y axis is given by the sine component of the angle. Thus knowing these components one can determine by taking the tan inverse of the ratio of the changes in the sine and cosine as shown in Eq. (14.7) (Soman et al. 2015b):

$$DL = \tan^{-1} \left( \frac{\Delta NAE_{yaxis}}{\Delta NAE_{xaxis}} \right) \quad (14.7)$$

where  $DL$  is the damage location in terms of angle ( $\phi$ ).

It should be kept in mind that the periodicity for sine and cosine is  $2\pi$  while that for tan ratio is  $\pi$  thus leading to loss of directionality. Thus a decision level data fusion is necessary, where the change in the directionality is overcome by proper study of the change in the NA location along both the sensor axes. The sign of the change in the NAE of both the axes determine the exact location of the damage.

### 14.2.4 Kalman Filter

The KF is a set of mathematical equations that provides an efficient computational (recursive) solution of the least squares method (Welch and Bishop 1995). Theoretically, KF combines a system's dynamic model (physical laws of motion) and measurements (sensor readings) to form an estimate of the systems varying quantities (system state) that is better than the estimate of the system obtained by measurement alone (Welch and Bishop 1995).

The KF allows estimation of the state variable  $\mathbf{x}$  of a discrete time controlled process governed by the linear stochastic difference equation. In the absence of the control scalar, it can be given by Eq. (14.8) (Brown and Hwang 1997):

$$\mathbf{x}_{k+1} = \mathbf{A}_k \mathbf{x}_k + \mathbf{w}_k \quad (14.8)$$

where  $\mathbf{A}$  is the state transition matrix and  $\mathbf{w}_k$  is the white process noise,  $k$  indicates the time step. The measurement equation is given by Eq. (14.9):

$$\mathbf{z}_k = \mathbf{H} \mathbf{x}_k + \mathbf{v}_k \quad (14.9)$$

where  $\mathbf{H}$  is the measurement matrix that relates to the observation  $\mathbf{z}_k$  and  $\mathbf{v}_k$  is the measurement noise.

The goal of using KF is to find an equation that computes a posteriori state  $\mathbf{x}_{k/k}$  as a linear combination of an a priori estimate  $\mathbf{x}_{k/k-1}$  and a weighted difference between an actual measurement  $\mathbf{z}_k$  and a measurement prediction  $\mathbf{H} \mathbf{x}_{k/k-1}$  as shown in Eq. (14.10):

$$\mathbf{x}_{k/k} = \mathbf{x}_{k/k-1} + \mathbf{K} (\mathbf{z}_k - \mathbf{H} \mathbf{x}_{k/k-1}) \quad (14.10)$$

where  $\mathbf{K}$  is the Kalman gain. The value of  $\mathbf{K}$  is chosen to minimise the error covariance. There are several forms of the  $\mathbf{K}$  matrix discussed in literature. One form of this matrix used for the gain computation is given by Eq. (14.11):

$$\mathbf{K}_k = \mathbf{P}_{k/k-1} \mathbf{H}_k^T (\mathbf{H}_k \mathbf{P}_{k/k-1} \mathbf{H}_k^T + \mathbf{R}_k)^{-1} \quad (14.11)$$

where,  $\mathbf{P}$  is the error covariance matrix, and  $\mathbf{R}_k$  is the measurement noise covariance matrix.

Figure 14.2 concisely explains the implementation of the KF in the present application.

The state estimate variable is  $\mathbf{X}_k = [NAE, 1, \theta]^T$ , NAE in undamaged condition should remain constant independent of the applied loads, the second variable tracked is the constant value 1. This constant is incorporated to ensure, correct relation between the state estimation matrix, the observation matrix and the measurement matrix. The added benefit of the constant is, it makes the measurement matrix square, which allows faster computations. The third component of the vector is the

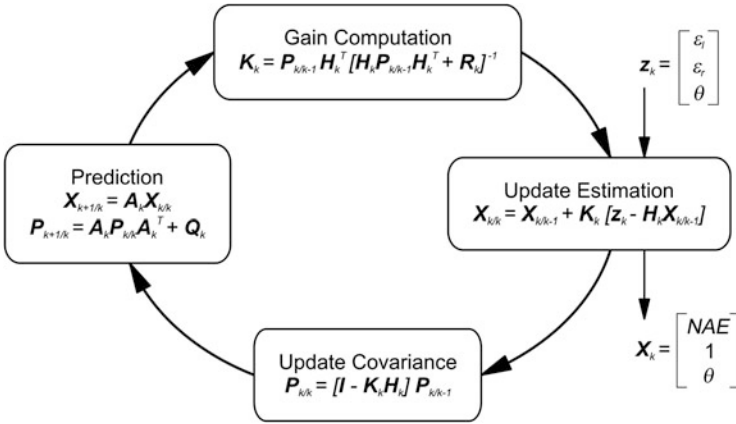


Fig. 14.2 Flow chart for the implementation of the KF (Soman et al. 2014a)

variable  $\theta$  for the yaw angle. It is a linear estimate of the measurement from the sensor. The input for the KF algorithm is essentially the state transition matrix ( $A$ ), which relates the state estimate variable in time. In this case,  $A$  is a unity matrix of dimension 3 as the state estimates are random and not co-related in time. The other input is the measurement matrix ( $H$ ) which links the state estimation variable  $X_k$ , and the measurement variable ( $Z_k$ ) at each time step (measurement from the sensors).

The H matrix takes into consideration the observability of the NA based on the locations of the sensors and is designed for accurate system modelling while maintaining the linearity of the measurement step. In the present case,  $Z_k = [\epsilon_l, \epsilon_r, \theta]^T$  vector consisting of the strain measurements from the left ( $\epsilon_l$ ) and the right side ( $\epsilon_r$ ) of the tower and the yaw angle measurement ( $\theta$ ) of the nacelle.

### 14.3 Structure Modelling

The mathematical formulation and the theory discussed in Sect. 14.2 was applied on a FE model of the DTU 10 MW Reference Wind Turbine (RWT) (Bak et al. 2013) for numerical validation. The theory was later validated on the real strain data from the Nordtank NTK 500/41 wind turbine (Paulsen 2011). This section gives the overview of the structures used for the validation and the details of the FE modelling of these structures.

### ***14.3.1 DTU 10 MW RWT***

The tower was modelled using the geometric and material properties from the design drawings in commercial FE software ABAQUS. The tower structure was modelled with S4R shell elements. For studying the behavior of the tower to wind loading the dynamic direct analysis was to be carried out. The dynamic analysis uses the modal superposition for estimating the displacements and the strain, so in order to achieve accurate results, and limit the computational load the number of extracted mode shapes was 50. The mesh size of the element was then chosen in order to achieve stable and smooth mode shapes for the extracted modes. The tower was divided in to 82 elements along the height and 48 elements around the circumference. This allowed a reasonable aspect ratio of the shell elements, which lead to a more stable and reliable computation. The tower was encased at the bottom (all DOFs at bottom fixed). The nacelle and hub loads were applied as point loads, at specified eccentricity and height indicated from the design specifications. The wind loads were simulated as random loads using Euro-codes (Standards Norway 2009). A peak wind pressure was selected and applied on the surface area facing the wind, in order to compute the force. The force increases according to the power law along the height of the tower (Sen et al. 2012). The blades, however, were assumed to be pitched into a full aerodynamic brake position to ensure minimal rotor motion and consequent change in mass distribution, which may affect the NA (Bas et al. 2012).

### ***14.3.2 Nordtank NTK 500/41 Wind Turbine***

The methodology proposed in Sect. 14.2 was validated from real strain data from the Nordtank wind turbine. The test wind turbine, is located at Risø Campus, Roskilde, and is a traditional Danish three-bladed stall regulated Nordtank (see specifications in Table 14.1).

The wind turbine is instrumented with a variety of sensors on the blades, in the gearbox and on the tower for measuring the different response of the structure and the ambient conditions like strain, the acceleration response to wind loading, the wind speed and direction, the yaw angle, temperature etc. Some of these sensors, namely the strain sensors at the bottom of the tower, the wind speed and direction sensors and the yaw angle measurements have been used for the validation of the methodology. The type of the sensor and its description is given in Table 14.2

**Table 14.1** Nordtank NTK 500/41 specifications (Paulsen 2011)

<b>Wind turbine</b>	
<b>8 Risø-R-1593(EN)</b>	
Mechanical brake	High speed shaft, operated in FS-mode
Power regulation	Passive aerodynamic stall
Gearbox	Flender; ratio 1:55.35
Generator	Siemens 500 kW, 4 poles, 690 V
Blade profile	NACA 63-4xx & NACA FF-W3, equipped with vortex generators
<b>Tower type</b>	
Conical steel tube	33.8 m
Hub height	36.0 m
<b>Masses</b>	
Blade weight	1960 kg
Rotor including hub	9030 kg
Tower head mass	24,430 kg
Tower mass	22,500 kg

**Table 14.2** Relevant sensor specifications (Paulsen 2011)

Measurement	Sensor	Signal type	Conversion principle	Transmitter
Wind speed nacelle	Risø cup anemometer P2546A with Reed relay	Digital	2 magnets on turning shaft controls the contact closure timings of the relay per revolution	Risø P2858A DAU configured to periodic time measurement
Wind direction nacelle	Vector Wind vane F2819A	Analogue	Measuring on resistive viper path relative to one full turn	Voltage divider
Tower bottom bending moment X	Micro Measurement Strain Gauge CEA-06-250C-350	Analogue	Semiconductor foil subjected to resistive change due to bending	Risø P2912B SG Amplifier
Tower bottom bending moment Y	Micro Measurement Strain Gauge CEA-06-250UW-350	Analogue	Semiconductor foil subjected to resistive change due to bending	Risø P2912B SG Amplifier
Position of nacelle	Resistor with gearbox attached to yaw drive	Analogue	Measuring on resistive path	Voltage divider

## 14.4 Numerical Simulations

The methodology highlighted in Sect. 14.2 was applied on the numerical models described in Sect. 14.3.1. The goals of the simulations were to:

- Establish the need for KF based NA tracking
- Establish NA as a damage sensitive feature
- Perform Level II damage detection using Bi-Axial NA tracking
- Establish the robustness of KF based NA tracking methodology

### 14.4.1 Need for KF tracking

The KF as explained in Sect. 14.2.4 combines the previous estimate of the state and the new estimate based on the measurements. Thus in noisy conditions, the KF based estimation is much more stable than the direct estimation. Also, in the second section it was outlined how one can estimate the NA from the instantaneous measured strains. This section compares the NA estimation by these two methods in different simulated conditions. The measured strains and the yaw angle were taken as input to the system and the NA location was estimated by both the methods. The measured signal was contaminated with different levels of white noise in order to simulate real conditions. Table 14.3 shows the statistical performance of the two estimation methods.

As can be seen, the KF needs some initial time for the convergence, but once the convergence is achieved the estimation is more stable. This can be seen from the lower standard deviation in the NA estimate observed while using the KF estimation than that using the direct estimation. Furthermore, it can also be seen that the mean NA position for the KF based estimation is more stable than that using direct estimation. The more stable mean will allow us to set lower thresholds for the change in NA position. This in turn will allow detection of small levels of damage in the tower structure.

Thus, use of KF improves the estimation, and as such, is recommended for accurate NA tracking. Furthermore, the KF algorithm is ideally suited for data

**Table 14.3** Statistical performance of estimators (Soman et al. 2015a)

Scenario	KF estimation standard deviation (mean)	Direct estimation standard deviation (mean)
0 % Noise for strain and 0 % noise for yaw angle	0.0444 (1.633)	0.1064 (1.637)
5 % Noise for strain and 0 % noise for yaw angle	0.0474 (1.633)	0.1862 (1.622)
10 % Noise for strain and 0 % noise for yaw angle	0.0507 (1.635)	0.4527 (1.666)
0 % Noise for strain and 5 % noise for yaw angle	0.0444 (1.633)	0.1168 (1.641)
5 % Noise for strain and 5 % noise for yaw angle	0.0499 (1.633)	0.211 (1.686)

fusion, and hence the yaw angle tracking can be seamlessly included in the algorithm in order to increase the confidence level in the NA tracking.

### 14.4.2 NA as a Damage Sensitive Feature

As explained in the earlier section, the NA of the cross-section of the tower is the property of the condition of the structure and may be used as a damage indicator. In order to validate the use of NA as damage indicator, artificial damage was introduced in one element of the tower, by reducing the flexural rigidity of that particular element by 20%. The simulated damage was detected by comparing the NAE of the damage and the undamaged element. The relative change in the location of the NA is given in Table 14.4.

The damage is detected if the change in the NA estimation of the damaged and undamaged state is more than a specified threshold, which is determined based on simulated studies of different damage scenarios (Soman et al. 2015a). As can be clearly observed, even in the presence of measurement noise, there is significant difference in the change of the NAE of the damage element and the others, so the

**Table 14.4** NA based damage detection in presence of noise (Soman et al. 2014a)

Sensor location (m)	NAE (%)			
	0 % Noise	1 % Noise	5 % Noise	10 % Noise
2.875	-0.0177	-0.0694	-0.2029	0.5403
8.625	-0.1546	-0.1266	-0.3123	0.3565
14.375	-0.0820	-0.0576	-0.1811	0.1504
20.125	-0.2128	-0.2161	-0.3438	-1.0455
25.875	-0.0252	-0.0508	-0.0135	0.5836
31.625	-0.4384	-0.4577	-0.4394	0.7286
37.375	-0.9947	-1.0899	-1.0932	-1.1910
<b>43.125</b>	<b>5.4836</b>	<b>5.4674</b>	<b>5.4675</b>	<b>5.3286</b>
48.875	-1.0367	-1.0491	-0.9949	-0.7893
54.625	-0.4416	-0.5153	-0.6243	-0.1339
60.375	-0.0422	0.0151	-0.1978	0.1797
66.125	-0.2413	-0.2820	-0.2334	-0.3370
71.875	-0.1271	-0.0716	0.1087	0.3750
77.625	-0.1664	-0.1475	-0.1069	-0.0487
83.375	-0.0417	-0.0639	-0.0125	-0.2715
89.125	-0.0770	-0.1277	-0.0120	-0.4831
94.875	0.0101	0.0301	0.1279	-0.2785
100.625	-0.0121	-0.0271	-0.3458	0.1291
106.375	0.0584	0.0463	0.0330	0.0299
112.440	-0.0368	0.0684	0.1646	0.7457



chances for a false detection are quite minimal and as such a lower threshold may be possible 1% in the case where yaw angle is being tracked as well. Thus NA can be used as a robust damage sensitive feature.

### 14.4.3 Bi-axial NA tracking

NA may be used as a damage sensitive feature. Table 14.2 only gives the location of the damage along the altitude. In order to isolate the damage even further, bi-axial NA tracking is necessary. For bi-axial NA tracking, two mutually perpendicular sensor pairs are necessary as explained in Sect. 14.2.3. Then the change in NA can be mapped along the two axes and the exact location determined. In order to show the methodology, four different damage scenarios were simulated, as shown in Fig. 14.3.

Table 14.5 shows the change in NA along the two axes, and as can be seen through decision level data fusion, we can easily isolate the damage accurately.

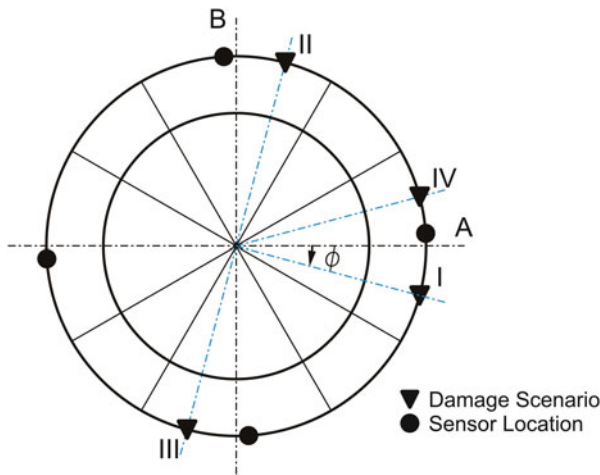


Fig. 14.3 Damage scenarios indicating the need for bi-axial NA tracking (Soman et al. 2015b)

Table 14.5 Bi-axial NA tracking for damage detection (Soman et al. 2015b)

Damage scenario	$\Delta\text{NAE}_A$ (%)	$\Delta\text{NAE}_B$ (%)	Damage location (°)	Damage location predicted (°)		Error in detection (°)	
				Fusion	W/o fusion	Fusion	W/o fusion
I	6.264	-2.020	-15	-17.9	-17.9	2.9	2.9
II	2.003	6.206	75	72	72	3	3
III	-2.301	-6.607	-105	-109	<b>70.7</b>	4	<b>-175.7</b>
IV	12.800	<b>0.875</b>	15	<b>3.8</b>	<b>3.8</b>	<b>11.2</b>	<b>11.2</b>

The damage scenario I and II indicate the validity of the decision level data fusion, and taking the ratio of the changes in NA, is a valid technique for fusion. The damage isolation for case I and II is valid without fusion as the damage lies in the  $-90^\circ$  to  $90^\circ$  range. Damage scenario III is a point diametrically opposite to II and it shows the significance of decision level data fusion. If the signs corresponding to the change of the location are not taken into account the isolation give a diametrically opposite point which may be termed as false isolation of the damage (shown in bold values in Table 14.5) and hence the decision level data fusion is necessary. Damage scenario IV indicates that when the damage is at locations perpendicular to one of the axes, the results obtained for the isolation are not accurate, but this in essence proves that bi-axial tracking is indeed necessary.

It can be noted that the change in the location of NA in scenario IV, in the estimate at A, is significant and hence false detection of the damage is highly unlikely. The high change exceeding 10 % also indicates very close proximity of the damage to the strain sensors and gives further idea about the location of the damage. Furthermore, the decision level data fusion will recognize that the threshold for the damage detection has not been exceeded (shown in bold values in Table 14.5) and as such the data should not be used, thus making the decision level data fusion based strategy more robust against false localization.

#### ***14.4.4 Robustness of KF***

The ideal SHM methodology should need limited operator skill and should be objective in nature. The previous section formally introduced a methodology for the selection of the threshold for damage detection which allows the methodology to be objective. In order to make it independent of operator skill the methodology should be robust in nature. This section shows how the KF is a robust methodology requiring limited operator skill for setting up. The Kalman Filter is a powerful tool for the estimation of the state variables especially in the presence of measurement noise. The NA estimate is independent of the initial setting up of the NA, and as such this makes the damage detection methodology robust. Figure 14.4 shows the evolution of the prediction under different parameters of the KF initiation.

Figure 14.4a shows the estimate of NA for different initial guess locations of the NA. As can be seen NA estimate is independent of the starting position, and converges to the true value in relatively short time and as such the damage detection methodology is not affected. Figure 14.4b shows the independence of the initial NA estimate to the uncertainty of the initial guess location or in other words the covariance of the state matrix. The value affects the rate at which the convergence is achieved.

As can be seen lower the value of the covariance quicker the convergence is achieved. Figure 14.4 shows the effect of the uncertainty in the strain measurements on the NA estimate. This uncertainty is termed as measurement noise.

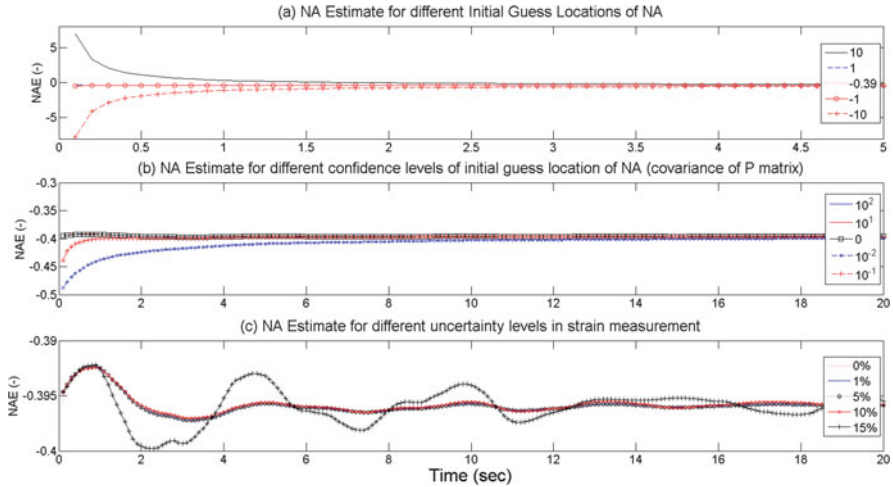


**Fig. 14.4** Sensitivity of NAE to KF parameters (Soman et al. 2015a)

It is intuitive to think that greater the measurement noise, more unsteady is the NA estimate, which in turn affects the threshold value for damage detection. It can be seen that even at 10 % measurement noise, the KF estimate is more or less stable, which points towards the robustness of the KF based methodology.

## 14.5 Validation

The success of the methodology for damage detection was checked on simulated damage scenarios. But the methodology needs to be validated with application on real structure. This chapter thus aims at validating the methodology with available strain data from the NTK 500/41 Wind Turbine.

The sensors were placed on the wind turbine as explained in Sect. 14.3, and are capable of measuring only the bending moments. Also, it is not feasible to introduce any damage in the structure, as the structure is in-service. Also the insurance for the machine will be void if such changes are made to the system. Hence, the study is limited to validating the need for KF based NA tracking. The results are shown and discussed in detail in the subsequent sections.

### 14.5.1 Need for KF Based NA Tracking

As explained earlier the direct estimation method for the NA tracking estimates the NA position based on the instantaneous strain measured by the system. In

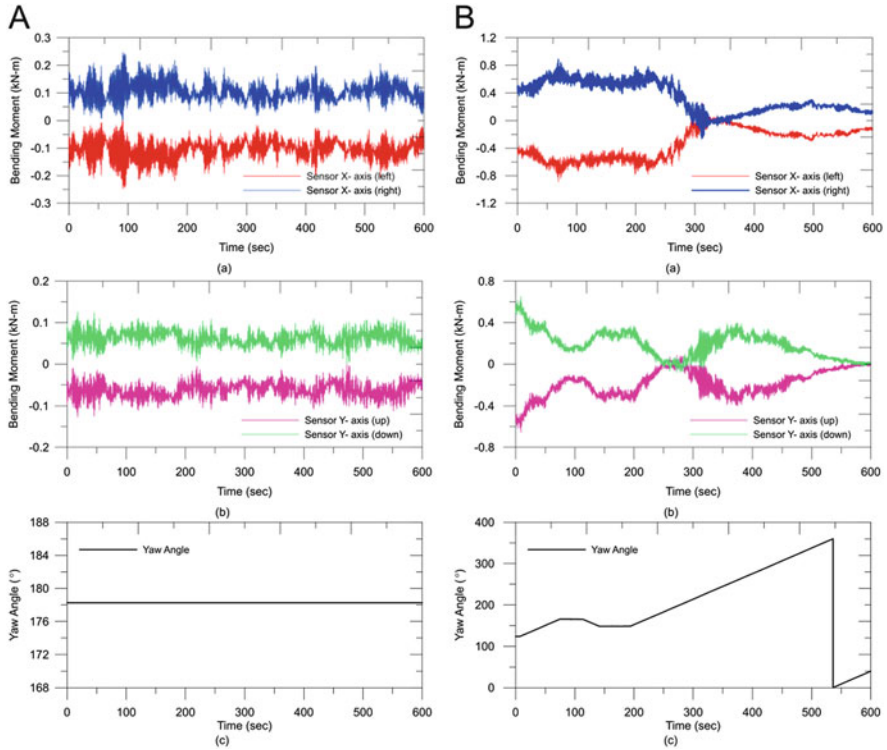


**Fig. 14.5** Measurements from Nordtank NTK 500/41 wind turbine. (A) Fixed yaw angle condition, (B) changing yaw angle condition. (a) Bending moment along x-axis, (b) bending moment along y-axis, (c) yaw angle measurement

the presence of measurement noise, this may lead to inaccurate NA estimation. On the other hand KF makes use of some component of the earlier estimate and then incorporates the new measurements of strain, in order to yield a more stable estimation.

In order to ascertain the performance of the two methods, the strain and yaw angle measurements from the Nordtank NTK 500/41 wind turbine were used for the NA estimation. Figure 14.5A(a) and (b) show the strains measured when the yaw angle was more or less constant (Fig. 14.5A(c)). Figure 14.5B(a) and (b) show strain measurements for the condition when the yaw angle was changed constantly (Fig. 14.5B(c)).

Based on these inputs the NA was tracked using the two methods. Figure 14.6 shows the performance of the direct estimation and KF estimation methods for the fixed yaw angle condition and Fig. 14.7 shows the performance in changing yaw angle conditions. The NA estimation is more stable in both the methods for fixed yaw angle conditions as the mass distribution is constant and the bending strains are more or less constant. Also, it can be clearly seen the NAE is more stable using

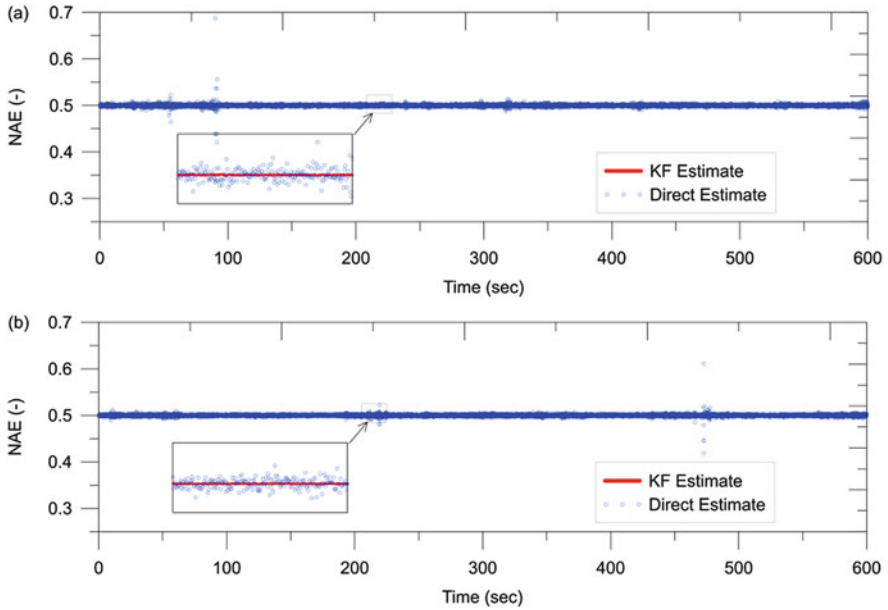
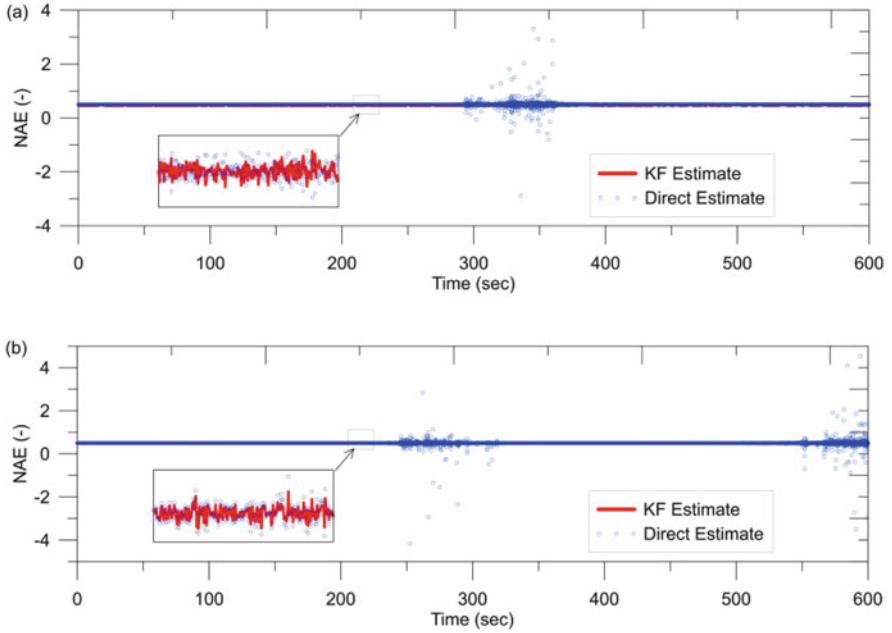


**Fig. 14.6** Comparative performance for NA estimation for fixed yaw angle condition (a) along x-axis (b) along y-axis (Soman et al. 2015c)

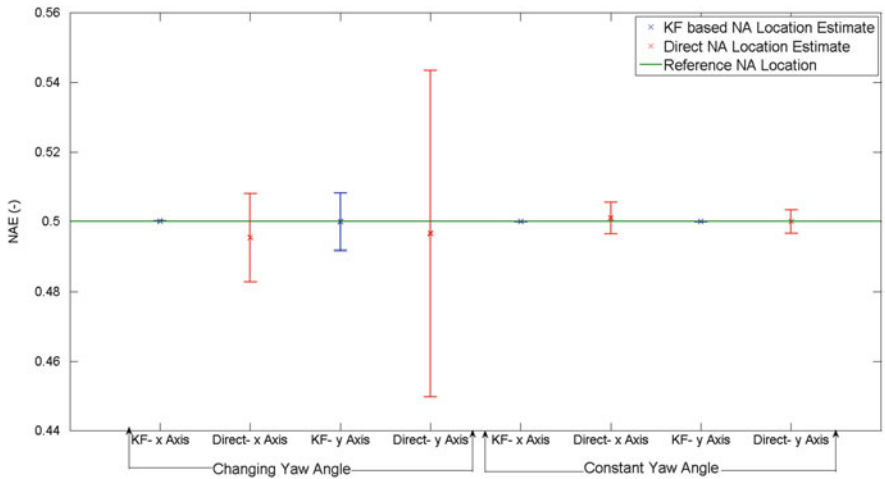
the KF estimate. The direct method gives erroneous estimation especially when the strain values are close to 0. This is in keeping with intuition, as when the measured strain is low, the effect of sensor noise and localized changes becomes significant leading to false estimations.

Figure 14.8 gives the comparative performance of the two methods under both the working conditions. It can be clearly observed that the standard deviation of the KF based estimation method is orders of magnitude better than the direct estimation method. Also, the mean of the KF based estimate is more accurate than the direct method.

The more accuracy in the estimation allows us, in turn, to have stricter thresholds for the damage detection. The lower thresholds allow earlier damage detection. Also, in the case of direct estimation, where the standard deviation of the estimate is higher, there is a higher possibility of a false negative damage detection, which leads to higher downtime and lower availability.



**Fig. 14.7** Comparative performance for NA estimation for changing yaw angle condition (a) along x-axis (b) along y-axis (Soman et al. 2015c)



**Fig. 14.8** Statistical performance comparison for NA estimation (Soman et al. 2015c)

## 14.6 Conclusions

The present research presents a complete damage detection methodology for tower structures of offshore wind turbine structures. The methodology makes use of NA as a damage sensitive feature. The NA as a damage sensitive feature has been proposed in literature for bridges (Sigurdardottir and Glisic 2013, 2014), but the innovation of the research is the customization of the NA tracking to the wind energy applications. The method makes use of KF for accurate NA tracking. The KF is robust tool ideally suited for data fusion and allows us to seamlessly combine the yaw angle measurement in the NA estimation and in turn improve the confidence level of the NA estimate. The KF uses the instantaneous strain measurements and a part of the previous estimate of NA location to give a more stable estimate than the one given by the direct method. The KF based estimations are shown to be more precise and accurate as compared to the estimation by the direct estimation. This has been shown through several simulated studies under different conditions of measurement noise as well as through actual strain measurements.

The NA seems to be a robust indicator and is not affected by the ambient loads as well as temperature conditions. Also, through the use of decision level data fusion, one can easily isolate the damage. The method also highlights a method to determine the threshold for the damage detection alarm to be raised. The threshold is chosen based on the trade-off of false detections and this threshold has been successfully implemented on the data from the Nordtank NTK500/41 wind turbine.

In the present study only the bulk temperature effects have been considered, and any temperature gradient effects are expected to be negligible because of the metallic construction and relatively thin cross section. Lastly the blades have been considered to be in braked condition in order to avoid any rotation and the resultant change in mass of the system. It is envisaged that the rotation effects can be easily incorporated through the data fusion of the rotation speed and a wavelet based filtering of the strain cycles due to the rotation. In addition, the present damage detection studies have been limited to reduction in the flexural rigidity of one element of the tower. Although this approach is commonly used in SHM of structures, is not a realistic damage scenario. Thus the performance of the NA tracking methodology must be validated for the detection of some realistic damage scenarios like fatigue cracks, or loosening of the bolts at the connecting flange. These are two areas identified for the future work, along with validation on strain data from a damaged tower structure.

**Acknowledgments** The authors would like to acknowledge the European Commission for their research grant under the project FP7-PEOPLE-20120ITN 309395 “MARE-WINT” (new Materials and REliability in offshore WIND Turbines technology). The authors would also like to thank DTU Wind Energy, for providing valuable information for the modeling of the 10 MW RWT tower for the purpose of this study. The authors are also grateful to TASK-CI for allowing the use of their computational resources. The opinions expressed in this paper do not necessarily reflect those of the sponsors.

**Open Access** This chapter is distributed under the terms of the Creative Commons Attribution-NonCommercial 4.0 International License (<http://creativecommons.org/licenses/by-nc/4.0/>), which permits any noncommercial use, duplication, adaptation, distribution and reproduction in any medium or format, as long as you give appropriate credit to the original author(s) and the source, provide a link to the Creative Commons license and indicate if changes were made.

The images or other third party material in this chapter are included in the work's Creative Commons license, unless indicated otherwise in the credit line; if such material is not included in the work's Creative Commons license and the respective action is not permitted by statutory regulation, users will need to obtain permission from the license holder to duplicate, adapt or reproduce the material.

## References

- Adeuyi A, Wu Z, Serker N (2009) Assessment of vibration-based damage identification methods using displacement and distributed strain measurement. *Struct Health Monit* 8(6):443–461
- Bak C, Zahle F, Bitsche R et al (2013) The DTU 10-MW reference wind turbine. In: DTU orbit—the research information system. Available via Technical University of Denmark. [http://orbit.dtu.dk/files/55645274/The\\_DTU\\_10MW\\_Reference\\_Turbine\\_Christian\\_Bak.pdf](http://orbit.dtu.dk/files/55645274/The_DTU_10MW_Reference_Turbine_Christian_Bak.pdf). Accessed 06 Apr 2016
- Bas J, Cariveau R, Cheng S et al (2012) Strain response of a wind turbine tower as a function of nacelle orientation. In: Dini P, Lorenz P (eds) *Proceedings of BIONATURE 2012: the 3rd international conference on bioenvironment, biodiversity and renewable energies*, St Maarten, 2012
- Brown R, Hwang P (1997) *Introduction to random signals and applied Kalman filtering*. Wiley, New York
- Cho S et al (2010) Structural health monitoring of cable-stayed bridge using acceleration data via wireless smart sensor network. In: Frangopol DM, Sause R, Kusko CS (eds) *Bridge maintenance, safety, management and life-cycle optimization: proceedings of the 5th international conference on bridge maintenance, safety and management*, Philadelphia, July 2010. CRC Press, London, p 85
- Doebling S, Farrar C, Prime M (1998) A summary review of vibration based damage identification techniques. *Shock Vib Dig* 30(2):91–105
- Paulsen U (2011) Verification of long-term load measurement technique: work package 1B.2 under the European Commission, integrated wind turbine design (UPWIND). In: DTU orbit—the research information system. Available via Technical University of Denmark. <http://orbit.dtu.dk/files/5712228/ris-r-1782.pdf>. Accessed 10 Apr 2016
- Sen Z, Altunkaynak A, Erdik T (2012) Wind velocity vertical extrapolation by extended power law. *Adv Meteorol*. doi:10.1155/2012/178623
- Sigurdardottir D, Glisic B (2013) Neutral axis as damage sensitive feature. *Smart Mater Struct*. doi:10.1088/0964-1726/22/7/075030
- Sigurdardottir D, Glisic B (2014) Detecting minute damage in beam-like structures using the neutral axis location. *Smart Mater Struct*. doi:10.1088/0964-1726/23/12/125042
- Soman R, Malinowski P, Ostachowicz W (2014a) Neutral Axis Tracking for damage detection in wind turbine towers. Paper presented at the European Wind Energy Conference and Exhibition (EWEA), Barcelona, 10–13 March 2014
- Soman R, Malinowski P, Ostachowicz W (2014b) Kalman Filter based data fusion for neutral axis tracking for damage detection in wind-turbine towers. In: *Abstracts of the 7th European workshop on structural health monitoring, EWSHM, Nantes, 8–11 July 2014*
- Soman R, Malinowski P, Ostachowicz W (2015a) Threshold determination for neutral axis tracking based damage detection in wind turbine towers. Poster presented at the Offshore 2015. European Wind Energy Association, Copenhagen, 10–12 March 2015



- Soman R, Malinowski P, Ostachowicz W (2015b) Bi-axial neutral axis tracking for damage detection in wind-turbine towers. *Wind Energy* 9(4):639–650
- Soman R, Malinowski P, Ostachowicz W et al (2015c) Kalman filter based data fusion for neutral axis tracking in wind turbine towers. In: Kundu T (ed) *Proceedings of the SPIE 9438, health monitoring of structural and biological systems*, California, 2015
- Standards Norway (2009) Eurocode 1: actions on structures—part 1–4: general actions—wind actions. NS-EN 1991-1-4:2005+NA:2009, Lysaker
- Welch G, Bishop G (1995) An introduction to the Kalman filter. In: Technical reports, Department of Computer Science University of North Carolina at Chapel Hill. Available via UNC CS. [https://www.cs.unc.edu/~welch/media/pdf/kalman\\_intro.pdf](https://www.cs.unc.edu/~welch/media/pdf/kalman_intro.pdf). Accessed 10 Apr 2016
- Xia H, Ni Y, Ye X (2012) Neutral-axis position based damage detection of bridge deck using strain measurement: formulation of a Kalman filter estimator. Paper presented at the 6th European workshop on structural health monitoring, Dresden, 3–6 July 2012

**Part IV**  
**Reliability & Preventive Maintenance**  
**of Offshore Wind Turbines**

# Chapter 15

## Reliability and Preventive Maintenance

**Itamar Esdras Martínez García, Alejandro Sánchez Sánchez, and Stefano Barbati**

**Abstract** In this chapter, the authors explain how to perform the core analysis of a Reliability Centered Maintenance (RCM) process for an offshore wind turbine. The aim is to provide an engineering guide which can improve the maintenance of the system, and consequently increases its availability and the production of energy. The initial investigations have been carried out using a database for an onshore 5 MW wind turbine; the data has then been converted using a proper conversion factor, so that it can be used for a 10 MW offshore turbine case. The reliability and availability of the entire offshore wind turbine have been calculated through Reliability Prediction and a Reliability Block Diagram (RBD). In addition, a failure mode analysis is done using FMECA, in order to identify the most important failure modes in a risk priority order, and to note the effect of propagation of each functional failure. The maintenance part of the RCM analysis has also been studied, to facilitate the creation of an optimum packaging of preventive maintenance tasks, which can help to avoid the functional failures of items throughout the system. Although the main target of the RCM is to reduce the downtime of the wind turbine, a reduction in Life Cycle Costs can be also accomplished through this process.

### Nomenclature

### Acronyms

4 M	Four Months
6 M	Six Months
2 Y	Two Years
5 Y	Five Years
6 Y	Six Years
A	Annually
A <sub>A</sub>	Achieved Availability
A <sub>I</sub>	Inherent Availability

---

I.E. Martínez García (✉) • A.S. Sánchez • S. Barbati  
Relex Italia SRL, Via Val Seriana, 4, 00141 Rome, Italy  
e-mail: [i\\_e\\_mg@hotmail.com](mailto:i_e_mg@hotmail.com); [alejandrofot@hotmail.com](mailto:alejandrofot@hotmail.com); [s.barbati@rellexsoftware.it](mailto:s.barbati@rellexsoftware.it)

A <sub>O</sub>	Operational Availability
A <sub>E</sub>	Age Exploration
CONV	Converter
DFIG	Doubly Fed Induction Generator
FF	Failure Finding
FTA	Fault Tree Analysis
FMECA	Failure Mode Effects and Criticality Analysis
GE	Generator
HT	Hard Time
IGBT	Insulated Gated Bipolar Transistor
L	Lubrication
LCC	Life Cycle Cost
LOR	Level Of Repair
LRU	Line Replaceable Unit
LSA	Logistic Support Analysis
LSAR	Logistic Support Analysis Record
MDT	Mean Down Time
MTA	Maintenance Task Analysis
MTBF	Mean Time Between Failure
MTTR	Mean Time to Repair
MVS	Medium Voltage Switchgear
OC	On Condition
OWT	Offshore Wind Turbine
PCNR	Percentage of Component Nominal Rating
PFC	Power Feeder Cables
PHS&T	Packaging Handling Storage and Transportation
PM	Preventive Maintenance
RBD	Reliability Block Diagram
RCM	Reliability Centered Maintenance
RPN	Risk Priority Number
S	Servicing
SF	Significant Function
TRANS	Transformer
WT	Wind Turbine

## Definitions

Availability	Probability that an item will perform its required function under given conditions at a stated instant of time
Corrective maintenance	Actions required to restore the proper operation of an item which has failed, either changing the failed item for a new one or fixing it
Failure rate	Number of failures per million of hours

MTBF	Defines the mean time between failures
MTTF	Represents the average time until a failure occurs
RCM	Process created by the aviation industry in order to develop and improve maintainability programs and ensuring safe operations with low costs
Reliability	The ability of an item to perform a required function under stated conditions for a given time interval. Reliability is expressed as a probability value (a value between 0 and 1)

## 15.1 Overview

During last 20 years, a great number of new technologies have been introduced in the field of green energy systems. The gradual appearance of different devices for energy production using renewable resources, have required novel research into improving the efficiency, in terms of both performances and costs. Taking such developments into consideration, reliability, availability and maintainability studies represent an essential investigation in order to identify how to optimize the design and the life cycle management from a cost/efficiency point of view.

The relevance of this topic has been well understood by the European Commission, as they promoted a research project named Reliawind (2011) between 2008 and 2011, for an on-shore wind turbine generator system. One of the aims of this research, in the work package led by Relex Italia s.r.l., was to assess the reliability for a 5 MW onshore wind turbine by creating a reliability model.

In 2014, the industry took a further step forward when the MARE-WINT project was approved. A new complete study on a wind turbine generator has been planned increasing generated power capacity to 10 MW and moving the wind turbine from onshore to an offshore environment. These changes reflect the improving design and concept for wind energy generation.

For a better explanation, Fig. 15.1 depicts the supportability analysis method derived from the procedure applied in the aeronautics and aerospace industries. This method has been used to initiate the current research; however, this method is quite extensive, and it was not possible to feasibly fulfill each and every component. Therefore, the attention has been focused on the core of this procedure (colored in pink) which can reasonably be considered the essential part.

As shown in Fig. 15.2, the knowledge acquired during Reliawind project, the reliability model, and the database have been used as starting point for the current work. An accurate study on the best power and environmental conversion factor has been conducted and a new reliability model, for reliability prediction and reliability block diagram studies, has been developed. Meanwhile an investigation into failure modes, classified by severity, has been conducted in order to identify riskiest failures for the system both from safety/environmental and economic/operational point of view. The second and third part of the research mainly consists of the

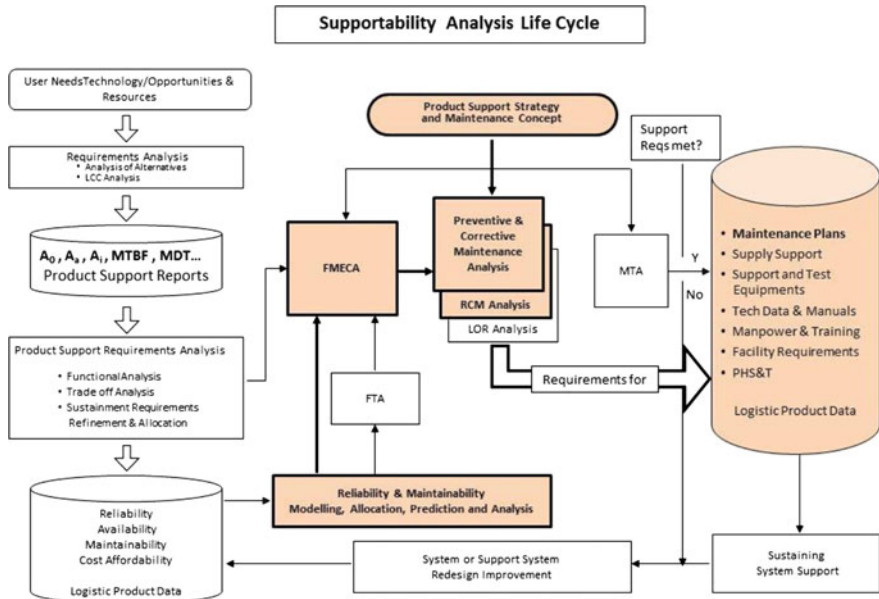


Fig. 15.1 Supportability analysis method

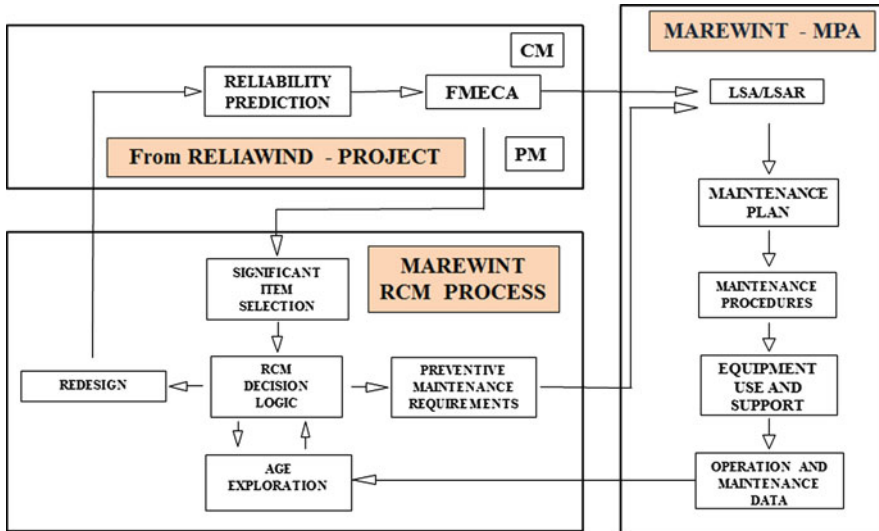


Fig. 15.2 MARE-WINT research

Reliability Centered Maintenance analysis—which has made it possible to optimize a maintenance plan with respect to all information collected in the previously analysis. The detailed procedure is described in the following chapter.

## 15.2 Offshore Wind Turbine Configuration

There are several wind turbine configurations which could be studied and compared in future works.

Figure 15.3 shows the whole hierarchy system which has been used in order to develop the reliability model. Main assembly and sub-assembly characteristics have

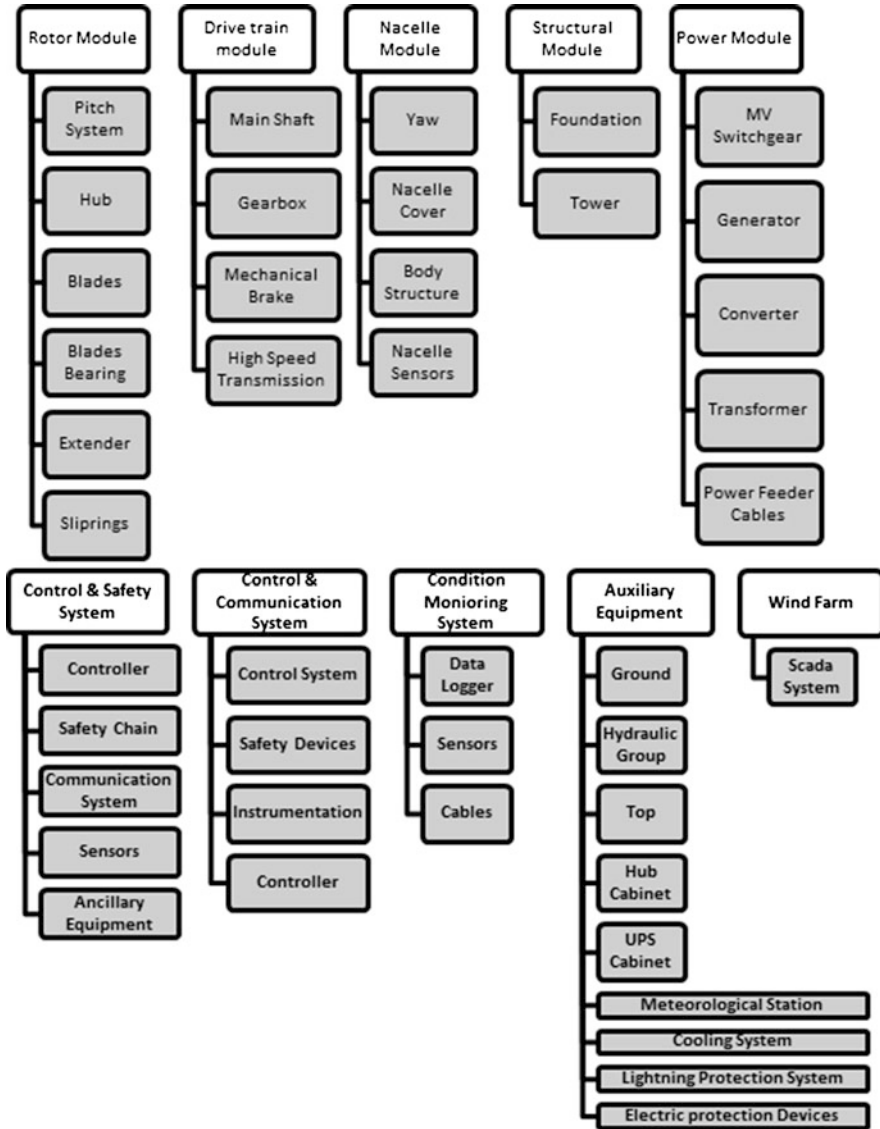


Fig. 15.3 Whole hierarchy offshore wind turbine

been described as follows:

- The Rotor Module is composed of a hydraulic pitch system which optimizes the position of the blades based on the wind direction. It is also the primary brake system for the wind turbine.
- The Drive Train Module transmits wind forces and torque from the rotor to the main shaft. It is done through a gearbox which is a combination of a planetary stage, followed by two parallel stages, and a mechanical brake.
- Four electrical yaw gears with motor brakes are included into the Nacelle Module. The yaw system rotates the top part of the nacelle into the upwind direction to maximize power production and minimize loads.
- A doubly fed induction generator (DFIG) with rated power 10 MW Power Module has been selected.
- A converter is connected between the generator and the grid. It is a four quadrant converter with the insulated gated bipolar transistor (IGBT) on the generator-side. An active crowbar unit is placed on the generator-side to ensure the compliance with grid requirements. The converter is located in the rear part of the nacelle.

### 15.3 Reliability Prediction

Reliability prediction is a quantitative analysis technique that has been used to predict the failure rate ( $\lambda$ ) of an offshore wind turbine (OWT) using an established model with defined operating conditions. The goal of reliability prediction is to predict the rate at which components and systems fail.

#### 15.3.1 Definition and Assumptions

The general formulation for the reliability through time is shown as Eq. (15.1):

$$R(t) = e^{-\int_0^t \lambda(x) dx} \quad (15.1)$$

where  $R$  is the reliability and  $\lambda$  is the failure rate (number of failures per million of hours) and  $t$  is the time.

A component's lifetime is often described by three phases. During first phase, the failure rate decreases down early with time and failures are attributable to manufacturing and quality problems. After that in the second phase, failure rate  $\lambda(t)$  is approximately constant (chance failures). In the third phase, the failure rate increases with time due to aging, wear out, fatigue, etc. If it is assumed that the



failure rate is constant along time (2nd phase), we get Eq. (15.2):

$$\lambda(t) = \lambda \quad (15.2)$$

Using Eq. (15.2), the reliability function shown in Eq. (15.1) can be expressed as Eq. (15.3):

$$R(t) = e^{-\lambda t} \quad (15.3)$$

The reliability exponential function (Eq. 15.3) has been selected as the way to describe the component's reliability.

### 15.3.2 Reliability Prediction Data-Base

Since published reliability data of offshore wind farms does not exist, it has been necessary to convert the failure rate data from onshore to offshore using published data of onshore wind turbines. Before starting the reliability prediction, a literature review of published data sources (e.g. Windstats, WMEP, LWP and Swedish Wind) was conducted, and the Reliawind data-base was chosen as being the most suitable for this research.

#### 15.3.2.1 Reliawind Data-Base

Reliawind is a project in which the reliability of large wind turbines (5 MW) was investigated. Recommended methods of measuring reliability and processing data from onshore wind turbines and wind farms were studied. During this project a large data-base, containing data on more than a thousand items, was developed. The project ran from 2008 to March, with active involvement of ten partners.

#### 15.3.2.2 Conversion Factor

Since our current turbine operates in a different environment, and has different parameters compared to the Reliawind turbine, a conversion factor has been introduced to convert the database data of the 5 MW *onshore* wind turbine to that of a 10 MW *offshore* wind turbine. This factor has been derived as combination of two parameters (Karyotakis 2011; Davidson and Hunsley 1994). The first parameter “ $K_1$ ”, takes into consideration the environmental stress; “ $K_2$ ” is based on the power rating stress.

$K_{1\text{ offshore}}$  is the environmental stress factor and it is defined as the effect of environmental condition (e.g. weather and humidity condition) on the offshore wind turbine.

**Table 15.1** Environmental stress factor

Environmental conditions	Environmental stress factor $K_1$
Ideal, static conditions	0.1
Vibration free, controlled environment	0.5
Ground-based	1
Naval Sheltered	1.5
Naval Exposed	2
Road	3
Rail	4
Air	10
Missile	100

$K_{2\text{ offshore}}$  is the power rating stress factor that depends on the operating power ranges of the wind turbine.

It is well known that offshore wind farms are exposed to higher power rating stress factor and adverse environment. Thus, Eq. (15.4) is used to describe the failure rate for the offshore wind turbine:

$$\lambda_{\text{offshore}} = \lambda_{\text{onshore}} \cdot (K_{1\text{ offshore}} \cdot K_{2\text{ offshore}}) \quad (15.4)$$

Table 15.1 shows how the value of the environment stress conversion factors varies, depending on the environmental conditions.

In our case,  $K_1$  is considered to be ‘Naval Sheltered’ for items within the nacelle. ‘Naval Exposed’ is chosen for the items that are fully exposed to marine environment.  $K_{1\text{ onshore}}$  is considered to be ‘Ground Based’ ( $K_{1\text{ onshore}} = 1$ );  $K_{1\text{ offshore}}$  is assumed to be between naval sheltered and exposed ( $1, 5 \leq K_{1\text{ offshore}} \leq 2$ ).

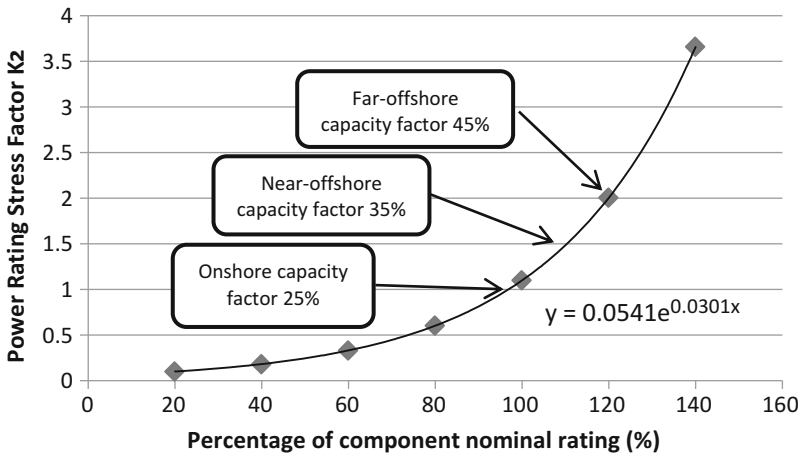
The other parameter,  $K_2$ , is obtained by taking into consideration the ‘windiness’ of the wind farm site. The windiness of the OWT is measured by the capacity factor of the wind turbine. This average capacity factor is assumed to be 25 % for onshore, 35 % for near-offshore and 45 % for far-offshore (Boccard 2009; BWEA 2000; CA-OWEE 2001; DTI 2002); in our case, the wind farm is considered to be ‘near-offshore’.

Table 15.2 shows the exponential relationship between the power rating stress factor and the component nominal rating. Values from Table 15.2 are plotted on Fig. 15.4 and the equation of the curve can be derived from the values showed in Table 15.2. As per the previous considerations, the difference between the average capacity factor for ‘far-offshore’ and ‘onshore’ is 20 % (45 %–25 %). Accepting a capacity factor of 25 % as the average onshore (assumed as a PCNR value of 100 %), and assuming that  $K_{2\text{ onshore}}$  is equal to 1 (from Table 15.2), the PCNR of far-offshore is calculated as: 45% – 25% + 100% = 120%.

Similarly, if—from Table 15.2— $K_{2\text{ far-offshore}}$  is equal to 2, the PCNR of near offshore can be calculated by using the same method which has been used for the far-offshore case; assuming a near offshore capacity factor of 35 %; the PCNR of

**Table 15.2** Power rating stress factor for mechanical components

Percentage of component nominal rating (PCNR)	Power rating stress factor $K_2$
140	4
120	2
100	1
80	0.6
60	0.3
40	0.2
20	0.1



**Fig. 15.4** Percentage of component nominal rating plotted against stress factor  $K_2$ . Graph constructed based on the data presented in Table 15.2

near-offshore is then:  $35\% - 25\% + 100\% = 110\%$ .  $K_{2 \text{ near-offshore}}$  is then calculated through Eq. (15.5), using this PCNR value of 110%:

$$K_2 = 0.0541 \cdot e^{0.0301 \cdot \text{PCNR}} \tag{15.5}$$

As a result,  $K_{2 \text{ near-offshore}}$  is equal to 1.483. Then, Eq. (15.6) can be obtained by introducing  $K_{2 \text{ near-offshore}}$  into Eq. (15.4):

$$\lambda_{\text{offshore}} = \lambda_{\text{onshore}} (K_{1 \text{ offshore}} \cdot 1.483) \tag{15.6}$$

### 15.3.3 Reliability Prediction Results

The system failure rate value obtained from the reliability prediction analysis is **1866.36 failures per million hours**. Figure 15.5 shows the number of failures per

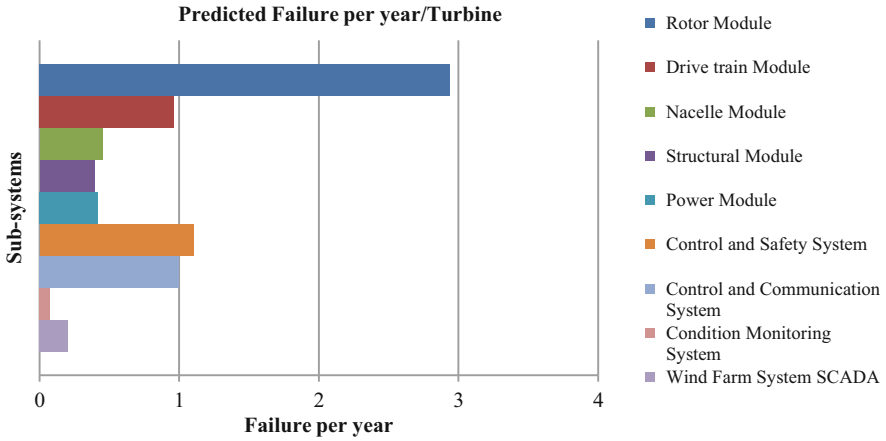


Fig. 15.5 Results reliability prediction on sub-systems

year associated with each sub-system (the failures of the auxiliary equipment are not included in Fig. 15.5).

## 15.4 Reliability Block Diagram

### 15.4.1 Definition and Assumptions

A Reliability Block Diagram (RBD) is a visual representation of the parts of the system, through blocks (representing items) linked together (Fig. 15.6). An RBD also shows how various parts are connected logically to fulfill the system requirements.

Since reliability predictions assume that all components in a system are in series, they cannot be used to analyze a system with redundant components. RBDs are used to evaluate the reliability of systems that are complex in their configurations. RBDs also provide an efficient and effective way to compare various configurations to identify the best overall system design. An example of a RBD for the OWT that presents redundancies is depicted in Fig. 15.7. The pitch system RBD shows how the main line is connected in standby configuration with the emergency line. A functional reliability model is created in order to evaluate the real configuration on the typical 10 MW wind turbine, and shown in Fig. 15.8.

The goal of the Reliability Block Diagram is to determine the reliability and maintainability metrics—such as Reliability, Availability, Failure rate and MTTR (mean time to repair)—for a complete system. The elements which are necessary for the required function are connected in series, while elements which can fail with

**Fig. 15.6** Development of RBD within a system

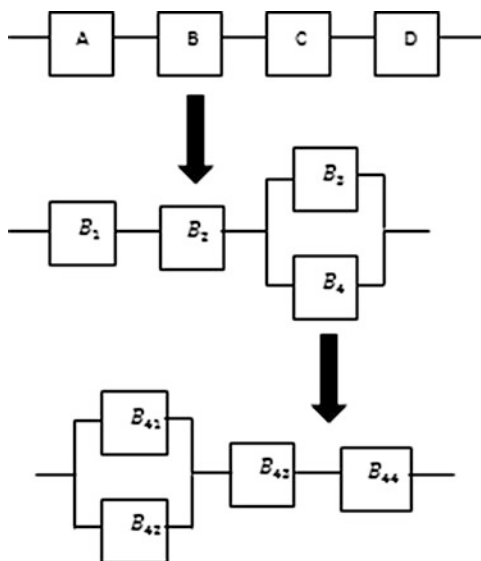
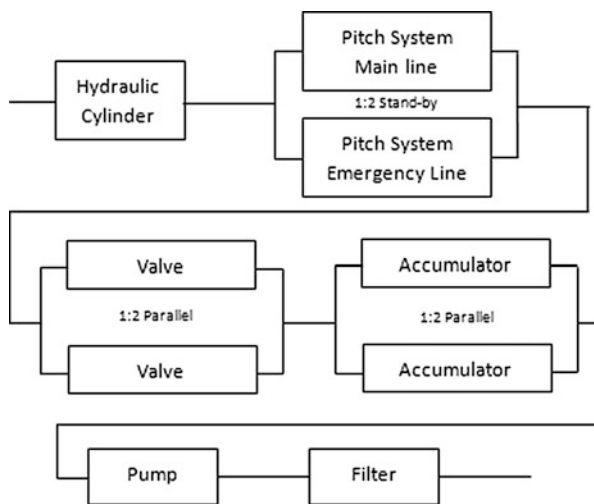


**Fig. 15.7** Pitch system RBD



no effect on the required function are connected with redundancies. There are three types of redundancies: parallel, load sharing and standby.

### 15.4.2 Inherent Availability

The Availability is the probability that the system is operating satisfactorily at any point in time when used under stated conditions; here, the time considered includes

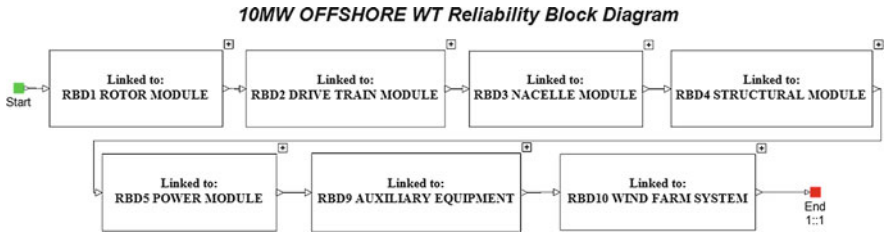


Fig. 15.8 Main RBD of the offshore wind turbine

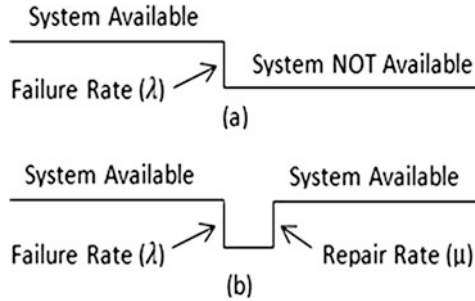


Fig. 15.9 (a) Non-reparable system and (b) reparable system

operating time, active repair time, administrative time and logistic time. Through this parameter, one can calculate the inherent availability, in which the proportion of the total time that the item is available is the steady-state availability. Therefore, the availability of an item is a function of its failure rate  $\lambda$  and of its repair or replacement rate  $\mu$ . The difference between repairable and non-repairable system is illustrated graphically in Fig. 15.9. For a simple unit with a constant failure rate and a constant mean repair rate,  $\mu$  is shown as Eq. (15.7):

$$\mu = \frac{1}{MTTR} \tag{15.7}$$

Then, Eq. (15.8) can be derived to calculate the steady-state availability:

$$A = \frac{MTBF}{MTBF + MTTR} = \frac{\mu}{\lambda + \mu} \tag{15.8}$$

### 15.4.3 Reliability Block Diagram Results

RBD results for our study are shown in Figs. 15.10 and 15.11. From Fig. 15.11, it can be seen that the MTBF is equal to 3723.37 h (2.37 failures per year). According to theory, the value of MTBF is the time at which the reliability value is 0.37. The

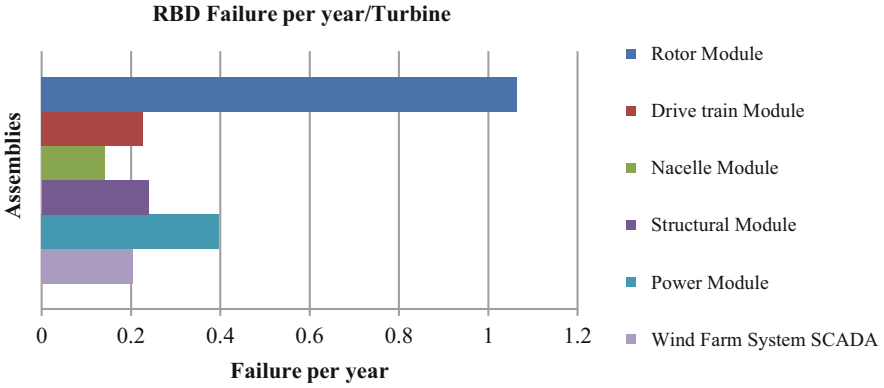


Fig. 15.10 Results RBD on sub-systems

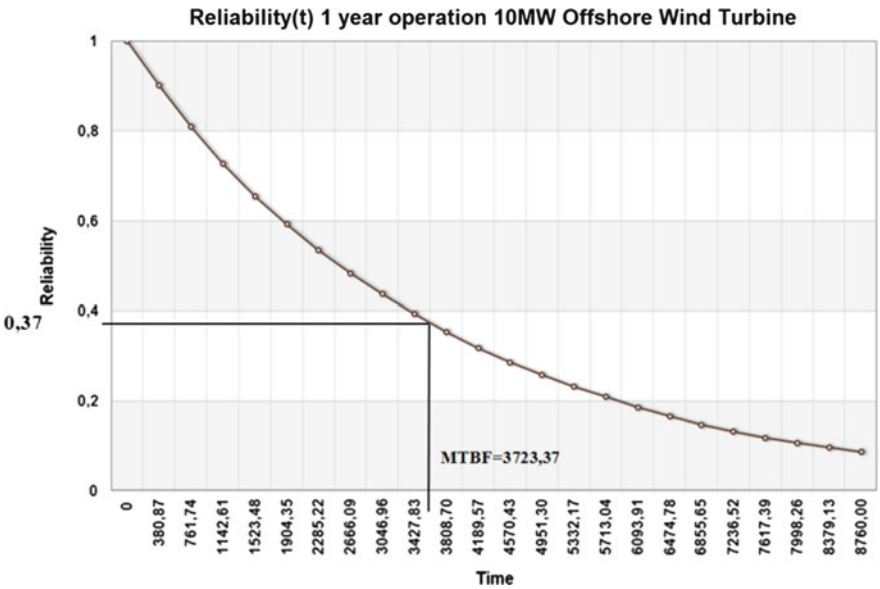


Fig. 15.11 Reliability through time in a year operation

inherent availability is calculated with a year mission time (8760 h), and at that time the value of inherent availability is about 99 %.

## 15.5 Failure Mode, Effects and Criticality Analysis

### 15.5.1 Definition

A Failure Mode, Effects and Criticality Analysis (FMECA) is one of the most used analysis tools in the engineering field for developing designs, processes and services. To develop a FMECA, potential failure modes are analyzed to determine their effects all along the system, and classified according to their severity (FMEA) and probability of occurrence (FMECA).

### 15.5.2 Objectives

The main target of this analysis is to identify the weakest parts of the OWT, understand their failure modes and the associated effects, and then improve their availability by introducing possible redundancies or design changes, and updating the preventive maintenance. Other objectives that are possible to achieve through this analysis are:

- Anticipate the most important problems.
- Prevent failures from occurring.
- Minimize the failure consequences as cost effectively as possible.
- Give technical information to maintenance personnel about failures that might come out during system life.
- Compare results with previous maintenance reports and update the analysis.
- Provide necessary information to create a cost/benefit analysis.
- Provide those modes that need preventive maintenance in a risk priority order.

### 15.5.3 Method

A FMECA is a bottom up approach analysis by which the system design and performance are studied. With this analysis the potential failure modes are defined, as well as the occurrence and severity of each failure effect associated to them. The analysis can be done in two ways: component level (referred as component FMEA) or functional level (referred as functional FMEA). A component FMECA has been chosen based on the tasks 101 and 102 (Table 15.3) of the military standard MIL-STD-1629A from the Department of Defense of USA (DoD 1980).



**Table 15.3** FMECA MIL-STD-1629 tasks

Task	Description
Task 101	Failure Mode and Effects Analysis. The purpose of the Failure Mode and Effects Analysis (FMEA) is to study the results or effects of item failure on system operation and to classify each potential failure according to its severity
Task 102	Criticality Analysis. The purpose of the Criticality Analysis (CA) is to rank each potential failure mode identified in the FMEA according to the combined influence of severity classification and its probability of occurrence

Source: DoD (1980)

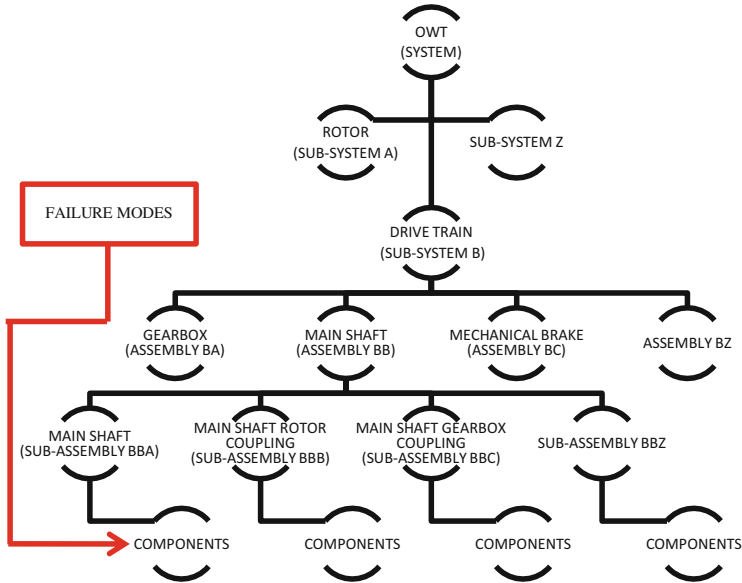


**Fig. 15.12** Example of the hierarchy structure used to perform the FMECA

### 15.5.4 Approach

A FMECA can be initiated at any system level but due to the complexity, huge amount of components and the lack of data, a proper level of indenture of our OWT has been chosen: the FMEA has been performed starting from the component level, while the FMECA starts from the line replaceable unit (LRU) level. A bottom-up approach is used, noting the failure modes of the lowest level items of the system and then moving up the hierarchy and noting the effect of the failure to the end item (the OWT itself). Figure 15.12 illustrates the distribution mentioned before.

### 15.5.5 Criticality

A criticality analysis completes the FMEA by using two parameters: occurrence and severity. With these parameters the risky parts of the systems are identified. *Calculating* criticality numbers gives us the possibility to define the criticality of each item and its associated failure modes from a quantitative point of view; however, this method is only used when enough data is available. The mode criticality number “C<sub>m</sub>” and the item criticality number “C<sub>r</sub>” (see Table 15.4), can be calculated according to definitions in MIL-HDBK-1629 (DoD 1980).

These numbers are defined using Eqs. (15.9) and (15.10):

$$C_m = \alpha * \beta * \lambda_p * t \tag{15.9}$$

$$C_r = \sum_n^j (C_m)_n \text{ for } n = 1, 2 \dots j \tag{15.10}$$

- C<sub>r</sub> = Criticality number for the item
- C<sub>m</sub> = Criticality number for a failure mode under a particular severity classification.
- α = Failure mode ratio. The probability, expressed as a decimal fraction, that the part or item will fail in the identified mode.
- λ<sub>p</sub> = Part failure rate.
- β = Conditional probability of mission loss given that the failure mode has occurred. Table 15.5 defines β values.
- t = Mission time.
- n = Failure modes in the items that fall under a particular severity classification.
- j = Last failure mode in the item under the severity classification.

**Table 15.4** Criticality numbers description from MIL-HDBK-1629

Criticality number	Description
C <sub>m</sub>	The portion of the “C <sub>r</sub> ” number due to one of its failure modes under a particular severity classification
C <sub>r</sub>	Number of system failures of a specific type expected due to the item’s failure modes

Source: DoD (1980)

**Table 15.5** β classification from MIL-HDBK-1629

β value	Failure effect
1	Actual loss
1-0.1	Probable loss
0.1-0	Possible loss
0	No effect

Alternatively, a qualitative method can be used, which allows us to represent the criticality results using a Risk Matrix. The matrix is constructed by inserting the total number of OWT failure modes in the matrix areas representing the severity classification and the frequency level assigned. The frequency is calculated as the ratio between failure mode probability of occurrence in a certain time interval, and the overall system probability of occurrence in the same time interval, as Eq. (15.11):

$$f = \frac{\lambda_p * \alpha * t}{\lambda_s * t} = \frac{\lambda_p * \alpha}{\lambda_s} \tag{15.11}$$

- f = Frequency
- $\alpha$  = Failure mode ratio. The probability, expressed as a decimal fraction, that the part or item will fail in the identified mode.
- $\lambda_p$  = Part failure rate.
- $\lambda_s$  = Total system failure rate.

The results of the analysis for our OWT are summarized in the Criticality Matrix shown in Fig. 15.13, in which three risk areas can be identified:

- Green area (Low occurrence and low severity) indicates that the risk associated to that failure mode located on it, is acceptable or well controlled. This area refers to those placed in minor severity with frequency from I to III, marginal severity with frequency I and II, critical severity with frequency I.
- Red area (High occurrence and high severity) indicates that actions must be taken to decrease the severity associated to that failure mode and occurrence of the failure modes placed on it. This area refers to those placed in marginal severity with frequency V, in critical severity with frequency IV and V and catastrophic severity with frequency from III to V.
- Yellow area (Medium risk) gathers those failure modes which must be monitored and controlled. This area refers to those modes placed in minor severity with

Frequency	Frequent (V)		1	1	
	Reasonably probably (IV)				
	Occasional (III)	3	4	2	1
	Remote (II)	6			1
	Extremely Unlikely (I)	8	1	6	
		Minor	Marginal	Critical	Catastrophic
		Severity			

Fig. 15.13 Risk matrix

**Table 15.6** Severity classification

Severity	Definition	Value associated with RPN analysis
Catastrophic	A failure mode which causes death, system loss, severe environmental damage, damage over 900,000 € or downtime over 2 days	250
Critical	A failure mode which causes severe injury, major system or environmental damage, mission loss, damage over 90,000 € but less than 900,000 € and loss of availability between 24 hours and 7 days	175
Marginal	A failure mode which causes minor injury, minor system and environmental damage, mission degradation, damage between 90,000 € and 9000 € and loss of availability between 24 h and 4 h	100
Minor	Only unscheduled maintenance or repair, damage under 9000 € and loss of availability under 4 h	25

frequency IV and V, marginal severity with frequency III and IV, critical severity with frequency II and III, and catastrophic severity with frequency I and II.

The matrix provides a way to identify and compare failure modes, with respect to their associated severity and frequency. Severity degrees assigned to failure modes are described in Table 15.6. A classification of frequency is given in Table 15.7.

### 15.5.6 Process

The ‘bottom-up’ procedure for component FMECA is the following:

1. Construct a OWT FMECA system tree;
2. Identify all potential items;
3. Evaluate failure modes (from mode library) of each component;
4. Evaluate the local effect for each component failure mode;
5. Roll-up all local effects at higher level (at higher level, the rolled-up effect becomes the failure mode at that level);
6. Repeat step 5 until system level;
7. For each end effect at system level identify the detection, severity and occurrence;
8. Build down the FMECA by transferring all the end system effects and severity to sub-system, assembly and component level.

**Table 15.7** Frequency/occurrence classification

Frequency	Description	Value associated with RPN analysis
Frequent	A high probability of occurrence during the item operative time interval. High probability may be defined as a single failure mode probability greater than 0.20 of the overall probability of failure during the item operative time interval	4
Reasonably probable	A moderate probability of occurrence during the item operative time interval. Probable may be defined as a single failure mode probability of occurrence which is more than 0.10 but less than 0.20 of the overall probability of failure during the item operative time	3
Occasional	An occasional probability of occurrence during item operative time interval. Occasional probability may be defined as a single failure mode probability of occurrence which is more than 0.01 but less than 0.10 of the overall probability of failure during the item operative time	2
Remote	An unlikely probability of occurrence during item operative time interval. Remote probability may be defined as a single failure mode probability of occurrence which is more than 0.001 but less than 0.01 of the overall probability of failure during the item operative time	1
Extremely unlikely	A failure whose probability of occurrence is essentially zero during item operative time interval. Extremely unlikely may be defined as a single failure mode probability of occurrence which is less than 0.001 of the overall probability of failure during the item operative time	0

### 15.5.7 Limitations

FMEA takes into consideration only non-simultaneous failure modes. In other words, each failure mode is considered individually, assuming that other system items work as usual. Effects of multiple item failures on wind turbine functions and redundant items are not covered by FMEA. These events are usually studied for those systems or sub-systems that perform safety functions by the Fault Tree Analysis (FTA) and Markov analysis.

## 15.5.8 Results

Due to the complexity of the full FMECA just the consequential results are shown in this section, which are related to the hierarchical structure described in Sect. 15.5.4.

### 15.5.8.1 Risk Matrix and Criticality Evaluation

A risk matrix is probably one of the most widespread tools for risk evaluation. Figure 15.13 reports the number of failure modes that lead to the end effect with each particular combination of severity and frequency values.

Figure 15.13 shows seven failure modes located in yellow zones where actions to control or monitor them must be taken (three of them are: The Drive train Module Failure, the Power Module Failure and the Structural Module Failure). Twenty-four failure modes, whose risk is considered to be low are in the green areas. Three failure modes are located in the red areas where mitigating actions must be taken (The Auxiliary Power Equipment Failure in Marginal-Frequent, The Rotor Module Failure in Critical-Frequent, and the Nacelle Module Failure in Catastrophic-Occasional).

The results of the Auxiliary Power Equipment are due to the large amount of items contained within it, while for the Rotor Module this result is due to the high failure rate of the Blades assembly. For the Nacelle Module Failure, the reason why it is placed in a red zone is because the Nacelle is one of the main structures of the WT where the majority of the main assemblies are located.

From what is presented in Sect. 15.4.3, the MTBF of the system is 3723.37 h (2.37 failures per year). For this reason, the time until system fails has been taken as the mission time.

As mentioned in Sect. 15.5.5, another quantitative analysis has been performed, the results of which are shown in Fig. 15.14. From Fig. 15.14, it can be seen that:

- Six marginal failure modes have the highest criticality number for the system.
- Nine critical failure modes have almost the same criticality number as Marginal failure modes.
- Seventeen ‘minor’ failure modes have more than three times criticality compared to the two ‘Catastrophic’ failure modes, but less than half the value of criticality number compared to Marginal and Critical failure modes.

Equation (15.12) is derived from Eqs. (15.9), (15.10) and (15.11), and it can help to explain why the item criticality numbers are so high for the less severe modes:

$$C_r = \sum_n^j (f_n * t * \beta * \lambda_s) \quad (15.12)$$

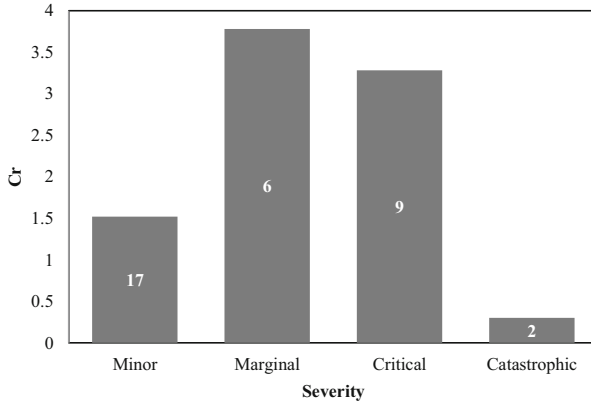


**Fig. 15.14** Item criticality number (Cr) distribution

Considering that “t” does not change,  $\lambda_s$  is constant and  $\beta$  values are the same for all failure modes, one can obtain Eq. (15.13):

$$C_r = k * \sum_n^j f_n \tag{15.13}$$

Therefore, for the marginal classification, high values of frequency and a high number of failure modes are the reason for high item criticality numbers.

**15.5.8.2 Mode Criticalities at System Level**

The ten modes with the highest criticalities are reported in Fig. 15.15. Blades are well known as the parts that most suffer in wind turbines due to their continuous work under adverse environmental conditions; in fact Rotor Module Failure (which includes the Blades) is characterized by the highest mode criticality value (mode criticality of 2.88).

Unifying all Auxiliary Equipment failure modes would lead to the highest mode criticality (3.41), simply due to the large amount of assemblies contained in this sub-system; however these failure modes have been sorted based on the equipment in which they can manifest.

Even with the aforementioned equipment separated, the second highest mode criticality belongs to Auxiliary Power Equipment Failure, while the third and fourth positions are taken by WT Auxiliary Equipment Failure and Air Conditioning Equipment Failure, respectively.

The remaining failures with the lowest values of mode criticality belong to Condition Monitoring System Failure, Control and Safety System Failure, Nacelle Module Failure, Drive Train Module Failure and Power Module Failure.

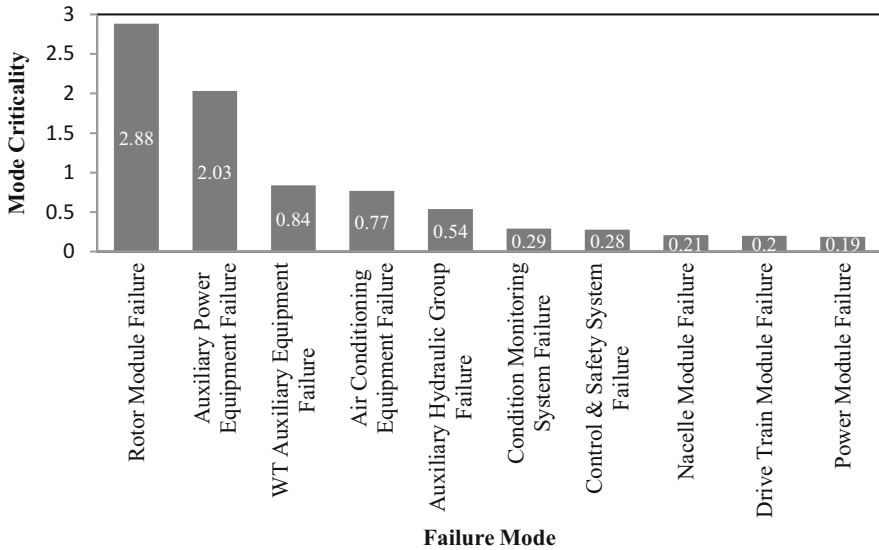


Fig. 15.15 Top 10 mode criticalities

### 15.5.8.3 Risk Priority Number (RPN)

RPN is a criticality study in which the severity, occurrence and detection are multiplied in order to obtain information about the riskiest failure modes. Thus, greater attention is paid to critical parts. Equation (15.14) is used to obtain RPN numbers:

$$RPN = \text{Severity} * \text{Occurrence} * \text{Detection} \tag{15.14}$$

Figure 15.16 shows the consequent risk priority classification with the highest RPNs of the OWT.

In this case, Rotor Module Failure is still in first position because of its high occurrence and severity and also its low detection level comparing to the others, followed now by the Structural Module Failure and the Nacelle Module Failure due to its high severity and low detection. The rest of the failure modes have such combinations that give them a gradual position on the graph until getting a value of 200 for the last two modes.

It is important to note that the mode criticality graph and the RPN graph give different lists of the riskiest failure modes of the OWT. This is because the mode criticality analysis focuses on the probability of occurrence, while the RPN analysis considers the detection parameter combined with severity and occurrence. All RPN values related to severity, occurrence and detection, and used to perform this analysis, are listed in Tables 15.6, 15.7 and 15.8 respectively.



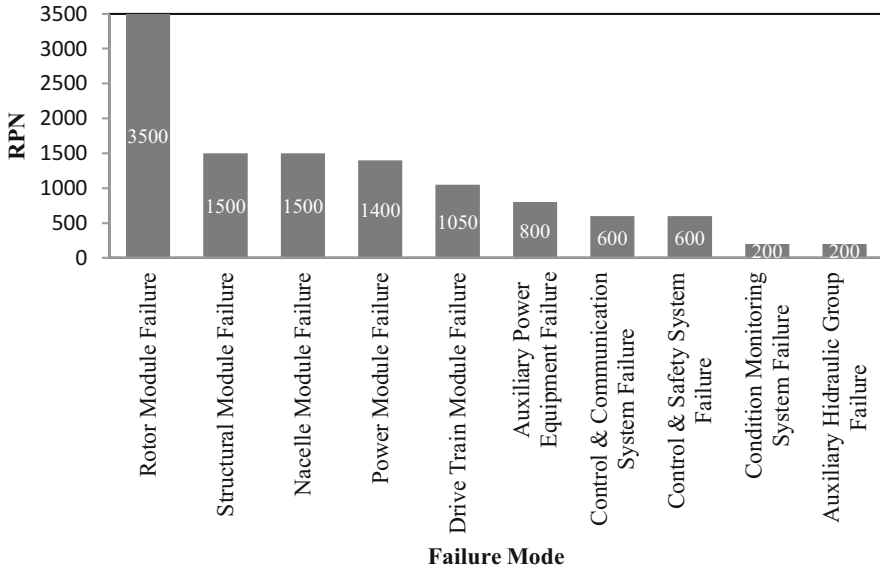


Fig. 15.16 Top 10 RPN

Table 15.8 Detection classification

Detection	Description	Value associated with RPN analysis
Almost certain	Inspections will almost certainly detect a functional failure	1
Very high	Very high chance the inspections will detect a functional failure	2
High	High chance the inspections will detect a functional failure	3
Moderately high	Moderately high chance the inspections will detect a functional failure	4
Moderate	Moderate chance the inspections will detect a functional failure	5
Low	Low chance the inspections will detect a functional failure	6
Very low	Very low chance the inspections will detect a functional failure	7
Remote	Remote chance the inspections will detect a functional failure	8
Very remote	Very remote chance the inspections will detect a functional failure	9
Absolutely impossible	Inspections will not and/or cannot detect a functional failure or there are no the inspections	10

## 15.6 Preventive Maintenance (PM)

During the Wind Turbine life different types of maintenance tasks are required in order to retain or restore its operation. In this section, we explain how to apply the “NAVAIR 00-25-403” procedure to define the PM tasks for our OWT (NAVAIR 2003). This standard explains a complete reliability centered maintenance (RCM) process which can be applied for almost any system.

### 15.6.1 Definition

Preventive Maintenance looks at actions that can be used to extend the useful life of system with a good cost-benefit relation, whilst simultaneously ensuring the safety of the system. PM tasks are generally performed during an intended downtime, though they can also be performed during corrective maintenance and even while the system is running (Predictive Maintenance using nondestructive inspection techniques).

### 15.6.2 Preventive Maintenance Tasks Classification

#### 15.6.2.1 Scheduled Tasks

Scheduled tasks are those which are performed in set intervals of time. These intervals can be measured in different units depending on how the system operates (e.g. cycles, time and events). The main units used in the Wind Turbine tasks are units of time: hours, days, months and years. Scheduled tasks include:

- Servicing (S): this task involves the replenishment of consumables that are wasted overtime, as for example oil and fuel. Usually no further analysis should be done for these tasks due to they should be performed according to their manufacturer’s instructions, which include information about how often, how to do it, level of disassembly, operator skills and other maintenance requirements.
- Lubrication (L): this task is applied to those components that must be lubricated periodically according to design specifications. As for S tasks, manufacturers give the instructions to perform it as well as its intervals to be applied
- Hard Time (HT): It consists of the replacement or restoration of the item before it fails. This task is performed when the degradation of the item cannot be detected. The degradation phase of the item is called “Wear Out”, which shows different increases of the probability of failure with time depending on the type of component. The time to perform the task is established according to the consequences of the effects that the item failure causes. If the consequences are safety/environmental related, the limit time to perform the task

will be established before the wear out age while if the consequences are operational/economic related the limit time will be flexibly established before the functional failure.

- Failure Finding (FF): this schedule task allows finding functional failures that have already occurred but are not apparent to the operators/maintainers, also called hidden failures. Emergency or back-up systems such as firefighting system or pumps in the hydraulic system are examples of elements that are subjected to Failure Finding task.

### 15.6.2.2 On Condition Task

On Condition (OC) tasks are periodical or continuous inspections. In contrast to HT tasks, these have a well-defined degradation period where the potential failure indicates that a functional failure will occur. Periodic and continuous inspections ensure that the items work until a potential failure comes along, extending its useful life, and therefore decreasing its maintenance costs. Once the potential failure is found, the next inspections are performed with flexible intervals of time in order to find the right time to take corrective actions. Periodical inspections range from simple visual checks to non-destructive inspections which need specialized equipment. The most used continuous inspection in wind turbines is condition monitoring. Condition monitoring is usually used for failure modes whose functional failures have environmental/safety-related effects, as these need to be continuously controlled.

### 15.6.3 Significant Function Selection

System failures may have different levels of function losses. Hence, functions are classified as “Significant Function (SF)” or “Non-SF”, depending on whether the consequences of these failures may lead to any losses of function, or effects, in terms of safety, environment, operations or economic impacts.

#### 15.6.3.1 Significant Function (SF) Logic

Function failures have been analyzed through several questions which identify all significant failures. Items may have more than one significant function and each one should be analyzed individually. Functions which are not significant are not taken into consideration. The logic diagram shown in Fig. 15.17 has been followed in order to identify all significant functions.

The diagram is composed of four questions, that point out which loss of function has adverse effects on safety, environment, operations and economic impacts—and if the function is already protected by an existing PM task. The significant

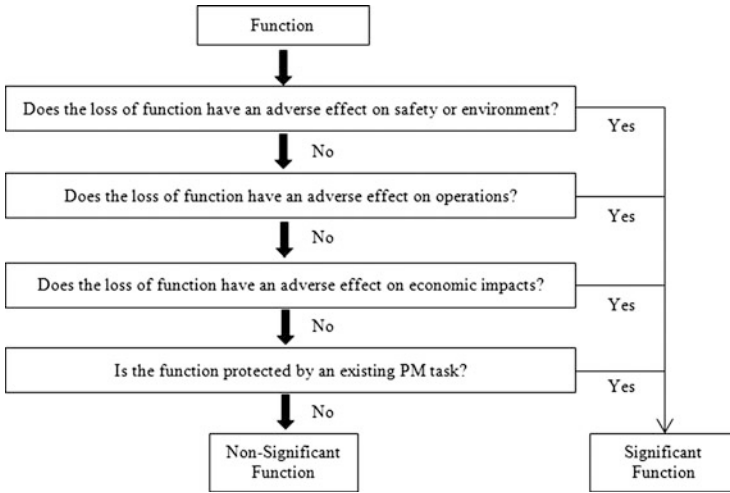


Fig. 15.17 Significant function selection logic diagram

function selection logic diagram is represented in Fig. 15.17. All functions are followed through the diagram in order to classify them in “SF” or “Non-SF”. If the four questions’ in Fig. 15.17 are answered as “No”, the function is classified as “Non-SF”. A positive answer is enough to consider the function as a “SF”. The SF Identification process ensures that all functions and effects have been taken into consideration before a Task Evaluation analysis is developed.

### 15.6.4 Task Evaluation

A ‘task decision logic’ process must be undertaken using the Decision Logic Diagram (Fig. 15.18), after SFs have been identified.

An appropriate failure management strategy is implemented in order to accept, eliminate or decrease the consequences of functional failures. All possible Predictive Maintenance tasks have been studied to cover each functional failure through the Decision Logic Diagram shown in Fig. 15.18.

The study of each functional failure or failure mode effect goes through different branches depending on its circumstances, which finally identifies the suitable options in a two-step process. A failure that is not apparent under normal circumstances is classified as “hidden” because it only appears when a dormant function is activated. Both evident and hidden failures have adverse impacts which require actions, but if for each mode more than one action is possible, an economic and operational impact study is required to identify the best option.

The Decision logic branches identify four types of PM tasks: Lubrication tasks, OC tasks, HT tasks, and FF tasks which have been explained before. Task

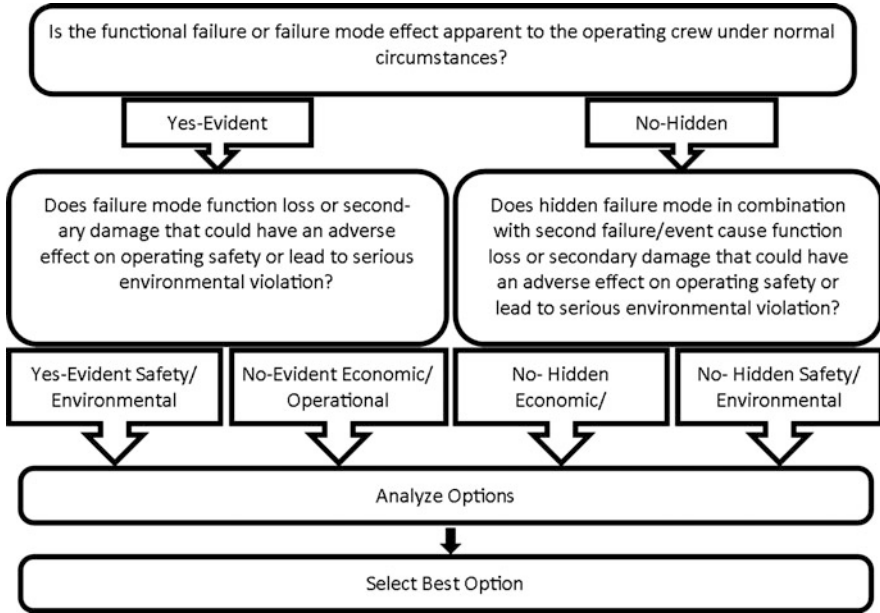


Fig. 15.18 Decision logic

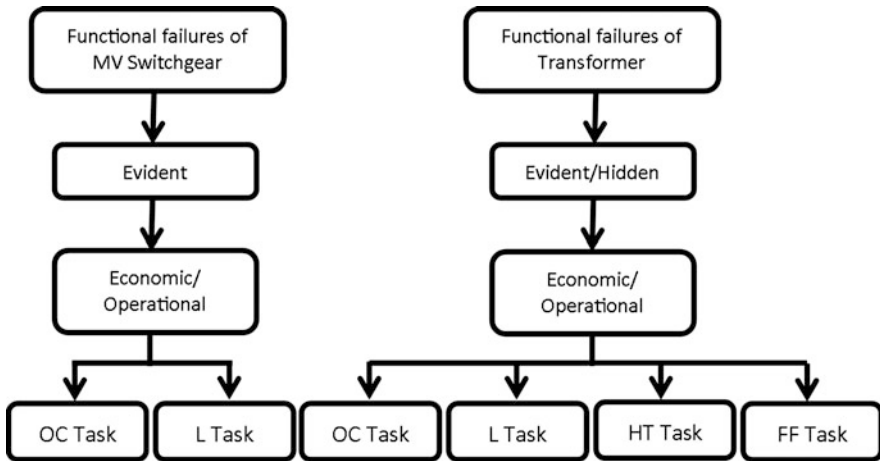


Fig. 15.19 Example of decision logic for the MV Switchgear and Transformer

evaluations are shown for the MV Switchgear and Transformer in Fig. 15.19; evaluating all the failure effects and reporting that the failures on these parts are “evident” for the crew with an economic/operational impact, is what the decision logic shown in Fig. 15.19 can provide, as an example.

In other words, this is the process in which the best suited task is selected to prevent and deal with each failure mode. If tasks cannot completely prevent the functional failure, the consequences must be reduced until they are acceptable. The available suitable tasks are identified in order to deal with each failure mode through the task selection in the next Sect. 15.6.5.

### 15.6.5 Task Selection

Once all possible maintenance tasks are known, the following step is the task selection. This evaluation process is done by looking through suitable tasks and taking into account cost analysis and operational consequences, thus determining which one deals better with a given failure mode.

#### 15.6.5.1 Cost

Costs are evaluated for each task, including consumables cost, charter cost for the kind of vessel that is used for the preventive tasks, crew cost, energy losses cost and transportation cost. Costs are measured in euros (€). Special attention has been paid to those activities or resources which play an important role in offshore maintenance: for instance, the energy losses during activity maintenance have been taken under consideration as well as fuel consumptions. All costs have been assumed under a literature review (Krohn et al. 2009; Malcolm and Hansen 2006; Myhr et al. 2014; Poore and Walford 2008; IRENA 2012; RAB 2010; The Crown Estate 2010). Equation (15.15) shows how the overall cost is based on associated costs:

$$C = C_{\text{Consumables}} + C_{\text{Vessel}} + C_{\text{transportation}} + C_{\text{Crew}} + C_{\text{Losses}} \quad (15.15)$$

$C_{\text{Consumables}}$  is the cost of the consumables. Assuming that vessels and equipment are needed, costs such as the rental vessel and equipment cost— $C_{\text{Vessel}}$ —are also taken into account.  $C_{\text{transportation}}$  is the cost based on transportation from the harbor to the wind farm. It is represented by Eq. (15.16):

$$C_{\text{Transportation}} = d \cdot C_1 \quad (15.16)$$

- $d = \text{Distance from harbor to wind farm and come back (km)}$ .
- $C_1 = \text{Fuel cost } (\text{€}/\text{Km})$ .

$C_{\text{Crew}}$ , the crew cost is based on Eq. (15.17):

$$C_{\text{Crew}} = t \cdot C_d (t_d + t_0 + t_r) \quad (15.17)$$

- $t$  = Number of technicians.
- $C_d$  = Cost technicians per hour ( $\text{€}/\text{hours}$ ).
- $t_d$  = Transportation time, round trip (hours).
- $t_0$  = Time to adjust the actions (hours). It has been assumed as 2 h.
- $t_r$  = Time to develop the preventive task (hours).

$C_{\text{Losses}}$ , the cost associated with losses of energy can be calculated via Eq. (15.18):

$$C_{\text{Losses}} = (t_r) \cdot C_L \tag{15.18}$$

- $C_L = W \cdot E \cdot C_{\text{factor}}$ .
- $W$  = Power Ratio(MW).
- $E$  = Electricity price =  $\text{€}/\text{MWh}$ .

Table 15.9 shows assumptions about  $C_{\text{Crew}}$  and  $C_{\text{Losses}}$ . Other general assumptions have been established as follows:

- The nominal power of the offshore wind turbine is 10 MW.
- A distance from harbor to wind farm of 30 Km.
- Logistic delays have not been taken into account.
- The weather window is always perfect to develop the replacement and there is no environmental condition by which to wait in onshore until the maintenance could begin (e.g. wave height).

A Crew Transfer Vessel has been selected in order to carry out the preventive tasks. This vessel is selected for the replacement of items with small and low weight. The role is to transport the crew to the OWT and items of a few tones. Characteristics of the selected vessel are shown in Table 15.10.

**Table 15.9** General assumptions

$C_d$ = Technicians Cost ( $\text{€}/\text{hour}$ )	90 $\text{€}/\text{h}$
Electricity price ( $\text{€}/\text{MWh}$ )	83 $\text{€}/\text{MWh}$
Capacity factor	45 %

**Table 15.10** Crew Transfer Vessel features

CTV—Crew Transfer Vessel	
Fuel cost, round trip ( $\text{€}$ )	145.72 $\text{€}$
Charter cost ( $\text{€}$ )	3.373 $\text{€}$
Number of technicians	G1 = 2; G2 = 1
$t_d$ = Transportation time, round trip (hours)	1.3
Operational speed	24 knots
Fuel consumption	0.24 mt/h (metric ton/h)

### 15.6.5.2 Operational Consequences

The right tasks have to ensure that there are no operational consequences in the OWT. A balance between cost and operational impact should be chosen: a less expensive task will not be selected unless it fits in a work package without operational consequences. As an example, the most suited maintenance tasks associated with each failure mode are shown in Table 15.11, for several Transformer parts.

**Table 15.11** Maintenance task assignation

Transformer	Maintenance tasks	Failure modes
THV	“Use vacuum to remove dirt”	Oil Insulation Failure; Cooling System Failure, Mechanical damage and faults in insulation
	“Do an infrared scan and compare it with previous reports. Test temperature. Check ground connections. Check for discolored copper and discolored insulation. Check for carbon tracking on insulators”	Mechanical damage and faults in insulation; Short circuit, personal safety; Bushings Failure; Tank Failure; Oil Insulation Failure; Possible fire; Winding deformation
	“Visual check around the transformer area”	Bushings Failure; Mechanical damage and faults in insulation; Loss of efficiency
	“Test fans and controls for proper operation”	Cooling System Failure
MV Winding & LV Winding	“Carry out ratio test of windings in all tap positions to ensure accuracy according to manufacturer’s data. Compare test data”	Drift; Mechanical Failure
	“Remove dirt using vacuum cleaner, blower or compressed air. Clean the areas of contact and tighten bolts and nuts. Apply air dry varnish”	Mechanical Failure
Transformer	“Vibration test”	Increased core temperature
	“Check diaphragm or bladder for leaks if there is conservator”	Increased core temperature
	“Check heat exchangers operation”	Increased core temperature
	“Check voltage and adjust it to the most suitable tap”	Opened; Shorted
Bushings	“Clean surfaces using brush or wiping with lint free cloth”	Worn Out



### 15.6.6 Packaging

After selecting the best-suited tasks the next step is to adjust all these tasks in work packages by different criteria in an optimal way. In the first phase of packaging, a proper metric for all the tasks must be selected in order to organize them along the timeline. When converting the metrics of an environmental/safety-related task, special care should be taken, ensuring that the time to perform the task is not exceeded with the new metric. Although the first timeline graph with all the maintenance tasks can suggest a first packaging strategy based on the frequency of the maintenance tasks, the second phase includes other criteria to group the tasks that should also be taken into consideration.

In the second phase, tasks with common characteristics are grouped according to their maintenance level, kind of skills needed, equipment required, task intervals, transportation, etc. While grouping maintenance tasks, the environmental/safety related ones usually set the time for other tasks, due to their less flexible intervals of time which cannot be exceeded.

In the third and last step, the final packaging is developed, introducing other important factors such as the operational impact of the work package (e. g. downtime) or the ability to perform tasks in parallel, managed by previous analysis and engineering criteria. The target, at this point, is to reduce the downtime of the wind turbine as much as possible while maintenance tasks are being performed. The more the maintenance time is reduced, the lesser costs of maintenance; consequently the availability of the wind turbine, and the energy produced, is also greater.

However, factors, such as labor hours (7–9 h and sometimes more) or the reduced spaces to work (limited crew) can make it difficult to obtain optimal packages. Sometimes tasks do not fit into the established work packages, and may have to be performed as “Special Inspections”. Usually, these inspections have:

- A different kind of vessel: Depending on the component, on which the task is going to be performed, the necessities and equipment needed to access it may be different; consequently, the vessels used will also vary. Usually, three or four kinds of vessels take part in PM programs.
- A different interval: Sometimes, the time to perform a preventive task is very different from the time required for other tasks. This may be due to the item operation, environment requirements, etc. This makes it harder to couple the task to others.

When new tasks or changes on them are being implemented, and they contain the usage of hazardous materials or the emission of contaminant, special authorizations are required. For instance, during the recoating of blades, the use of solvents, certain types of lubricants, and some non-destructive inspection materials may need to be regulated and/or certificated before the task is performed.

In the following example, 59 maintenance tasks from the power module have been packaged. The power module is divided in five parts: Medium Voltage Switchgear (MVS), Generator (GE), Converter (CONV), Transformer (TRANS)

**Table 15.12** Maintenance task classification by sub-systems

MVS	GE	CONV	TRANS	PFC
1–6	7–25	26–34	35–57	58–59

and Power Feeder Cables (PFC). The maintenance tasks are numbered as shown in Table 15.12.

The descriptions of some key tasks are shown in Table 15.13. In this case, the system is already operating and the intervals are taken from manufacturers' manuals. If the system is in an early design phase, other analyses should be performed to define task intervals. When all the intervals are identified, they are grouped every four months (4 M), six months (6 M), annually (A), two years (2 Y), three years (3 Y), and five years (5 Y) and six years (6 Y). Table 15.14 shows the first packaged tasks by their intervals for the Medium Voltage Switchgear and the Generator.

The tasks using common equipment are highlighted with the same colors. In Table 15.14, the red color (task number 1) refers to cleaning products and tools for cleaning; the yellow color (task number 2) means advanced tools for electrical tests; green indicates (task number 3, 10 and 11) basic tools for electrical tests; flesh color (task number 4 and 17) indicated lubricants; blue color (task number 12, 15, 18 and 19) depicts temperature and vibration test tools; and purple color pertains to advanced test tools.

Once the tasks are defined and classified by intervals of time, they have to be arranged in a lifeline. In our case, the tasks have been organized for 6 years (the maximum interval) and distributed over 3 different months with 2 days of work in each one. The simple reason why the workload is distributed in 2 days is because the work package has many working hours that do not fit in the limited labor hours. The months to perform the work packages are chosen based on the best weather periods of the year; the same for applies for the working days in each month, as certain weather conditions must be met. Table 15.15 shows the distribution of tasks for the first month (March) of work and for the first 6 years. The tasks highlighted in Table 15.15 are in accordance with the previous ones shown in Tables 15.13 and 15.14 (which follow the criteria previously explained for the packaging).

The crew on board the vessel is divided in two teams which work in parallel—thus the time to perform the maintenance tasks is considerably reduced. Table 15.16 summarizes the working time for each year, for the first month and each work team.

Consider the second working day and first work team, with a short working time of 1.8 h. The 1.8 h could have been better packaged with just one work team; however, further analyses for other sub-systems led to other maintenance tasks, that also need to be packaged with the same work team; additionally, there is the possibility that the labor time of the day can be limited to around 8 h.

Table 15.17 shows the different cases taken into account when packaging. In the case of October, a more flexible labor time is assumed (where it reaches 11 labor hours)—and so there is only one day of work. However, as it was mentioned before, when the maintenance plan is also performed for the rest of the sub-systems, these

**Table 15.13** Maintenance task descriptions

Assembly	Sub assembly	Task number	Maintenance task	Description
MVS	MV Switchgear	1	OC	“Check for accumulations of dirt especially on insulating surfaces. Remove filings. Use suitable cleaners in contacts”
		2	OC	“Inspect for proper grounding of the equipment. Megger test: insulators to ground, bussing phase to ground, and phase to phase. Test contact resistance across bolted sections of bars”
		3	OC	“Check electrical operation of: relays, auxiliary contacts, visual indicators, interlocks, cell switches and lighting. Visually inspect arrestors, C/T’s and P/T’s for signs of damage. Check cable and wiring condition, appearance, and terminations”
		4	L	“Lubricate doors”
		5	OC	“Inspect insulators and insulating surfaces for cleanliness and cracks. Remove drawout breakers and check drawout equipment. Check condition of bushings for signs of overheating, moisture or other contamination, for proper torque and clearance to ground”
		6	OC	“Check condition of contacts, connections, starters, and circuit breakers in accordance with test reports and manufacturer’s data. Check physical appearance of doors”
GE	Stator windings	12	OC	“Measure temperature at provided measuring points. Measure endwinding vibration”
	Bearings	15	OC	“Measure and record temperature at provided measuring points. Measure machine vibration. Measure and record condition of bearings using shock-pulse-method. Check bearing seals for oil leakage and clean if dirty. Check for rust”
	External fans	18	OC	“Visual inspection for rust and dirt. Check the vibration level”
	Internal fans	19	OC	“Visual inspection for rust and dirt. Check the vibration level”
TRANS	Cooling system	52	OC	“Clean the cooling air channels. Check the cooling air circulation ducts/openings for proper size and obstructions”

**Table 15.14** Packaged tasks by intervals for MVS and GE

INTERVAL	MVS		GE	
	TIME(h)	TASK N°	TIME(h)	TASK N°
4M	3	1,3,6	7.2	7,9,11,12,15
6M			1.8	16,20,24,25
A	2.7	2,5	4.6	8,10,13,14,17,21,22,23
2Y			1	18,19
3Y	0.25	4		
5Y				
6Y				
TOTAL	5.95	6	14.6	19

**Table 15.15** Packaged tasks for the first 6 years

Year	First day	Second day
0	<u>1,3,6,7,9,11,12,15,38,49,52</u>	<u>16,20,24,25,29,33,37,40,41,44,48,54,57,59</u>
1	<u>1,2,3,5,6,7,9,11,12,15,38,49,52</u>	<u>16,20,24,25,29,33,37,40,41,44,48,54,57,59</u>
2	<u>1,2,3,5,6,7,9,11,12,15,18,19,38,49,52</u>	<u>16,20,24,25,29,33,37,40,41,44,48,54,57,59</u>
3	<u>1,2,3,4,5,6,7,9,11,12,15,38,49,52</u>	<u>16,20,24,25,29,33,37,40,41,44,48,54,57,59</u>
4	<u>1,2,3,5,6,7,9,11,12,15,18,19,38,49,52</u>	<u>16,20,24,25,29,33,37,40,41,44,48,54,57,59</u>
5	<u>1,2,3,5,6,7,9,11,12,15,38,49,52</u>	<u>16,20,24,25,29,33,37,40,41,44,48,54,57,59</u>
6	<u>1,2,3,4,5,6,7,9,11,12,15,18,19,38,49,52</u>	<u>16,20,24,25,29,33,37,40,41,44,48,54,57,59</u>

**Table 15.16** Working hours for the first 6 years

First day	Year 0	Year 1	Year 2	Year 3	Year 4	Year 5	Year 6
Work team 1 (hours)	7.2	7.2	8.2	7.2	8.2	7.2	8.2
Work team 2 (hours)	4.2	6.9	6.9	7.15	6.9	6.9	7.15
Second day	Year 0	Year 1	Year 2	Year 3	Year 4	Year 5	Year 6
Work team 1 (hours)	1.8	1.8	1.8	1.8	1.8	1.8	1.8
Work team 2 (hours)	7.1	7.1	7.1	7.1	7.1	7.1	7.1

times will be readjusted. In the case of July, the two working teams cannot work in parallel because of the limited space in the nacelle; therefore they are separated in 2 days of work.

### 15.6.7 Age Exploration (AE)

In the process to elaborate PM programs, assumed data is necessary. An AE updates the data during different analyses.

**Table 15.17** Packaging overview for year 0

Year 0	Month	Day	Working team	PM tasks	Hours
	March	Day 1	Group 1	OC × 5	7.2
			Group 2	OC × 6	4.2
		Day 2	Group 1	OC × 4	1.8
			Group 2	OC × 10	7.1
	July	Day 1	Group 1	OC × 5	7.2
			Group 2	–	–
		Day 2	Group 1	–	–
			Group 2	OC × 6	4.2
	October	Day 1	Group 1	OC × 12	10.9
			Group 2	OC × 13	9.4
		Day 2	Group 1	–	–
			Group 2	–	–

### 15.6.8 Repackaging

In order to improve the work packages there are periodic reviews of:

- Time to perform the task
- Task interval
- Work package interval
- Maintenance process
- Techniques and technologies used

The maintenance documentation from field, which contains the information as previously mentioned, should be reviewed with maintainers to verifying whether the analysis results are realistic.

## 15.7 Conclusions

The reliability analysis for a 10 MW offshore wind turbine has identified which sub-systems, assemblies and sub-assemblies have a high failure rate. The sub-systems with highest failure rate are Rotor Module, and Drive Train Module. In particular, the Rotor Module is exposed to high stress and fatigue during its operation time due to uneven high air pressure around it. It should be also noted that the gearbox does not appear to be one of the less reliable assemblies of an OWT as it might be expected. These results also verify the results of the Reliawind project.

The RBD shows an OWT failure rate of 2.37 failures per year, which is about twice as large as an onshore wind turbine failure rate. This value could be accepted for an onshore wind turbine; however it is a high failure rate for an OWT due to the limited accessibility to perform preventive or corrective maintenance.

The huge dimensions of the wind turbine, its complexity and the environment increase the failure rate of the system. Through quality improvements of components, and by using condition monitoring on critical assemblies, the downtime can be reduced—allowing for an accurate scheduled maintenance to be developed.

Nowadays, availability improvements have been sought, in order to reduce energy losses and make offshore wind energy more profitable. In general, commercial offshore wind turbines can achieve an availability value of about 90 %, but, depending on the maintenance assumptions, this value can increase to 95 %. However in this analysis, logistic delays, maintenance delays and supply delays have not been taken into account; therefore, an availability value (inherent availability) of 99 % has been achieved.

Regarding the FMECA study, it can be concluded that the change in environment increases the probability of certain failures, directly or indirectly. For the Rotor Module and the Structural Module, the analysis confirms that their failures are mainly caused by the hazardous environment. For the Drive Train Module and Rotor Module, the abrupt changes in wind direction lead to continuous variation on their load conditions, and consequently cause stress and fatigue. As the OWT usually works in extreme temperature conditions, the Air Conditioning Equipment has to increase its power to maintain suitable environmental conditions, and this leads to an increase in its failure rate.

From the result of the RPN and Mode Criticalities analysis, it can be seen how each method can give different lists of riskiest parts of the system; for this reason both analysis are suggested in order not to leave any important failure mode out of consideration.

A successfully scheduled PM program can reduce maintenance costs and increase the availability of the OWT without risks for the system, personnel or environment. Throughout the packaging study, it has been seen that clear criteria combined with expert engineering judgment can make the process much easier.

The fact that the wind turbine is placed in an offshore environment affects the PM program due to drawbacks such as limited labor hours, expensive means of transport, expensive maintenance tasks, the difficulty to proceed with certain corrective actions, and the difficulty to perform some preventive tasks, amongst other factors. Nonetheless, with the right tools and procedures, offshore wind can be made more reliable and feasible.

**Open Access** This chapter is distributed under the terms of the Creative Commons Attribution-NonCommercial 4.0 International License (<http://creativecommons.org/licenses/by-nc/4.0/>), which permits any noncommercial use, duplication, adaptation, distribution and reproduction in any medium or format, as long as you give appropriate credit to the original author(s) and the source, provide a link to the Creative Commons license and indicate if changes were made.

The images or other third party material in this chapter are included in the work's Creative Commons license, unless indicated otherwise in the credit line; if such material is not included in the work's Creative Commons license and the respective action is not permitted by statutory regulation, users will need to obtain permission from the license holder to duplicate, adapt or reproduce the material.

## References

- Boccard N (2009) Capacity factor of wind power, realized values vs. estimates. *Energy Policy* 37:2679–2688. doi:10.1016/j.enpol.2009.02.046
- BWEA (2000) Prospects for offshore wind energy: a report written for the EU (Altener contract XVII/4.1030/Z/98-395) by the British Wind Energy Association. In: Reports. Offshore wind energy. Available via OWE. [http://www.offshorewindenergy.org/reports/report\\_026.pdf](http://www.offshorewindenergy.org/reports/report_026.pdf). Accessed 10 Apr 2016
- CA-OWEE (2001) Offshore wind energy: ready to power a sustainable Europe. Final report concerted action on wind energy in Europe NNE5-1999-562. In: Offshore wind energy CA-OWEE reports. Available via OWE. [http://www.offshorewindenergy.org/ca-owee/indexpages/downloads/CA-OWEE\\_Complete.pdf](http://www.offshorewindenergy.org/ca-owee/indexpages/downloads/CA-OWEE_Complete.pdf). Accessed 10 Apr 2016
- Davidson J, Hunsley C (eds) (1994) The reliability of mechanical systems. Mechanical Engineering Publications, London
- Department of Trade and Industry (DTI) (2002) Future offshore: a strategic framework for the offshore wind industry. Available via Tethys, Pacific Northwest National Laboratory (PNNL). <https://tethys.pnnl.gov/publications/future-offshore-strategic-framework-offshore-wind-industry>. Accessed 10 Aug 2016
- DoD (1980) Military standard MIL-STD-1629A: procedures for performing a failure mode, effects and criticality analysis. Department of Defense, United States. Alion System Reliability Center Publications. Available via SRC. <https://src.alionscience.com/pdf/MIL-STD-1629RevA.pdf>. Accessed 10 Apr 2016
- IRENA (2012) Wind power, renewable energy technologies cost analysis series, vol 1: power sector, Issue 5/5. In: International renewable energy agency. Available via IRENA. [https://www.irena.org/documentdownloads/publications/re\\_technologies\\_cost\\_analysis\\_wind\\_power.pdf](https://www.irena.org/documentdownloads/publications/re_technologies_cost_analysis_wind_power.pdf). Accessed 10 Apr 2016
- Karyotakis A (2011) On the optimization of operation and maintenance strategies for offshore wind farms. Dissertation, University College of London
- Krohn S, Morthorst PE, Awerbuch S (2009) The economics of wind energy: a report by the European Wind Energy Association. Available via EWEA. [http://www.ewea.org/fileadmin/ewea\\_documents/documents/publications/reports/Economics\\_of\\_Wind\\_Main\\_Report\\_FINAL-lr.pdf](http://www.ewea.org/fileadmin/ewea_documents/documents/publications/reports/Economics_of_Wind_Main_Report_FINAL-lr.pdf). Accessed 10 Apr 2016
- Malcolm DJ, Hansen AC (2006) WindPACT turbine rotor design study: June 2000–June 2002. Subcontract report NREL/SR-500-32495. In: National renewable energy laboratory documents. Available via NREL. <http://www.nrel.gov/docs/fy06osti/32495.pdf>. Accessed 10 Apr 2016
- Myhr A, Bjerkseter C, Agotnes A et al (2014) Levelised cost of energy for offshore floating wind turbines in a life cycle perspective. *Renew Energy* 66:714–728. doi:10.1016/j.renene.2014.01.017
- NAVAIR (2003) Naval air systems command fundamentals of reliability centered maintenance process (RCM) analysis: NAVAIR 00-25-403. <http://www.navair.navy.mil/logistics/rcm/index.cfm>. Accessed 10 Apr 2016
- Poore R, Walford C (2008) Development of an operations and maintenance cost model to identify cost of energy savings for low wind speed turbines. In: National renewable energy laboratory documents. Available via NREL. <http://www.nrel.gov/docs/fy08osti/40581.pdf>. Accessed 10 Apr 2016
- RAB (2010) Value breakdown for the offshore wind sector: a report commissioned by the Renewables Advisory Board (RAB). In: Gov.UK corporate reports. Available via Gov.UK. [https://www.gov.uk/government/uploads/system/uploads/attachment\\_data/file/48171/2806-value-breakdown-offshore-wind-sector.pdf](https://www.gov.uk/government/uploads/system/uploads/attachment_data/file/48171/2806-value-breakdown-offshore-wind-sector.pdf). Accessed 10 Apr 2016
- Reliawind (2011) Final report—Reliawind (reliability focused research on optimizing wind energy systems design, operation and maintenance: tools, proof of concepts, guidelines and methodologies for a new generation): 212966, FP7-Energy. European Commission, Community

Research and Development Information Service Publications. Available via CORDIS. [http://cordis.europa.eu/publication/rcn/14854\\_en.html](http://cordis.europa.eu/publication/rcn/14854_en.html). Accessed 10 Apr 2016

The Crown Estate (2010) A guide to an offshore wind farm. The Crown Estate Publications. Available via The Crown Estate. <http://www.thecrownestate.co.uk/media/5408/ei-a-guide-to-an-offshore-wind-farm.pdf>. Accessed 10 Apr 2016



**Part V**  
**CFD Analysis of a Complete Offshore**  
**Wind Turbine**

# Chapter 16

## An Overview of the CFD Analyses in the MARE-WINT Project

George N. Barakos

**Abstract** In the MARE-WINT project, two early stage researchers, researched and developed CFD methods for complete offshore wind turbine configurations. This brief chapter provides an overview of the work conducted by these two fellows.

The subsequent two chapters detail the work carried out during the MARE-WINT project on the CFD simulation of complete wind turbines. The term ‘complete’ needs to be clearly defined, since it is used here only in relation to the current CFD state-of-the-art. Often, Wind Turbine (WT) blades are analysed using grid-based Navier–Stokes methods under the assumption of steady flow with spatial symmetry between blades. The inflow to the blades is uniform, the tower, spinner and nacelle are typically ignored and the aeroelastic effects are absent.

The work at MARE-WINT progressed beyond the current state-of-the art by presenting results for configurations that include all blades, the tower and nacelle, aeroelasticity and even the effect of the wind turbine motion due to waves for floating off-shore configurations. An additional feature of the current work is that large scale wind turbines are considered in contrast to past CFD works that mainly simulated scaled wind turbines used for validation of CFD against wind tunnel data.

Two fellows contributed to this task, and one common theme between their works is that they both used compressible CFD solvers. This was driven by two reasons. On one hand, the solvers were readily available and well-validated for high speed aerodynamic flows (compressible flows) like flows around transonic aerofoils, cascades, helicopter rotors etc. The methods used low-Mach and all-Mach schemes to account for the relatively low speed flow around wind turbines. Both methods used multi-block structured grids with sliding grids to account for the relative motion between blades and the tower. The solvers used turbulence models of the  $k-\omega$  family for their work. The use of structured grids was combined with the use of aeroelastic methods. These fall within the established Fluid/Structure Interaction methods that are common in aerospace applications. The methods include not only modal-based representations of the blades but also mesh deformation, interpolation

---

G.N. Barakos (✉)  
Division of Aerospace Sciences, School of Engineering, University of Glasgow,  
James Watt South Building, Glasgow G12 8QQ, UK  
e-mail: [george.barakos@glasgow.ac.uk](mailto:george.barakos@glasgow.ac.uk)

and motion methods to accommodate the dynamic change of the blade shape during its motion.

One of the researchers went even further by considering flaps on the blades as described in other paragraphs of this book. Furthermore, the CFD methods were coupled with a hydrodynamic method to allow for the simultaneous solution of the liquid domain near the water-surface of off-shore cases. Additional modelling elements worth of mention here, include the use of a multi-body dynamics tool to allow for the effect of mooring lines and the overall rigid motion of the complex WT system to be accounted for effectively. The use of multi-body simulation is common in the context of simpler engineering methods than CFD, where the blade-element momentum theory is used to estimate the blade loads but it has so far been unexplored for grid-based Navier–Stokes methods.

To close the introduction to this part it should be mentioned that more elaborate models of complete wind turbines would include a time-varying inflow as well as a model of the drive-train and the control system of the WT. These are extensions that should be attempted by the fellows of MARE-WINT in the future as their work progresses and their skills are advancing. Needless to mention here that the CFD analyses of the complete wind turbines are to benefit from parallel computing and especially the use of new processor technologies like Graphical Processing Units as well as many-core machines like the Intel phil.

Extrapolating from this work, one expects to see in the future, work on extreme and fatigue loads with CFD replacing some of the BEM methods that are now used due to the large number of cases necessary to be computed for the overall loads envelope of a WT. Additional applications will include active rotors with flaps and flow control systems, as well as, direct simulation of wind turbine noise. Farm analysis is also expected to move away from the free-wake and actuator disk LES-like simulations, to properly resolved blades with high order schemes able to capture and maintain wakes for the necessary length of time and space.

**Open Access** This chapter is distributed under the terms of the Creative Commons Attribution-NonCommercial 4.0 International License (<http://creativecommons.org/licenses/by-nc/4.0/>), which permits any noncommercial use, duplication, adaptation, distribution and reproduction in any medium or format, as long as you give appropriate credit to the original author(s) and the source, provide a link to the Creative Commons license and indicate if changes were made.

The images or other third party material in this chapter are included in the work's Creative Commons license, unless indicated otherwise in the credit line; if such material is not included in the work's Creative Commons license and the respective action is not permitted by statutory regulation, users will need to obtain permission from the license holder to duplicate, adapt or reproduce the material.

# Chapter 17

## CFD Investigation of a Complete Floating Offshore Wind Turbine

Vladimir Leble and George N. Barakos

**Abstract** This chapter presents numerical computations for floating offshore wind turbines for a machine of 10-MW rated power. The rotors were computed using the Helicopter Multi-Block flow solver of the University of Glasgow that solves the Navier-Stokes equations in integral form using the arbitrary Lagrangian-Eulerian formulation for time-dependent domains with moving boundaries. Hydrodynamic loads on the support platform were computed using the Smoothed Particle Hydrodynamics method. This method is mesh-free, and represents the fluid by a set of discrete particles. The motion of the floating offshore wind turbine is computed using a Multi-Body Dynamic Model of rigid bodies and frictionless joints. Mooring cables are modelled as a set of springs and dampers. All solvers were validated separately before coupling, and the loosely coupled algorithm used is described in detail alongside the obtained results.

### Nomenclature

#### Latin

d	distance between particles (m)
I	inertia tensor ( $\text{kg m}^2$ )
m	mass (kg)
w	relative weight between the fluid and body particles (–)

#### Greek

$\alpha$	artificial viscosity parameter (–)
$\gamma$	adiabatic index (–)

---

V. Leble • G.N. Barakos (✉)  
Division of Aerospace Sciences, School of Engineering, University of Glasgow,  
James Watt South Building, Glasgow, G12 8QQ UK  
e-mail: [v.leble.1@research.gla.ac.uk](mailto:v.leble.1@research.gla.ac.uk); [george.barakos@glasgow.ac.uk](mailto:george.barakos@glasgow.ac.uk)

$\omega$	rotational velocity (rad/s)
$\tau$	gyroscopic torque (Nm)

## Acronyms

BEM	Blade Element Momentum method
BILU	Block-Incomplete Upper Lower factorisation
FOWT	Floating Off-shore Wind Turbine
FSI	Fluid Structure Interaction
GCG	Generalised Conjugate Gradient
GMRES	Generalised Minimal Residual method
HMB3	Helicopter Multi-Block CFD Solver
HPC	High Performance Computer
IBQN-LS	Interface Block Quasi-Newton with an approximation for the Jacobian from a Least-Squares mode
IQN-ILS	Interface Quasi-Newton algorithm with an approximation for the inverse of the Jacobian from a Least-Squares model
MBDM	Multi-Body Dynamic Model
MPI	Message Passing Interface library
SPH	Smoothed Particle Hydrodynamics Method

## 17.1 Motivation and Objectives

Over the years, offshore wind farms have moved further from the shore and into deeper waters. At the end of 2014, the average water depth of grid connected wind farms was 22.4 m and the average distance to shore 32.9 km. Projects under construction, consented and planned confirm that average water depths and distances to shore are likely to increase (Arapogianni et al. 2013). Shallow water regions suitable for seabed-fixed, offshore wind turbines are limited, and for sea depths exceeding 30–60 m, floating structures become more economic. Hence, emphasis is placed on the development of floating offshore wind turbines (FOWTs) with several prototypes already operational across the world (Arapogianni et al. 2013). Unlike onshore machines, the FOWT is a highly dynamic system subjected to the wind and wave loads and only constrained by a mooring system. Further, the rotor frequency is low due to the large size of the blades, and wave frequencies may come close or coincide with the rotational frequency of the rotor. It is, therefore, important to develop a method for the analysis of this air-structure-water system.

The common approach is to combine simplified tools into one hybrid model to predict wind turbine responses under wind and wave loads. The Blade Element Momentum (BEM) method is frequently used to calculate aerodynamic loads on the blades and tower (Jonkman 2007; Skaare et al. 2007; Karimirad and Moan 2013).

Sometimes analytical models are used that take the form of algebraic equations for the applied thrust that is proportional to the area of the rotor and the relative velocity between the wind and the hub as in Roddier et al. (2009) and Karimirad and Moan (2012). If aero-elasticity is considered, it is often included in BEM methods, where the structure is described by a multi-body formulation, in which wind turbine structures are subdivided into a number of bodies and each body consists of an assembly of Timoshenko beam elements (Larsen and Hanson 2007). Another approach is to characterise flexible bodies using linear modal representation, which usually assumes small deflections.

The hydrodynamic loads on the support structure are often modelled with a linear potential theory assuming inviscid, incompressible and irrotational flow, also known as Airy wave theory (Jonkman 2007; Rieper 2011; Karimirad and Moan 2013). In this case, frequency dependent hydrodynamic-added-mass and hydrodynamic-damping matrices, along with wave-excitation force vector are precomputed for a given problem, and serve as input to the coupled model. At the beginning of the computation, the wave-radiation-retardation kernel is obtained by integrating user-supplied added-mass or damping coefficients (Jonkman 2007). This way, external computer routines can be linked to the aerodynamic solver as a function that employs convolution integrals and returns hydrodynamic loads at given instances. The non-linear hydrodynamic viscous drag is included from Morison's equation (Morison et al. 1950) using strip theory. The drag coefficient involved in Morison's equation is often determined based on experiments. Since the drag coefficient depends on many factors, including the Reynolds number, geometry, and the presence of a free surface and a free end of a body, the experimental data is not always directly applicable. The drag coefficient can be obtained from a CFD computation for given support platform and then applied to Morison's equation improving the results as was shown by Benitz et al. (2015).

Linearization of the hydrodynamic problem implies that the translational displacements of the support platform are small relative to the size of the body, and that amplitudes of the incident waves are much smaller than their wavelengths i.e. steep or breaking waves cannot be modelled. Some extensions to the second-order potential flow was performed e.g. by Marino et al. (2011) and Roald et al. (2013). Even with second-order hydrodynamic terms included, however, the potential hydrodynamic theory might not completely apply to floating wind turbine platforms due to the large displacements encountered (Matha et al. 2011). Mooring lines constraining the FOWT can be modelled using springs (Savenije et al. 2010), flexible beams (Skaare et al. 2007) or multi-body chains of rigid bodies (Matha et al. 2011). Sometimes, precomputed nonlinear force-displacement relationships are employed, as in Karimirad and Moan (2012). Some of the works in the field of FOWT modelling are summarised in Table 17.1.

The purpose of this chapter is to present a coupling algorithm that brings together two Navier-Stokes solvers. For this, the Helicopter Multi-Block (HMB3) solver (Barakos et al. 2005) is used to solve for the aerodynamic forces acting on the wind turbine (WT) blades. Hydrodynamic forces on the support platform are solved using the Smoothed Particle Hydrodynamics (SPH) method (Gomez-Gesteira et al. 2012;

**Table 17.1** Works relevant for the complete FOWT models

Author(s)	Aerodynamic method	Hydrodynamic method
Jonkman (2007)	BEM	Linear potential
Skaare et al. (2007)	BEM	Linear potential
Roddir et al. (2009)	BEM	Linear potential
Karimirad and Moan (2013)	BEM/Analytical	Linear potential/Second-order potential/Morison's equation

Woodgate et al. 2013). Both solvers are coupled by exchanging information while the FOWT is represented by a lumped mass model.

## 17.2 Numerical Methods

HMB3 is a 3D multi-block structured solver for the Navier-Stokes equations in 3D. HMB3 solves the Navier-Stokes equations in integral form using the arbitrary Lagrangian-Eulerian formulation for time-dependent domains with moving boundaries (Dehaeze and Barakos 2012a, b; Carrión et al. 2014a). The solver uses a cell-centred finite volume approach combined with an implicit dual-time method (Jameson 1991). Osher's upwind scheme (Osher and Chakravarthy 1983) is used to resolve the convective fluxes. Central differences (CD) spatial discretisation is used for the viscous terms. The non-linear system of equations that is generated as a result of the linearization is solved by integration in pseudo-time using a first-order backward difference method. A Generalised Conjugate Gradient (GCG) method is then used (Eisenstat et al. 1983) in conjunction with a Block Incomplete Lower-Upper (BILU) factorisation as a pre-conditioner (Axelsson 1994). The HMB3 solver has a library of turbulence closures including several one- and two- equation models. Turbulence simulation is also possible using either the Large-Eddy or the Detached-Eddy simulation approach (Spalart et al. 1997). The solver was designed with parallel execution in mind and the MPI library along with a load-balancing algorithm are used to this end. The flow solver can be used in serial or parallel fashion for large-scale problems. Depending on the purposes of the simulations, steady and unsteady wind turbine CFD simulations can be performed in HMB3 using single or full rotor meshes generated using the ICEM-Hexa tool. Rigid or elastic blades can be simulated using static or dynamic computations. HMB3 allows for sliding meshes to simulate rotor-tower interaction cases as described in Steijl and Barakos (2008). Alternatively, overset grids can be used with the details presented in Jarkowski et al. (2013). To account for low-speed flows, the Low-Mach Roe scheme (LM-Roe) developed by Rieper (2011) is employed for wind turbine cases (Carrión et al. 2013). The chosen methodology allows for easy updating of the solver with new functions. One example presented here, is the coupling with a hydrodynamic solver.

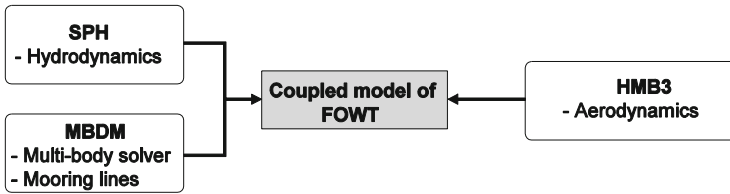


Fig. 17.1 Schematic of the solvers employed in the floating offshore wind turbine model

The sea is modelled with the SPH method (Gomez-Gesteira et al. 2012). Each SPH particle has individual material properties and moves according to the Navier-Stokes equations solved in the Lagrangian form. SPH offers a variety of advantages for fluid modelling, particularly those with a free surface and moving bodies. Due to the Lagrangian nature of the SPH method, the free surface requires no special treatment. Further, submerged bodies can be represented with particles. Therefore, it is natural for the method to include floating objects.

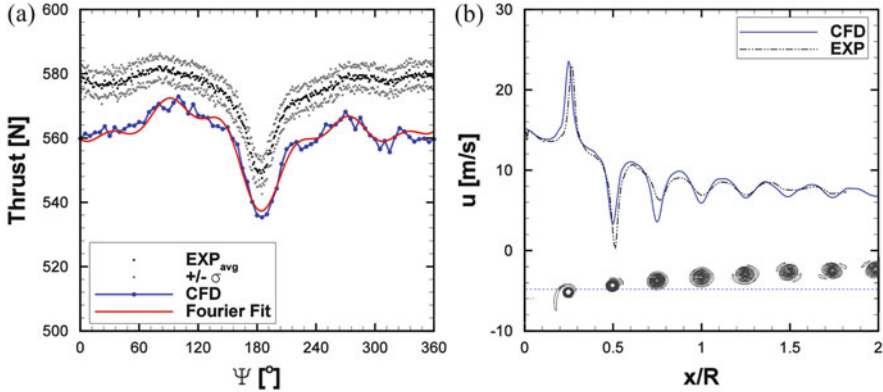
The motion of the FOWT components is computed with a multi-body model (MBDM) of rigid bodies and frictionless joints. Mooring cables are modelled as a set of springs and dampers, according to Savenije et al. (2010). The coordinate partitioning method of Nikraves (1988) is used to solve the resulting system of mixed differential-algebraic equations. The time integration scheme for independent variables is explicit and various schemes are implemented up to the Runge-Kutta method of fourth order. The non-linear position equations for dependent variables are solved using the Newton-Raphson method with exact, an analytical, Jacobian.

The current implementation is schematically presented in Fig. 17.1, where coupling is between both fluids. Another option would be to employ a multi-phase solver (e.g. Volume of Fluid as in Beyer et al. (2013)). This approach does not tackle the problem of coupling, but shifts it to the structure-fluid side.

### 17.2.1 Validation of the Aerodynamic Solver

The HMB3 CFD solver has so far been validated for several wind turbine cases, including the NREL Annex XX experiments (Gómez-Iradi et al. 2009), where the effect of the blades passing in front of the tower was captured, as can be seen by the deficit of the thrust values presented in Fig. 17.2a. The under-prediction of 3% is due to the fact that computations were performed at the nominal conditions for the experiment, and not for the measured pitch. A small change of pitch accounts for this difference. The pressure and PIV data of the MEXICO project (Schepers and Snel 2007, 2012) have also been used for validation (Carrión et al. 2014b), where the wake was resolved on a fine mesh capable to capture and preserve the vortices downstream the rotor (Fig. 17.2), which enabled the prediction of the onset of wake instabilities (Carrión et al. 2015).





Deficit in thrust of the NREL Annex XX blade when passing in front of the tower with corresponding Fourier series fit of five modes.

Axial velocity profile passing through the first vortex generated by the MEXICO blade.

**Fig. 17.2** Thrust prediction over a full revolution of the NREL Annex XX wind turbine at 7 m/s wind speed (a); and prediction of MEXICO rotor wake, including axial velocity profile (b) (Carrión et al. 2015)

### 17.2.2 Validation of the Hydrodynamic Solver

The hydrodynamic loads are estimated using the SPH method validated against the experiments of Greenhow and Lin (1983) for the high speed entry of a half-buoyant solid cylinder into calm water. As shown in Fig. 17.3a a cylinder of density of  $500 \text{ kg/m}^3$  was allowed to fall freely from the height of 0.8 m under gravity acceleration; the water depth was 0.3 m. The density of the cylinder was assigned by defining the relative weight between fluid and cylinder particles to be  $w = 0.5$ . Simulations were run with a cubic spline kernel, artificial viscosity with viscosity parameter  $\alpha = 0.1$ , adiabatic index  $\gamma = 7$ , and Courant-Friedrichs-Lewy number  $\text{CFL} = 0.2$ . The viscosity between the cylinder SPH particles and the fluid particles was neglected. Five cases were compared with different distances  $d$  between the particles. The penetration depth of the cylinder for all cases, along with the experimental results, are shown in Fig. 17.3b, whereas Fig. 17.4 shows the water surface deformation. The results were used for estimating the particle density and viscosity necessary for computations of floating bodies. Note that the best agreement with the experiment was obtained with distances between the particles  $d = 0.23 \text{ cm}$ , what corresponds to 25 particles per radius of the cylinder.

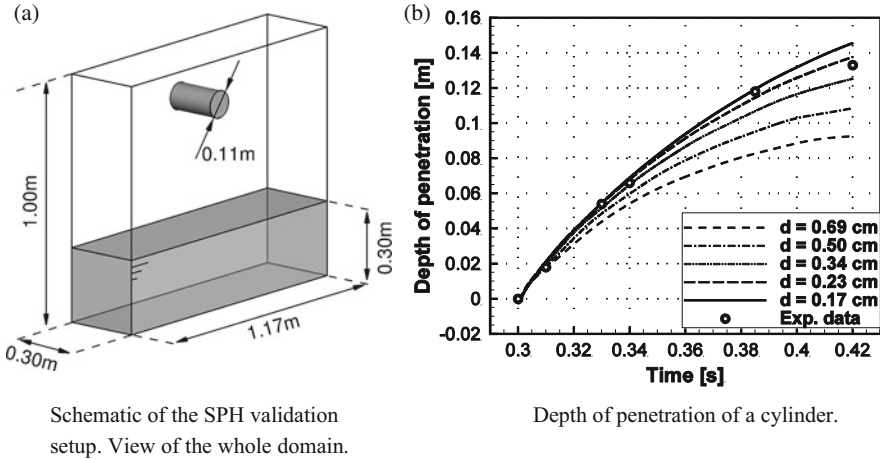


**Fig. 17.3** Validation case for the SPH solver. (a) Schematic of the SPH validation setup; (b) Depth of penetration of a cylinder of density  $500 \text{ kg/m}^3$ : SPH results for different distances between particles  $d$  and experimental results of Greenhow and Lin (1983)

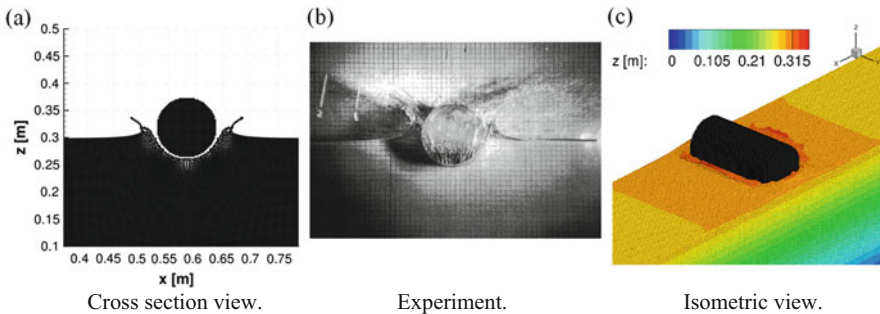


**Fig. 17.4** Surface deformation during water entry of a cylinder for time  $t = 0.32\text{s}$  from the beginning of the fall. Comparison between CFD results with distance  $d = 0.23 \text{ m}$  between particles

### 17.2.3 Validation of Multi-body Dynamics Solver

The MBDM was validated using simple mechanical systems of known solution as presented in Leble and Barakos (2016) like 2D and 3D slider-crank mechanisms. The gyroscopic wheel mechanism was used to validate that the gyroscopic effect is properly accounted for in the multi-body formulation. The ground body was placed at the origin at the global coordinate system. A short rod of length 0.1 m was attached to the ground body at height 1.0 m using a universal joint. The other end of the rod was connected to the centre of mass of the steel wheel with a revolute joint. A constant rotational speed of 60 rad/s was applied to the wheel by a revolute driver.

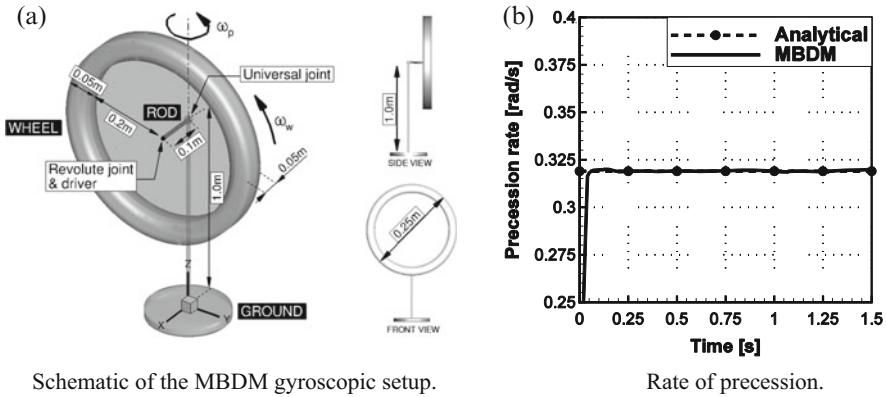


**Fig. 17.5** Validation of the MBDM to account for the gyroscopic effect. Test case setup (a), and rate of precession of the wheel (b)

**Table 17.2** Properties of the bodies employed to model the gyroscopic effect

Name	Mass (kg)	Inertia tensor (kg m <sup>2</sup> )
Wheel	28.3	$\begin{bmatrix} 1.45 & 0 & 0 \\ 0 & 0.73 & 0 \\ 0 & 0 & 0.73 \end{bmatrix}$
Rod	0.1	$\begin{bmatrix} 10^{-6} & 0 & 0 \\ 0 & 8.3 \times 10^{-5} & 0 \\ 0 & 0 & 8.3 \times 10^{-5} \end{bmatrix}$

The gravitational force acting in negative z direction was applied to all bodies, and at time  $t = 0$  system was assumed to have no precession.

The system is presented in Fig. 17.5a, while the mechanical properties of all bodies are shown in Table 17.2. The analytical solution was obtained from Eq. (17.1) using the gyroscopic approximation, i.e. assuming that precession is much slower than rotation of the wheel  $\omega_p \ll \omega_w$ , so that the magnitude of the angular velocity  $|\vec{\omega}| \cong |\omega_w|$  and that precession and rotation rates are nearly constant. Eq. (17.1) is shown below:

$$\omega_p = \tau/L = m_w g l / I_{xx} \omega_w \tag{17.1}$$

In Eq. (17.1),  $\omega_p$  is the angular velocity of precession,  $\tau$  is the moment due to gravity about the pivot point, and  $L$  is the angular momentum of the wheel. The expansion to the right-hand side involves the mass of the wheel  $m_w$ , the length of the rod  $l$ , the gravitational acceleration  $g$ , the mass moment of inertia of the wheel about the axis of rotation  $I_{xx}$ , and the rotational velocity of the wheel  $\omega_w$ . Substitution of values from Table 17.2 into Eq. (17.1) yields the rate of precession as  $\omega_p \approx 0.319$  rad/s. The results are presented in Fig. 17.5b, where the Runge-Kutta

integration scheme of fourth order was employed, with a time step  $\Delta t = 0.0001$ s. As can be seen, the rate of precession developed in less than 0.05s, and then maintained almost constant value that agreed with the one obtained using the gyroscopic approximation.

### 17.2.4 Coupling Algorithms

Coupling problems arise in many engineering problems, like fluid-structure interaction (FSI), but can also result from domain decomposition, where each sub-domain employs different discretisation or is solved with different method (Zienkiewicz et al. 2005). A multi-physics problem with adjacent domains can be simulated in a monolithic or in partitioned way. The former refers to the flow equations and structural equations being solved simultaneously, while the latter means that they are solved separately. The monolithic approach requires a specific solver for each particular combination of physical problems, whereas the partitioned approach allows for solver modularity. The partitioned approach also allows one to solve the fluid equations with different techniques developed specifically for the air and water. Further, this approach reduces the computational complexity per time-step, simplifies explicit/implicit treatment, facilitates sub-cycling, and eases replacements when better mathematical models and methods emerge in the fluid sub-disciplines. On the other hand, the partitioned simulation requires a special treatment to account for the interaction between the involved domains. Hence, computational efficiency over a monolithic approach is not necessarily guaranteed (Fellipa et al. 1999). The monolithic solution—which is the ultimate form of strong coupling, does not recognise the differences between the mathematical properties of the subsystems. Furthermore, it tends to ignore the issues of software modularity, availability, and integration, even though each of these issues can be in practice a major obstacle (Farhat et al. 2006). Considering that two available and validated solvers (HMB3 and SPH) can be used in this work, the emphasis is placed on partitioned algorithms.

Partitioned coupling can be weak or strong. Explicit algorithms are weak (or loose) as the solvers exchange information once per time step, and the coupled equations are not exactly satisfied due to explicit treatment. Depending on the formulation, one side of the coupling boundary conditions is usually lagging behind another. This can be improved with staggering or extrapolation techniques, but the scheme remains weak, and coupling errors may be introduced. However, loosely coupled algorithms are attractive, since among all solution methods, they are the simplest to implement for realistic applications, and the most computationally inexpensive per time step.

Implicit algorithms are strong (or tight), and enforce exactly the coupling conditions at each time level. This is obtained by conducting iterations until boundary equations are satisfied to certain, prescribed accuracy. The coupling problem can be formulated either as fixed-point or root-finding problem. For the former, fixed-point Jacobi or Gauss-Seidel methods can be employed. Although easy to implement,

those methods converge slowly if at all. Under-relaxation techniques can be used to improve convergence of the fixed-point iterations. Methods like fixed under-relaxation, adaptive Aitken's under-relaxation or steepest descent relaxation are some of the possible choices (Küttler and Wall 2008; Degroote et al. 2010). Newton's method can also be used. This method requires Jacobians relating the solutions of both solvers that are usually not known. This can be circumvented by employing approximation of Jacobian or Jacobian-vector product. Those types of coupling methods are called Quasi-Newton. Recently, new strongly coupled algorithms have been proposed.

Vierendeels et al. (2007) proposed an Interface Quasi-Newton algorithm with an approximation for the inverse of the Jacobian from a Least-Squares model (IQN-ILS). This approach was further investigated by Degroote et al. (2010), where they compared its performance with the Interface Block Quasi-Newton with an approximation for the Jacobian from a Least-Squares model (IBQN-LS), Aitken relaxation, and the Interface Generalised Minimal Residual method (Interface-GMRES(R)) algorithms. Demonstrated results showed that IQN-ILS and IBQN-LS performed similarly, using three times less evaluations and converging four times faster than the Aitken's relaxation method. IQN-ILS and IIBQN-LS were also found to use two times less evaluations and be almost three times faster than the Interface-GMRES algorithm.

Fernández and Moubachir (2005) reformulated fluid-structure interaction as a non-linear problem in the state of the structure, with the flow states considered as internal variables of the problem. This system was subsequently solved with the Newton-Raphson method using an exact Jacobian. The performance of this algorithm was compared with the performance of the Aitken relaxation and Quasi-Newton GMRES methods, for the inviscid flow in an elastic tube. Results showed that Aitken's relaxation was twice as slow as the Quasi-Newton and the exact Jacobian methods, and required almost 40 times more iterations. Further, for time steps of  $\Delta t = 10^{-4}$  s, both latter algorithms showed similar behaviour in convergence. However, for time steps of  $\Delta t = 10^{-3}$  s, the fixed-point and Quasi-Newton algorithms failed to converge. This implies sensitivity of the methods to the employed Jacobian.

The strong coupling may be important if the phenomena occurring in both fluids have similar time scales. Due to frequency similarities, resonances may occur and the exact response of a system will deviate from what is predicted by a loosely coupled algorithm. On the other hand, if time scales are largely different, loosely coupled algorithm may be sufficient. The exact bounds when the strong coupling is required for particular FOWT must be carefully assessed. Some indication comes from the waves and rotor frequency analysis. The sea state, wave height, wave frequency, and wind speed are empirically related in terms of range and most probable values e.g. in Lee et al. (1985). On the other hand, every wind turbine is designed to operate at a particular rotational frequency for a given wind speed. This allows one to construct a "Campbell" diagram for the FOWT investigated in this work (Fig. 17.6). It is clear that for sea states between 3 and 4 (or wind speed about 9 m/s) resonances may occur. The rated power production for this 10-MW

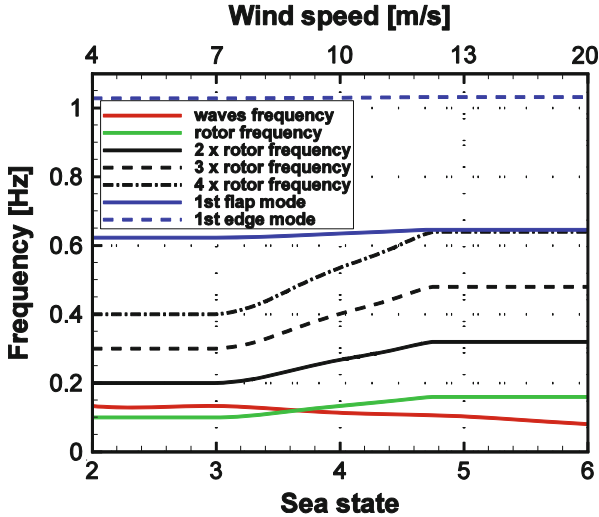


**Fig. 17.6** Campbell diagram for the investigated FOWT showing frequencies of the rotor and the waves as function of sea state and wind speed

FOWT corresponds to the wind speed of 11.4 m/s, or sea state 4. This indicates that for rated conditions, the weakly coupled algorithm may be sufficient.

### 17.2.5 Coupling Scheme and Its Implementation

In general, the exchange of information without stopping the computations can be implemented in three ways: through files, shared memory or the Message Passing Interface (MPI). Writing a file is the simplest solution. Both solvers can be launched separately and write files whenever exchange of information is required. This approach calls for very minor changes to both codes.

In the shared memory approach multiple processes have access to the same memory, allowing them to change it and read changes made by other processes. If the random access memory (RAM) is to be used, it requires a shared memory machine, which may not be available on a general High Performance Computer (HPC). The file system can be used instead by mapping the memory on the hard drive. This approach suffers from the same drawback as the case of writing files. That is, writing and reading from hard drive creates a bottleneck, and slows down the computation especially if information is exchanged often, and large amount of data is to be exchanged.

Both employed CFD solvers are parallelised using MPI and the Single Program, Multiple Data (SPMD) paradigm, where each instance of the solver is assigned to perform the same task on different sets of data. Therefore, the easiest way to

combine solvers is to employ MPI, but in Multiple Program, Multiple Data (MPMD) approach, where different programs operate on different sets of data.

However, direct MPMD implementation of SPMD solvers requires additional effort to split the global communicator, such that each of the solvers is in a separate communicator (MPI COMM WORLD) with a separate ordering of processes, as detailed in Castain et al. (2015). This can be avoided by dedicating one process to be in charge of executing both solvers with MPI\_Comm\_spawn routine.

In the present work, the communication between the solvers was established through the Message Passing Interface (MPI), where the MBDM is executed as a single process and is dedicated to start SPH and HMB3 parallel solvers. The data flow diagram of the implementation is presented in Fig. 17.7.

The communication was validated by executing separately SPH or HMB3 and comparing with the results were the body motion was introduced by MBDM. Due to the Lagrangian nature of the SPH method, the submerged bodies can be represented with particles and do not require specific coupling. Therefore, by utilising MPI, the MBDM substituted the body motion routines of the SPH solver and reduced the number of coupled codes to two—SPH and HMB3. This implies that MBDM is advancing in time with the same integration scheme as SPH using a symplectic method in this case (Leimkuhler et al. 1996).

In the present work, a weakly coupled approach is employed, namely the parallel, conventional, staggered method shown in Fig. 17.8. Both solvers are advancing with different but constant time steps. SPH employs a time step of  $\Delta t_{SPH} = 2 \times 10^{-4}$  s with CFL = 0.2, whereas HMB3 employs a time step of  $\Delta t_{HMB3} = 2 \times 10^{-2}$  s = 100 $\Delta t_{SPH}$  with implicit CFL = 5.0. The small time step for the SPH method is required by the explicit integration scheme. The HMB3 solver employs an implicit dual-time method by Jameson (1991) that is superior for larger time steps. Synchronisation of the solvers is performed at the end of each HMB3 step.

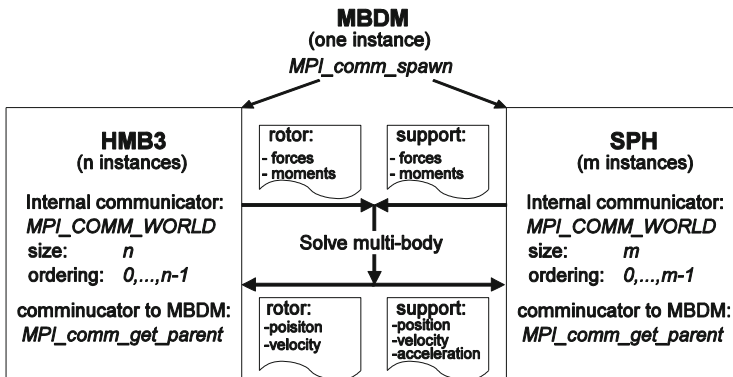


Fig. 17.7 Flow chart of the MPI implementation and data exchange for coupled model

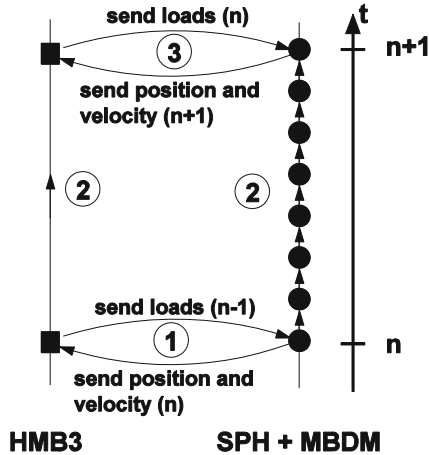


Fig. 17.8 The parallel conventional staggered method employed in present work

At the beginning of each synchronisation time step, the position and velocities of the rotor are transferred to the HMB3 aerodynamic solver, and forces and moments on the rotor are passed to the SPH. The two solvers are then advancing to a new time level with different methods and different number of steps. SPH performs 100 symplectic steps, while HMB3 performs 350 implicit pseudo-time steps. During the symplectic steps of the SPH code, the aerodynamic loads are kept constant (frozen). In return, the position and velocities of the rotor are kept constant during the implicit steps of HMB3. Once the synchronisation point is reached, the new position and velocities of all bodies, and rotor loads are obtained. Then, the algorithm proceeds to the new time level and information between the solvers is exchanged.

### 17.3 Test Case Description

A 10-MW wind turbine design by Bak et al. (2013) was used in this work. The blade consists of the FFA-W3 aerofoil family (Björck 1990) with the thickness ranging from 24 to 60 % of the chord. The blade has a non-linear distribution of the chord, the relative thickness of the section and the twist. The rotor diameter is 178.3 m, and the wind turbine operates at a wind speed of 11 m/s with a rotational speed of 8.8 rpm. The blades have a pre-coning of  $2.5^\circ$  and nonlinear pre-bending with 3.3 m displacement at the blade tip. The mass of the rotor is 228 tons, whereas mass of the nacelle and tower is 446 tons and 605 tons, respectively. The tilt of the nacelle in the original design is  $5^\circ$  nose up, but this was not included in the present model.

The wind turbine is attached to the floating support which consists of three cylindrical floats that increase the buoyancy and stability of the structure. A similar concept of the support platform was investigated by Roddier et al. (2009). Unlike



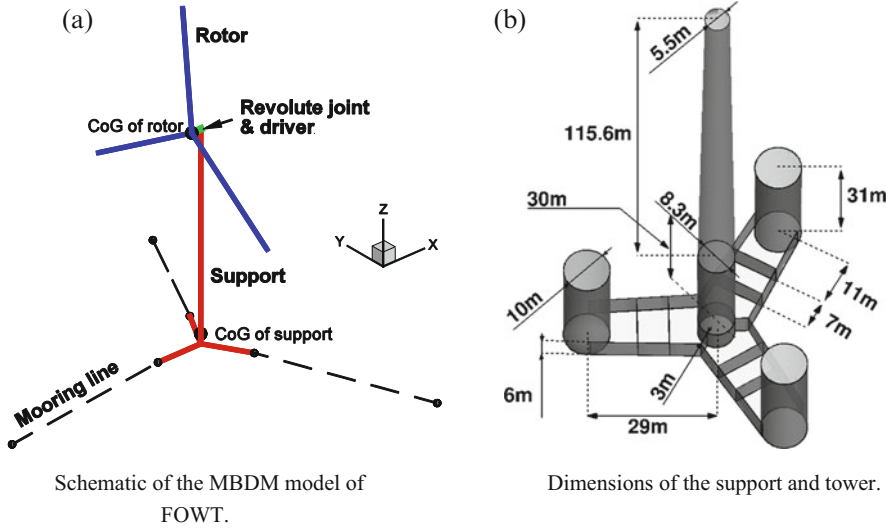


**Fig. 17.9** Schematic of the employed model of FOWT (a), and dimensions of the semi-submersible support and tower (b). FOWT model consists of three mooring lines and two rigid bodies: the rotor (blue) and combined body representing nacelle, tower and support (red). Adapted from Leble and Barakos (2016)

that design, the present support is simplified to be symmetric with respect to the location of the tower and the floats are connected to the base of the tower with a solid frame. The size of the tower is taken from Bak et al. (2013), and the dimensions of the support were calculated to provide sufficient buoyancy. A schematic of the studied FOWT is shown in Fig. 17.9.

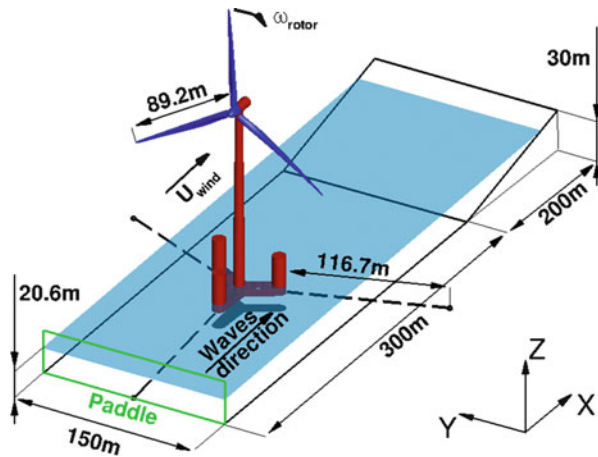
In the present model, the FOWT is represented by three mooring lines and two bodies, as shown in Fig. 17.9a. The first body represents the rotor (three blades with the spinner), and the second body represents the combined nacelle, tower and floating support rigidly linked to each other. The two bodies are connected by a revolute joint and a constraint of constant rotational speed is applied to the rotor. The resulting system has 6 unconstrained degrees of freedom. The mechanical properties of the bodies and mooring lines are presented in Table 17.3.

The FOWT is placed in a shallow tank of length 500 m, width 150 m and height 30 m. The tank is filled with water to a depth of 20.6 m. The waves are generated using a paddle on one side, and dissipated using a beach-like slope on the other side of the tank. The tank is presented in Fig. 17.10. Waves are generated to represent the specific sea state corresponding to a given wind speed. Based on the measurements of annual sea state occurrences in the North Atlantic and North Pacific (Lee et al. 1985), the wind speed of 11 m/s corresponds to a sea state 4 with a mean wave height of 1.88 m and a period of 8.8 s.

**Table 17.3** Mechanical properties of the employed bodies and mooring lines

Rotor	
m (kg)	227,962
I (kg m <sup>2</sup> )	$\begin{bmatrix} 1.56 \times 10^8 & 0 & 0 \\ 0 & 7.84 \times 10^7 & 0 \\ 0 & 0 & 7.84 \times 10^7 \end{bmatrix}$
Nacelle, support and tower	
m (kg)	4,223,938
I (kg m <sup>2</sup> )	$\begin{bmatrix} 2.03 \times 10^{10} & 0 & 0 \\ 0 & 2.03 \times 10^{10} & 0 \\ 0 & 0 & 2.81 \times 10^9 \end{bmatrix}$
Mooring lines	
120.0	Angle between adjacent lines (°)
20.6	Depth of anchors below SWL (m)
7.0	Depth of fairleads below SWL (m)
116.73	Length of the relaxed line (m)
400×10 <sup>6</sup>	Mooring line extensional stiffness (N/m)
40,000	Mooring line damping coefficient (Ns/m)

**Fig. 17.10** The FOWT model placed in a shallow tank. Mooring lines are shown with *dashed lines*. Adapted from Leble and Barakos (2016)



### 17.3.1 CFD Mesh

The aerodynamic grid consists of the rotor and nacelle i.e. the tower is not included and the effect of the blade passing on the tower is not investigated. The grid consists of 8M cells, where 24 cells are used in the first layer, and 166 cells are distributed around the aerofoil section as presented in Fig. 17.11a. The surface of the blade is resolved with 90 cells along the span, as shown in Fig. 17.11b. The size of the first cell in the direction normal to the surface was  $10^{-5}c$ , where  $c = 6.2$  m is the

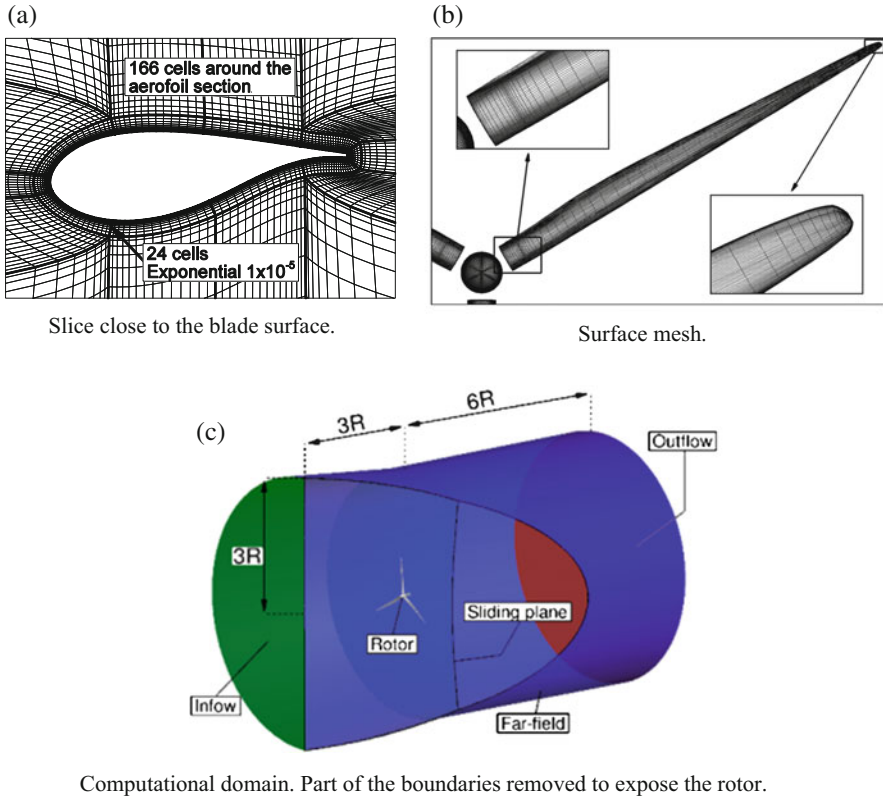


**Fig. 17.11** 8M mesh used to solve for aerodynamic loads. Slice through the volume close to the blade surface (a), surface mesh (b), and computational domain (c)

maximum chord of the blade. Based on the free-stream condition and the size of the first cell, the  $y^+$  parameter was estimated to be  $y^+ = 1.2$ . It must be noted that the grid was relatively coarse as compared with the one used by Carrión et al. (2015) to capture the wake of the MEXICO rotor. However, a grid convergence study showed that this density is sufficient to produce meaningful, grid-independent results.

The density of the air was assumed to be  $\rho = 1.225 \text{ kg/m}^3$ , the dynamic viscosity of the air was assumed to be  $\mu = 1.8 \times 10^{-5} \text{ Ns/m}^2$ , and the speed of sound was assumed to be 340 m/s. Further, the  $k-\omega$  SST turbulence model was employed with the free-stream level of turbulence at 2.6%. The flow was assumed to be fully turbulent, and the atmospheric boundary layer was not modelled. The uniform inflow boundary was set  $3R$  upstream of the rotor, and the outflow boundary was set  $6R$  downstream of the rotor, where  $R$  is the radius of the blade. The far-field boundary was assigned  $3R$  from the centre of rotation. In addition, the sliding plane was used to connect rotor to the nacelle and allow relative motion. The computational domain with corresponding boundaries, a slice through the mesh

close to the blade surface, and the surface mesh of the blade are presented in Fig. 17.11.

### 17.3.2 SPH Setup and Resolution

The hydrodynamic domain is resolved using 5M particles with initial uniform spacing of  $d = 0.625$  m. Note that the best agreement with experimental data was obtained for 25 particles per radius of the cylinder, as shown in Sect. 17.2.2. Here, the employed spacing corresponds to 9 particles per radius of the cylindrical leg, or to spacing  $d = 0.69$  cm in Fig. 17.3b. The coarse particle distribution was chosen for economies in CPU time, where coarse domain is obviously solved faster, but tends to under-predict the slamming loads on the structure. Three test were performed to investigate the influence of the domain width and particle spacing on the force acting on the support structure, as presented in Table 17.4. The average hydrodynamic forces acting on the support during 1 s of simulation were used for comparison. This time interval was chosen such that it leads to direct comparison of the average loads per unit of time. Percentage difference is computed relative to the size and spacing employed for the coupled computation. As can be seen, the size of the hydrodynamic domain has little effect on the average hydrodynamic force. On the other hand, improving the spatial resolution results in about 18 % difference in the hydrodynamic force. This agrees with observations made in Sect. 17.2.2. A spacing of  $d = 0.3125$  m would have been better, but to improve computational performance a spacing of  $d = 0.625$  m was employed.

### 17.3.3 Initial Conditions

Each of the solvers was executed separately before coupling to obtain a periodic solution of the loads. During this phase of computation the floating support was fixed, and the waves were generated for approximately 30 s. The rotor was set to spin about the axis aligned with the direction of the incoming wind, and was first solved using HMB3 “hover” formulation with 20,000 steps during which the L2 norm of the residual vector dropped below  $10^{-6}$ . Then, the unsteady computation was

**Table 17.4** Test cases investigating the influence of the domain width and particle spacing on the forces acting on the support structure

Domain size $x \times y$ (m)	Spacing $d$ (m)	1s averaged hydrodynamic force (N)	Difference (%)
500 × 150	0.6250	$1.070 \times 10^7$	–
500 × 300	0.6250	$1.068 \times 10^7$	0.20 %
500 × 150	0.3125	$1.267 \times 10^7$	18.40 %

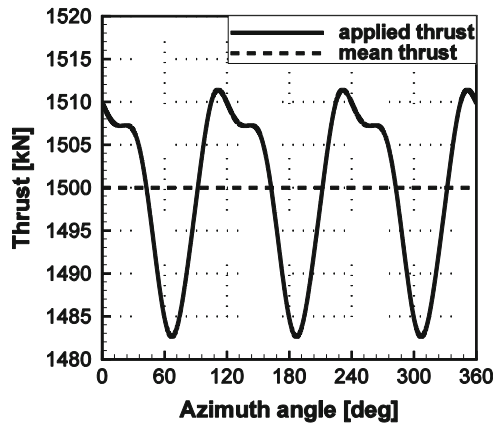
initiated and the flow was solved for an additional  $30^\circ$  of azimuth. The aerodynamic loads were almost constant during unsteady computation. Once the initial conditions were obtained, the coupled computations were initiated.

### 17.3.4 Demonstration Cases

The first demonstration case of the FOWT has the described configuration (see Fig. 17.10) with the difference that rotor was not included in multi-body formulation. Instead, the mass of the rotor was concentrated in the centre of gravity of the support to produce correct mass of the floating structure. In this way, the shift of the centre of mass due to rotor overhung was not considered. Further, the rotor inertia was not included, and the associated gyroscopic effects were not taken into account. The importance of these effects for the system at hand is assessed in the results section. Calm sea was considered, and the time varying thrust with the mean value of 1500 kN was applied at the location of the rotor. The thrust variation is shown in Fig. 17.12, and was estimated from a separate CFD computation of the rotor with the tower included.

This test case was solved for 150 s. Note that the demonstration case is not a coupled simulation, since the thrust force is prescribed and independent of the platform motion. The last test case was a coupled computation, as described in Sect. 17.2.5. This case was solved for 60 s, and allowed for almost 7 wave passages and about 9 revolutions of the rotor.

**Fig. 17.12** Thrust as function of azimuth angle of the rotor for decoupled case



## 17.4 Results and Discussion

### 17.4.1 Decoupled Case

The results of the first case are presented in Fig. 17.13. As can be seen, the FOWT moves in the direction of the thrust by about 0.215 m (displacement in  $x$ ). The FOWT also sinks in the water for about 0.603 m (displacement in  $z$ ), and tends to settle at a pitch angle of around 0.09 rad or  $5.2^\circ$  (rotation about  $y$  axis). The SPH particles are settling for the first 15 s as is visible in the acceleration plot. This cannot be avoided even if the floating body is fixed and particles are let to settle. This is because releasing the floating structure is equivalent to a drop, and therefore does not represent equilibrium.

The last 20s of lateral and rotational accelerations are presented in Fig. 17.14. The effect of time varying thrust on the angular acceleration in pitch (about  $y$  axis) can be seen in Fig. 17.14c. The variation in the shape and frequency corresponds to the applied time dependent thrust. The effect of time varying thrust on the lateral accelerations can be seen in Fig. 17.14. Again, the frequency of accelerations corresponds to the frequency of the thrust, but some phase shift is present and the shape of the response does not follow the shape of the thrust. This is because the motion in heave is linked to the applied thrust only through the rotational motion of the support i.e. through the second time integral of the angular acceleration that does follow the shape of the thrust as shown in Fig. 17.14c.

The acceleration in the  $x$  direction is directly linked to the applied thrust, and the frequency dependence on thrust without the phase shift is clearly visible. However, the shape of the acceleration is not following the shape of applied thrust. This is a result of high stiffness of the mooring lines in this direction, where high frequency response of the mooring system augments the overall response of the support platform.

There are three sources of momentum for the decoupled computation: hydrodynamics, prescribed aerodynamics and mooring lines. Time histories of forces and moments are presented in Fig. 17.15. Note that for clarity, the time starts at 25 s. Also, note the differences in magnitude of the computed moments, where moments about  $y$  axis are three orders of magnitude bigger, as compared to the other moment components.

First, it should be noted that mooring lines are in general opposing the hydrodynamic forces introduced by the SPH solver. This is not true for the pitching moment, where hydrodynamics and mooring lines are acting together to counter the imbalance of the moment due to the thrust. For the mooring lines, moment is created by the displacements of the fairleads, whereas for the hydrodynamics, moment is created by the change of the buoyancy introduced by the rotation of the support. As can be seen, the mooring lines contribute about 30%, whereas buoyancy about 70% of the restoring moment in this system. One would expect similar, cooperative behaviour for the forces in surge (in  $x$  direction). The obtained

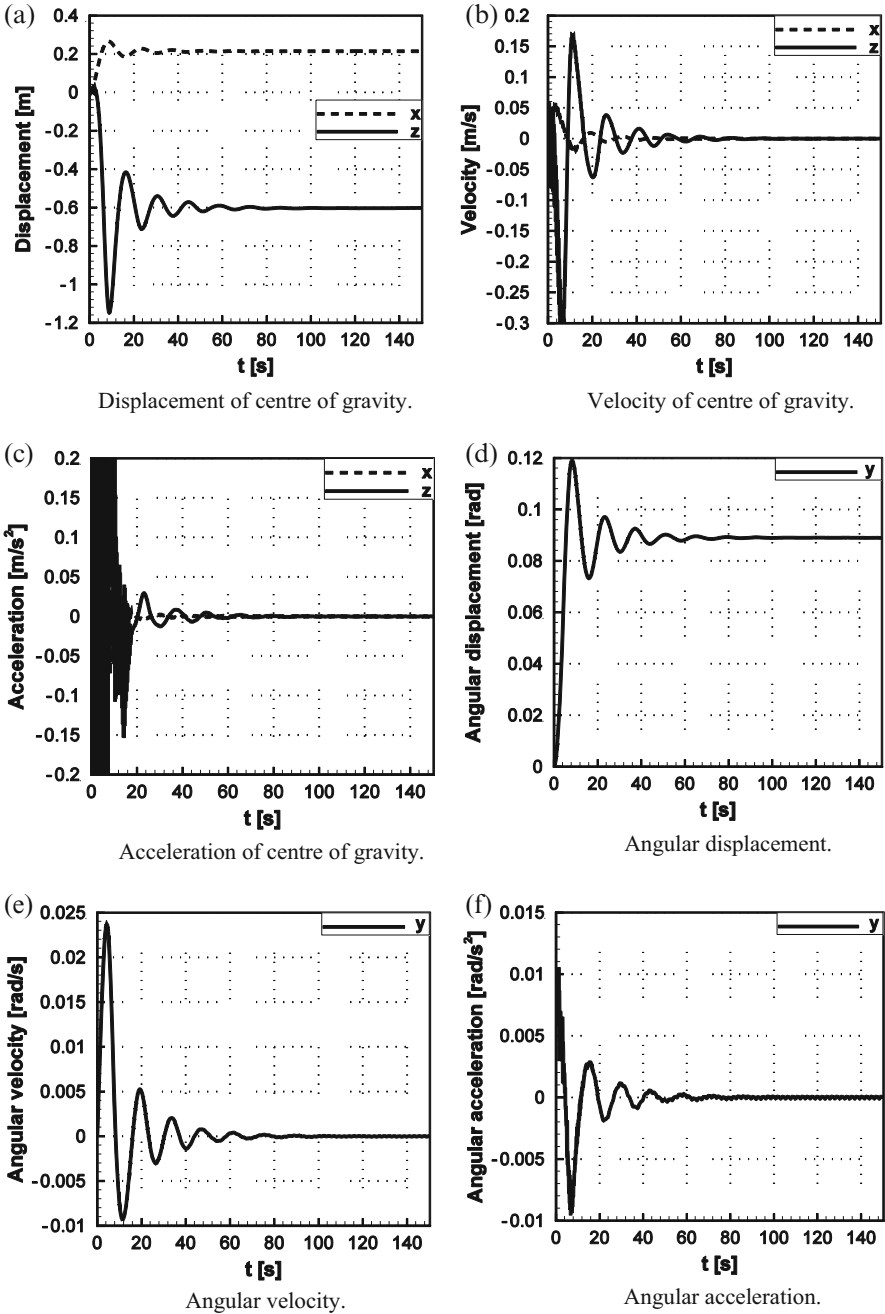
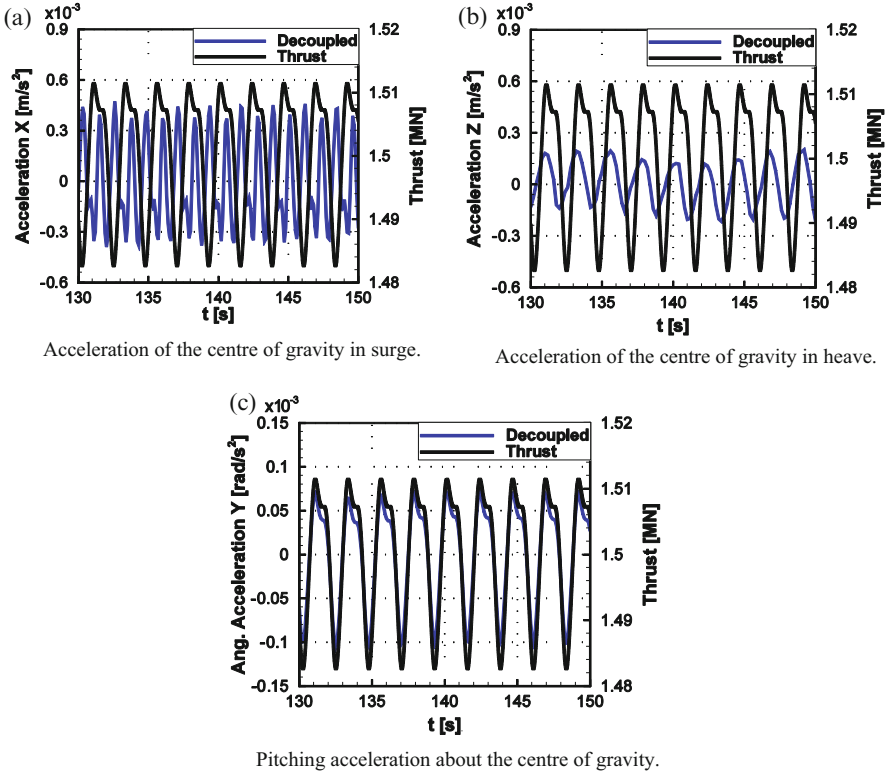


Fig. 17.13 Lateral and rotational dynamics of the support for decoupled case



**Fig. 17.14** The last 20 s of lateral and rotational accelerations of the support for decoupled case

results suggest otherwise, as shown in Fig. 17.15a. As can be seen, only the mooring lines are responsible for balancing the thrust force.

Since the water is considered calm for the decoupled case, the only source of hydrodynamic force acting in x direction is the hydrodynamic damping. Therefore, it is acting in the opposite direction of the motion, and as a result in opposite direction to the mooring force, which is a main source of motion in this direction. Lastly, small spurious moments and forces are noted, e.g. force in sway (y direction), which is normal to the plane of symmetry of the support. This is due to the SPH, where motion of the particles is never indeed symmetric. However, these discrepancies diminish with the number of particles, as was seen when test cases from Table 17.4 were computed.

Further, the SPH method is known for its pressure instabilities, where the pressure field of the particles exhibits large pressure oscillations due to acoustic waves present in compressible fluids. This is commonly tackled with solution smoothing techniques, also termed particles smoothing. Schemes up to the second order were proposed in the literature (Belytschko et al. 2000; Bilotta et al. 2011). In the present work, no particles smoothing was applied, including validation test



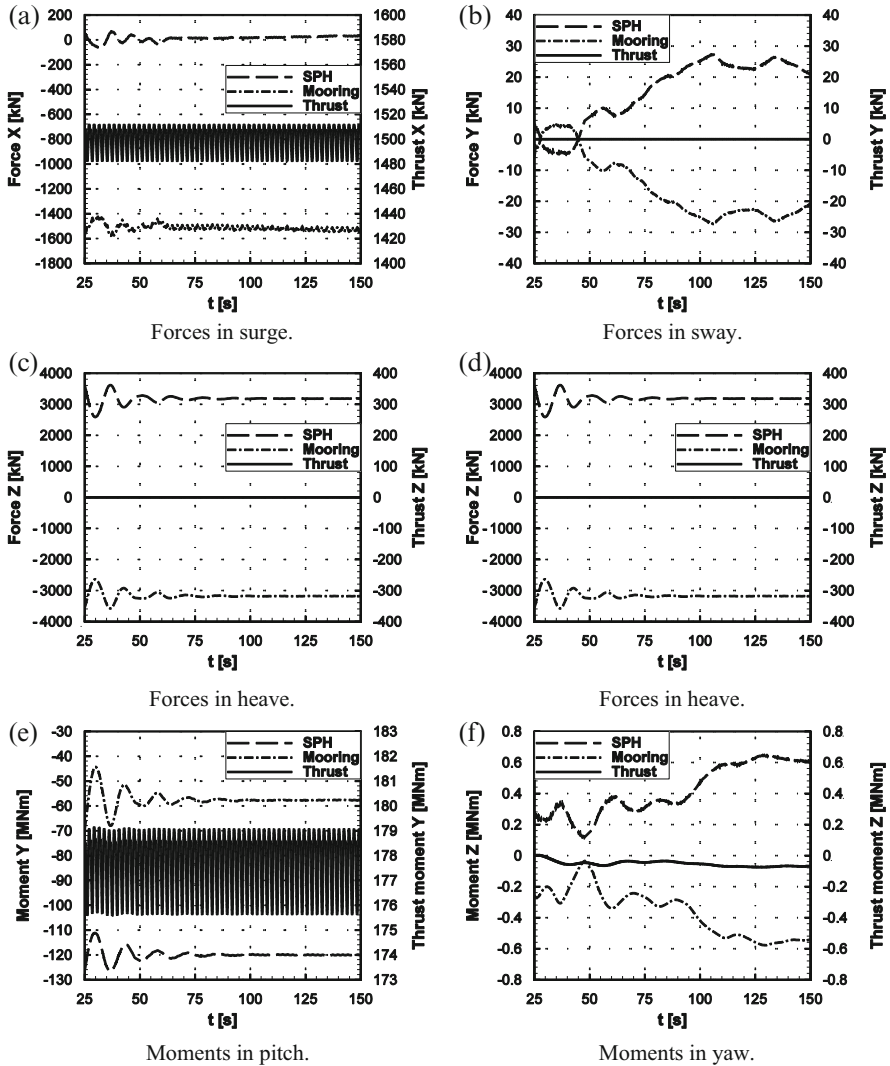


Fig. 17.15 Forces and moments acting at CoG of the support for decoupled case

cases. In fact, stability issues were encountered when a zero-order Shepard density filter was applied to the decoupled test case every 50 and 100 SPH steps. However, smoothing was shown to have a small effect on the overall pressure distribution for the artificial viscosity formulation used in this work (Gomez-Gesteira et al. 2012).

### 17.4.2 Coupled Case

Coupled computations were also performed, and results are presented in Fig. 17.16. As was mentioned in Sect. 17.2.5, the time step for SPH was set to  $\Delta t_{\text{SPH}} = 2 \times 10^{-4}$  s, whereas HMB3 employed a time step of  $\Delta t_{\text{HMB3}} = 2 \times 10^{-2}$  s =  $100\Delta t_{\text{SPH}}$ , or  $1.06^\circ$  of revolution per time step. The aerodynamic forces acting on the rotor as functions of time are shown in Fig. 17.17a. The platform motion shows similar trend as for the previous, decoupled test case. However, the rotor thrust is now dependent on the position and velocity of the rotor. As the wind turbine pitches under the thrust force, the rotor moves in the direction of the wind (velocity in x direction in Fig. 17.17b). In return, the thrust force decreases due to the reduced inflow speed and the orientation of the rotor disk. As the applied force is reduced, the rotor velocity decreases. The inverse relation between the aerodynamic force and velocity of the hub in x direction is clear in Fig. 17.17. Further, due to the pitch angle, a component of the thrust is acting along the z axis. As a result, the FOWT experiences higher displacement in heave:  $-0.8$  m as compared to  $-0.6$  m for the decoupled solutions. The initial motion of the FOWT is dominated by the imbalance of the forces due to the applied thrust, and the effect of the first wave passage is not visible. However, the effect of every consecutive wave is clearly visible in periodic variation of the moment about the y axis, as shown in Fig. 17.16f.

To facilitate the analysis of forces and moments acting on the system, the aerodynamic moments were transferred to the centre of gravity of the support platform. The resulting time histories of forces and moments for the coupled test case are presented in Fig. 17.18. First, we observe lasting for about 10 s high frequency hydrodynamic forces and moments due to initial particles settling. Similar was observed for decoupled test case. After an initial phase, the hydrodynamic forces show periodic variation related to the frequency of the passing waves. Next, the mooring line forces are opposing the SPH forces in all directions. Finally, periodic variation of the aerodynamic forces with frequency of the waves is noted. A phase shift is present, since the aerodynamic forces are dependent on velocity and position, rather than on forces, as was discussed in previous paragraphs.

For the moments, pitching moment (about y) is dominating and after the initial phase the solvers tend to a periodic solution. The aerodynamic moment follows the inverse relation to the hydrodynamic pitching moment. The phase shift for the mooring lines moment is present, as it depends on the orientation of the support. The aerodynamic moment about x axis applied at the rotor is a result of a driving force created by the lift and drag. Clearly, the driving force follows the same trend as the thrust force i.e. inverse relation with the velocity of the hub. The aerodynamic moment is transferred to the structure, and hydrodynamic and mooring lines moments are trying to compensate for this moment. Finally, the mooring lines are opposing the hydrodynamic moments for the moment about z axis (yawing).

Note that no significant gyroscopic effect was observed for this FOWT. The value of gyroscopic moment can be estimated using gyroscopic approximation as

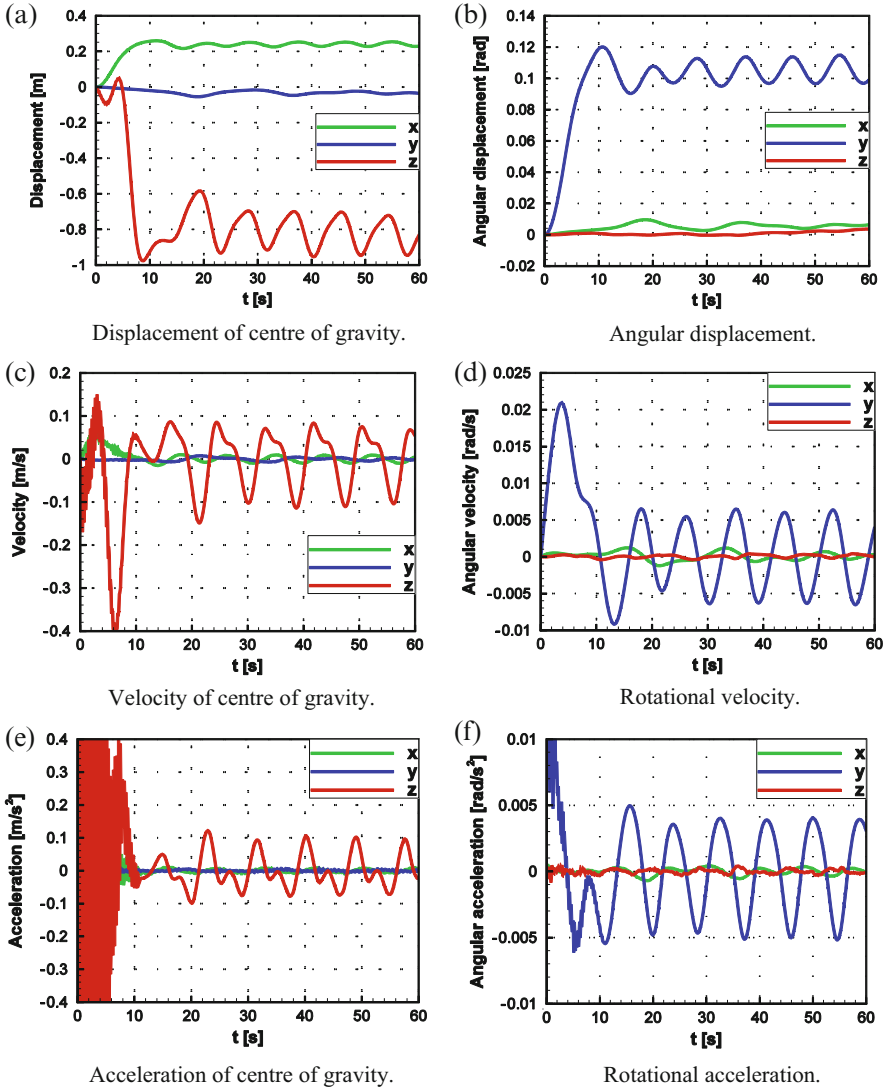
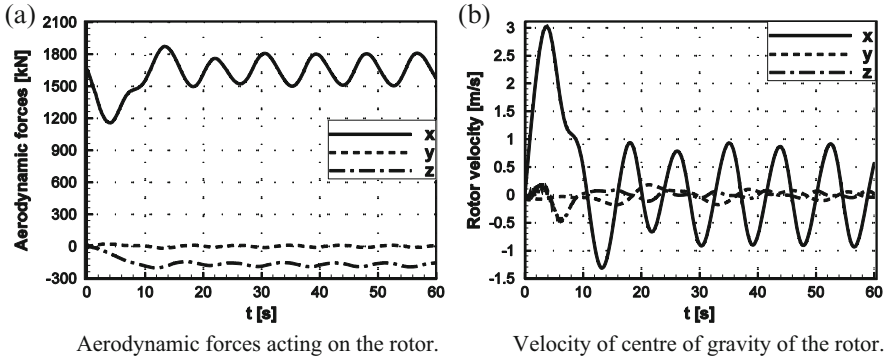


Fig. 17.16 Lateral and rotational dynamics of the support platform for coupled test case

$\tau = I_{zz}\omega_r\omega_p$ . In this case the precession rate  $\omega_p$  is caused by the waves, and gyroscopic torque  $\tau$  should develop about body-fixed yaw axis. The pitching angular velocity is shown in Fig. 17.16d and follows sinusoidal shape with amplitude  $\omega_p \approx 0.006$  rad/s. Given that the angular velocity of the rotor  $\omega_r = 0.92$  rad/s  $\gg \omega_p$ , some of the gyroscopic approximation assumptions are still valid. Substituting the above values and the mass moment of inertia of the rotor from Table 17.3 into the



**Fig. 17.17** Forces acting on the rotor and velocity of centre of gravity of the rotor as function of time for coupled computation

equation of gyroscopic approximation, it follows that the amplitude of gyroscopic torque is  $\tau = 0.86$  MNm.

Since FOWT is oscillating about a mean pitch angle of about  $0.11$  rad ( $6.3^\circ$ ), the gyroscopic torque has two components when projected on the direction of global axes: one about the global z-axis  $\tau_z = 0.77$  MNm, and one about the global x-axis  $\tau_x = 0.09$  MNm. As can be seen, the estimated magnitude of the rolling gyroscopic torque is about  $0.75\%$  of the mean aerodynamic moment in roll. Therefore, it can be considered negligible. On the other hand, the gyroscopic torque in yaw is comparable to other moments about the z-axis. However, those small moments did not cause significant rotation of the FOWT about this axis due to large inertia of the floater. The estimated magnitude of the gyroscopic torque is about  $0.35\%$  of the mean aerodynamic moment in pitch. This agrees with the observations made by Velazquez and Swartz (2012) that gyroscopic effect and resulting moment is small (less than  $5\%$ ) as compared to the pitching moment for horizontal axis wind turbines with low speed rotors.

Figure 17.19 presents different positions of the FOWT during the computation. The wave breaking effect of the support structure is visible, and the recovery of the waves behind the FOWT can be seen. The change of the pressure on the rotor can also be observed, especially at the tip of the nacelle. Note that the tower was not included in the aerodynamic domain; it is, however, shown in the figure, as the presence of the tower was accounted for in the multi-body model.

### 17.4.3 Computational Performance

For all cases, the SPH solver with MBDM were executed on a single 8 cores Intel<sup>®</sup> Xeon<sup>®</sup> CPU machine with 16 threads. Each of the CPU cores had a clock rate of 2 GHz, and 6.6 GB of dedicated memory. As no interconnect switch was

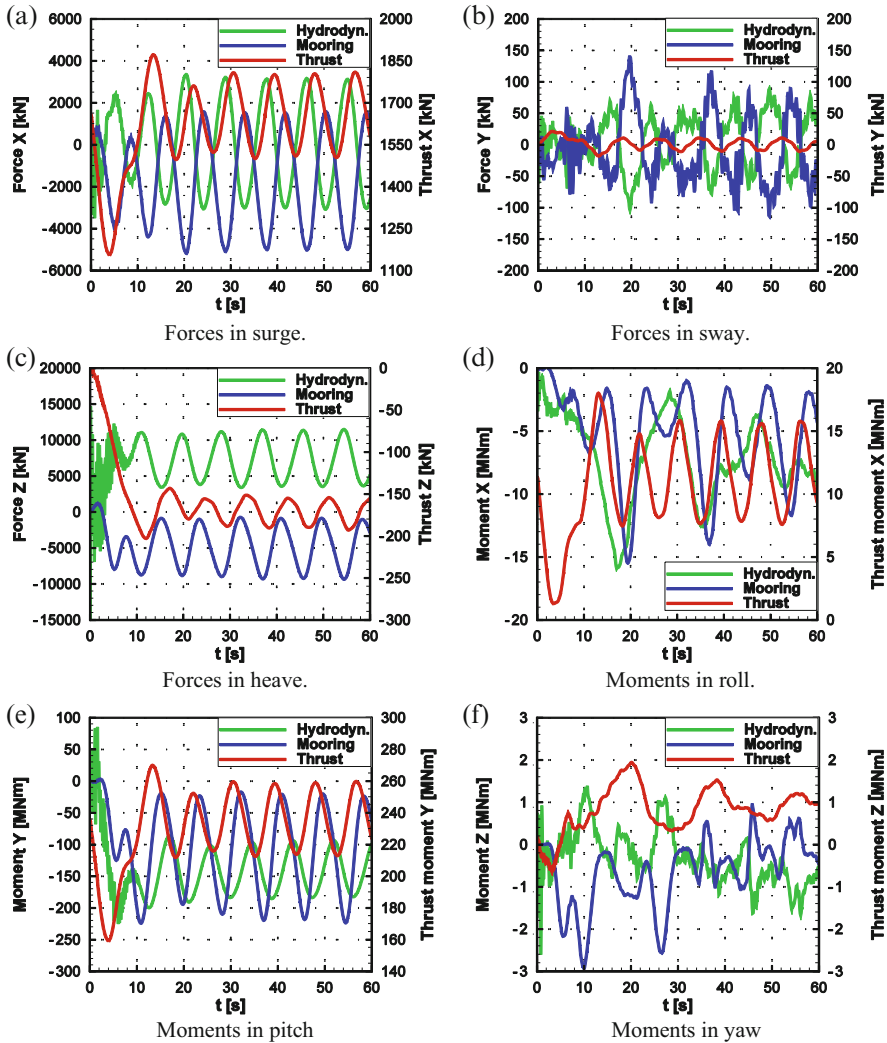
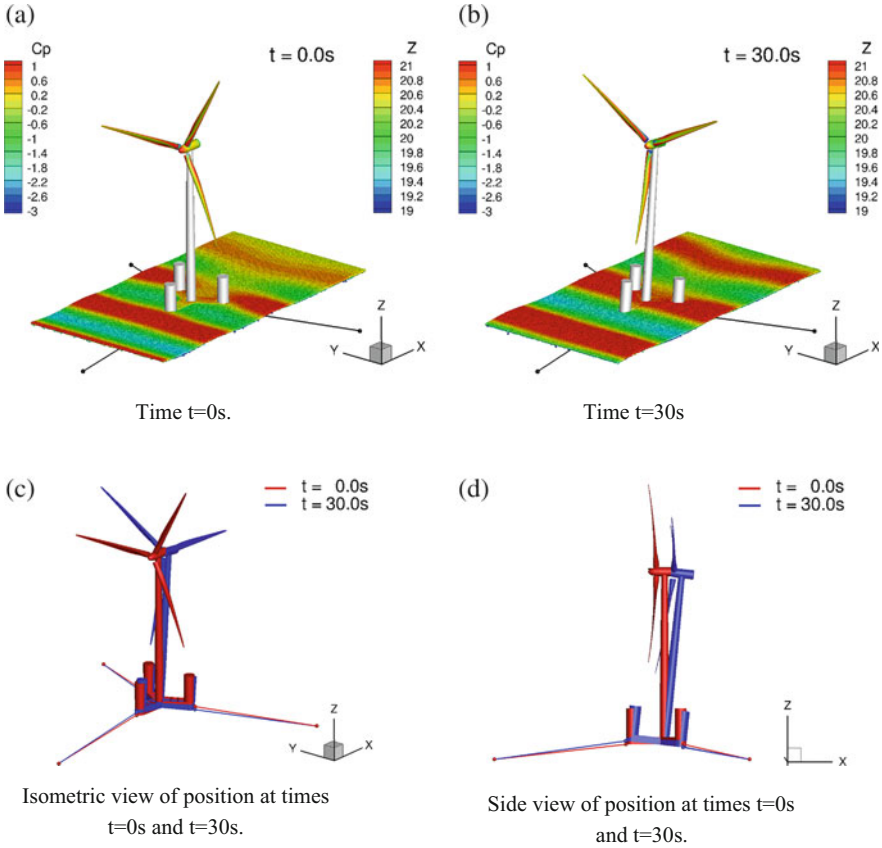


Fig. 17.18 Forces and moments acting at CoG of the support for the coupled test case

involved, the message passing delay between SPH and MBDM solvers was reduced to minimum. For the coupled case, HMB3 was executed on 29 dual-core AMD Opteron™ processors with 4 threads, giving in total 116 parallel instances of the solver. Each of the CPU cores had a clock rate of 2.4 GHz, and 4 GB of random access memory. It should be noted that the SPH method requires only local (limited by the kernel function) weighted average in the vicinity of the given particle, whereas HMB3 solves the complete set of equations involving all the cells in the



**Fig. 17.19** Position and orientation of the FOWT at times  $t = 0\text{ s}$  and  $t = 30\text{ s}$  during coupled computation. Contours on the rotor correspond to pressure coefficient  $C_p$ , contours on the water surface correspond to surface elevation  $z$  in meters

domain. Hence, more processing units were assigned to the aerodynamic side of the coupled problem.

The average time required to compute a second of the solution for the coupled case is 27.26 h, where about 27.25 h were spent to solve aerodynamics, 21.3 h to solve hydrodynamics, and 0.24 h to solve multi-body equations. The average time spent to exchange information for a second of the solution is 0.53 s, and was mostly dictated by the communication between the SPH and the MBDM solvers.

It should be noted that time accuracy can be improved, if the coupling step is reduced. In the presented coupled case, the information is exchanged every 100 SPH steps ( $\Delta t = 2 \times 10^{-2}$ ). When information between the solvers is exchanged every 50 SPH steps ( $\Delta t = 1 \times 10^{-2}$ ), the average time required to compute a second of the solution becomes 45.0 h. If information is exchanged every single SPH step ( $\Delta t = 2 \times 10^{-4}$ ), the average time per one second extends to about 438.9 h.

**Table 17.5** Computational performance of the coupling algorithm for various coupling time steps

Coupling $\Delta t$ (s)	HMB3 CFL no.	HMB3 Newton steps	SPH steps	Time per coupling step (s)	Time per 1s of solution (s)
$2 \times 10^{-2}$	5.0	315	100	$1.95 \times 10^3$	$9.81 \times 10^4$
$2 \times 10^{-2}$	10.0	350	100	$2.29 \times 10^3$	$1.15 \times 10^5$
$1 \times 10^{-2}$	5.0	237	50	$1.61 \times 10^3$	$1.62 \times 10^5$
$1 \times 10^{-2}$	10.0	105	50	$1.04 \times 10^3$	$1.06 \times 10^5$
$2 \times 10^{-4}$	5.0	45	1	$3.13 \times 10^2$	$1.58 \times 10^6$
$2 \times 10^{-4}$	10.0	23	1	$1.59 \times 10^2$	$7.97 \times 10^5$

In the former case, HMB3 requires on average 237 pseudo-time steps to achieve the level of convergence below  $10^{-2}$ , and 45 pseudo-time steps for the latter case. The convergence is defined as L2-norm of the residual vector. This suggests that computational cost can be further reduced by employing explicit schemes for both solvers and performing less evaluations (four for Runge-Kutta scheme of 4th order). However, the biggest possible explicit step for HMB3 that would satisfy explicit CFL condition of 0.4 for the smallest cell in the domain is about  $3.6 \times 10^{-9}$  s. Therefore, the aerodynamic time-step becomes the limiting factor for this approach and for the problem at hand. More information about the computational performance is presented in Table 17.5. Stability issues were encountered for a time step  $\Delta t = 2 \times 10^{-2}$  and HMB3 implicit CFL number 10.0, where the residual vector does not converge as fast as for CFL number 5.0. This indicates that CFL number of about 8.0 would be an optimal choice for this time step.

## 17.5 Conclusions

The chapter presented a coupling method for the analysis of the dynamics of floating offshore wind turbines. The HMB3 CFD solver was used for the analysis of blade aerodynamics and via a multi-body dynamics method it was coupled to a smoothed particle hydrodynamics tool to model the floating part of the turbine. The results showed that the weak coupling method is adequate for the solution of the problem at hand. Due to the lack of experimental data for a coupled system, validation was only possible for the components of the model. Data from the MEXICO project were used for aerodynamics; good overall agreement has been seen between CFD and test data. For the hydrodynamics solver, experiments related to drops of solid objects in water were used. Again, with a refined set of particles, the SPH method delivered good results. The third component of the method was the multi-body dynamics and this was validated using simple slider-crank problems.

Presented results demonstrated that a FOWT is a highly dynamic system. To obtain a deeper understanding of how rotor thrust and torque vary under dynamic conditions, efforts should be put forward to study the aerodynamic flow and loads as a wind turbine undergoes prescribed motion in pitch and yaw. It should be noted

that the spatial resolution of water employed in this work can be improved. In the future, a finer set of SPH particles will be employed and the tower will be included in the aerodynamic domain. Also, in the future, the work will continue with the validation of the method against experimental data, when available, and comparisons with a strong coupling technique. Another aspect that should be addressed is the experimental measurements. Clearly, each of the components can be validated separately, but the set of comprehensive data for the complete FOWT system is crucial for the model validation. The following measurements would be an asset: forces and moments due to the mooring system, water basin tests with small- or full-scale wind turbine including pressure distributions on support and rotor, and the overall FOWT time response including transient and periodic states.

**Acknowledgments** Results were obtained using the EPSRC funded ARCHIE-WeSt High Performance Computer ([www.archie-west.ac.uk](http://www.archie-west.ac.uk)). EPSRC grant no. EP/K000586/1.

**Open Access** This chapter is distributed under the terms of the Creative Commons Attribution-NonCommercial 4.0 International License (<http://creativecommons.org/licenses/by-nc/4.0/>), which permits any noncommercial use, duplication, adaptation, distribution and reproduction in any medium or format, as long as you give appropriate credit to the original author(s) and the source, provide a link to the Creative Commons license and indicate if changes were made.

The images or other third party material in this chapter are included in the work's Creative Commons license, unless indicated otherwise in the credit line; if such material is not included in the work's Creative Commons license and the respective action is not permitted by statutory regulation, users will need to obtain permission from the license holder to duplicate, adapt or reproduce the material.

## References

- Arapogianni A, Genachte AB, Ochagavia RM et al (2013) Deep water – the next step for offshore wind energy. In: European Wind Energy Association Publications. Available via EWEA. [http://www.ewea.org/fileadmin/files/library/publications/reports/Deep\\_Water.pdf](http://www.ewea.org/fileadmin/files/library/publications/reports/Deep_Water.pdf). Accessed 11 Apr 2016
- Axelsson O (1994) Iterative solution methods. Cambridge University Press, Cambridge
- Bak C, Zahle F, Bitsche R et al (2013) The DTU 10-MW reference wind turbine. In: DTU orbit – the research information system. Available via Technical University of Denmark. [http://orbit.dtu.dk/files/55645274/The\\_DTU\\_10MW\\_Reference\\_Turbine\\_Christian\\_Bak.pdf](http://orbit.dtu.dk/files/55645274/The_DTU_10MW_Reference_Turbine_Christian_Bak.pdf). Accessed 06 Apr 2016
- Barakos G, Steijl R, Badcock K et al (2005) Development of CFD capability for full helicopter engineering analysis. In: Abstracts of the 31st European Rotorcraft Forum 2005, AIDAA, Florence, 13–15 September 2005
- Belytschko T, Guo Y, Kam Liu W et al (2000) A unified stability analysis of meshless particle methods. *Int J Numer Methods Eng* 48(9):1359–1400
- Benitz M, Schmidt D, Lackner M et al (2015) Validation of hydrodynamic load models using CFD for the OC4 – DeepCwind Semisubmersible. Paper presented at the 33rd international conference on ocean, offshore and arctic engineering, ASME, St. John's, May 31–June 5 2015



- Beyer F, Arnold M, Cheng PW (2013) Analysis of floating offshore wind turbine hydrodynamics using coupled CFD and multibody methods. In: Chung JS, Langen I, Kokkinis T et al (eds) Proceedings of the twenty-third (2015) international offshore and polar engineering conference, Anchorage, June–July 2013. ISOPE, California, p 261
- Bilotta G, Russo G, Herault A et al (2011) Moving least-squares corrections for smoothed particle hydrodynamics. *Ann Geophys*. doi:[10.4401/ag-5344](https://doi.org/10.4401/ag-5344)
- Björck (1990) Coordinates and calculations for the FFA-W1-xxx, FFA-W2-xxx and FFA-W3-xxx series of airfoils for horizontal axis wind turbines. Technical report, The Aeronautical Research Institute of Sweden. In: National Renewable Energy Laboratory documents. Available via National Wind Technology Center's Information Portal (NWTc). <https://wind.nrel.gov/airfoils/Documents/FFA%20TN%201990-15%20v.1-2%20c.1.pdf>. Accessed 11 Apr 2016
- Carrión M, Woodgate M, Steijl R et al (2013) Implementation of all-mach roe-type schemes in fully implicit CFD solvers – demonstration for wind turbine flows. *Int J Numer Methods Fluids* 73(8):693–728. doi:[10.1002/fld.3818](https://doi.org/10.1002/fld.3818)
- Carrión M, Steijl R, Woodgate M et al (2014a) Aeroelastic analysis of wind turbines using a tightly coupled CFD-CSD method. *J Fluid Struct* 50:392–415
- Carrión M, Steijl R, Woodgate M et al (2014b) Computational fluid dynamics analysis of the wake behind the MEXICO rotor in axial flow conditions. *Wind Energy* 18(6):1023–1045. doi:[10.1002/we.1745](https://doi.org/10.1002/we.1745)
- Carrión M, Woodgate M, Steijl R et al (2015) Understanding wind-turbine wake breakdown using computational fluid dynamics. *AIAA J* 53(3):588–602
- Castain R, Ladd J, Solt D et al (2015) Supercomputing 2015 PMix BoF slides. In: Open MPI super computing papers. Available via Open MPI. <https://www.open-mpi.org/papers/sc-2015-pmix/PMix-BoF.pdf>. Accessed 11 Apr 2016
- Degroote J, Haelterman R, Annerel S et al (2010) Performance of partitioned procedures in fluid-structure interaction. *Comput Struct* 88(7-8):446–457
- Dehaeze F, Barakos GN (2012a) Hovering rotor computations using an aeroelastic blade model. *Aeronaut J* 116(1180):621–650
- Dehaeze F, Barakos GN (2012b) Mesh deformation method for rotor flows. *J Aircraft* 49(1):82–92. doi:[10.2514/1.C031251](https://doi.org/10.2514/1.C031251)
- Eisenstat SC, Elman HC, Schultz MH (1983) Variational iterative methods for nonsymmetric systems of linear equations. *SIAM J Numer Anal* 20(2):345–357. doi:[10.1137/0720023](https://doi.org/10.1137/0720023)
- Farhat C, Van der Zee K, Geuzaine R (2006) Provably second-order time-accurate loosely-coupled solution algorithms for transient nonlinear computational aeroelasticity. *Comput Methods Appl Mech* 195:1973–2001
- Fellippa CA, Park KC, Farhat C (1999) Partitioned analysis of coupled mechanical systems: Technical Report CU-CAS-99-06. In: University of Colorado, Department of Aerospace Engineering Sciences, Center for Aerospace Structures (CAS), Publications. Available via CAS. <http://www.colorado.edu/engineering/CAS/Felippa.d/FelippaHome.d/Publications.d/Report.CU-CAS-99-06.pdf>. Accessed 11 Apr 2016
- Fernández MA, Moubachir M (2005) A newton method using exact Jacobians for solving fluid-structure coupling. *Comput Struct* 83:127–142. doi:[10.1016/j.compstruc.2004.04.021](https://doi.org/10.1016/j.compstruc.2004.04.021)
- Gomez-Gesteira M, Rogers BD, Crespo AJ et al (2012) SPHysics – development of a free-surface fluid solver – part 1: theory and formulations. *Comput Geosci* 48:289–299. doi:[10.1016/j.cageo.2012.02.029](https://doi.org/10.1016/j.cageo.2012.02.029)
- Gómez-Iradi S, Steijl R, Barakos GN (2009) Development and validation of a CFD technique for the aerodynamic analysis of HAWT. *J Sol Energy Eng*. doi:[10.1115/1.3139144](https://doi.org/10.1115/1.3139144)
- Greenhow M, Lin WM (1983) Nonlinear-free surface effects: experiments and theory. Technical Report 83–19, Massachusetts Institute of Technology, Department of Ocean Engineering. In: US Department of Defense publications. Available via Defense Technical Information Center (DTIC). <http://www.dtic.mil/dtic/tr/fulltext/u2/a161079.pdf>. Accessed 11 Apr 2016
- Jameson A (1991) Time dependent calculations using multigrid, with applications to unsteady flows past airfoils and wings. In: Abstracts of the 10th computational fluid dynamics conference, fluid dynamics and co-located conferences, AIAA, Honolulu, 24–26 June 1991

- Jarkowski M, Woodgate MA, Barakos GN et al (2013) Towards consistent hybrid overset mesh methods for rotorcraft CFD. *Int J Numer Methods Fluids* 74(8):543–576. doi:[10.1002/flid.3861](https://doi.org/10.1002/flid.3861)
- Jonkman J (2007) Dynamics modeling and loads analysis of an offshore floating wind turbine, technical report NREL/TP-500-41958. In: National Renewable Energy Laboratory Documents. Available via NREL. <http://www.nrel.gov/docs/fy08osti/41958.pdf>. Accessed 11 Apr 2016
- Karimirad M, Moan T (2012) A simplified method for coupled analysis of floating offshore wind turbines. *Mar Struct* 27(1):5–63
- Karimirad M, Moan T (2013) Modeling aspects of a floating wind turbine for coupled wave – wind-induced dynamic analyses. *Renew Energy* 53:299–305
- Küttler U, Wall WA (2008) Fixed-point fluid–structure interaction solvers with dynamic relaxation. *Comput Mech* 43(1):61–72
- Larsen TJ, Hanson TD (2007) A method to avoid negative damped low frequent tower vibrations for a floating, pitch controlled wind turbine. *J Phys Conf Ser.* doi:[10.1088/1742-6596/75/1/012073](https://doi.org/10.1088/1742-6596/75/1/012073)
- Leble V, Barakos G (2016) Demonstration of a coupled floating offshore wind turbine analysis with high-fidelity methods. *J Fluid Struct* 62:272–293
- Lee WT, Bales SL, Sowby SE (1985) Standardized wind and wave environments for North Pacific Ocean Areas. David W Taylor Naval Ship Research and Development Center. Technical Report DTNSRDC/SPD-0919-02. In: US Department of Defense publications. Available via Defense Technical Information Center (DTIC). <http://www.dtic.mil/cgi-bin/GetTRDoc?Location=U2&doc=GetTRDoc.pdf&AD=ADA159393>. Accessed 11 Apr 2016
- Leimkuhler BJ, Reich S, Skeel RD et al (1996) Integration methods for molecular dynamics springer. In: Schulten K, Sumners DW (eds) *Mathematical approaches to biomolecular structure and dynamics*. The IMA volumes in mathematics and its applications, vol 82. Springer, New York, p 161
- Marino E, Borri C, Peil U (2011) A fully nonlinear wave model to account for breaking wave impact loads on offshore wind turbines. *J Wind Eng Ind Aerod* 99(4):483–490
- Matha D, Schlipf M, Cordle A et al (2011) Challenges in simulation of aerodynamics, hydrodynamics, and mooring-line dynamics of floating offshore wind turbines. Paper presented at the 21st offshore and polar engineering conference, Maui, 19–24 June 2011
- Morison J, O’Brein M, Johnson J et al (1950) The force exerted by surface waves on piles. *J Petrol Technol* 2:149–154
- Nikravesh PE (1988) *Computer-aided analysis of mechanical systems*. Prentice Hall, Upper Saddle River
- Osher S, Chakravarthy S (1983) Upwind schemes and boundary conditions with applications to Euler equations in general geometries. *J Comput Phys* 50(3):447–481
- Rieper F (2011) A low-Mach number fix for Roe’s approximate Riemann solver. *J Comput Phys* 230(13):5263–5287. doi:[10.1016/j.jcp.2011.03.025](https://doi.org/10.1016/j.jcp.2011.03.025)
- Roald L, Jonkman J, Robertson A et al (2013) The effect of second-order hydrodynamics on floating offshore wind turbines. *Energy Procedia* 35:253–264
- Roddier D, Cermelli C, Weinstein A (2009) WindFloat: a floating foundation for offshore wind turbines – part I: design basis and qualification process. In: Abstracts of the ASME 2009 28th international conference on ocean, offshore and arctic engineering, ASME, Honolulu, 31 May–5 June 2009
- Savenije LB, Ashuri T, Bussel GJ et al (2010) Dynamic modeling of a spar-type floating offshore wind turbine. Paper presented at the European Wind Energy Conference and Exhibition (EWEC), Warsaw, 20–23 April 2010
- Schepers JG, Snel H (2007) Model experiments in controlled conditions, final report ECN-E-07-042. In: Energy Research Center of the Netherlands (ECN) reports. Available via ECN. <http://www.ecn.nl/docs/library/report/2007/e07042.pdf>. Accessed 11 Apr 2016

- Schepers JG, Snel H (2012). Final report of IEA Task 29, MexNext (Phase I): analysis of Mexico wind tunnel measurements. Technical Report, Energy Research Center of the Netherlands, ECN. In: Energy Research Center of the Netherlands (ECN) reports. Available via ECN. [http://www.mexnext.org/fileadmin/mexnext/user/documents/FinRep\\_Mexnext\\_v6\\_opt.pdf](http://www.mexnext.org/fileadmin/mexnext/user/documents/FinRep_Mexnext_v6_opt.pdf). Accessed 11 Apr 2016
- Skaare B, Hanson T, Nielsen F et al (2007) Integrated dynamic analysis of floating offshore wind turbines. Paper presented at the European Wind Energy Conference and Exhibition (EWEC), Milan, 07–10 May 2007
- Spalart P, Jou W, Strelets M et al (1997) Comments on the feasibility of LES for wings, and on a hybrid RANS/LES approach. In: Liu C, Liu Z (eds) Proceedings of the first AFOSR international conference on DNS/LES, Louisiana, 1997
- Steijl R, Barakos G (2008) Sliding mesh algorithm for CFD analysis of helicopter rotor-fuselage aerodynamics. *Int J Numer Methods Fluids* 58:527–549. doi:10.1002/flid.1757
- Velazquez A, Swartz RA (2012) Gyroscopic effects of horizontal axis wind turbines using stochastic aeroelasticity via spinning finite elements. In: Abstracts of the ASME 2012 conference on smart materials, adaptive structures and intelligent systems, ASME, Stone Mountain, 19–21 September 2012
- Vierendeels J, Lanoye L, Degroote J et al (2007) Implicit coupling of partitioned fluid-structure interaction problems with reduced order models. *Compos Struct* 85:970–976. doi:10.1016/j.compstruc.2006.11.006
- Woodgate MA, Barakos GN, Scrase N et al (2013) Simulation of helicopter ditching using smoothed particle hydrodynamics. In: Abstracts of the 39th European Rotorcraft Forum 2013. AIDAA, Moscow, 3–6 September 2013
- Zienkiewicz O, Taylor R, Zhu JZ (2005) *The Finite element method*, 6th edn. Butterworth-Heinemann, Oxford

# Chapter 18

## CFD Study of DTU 10 MW RWT Aeroelasticity and Rotor-Tower Interactions

Sergio González Horcas, François Debrabandere, Benoît Tartinville, Charles Hirsch, and Grégory Coussement

**Abstract** A numerical analysis of the DTU 10 MW RWT wind turbine aerodynamics is presented in this work. The development of an innovative methodology based on three-dimensional computational fluid dynamics allowed to tackle two challenging problems related to this application. On one hand, the impact of blade deflections on rotor performance was assessed in a *rotor-only* context. Different blade configurations were studied, including the installation of *Gurney flaps* and the consideration of *prebending* and *preconing*. On the other hand, flow unsteadiness of the *full machine* (i.e. including the tower) was modeled by means of the *Non-Linear Harmonic* method. This approach allowed to characterize local aspects of the flow and the impact of *rotor-tower interactions* on the computed loads.

### 18.1 Introduction

Industry standards for the aeroelastic simulations of horizontal axis wind turbines are based on the *Blade Element Momentum* (BEM) theory. For classical machine designs, such a method offers a very good computational efficiency and an acceptable flow response. BEM base formulation has been improved along with *onshore* wind turbines evolution, thanks to the introduction of additional sub-models (Jonkman and Buhl 2007; Heege et al. 2013). The accuracy of this approach is however limited when dealing with large *Offshore Wind Turbine* (OWT) rotors due to the existence of highly skewed flows and heavy detachments. Hence, the use of more sophisticated *Computational Fluid Dynamics* (CFD) techniques is justified.

---

S.G. Horcas (✉) • F. Debrabandere • B. Tartinville • C. Hirsch  
NUMECA International, 189 Ch. de la Hulpe, B-1170 Bruxelles, Belgium  
e-mail: [sergio.horcas@gmail.com](mailto:sergio.horcas@gmail.com); [francois.debrabandere@numeca.be](mailto:francois.debrabandere@numeca.be);  
[benoit.tartinville@numeca.be](mailto:benoit.tartinville@numeca.be); [charles.hirsch@numeca.be](mailto:charles.hirsch@numeca.be)

G. Coussement  
Faculty of Engineering, Fluids-Machines Department, University of Mons, 53 Rue du Joncquois,  
B-7000 Mons, Belgium  
e-mail: [gregory.coussement@umons.ac.be](mailto:gregory.coussement@umons.ac.be)

Due to the continuous upscaling of modern OWTs, important *aeroelastic effects* are also expected. Traditional CFD approaches do not consider the flexibility of the rotor. However, blade deflections can have a non negligible impact on the machine performance, and a possible *blade-tower impact* should be considered at the design stage. This requires the consideration of rotor structural models in CFD computations. Due to the lack of publicly available *industrial* configurations, previous studies concerning wind turbines *aeroelasticity* are based on the so-called *academic* or *reference* designs. In this group we find the works of Corson et al. (2012) for the SNL-100-00 blade and the studies of the NREL 5 MW performed by Hsu and Bazilevs (2012) and Yu and Kwon (2014). In all these publications, blade deflections were found to have a direct impact on the final rotor performance.

Previous CFD studies of wind turbine rotors are based on steady flow *rotor-only* simulations (where only blades, hub and nacelle geometries are considered). Thanks to the problem periodicity when assuming an incoming wind aligned with the rotor axis, a single *blade passage* is normally meshed. These simulations allow to characterize the local flow behaviour around the wind turbine and its impact on global rotor performance with a reduced computational effort. However, by omitting the tower geometry the main source of flow unsteadiness is also neglected. Indeed, due to the proximity of the rotor to the tower, the generation of complex unsteady flow phenomena is expected. This mechanism is often referred as *rotor-tower interactions*. First NREL Phase VI publications assessing this topic revealed the existence of both blade and tower *shedding* phenomena and fluctuating loads generation related to the *blade-tower alignment* event (Zahle et al. 2009; Lynch 2011; Wang et al. 2012; Hsu et al. 2014; Li 2014). Similar unsteady effects were computed for the NREL 5 MW studies of Hsu and Bazilevs (2012) and Yu and Kwon (2014), and in the *industrial* wind turbines publications of Zahle and Sørensen (2008, 2011).

In this chapter high fidelity CFD models were used in order to characterize the rotor aerodynamics of the DTU 10 MW RWT *reference* wind turbine (Bak et al. 2013), whose main parameters are summarized in Table 18.1. *Aeroelasticity* and *rotor-tower interactions* problems were assessed in two independent numerical studies. In Sect. 18.2, *rotor-only* simulations were performed based on the computational framework for OWT rotors *static aeroelasticity* analysis developed by Horcas et al. (2014). In particular, the impact of *Gurney flaps* installation and the effect of *prebending* and *preconing* on rotor performance were evaluated. This work can be understood as a continuation of previous DTU 10 MW RWT studies (Horcas et al. 2015a,b). In Sect. 18.3, the flow unsteadiness related to *rotor-tower interactions* was characterized by means of the *Non Linear Harmonics* (NLH) method presented by Vilmin et al. (2006).

The present computational analysis was performed using the commercial CFD package FINE™/Turbo (NUMECA International 2013b). This tool was previously validated in the framework of NREL Phase VI *rotor-only* simulations by other authors (Fan and Kang 2009; Elfarra et al. 2014; Suárez et al. 2015a,b). The FINE™/Turbo solver is a three-dimensional, density-based, structured, multi-

**Table 18.1** DTU 10 MW RWT main parameters

Parameter description	Parameter value
Cut in wind speed	4 m s <sup>-1</sup>
Cut out wind speed	25 m s <sup>-1</sup>
Rated wind speed	11.4 m s <sup>-1</sup>
Rated power	10 MW
Number of blades	3
Rotor diameter	178.3 m
Min. rotor speed	6 RPM
Max. rotor speed	9.6 RPM
Hub height	119 m
Tower diameter top	5.5 m
Tower diameter base	8.3 m
Tower clearance	18.26 m

block finite volume code. A central-difference scheme is employed for the spatial discretization with Jameson type artificial dissipation. A four-stage explicit Runge-Kutta scheme is applied for the temporal discretization. Multi-grid method, local time-stepping and implicit residual smoothing are used in order to speed-up the convergence.

## 18.2 DTU 10 MW RWT Rotor-Only Analysis

In this section, a complete characterization of DTU 10 MW RWT aeroelasticity in a *rotor-only* framework is presented. A *Reynolds Averaged Navier Stokes* (RANS) approach was used in order to perform steady flow simulations of this OWT. Turbulence was considered by means of the Spalart–Allmaras model (Spalart and Allmaras 1992). Rotor was considered either as *rigid* or *flexible*. For the latter case, the consideration of a blade structure sub-model was necessary. Mesh deformation was carried out by the 3-steps *hybrid method* described in Horcas et al. (2015a).

First computations included in Sect. 18.2.1 were based on the standard DTU 10 MW RWT rotor, assuming a *rigid* configuration. *Straight* blades were considered, equipped with the so-called *Gurney flaps* devices at low span range [20 %, 30 %] (see Fig. 18.1). Obtained results were compared with three-dimensional CFD simulations performed by other authors. The same methodology was used in Sect. 18.2.2 to compare the performance of this standard blade with a *clean* variant, where the *Gurney flaps* were removed. Both *rigid* and *flexible* rotor configurations were studied. Finally, in Sect. 18.2.3 the impact of of *prebending* and *preconing* on DTU 10 MW RWT aeroelastic behaviour is assessed.

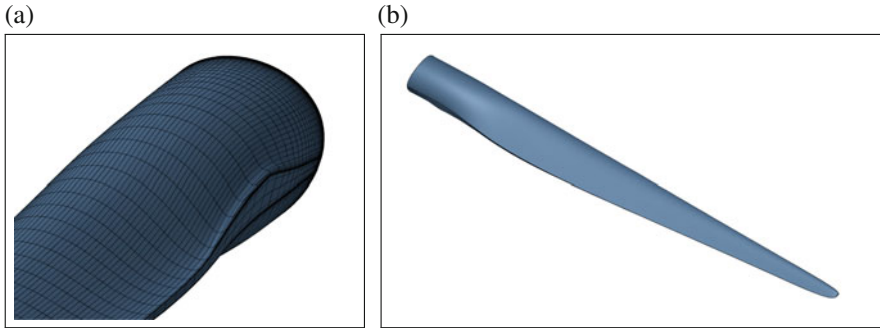


**Fig. 18.1** DTU 10 MW RWT *straight* blade geometry equipped with *Gurney flaps*. (a) Low span zoom. (b) Global view

**Table 18.2** DTU 10 MW RWT aerodynamic load cases definition

DLC Identifier	Wind speed [ $\text{ms}^{-1}$ ]	RPM
FT_WSP07	7	6.000
FT_WSP08	8	6.426
FT_WSP09	9	7.229
FT_WSP10	10	8.032
FT_WSP11 <sup>a</sup>	11	8.836

<sup>a</sup> FT\_WSP11 being very close to the wind turbine design point, it is referred in this document as *rated speed*

### 18.2.1 Steady Aerodynamics, Standard Geometry

In this section, the DTU 10 MW RWT standard rotor was studied for the  $0^\circ$  pitch operating range compiled in Table 18.2. The hypothesis of *rigid* blades was made.

Autogrid5<sup>TM</sup> structured grids generator was used in order to perform a three-dimensional mesh of the DTU 10 MW RWT rotor (NUMECA International 2013a). Blade surfaces as well as original nacelle and hub geometries were included in this process. A blocking topology was established around the blade, putting special attention in the local mesh around the blunt edge and blade tip. A single blade passage was meshed, accounting for  $7.2 \times 10^6$  nodes and 24 blocks. A first cell size of  $3.0 \times 10^{-5}$  m was imposed around the considered geometry, in order to properly describe the boundary layer for the studied wind speed range. Flow inlet and outlet were located at 2.2 and 3.2 blade radius from the nacelle respectively. Figure 18.2 shows a global overview of the mesh. For clarity purposes the three blades are displayed, and 1 out of 2 grid lines are skipped. In Fig. 18.3a, the cross-section mesh at mid-span is illustrated. The geometry of *Gurney flaps* at 20% of span together with the surrounding cross-section mesh are shown in Fig. 18.3b.

A good agreement in terms of loads prediction with respect to the three-dimensional RANS computations described in Bak et al. (2013) and performed with



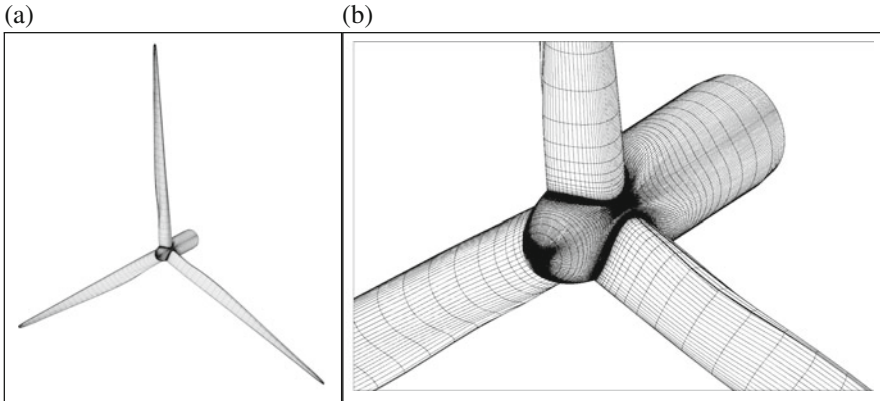


**Fig. 18.2** DTU 10 MW RWT surface mesh overview (displayed 1 every 2 grid lines). (a) Global view. (b) Detail of nacelle and low blade span range

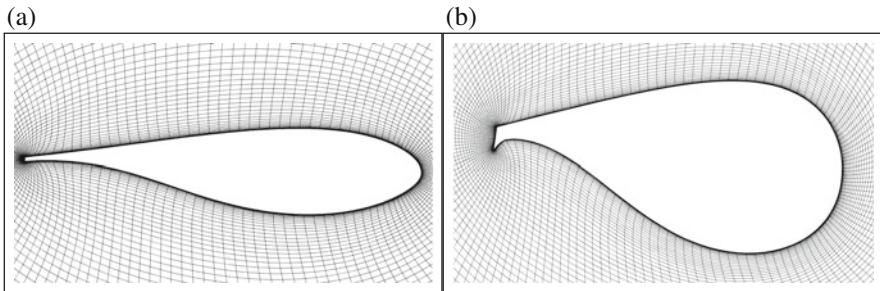


**Fig. 18.3** DTU 10 MW RWT cross-section meshes, 20 and 50% span. (a) 50% span. (b) 20% span

EllipSys3D (Sørensen 1995) was observed. A global loads comparison for all the studied operating points is included in Fig. 18.4.

Recirculations were observed near blade trailing edges at low span range. To illustrate this issue, Fig. 18.5 shows the friction streamlines around the DTU 10 MW RWT for the *rated speed* operating point. This observation is in-line with EllipSys3D computations performed by Zahle et al. (2014), where an important 3D flow behaviour was found up to an approximated radius of 30 m.

### 18.2.2 Static Aeroelasticity, Impact of Gurney Flaps

Original DTU 10 MW RWT blade geometry is equipped with the so-called *Gurney flaps* at low span range [20%, 30%]. This device, originally developed for race car applications, consists on a small plate located at the trailing edge. It is used to



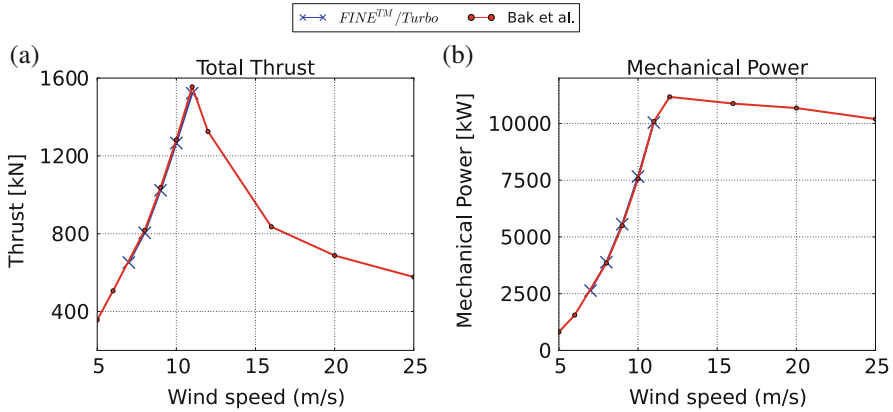


**Fig. 18.4** DTU 10 MW RWT total rotor thrust and mechanical power versus wind speed. (a) Total thrust. (b) Mechanical power

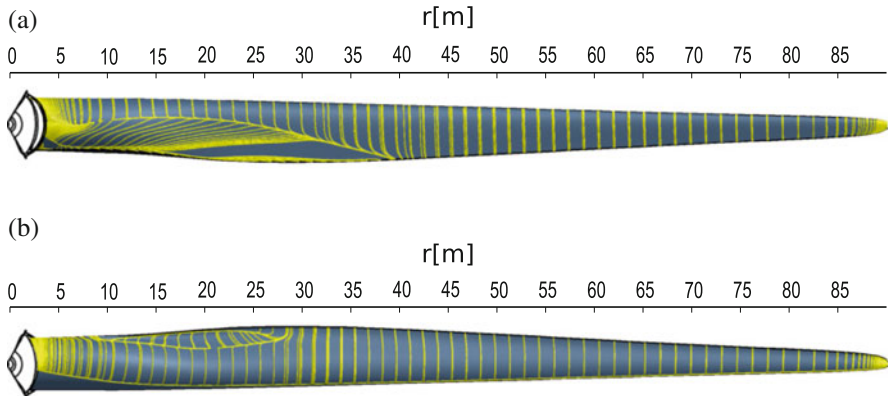


**Fig. 18.5** Friction streamlines at *rated speed*. (a) Suction surface. (b) Pressure surface

increase the lift produced by the airfoil when operating in separated flow conditions. A low drag penalty is expected. First studies characterizing the performance of this passive device were performed by Liebeck (1978). Figure 18.6 reproduces the conclusions of this work. The beneficial effects of the *Gurney flaps* installation are explained by the re-attachment of suction side flow close to the trailing edge. In order to evaluate the behaviour of the DTU 10 MW RWT *Gurney flaps* the load cases of Table 18.2 were studied again in a mesh with *clean trailing edges*, and compared with previous results. This comparison was performed not only under the hypothesis of *rigid* blades, but also by considering a *flexible* rotor.

A new mesh was generated with the same set-up described in Sect. 18.2.1, but based on a variant geometry of the DTU 10 MW RWT where the *Gurney flaps* were replaced by the unmodified blade profiles definition. This new mesh is referred in

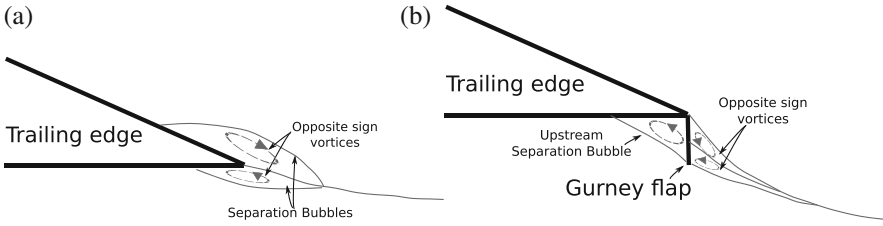


**Fig. 18.6** Expected effects on trailing edge flow due to *Gurney flaps* installation. (a) Clean trailing edge. (b) Trailing edge accounting for a *Gurney flap*

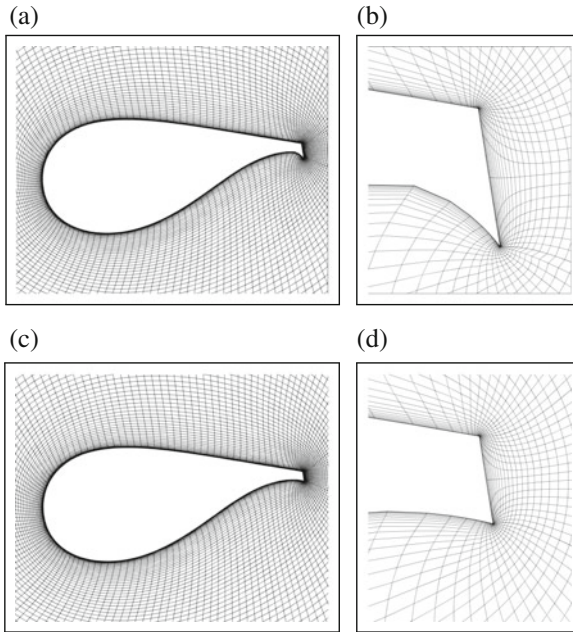


**Fig. 18.7** Cross-section meshes at 25% span for *G* (*Gurney*) and *NG* (*no-Gurney*) configurations. (a) *G* cross-section mesh. (b) *G* trailing edge. (c) *NG* cross-section mesh. (d) *NG* trailing edge

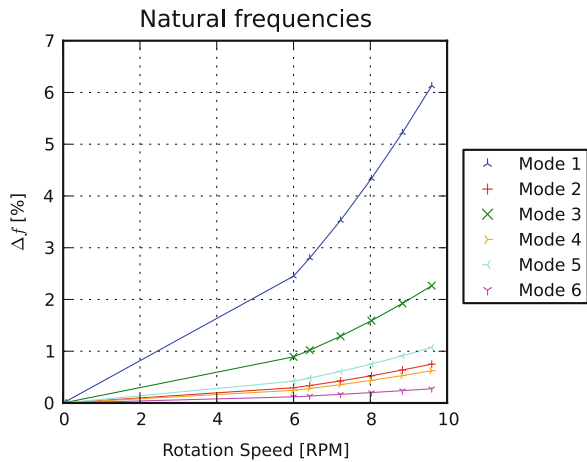
this section as *no-Gurney*, or *NG*. For clarity purposes, the one initially created in Sect. 18.2.1 is referred as *Gurney* or *G*. In order to illustrate the differences between *G* and *NG* configurations, Fig. 18.7 displays a cross-section of the mesh corresponding to a 25% of blade span.

For the considered aeroelastic simulations, the blade structure was linearized by means of the *Reduced-Order Model* (ROM) developed by Debrabandere (2014). A modal analysis was performed within the commercial package Abaqus (Simulia 2008) based on the model provided by Bak et al. (2013). Obtained natural frequencies were compared against the results of the aeroelastic computations of HAWC2 (Larsen and Hansen 2007), a third party software based on *blade element*

**Table 18.3** DTU 10MW RWT blade modes, comparison in the absence of rotation

Natural frequency [Hz]		Isolated blade modes	
Abaqus	Bak et al. (2013)	Identifier	Description
0.61	0.61	1	1 <sup>st</sup> flap
0.96	0.93	2	1 <sup>st</sup> edge
1.75	1.74	3	2 <sup>nd</sup> flap
2.88	2.76	4	2 <sup>nd</sup> edge
3.58	3.57	5	3 <sup>rd</sup> flap
5.71	5.69	6	1 <sup>st</sup> torsion
5.75	–	7	Mixed flap/torsion
6.16	6.11	8	4 <sup>th</sup> flap
–	6.66	9	3 <sup>rd</sup> edge

**Fig. 18.8** Evolution of DTU 10 MW RWT blade frequencies in function of rotational speed (first six modes plotted)



*momentum* (BEM) theory. Computed frequencies for each identified mode are compiled in Table 18.3. To reduce the computational cost attached to aeroelastic simulations, only the first six frequencies of the obtained modal basis were used to model blade flexibility. A mixed mode was found between first torsion and fourth flap. No pure third edge mode was identified within the considered frequency range. These differences could be explained by the complexity of the astructural models used for natural frequencies extraction.

Additional modal analysis were performed taking into account the *centrifugal effects* of each one of the analyzed rotor RPMs. This allowed to include the *initial blade deformation* due to the rotation. In addition, a slight structural frequencies shift was observed. This effect is illustrated in Fig. 18.8, where the variations of blade frequencies against non-rotating frequency are plotted at every RPM. Even if this frequency shifting is not as important as in other rotatory applications including large blade deformations (such as helicopters), a non-negligible value is observed

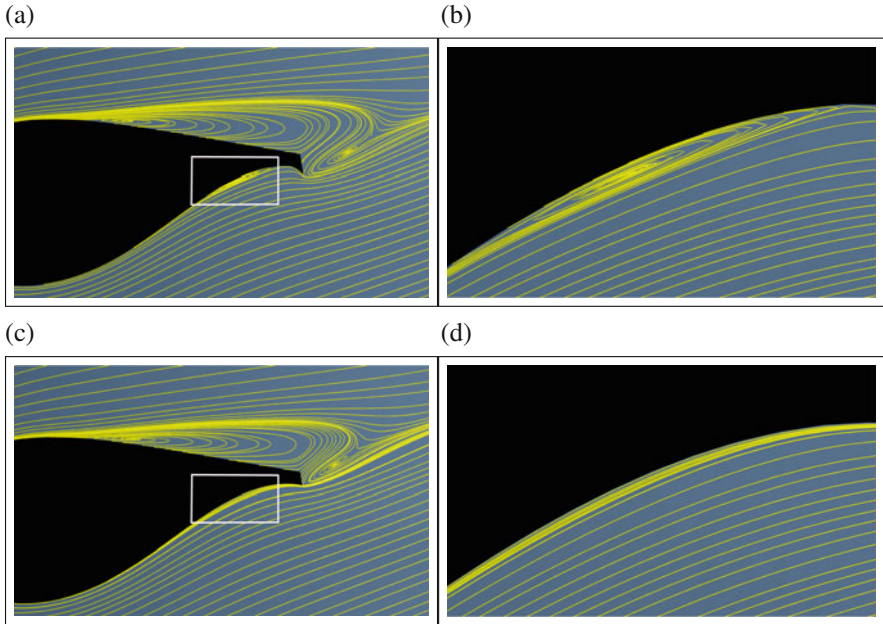


**Fig. 18.9** Cross-section streamlines for  $r = 23$  m at rated speed. Rigid simulations. (a) *G* (Gurney), global view. (b) *G* (Gurney), pressure side zoom. (c) *NG* (no-Gurney), global view. (d) *NG* (no-Gurney), pressure side zoom

for the first modes. As an example a difference up to 6.12% was found for the first mode at 9.6RPM.

In order to check if the *Gurney flaps* flow control mechanism illustrated in Fig. 18.6 was reproduced in the DTU 10MW RWT geometry, a detailed analysis of the *rigid* configuration at *rated* speed was performed. Figure 18.9 shows a comparison of the cross-section streamlines at  $r = 23$  m. The generation of the pressure surface separation bubble was visible for the *G* configuration. A detailed view of this phenomenon is included in Fig. 18.9b. The suppression of the suction surface recirculation, expected after the installation of the *Gurney flaps*, was not observed. This behaviour was found for the whole low span range, as it can be deduced from the comparison of blade surface streamlines of Fig. 18.10a and b. Indeed, the removal of the *Gurney flaps* led to a slight decrease of the maximum radius of the suction surface separation (passing from 39.7 m for *G* to 38.1 m for *NG*). In addition, the flow around the pressure surface of *NG* remained attached for the whole blade span, except for a small recirculation bubble located at  $r = [14.9, 20.3]$  m (see Fig. 18.10d). A similar flow pattern was observed for all the operating points of Table 18.2.

The benefits of the *no-Gurney NG* configuration on flow behavior had a direct impact on global rotor performance. Figure 18.11a and b show the global thrust

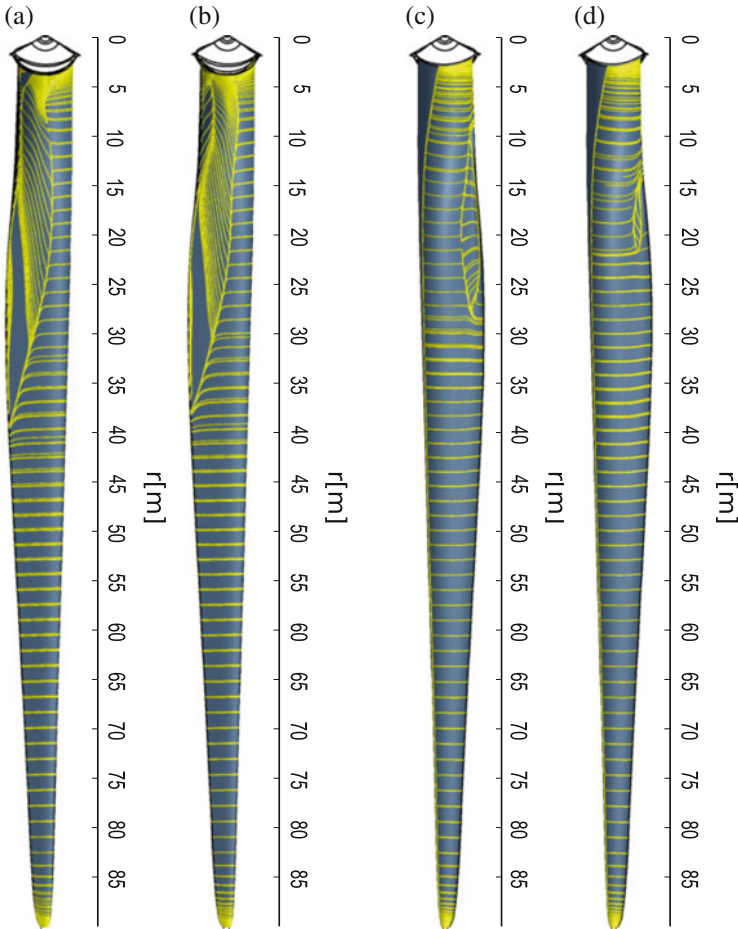


**Fig. 18.10** Friction streamlines at *rated speed* for suction and pressure surfaces (referred as *SS* and *PS* respectively). *Rigid* simulations of *G* (Gurney) and *NG* (no-Gurney) configurations. (a) *SS-G*. (b) *SS-NG*. (c) *PS-G*. (d) *PS-NG*

and mechanical power coefficients, computed for both *G* and *NG* configurations. The results for *rigid* and *flexible* blade models are included. Global load coefficients were computed based on the following equations:

$$C_{t,global} = \frac{BT}{0.5\rho U_{\infty}^2 \pi R^2}, C_{p,global} = \frac{B\tau\Omega}{0.5\rho U_{\infty}^3 \pi R^2}, \quad (18.1)$$

Where  $T$  stands for the thrust force generated per blade,  $\tau$  is the torque per blade,  $B$  stands for the number of blades,  $U_{\infty}$  is the incoming fluid speed,  $\rho$  is the fluid density,  $R$  is the total blade span and  $\Omega$  is the rotating speed.

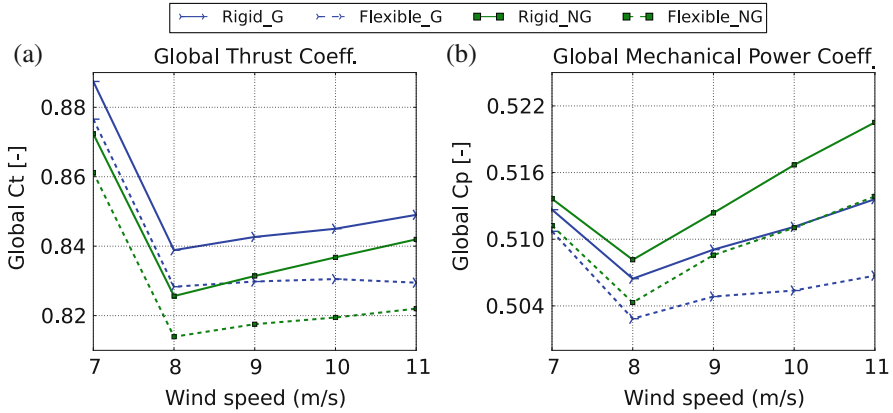


**Fig. 18.11** Global load coefficients in function of wind speed for *G* (*Gurney*) and *NG* (*no-Gurney*) configurations. (a) Global thrust coefficient. (b) Global mechanical power coefficient

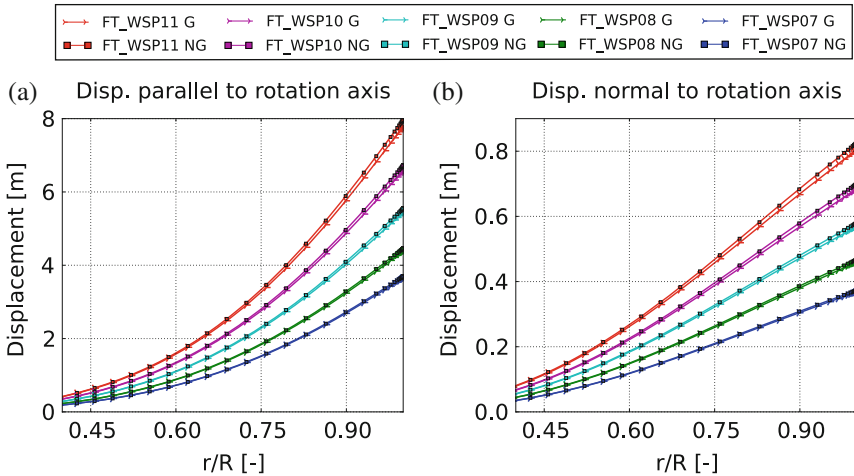


**Fig. 18.12** DTU 10MW RWT blade deformation in function of normalized radius. *G* (*Gurney*) and *NG* (*no-Gurney*) configurations. (a) Blade axis displacement parallel to rotor axis. (b) Blade axis displacement normal to rotor axis

At rated speed and for the rigid blade model, the installation of *Gurney flaps* decreased the mechanical power of 1.4 %, while the thrust was increased of 0.8 %. A similar trend was observed for lower wind speeds. Same remarks concerning the efficiency of *Gurney flaps* could be made when considering blade elasticity.

A global thrust and mechanical power decrease was observed for both *G* and *NG* configurations when considering aeroelasticity. This is related to the important blade deflections experienced by the blade. Figure 18.12 displays the

computed displacements parallel and normal to the rotor axis (often referred as out-of-rotor plane and in-rotor plane respectively). No significant differences were observed between the deflections corresponding to *G* and *NG* geometries. For both configurations, deformation parallel to rotor axis reached the 44 % of the blade tip/tower distance (18.26 m) at the *rated speed* operating point.

Based on the presented results, a decrease of the performance of the DTU 10 MW RWT rotor is expected after the integration of the *Gurney flaps*. Other alternatives in order to avoid the observed flow separation can be found in the literature. In Gaunaa et al. (2013), the use of leading edge slats at low span regions  $r/R = [0.8, 0.32]$  was studied. Troldborg et al. (2015) considered the installation of *vortex generators* in order to control flow separation.

### 18.2.3 *Static Aeroelasticity, Impact of Prebending and Preconing*

The distance between the blade tip and the tower is often referred in the wind energy context as the *tower clearance*. In order to increase this gap (especially when dealing with large rotors), wind turbine designers use to introduce three geometrical considerations on the assembly:

- **Tilt angle:** Angle between rotor axis and tower
- **Precone angle:** Angle between blade axis and rotor axis
- **Prebending:** Blade deflection towards the incoming wind direction imposed during the blade design stage

The DTU 10 MW RWT accounts for all of them, as shown in Fig. 18.13a, where a sketch from the definition document of Bak et al. (2013) is reproduced. The geometrical effects of *prebending*, *tilt* and *preconing* are highlighted. In an operating wind turbine, the combination of all these modifications will try to align the deformed blade with the tower, as shown in Fig. 18.13b.

The aim of this section is to analyze how these geometrical considerations will impact rotor performance. The results of the already studied *straight* configuration were compared against a new and more *realistic* variant, accounting for *tower clearance* increase devices. Based on the conclusions of Sect. 18.2.2, new simulations were based on a blade geometry without *Gurney flaps*. In order to explore the whole  $0^\circ$  operating range of the machine, the load cases from Table 18.2 were analyzed again and compared with the *straight-NG* configuration results. Both *rigid* and *flexible* blades were analyzed.

A new mesh was generated with the same characteristics as the one described in Sect. 18.2.1. Since the introduction of the tilt angle was not compatible with the angular periodicity hypothesis, only the *prebending* and the *preconing* were considered. Based on the design specifications from Bak et al. (2013), the new



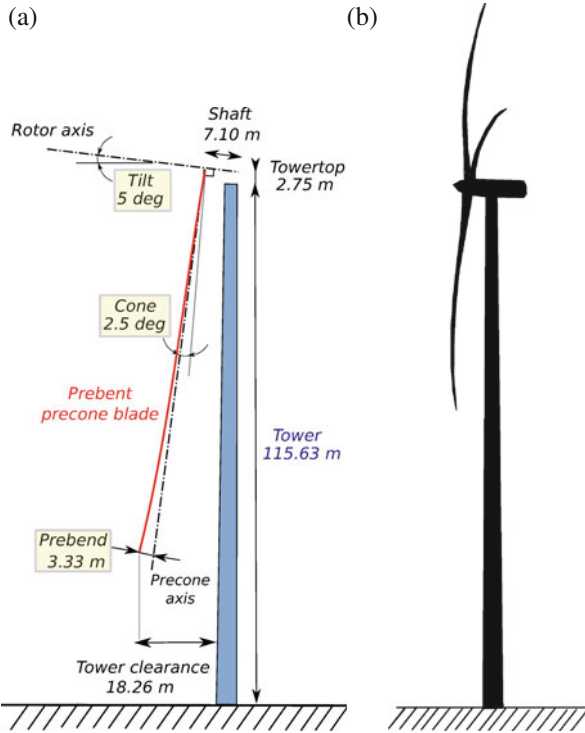


**Fig. 18.13** Examples of whole wind turbine assemblies. (a) Sketch of the DTU 10 MW RWT assembly. (b) Representative sketch of a working wind turbine

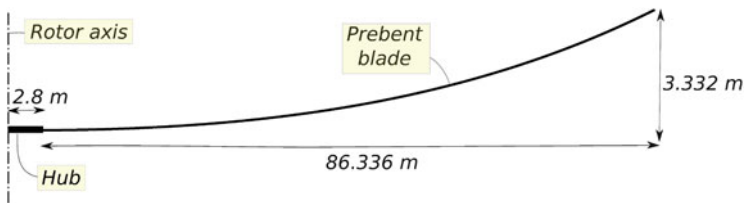


**Fig. 18.14** DTU 10 MW RWT axis prebending definition, (reproduced from Bak et al. 2013)

considered geometry was generated by the application of the following geometrical operators on the standard DTU 10 MW RWT configuration:

1. Application of the prebending law definition on the *straight* blade (see Fig. 18.14)
2. Application of the  $2.5^\circ$  precone angle to the already prebent blade

Due to the significant geometrical modifications performed on the new *prebent-precone* blade, a new set of natural structural frequencies and mode shapes was required. The methodology described in Sect. 18.2.2 was used in order to perform



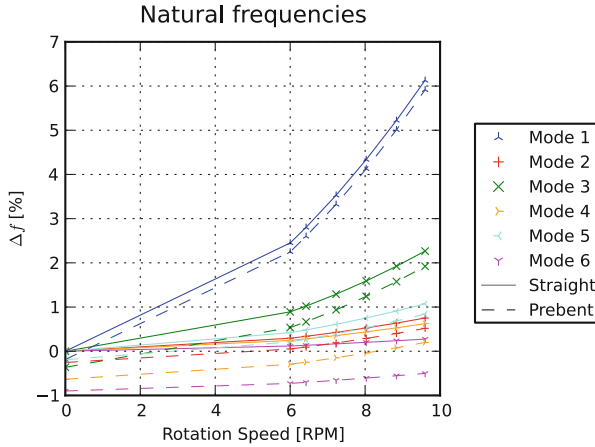


**Fig. 18.15** Evolution of DTU 10 MW RWT blade frequencies in function of rotational speed, *straight* and *prebent-precone* blades (first six modes plotted)



**Fig. 18.16** DTU 10 MW RWT modal analysis initial deformation (*blue-yellow*), superposed to the blade geometry reference (*red*) at *rated speed*. (a) *Straight* blade. (b) *Prebent-precone* blade

modal analysis for each one of the considered RPM. The same blade modes identified for the *straight* blade were observed for the new geometry. As previously shown in Fig. 18.8 for the *straight* configuration, a small RPM dependency was observed. In Fig. 18.15, the relative variations of natural frequencies corresponding to both configurations are compared. They are normalized by the frequency of the non-rotating *straight* blade. The evolutions of the frequencies with the rotation speed were very similar. Only a constant shift between *straight* and *prebent-precone* configuration was observed. This shift tended to increase with the mode number.

A more significant difference was related to the *centrifugal effects* included in the performed modal analysis. Indeed, an important *initial deformation* was observed for the *prebent-precone* configuration, due to offset of the blade geometry. In Fig. 18.16, the initial deformation (in *blue-yellow*) is superposed to the corresponding blade geometries (in *red*) for the *rated speed* operating point. While no difference was visible for the *straight* configuration (Fig. 18.16a), the *centrifugal effects* tended to straighten up the blade (Fig. 18.16b). As performed in the previous

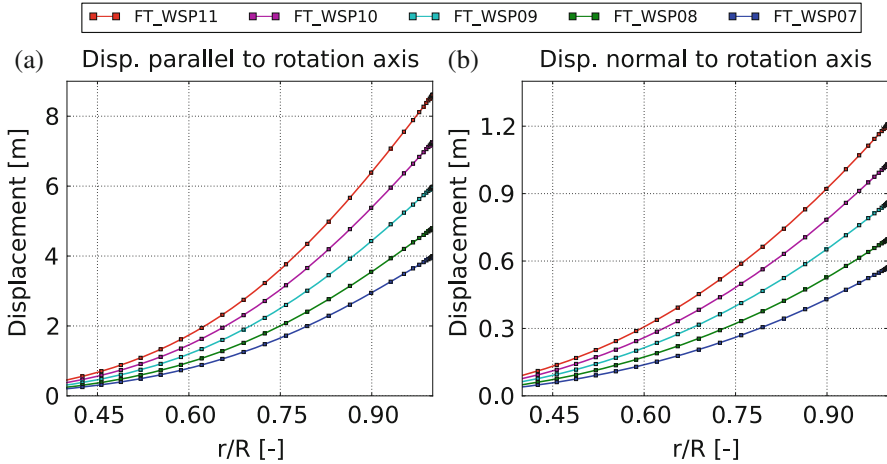


**Fig. 18.17** DTU 10MW RWT blade deformation in function of normalized radius for the *prebent-precone* configuration. **(a)** Blade axis displacement parallel to rotor axis. **(b)** Blade axis displacement normal to rotor axis

section, only the first six frequencies of the computed modal basis were used to model blade flexibility in the simulations.

Figure 18.17 shows the blade deformations for the *flexible* simulations of the *prebent-precone* rotor. Computed deformations were slightly higher than the ones corresponding to the *straight* rotor and previously displayed in Fig. 18.12. However, higher deformed blade tip/tower distances were observed for the *prebent-precone* configuration, due to its more conservative initial *tower clearance*. In order to illustrate this fact, Fig. 18.18 shows the reference (i.e. undeformed) and deformed blade axis coordinates for each of the presented aeroelastic computations. A global view is provided as well as a close zoom in order to properly contextualize the magnitude of the deformations. For the *prebent-precone* configuration, a blade tip/blade root alignment was observed for for the  $10 \text{ m s}^{-1}$  simulation. This operating point is indeed very close to the *rated speed* of the machine, verifying the prebending law defined at the design stage.

Computed global mechanical power coefficients of *straight* and *prebent-precone* configurations are shown in Fig. 18.19, together with a diagram superposing reference and deformed rotor geometries at *rated speed*. When considering the blades as *rigid*, a decrease in power was observed when introducing blade *prebending* and *preconing*. For the *straight* rotor, accounting for blade flexibility led to a reduction of the total power. This trend was reversed for the *prebent-precone* configuration, since the effect of flexibility tended to deform the blade towards a more orthogonal geometry with respect to the incoming flow (Fig. 18.19b). At *rated speed*, the power produced by the *flexible prebent-precone* blade was very close to the one computed for the *rigid straight* blade. An analogous plot regarding rotor global

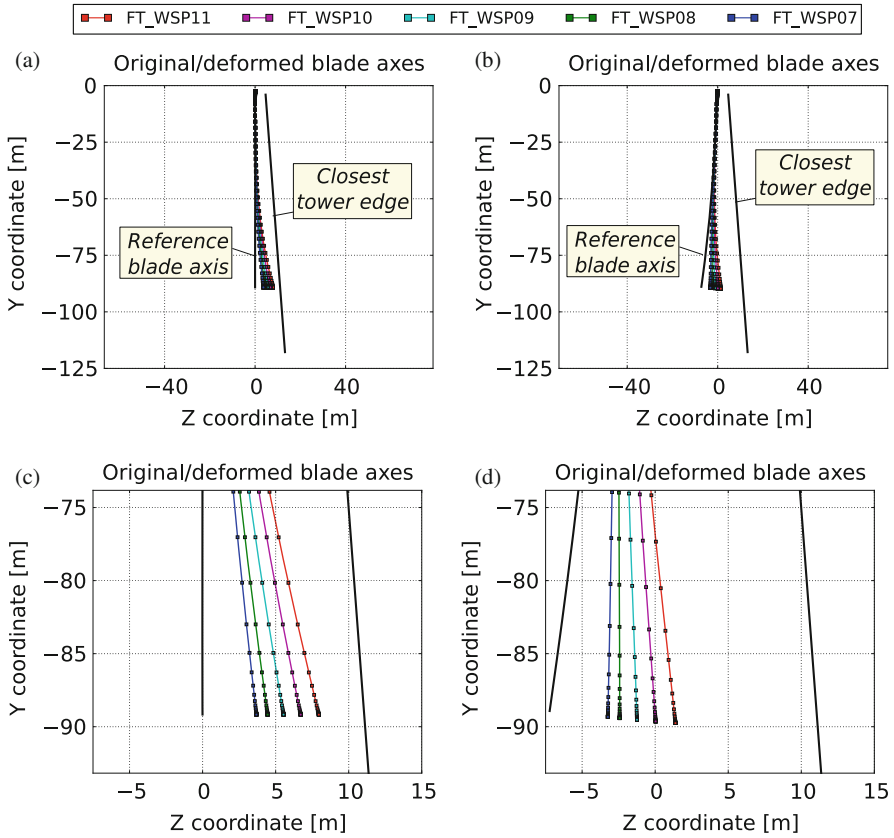


**Fig. 18.18** Reference and deformed DTU 10MW RWT blade axis coordinates with respect to closest tower edge. (a) *Straight* rotor (global view). (b) *Prebent-precone* rotor (global view). (c) *Straight* rotor (zoom). (d) *Prebent-precone* rotor (zoom)

thrust coefficient is included in Fig. 18.20. Lower thrust values were computed for the *prebent-precone* configuration with respect to the *straight* rotor. No significant differences between *flexible* and *rigid* simulations were observed for the *prebent-precone* configuration.

As a global conclusion, presented results show that aeroelastic analysis of DTU 10MW RWT cannot be performed without considering the *prebending* and the *preconing* of the blades. Indeed, even if it does not largely affect the natural frequencies of the blade, its shape modification influences the performances of the wind turbine.

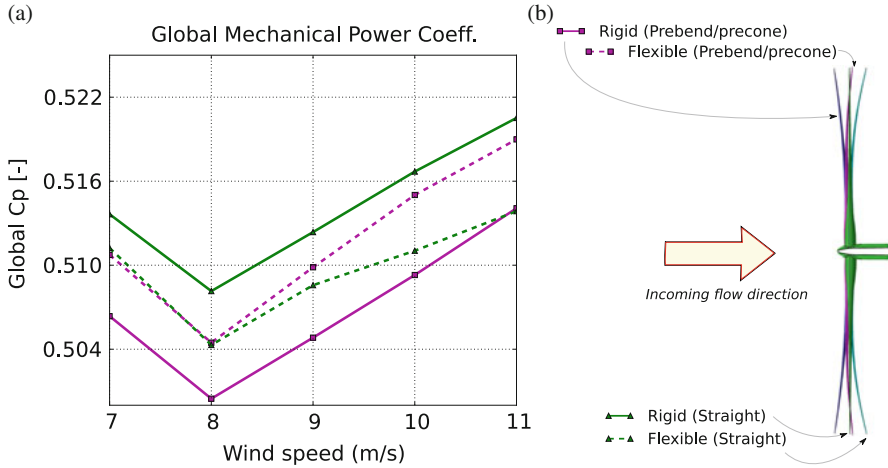


**Fig. 18.19** Mechanical power coefficient of the DTU 10MW RWT rotor, effects of *prebending-preconing* and flexibility. (a) Global mechanical power coefficient. (b) View of deformed blades at *rated speed*

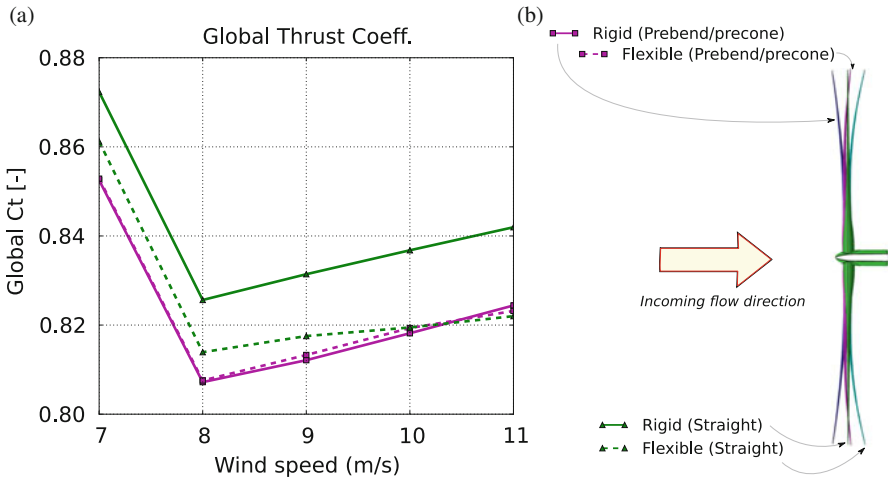


**Fig. 18.20** Global thrust coefficient of the DTU 10MW RWT rotor, effects of *prebending-preconing* and flexibility. (a) Global thrust coefficient. (b) View of deformed blades at *rated speed*

### 18.3 DTU 10 MW RWT Rotor-Tower Interactions Analysis

In this section, flow complexity was increased by considering the DTU 10MW RWT tower in the computational domain. This more realistic scenario introduced an important unsteadiness in the flow due to the so-called *rotor-tower*

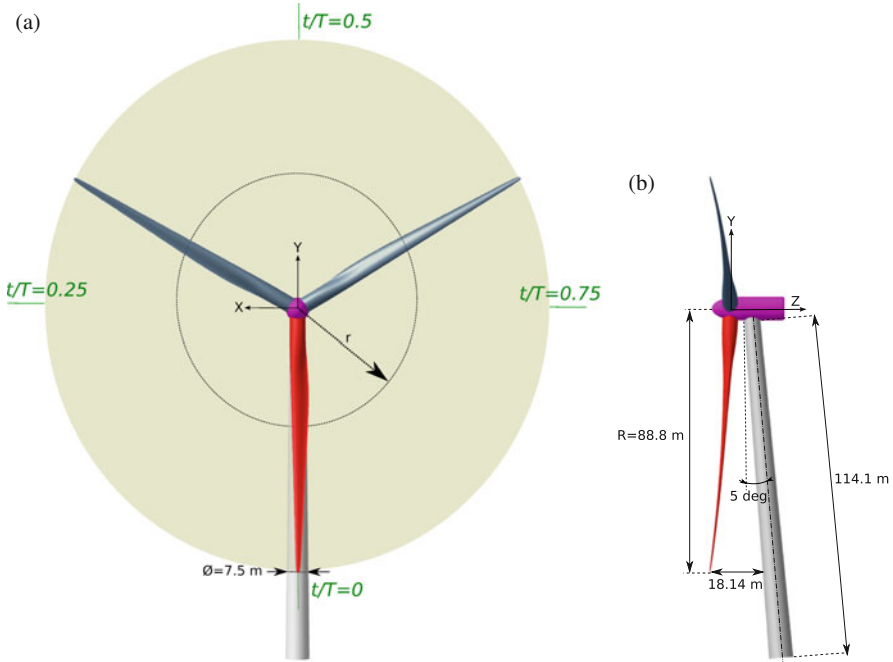


**Fig. 18.21** Sketch of the DTU 10 MW RWT assembly. (a) Front view. (b) Side view

*interactions*. Hence, the use of more sophisticated numerical methods was required. In particular, the *Non-linear Harmonic* (NLH) approach presented by Vilmin et al. (2006) was used. In the NLH method, unsteady flow perturbations are Fourier decomposed. Navier-Stokes equations are then cast in the frequency domain, leading to the extraction of a set of transport equations for each harmonic. A single *blade passage* mesh is required. As a first approach and in order to keep the rotational periodicity of the problem, the incoming wind was assumed to be aligned with rotor axis. The hypothesis of *rigid* rotor blades was also made. The studied operating point was characterized by the following parameters:

- **Incoming wind speed:**  $10.5 \text{ m s}^{-1}$
- **Rotor speed:** 8.836 RPM
- **Blade pitch:**  $0^\circ$

Figure 18.21 illustrates the main geometrical properties of the studied DTU 10 MW RWT assembly, based on its definition from Bak et al. (2013). The rotor axis was co-linear with Z axis. A *tilt angle* of  $5^\circ$  was considered between rotor and tower axes. Blades accounted for a *precone* angle of  $2.5^\circ$  as well as a distributed *prebending*. Based on the disadvantageous effects on rotor performance found in Sect. 18.2.2, *Gurney flaps* were removed from blade geometry. In order to present the unsteady results of this section, the normalized time  $t/T$  was used. In this context,  $t$  is defined

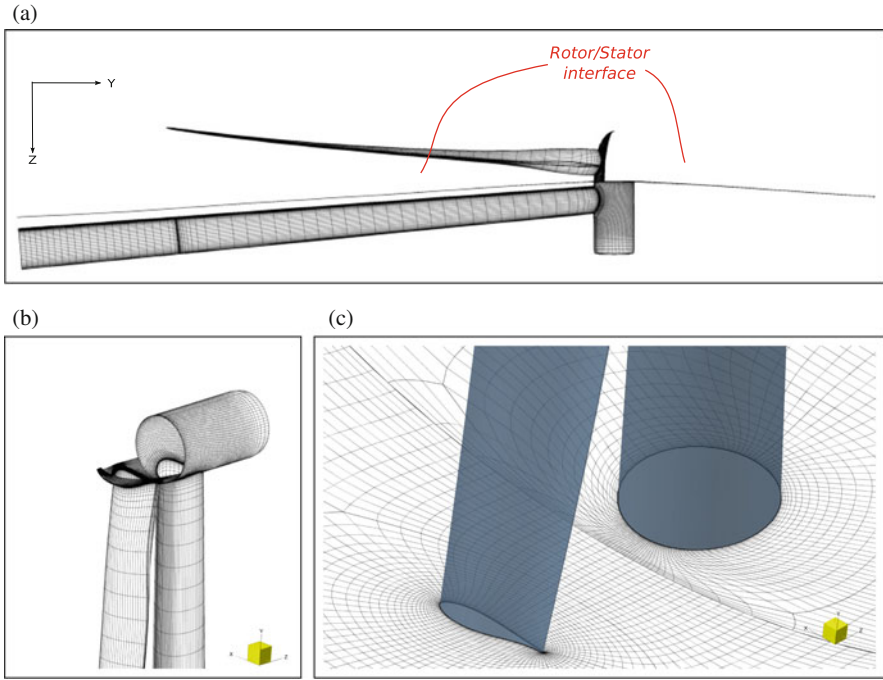


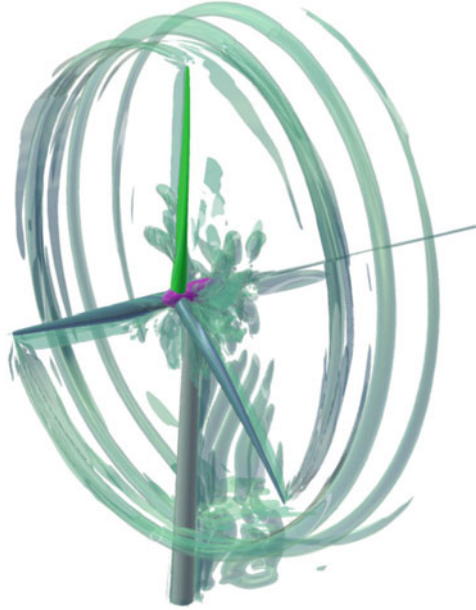
**Fig. 18.22** DTU 10 MW RWT assembly mesh, 1 out of 2 mesh lines are skipped. (a) Surface mesh, global view. (b) Surface mesh, rotor detail. (c) Half-span cross-section grid line

as the already lapsed time in the current revolution and  $T$  refers to the period of rotation. The DTU 10 MW RWT operates in clockwise rotation, and it was assumed that at  $t/T = 0$  one of the blades was aligned with the tower axis. This particular blade, displayed in red in Fig. 18.21, is referred in this document as the *observed blade*.

To generate a suitable mesh for NLH computations, DTU 10 MW RWT blade sections defined in Bak et al. (2013) were imported in Autogrid5™ structured grids generator (NUMECA International 2013a). Original nacelle, hub and tower geometries were also considered in the mesh generation process. To properly describe the boundary layer for the considered operating point, a first cell size of  $3.0 \times 10^{-5}$  m was imposed around the blade. A *rotor/stator interface* crossing the DTU 10 MW RWT nacelle was defined in order to connect rotating and non-rotating computational domains. A single *blade passage* was meshed in the rotor side, while a  $360^\circ$  grid was generated for the tower (or *stator*) region. Flow inlet and outlet were located at 2.2 and 3.2 blade radius from the nacelle, respectively. Figure 18.22 shows the complete generated mesh, accounting for 13 millions of nodes. For clarity purposes, 1 out of 2 mesh lines were skipped.

A total of nine harmonics were considered. The Spalart–Allmaras turbulence model (Spalart and Allmaras 1992) was used. A full non-matching non-reflecting

**Fig. 18.23** Iso-surface of 0.5 Q-criterion at  $\frac{t}{T} = 0.50$



approach was employed for the modeling of the *rotor/stator interface* (Vilmin et al. 2006). First resolved rotor harmonic was located at 0.15 Hz, corresponding to the rotational speed at the considered operating point. Since the DTU 10 MW RWT has a three-bladed rotor, a frequency of 0.45 Hz was observed for the first tower harmonic. Even if flow variables are solved in the frequency domain, NLH results can be easily reconstructed in time in order to perform a more comprehensive postprocessing. This process is referred in this document as the *time solution reconstruction*.

The complexity of this unsteady problem could be already pointed out with the visualization of the flow at a given time. Figure 18.23 illustrates the iso-surfaces of Q-criterion for a value of 0.5 of the time reconstructed solution at  $\frac{t}{T} = 0.50$ . Important vortical structures could be observed downstream of the tower. These were present all along the tower height. High vorticity regions were identified at low blade span range (where the DTU 10 MW RWT is equipped with thicker airfoils). The generation of blade tip vortex was clearly visible. The collision of this structure with the tower led to an important increase of downstream vorticity.

The observed vorticity at low blade span can be related to the *shedding* phenomenon. Figure 18.24 shows the streamlines around the *observed blade* for a  $r = 20\text{ m}$  cross-section. Indeed, the low span suction side recirculation already identified for the *rotor-only* RANS computations was shed from the blade. This effect was especially visible when the blade approached the tower (i.e. for  $\frac{t}{T} = 0.00$  and  $\frac{t}{T} = 0.76$ ). A similar *vortex shedding* phenomenon was identified downstream of the tower all along its height.

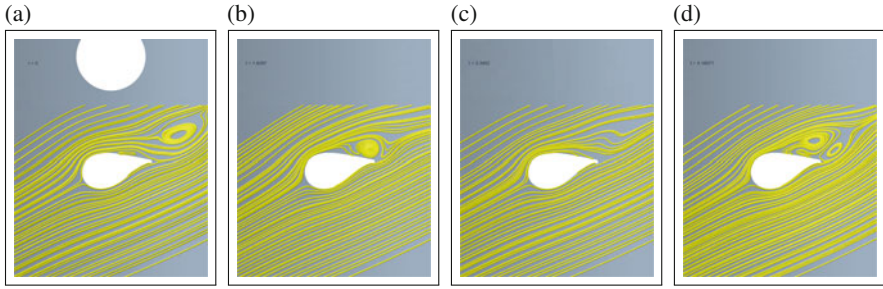


**Fig. 18.24** Relative velocity streamlines around the *observed blade* for a  $r = 20$  m cross-section. (a)  $\frac{t}{T} = 0.00$ . (b)  $\frac{t}{T} = 0.24$ . (c)  $\frac{t}{T} = 0.50$ . (d)  $\frac{t}{T} = 0.76$

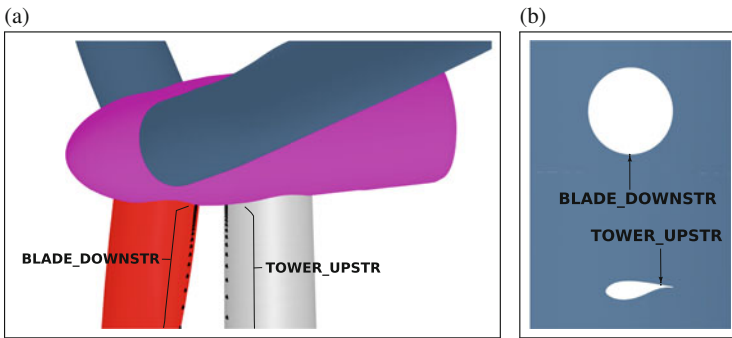


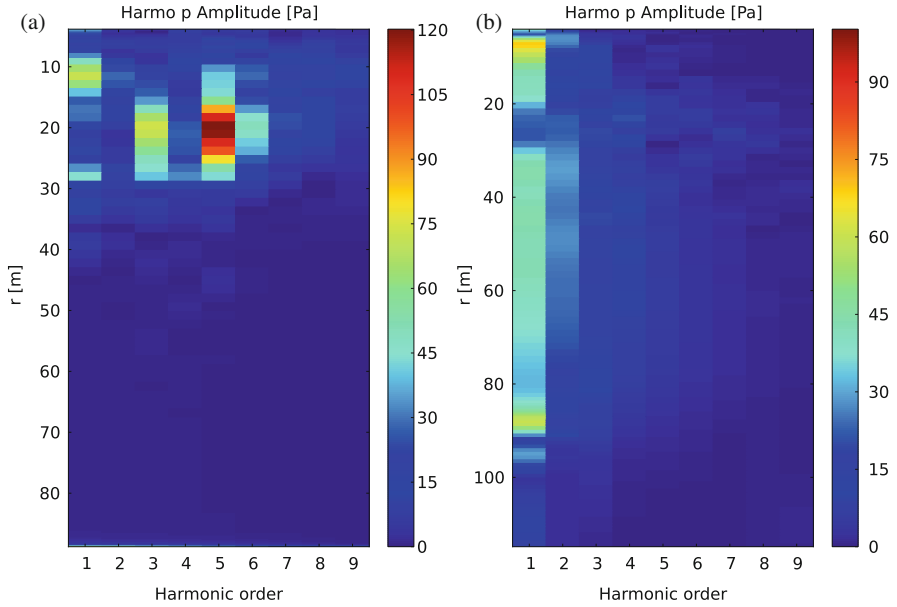
**Fig. 18.25** Location of BLADE\_DOWNSTR and TOWER\_UPSTR sets of sensors. (a) DTU 10 MW RWT front view. (b) Cut at  $r = 44.5$  m

When characterizing the frequency content of the blade *shedding*, an important spanwise dependency was observed. Two sets of sensors were defined in order to have an overview of this relation: BLADE\_DOWNSTR and TOWER\_UPSTR, both installed all along a mesh line. While BLADE\_DOWNSTR was positioned at the observed blade *shedding* location, TOWER\_UPSTR intended to analyze the impact of the rotor perturbation on the tower (see Fig. 18.25).

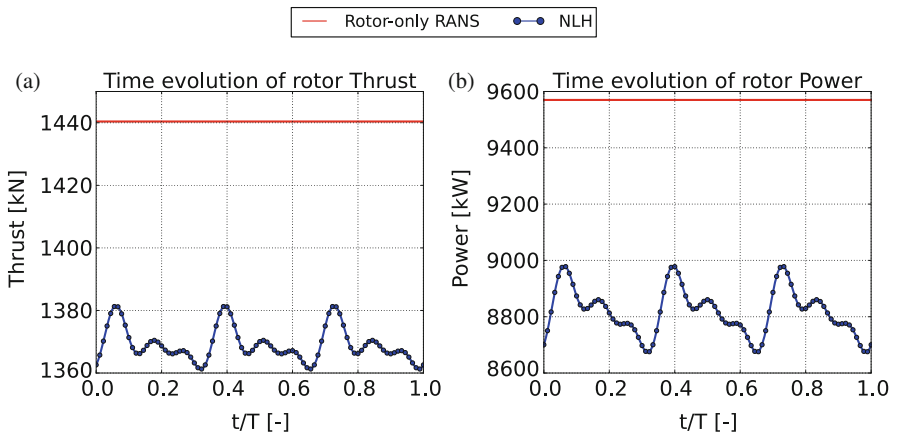
Figure 18.26 illustrates the harmonic pressure amplitudes for every point included in BLADE\_DOWNSTR and TOWER\_UPSTR. The results are expressed as a function of the considered harmonic (referenced here as *Harmonic order*), and of the radial position of each point. The blade *shedding* phenomenon could be identified for BLADE\_DOWNSTR at the vicinity of 20 m. In this region, important harmonic amplitudes corresponding to the fifth harmonic were observed. The influence of *blade shedding* on the tower was visible in TOWER\_UPSTR, where a shifting of the harmonic content towards higher frequencies was observed at low span.

Figure 18.27 shows rotor loads time evolution, where the effects of the *blade-tower alignment* event are clearly visible at  $\frac{t}{T} = 0, \frac{1}{3}, \frac{2}{3}$ . The corresponding result





**Fig. 18.26** Harmonic pressure amplitude [Pa] for the defined sets of sensors, as a function of  $r$  [m]. (a) BLADE\_DOWNSTR. (b) TOWER\_UPSTR



**Fig. 18.27** DTU 10 MW RWT rotor loads as a function of normalized time. (a) Thrust [kN]. (b) Power [kW]

for a *rotor-only* RANS simulation based on the set-up of Sect. 18.2 is included for reference. Relative loads fluctuation amplitudes of 1% for the rotor thrust and 2% for the mechanical power were computed. The presence of the tower led to a time-averaged decrease of 5% of rotor thrust and 8% of mechanical power with

respect to the corresponding *rotor-only* simulation. Therefore it can be concluded that the influence of the tower is not negligible when assessing the wind turbine performance.

## 18.4 Conclusions and Future Work

A numerical analysis of the DTU 10 MW RWT *reference* wind turbine aerodynamics was presented and discussed. A three-dimensional CFD-based methodology was developed in order to tackle two challenging problems. On one hand, the impact of large OWT blade deflections on rotor performance (the so-called *aeroelastic effects*). On the other hand, the modeling of flow unsteadiness coming from the consideration of the tower in the CFD set-up (also referred as *rotor-tower interactions*).

The issue of aeroelasticity was studied in a *rotor-only* framework. First simulations aimed to verify the obtained results for a *straight* and *rigid* configuration regarding to CFD simulations performed by other authors. For both methodologies, computed flow separation and rotor loads were in good agreement. After this initial comparison the developed tool was extended by including a structural model of the blade, represented by its natural frequencies and deformed shapes. This enhanced numerical approach was used in order to study the influence of two different geometrical modifications of the blade on final rotor performance and aeroelastic response. First, the impact of *Gurney flaps* installation was discussed. No re-attachment of the suction surface separation bubble was observed after the introduction of these devices, and a wider pressure surface recirculation zone was identified. The evaluation of the total mechanical power and thrust showed that *Gurney flaps* reduced the global performance of the DTU 10 MW RWT rotor for the considered operating points. This remark could be made for both *rigid* and *flexible* configurations. For the latter case blade tip deformations of 8 m were computed at *rated speed*, leading to a power production decrease of 1.4%. It can be concluded that the consideration of blade *flexibility* is necessary in order to properly estimate the final rotor performance. Secondly, the results of a *prebent-precone* rotor were compared with the standard *straight* configuration. When considering the blades as *rigid*, the combination of both geometrical modifications led to a decrease of the computed rotor loads. At *rated speed*, reductions of 1% of thrust and 2% of mechanical power were observed. When analyzing the corresponding *flexible* blade configurations, the effect of aeroelasticity on rotor performance was reversed. Indeed, while a reduction in the generated power was observed for the deformed *straight* rotor, an increase was found for the *prebent-precone* configuration. This inversion was explained by the deformed rotor geometries, since for the *prebent-precone* simulations the blade flexibility tended to recover the orthogonality with respect to the incoming flow. These results show that aeroelastic analysis of DTU 10 MW RWT cannot be performed without considering the *prebending* and the *preconing* of the blades.

Finally, the NLH method was applied in order to study the whole DTU 10 MW RWT assembly (including the tower). This approach was able to capture the complex unsteady aerodynamics related to *rotor-tower interactions*. The presence of the tower had a direct impact on rotor performance, justifying the numerical analysis of the *full machine*. Decreases of around 5 % of time-averaged rotor thrust and 8 % of power were computed. These reductions are in line with previous studies based on other wind turbines (Hsu and Bazilevs 2012; Hsu et al. 2014; Carrión 2014; Li 2014). Local unsteady flow patterns around the whole DTU 10 MW RWT assembly were also characterized. In particular, both tower and blade *shedding* phenomena were identified. The latter effect was found to be related to high frequencies. In particular, the considered operating point revealed a blade *shedding* frequency corresponding to the fifth harmonic. This harmonic order is coherent with the results of previous CFD computations of the NREL Phase VI (Le Pape and Lecanu 2004; Li 2014). Regarding the *blade-tower alignment* event, loads fluctuation relative amplitudes of 1 % for the rotor thrust and 2 % for the mechanical power were computed.

Future work will be devoted to extend the capabilities of the NLH method to account for a structural model of the blades, in order to assess the combined impact of rotor flexibility and flow unsteadiness on rotor performance. Additionally, the studied DTU 10 MW RWT operating range will be extended to higher wind speeds to evaluate the performance of the presented methodology when considering more important angles of attack.

**Acknowledgements** The authors acknowledge the *European Commission* for their research grant under the project FP7-PEOPLE-2012-ITN 309395 *MARE – WINT (new MAterials and REliability in offshore WIND Turbines technology)*, as well as all the members from FINE™/Turbo team of NUMECA International for their valuable and active contribution.

**Open Access** This chapter is distributed under the terms of the Creative Commons Attribution-NonCommercial 4.0 International License (<http://creativecommons.org/licenses/by-nc/4.0/>), which permits any noncommercial use, duplication, adaptation, distribution and reproduction in any medium or format, as long as you give appropriate credit to the original author(s) and the source, provide a link to the Creative Commons license and indicate if changes were made.

The images or other third party material in this chapter are included in the work's Creative Commons license, unless indicated otherwise in the credit line; if such material is not included in the work's Creative Commons license and the respective action is not permitted by statutory regulation, users will need to obtain permission from the license holder to duplicate, adapt or reproduce the material.

## References

- Bak C, Zahle F, Bitsche R, et al (2013) The DTU 10-MW reference wind turbine. In: DTU orbit - the research information system. Available via Technical University of Denmark. [http://orbit.dtu.dk/files/55645274/The\\_DTU\\_10MW\\_Reference\\_Turbine\\_Christian\\_Bak.pdf](http://orbit.dtu.dk/files/55645274/The_DTU_10MW_Reference_Turbine_Christian_Bak.pdf). Accessed 08 Apr 2016

- Carrión M (2014) Low Mach number CFD for wind turbine analysis. Dissertation, University of Liverpool
- Corson D, Griffith DT, Ashwill T, et al (2012) Investigating aeroelastic performance of multi-mega watt wind turbine rotors using CFD. Paper presented at the 53rd AIAA/ASME/ASCE/AHS/ASC structures, structural dynamics and materials co-located conferences, Honolulu, 23–26 April 2012
- Debrabandere F (2014) Computational methods for industrial fluid-structure interactions. Dissertation, Université de Mons (UMONS)
- Elfarrar MA, Sezer-Uzol N, Akmandor IS (2014) NREL VI rotor blade: numerical investigation and winglet design and optimization using CFD. *Wind Energy* 17(4):605–626
- Fan Z, Kang S (2009) Numerical simulations of the aerodynamics performance of Horizontal Axis Wind Turbines. In: Tao Y, Ma C (eds) UECTC 2009. Inaugural US-EU-China thermophysics conference-renewable energy, Beijing, May 2009. American Society of Mechanical Engineers (ASME), Houston. doi:10.1115/1.802908.paper16
- Gaunaa M, Zahle F, Sørensen NN, et al (2013) Rotor performance enhancement using slats on the Inner part of a 10 MW rotor. Paper presented at the European wind energy conference and exhibition (EWEA), Vienna, 4–7 February 2013
- Heege A, Gaull A, Horcas SG, et al (2013) Experiences in controller adaptations of floating wind turbines through advanced numerical simulation. Paper presented at the AWEA WINDPOWER 2013 conference and exhibition, Chicago, 5–8 May 2013
- Horcas SG, Debrabandere F, Tartinville B, et al (2014) Mesh deformation tool for Offshore Wind Turbines fluid-structure interaction. In: Abstracts of the 11th World Congress on Computational Mechanics (WCCM XI), Barcelona, 20–25 July 2014
- Horcas SG, Debrabandere F, Tartinville B, et al (2015a) A new, high fidelity offshore wind turbines aeroelasticity prediction method with significant CPU time reduction. Poster presented at the Offshore 2015. European Wind Energy Association, Copenhagen, 10–12 March 2015
- Horcas SG, Debrabandere F, Tartinville B, et al (2015b) Hybrid mesh deformation tool for offshorewind turbines aeroelasticity prediction. In: Ferrer E, Montlaur A (eds) CFD for wind and tidal offshore turbines SE - 8, Springer tracts in mechanical engineering. Springer, Heidelberg, pp 83–94
- Hsu MC, Bazilevs Y (2012) Fluid-structure interaction modeling of wind turbines: simulating the full machine. *Comput Mech* 50(6):821–833
- Hsu MC, Akkerman I, Bazilevs Y (2014) Finite element simulation of wind turbine aerodynamics: validation study using NREL Phase VI experiment. *Wind Energy* 17:461–481
- Jonkman JM, Buhl ML (2007) Development and verification of a fully coupled simulator for offshore wind turbines, NREL/CP-500-40979. In: National Renewable Energy Laboratory documents. Available via NREL. <http://www.nrel.gov/docs/fy07osti/40979.pdf>. Accessed 11 Apr 2016
- Larsen T, Hansen A (2007) How to HAWC2, the User's manual. In: DTU orbit - the research information system. Available via Technical University of Denmark. [http://orbit.dtu.dk/files/7703110/ris\\_r\\_1597.pdf](http://orbit.dtu.dk/files/7703110/ris_r_1597.pdf). Accessed 11 Apr 2016
- Le Pape A, Lecanu J (2004) 3D Navier-Stokes computations of a stall-regulated wind turbine. *Wind Energy* 7(4):309–324
- Li Y (2014) Coupled computational fluid dynamics/multibody dynamics method with application to wind turbine simulations. Dissertation, University of Iowa
- Liebeck RH (1978) Design of subsonic airfoils for high lift. *J. Aircraft* 15(9):547–561
- Lynch CE (2011) Advanced CFD methods for wind turbine analysis. Dissertation, Georgia Institute of Technology
- NUMECA International (2013a) Autogrid5™ v9.0 User Manual, NUMECA, Brussels
- NUMECA International (2013b) FINE™/Turbo v9.0 User Manual, NUMECA, Brussels
- Simulia DSC (2008) Abaqus Analysis version 6.8 User's Manual, Simulia, Waltham
- Sørensen NN (1995) General purpose flow solver applied to flow over hills. Risø National Laboratory, Roskilde

- Spalart P, Allmaras S (1992) A one-equation turbulence model for aerodynamic flows. In: Abstracts of the 30th AIAA aerospace sciences meeting and exhibit, AIAA, Reno, 6–9 January 1992
- Suárez JM, Doerffer P, Szulc O (2015a) CFD validated technique for prediction of aerodynamic characteristics on horizontal axis wind energy turbines. Poster presented at the Offshore 2015. European Wind Energy Association, Copenhagen, 10–12 March 2015
- Suárez JM, Doerffer P, Szulc O, et al (2015b) Aerodynamic analysis of wind turbine rotor blades. *Task Quart* 19(2):129–140
- Troldborg N, Zahle F, Sørensen NN (2015) Simulation of a MW rotor equipped with vortex generators using CFD and an actuator shape model. In: 53rd AIAA Aerospace Sciences Meeting, American Institute of Aeronautics and Astronautics, Kissimmee, 5–9 July 2015
- Vilmin S, Lorrain E, Hirsch C, et al (2006) Unsteady flow modeling across the rotor/stator interface using the nonlinear harmonic method. In: Abstracts of the ASME Turbo Expo 2006: power for land, sea and air, American Society of Mechanical Engineers, Barcelona, 8–11 May 2006
- Wang Q, Zhou H, Wan D (2012) Numerical simulation of wind turbine blade-tower interaction. *J Mar Sci Appl* 11(3):321–327
- Yu DO, Kwon OJ (2014) Predicting wind turbine blade loads and aeroelastic response using a coupled CFD-CSD method. *Renewable Energy* 70:184–196
- Zahle F, Sørensen NN (2008) Overset grid flow simulation on a modern wind turbine. In: Abstracts of the 26th AIAA applied aerodynamics conference, guidance, navigation, and control and co-located conferences, American Institute of Aeronautics and Astronautics, Honolulu, 18–21 August 2008
- Zahle F, Sørensen NN (2011) Characterization of the unsteady flow in the nacelle region of a modern wind turbine. *Wind Energy* 14(2):271–283
- Zahle F, Sørensen NN, Johansen J (2009) Wind turbine rotor-tower interaction using an incompressible overset grid method. *Wind Energy* 12(6):594–619
- Zahle F, Bak C, Guntur S, et al (2014) Comprehensive aerodynamic analysis of a 10 MW wind turbine rotor using 3D CFD. In: Abstracts of the 32nd wind energy symposium, American Institute of Aeronautics and Astronautics, National Harbor, 13–17 January 2014

**Part VI**  
**Offshore Wind Farm Design**

# Chapter 19

## An Overview of Offshore Wind Farm Design

Gregor Giebel and Charlotte Bay Hasager

**Abstract** For offshore wind energy to be viable, the design of wind turbines is not the only important factor—rather, the design of wind *farms* is also crucial. The current chapter discusses the challenges of designing an optimum wind farm and identifies the various factors that need to be considered. Lastly, the chapter presents the novel EERA-DTOC tool for designing offshore wind farm clusters.

### 19.1 An Overview of Offshore Wind Farm Design

There are two stages in the design of offshore wind farms, run by two different stakeholders. The first stage is often the choice of sites for tendering through a national authority, such as the Danish Energy Agency or the Crown Estate in the UK. During this stage, a number of different exclusion zones have to be managed, such as nature reserves, shipping lanes, oil exploration areas, light house cones, risks of unexploded ordnance or the chances for finding archaeological remains. Typically, the locations thus determined will be opened in a call for tenders, where the second stage of the wind farm design is done at the wind power developers. They now look into wind, wave and sea bed conditions, availability of foundation and turbine types and installation ships, layout of the wind farm, both taking wakes and cabling into account, projected operation and maintenance cost, and try to roll all of this information into typically a bid for a price per produced kWh. In some jurisdictions, the cost of transporting the power onshore is priced in with the wind farm, in other places the transmission system operator will have the duty of providing a suitable grid connection point in the vicinity of the wind farm. Usually, the cheapest bidder will be awarded the contract. Once that has happened, the detailed design of the wind farm will go on, including in-depth investigations of the sea bed, contracting of suppliers of hardware and services, detailed layouting of the farm, and finally the construction. As the last step before power delivery, the transmission system operator will check for grid code compliance, together with the checkout of the

---

G. Giebel (✉) • C.B. Hasager  
Department of Wind Energy, Technical University of Denmark (DTU), DTU Risø Campus,  
Frederiksborgvej 399, 4000 Roskilde, Denmark  
e-mail: [rgi@dtu.dk](mailto:rgi@dtu.dk); [CBHA@dtu.dk](mailto:CBHA@dtu.dk)

suppliers. Then, the wind farm will go into an operational state and will produce power for the next 25 years.

## 19.2 Strategic Planning

The first real offshore wind farm was built in Denmark, in 1991 in Vindeby. It consists of 9 Bonus 450 kW turbines on gravity foundations. It was followed by the similar sized wind farm at Tunø Knob in 1995. Both sites are in relatively protected Danish waters, and are now owned and operated by DONG Energy. Also for the permitting of the wind farm, the process was new and had to be a collaborative work of the Danish Energy Agency (DEA) as the permitting government authority and Elkraft, then the executing developer. A similar process still exists in Denmark under the name of Open-Door Policy, where new projects can be proposed and then will make their way through the permitting process. However, the more relevant process in recent years is the tendering process, where first parliament agrees on the size and overall location of the next Danish offshore farm, and then the DEA investigates the area and designs a call for tender. This was the procedure for the first large-scale offshore wind farm at Horns Rev in 2002, with 80 turbines and 160 MW total, and it has been refined ever since. The developer bids in with a price per kWh produced by the offshore wind farm. In this way it is hoped that the overall prices for offshore wind power come down over time.

Uncertainty about the input parameters for the wind farm design leads to higher prices from the developers. Therefore, already for the tender for the Anholt wind farm the Danish Climate and Energy Ministry changed the process so that the relevant sea bed investigations and the Environmental Impact Assessment (EIA) was handled and the outcome be known before the bids were given (Energinet.dk 2010). In this EIA, coordinated by the Danish Transmission System Operator Energinet.dk, a larger area was investigated in detail before the final call for tenders was published with regard to sea bed conditions, hydrography, geomorphology, coastal morphology, water quality, marine life and vegetation, benthic habitats, fish, birds, marine mammals, landscape issues, raw materials, marine archaeology, recreational areas, protected areas, ship and aerial traffic, fishery and others, during construction, operation and dismantling.

The influence of uncertainty on the price was exposed during the process leading to the Anholt wind farm. In this case, the Danish parliament required a new offshore wind farm to be built in too short a time to get a good process underway. This resulted in only one bidder (DONG Energy), who then claimed that the preparation time was too short to bring the uncertainties down, and added a significant mark-up to the best guess price. The next tender leading to the Horns Rev 3 wind farm had longer time for bidding, and subsequently for construction, and therefore attracted several bids. The outcome was 32 % cheaper than the price at Anholt. This price means, according to the Danish Ministry for Climate, Energy and Buildings, an economic benefit for rate payers in the order of 2.2 billion kroner over the lifetime



of the wind farm, in comparison to previous cost estimates (EFKM Denmark 2015). While this in part is due to moving technology (larger turbines were available since) and a better wind climate, reduced uncertainties also were a factor.

In the UK, the Crown Estate administers all the sea bed outside the 12-mile zone, and thus is the regulating authority for offshore wind farms in the UK. In three tendering rounds, the Crown Estate has increased the size of the area one could bid for, to the current Round 3 sites with over 1 GW potential each. Wind farms in the UK, despite an at least comparable wind resource to Denmark, are netting a higher strike price (in a “Contracts for Difference” scheme, the fixed price paid per kWh for the first e.g. 15 years; the premium is then the difference between the market price and the strike price) than their Danish counterparts. One important difference is that the transmission is in Denmark, but also in e.g. Germany, taken care of by the TSO. Thereby, the cost of transmission is spread over the total customer base of the TSO. In the UK, the transmission is a part of the strike price and therefore has to be financed as part of the wind farm investment.

### 19.3 Offshore Wind Farm Design

The main driver for wind farm design is the cost of energy. A simple model for the Levelised Cost of Energy, LCOE, is shown in Eq. (19.1):

$$LCOE = \frac{CaPEX \bullet CRF + OpEX}{AEP} \quad (19.1)$$

where CaPEX is the Capital Expenditure (i.e. the cost of wind turbines, foundations, cables, transmission system etc., their installation and financing), CRF is the Capital Recovery Factor (essentially a simplified representation of the discounted cash flow), OpEX are the Operating Expenses (i.e. operation and maintenance expenses), and AEP is the Annual Energy Production. Within this model, several sub-models are amenable to optimization. For example, in a radial cabling layout in the wind farm, where one radial connects a string of turbines to the substation, the cables further from the substation carry less electricity and could therefore be of smaller diameter. However, the installation cost can be double the cost per metre than the cable itself, and changing the cable on the installer ship incurs lost time too, so the optimization is less straightforward than just determining the electrical needs.

Construction of the offshore farm is a major cost factor. The industry has moved to dedicated ships installing the foundations and turbines, working as jack-up barges (Fig. 19.1) for a stable working platform in up to 30+ m water depth. Those ships can cost up to 200,000 €/day, and can install up to 2 turbines a day in optimal weather conditions. In larger wind farms, many processes work in parallel, installation of foundations, cable laying, removal of Unexploded Ordnance (UXO), diving for cable connection or inspection of the works done, and other things. For example, at the peak of construction of the currently largest offshore wind farm,



**Fig. 19.1** A2SEAs SEA JACK during the construction of the Gwynt y Mor wind farm. Image Source: A2SEA (2016)

there were 1000 people working simultaneously on 60 vessels in the London Array (2016) site.

The OpEX is, to a large degree, determined by maintenance cost—both scheduled preventive and corrective maintenance, and the related lack of availability. The optimization of those depends heavily on the weather windows for accessibility of the farm. Already in 2001, Risø National Laboratory (now part of DTU) presented a tool to estimate weather windows and calculate the corresponding availability and outages of the turbines (Christensen and Giebel 2001). A main factor was the wave pattern at the site, as the significant wave height was more often a determining factor than too high winds. In 2012, researchers from University of Strathclyde (Dinwoodie et al. 2012) presented a similar picture using actual data: the availability in winter for three actual wind farms was significantly lower than in summer, which was attributed to the lack of accessibility to the sites (Fig. 19.2). In a notional 300 MW wind farm, this difference would mean over 2 million euros per month in lost production.

Finally, the last factor going into the determination of the LCOE is the AEP. Since usually, the wind distribution is mostly given by the choice of site by the national authority, and since the wind speed is not varying strongly across the area offshore (at least for current wind farm sizes sufficiently away from the shore), the most determining factor are the wake effects. By their very nature, wind turbines extract energy out of the wind, which means that the wind behind a turbine is less strong. If that diminished wind speed then comes to the next turbine, that turbine will produce less than if it was in free flow conditions. Researchers developed models to calculate this effect already in the 1980s, and by now a wealth of models with

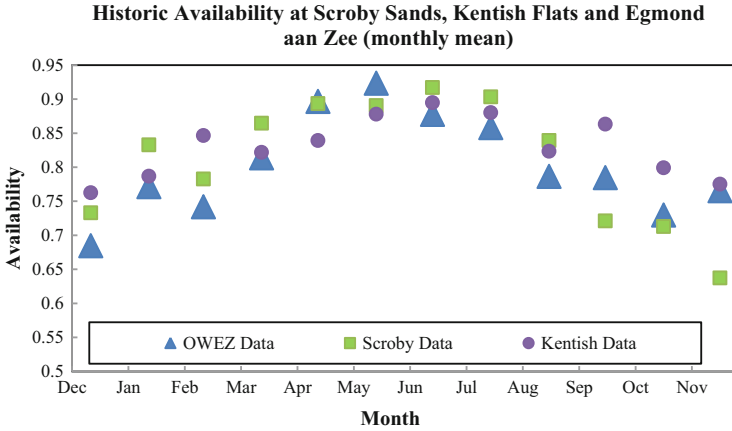


Fig. 19.2 Availability of three wind farms in the Netherlands and the UK. Source: Dinwoodie et al. (2012)

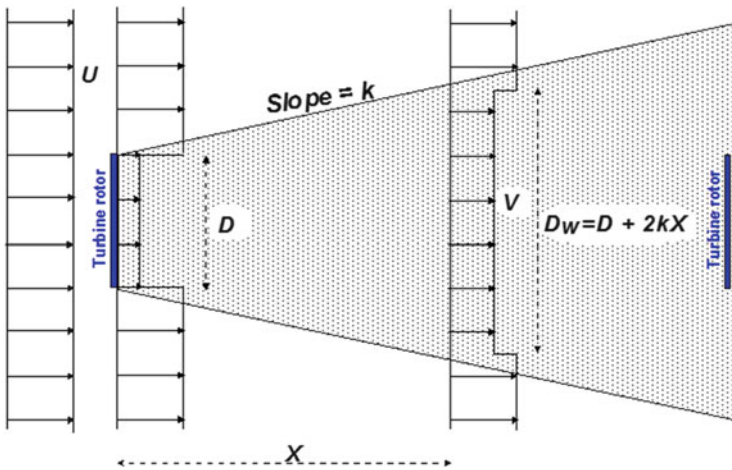
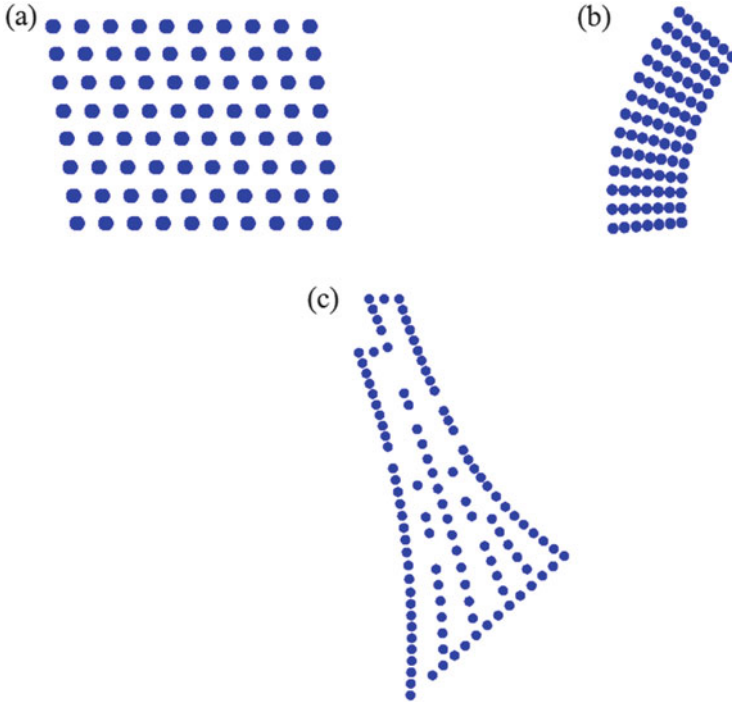


Fig. 19.3 Wake deficit and expansion as modelled by the PARK model of N.O. Jensen

varying degrees of sophistication have been developed. One of the simplest models is the PARK model developed by N.O. Jensen (Fig. 19.3), embodied in the siting software WAsP (2016). In reality, the wake expansion covers the fact that the wake expands relatively little, but meanders right and left in the atmospheric turbulence, which in the 10-min averages usually used for the AEP calculations gives the average wake loss given by the picture. Offshore, due to the reduced turbulence, the expansion parameter  $k$  is different from its onshore value. On the other end of the scale, Computational Fluid Mechanics (CFD) and Large Eddy Simulation (LES) models can calculate the wind flow in a wind farm with much higher resolution, but require significantly more running time, up to weeks on a supercomputer.



**Fig. 19.4** The layouts of the (a) Horns Rev 1, (b) Horns Rev 2 & (c) Anholt OWFs. Source: Nygaard (2015)

Some major parameters with which to influence the total wake loss in a wind farm are the turbine spacing and layout. One can distinguish different generations of designs when looking at the development of the Danish offshore wind farms.

The first attempts were regular layouts like the one at Horns Rev 1 (and Nysted, built a year later), as shown in Fig. 19.4a. However, since the wake effects are very sensitive to the wind direction, already small changes in wind direction (as they happen frequently) will change the power output of the farm significantly, making the power less predictable and more difficult to integrate into the grid. This insight led to a second generation layout like the Horns Rev 2 (Fig. 19.4b), and Rødsand wind farms. Since the straight lines in the wind farm are not pointing into the same direction, the sensitivity towards wind direction changes is much reduced.

For the Anholt wind farm (Fig. 19.4c), built in 2012, developer DONG Energy chose a different layout. A more thorough assessment of the wake effects led to a perimeter centred layout, based on the notion that the second row shows the strongest wake effects, so an elimination of the second row will reduce the overall wake effects. However, this is not precedence for future wind farms. Also after Anholt there were farms planned in the UK with more regular layouts.

RS-2 20130430 17:41:53 UTC SAR intensity image

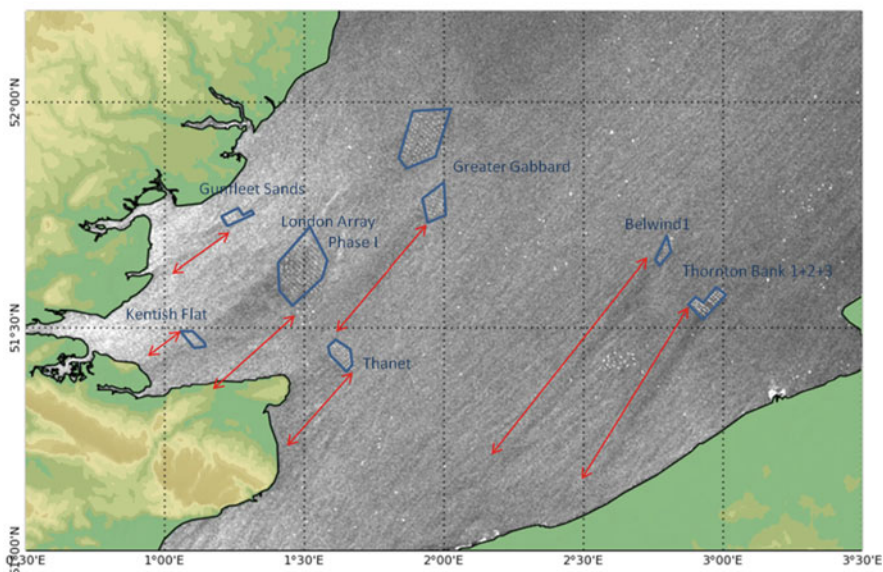


**Fig. 19.5** RADARSAT-2 intensity map of the southern North Sea observed 30 April 2013 at 17:41 UTC. The *blue lines* outline wind farms and the *red arrows* the wind farm wake. The SAR-wind processing chain was set up by Collecte Localisation Satellites (CLS). Source: Hasager et al. (2015)

Wakes are not only an issue within a wind farm, they also extend for many km down-drift of the wind farm. The wind speed near the sea surface can be measured using Synthetic Aperture Radar (SAR), e.g. mounted on satellites (Hasager et al. (2015)). In certain weather situations, the area of reduced production can extend several tens of kilometres. At Belwind wind farm the wake is around 55 km long, at Thornton Bank 45 km, at London Array 15 km, at Thanet 14 km and at Kentish Flat 10 km (but probably continues inland). It is the intensity image where the darker area is due to lower wind speed (Fig. 19.5).

## 19.4 EERA-DTOC and Wind & Economy

Over the last 3.5 years, the European Energy Research Alliance (EERA) integrated many of the institutes' softwares into a common Design Tool for Offshore Clusters (eera-dtoc.eu) in a project sponsored by the EU in years 2012–2015 (project budget 4 million euro). While strategic planners were envisaged as a potential target group, owing to the consortium membership in the EERA-DTOC project, the main emphasis went into making a good tool for offshore wind farm developers

(DTU Vindenergi 2016). Therefore, it integrated the workflow and the models from different planning aspects, i.e., wind climate, wakes and electrical models from grid to turbine plus a LCOE model, which currently embodies the cost function of an offshore developer. A number of EERA members’ state-of-the-art models and software products, most notably DTU Wind Energy’s own but also tools for the design of the grid inside the farm and the connection to the shore were integrated in the Design Tool for Offshore Clusters (DTC) (Hasager and Giebel 2015). The tool, also commercially available under the name *Wind & Economy* (Wind and Economy 2016), was designed, integrated and developed by Overspeed, a SME from Oldenburg with specialty in wind consultancy and wind related software development.

The EERA-DTC tool was designed based on input from end users. Its aim is to support the optimisation of LCOE by comparing different variants for the farm layout. A central concept of the DTC tool is the organization of wind farm variants as scenarios and scenario trees. The single scenario is a fine-grained project variant, distinguished by all project parameters and the employed model chain including the model parameters. Scenarios can be cloned or duplicated, and inherit the settings from the higher level scenario.

This philosophy supports one of the central user stories (i.e., use cases): ‘As a developer I can determine the optimum spacing, position, turbine model and hub height of turbines within an offshore wind farm’.

The DTC software supports the generation and comparison of the calculation results of many design scenarios. Comparative reporting of those results enables then the selection of optimized configurations. The work flow to optimize through comparing LCOE is shown in Fig. 19.6.

In order to calculate the LCOE, the submodels for e.g. cabling, AEP and grid compliance have to be called for each scenario. GIS data is also integrated in the tool, taking thus e.g. bathymetry into account. The runs start with the calculation of the wind climate calling a remote WRF installation at one of the three offering centres (DTU Wind Energy, CENER or CIEMAT). Typically, two or three runs are made, one run calculating a wind climate without any wind farms, one run with all currently running farms, and one run also including future wind farms planned in the

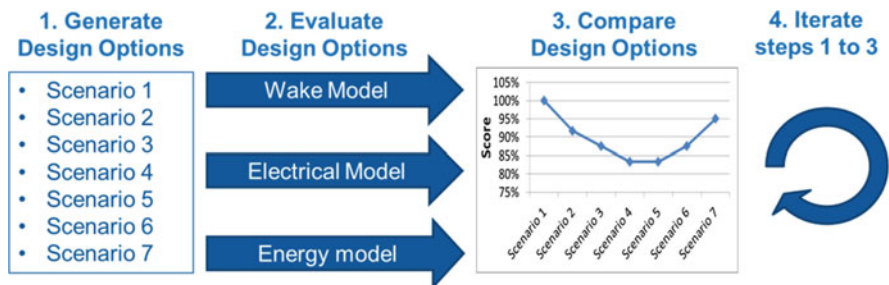


Fig. 19.6 Work flow for the DTC-tool based optimization process



area. In this way, a timeline can be established when the production is going to drop due to wake effects from new wind farms. Since this wind climate is notionally the same for all wind farm configurations, it is run only once. This wind climate is then put into different farm layout options, which are compared according to Fig. 19.6. Therefore, instead of having to convert data from one program to the next, the user can handle many more scenarios before the bidding process begins.

**Acknowledgments** The authors would like to acknowledge funding from the EuroTech Greentech Wind initiative.

Satellite images from RADARSAT-2 from Data and Products © MacDonald, Dettewiler and Associates Ltd.

Support from the European Energy Research Alliance - Design Tools for Offshore wind farm Clusters (EERA DTOC) project FP7-ENERGY-2011-1/ n°282797 is acknowledged.

**Open Access** This chapter is distributed under the terms of the Creative Commons Attribution-NonCommercial 4.0 International License (<http://creativecommons.org/licenses/by-nc/4.0/>), which permits any noncommercial use, duplication, adaptation, distribution and reproduction in any medium or format, as long as you give appropriate credit to the original author(s) and the source, provide a link to the Creative Commons license and indicate if changes were made.

The images or other third party material in this chapter are included in the work's Creative Commons license, unless indicated otherwise in the credit line; if such material is not included in the work's Creative Commons license and the respective action is not permitted by statutory regulation, users will need to obtain permission from the license holder to duplicate, adapt or reproduce the material.

## References

- A2SEA (2016) A2SEA Gwynt y Mor SEA-JACK. [w.a2sea.com/wp-content/uploads/2014/07/A2SEA\\_Gwynt\\_y\\_Mor\\_SEA-JACK.jpg](http://w.a2sea.com/wp-content/uploads/2014/07/A2SEA_Gwynt_y_Mor_SEA-JACK.jpg). Accessed 12 Apr 2016
- Christensen P, Giebel G (2001) Availability of wind turbines in remote places. A statistical and a real-time view. Paper presented at the 2001 European wind energy conference and exhibition, Copenhagen, 2–6 July 2001
- EFKM Denmark (2015) Danmark får billigere strøm fra havvindmøller. <http://www.kebmin.dk/nyheder/danmark-faar-billigere-stroem-havvindmoeller>. Accessed 12 Apr 2016
- Dinwoodie I, Quail F, McMillan D (2012) Analysis of offshore wind turbine operation and maintenance using a novel time domain meteo-ocean modeling approach. Paper presented at the ASME Turbo Expo 2012: Turbine technical conference and exposition, Copenhagen, 11–15 June 2012
- Energinet.dk (2010) Anholt Havmøllepark – Vurdering af virkninger på miljøet, VVM redegørelse. In: Energy Styrelsen Denmark files on renewable-energy, wind-power, offshore-wind-power and environmental-impacts. Available via ENS DK. [http://www.ens.dk/sites/ens.dk/files/supply/renewable-energy/wind-power/offshore-wind-power/environmental-impacts/anholt\\_havmoellepark\\_vvm-redegoerelse.pdf](http://www.ens.dk/sites/ens.dk/files/supply/renewable-energy/wind-power/offshore-wind-power/environmental-impacts/anholt_havmoellepark_vvm-redegoerelse.pdf). Accessed 12 Apr 2016
- Hasager CB, Giebel G (eds) (2015) EERA-DTOC final summary report. In: European Energy Research Alliance – Design Tool for Offshore Wind Farm Cluster files (EERA-DTOC). Available via EERA-DTOC. <http://www.eera-dtoc.eu/wp-content/uploads/files/D7-20-EERA-DTOC-final-summary-report-web-version.pdf>. Accessed 12 Apr 2016
- Hasager CB, Vincent P, Badger J et al (2015) Using satellite SAR to characterize the wind flow around offshore wind farms. *Energies* 8(6):5413–5439. doi:10.3390/en8065413

- London Array (2016) Offshore construction. <http://www.londonarray.com/the-project-3/offshore-construction/>. Accessed 12 Apr 2016
- Nygaard NG (2015) Wake model uncertainty quantification – a systematic approach. Paper presented at the EWEA offshore 2015 conference, Copenhagen, 10–12 Mar 2015
- DTU Vindenergi (2016) Streamlining project planning of offshore wind farms. <http://www.vindenergi.dtu.dk/Nyheder/Nyhed?id=C3435BFD-EF12-42CF-8F39-FD5FA8E948C8>. Accessed 12 Apr 2016
- WAsP (2016) WAsP website. [www.wasp.dk](http://www.wasp.dk). Accessed 12 Apr 2016
- Wind And Economy (2016) Wind and economy. <http://wind-and-economy.com/home/>. Accessed 12 Apr 2016



# Chapter 20

## Large Eddy Simulation of Wind Farm Aerodynamics with Energy-Conserving Schemes

Dhruv Mehta

**Abstract** In order to truly realise the potential of wind power, it is vital to understand the aerodynamic losses over a wind farm. The current chapter highlights the importance of aerodynamic analysis of offshore wind farms, and presents a summarized review of Large Eddy Simulation literature. Furthermore, the chapter presents the objectives of the current research and concludes with a case study.

### 20.1 Introduction

This chapter presents a study on the Large Eddy Simulation of wind farm aerodynamics. Wind farm aerodynamics (WFA) deals with the interaction between wind turbine wakes and the atmospheric boundary layer (ABL), as they develop across the length of the wind farm. At times, the wakes also interact with each other and with other wind turbines (Mehta et al. 2014).

The study of WFA is crucial as it provides insight into the air flow through a wind farm, which eventually provides the energy that is converted into electricity by wind turbines. Therefore, one can assess the power produced by a wind farm by aerodynamically analysing the flow through the farm. The study of WFA requires aerodynamic data, which is generally gathered through meteorological masts in existing wind farms.

With the apparatus placed on these masts, we can measure the velocity and turbulence intensity (TI)—albeit at only a single point. In case the apparatus is an array of instruments, one may be able to measure the velocity (and TI) at more than a single point. Nonetheless, even in the best cases, the aerodynamic data for a few points on a wind farm is not enough to assess the power produced by the wind farm. Further, the erratic nature of the atmosphere makes it hard to relate the measured velocity (or TI) to its cause. For example, one cannot be certain whether

---

D. Mehta (✉)

Wind Energy Research Institute (DUWIND), Delft University, Kluyverweg 1, 2629 HS Delft, Netherlands

Energy Research Centre of the Netherlands (ECN), Westerduinweg 3, 1755 LE Petten, Netherlands

e-mail: [d.mehta@tudelft.nl](mailto:d.mehta@tudelft.nl)

the measured velocity (or TI) is from a single turbine’s wake, or due to a sudden gust through the farm etc. Thus, for a complete insight, it is important to complement experimental data with numerical data from simulations.

## 20.2 Simulation

To simulate the flow through a wind farm, one must numerically resolve the various eddies within the air flow. These eddies represent the different scales of turbulence. For a high Reynolds number flow, these eddies can be of various sizes (Pope 2000). In case of a wind farm, this difference in eddy sizes can be between a few millimetres corresponding to boundary layer on a turbine’s blade, and a kilometre corresponding to the height of the boundary layer. When the energy of these scales is plotted against their size, one obtains the energy spectrum as shown in Fig. 20.1.

The largest scales are the energy-containing integral range and the smallest ones are the dissipative, Kolmogorov scales (Tennekes and Lumley 1972). In between lies the inertial range. On a wind farm, these scales are about a few centimetres in size.

It is computationally impossible (with today’s resources) to resolve all these scales feasibly. Therefore, the wisest approach would be to numerically resolve only the large energy containing scales (and a part of inertial range), to gain insight into WFA. This approach is known as Large Eddy Simulation (LES); an example of

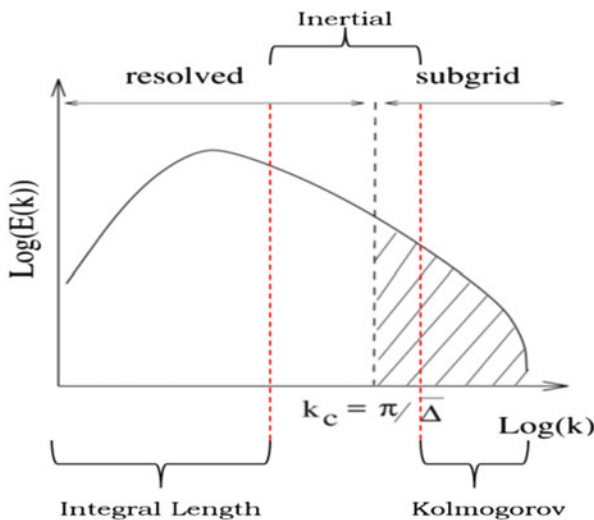


Fig. 20.1 The energy of the various eddies (y-axis) in a flow, plotted against their size (x-axis)

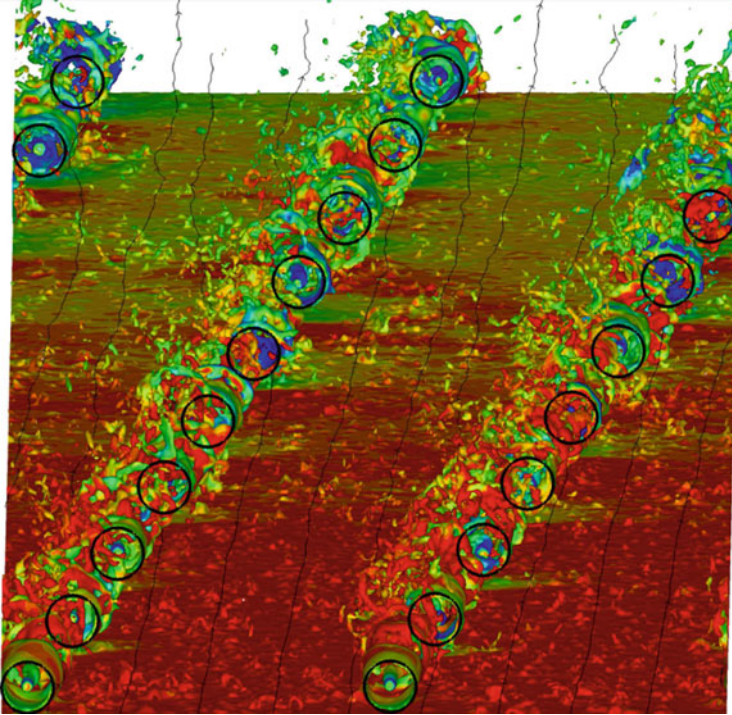


Fig. 20.2 Large Eddy Simulation of the Horns Rev wind farm [Source: Ivanel (2009)]

LES is shown in Fig. 20.2. As shown in Fig. 20.1, the scales that are numerically calculated are called the ‘resolved scales’ and the rest are known as the ‘subgrid scales’. The latter are numerically modelled with a subgrid scale (SGS) model.

### 20.3 Literature Review

A comprehensive literature review on LES was conducted by Mehta et al. (2014). We summarize the key points below:

- Wind farms simulations have been performed predominantly with eddy-viscosity models. Even the simple Smagorinsky’s model is sufficient for qualitative analyses of wind farm aerodynamics. But for accuracy, researchers must rely on more advanced SGS models.
- With proper ABL modelling, LES can help assess the performance of wind farms in off-design conditions like non-neutral ABLs and gusts. Effective coupling with aeroelastic codes could provide great insight into turbine loading in such situations.

- Wind farm simulations rely on accurate wake-ABL interaction, which is possible only with a correct ABL model. This is of great consequence for simulating large wind farms on which the ABL evolves into a wind turbine-ABL. Generating a synthetic ABL requires lesser computational effort than precursor simulations with LES, but lacks the statistical correlations that exist in a physical ABL.
- Using the Scale Dependent Dynamic model with Lagrangian averaging generates an ABL that is accurate enough for wind farm simulations, but is computationally expensive. Nonetheless, it retains its precision even on coarse grids making it suitable for LES.
- From simulations of the Horns Rev wind farm, it is apparent that the performance of engineering models is comparable to that of certain LES codes, as far as generating averaged statistics. When done with accurate ABL modelling and with advanced SGS models, on relatively refined grids, LES delivers a substantially better performance.
- LES data can be utilised to enhance simple engineering models to retain computational efficiency but ensuring better accuracy.
- Numerical schemes for LES must ensure zero numerical dissipation for high accuracy. Pseudo-spectral and Energy-Conserving spatial discretisation schemes are useful in this regard; the latter however requires a higher-order formulation to be as accurate as the former. Additionally, energy-conserving time integration with zero dissipation would help speed up computations, but requires further modifications to avert loss in accuracy and stability.
- A stress-free upper boundary is most appropriate for wind farm simulations. Periodic boundaries required by spectral schemes can be avoided with Energy-Conserving schemes, which are however not as accurate as the former.
- SGS models have been compared in terms of their ability to simulate the ABL. It is clear that above beyond a certain resolution, the effect of the SGS model on ABL is nullified and even a simple model is sufficient for an ABL simulation. However, such a conclusion with regard to wind farm simulations is yet to be drawn.

Concerning LES, it is certain that no SGS model is complete and their efficacy is situation-dependent. Smagorinsky's model and its derivatives are popular as they are easily implementable and capable of producing good data on wind farm aerodynamics, despite their assumptions lacking conclusive evidence. Regarding coarse grids, it would be wise to develop numerical schemes instead of relying on excess computational power. LES codes cannot count on upwind schemes of stability because the numerical dissipation will dampen the resolved scales, more so on coarse grids. High-order spectral methods are thus common in LES but are computationally expensive. On the other hand, Energy-conserving schemes are free from numerical dissipation and permit the use of non-periodic boundaries, but require further investigation at this stage.

In terms of boundary conditions, Monin-Obukov’s (Panofsky and Dutton 1984) approach remains the only option for modelling the ABL, despite being deemed unsuitable for LES. Lately, research has been focussed on developing a more appropriate technique that could be adapted for inhomogeneous terrains, but experiments would be more instrumental in enhancing the existing approach.

### 20.4 Power Losses and Observations

Figure 20.3 shows the power generated by the various rows of wind turbines simulated as shown in Fig. 20.2. It can be observed that the power generation is the highest for turbines in the front row, which is exposed directly to the freestream ABL flow. However, turbines within this row generate a wake, which develops with downstream distance and interacts, in the case of Horns Rev, within downstream turbines.

Therefore, there is a sudden decrease in power generation by the second row. This is due to the reduced velocity in the wake. However, a wake not only bears a reduced velocity but also a higher turbulence intensity. This fact has been confirmed experimentally by Chamorro and Porté-Agel (2011) and numerically through LES by Stevens et al. (2013).

This increased turbulence promotes the mixing of the slower wake with the faster freestream ABL flow, leading to the reduction of the velocity deficit in the wake and increased velocity. This is the reason why the second row (Horns Rev,

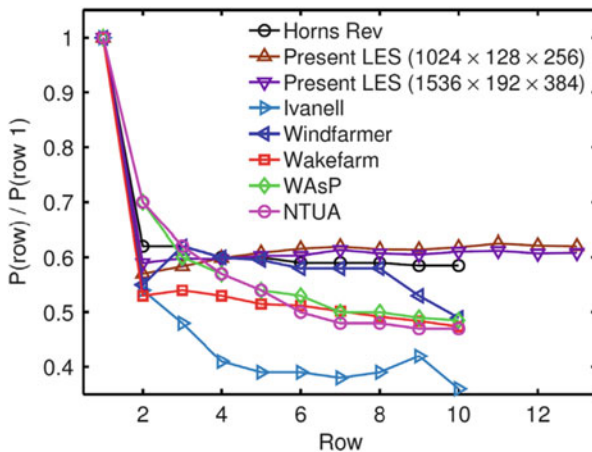


**Fig. 20.3** The power output on the Horns-Rev wind farm predicted by an LES codes (present LES, and Ivanell (2009)) and various engineering models, adapted from Stevens et al. (2013). The power output on the y-axis has been normalised by the power output of the turbines in the first row. One notices the discrepancy between LES and simple engineering models

black line in Fig. 20.3), generates the highest power amongst all downstream rows. Further, the increased turbulence reaches a peak value after the wake from the first turbine interacts with the second turbine, leading to a slower wake; thus, after one wake-turbine interaction. At times, this could happen after two such wake-turbine interactions, in case the inflow turbulence is low (Mehta et al. 2014).

Once, the wake generated turbulence reaches its peak value, the recovery of the reduced velocity in the wake also reaches its limit. Therefore, after one or two wake-turbine interactions, the wake does not recover much, as a result, one notices a decline in power production across the rows on a wind farm. Nevertheless, the decrease is not steep as compared to the one noticed within the first two rows. The fact that the added turbulence has reached a steady peak value, ensures that the wake recovers after every wake-turbine interaction, to a value that is more or less similar to the inflow value. In effect, beyond the second or third row, the horizontal flow is fully developed, leading a similar power prediction as seen in Fig. 20.3 (Calaf et al. 2010).

Figure 20.3 also compares the data from LES and engineering models. These models are very simple and built upon the simplification of the flow phenomena. As a result, these models are fast and computationally efficient but not very accurate. Further, their accuracy is mostly related to the prediction of the average power output over a range of wind directions, and not for a particular inflow direction, which requires the application of LES (Barthelmie et al. 2009).

## 20.5 Research Objectives

The current research involves three phases:

- Implementing an SGS model in the Energy-Conserving Navier-Stokes (ECNS) code.
- Analysing energy-conserving (EC) spatial discretisation and EC time integration in terms of accuracy and efficiency.
- Validating the combination of the ECNS and the chosen SGS model for wind farm simulations.

## 20.6 Tests and Results

The following are the tests conducted, the results obtained and the conclusions drawn.

### 20.6.1 EC Time Integration

EC time integration available within the ECNS code is unconditionally stable for any time step. Further, it introduces no numerical dissipation during the simulation (Sanderse 2013). However, according to the literature, most existing LES codes would rely on non-EC time integration.

We therefore, used the case of decaying isotropic homogeneous turbulence, to assess whether an EC time integration scheme offers any advantage, in terms of accuracy. We observed that an implicit EC time scheme (4th order accurate), has a lower global error than a 4th order accurate, non-EC explicit time scheme. This error corresponds directly to the numerical dissipation (Fig. 20.4).

However, as shown in Fig. 20.4, the computational time required by the implicit EC time schemes, are much larger than those required by the explicit non-EC schemes. This disproportionality is such that, one is better off using a non-EC explicit time integration scheme (as done by existing LES codes) with a smaller time step, as opposed to an implicit EC scheme.

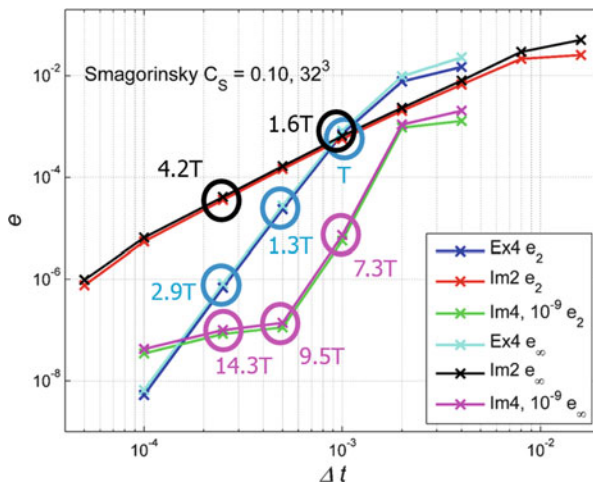


**Fig. 20.4** A plot of the error vs. the time step use with three time integration methods: Ex4, explicit 4th order non-EC Runge-Kutta scheme; Im2, implicit 2nd order EC Gauss scheme and Im4, implicit 4th order EC Gauss scheme. T is the computational time take by Ex4 at a time step of 0.001 s



### 20.6.2 EC Spatial Discretisation

EC spatial discretisation done on a Cartesian staggered grid, is dissipation free for any grid size (Sanderson 2013). However, the scheme itself, is essentially a simple central difference scheme (Perić and Ferziger 2002).

We checked if using an EC spatial discretisation on a Cartesian staggered grid, is the same as using a simple central difference on a collocated Cartesian grid. Using a series of tests on inviscid vortices, we noticed that both the schemes are numerically alike. By extension, the absence of numerical dissipation in either scheme, reduces the grid dependence in tuning the Smagorinsky SGS model chosen for the ECNS (Fig. 20.5).

Therefore, we were able to tune the Smagorinsky model in the ECNS, to a value of the Smagorinsky constant,  $C_S = 0.12$ . Over a range of grid resolutions, this value of the Smagorinsky constant was reasonable enough to predict the behaviour of the large energy-containing scales, correctly.

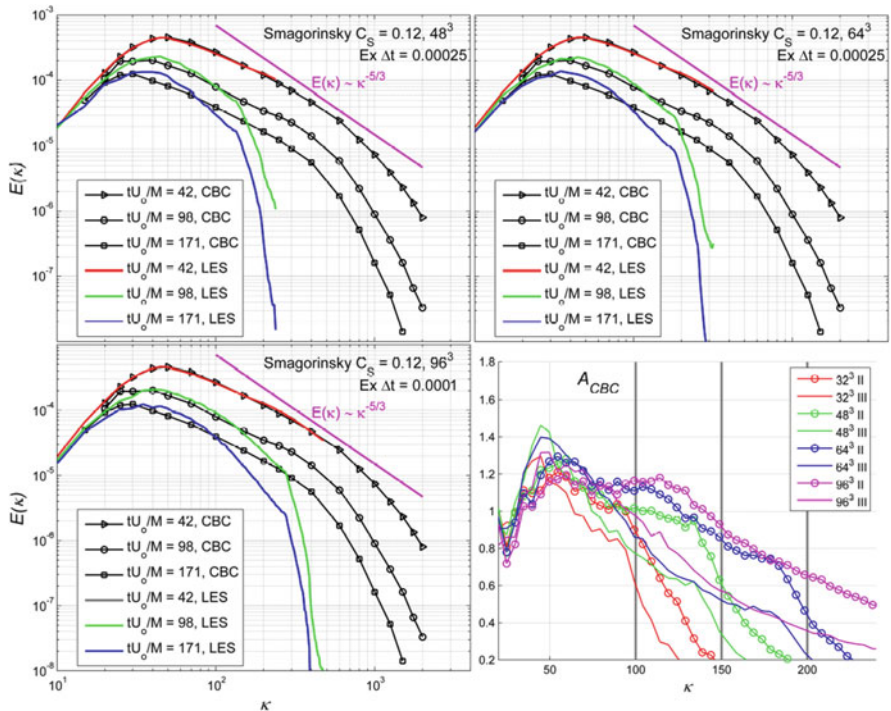


**Fig. 20.5** Clockwise from *top-left*: the energy spectra obtained through experiments (Comté-Bellot and Corrsin 1971) compared against results with the ECNS and a Smagorinsky constant of 0.12, and three different grid resolutions. *Bottom-left*: the ratio of the simulated value of the energy at a given wavenumber to the experimentally obtained value at the same wavenumber



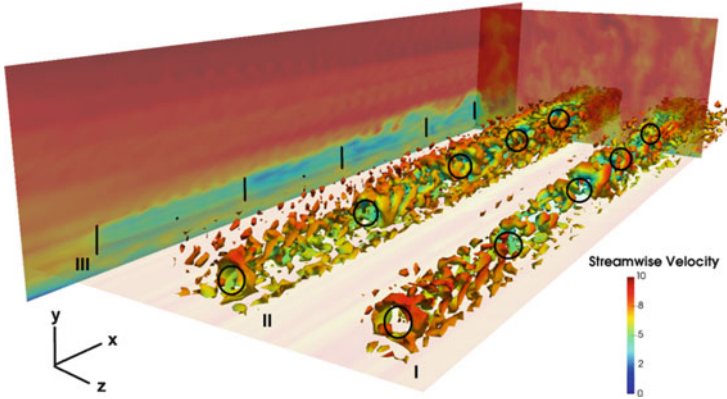


**Fig. 20.6** Isosurfaces of Q-Criterion coloured by streamwise velocity in the wake of turbines on a simple wind farm. The ABL is neutral and runs through a wind farm with 15 turbines

### 20.6.3 Validation

The code with the chosen value of the Smagorinsky constant was validated against two test-cases.

- The simulation of an actuator disk's wake validated against particle image velocimetry measurements in the wake of a porous disc within a wind tunnel, designed to emulate the actuator disk concept (Lignarolo et al. 2014).
- The simulation of a neutral-ABL with the ECNS-Smagorinsky model, to obtain the correct velocity profile and turbulence statistics (Meyers 2011).

The value of the Smagorinsky constant is fit for either case; as a result, we are able to simulate the combination of the actuator disk method and the neutral atmospheric boundary layer (Fig. 20.6).

## 20.7 Case Study: EWTW

We use the validated ECNS-Smagorinsky LES code to simulate the turbines at the ECN Wind Turbine Test-Site Wieringermeer (EWTW) (Bot 2015). It has five turbines of diameter  $D = 80$  m, separated in the streamwise direction by 305 m or  $3.812D$ . We simulate the turbines with an inflow velocity of  $8 \text{ m s}^{-1}$  at hub-height

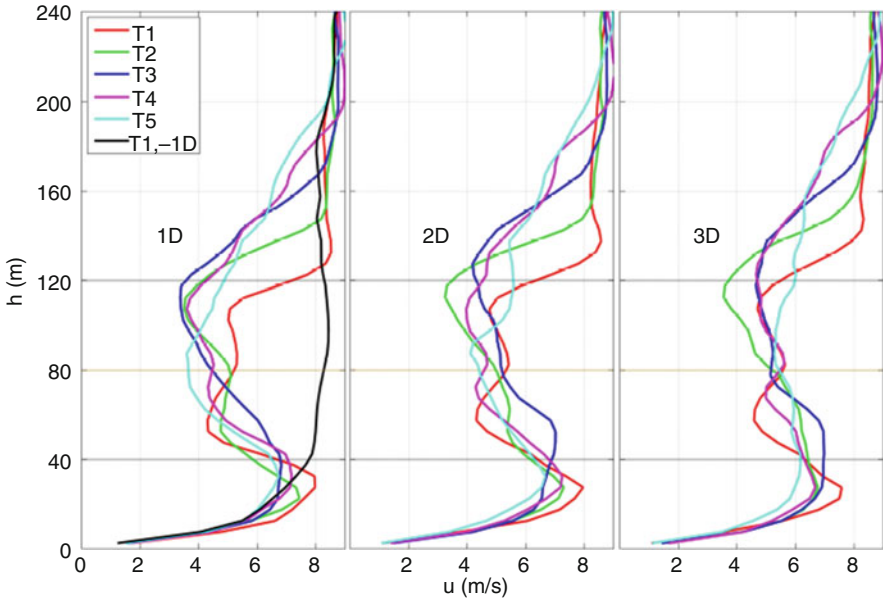


**Fig. 20.7** Profiles of streamwise wake velocity behind the turbines at the EWTW

and a thrust coefficient of 0.789. We do not have ample experimental data to validate the ECNS, however, we do notice trends in the prediction of the wake velocity and turbulence intensity that are relevant to wake-turbine interaction across a row of turbines.

Figures 20.7 and 20.8 show the variation in velocity and turbulence intensity, respectively, with the vertical distance from the ground, behind 5 turbines, T1 to T5, at three downstream distances, 1D, 2D and 3D. In the leftmost plot within Figs. 20.7 and 20.8, the inflow profile has also been plotted (in black) at 1D before the first turbine, T1, or -1D. One notices trends similar to those explained in Sect. 20.4, regarding the recovery of velocity deficit, which is maximum behind the first turbine. However, the velocity recovers more rapidly behind the downstream turbines, as the turbulence intensity develops and reaches a fixed value, which aids the recovery of wake velocity.

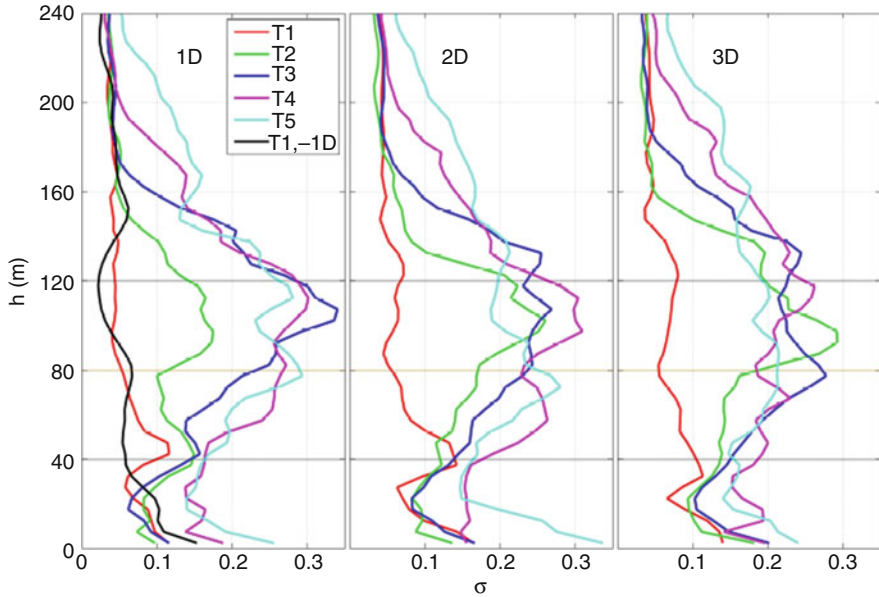


Fig. 20.8 Profiles of turbulence intensity behind the turbines at the EWTW

## 20.8 Conclusions and Recommendations

Based on the research we conclude the following:

- EC time integration is beneficial for averting numerical dissipation, which can lead the spurious decay of energy during wind farm simulations, and eventually, producing a wrong estimate of power generation. However, a non-EC time integration scheme can also guarantee minimal numerical dissipation at a small time step, at significantly lower computational costs.
- EC spatial discretisation helps tune the Smagorinsky model for a range of grid resolutions owing to the absence of numerical dissipation, which varies with grid resolution and must be accounted for while tuning.
- The Smagorinsky constant obtained through tuning the model for decaying isotropic homogeneous turbulence, can be used to simulate a neutral-ABL and the wake of an actuator disk and therefore, by extension, the flow through a wind farm.

For research in the future, we recommend the following:

- Developing an optimised method to using the EC time integration schemes more efficiently. Although non-EC schemes are a fine alternative, they are restricted by a stability criterion that prevents the use of local grid refinement. Such, refinement can help gain insight into critical phenomena in the wake and the

ABL as a whole. Using an EC time scheme that is implicit, will not only remove the restriction on grid refinement but also avert numerical dissipation.

- Simple schemes such as the central difference scheme in OpenFOAM can readily be used for wind farm aerodynamics, instead of developing new computational methods.

**Open Access** This chapter is distributed under the terms of the Creative Commons Attribution-NonCommercial 4.0 International License (<http://creativecommons.org/licenses/by-nc/4.0/>), which permits any noncommercial use, duplication, adaptation, distribution and reproduction in any medium or format, as long as you give appropriate credit to the original author(s) and the source, provide a link to the Creative Commons license and indicate if changes were made.

The images or other third party material in this chapter are included in the work's Creative Commons license, unless indicated otherwise in the credit line; if such material is not included in the work's Creative Commons license and the respective action is not permitted by statutory regulation, users will need to obtain permission from the license holder to duplicate, adapt or reproduce the material.

## References

- Barthelmie RJ, Frandsen ST, Hansen K et al (2009) Modelling the impact of Wakes on Power Output at Nysted and Horns. Paper presented at the EWEC 2009, European wind energy conference and exhibition, Marseille 16–19 March 2009
- Bot ETG (2015) FarmFlow validation against full scale wind farms, Technical Report ECN-E-15-045. In: Energy research Centre of the Netherlands publications. Available via ECN. <https://www.ecn.nl/publications/PdfFetch.aspx?nr=ECN-E--15-045>. Accessed 12 Apr 2016
- Calaf M, Meneveau C, Meyers J (2010) Large Eddy Simulation study of fully developed wind-turbine array boundary layers. *Phys Fluids*. doi:[10.1063/1.3291077](https://doi.org/10.1063/1.3291077)
- Chamorro LP, Porté-Agel F (2011) Turbulent flow inside and above a wind farm: a wind tunnel study. *Energies* 4:1916–1936
- Comté-Bellot G, Corrsin S (1971) Simple Eulerian time correlation of full and narrow band velocity signals in grid generated isotropic turbulence. *J Fluid Mech* 48:272–337
- Ivanell SSA (2009) Numerical computations of wind turbine wakes. In: Technical reports from the Royal Institute of Technology, Linné Flow Centre, Department of Mechanics, Stockholm. Available via KTH. <https://sverigesradio.se/diverse/appdata/isidor/files/3345/10845.pdf>. Accessed 12 Apr 2016
- Lignarolo L, Ragni D, Krishnaswami C et al (2014) Experimental analysis of a horizontal axis wind-turbine model. *Renew Energ* 70:31–46
- Mehta D, van Zuijlen AH, Koren B et al (2014) LES of wind farm aerodynamics: a review. *J Wind Eng Ind Aerod* 133:1–17
- Meyers J (2011) Error-landscape assessment of large-eddy simulations: a review of the methodology. *J Sci Comput* 49:65–77
- Panofsky H, Dutton J (1984) Atmospheric turbulence: models and methods for engineering applications. Wiley, New York
- Perić M, Ferziger J (2002) Computational methods for fluid dynamics. Springer, Berlin
- Pope SB (2000) Turbulent flows. Cambridge University Press, Cambridge
- Sanderse B (2013) Energy conserving discretisation methods for the incompressible Navier-Stokes equations: application to the simulation of wind-turbine wakes. Dissertation, Eindhoven University of Technology
- Stevens RJAM, Gayme DF, Meneveau C (2013) Effect of turbine alignment on the average power output of wind farm. In: Abstracts of the ICOWES 2013 international conference on aerodynamics of offshore wind energy systems and wakes, Lyngby, 17–19 June 2013
- Tennekes H, Lumley JL (1972) A first course in turbulence. MIT Press, London

# Chapter 21

## A Theoretical Risk Management Framework for Vessels Operating Near Offshore Wind Farms

Raza Ali Mehdi and Jens-Uwe Schröder-Hinrichs

**Abstract** The design of an offshore wind farm (OWF) can have a major impact on the safety of maritime operations in the vicinity. Factors such as the number of turbines, turbine spacing, and tower design can all have an effect the probability and consequences of various maritime accidents. The current chapter describes the potential effects of offshore wind farms on maritime traffic—particularly in a safety, reliability and risk context. The chapter also reviews existing methods, models and frameworks that can be used to assess the risk to maritime operations. Lastly, the authors propose an improved theoretical risk management framework that addresses some present concerns.

### 21.1 The Need for Maritime Risk Management Around Offshore Wind Farms

In this first section, the status of the OWF industry and the need for maritime risk management around wind farms is described.

#### 21.1.1 Trends in the OWF Industry

Over the past few decades, there has been a sharp increase in the use of renewable energy—driven not only by a more mindful society, but also by strong policy instruments and decisions. One of the most popular renewable energy schemes is wind energy. As the demand for energy generation grows, an increasing number of wind turbines are being installed offshore. OWFs offer several advantages over their onshore equivalents. There is better wind resource, and the wind speeds are more consistent out at sea. Potentially, wind turbines can also be scaled up to much

---

R.A. Mehdi (✉) • J.-U. Schröder-Hinrichs  
Maritime Risk and System Safety (MaRiSa) Research Group, World Maritime University,  
Fiskehamngatan 1, 21118 Malmö, Sweden  
e-mail: [rm@wmu.se](mailto:rm@wmu.se); [jush@wmu.se](mailto:jush@wmu.se)

greater sizes than would be possible onshore—leading to increased, more efficient, energy generation. In Europe, on average, an offshore wind turbine has a capacity of 3.6 MW and generates 12,961 MWh of energy annually; by comparison an onshore turbine has an average capacity of 2.2 MW, and generates around 4702 MWh of energy (EWEA 2015).

OWFs can also be constructed close enough to heavily populated shores to reduce energy transport cost, and yet be distant enough not to cause visual and noise pollution (Anderson 2013). These factors, combined—to some extent—with limited space on land, have led to an increased exploitation of marine areas for wind energy generation. As a result, offshore wind turbines are increasingly rapidly in size and numbers. Wind farms are also getting larger and moving further ashore so as to better exploit wind resource.

There are, however, certain drawbacks of OWFs that also need to be taken into account. The drawbacks include harsh environmental conditions for construction and maintenance, limitations in deep water installation technology, and impacts on the marine environment (Anderson 2013). These disadvantages, coupled with the high cost of capital investment, maintenance and reliability mean that OWFs are not as cost-effective or efficient as their onshore equivalents today; in fact, by certain estimates, the costs of operation and maintenance (O&M) for OWFs may be 2–6 times higher than those for onshore wind (Dalgic et al. 2013).

### ***21.1.2 The Need for Maritime Risk Assessment and Management***

Building an OWF has an impact on vessel operations in the vicinity. A wind farm leads to more obstructions in the water for ships to avoid; the presence of a wind farm near a shipping lane effectively narrows the area in which vessels can operate, therefore increasing the traffic density. This may lead to additional costs for the maritime industry—if for example, the vessels have to be diverted to sail along a longer route.

Perhaps more importantly, there is also an increased risk of accidents due to the increased maritime traffic as a result of activities related to OWFs. In addition to the increased traffic density, and reduced sea space, wind turbines may also cause problems with a ship's on-board navigation equipment. In fact, the potential accidents that maritime operations face due to offshore wind farms can be classified into five different categories.

- Navigational accidents involving passing vessels (Powered and Drifting)
- Navigational accidents involving wind farm support vessels
- Accidents during OWF installation and decommissioning operations
- Accidents during emergency maritime operations such as SAR
- Accidents in harbours and ports that deal with offshore activities

In addition to the risk-areas mentioned above, an OWF may also affect the safety of pleasure vessels and fishing operations; these areas, however, are beyond the scope of the current research.

Any of the maritime accidents listed above, if they occur in the vicinity of an OWF, may cause a farm-wide shutdown, or lead to a severe delay in installation, repair or maintenance services—thus leading to higher costs. In the worst case scenarios, maritime accidents may not only damage the vessels, but also the turbines—leading to further downtime and increased repair costs, thereby reducing the reliability of offshore wind even further. According to the findings of Dai et al. (2013), a fairly small support vessel with 230 tones displacement, colliding head-on with the landing structure on a turbine tower at a speed of just 0.48 m/s, would be enough to induce local yield in the structure; colliding a speed of 0.84 m/s with the landing structure would induce global yield. Conversely, the same vessel colliding head-on directly with the tower would cause local yield and global yield at speeds of 0.34 m/s and 0.55 m/s respectively. Such reports clearly highlight the need for thorough risk management.

Risk management may also be a legal or regulatory necessity—national, and international standards, e.g. BSH (2015) and MCA (2013), may require wind farm owners to demonstrate that their OWF will not impede the safety of maritime operations. In Germany, for instance, there are very clear guidelines which state that accidents near OWFs should not happen more than once every 100 years. Wind turbines installed in Germany must also be *collision-friendly*—if an accident does occur, it is preferable for the turbine to be damaged, so the vessel does not rupture or cause an oil spill<sup>1</sup> (BSH 2015).

In summary, a thorough risk management process can serve two very important purposes—avoiding costly accidents, and demonstrating the safety and reliability of an OWF. This makes good risk management frameworks invaluable to stakeholders from both the maritime and OWF industries.

## 21.2 Literature Review

When discussing risk management, it is firstly important to define the term *risk* in a theoretical context. Based on a thorough literature review, risk has been defined as ‘*a combination of the probability and consequences of undesirable events that arise due to a permutation of passive hazards and active failures in a system or a process*’ by the current authors.

---

<sup>1</sup>A 160,000 DWT vessel drifting sideways into a turbine at a speed of 2 m/s is often considered as a typical reference case, unless the vessels on a particular route significantly differ in size.

Risk, as a concept, has been widely researched in recent decades. Despite the varying opinions about the actual definition of the term, most authors agree that no system or process is ever risk-free. The risk associated with one system or a process may also have an impact on *other* ‘external’ systems or processes.

Subsequently, *risk assessment* and *risk management* have emerged as two very vital concepts. *Risk assessment* is an integral part of risk management and refers to the use of tools, methods, models and frameworks to *assess* the risk associated with a system. Once the risk to a system has been assessed, the next step is to evaluate, control and/or monitor the risk; the combination of these latter three steps and the risk assessment process is risk management. The International Risk Governance Council (IRGC) defines risk management as ‘*the process of analysing, selecting, implementing, and evaluating actions to reduce risk*’ (IRGC 2006).

To develop a risk management framework, one must also understand the differences between the three terms *methods*, *models* and *framework*.

A risk assessment *method* can be thought of as a recipe—it provides step-by-step guidance on assessing the risk associated with a system or a process. A non-exhaustive list of risk assessment methods would include Fault Tree Analyses (FTAs), Event Tree Analyses (ETAs), Risk Contribution Trees (RCTs), Failure mode, effects and criticality analyses (FMEAs/FMECAs), and Bayesian Networks (BNs).

Risk assessment *models*, on the other hand, are replications of real-life systems and processes. Models can be developed using the step-by-step approach provided by a method, although this is not always the case—some simpler models can be developed without the explicit help of a specific method.

A *framework* is an overarching ‘outline’ which can consist of several methods, models and other tools. A risk *assessment* framework may include guidance as to what should be done before and after the actual risk assessment. For example, a framework may specify what data needs to be collected for an assessment and where/how it can be obtained. Similarly, a risk *management* framework might elaborate on what to do with the results of the risk assessment, and how to interpret them in a meaningful manner, through the use of tools such risk matrices and principles such as ALARP (As Low As Reasonably Practicable). A risk management framework may also contain guidance on the selection and evaluation of different risk control measures, through techniques such as cost-benefit analysis.

Although a detailed review of risk assessment *methods* is out of scope for this book chapter, a review of different risk, probability and consequence assessment *models* and *frameworks* is presented in the following sections.

### **21.2.1 Maritime Risk Assessment Models for OWFs**

Various authors, over the years, have developed maritime risk assessment models for many scenarios—so much so that a complete, exhaustive review is nigh impossible. Review texts range from complete books, to comparison and review



papers (Goerlandt and Montewka 2015; Amdahl et al. 2013; Li et al. 2012; Pedersen 2010; Wang et al. 2002; Soares and Teixeira 2001). It is therefore unfeasible, and redundant, to have a detailed discussion of the various risk assessment models in this report. A brief, categorical overview is, however, prudent.

Risk assessment models can be categorized in many different ways. Some models can be used to calculate the probability of maritime accidents, whilst others focus on the consequences of these accidents. There are models that deal exclusively with a given type of accident, and some models that are applicable to many different types of accidents. For the purpose of this chapter, the author has categorized the risk assessment models based on whether they evaluate the probability, or consequences of accidents. Only models that can be used for maritime risk assessment of maritime operations around offshore wind farms are discussed. The models reviewed cover the risk of contact, collision and grounding events.

### 21.2.1.1 Probability Models

#### Geometric – Causation Probability Models for Powered Accidents

A commonly-used method to assess the probability of navigational accidents was proposed by MacDuff (1974). He suggested that the total probability of an accident along a waterway could be expressed as a multiplication of two factors—the ‘geometric probability of accident’, multiplied by a ‘causation probability’. This class of methods is applicable to powered accidents—where a vessel is still under the control of the crew.

#### *Geometric Probability of Accidents*

The geometric probability of accidents is simply the probability of an accident occurring if *no evasive measures are taken*. It essentially indicates how often, and how many, vessels deviate from their ‘normal’ route onto a course that could lead to an accident. Depending on the type of accident, there are many different ways to assess and calculate the geometrical probability of accidents. The most common method is to look at vessel AIS (Automatic Identification System) data for an area, and see how many vessels deviate from their course over a given period of time.

The deviation of the vessels generally depends not only on physical and technical factors related to vessel ways (width of vessel way, marking of objects, aids to navigations, etc.), but also on human factors. A probability distribution of vessel deviations can be created using AIS information, which can be used to assess future case scenarios. Generally, AIS data and probability distributions are enough to calculate the geometric probability of contact (accidents between ships and fixed structures) and grounding accidents (Ellis et al. 2008b; Christensen 2007; Kleissen 2006; ANATEC 2014). AIS data can also be combined with marine spatial data, and information such as bathymetry and geography, to assess the risk of contact or grounding events (Hansen et al. 2013).

The calculation of the geometric probability of accidents can be enhanced by taking into account additional factors—particularly in collision scenarios. For instance, MacDuff (1974) derived a simplified equation to determine the geometric collision candidates based on the manoeuvrability of a vessel, and the width of a channel. Fujii and Tanaka (1971) proposed an equation which took into consideration the traffic density, and the relative speed of colliding vessels. Fujii and Tanaka (1971) also pioneered the concept of a ‘collision diameter’ or ‘ship domain’. A ‘collision diameter’ is essentially an area enveloping a ship, which—if encroached by another ship—would lead to an imminent collision; this diameter or domain can be calculated using factors such as ship size, manoeuvring capabilities, waterway geometry, and laws of motion (Li et al. 2012).

The concept of a ‘collision diameters’ and ‘ship domains’ has been developed further by authors such as Pedersen (2010), Kaneko (2002, 2013) and Montewka et al. (2010b, 2011, 2012)—who have derived their own equations to estimate the number of geometric collision candidates; the latter have developed a concept called ‘Minimum Distance to Collision’ (MDTC), which incorporates the physical properties of vessels, ship dynamics and even the traffic patterns in an area to assess the risk of ship-ship collisions (Montewka et al. 2012). Equations that incorporate principles of ship domain, in combination with vessel traffic data, are also often used in tools like iWRAP (Friis-Hansen 2008).

### *Causation Probability of Accidents*

The geometric probability, alone, is not enough to assess the probability of an accident; another important value that needs to be assessed is the causation probability. If a vessel is on an accident course, but manages to correct the course in time, the accident can be avoided; thus, the causation probability is essentially the *probability of evasion measures being undertaken* by a vessel on an accident course. When the values of geometric probability and causation probability are combined, one can calculate the *total* probability of a given type of accident.

Causation probabilities are often harder to quantify. MacDuff (1974), Fujii and Yamanouchi (1974), and Fujii et al. (1974) determined causation probabilities through observations, and by considering historical data, to see how often ‘incorrect’ vessel deviations were corrected before an accident occurred. They came up with specific values of causation probabilities, which are tabulated and still commonly used in modern risk assessment studies and tools—despite the fact that these values were for *specific* maritime areas, from a time long gone. To compensate for this, these outdated causation probability values may be multiplied by a constant factor to provide a conservative estimate, and to reflect the assumption that modern technology has made navigation safer.

Rather than estimating a causation probability based on observations alone, some authors prefer to calculate it instead. Depending on the *type* of accident being analysed, causation probabilities can be calculated in different ways. Calculating causation probability of contact incidents, for example, requires one to take into consideration factors such as the location, and size of a fixed object. Similarly,

to calculate the probability of grounding events, one may have to consider the hydrographic and bathymetric features of a sea area. Causation probabilities equations may be functions of various physical parameters such as vessel speed, vessel type, distance between vessel and accident area/object, and traffic density.

Causation probabilities are also heavily dependent on the so-called ‘human element’—i.e.—the capabilities of human beings on board the ship. Human reliability techniques such as HEART (Human error assessment and reduction technique) and THERP (Technique for human error-rate prediction) can be used to quantify the frequency of human error.

Various studies have also quantified the effect of factors such as weather, and bad visibility conditions, on the causation probability (Larsen 1993). Some recent studies of causation probabilities also take into account the effect of technical and technological factors, such as coastal state facilities, VTS, and aids to navigation (Lehn-Schiøler et al. 2013). Technical factors - such as rudder or engine failure - can also influence the causation probability (Hänninen and Kujala 2012).

The socio-technical factors required to estimate causation probabilities may be intrinsically linked. As such, causation probabilities are often calculated through sophisticated risk assessment methods such as Fault Trees, Event Trees (Fowler and Sørgård 2000; Haugen 1991) and Bayesian Networks (Akhtar and Utne 2013; Dai et al. 2013; Hänninen et al. 2013; Hänninen and Kujala 2012; Szwed et al. 2006; Friis-Hansen 2000; Friis-Hansen and Simonsen 2002). Using risk assessment methods can allow various factors—such as human and organizational errors, configuration of the navigational area, navigational aids and markings, bathymetry, and coastal state features such as VTS—to be taken into consideration (Friis-Hansen 2008).

To a certain extent, even the most sophisticated causation probability estimates rely on historical data, and the best way to quantify such data is through the use of accident investigation models—best demonstrated by authors such as Mazaheri et al. (2015b), and Schröder-Hinrichs et al. (2011). Data gathered through accident investigation models can, in turn, be used as an input to risk assessment methods—and thus augment causation probability calculations further.

### Other Probability Models for Powered Accidents

The overarching principle to assess the probability of accidents—by combining the geometrical and causation probabilities, as suggested by MacDuff—is still widely used today. There are, however, other ways to assess the probability of accidents in the maritime domain as well.

ANATEC (2014), for example, calculate the probability of collisions by dividing a sea area into a number of cells, and considering the traffic density and number of potential encounters in each cell based on AIS data.

One may also rely *solely* on past accident data to identify a potentially dangerous sea area. A good example for such proactive accident data use can be found in the work of Schröder-Hinrichs et al. (2011); in this study, the authors assessed previous

occurrences of engine room fires to determine what equipment and ship areas were most susceptible to such accidents.

Ohlson (2013) suggests the use of risk assessment methods like FMECA to calculate, amongst other factors, the probability of accidents close to OWFs. Van LU (2012) analysed and compared the usefulness of methods such as FMECA, FTA, ETA, Checklist Method and SWIFT. He also extended his work to cover human reliability methods such as THERP, HEART, ASEP and SPAR-H.

Geijerstam and Svensson (2008) identified several factors that should be taken into consideration when performing a qualitative risk assessment for OWFs; in some cases, such factors, combined with simple expert judgements can be used to qualitatively determine if the chances of accidents are ‘high’ or ‘low’, for instance.

### Probability Models for Drifting Accidents

Drifting accidents are accidents in which the crew is no longer able to control the vessel—usually due to an engine or steering system/rudder failure. Drifting vessels are more prone to contact and grounding incidents.

Therefore, the first step in calculating the probability of drifting accidents is to calculate the probability of engine or rudder failure, whilst a vessel is in an area where there are other structures or shallow water depths.

One should also take into consideration the sea space available, and the wind and weather conditions in an area—as these factors determine how much a time is available for the vessel to perform corrective action or repairs. If for example, the wind and wave conditions are favourable, and the drift speed is very low, the crew may actually be able to repair the engine or rudder before an accident takes place.

The probability of a vessel anchoring safely before a drifting accident occurs, or being towed to safety by tug vessels, should also be considered. Most modern drifting models and frameworks have specific time functions based on historic ship data, which allow users to assess the time available to a drifting vessel based on all the aforementioned factors (SAFESHIP 2006; Kleissen 2006; van der Tak 2010; Christensen 2007; Ellis et al. 2008b).

#### 21.2.1.2 Consequence Models

Work on modelling the consequences of maritime accidents was pioneered by in the 1950s (Minorsky 1959). Since then, various authors have developed many different consequence assessment models.

As demonstrated by Wang et al. (2002), consequence models can be categorized in many different ways. There are models, for instance, that deal with either internal or external mechanics of ship collisions. Some models take into consideration the deformation of a ship’s bow, whilst others may not. Alternatively, models may be classified depending on the type of accident they were developed for—collision, contact or grounding models. Lastly, models can be classified on the *type* of analysis they perform; this is the classification used in this chapter.

## Empirical, Analytical, and Probabilistic Consequence Models

Minorsky (1959) proposed to separate the external mechanics and internal mechanics of accidents. External mechanics are generally based on the equations of motions of, and the kinetic energy of the vessel(s) involved. Principles of conservation of energy, momentum and angular momentum (Wang et al. 2002) are generally applied when assessing the external mechanics of ship accidents. Pedersen and Zhang (1998), Zhang (1999), and Pedersen (2014) have done some pioneering work on the external mechanics of ship accidents. Other authors (Simonsen 1997; Paik and Thayamballi 2007) have developed equations for similar approaches.

The internal mechanics study the actual structural and material failure in given accidents. Analysis methods for internal mechanics can be further divided into many sub-categories, based on the type of analysis, and the equations used. Minorsky (1959), for instance developed empirical equations to model the internal mechanics of ship accidents—particularly damage length and penetration—based on past data. Pedersen and Zhang (1998) developed Minorsky’s work further, and Zhang (1999) derived semi-empirical, semi-analytical equations for internal mechanics, improving Minorsky’s original empirical equations for ship damage.

Pedersen (2002, 2010, 2013, 2014), Pedersen et al. (1993), Zhang (1999), Lützen (2001), Chen (2000), Brown (2001, 2002a, b), Brown and Chen (2002), and Lin (2008), amongst others, have also developed analytical models for analysis of internal mechanics problem.

The analytical models developed by Pedersen (2002, 2010, 2013, 2014) focus mainly on the kinetic energy dissipation, and are based on factors such as mass, speed, and angles and location of collision and contact along the ship length. Brown and Chen (2002) have further developed the programme SIMCOL (Chen 2000; Brown 2002a), which can quickly assess the damage length and penetration depth, with varying parameters such as angle of collision, and speed of ships. Ehlers and Tabri (2012) have developed a robust model to assess the damage to a ship through a semi-analytical, semi-numerical procedure. Tools like GRACAT (Friis-Hansen and Simonsen 2002) have also been developed based on analytical and empirical equations, and can help to assess, and visualize, the damage to ships in an integrated manner—users are able to calculate everything from the probability of collisions and grounding, to the oil outflows and capsizing time.

Aside from considering external and internal mechanics, probabilistic damage assessment is also very common when assessing the consequences of ship accidents. Such models are essentially an offshoot of empirical models, and rely primarily on past accident data. Ronza et al. (2003) and Ellis et al. (2008a) used Event Trees, developed using past-accident data, to predict *likely* future case accidents and consequences. Probabilistic models have been used by the IMO in Formal Safety Assessment studies—not only to predict environmental damage, but also to assess the stability of ships, effectiveness of evacuations and potential loss of lives (IMO 2008). Organizations like ANATEC (2014) also use accident statistics and subsequent predictive estimates to assess the consequences of maritime accidents near OWFs.

Goerlandt and Montewka (2014), amongst others, have developed thorough and robust probabilistic consequence models using methods such as Bayesian Networks, fault trees, and event trees (Li et al. 2012). Similar work has been carried out by Vanem and Skjong (2004), Mazaheri (2009), Montewka (2009), Montewka et al. (2010a, 2014a, b), van de Wiel and van Dorp (2011), Ståhlberg et al. (2013), and Helle et al. (2015), amongst other authors. Some of these aforementioned authors have combined tree-based diagrams with neural networks, and augmented their findings with past accident-data, for further validity.

### Finite Element (Numerical) Consequence Models

External and internal mechanics can also be assessed using simplified Finite Element Methods (FEM). Ito et al. (1985) and Paik et al. (1999)—amongst others—have done substantial work in this area. In recent years, with advances in computing, non-linear FEM simulations have become increasingly popular, for the level of detail they are able to capture. Authors like Xia (2001) and Kitamura (2002) have demonstrated the use of FEM for collision and grounding accidents.

Non-linear FEM offers a very robust solution to analyse complex systems like a turbine-vessel collision. Amongst others, Servis and Samuelides (1999) and Xia (2001) have developed FE models for ship-ship collisions, whilst Dalhoff and Biehl (2005), Biehl and Lehmann (2006), Dai et al. (2013), and Bela et al. (2015) have all published papers on FEM for ship-turbine collisions. FEM can also be used to model the damage on the turbine itself, as demonstrated by Ozguc et al. (2006), Le Sourne et al. (2015), Ren and Ou (2009), Ramberg (2011), Kroondijk (2012), Pichler et al. (2012), Samsonovs et al. (2014), Ding et al. (2014), and Hsieh (2015); such models are invaluable as they can incorporate factors such as blade rotation and soil-structure interaction, thus being able to provide an in-depth analysis of contact events. Cho et al. (2013) describe experimental investigations to validate numerical models of OWF collisions.

FE models can provide a comprehensive analysis of internal mechanics—and can thus be used to obtain accurate values for parameters such as damage length, damage height and penetration depth of damage to a ship. This information can then be used to calculate further consequences—e.g.—oil outflow, using models developed by Sirkar et al. (1997), Krata et al. (2012), and Tavakoli et al. (2008, 2010). One can also assess the ‘hull girder strength’ after an accident to assess the residual strength of a ship; although analytical, empirical and probabilistic equations for doing so are presented by many authors as described by Wang et al. (2002), FE models can provide a more detailed outlook.

Once the extent of damage (damage length, penetration) is known, equations, or software like HECSALV and Seatrack Web can also be used to assess further consequences—economical, environment and social—based on factors such as ship stability, oil outflow/drift, and water-inrush.

## Other Consequence Models

As with probability, it is possible to assess consequences of accidents qualitatively. Qualitative models are not commonplace, though they may sometimes be used during the preliminary stages of risk assessment. A qualitative model generally relies on a combination of expert judgements and past data. In his Licentiate, Ohlson (2013) describes a framework where consequences are calculated both quantitatively and qualitatively.

Probability and consequence models are many and varied, and it is safe to say that there is no ‘one solution fits all’ model. In an ideal framework, it is therefore prudent to select a variety of models that can complement each other and provide a very comprehensive overview of the situation. At the same time, the models should not be too resource intensive, as this would be very unfeasible.

### ***21.2.2 Existing Risk Management Frameworks***

From the get-go, thorough risk management of maritime operations OWFs has been considered an important task. Several different industrial organisations have developed integrated frameworks that can assess the risk associated with OWFs. Examples of such frameworks include SAMSON from MARIN (SAFESHIP 2006; Kleissen 2006; van der Tak 2010), CRASH/MARCS from DNV (SAFESHIP 2006; Christensen 2007), and COLLRISK from ANATEC (Ellis et al. 2008b; ANATEC 2014). The existing frameworks are often considered to be robust; they can provide users with very detailed and comprehensive probability calculations and estimates for various types of accidents around OWFs. The frameworks are also able to quantify the consequences in terms of parameters such as damage to property, environmental damage, loss of human lives, etc. to varying degrees of detail and accuracy. Furthermore, these frameworks are very adept at performing cost-benefit analyses of various risk control options.

#### **21.2.2.1 The Gap in Existing Risk Management Frameworks**

Despite all their benefits, the existing frameworks have some weaknesses. One concern that stakeholders often have is that the ship damage estimations in these frameworks are very simplistic—often relying on basic kinetic energy calculations, and past accident statistics. This raises doubts as to whether or not these frameworks are sophisticated and detailed enough to adequately assess the consequences of complex accidents, such as vessel-turbine collisions. The lack of adequately detailed consequence assessment may lead to over- or under-designed systems. Moreover, some of these frameworks may be insufficient as approval tools in countries like Germany, which require detailed consequence calculations.



The *transparency* of different frameworks is also a concern previously highlighted by the EU-funded SAFESHIP project and the findings of Ellis et al. (2008b). The latter report implied that it was impossible to replicate the calculation results of certain frameworks, as the equations and data values being used were not evident. Since the study by Ellis et al. (2008b), however, some stakeholders have made greater efforts to increase the transparency and validity of their models and frameworks. Both MARIN and DNV-GL—and even companies like ANATEC—for instance, have produced very clear and detailed reports about their calculation methods. Despite the significant progress in this area by major industry players, some of the frameworks widely used by other organisations and governments still do not conform to an adequate level of transparency. This prevailing lack of transparency does not bode well for a maturing industry.

Ellis et al. (2008b) also highlighted concerns about *harmonisation* of various risk management frameworks. It was noted that despite the initiation of the SAFESHIP project—which was set up to harmonize navigational risk assessment (NRA) models—a harmonized *framework* was not achieved. In their study, Ellis et al. (2008b) compared the risk assessment results for a specific transnational OWF—Krieger's Flak—shared between three different countries: Denmark, Sweden and Germany. It was noted that the NRA had been conducted by different organizations, and that the results of the NRA were quite different for the same wind farm. In fact, each different framework used different tools and models for the calculation of probability and consequences of various undesirable events. This difference in probability and consequence calculations arises because different countries and organizations have different calculation procedures. Going forward, this is clearly an issue that needs to be addressed particularly given the ambitious plans for transnational wind farm.

The lack of harmonization is also a bureaucratic burden as it means that OWF owners have to follow different procedures in different countries. For offshore wind to be viable, such administrative problems should be addressed urgently. The continuing rapid growth of OWFs, increasing sizes and complexity of turbines, and novel developments such as floating turbines (EWEA 2014) further underline the urgent need for harmonization. Thus, harmonizing various risk management frameworks is a high priority task—and one that is advocated by key players in both the maritime and OWF industries; harmonization concerns, for instance, have been highlighted repeatedly by organisations such as the European Wind Energy Association (EWEA 2007).

Lastly, the existing frameworks are often geared towards subject matter experts. This is not a negative *per se*; however, OWFs are complex socio-technical systems, which ideally require various groups of stakeholders from different backgrounds to work together towards an optimal solution. Bearing this in mind, more should be done to involve cross-industry stakeholders in the risk management process.

In summary, existing risk management frameworks have four broadly identifiable gap areas—lack of harmonization, poor transparency, insufficient stakeholder involvement, and inadequately detailed consequence calculations. In order to address these issues, the current chapter describes an improved, unified risk management framework for vessels operating near OWFs.



## 21.3 The Proposed Risk Management Framework

Based on the problems and research gap identified in the previous sections, a novel theoretical risk management framework has been developed. This framework is designed to provide a step-by-step approach towards harmonized and transparent risk management. Currently, the proposed framework describes the risk management process for vessels *passing* near offshore wind farms only. The authors plan to extend the same framework to include other core maritime risks associated with OWFs, as listed in Sect. 21.1.2.

Some of the steps shown in the following diagrams (Figs. 21.1–21.9) are already incorporated into various existing risk assessment models and frameworks. Therefore, where possible, the authors recommend the relevant tool(s) which can be used to fulfil the respective steps. It is important to note, however, there is no *single* existing model or framework which covers *all* of the steps—this, in fact, is the novelty of the current work.

Even though certain models are *recommended*<sup>2</sup> the current chapter does not provide any specific formulae or detailed explanation (although the reader is provided with appropriate references). This is primarily because the models and tools used have been developed by other authors, and detailed explanations of how the equations are derived are beyond the scope of this chapter. Furthermore, this framework is still *theoretical*—to reiterate, the premise of this chapter is to present the steps that could constitute an improved and unified risk management process. It is therefore intended that any equations will be presented at a future stage.

Figure 21.1 shows the ‘main’ flowchart of the risk management framework. The boxes in blue indicate the ‘pre-risk assessment’ or data collection stage. The green boxes are the core of the framework—the ‘risk assessment/estimation’ stage. The red boxes indicate the ‘risk evaluation’ and ‘risk management’ stages—i.e.—stages where decision makers decide if the estimated risk is acceptable, or if further measures are needed to mitigate the maritime risk associated with offshore wind farms.

### 21.3.1 Pre-risk Assessment (Blue): Steps 1–3

Before beginning any risk assessment, it is vital to collect data that can allow one to calculate the probabilities and consequences of various undesirable events.

The primary data that needs to be collected when performing a risk assessment around an OWF is, of course, data related to the wind farm itself. A project like MARE-WINT has a substantial advantage at this stage, since different researchers try and optimize various different parameters of the OWF. For instance, several

---

<sup>2</sup>The selection of the recommended tools/models is partly based on the input/output capabilities and reasonable resource costs.

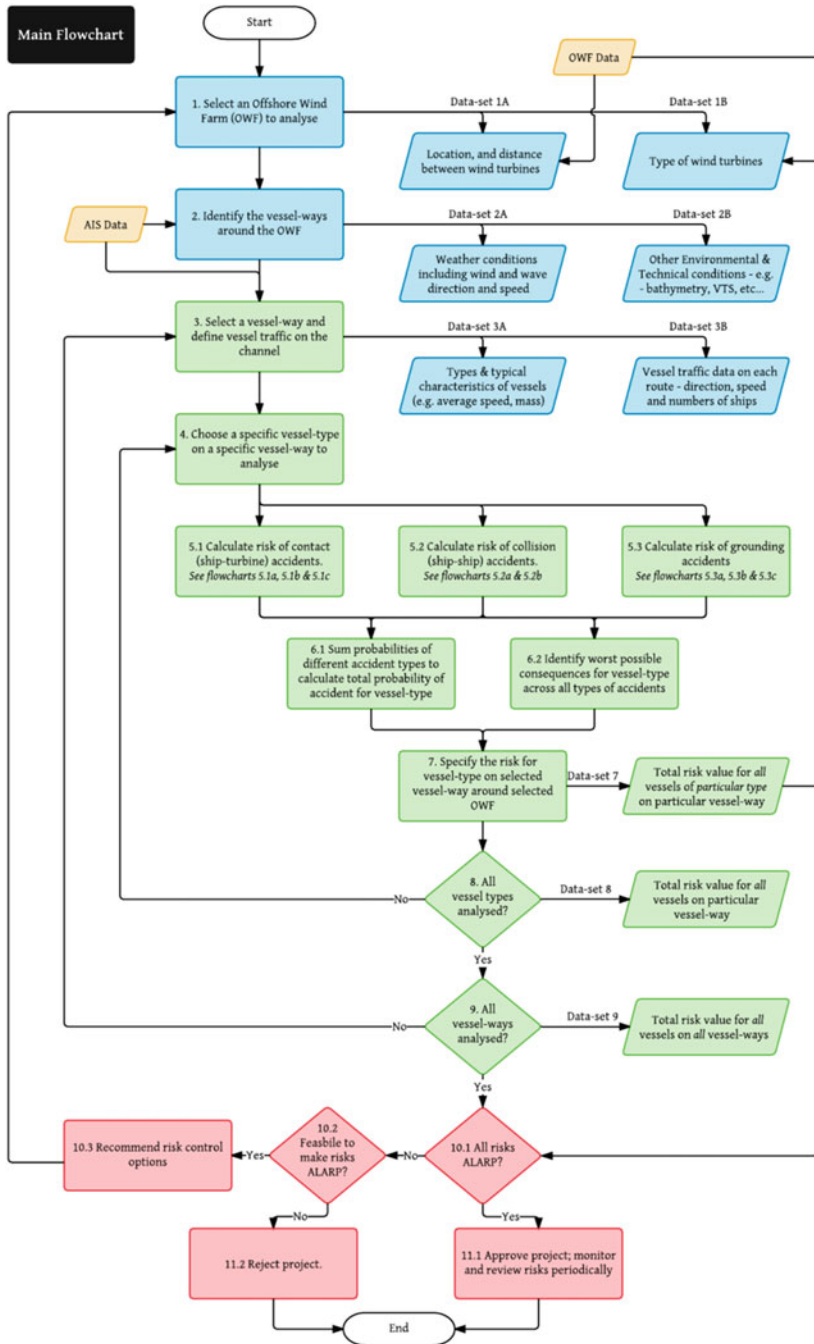


Fig. 21.1 The main/core flowchart for the proposed risk management framework

researchers work directly on the optimization of the support tower and substructure components of a turbine, based on the feedback they receive from other fellows working on blade, gearbox and nacelle design. The work of these researchers is immensely useful for the current research, as it provides structural information about the turbine—which allows one to study the consequences of ship collisions in detail. Similarly, another researcher’s work focused on large eddy simulations over the wind farm to optimize the wind farm layout. This work can help to identify the inter-turbine distance, and the proposed layout of the wind farm. The distance between the turbines can affect both the probability, and the consequences of maritime accidents. The output of the proposed framework can also be used to provide feedback *to* other researchers. This iterative approach can improve the design process for OWFs.

Apart from the feedback from other researchers, one of the most important sources of information is Automatic Identification System (AIS) data for vessels. AIS data includes vessel tracks over a given period of time, which can help users to create a statistical distribution of vessel traffic around a potential OWF site.

AIS data also contains other valuable information such as the speed and mass of vessels; it may even be possible to identify manoeuvring characteristics of a vessel, since AIS records the call-signs. AIS data, combined with metrological and hydrography data can allow for a detailed, enhanced risk assessment. All this data is collected and recorded by appropriate marine and maritime agencies, and can be obtained for risk assessment purposes.

### ***21.3.2 Risk Assessment/Estimation (Green): Steps 3–9***

The most crucial output from the risk assessment/estimation stage is data-set 7, as shown on Fig. 21.1. This data-set specifies a total risk value for each *type of vessel* on each *vessel way* around a wind farm. Obtaining this value is the core goal for the current framework.

In order to obtain this value, the first step is to define the various vessel ways and the traffic density on each way. This, as stated above, can be done using AIS recordings around the proposed wind farm area. Generally, AIS data recorded over a period of one year just prior to the risk assessment, is considered.

The next step is to define standard parameters for each *type*<sup>3</sup> of vessel that operates on each *vessel way*. This is done in step 4. A ‘standard’ vessel in this sense would refer to a vessel that is typical of a particular vessel-type. It is proposed that standard vessel data be developed by different member states for risk assessment purposes.

---

<sup>3</sup>Vessels can be classified into different types according to classifications present in literature. Usually, vessels are classified based on their role and the cargo they carry—e.g.—general cargo, bulk, oil tanker, etc . . . This classification is widely used, and is recommended for the proposed framework.

The primary parameters that define the ‘standard’ vessel include speed, mass, loading condition, and design and construction aspects. The last parameter can be obtained from IMO documents pertaining to minimum design standards; the other factors, such as average speed, can be obtained directly from AIS data, and vessel data over a given period of time. So if, for example, 10 different types of cargo ships operate on one route adjacent to a wind farm, step four would ‘average’ these 10 cargo ships into one standard cargo ship—which would then be used as a reference in all calculations involving that ship type. This helps to significantly reduce computation and analysis time, particularly if an area with high traffic needs to be assessed. Defining a standard vessel may also allow future case vessels to be taken into consideration. It is also recommended by the author that various coastal states maintain a database of 3D models for ‘standard’ vessels that can be used during the consequence assessment stage for FE (Finite Element) numerical calculations. These databases can also be regularly updated to accurately reflect the vessels in a given sea area.

Three main types of risks need to be estimated for each type of vessel, as indicated by steps 5.1, 5.2 and 5.3 in Fig. 21.1. The three risks are the risk of contact (an accident involving a vessel and a wind turbine), the risk of a collision (an accident involving 2 or more vessels), and the risk of grounding (an accident where a vessel runs aground). For each type of risk, the user is required to calculate the total probability of that risk, and then determine the worst-case consequences—for each separate type of vessel.

The next few pages contain further flow charts (Figs. 21.2, 21.3, 21.4, 21.5, 21.6, 21.7, 21.8, and 21.9) which explain, step-by-step, how to calculate the probability and consequence values associated with each type of risk. Each time a user goes through the entire *set* of flowcharts, they calculate the risk to all vessels of *one specific type*, on *one specific route* around the OWF. In order to do a complete risk assessment, the users should repeat the process for as many vessel-types as they expect, on as many routes there are around the OWF (steps 8 and 9, Fig. 21.1).

Once a user gets to step 6.1, they should add *all* the probability values for each specific vessel-type. In step 6.2, they should specify *only* the worst case consequences for each specific vessel-type, as quantified in step 5. Combined, these probability and consequence values will give the overall risk associated with all vessels of a particular type, on a particular vessel-way around a wind farm.

### **21.3.3 Risk of Contact Events: Figs. 21.2, 21.3 and 21.4**

The first risk that needs to be calculated is the risk from contact events. Contact events, as stated earlier, involve an accident between a fixed object—in this case, a turbine—and a ship. In order to calculate the overall risk of contact events, a user must first calculate the probability of both powered and drifting contact events individually (Figs. 21.2 and 21.3), and then calculate the consequences (Fig. 21.4).

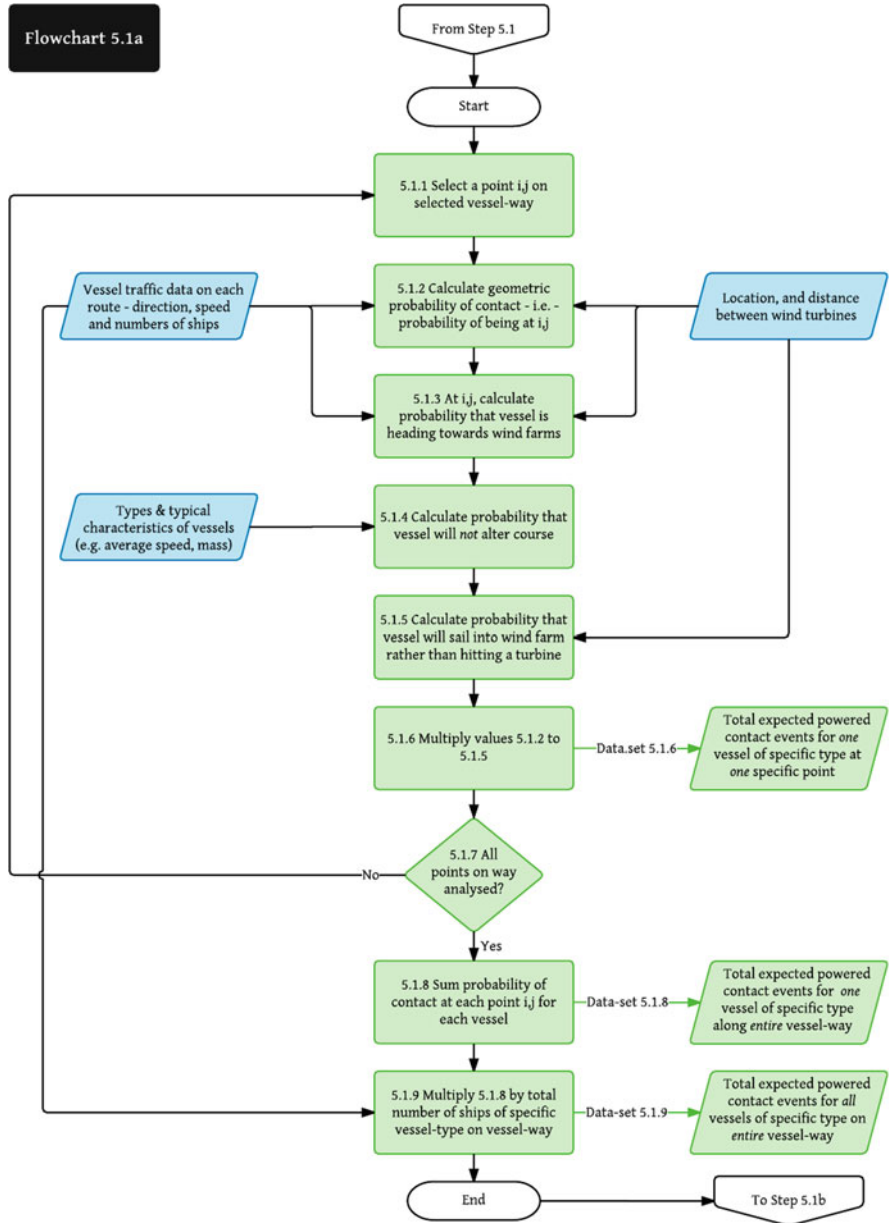
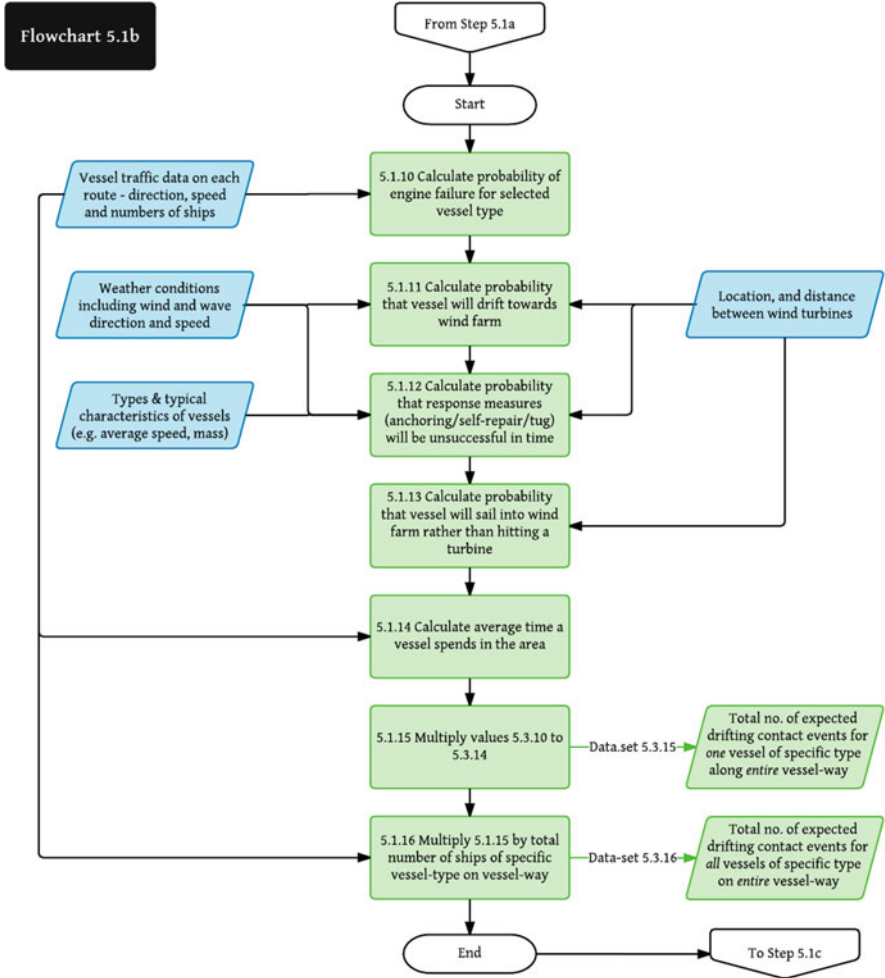


Fig. 21.2 Flowchart for step 5.1a: probability of powered contact



**Fig. 21.3** Flow chart for step 5.1b: probability of drifting contact

**21.3.3.1 Probability of Powered Contact: Fig. 21.2**

A powered contact generally occurs when a vessel is deviating from course and heading towards a wind farm, and this incorrect action is not corrected in time. Therefore, in order to calculate the probability the powered contact, it is recommended that the user follow the geometric-causation probability model as described in Sect. 21.2.1.1.1.

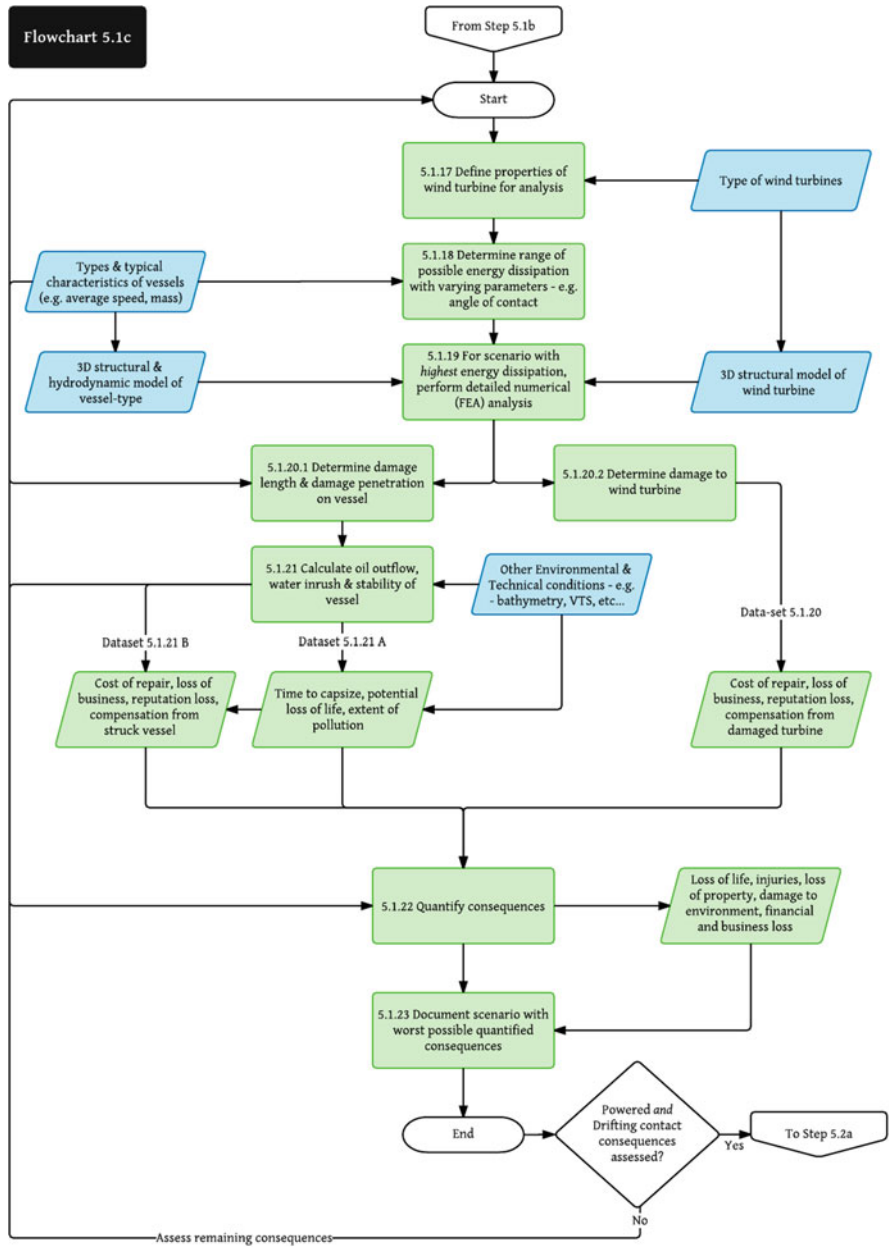
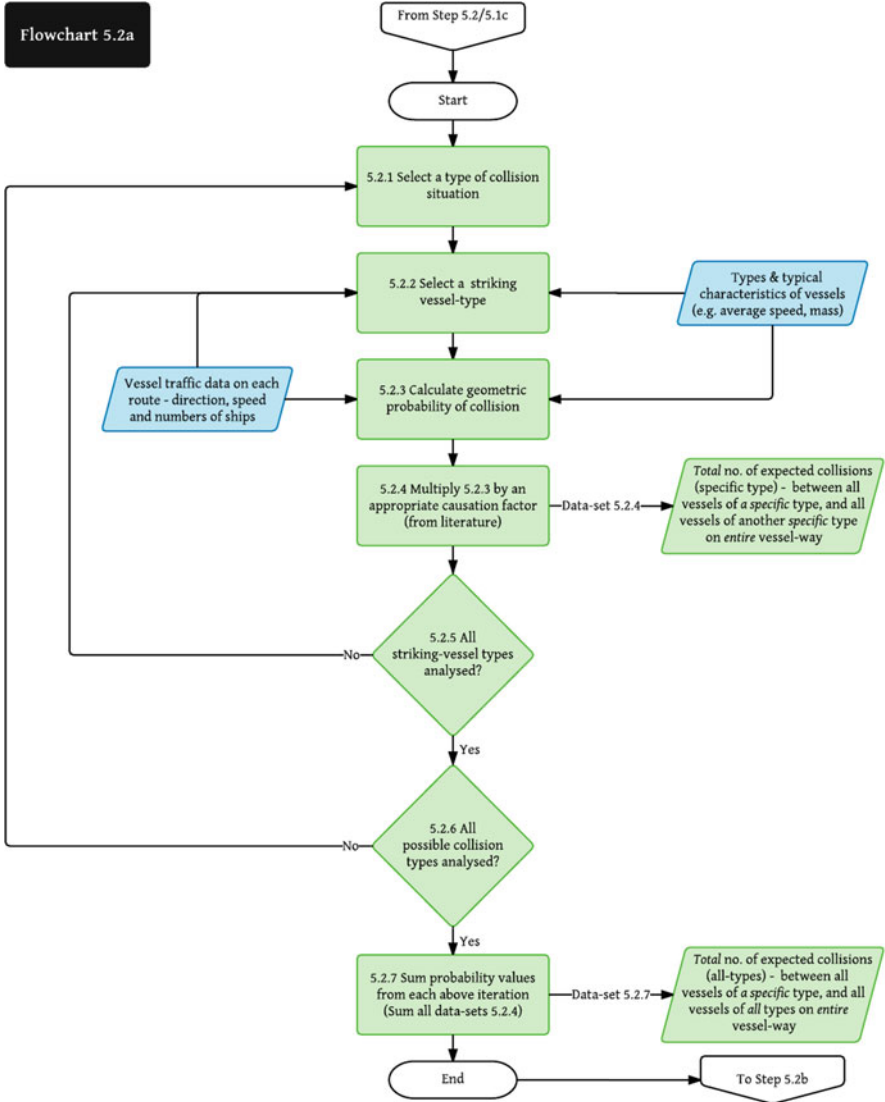


Fig. 21.4 Flowchart for step 5.1c: consequences of contact



**Fig. 21.5** Flowchart for step 5.2a: probability of powered collisions

Essentially, a user must first calculate the geometric probability of accident—i.e.—the probability that a vessel is *not* following its course and/or is offset from the vessel way (steps 5.1.2 and 5.1.3 in Fig. 21.2). This is generally done by looking at AIS data, and determining how many times vessels deviate from their route. The AIS data can be used to generate a probability distribution, which indicates how often vessels deviate or are offset from the median line of a vessel way. If AIS data is not available, it is reasonable to assume that vessel traffic is normally distributed along the width of the vessel-way.



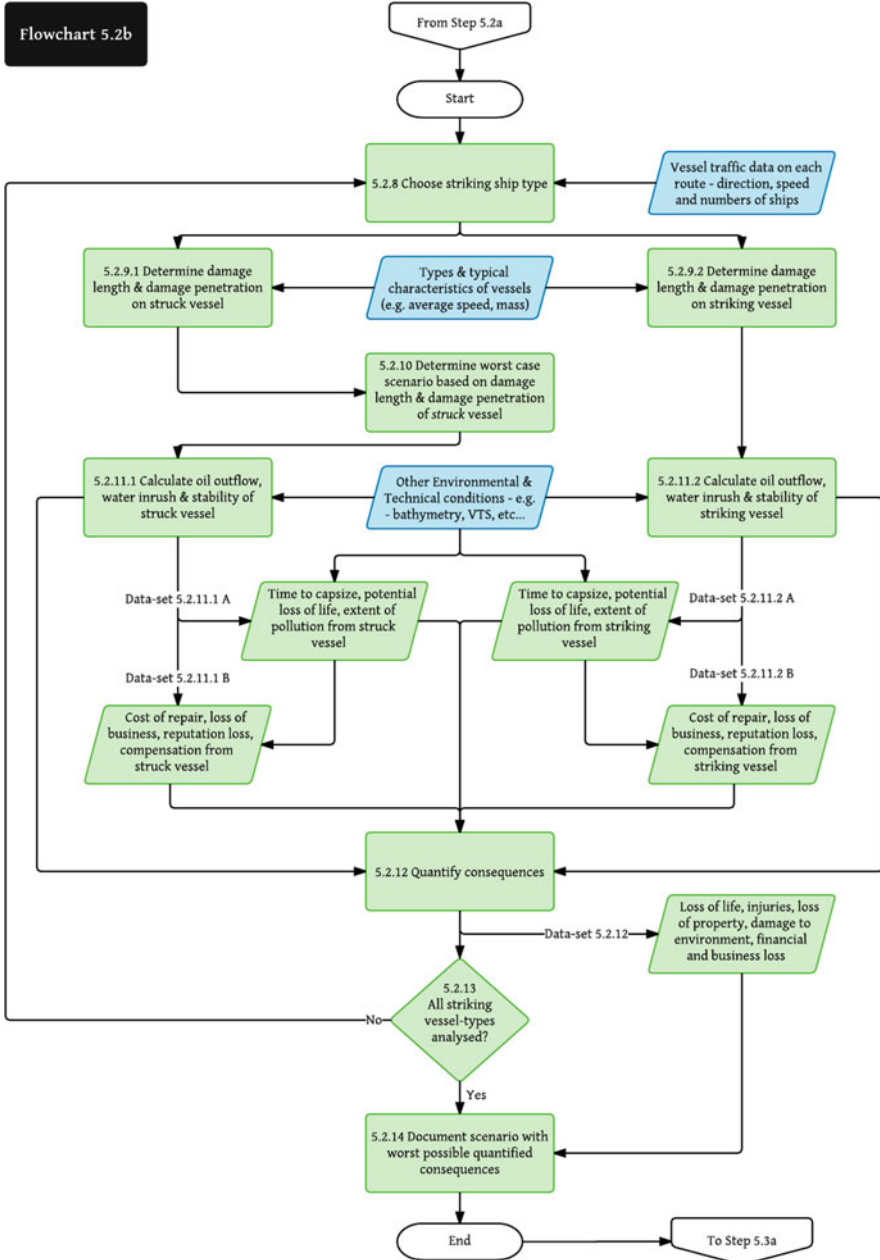


Fig. 21.6 Flowchart for step 5.2b: consequences of collisions

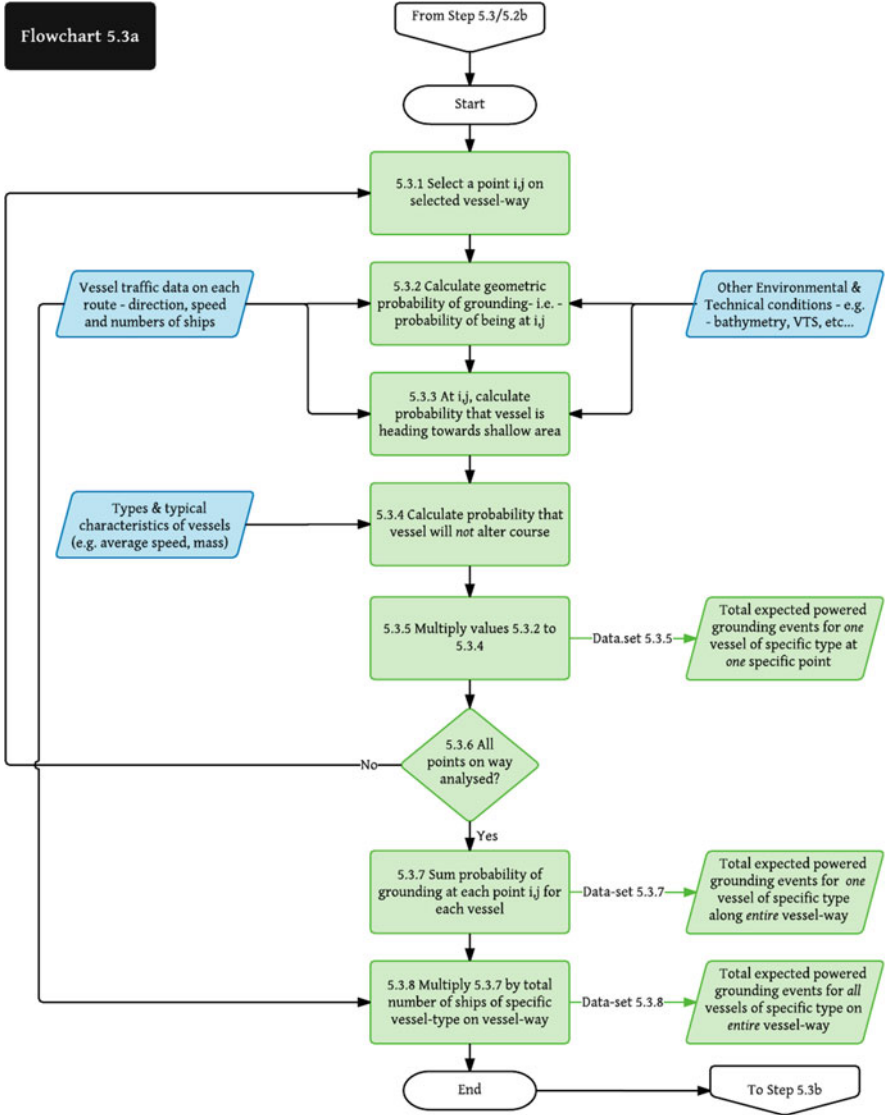
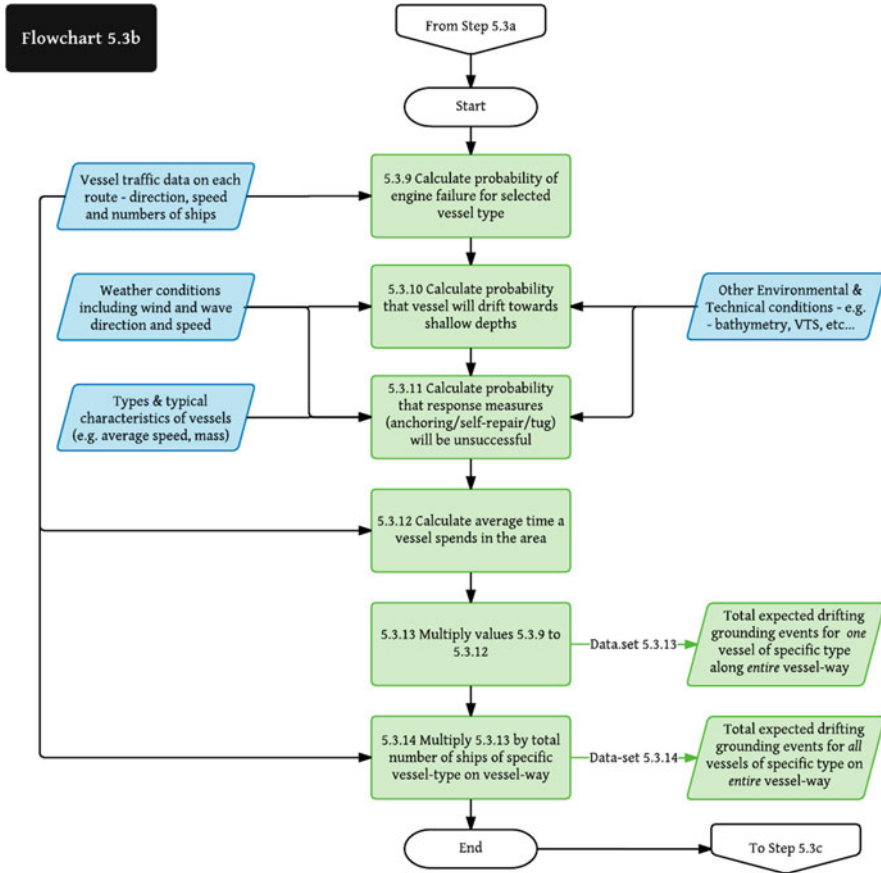


Fig. 21.7 Flowchart for step 5.3a: probability of powered grounding

Calculating the probability of a vessel *not* performing a corrective action, while deviating from its course (step 5.1.4 in Fig. 21.2), is slightly more challenging—particularly because this depends on both human and technical factors. A typical approach is to use a ‘causation probability’ value from literature; a more sophisticated and thorough approach is use to use risk assessment methods like Fault Trees, Event Trees and Bayesian Networks to estimate the causation probability (Friis-Hansen 2008).



**Fig. 21.8** Flowchart for step 5.3b: probability of drifting grounding

Once a user obtains a geometric probability of contact for all vessels over a given time period, and an appropriate causation probability, he or she can then multiply the two values to obtain a total probability of contact for that type of vessel over the given time period.<sup>4</sup>

A user of the framework can also multiply this total probability value by another given geometric equation to calculate the probability of actually hitting a wind turbine rather than just sailing into a wind farm (step 5.1.5 in Fig. 21.2). Equations for this purpose are also available in literature (Ellis et al. 2008b), and generally take into account various factors such as ship length, distance between turbines, and diameters of the turbine towers.

<sup>4</sup>The time period that the probability is calculated for is generally 1 year, and therefore the entire traffic over a period of 1 year must be considered (step 5.1.9 in Fig. 21.2).

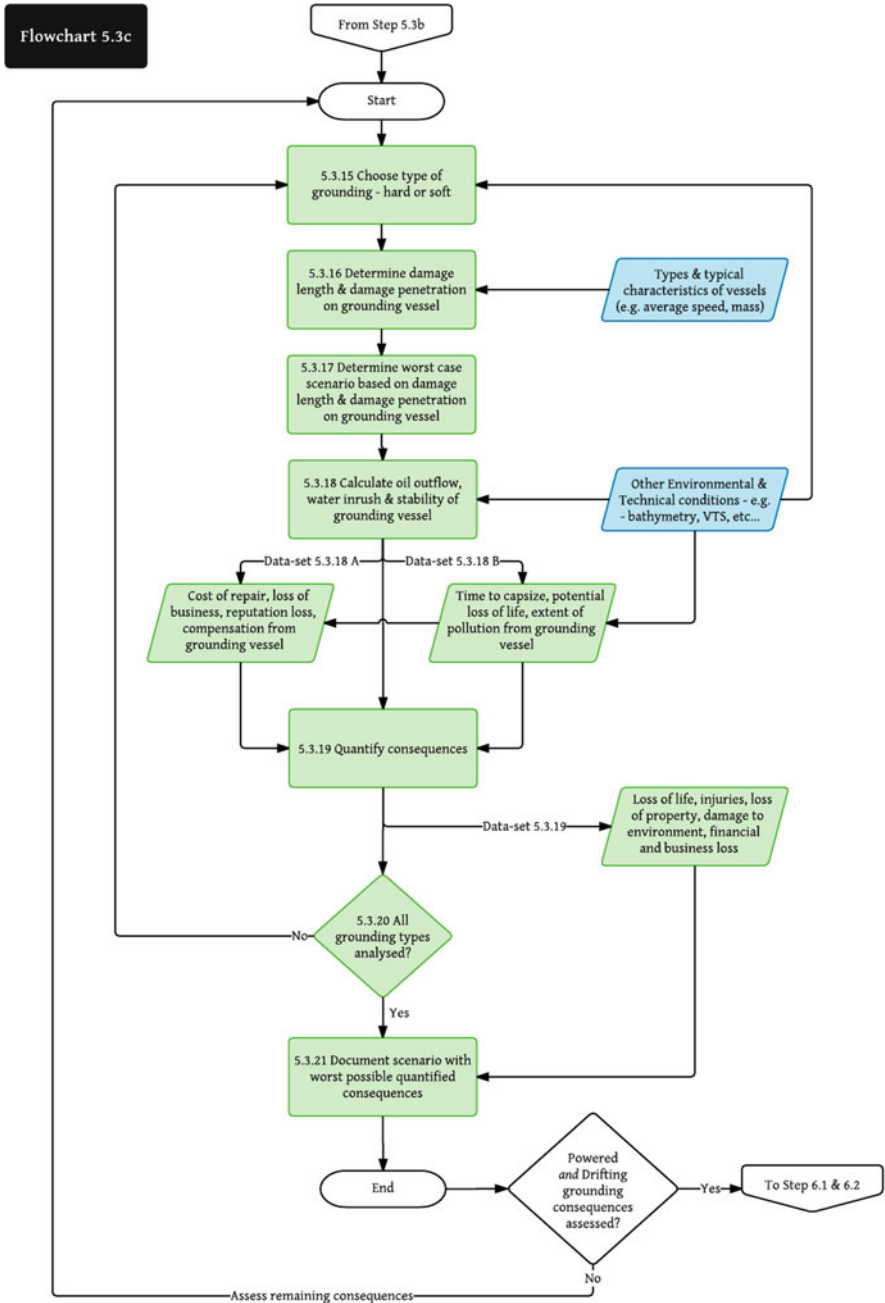


Fig. 21.9 Flowchart for step 5.3c: consequences of grounding

To calculate the probability of a powered contact, the researcher recommends using the model and equations developed by SSPA, as described by Ellis et al. (2008b).

### 21.3.3.2 Probability of Drifting Contact: Fig. 21.3

Once the probability of powered contact has been calculated, the next step is to calculate the probability of drifting contact (Fig. 21.3). A vessel is set to be ‘drifting’ when it suffers from loss of engine power. Therefore, in order to calculate the probability of a drifting contact event, a user must first calculate the probability of a vessel-type facing an engine breakdown (5.1.10 in Fig. 21.3). This data is generally available from maritime and ship records.

The next important parameter to calculate during a drifting-contact probability assessment is the probability that a vessel will actually drift *towards* an OWF (5.1.11 in Fig. 21.3). This probability is calculated by looking at wind and wave condition data, and seeing how often the wind or current flows in a direction that can carry ships towards an OWF.

Next, the user must calculate the time for which a vessel will drift—and whether or not this time is enough for a contact accident to occur. In order to do so, the users must consider the width of the traffic distribution on the route, and calculate the time it would take different vessels to reach the wind farm boundary based on their position on the route, and the wind and wave conditions. In the same step, one must also calculate the probability that emergency measures<sup>5</sup> will be unsuccessful or omitted in a given time period (5.1.12 in Fig. 21.3). A successful emergency measure—in time—will ensure that a certain proportion of the vessel traffic will not reach the wind farm to cause a contact incident.

Having obtained all the mentioned parameters, a user can multiply them to calculate the overall probability of a drifting contact for one vessel along an entire vessel way, over a given period of time. Similar to the powered contact procedure, the user can further multiply this product by an equation to obtain the probability of actually drifting and hitting a wind turbine, rather than just drifting into a wind farm area (5.1.13 in Fig. 21.3).

It is also important to predict the potential speed of the vessel in drift. This is vital in order to assess the consequences later. Equations from literature (Kleissen 2006; Christensen 2007; Ellis et al. 2008b) can be used to calculate the drift speed, which depends primarily on current and wind conditions.

For the drifting model, too, the researcher recommends the use of SSPA’s comprehensive model and equations, as detailed in Ellis et al. (2008b).

---

<sup>5</sup>Emergency measures generally include anchoring, repairing the ship in time, or getting help from a tug vessel. Each of these measures has a certain probability of success/failure depending on different parameters; typical values for these probabilities are also cited in literature (Ellis et al. 2008b).

To calculate the overall probability of a type of vessel suffering a contact event, a user should sum the probability of both, powered, and drifting contact events for that vessel-type.

### 21.3.3.3 Consequences of Contact: Fig. 21.4

After calculating the probability of contact, the next step is to calculate the consequences, using Fig. 21.4. To calculate the consequences to a given type of vessel, one should use a 'standard' reference vessel, as explained earlier in this section. A user should also consider the structural properties of a wind turbine (5.1.17 in Fig. 21.4).

The first step (5.1.18 in Fig. 21.4) whilst calculating the consequences is to assess a range of possible energy dissipation values. The energy dissipation values are derived from the range kinetic energy of the vessel when it collides with the turbine, and the energy that the turbine and vessel absorb. Of course, this dissipated energy depends primarily on the velocity and mass of the vessels. Since the speed and mass are assumed to be constant values for all vessels of a specific type, the other parameters that can influence the energy dissipation have to be considered—e.g.—the angle of collision between the ship and the turbine. Therefore, a user must use an equation that relates the mass, velocity *and* the angle of collision, as well as the location of collision, to the kinetic energy. Such equations have been developed by Pedersen and Zhang (1998), and by Pedersen (2002, 2010, 2013, 2014).

Once several kinetic energy values have been obtained, the next step is to perform a detailed numerical finite element analysis (FEA) for the worst case scenario (5.1.19 in Fig. 21.4)—i.e.—the scenario with the highest energy dissipation. Although there are simpler methods to calculate consequences—semi-analytical, probabilistic, and empirical equations being quite common—such methods are geared more towards ship-ship collisions. Without using FEA, it is hard to capture the complexity of a ship-turbine collision, and thus assess the consequences in sufficient detail. A turbine may have many different forces acting upon it, from the aerodynamics of the blades, to the structural integrity of the soil. Therefore, although FEA is more resource intensive, it is the method recommended by the current researcher. Moreover, substantial contemporary literature shows increasing progress when it comes to FEA analysis of ship-turbine contacts. In particular, Biehl and Lehmann (2006) have done significant work on describing numerical methods for ship-turbine collision analysis. Similarly, Dai et al. (2013) describe a procedure to calculate the damage to a turbine, using FEA, in a scenario where a support vessel collides with a wind turbine. Most recently, Bela et al. (2015) have used FEA to assess the crashworthiness of mono-piles.

It is interesting to note that all the above-mentioned papers use the FEA software LS-DYNA for their analysis. In fact, most of the FEA work on ship-turbine collision is done using the software LS-DYNA, as it has certain features (structural element types) which make it ideal for such analysis. Therefore, when it comes to this stage, the current researcher also recommends the use of LS-DYNA. In order to perform

a numerical analysis, the user is required to create a 3D model for each type of vessel, and for each type of wind turbine. The models should incorporate primarily the structural properties, but it is also important to include the hydrodynamic and aerodynamic properties for accurate calculations of consequences. A contact event can then be simulated to assess the energy dissipation in more detail, and to understand the damage to both structures.

A numerical analysis obviously requires a high level of computational resources. The intensity of resources is partially reduced since the FEA is only performed for the worst case scenario for each vessel type, although it is recommended that a user perform it at several different points along the vessel, and at various locations around the turbine to ensure the validity of the results. Developing 3D models and meshing then appropriately consumes a lot of time; in order to minimize this, the author proposes that various coastal states maintain a database of standard meshed 3D models for all vessel types operating in their waters. This can greatly help to reduce the resources required for FE modelling.

A numerical FE analysis allows the user to assess the damage to both the ship and the turbine (5.1.20.1 and 5.1.20.2 in Fig. 21.4). The damage to the wind turbine can determine the state of the turbine after a contact event, and whether it will collapse or not. Such information can be used to evaluate how much economical loss will be incurred.

From the FE calculations, the damage to the ship can be generally visualised, and quantified in terms of a certain damage length, damage height and a specific penetration depth. These parameters in turn define the oil and cargo outflow from a ship, as well as the water inrush. The water inrush can then determine the stability of a ship, and how much time is available until capsizes. Using all this information, one can quantify the consequences as described in Fig. 21.4. A similar procedure can be applied to damage incurred by the wind turbine.

For oil outflow, water in rush and stability calculations (5.1.21 in Fig. 21.4), there are equations and models present in literature (van de Wiel and van Dorp 2011; Wang et al. 2002; Li et al. 2012; Goerlandt and Montewka 2014) that can allow a user to model these events; such equations directly relate the extent of damage to the aforementioned parameters. The current researcher, however, uses the software HECSALV from Herbert-ABS to model these events. HECSALV is a rapid assessment tool, developed to perform rapid assessment of vessels in distress. It incorporates widely-used equations to assess several parameters which indicate the state of damage to a vessel. If the damage extent to a ship is known, HECSALV can provide oil outflow estimates, water inrush estimates, and time to capsizes estimates, amongst other factors.

The output from HECSALV can be used to estimate evacuation and emergency response times, and, when combined with Data-sets 2A and 2B from Fig. 21.1 (which can indicate the potential level of emergency response in the area), one can estimate the consequences in terms such as loss of lives, amount of total oil spill, and cumulative damage to ship. Methods described by the IMO (2008) can also be used to calculate the potential number of injuries and fatalities. The spreading of oil can be further modelled using tools like Seatrack Web—the official HELCOM oil drift forecasting system.

The consequences of an accident can also be quantified (5.1.22 in Fig. 21.4) as monetary figures, using ‘per-unit currency’ values given in literature for different types of losses and damages—e.g.—each tonne of oil spill costs approx. \$60,000 in a given sea area (Christensen 2007). Such monetary values can be obtained for a variety of consequences—such as loss of one life, loss of a turbine, and damage to environment. Further expert judgements can also be used to augment these monetary values.

Alternatively consequences can be quantified into various qualitative ‘levels’, although this approach is not recommended for the current framework.

Ideally, the process described by Fig. 21.4 should be repeated twice—once for drifting vessels, and once for powered vessels. The core difference between these two assessments would be speed of the standard colliding vessel—a vessel in drift is likely to have a lower collision speed with a turbine. After quantifying the consequences, it is recommended that *only* the worst-case consequence values be documented for the next stage in the framework—but if the user wishes, they can mention the worst-case consequences for both drifting and powered contact events separately.

### 21.3.4 Risk of Collision Events: Figs. 21.5 and 21.6

A ‘collision’ event refers to an accident between 2 or more ships—although the likelihood of there being more than 2 ships is extremely rare. When calculating the risk of collision, it is only necessary to assess the risk of powered collisions. Drifting collisions are extremely unlikely at sea, since it is highly improbable that two vessels will drift towards each other and collide.

#### 21.3.4.1 Probability of Powered Collision: Fig. 21.5

As with powered contact probability, the author recommends using the geometric-causation probability model as described in Sect. 21.2.1.1.1 to calculate the probability of powered collision. Thus, assessing the probability of a powered collision involves the multiplication of two main factors (5.2.4 in Fig. 21.5)—the *geometric collision candidates* and the *causation probability*.

The *causation probability*, as mentioned earlier, is the probability of corrective action being taken; values of causation probability can easily be obtained from various literature sources (Fujii et al. 1974, 1984; Fujii and Mizuki 1998; MacDuff 1974; Ellis et al. 2008b). Alternatively, it can be calculated using historical accident data and methods like Bayesian Networks (see Sect. 21.2.1.1.1.2).

The *number of geometric collision candidates* for collision indicates the likelihood of two vessels occupying the same space, at any given time, if no corrective action is taken. In literature (Pedersen 2010; Li et al. 2012), one can find many equations which provide values for the *geometric collision candidates*, based on the



AIS information for a given area. These equations are different for different types of collision situations; on any given vessel-way, there can be many potential types of collision situations—e.g.—head-on situations, overtaking situations, and crossing situations. It is therefore important, to clearly choose a type of collision situation (step 5.2.1) *before* beginning a collision assessment.

After a user has the values for geometric probability of collision, and appropriate values for causation factors, they can multiply the two values to obtain a *total* probability value. This probability value indicates the frequency of a *given type of collision*, between *all* vessels of *two specific types*, along an *entire* vessel-way, for a *given period of time*. The process should be repeated until all possible collision types and vessel-types have been analysed.

Once the probability of each different *type* of collision has been calculated, the user can sum all these values (step 5.2.7) to get a final probability value: this value would represent the frequency of *all types of collision*, between *one specific vessel type* and *all types of vessels*, along an *entire* vessel-way, for a *given period of time*.

The current researcher recommends using the software tool iWRAP, developed by IALA (Friis-Hansen 2008). iWRAP incorporates all of the steps indicated in Fig. 21.5. It allows users to assess the probability of different *types of collisions*, and can directly assess the geometric collision candidates based on AIS data. iWRAP also has several different causation factors values and ship domain data included, which allows users to perform integrated calculations. The theory and equations behind iWRAP are well-documented, and commonly used by many practitioners. Furthermore, iWRAP is endorsed and recommended by the IMO as an ideal tool to calculate the risk of collision and compare base and future case traffic scenarios—which makes it the perfect tool for the job.

#### 21.3.4.2 Consequences of a Collision: Fig. 21.6

Calculating the consequences for collisions is, in some ways, similar to calculating the consequences of a contact event. One major difference is that the user must select a type of striking ship (5.2.8 in Fig. 21.6), instead of a type of turbine.

Another prime difference is that there is no separate step for energy dissipation calculation. Instead, a range of values for the damage length and damage penetration to each ship are calculated from the very start (5.2.9.1 and 5.2.9.2 in Fig. 21.6). In literature, it is easy to find many equations that relate various parameters—ship speed, mass, loading condition, design, and angle of collision, to name but a few—to damage length and damage penetration in cases of ship-ship collisions (Wang et al. 2002; Pedersen 2010; Li et al. 2012). For the purposes of this framework, the researcher suggests using SIMCOL (Brown 2001, 2002a, b) to assess varying damage lengths and penetration depths with varying factors such as type of striking vessel and angle of collision. SIMCOL uses semi-analytical and empirical equations, which allows for extremely rapid assessment of collision situations with varying parameters.

Once the user has obtained a range of values for damage lengths and penetration depths, he or she should choose the case with the most severe damage to the struck vessel (5.2.10 in Fig. 21.6), to analyse further in terms of oil outflow, stability and water in rush (5.2.11 in Fig. 21.6). Since each type of vessel is analysed based on a standard model, only one case needs to be assessed in detailed. For the chosen case, the consequences can be calculated and quantified in a similar manner to the contact scenario (Sect. 21.3.3.3). It is again recommended to use HECSALV for oil outflow, water in rush and stability calculation, whilst tools like Seatrack Web from HELCOM can be used to model the spread of oil. In other words, 5.2.12 from Fig. 21.6 can be calculated in a similar manner to step 5.1.22 from Fig. 21.4.

Finally, the worst case consequences for each type of vessel, in case of collision events, should then be clearly recorded.

### **21.3.5 Risk of Grounding Events: Figs. 21.7, 21.8 and 21.9**

A grounding event is one where the ship runs into an area of shallow depth, thus causing the bottom of hull to scrape along solid ground, rock or reefs. This type of accident is typically *not* considered when analysing the operation of ships around offshore wind farms. As the number of wind farms increase, however, the limited sea space is reduced. Furthermore, OWFs are often built in shallow waters, and there is a risk of shifting sand banks in some areas. Such factors make an assessment of grounding risk a priority.

#### **21.3.5.1 Probability of Powered Grounding: Fig. 21.7**

It is easy to find an abundance of literature on models that calculate the probability of powered groundings (Mazaheri et al. 2014). The current framework recommends a simple approach for this assessment—by suggesting the user to assess the powered grounding probability in a manner similar to the one applied when assessing powered *contact* probability (Fig. 21.2). In fact, between the two approaches (Fig. 21.2 and 21.7), there is only one fundamental difference: when calculating the probability of powered contact, the users have an option to calculate the chance of a ship actually hitting a wind turbine, or just simply sailing into an OWF area; such an option is not available when calculating the powered grounding probability.

To ensure consistency, the researcher recommends the use of iWRAP, which provides a robust calculation procedure for powered grounding. Using iWRAP meets consistency criterion, as it is suggested for collision calculations as well. iWRAP is also able to calculate the probability of grounding for vessel ways with varying geometries and spatial features.

### 21.3.5.2 Probability of Drifting Grounding: Fig. 21.8

In order to be consistent, the current researcher recommends following a similar procedure to calculate the probability of drifting grounding, as was detailed for assessing the probability of drifting contact events (Fig. 21.3). Once again, the only difference between the process described in Fig. 21.3 and the one described in Fig. 21.8 is that the former allows users to calculate the probability of actually hitting an object, rather than just the probability of drifting into a general area—whereas the latter does not. The researcher again recommends the use of the iWRAP model and/or all its associated equations.

To calculate the overall probability of a type of vessel grounding, a user should sum the probability of powered and drifting grounding events, for that vessel-type.

### 21.3.5.3 Consequences of Grounding: Fig. 21.9

Many different approaches exist to calculate the consequences of grounding events (Mazaheri et al. 2013, 2014, 2015a, b; Zhu et al. 2002). To assess the consequences of the grounding in a rapid, novel manner, the current framework suggests following a similar approach as when assessing the consequences of a collision (Fig. 21.6)—with some differences, of course.

The major difference between the approach outlined in Figs. 21.6 and 21.9 is the exclusion of the ‘striking ship’ from the latter, and the inclusion of ‘grounding type’. Another crucial, but related difference is of course that the consequences are only calculated for one ship at a time, instead of two.

The researcher recommends the use of the same tools and models as used in Fig. 21.6, but with one exception: instead of using SIMCOL to assess the damage length and penetration depth, it is suggested that the procedure outlined by Zhu et al. (2002) is used instead. In this latter procedure, the authors developed equations to allow for a quick assessment of grounding damages (step 5.3.16 in Fig. 21.9), which makes it ideal for use in the current framework.

For the subsequent consequence quantification and assessment, it is once again recommended to use the tools HECSALV and Seatrack Web, along with the per-unit values provided in literature, for various different types of losses.

Ideally, a user should go over Fig. 21.9 twice—once for powered grounding accidents, and once for drifting grounding accidents. The only parameter that will significantly vary between the two cases will be the speed of the grounding. After quantifying the consequences, it is recommended that *only* the worst-case consequence values are documented for subsequent risk evaluation; if the user wishes, however, they can mention the worst-case consequences for both drifting and powered grounding events separately.

## 21.3.6 Risk Evaluation and Management (Red): Fig. 21.1

### 21.3.6.1 Risk Evaluation: ALARP and Acceptance Criteria

Having estimated the risk to each type of vessel (steps 5 to 9 in Fig. 21.1), the next steps (10–11) involve *evaluating* the probability and consequence values against certain ‘acceptability’ criteria. This allows users of the framework to judge whether the risk—to each particular type of vessel along each particular route near the OWF—is acceptably low enough, or not. If a risk to one or more types of vessels is deemed to be too high, the user can implement some risk control measures, and repeat the entire process as described by the framework.

Acceptability criteria are generally set out after consultation with various stakeholders. The International Maritime Organization (IMO) has conducted several studies in which the acceptable criteria for various vessel types are clearly set out (IMO 2006, 2007a, b, 2008). Thus far, however, there have not been any acceptability discussions on vessels specifically operating near OWFs, on an international level.

Despite this, during the planning of OWFs, governments may require the OWF developer to clearly state the acceptable risk. Therefore, companies that carry out navigational risk assessment studies for OWFs occasionally develop acceptability criteria, or matrixes, on a case-by-case basis (ANATEC 2014).

One of the most common ways of checking whether or not a risk is acceptable is through the use of an ALARP diagram (Ellis et al. 2008a). An ALARP diagram is a log-log graph with probability values on the x-axis, and consequence values on the y-axis.

An ALARP diagram can be divided into three sections—*Broadly Acceptable*, *ALARP (As Low as Reasonably Practicable)*, and *Unacceptable*. To demonstrate what an output from the current framework might look like, the author has developed an ALARP diagram using dummy data (Fig. 21.10).

The top right corner, above the white dotted line is the *Unacceptable* region. Risks in this area cannot be accepted by society and/or stakeholders. The region in the bottom left, below the other white dotted line, is the *Broadly Acceptable* region. Ideally, probability and consequence values should be in the region, but it might be unfeasible and costly to design the system for this to be the case. The region in the middle, bounded by the two white dotted lines is the ALARP region. This region indicates the levels of probability and respective consequences are acceptable, and feasible to achieve.<sup>6</sup>

The white ellipses can represent different types of vessels—passing vessels (bulk, general cargo, passenger, RO-PAX, etc.) but also support vessels, SAR vessels

---

<sup>6</sup>The aim of the current framework is to harmonize risk management procedures and *not* the acceptance criteria. Thus, the current framework does not specify limits for the different regions on an ALARP diagram—it is up to the individual maritime administrations and licensing authorities to decide what is ‘acceptable’ after close consultations with stakeholders.

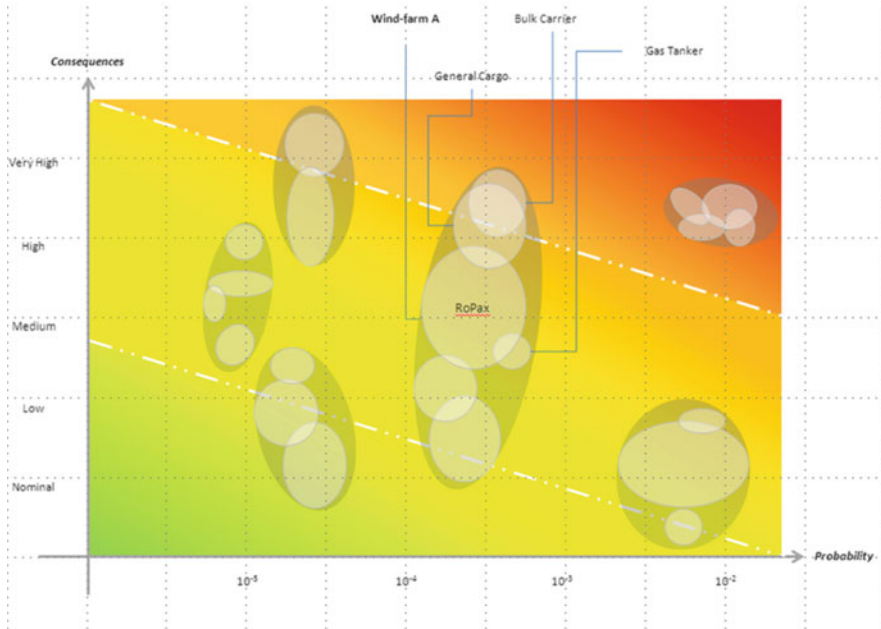


Fig. 21.10 A proposed output of the risk management framework, generated using dummy data

and installation and decommissioning vessels. Each of the grey ellipses indicates different OWF options—various wind turbine layouts, and the effect of various risk control options such as enhanced navigational aids and VTS. The size of the ellipses indicates the uncertainty associated with the calculations; the smaller the size, the more accurate a calculation or estimation is likely to be.

Even if the risk to all vessels is considered to be *acceptable*, it is still important to monitor and review the risks at regular periods over the lifecycle of an OWF. This is particularly important because, over time, some crucial parameters may change; changes may include variations in the standard types of vessels, climate conditions, and technological advances.

### 21.3.6.2 Risk Management

If a wind farm option lies in the *Unacceptable* region, OWF owners may attempt to mitigate and manage the risk to push it down to the ALARP region. Generally, there are four main ways in which risk can be managed, as identified by various authors and organisations, including the Health and Safety Executive (HSE UK): Risk Avoidance, Retention, Transfer or Reduction and Mitigation.

There is a fundamental difference between risk mitigation and risk avoidance—in the former, the system or process is ‘tweaked’ to deal with a risk, in the latter the system or process is changed so the risk is eliminated entirely, if possible.

To better understand and summarize the four risk management methods, consider a ship going from point A to B, and passing a wind-farm en-route. The ship therefore faces a possible risk of collision with the wind turbines. If the ship owner wishes to avoid this risk of collision, they might opt for a different route altogether, and thus eliminate a particular risk (although this might give rise to *other* risks). This would be an example of risk avoidance.

Alternatively, the ship owners may decide either that the ship colliding with wind turbines will not harm their interests, or the probability of collision is so low that they are not concerned; they thus decide to do *nothing* about the risk. This option would demonstrate risk retention.

A third option would be to get the ship insured, so that in the case of a collision, the insurance company is responsible for the consequences. This third option exemplifies risk transfer.

Lastly, the ship owner may simply implement some measures that reduce the probability or consequences of collision within the system itself, without eliminating the risk entirely. Such measures could include, for instance, a good captain or state-of-art equipment. This would be an example of risk reduction or mitigation.

To control risk then—primarily via risk avoidance, transfer and mitigation—there are several types of barriers that can be implemented: physical, administrative and supervisory or management barriers. Physical barriers, as the name implies, physically separate the hazard and potential target. Administrative and supervisory and management generally influence, and are influenced by, the human elements in systems and processes. Typically, barriers are designed to either improve the reliability of the system (reduce probability of failures and accidents), or to improve the safety of the system (reduce and mitigate the consequences in case of an accident)—although it is possible to have barriers that reduce *both* the probability and consequences of accidents.

Examples of typical barriers in the maritime domain, that can help to reduce the probability of accidents near OWFs, include measures such VTS (vessel traffic service) monitoring, pilotage, traffic separation schemes, and even sonars (Fricke and Rolfes 2013). There are several consequence-reducing measures as well, proposed by authors such as Graczykowski and Holnicki-Szulc (2009) and Ren and Ou (2009); both their papers describe and analyse the use of ‘crashworthiness devices’ around the turbine tower, which can minimize the impact of the vessel contact events. The effects of barriers and risk control options can be quantified by going through the process described in the framework (Fig. 21.1), and updating the probability and consequence values for each type of vessel, as necessary. The introduction of VTS, might for example, have an effect on the causation probability of accidents, and this would be reflected in the probability calculations of Fig. 21.1. Similarly, designing an implement to absorb the energy in contact events would mean updated calculations and results for the consequence assessment in Fig. 21.1

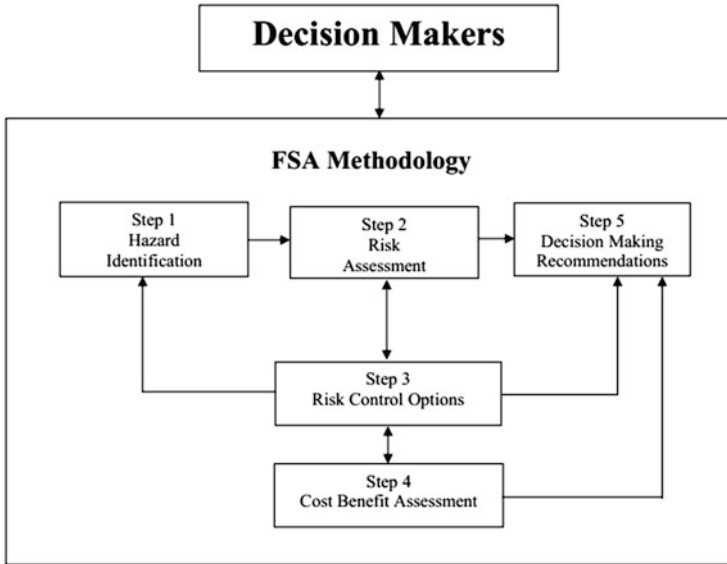


**Fig. 21.11** The FSA Process (IMO 2007a)

It is of course, important that risk management measures are feasible, and cost effective. In the maritime domain, the IMO's Formal Safety Assessment (FSA) process was developed for exactly this purpose—to assess the feasibility of risk reduction measures (and new system design). The FSA process consists of 5 steps, as shown in Fig. 21.11.

A detailed breakdown of each of the FSA steps is beyond the scope of this chapter. The risk management framework developed by the researcher attempts to cover all these steps. The risk estimation described by Figs. 21.1, 21.2, 21.3, 21.4, 21.5, 21.6, 21.7, 21.8, and 21.9 cover steps 1 and 2 of the FSA process, whilst the current sub-section deals with steps 3–5. Several IMO documents (IMO 2007a, b, 2008) include specific equations to calculate the 'cost' and 'benefit' of risk reduction measures.

Such analyses are also included in other literature sources such as reports by Christensen (2007) and Kleissen (2006). These equations help decision makers decide if risks associated with a project are worth reducing, or if a project should be abandoned.

## 21.4 Outlook and Conclusions

With the growing number and sizes of offshore wind farms and turbines, it has become increasingly necessary to conduct proactive risk assessment. Combining the growth of OWFs with developments such as floating wind turbines, and transnational wind farms, one can clearly see that existing frameworks are inadequate. In particular, existing frameworks are not capable of addressing transboundary issues, as risk assessment calculation procedures vary across countries.

This book chapter proposes an urgently-needed harmonized and transparent risk management framework for vessels operating near OWFs. Primarily developed to address the concerns with existing solutions (Sect. 21.2.2.1), the current framework outlines a step-by-step approach, and incorporates various recommended probability and consequence models in a cohesive manner.

Having one uniform framework across several different countries is a big step towards achieving continued growth of OWFs as it can simplify the administrative burdens that developers currently face. A clear, harmonized, step-by-step framework might also encourage smaller OWF owners to submit bids and tenders for OWFs. A simpler, transparent framework may also encourage greater participation from a broader range of stakeholders, thus allowing for a more comprehensive risk assessment. The outputs of this framework can be plotted an ALARP graph (Fig. 21.10)—which can enable quicker, more well-informed decisions from multiple stakeholders.

The proposed framework can, of course, be developed further. One of the immediate next steps will be to define specific equations for each relevant step. The authors also plan to expand this framework to take into account other maritime operations, rather than just vessels *passing* by OWFs. The ALARP diagram for the proposed framework will also be developed further to incorporate a third *cost* axis, which will visualize the results of cost-benefit analysis for various wind farm layouts and risk control options. The proposed framework is, so far, purely theoretical; however, the authors intend to apply this framework to a series of existing and proposed wind farms to validate the work practically in the near future.

Ultimately, the only way that the current levels of OWF growth can be sustained is if both the maritime and OWF industry understand the concerns of the other; the proposed framework is designed to enable just that. To continue building OWFs, we must demonstrate that they are viable, safe and reliable—and the way to do that is through proper, thorough risk management frameworks.

**Open Access** This chapter is distributed under the terms of the Creative Commons Attribution-NonCommercial 4.0 International License (<http://creativecommons.org/licenses/by-nc/4.0/>), which permits any noncommercial use, duplication, adaptation, distribution and reproduction in any medium or format, as long as you give appropriate credit to the original author(s) and the source, provide a link to the Creative Commons license and indicate if changes were made.



The images or other third party material in this chapter are included in the work's Creative Commons license, unless indicated otherwise in the credit line; if such material is not included in the work's Creative Commons license and the respective action is not permitted by statutory regulation, users will need to obtain permission from the license holder to duplicate, adapt or reproduce the material.

## References

- Akhtar MJ, Utne IB (2013) Human fatigue's effect on the risk of maritime groundings – A Bayesian Network modelling approach. *Saf Sci* 62:427–440
- Amdahl J, Ehlers S, Leira BJ (eds) (2013) Collision and grounding of ships and offshore structures. CRC Press/Taylor and Francis Group, London
- ANATEC, Royal Haskoning DHV (2014) FOREWIND Dogger Bank Teesside A and B – Environmental Statement – Shipping and Navigation (Chapter 16). F-OFL-CH-016 issue 4.1, application reference: 6.16. In: Forewind UK documents. Available via Forewind. [http://www.forewind.co.uk/uploads/files/TeessideAB/Application\\_Documents/6.Environmental\\_Statement/6.16\\_ES\\_Chapter\\_16\\_Shipping\\_and\\_Navigation.pdf](http://www.forewind.co.uk/uploads/files/TeessideAB/Application_Documents/6.Environmental_Statement/6.16_ES_Chapter_16_Shipping_and_Navigation.pdf). Accessed 06 Apr 2016
- Anderson S (2013) Comparing offshore and onshore wind. In: Harvey Mudd College papers. Available via HMC. <http://pages.hmc.edu/evans/andersonwind.pdf>. Accessed 06 Apr 2016
- Bela A et al (2015) Numerical crashworthiness analysis of an offshore wind turbine monopile impacted by a ship. In: Soares G, Sheno RA (eds) MARSTRUCT'15. 5th international conference on marine structures, Southampton, March 2015. Analysis and design of marine structures, vol 5. Taylor and Francis Group, London, p 661
- Biehl F, Lehmann E (2006) Collisions of ships with offshore wind turbines – calculation and risk evaluation. In: Köller J, Köppel J, Peters W (eds) Offshore wind energy: research on environmental impacts. Springer, Heidelberg, pp 281–304
- Brown AJ (2001) Collision scenarios and probabilistic collision damage. In: Pedersen PT, Lützen M, Simonsen BC et al (eds) Proceedings of the 2nd international conference on collision and grounding of ships (ICCGS), Copenhagen, 2001
- Brown AJ (2002a) Modelling structural damage in ship collisions. In: Ship structure committee reports. Available via SSC. <http://www.shipstructure.org/pdf/422.pdf>. Accessed 06 Apr 2016
- Brown AJ (2002a) Collision scenarios and probabilistic collision damage. *Mar Struct* 15:335–364
- Brown AJ, Chen D (2002) Probabilistic method for predicting ship collision damage. *Ocean Eng* 6:54–65
- BSH (2015) Minimum requirements concerning the constructive design of offshore structures within the Exclusive Economic Zone (EEZ). In: Federal Maritime and Hydrographic Agency, Germany standards. Available via BSH. <http://www.bsh.de/en/Products/Books/Standard/7005-15.pdf>. Accessed 06 Apr 2016
- Chen D (2000) Simplified ship collision model. Dissertation, Virginia Polytechnic Institute and State University
- Cho SR, Seo BS, Cerik BC et al (2013) Experimental and numerical investigations on the collision between offshore wind turbine support structures and service vessels. In: Amdahl J, Ehlers S, Leira BJ (eds) Collision and grounding of ships and offshore structures. CRC Press/Taylor and Francis Group, London, pp 281–288
- Christensen CF (2007) Navigational risk assessment – Rødsand 2 wind farm. In: Energy Styrelsen Denmark files. Available via ENS DK. [http://www.ens.dk/sites/ens.dk/files/undergrundforsyning/vedvarende-energi/vindkraft-vindmoeller/havvindmoeller/miljoepaavirkninger/Roedsand/navigational\\_risk\\_assessment.pdf](http://www.ens.dk/sites/ens.dk/files/undergrundforsyning/vedvarende-energi/vindkraft-vindmoeller/havvindmoeller/miljoepaavirkninger/Roedsand/navigational_risk_assessment.pdf). Accessed 06 Apr 2016
- Dai L, Ehlers S, Rausand M et al (2013) Risk of collision between service vessels and offshore wind turbines. *Reliab Eng Syst Safe* 109:18–31

- Dalgic Y, Lazakis I, Turan O (2013) Vessel charter rate estimation for offshore wind O&M activities. In: Soares G, Peña FL (eds) *Developments in maritime transportation and exploitation of sea resources*. CRC Press, Boca Raton, FL, pp 899–907
- Dalhoff P, Biehl F (2005) Ship collision, risk analysis – emergency systems – collision dynamics. In: *National Renewable Energy Laboratory Documents*. Available via NREL. [http://wind.nrel.gov/public/SeaCon/Proceedings/Copenhagen.Offshore.Wind.2005/documents/papers/Risk\\_management/P.Dalhoff\\_ShipCollision\\_riskanalysis.pdf](http://wind.nrel.gov/public/SeaCon/Proceedings/Copenhagen.Offshore.Wind.2005/documents/papers/Risk_management/P.Dalhoff_ShipCollision_riskanalysis.pdf). Accessed 06 Apr 2016
- Ding H, Zhu Q, Zhang P (2014) Dynamic simulation on collision between ship and offshore wind turbine. *Trans Tianjin Univ* 20:1–6
- Ehlers S, Tabri K (2012) A combined numerical and semi-analytical collision damage assessment procedure. *Mar Struct* 28:101–119
- Ellis J, Forsman B, Gehl S et al (2008a) A risk model for the operation of container vessels. *WMU J Marit Aff* 7:133–149
- Ellis J, Forsman B, Huffmeier J et al (2008b) Methodology for assessing risks to ship traffic from offshore wind farms. In: *Vattenfall reports*. Available via Vattenfall. [https://corporate.vattenfall.se/globalassets/sverige/om-vattenfall/om-oss/var-verksamhet/vindkraft/kriegers-flak/5-kriegers-flak-risk-assessment\\_11335732.pdf](https://corporate.vattenfall.se/globalassets/sverige/om-vattenfall/om-oss/var-verksamhet/vindkraft/kriegers-flak/5-kriegers-flak-risk-assessment_11335732.pdf). Accessed 06 Apr 2016
- EWEA (2007) *Delivering Offshore Wind Power in Europe: Policy recommendations for large-scale deployment of offshore wind power in Europe by 2020*. In: *The European Wind Energy Association (EWEA) reports and documents*. Available via EWEA. [http://www.ewea.org/fileadmin/ewea\\_documents/images/publications/offshore\\_report/ewea-offshore\\_report.pdf](http://www.ewea.org/fileadmin/ewea_documents/images/publications/offshore_report/ewea-offshore_report.pdf). Accessed 06 Apr 2016
- EWEA (2014) *Wind in power: 2013 European statistics*. In: *The European Wind Energy Association (EWEA) statistics*. Available via EWEA. <http://www.ewea.org/statistics/>. Accessed 06 Apr 2016
- EWEA (2015) *Wind in power: 2014 European statistics*. In: *The European Wind Energy Association (EWEA) statistics*. Available via EWEA. <http://www.ewea.org/statistics/>. Accessed 06 Apr 2016
- Fowler TG, Sörgård E (2000) Modelling ship transportation risk. *Risk Anal* 20:225–244
- Fricke MB, Rolfes R (2013) Investigation of sonar transponders for offshore wind farms: modeling approach, experimental setup, and results. *J Acoust Soc Am* 134:3536–3545
- Friis-Hansen A (2000) *Bayesian networks as a decision support tool in marine applications*. Dissertation, Technical University of Denmark
- Friis-Hansen P (2008) *IWRAP MK II – working document – basic modelling principles for prediction of collision and grounding frequencies*. In: *IALA-AISM technical products*. Available via IALA-AISM. [http://www.iala-aism.org/wiki/iwrap/images/2/2b/IWRAP\\_Theory.pdf](http://www.iala-aism.org/wiki/iwrap/images/2/2b/IWRAP_Theory.pdf). Accessed 06 Apr 2016
- Friis-Hansen P, Simonsen BC (2002) GRACAT: software for grounding and collision risk analysis. *Mar Struct* 15:383–401
- Fujii Y, Mizuki N (1998) Design of VTS systems for water with bridges. In: Gluver H, Olsen D (eds) *Proceedings of the international symposium on advances in ship collision analysis, Copenhagen, May 1998*. Ship collision analysis. A.A. Balkema, Rotterdam, p 177
- Fujii Y, Tanaka K (1971) Traffic capacity. *J Navig* 24:543–552
- Fujii Y, Yamanouchi H (1974) Visual range and the degree of risk. *J Navig* 27:248–252
- Fujii Y, Yamanouchi H, Mizuki N (1974) Some factors affecting the frequency of accidents in marine traffic. *J Navig* 27:239–248
- Fujii Y, Yamanouchi H, Matui T (1984) Survey on vessel traffic management systems and brief introduction to marine traffic studies. *Electron Navig Res Inst Pap* 45:1–48
- Geijerstam K, Svensson H (2008) *Ship collision risk - an identification and evaluation of important factors in collisions with offshore installations*. Dissertation, Lund University
- Goerlandt F, Montewka J (2014) A probabilistic model for accidental cargo oil outflow from product tankers in a ship-ship collision. *Mar Pollut Bull* 79:130–144

- Goerlandt F, Montewka J (2015) Maritime transportation risk analysis: review and analysis in light of some foundational issues. *Reliab Eng Syst Safe* 138:115–134
- Graczykowski C, Holnicki-Szulc J (2009) Protecting offshore wind turbines against ship impacts by means of adaptive inflatable structures. *Shock Vib* 16:335–353
- Hänninen M, Kujala P (2012) Influences of variables on ship collision probability in a Bayesian belief network model. *Reliab Eng Syst Safe* 102:27–40
- Hänninen M, Sladojevic M, Tirunagari S et al (2013) Feasibility of collision and grounding data for probabilistic accident modelling. In: Amdahl J, Ehlers S, Leira BJ (eds) *Collision and grounding of ships and offshore structures*. CRC Press/Taylor and Francis Group, London, pp 1–8
- Hansen MG, Randrup-Thomsen S, Askeland T et al (2013) Bridge crossings at Sognefjorden – ship collision risk studies. In: Amdahl J, Ehlers S, Leira BJ (eds) *Collision and grounding of ships and offshore structures*. CRC Press/Taylor and Francis Group, London, pp 9–18
- Haugen S (1991) Probabilistic evaluation of frequency of collision between ships and offshore platforms. Dissertation, University of Trondheim
- Helle I, Ahtianen H, Luoma E et al (2015) A probabilistic approach for a cost-benefit analysis of oil spill management under uncertainty – a Bayesian network model for the Gulf of Finland. *J Environ Manag* 158:122–132
- Hsieh JR (2015) Analytical formulations for ship-offshore wind turbine collisions. Dissertation, University of Liege
- IMO (2006) Possible improvements on FSA guidelines (MSC 82/INF.3). In: International Maritime Organization (IMO) documents. Available via IMO Docs. <https://docs.imo.org/>. Accessed 06 Apr 2016
- IMO (2007a) Consolidated text of the guidelines for Formal Safety Assessment (FSA) for use in the IMO rule-making process (MSC 83/INF.2). In: International Maritime Organization (IMO) documents. Available via IMO Docs. <https://docs.imo.org/>. Accessed 06 Apr 2016
- IMO (2007b) FSA – Liquefied Natural Gas (LNG) carriers (MSC 83/21/1). In: International Maritime Organization (IMO) documents. Available via IMO Docs. <https://docs.imo.org/>. Accessed 06 Apr 2016
- IMO (2008) FSA – cruise ships – details of the formal safety assessment (MSC 85/INF.2). In: International Maritime Organization (IMO) documents. Available via IMO Docs. <https://docs.imo.org/>. Accessed 06 Apr 2016
- IRGC (2006) Risk governance – towards an integrative approach. In: The International Risk Governance Council (IRGC) publications. Available via IRGC. [http://www.irgc.org/IMG/pdf/IRGC\\_WP\\_No\\_1\\_Risk\\_Governance\\_reprinted\\_version.pdf](http://www.irgc.org/IMG/pdf/IRGC_WP_No_1_Risk_Governance_reprinted_version.pdf). Accessed 06 Apr 2016
- Ito H, Kondo K, Yoshimura N et al (1985) A simplified method to analyze the strength of double hulled structures in collision (2nd report). *J Soc Nav Archit Jpn* 158:420–434
- Kaneko F (2002) Methods for probabilistic safety assessment of ships. *J Mar Sci Technol* 7:1–16
- Kaneko F (2013) An improvement on a method for estimating number of collision candidates between ships. In: Amdahl J, Ehlers S, Leira BJ (eds) *Collision and grounding of ships and offshore structures*. CRC Press/Taylor and Francis Group, London, pp 27–38
- Kitamura O (2002) FEM approach to the simulation of collision and grounding damage. *Mar Struct* 15:403–428
- Kleissen F (2006) NSW – MEP: Maritime and marine risk assessment of calamitous (oil) spills. In: NoordzeeWind knowledge, reports and data. Available via Noordzeewind. <http://www.noordzeewind.nl/en/knowledge/reportsdata/>. Accessed 06 Apr 2016
- Krata P, Jachowski J, Montewka J (2012) Modelling of accidental bunker oil spills as a result of ships bunker tanks rupture – a case study. *Int J Mar Navig Saf Sea Transp* 6(4):495–500
- Kroondijk R (2012) High energy ship collisions with bottom supported offshore wind turbines. Dissertation, Norwegian University of Science and Technology
- Larsen OD (1993) Ship collision with bridges – the interaction between vessel traffic and bridge structures (structural engineering documents (SED) 4). IABSE-AIPC-IVBH, Zurich

- Lehn-Schiøler T, Hansen MG, Melchild K et al (2013) VTS a risk reducer: a quantitative study of the effect of VTS Great Belt. In: Amdahl J, Ehlers S, Leira BJ (eds) Collision and grounding of ships and offshore structures. CRC Press/Taylor and Francis Group, London, pp 19–26
- Li S, Meng Q, Qu X (2012) An overview of maritime waterway quantitative risk assessment models. *Risk Anal* 32:496–512
- Le Sourne H, Barrera A, Maliakel JB (2015) Numerical Crashworthiness Analysis of an Offshore Wind Turbine Jacket Impacted by a Ship. *J Mar Sci Technol* 23(5): 694–704
- Lin H (2008) Simplified analysis and design of ships subjected to collision and grounding. Dissertation, Norwegian University of Science and Technology
- Lützen M (2001) Ship collision damages. Dissertation, Technical University of Denmark
- Macduff T (1974) Probability of vessel collisions. *Ocean Ind* 9(9):144–148
- Mazaheri A (2009) Probabilistic modelling of ship grounding – a review of the literature. In: Kotka Maritime Research Centre publications. Available via Merikotka. <http://www.merikotka.fi/safgof/ProbabilisticModelingofShipGrounding.pdf>. Accessed 06 Apr 2016
- Mazaheri A, Motewka J, Kujala P (2013) Correlation between the ship grounding accidents and the ship traffic – a case study Based on the Statistics of the Gulf of Finland. *Int J Mar Navig Saf Sea Transp* 7(1):119–124
- Mazaheri A, Montewka J, Kujala P (2014) Modelling the risk of ship grounding – a literature review from a risk management perspective. *WMU J Marit Aff* 13:269–297
- Mazaheri A, Montewka J, Kotilainen P et al (2015a) Assessing grounding frequency using ship traffic and waterway complexity. *J Navig* 68:89–106
- Mazaheri A, Montewka J, Nisula J et al (2015b) Usability of accident and incident reports for evidence-based risk modeling – a case study on ship grounding reports. *Saf Sci* 76:202–214
- MCA (2013) Methodology for assessing the marine navigational safety and emergency response risks of offshore renewable energy installations (OREI). In: GOV.UK, Maritime and Coastguard Agency (MCA) documents. Available via GOV.UK MCA. [https://www.gov.uk/government/uploads/system/uploads/attachment\\_data/file/372597/NRA\\_Methodology\\_2013.pdf](https://www.gov.uk/government/uploads/system/uploads/attachment_data/file/372597/NRA_Methodology_2013.pdf). Accessed 06 Apr 2016
- Minorsky V (1959) An analysis of ship collisions with reference to protection of nuclear power plants. *J Ship Res* 3:1–4
- Montewka J (2009) Predicting risk of collision for oil tankers in the gulf of Finland. *J KONBiN* 3:17–32
- Montewka J, Ehlers S, Tabri K (2010a) Elements of risk analysis for a LNG tanker maneuvering with tug assistance in a harbour. In: Abstracts of the 11th international symposium on practical design of ships and other floating structures COPPE/UFRJ 2010, Rio de Janeiro, 19–24 September 2010
- Montewka J, Hinz T, Kujala P et al (2010b) Probability modelling of vessel collisions. *Reliab Eng Syst Safe* 95:573–589
- Montewka J, Goerlandt F, Kujala P (2011) A new definition of a collision zone for a geometrical model for ship-ship collision probability estimation. *Int J Mar Navig Saf Sea Transp* 5(4):497–504
- Montewka J, Goerlandt F, Kujala P (2012) Determination of collision criteria and causation factors appropriate to a model for estimating the probability of maritime accidents. *Ocean Eng* 40:50–61
- Montewka J, Goerlandt F, Kujala P (2014a) On a systematic perspective on risk for formal safety assessment (FSA). *Reliab Eng Syst Safe* 127:77–85
- Montewka J, Ehlers S, Goerlandt F et al (2014b) A framework for risk assessment for maritime transportation systems – a case study for open sea collisions involving RoPax vessels. *Reliab Eng Syst Safe* 124:142–157
- Ohlson J (2013) Broadening horizons – The FMECA-NETEP model, offshore wind farms and the permit application process. Dissertation, Linnaeus University
- Ozguç O, Das P K, Barltrop N et al (2006) Numerical modelling of ship collisions based on finite element codes. In: Proceedings of the 3rd international ASRANet Colloquium, Glasgow, 10–12 July 2006

- Paik JK, Thayamballi AK (2007) Ship-shaped offshore installations – design, building, and operation. Cambridge University Press, Cambridge
- Paik JK, Chung JY, Choe IH et al (1999) On the rational design of double hull tanker structures against collision. In: The Society of Naval Architects and Marine Engineers (SNAME), technical resource library, technical papers. Available via SNAME. <http://www.sname.org/pubs/viewtechnicalpaper?DocumentKey=c7798c58-649e-4247-8d96-358e836552ad>. Accessed 06 April 2016
- Pedersen PT (2002) Collision risk for fixed offshore structures close to high-density shipping lanes. *Proc Inst Mech Eng M J Eng Marit Environ* 216:29–44
- Pedersen PT (2010) Review and application of ship collision and grounding analysis procedures. *Mar Struct* 2:241–262
- Pedersen PT (2013) Ship collisions against wind turbines, quays and bridge piers. In: Amdahl J, Ehlers S, Leira BJ (eds) *Collision and grounding of ships and offshore structures*. CRC Press/Taylor and Francis Group, London, pp 273–280
- Pedersen PT (2014) Risk assessment for ship collisions against offshore structures. In: Soares G, Santos TA (eds) *Maritime technology and engineering*. CRC Press/Taylor and Francis Group, London, pp 11–24
- Pedersen PT, Zhang S (1998) On impact mechanics in ship collisions. *Mar Struct* 11:429–449
- Pedersen PT, Valsgård S, Olsen D et al (1993) Ship impacts: bow collisions. *Int J Impact Eng* 13:163–187
- Pichler T, Pucker T, Hamann T et al (2012) High-performance Abaqus simulations in soil mechanics reloaded – chances and frontiers. In: *iMechanica papers*. Available via iMechanica. [http://imechanica.org/files/Pichler\\_TUHH\\_final\\_2222012.pdf](http://imechanica.org/files/Pichler_TUHH_final_2222012.pdf). Accessed 06 Apr 2016
- Ramberg HF (2011) High energy ship collisions with bottom supported offshore wind turbines. Dissertation, Norwegian University of Science and Technology
- Ren N, Ou J (2009) Dynamic numerical simulation for ship-OWT collision. In: Abstracts of the 8th international conference on reliability, maintainability and safety (ICMRS), Chengdu, 20–24 July 2009
- Ronza A, Félez S, Darbra RM et al (2003) Predicting the frequency of accidents in port areas by developing event trees from historical analysis. *J Loss Prevent Proc* 16(6):551–560
- SAFESHIP (2006) Reduction of ship collision risks for offshore wind farms: state of the art of risk models – Deliverable No. 5; Version 1, 2006-10-27, BV, Bunnik
- Samsonovs A, Giuliani L, Zania V (2014) Soil structure interaction in offshore wind turbine collisions. In: Cunha A, Caetano E, Ribeiro P et al (eds) *Proceedings of the 9th international conference on structural dynamics (EURODYN2014)*, Porto, 2014
- Schröder-Hinrichs JU, Baldauf M, Ghirxi KT (2011) Accident investigation reporting deficiencies related to organizational factors in machinery space fires and explosions. *Accid Anal Prev* 43(3):1187–1196
- Servis DP, Samuelides M (1999) Ship collision analysis using finite elements. In: GL Group research and advanced engineering. Available via GL Research Server. <http://research.gl-group.com/Projects/DEXTREMEL/publications/nantes-ntua.pdf>. Accessed 06 Apr 2016
- Simonsen BC (1997) Mechanics of ship grounding. Dissertation, Technical University of Denmark
- Sirkar J, Ameer P, Brown A et al (1997) A framework for assessing the environmental performance of tankers in accidental groundings and collisions. *SNAME Trans* 105:253–295
- Soares CG, Teixeira AP (2001) Risk assessment in maritime transportation. *Reliab Eng Syst Saf* 74:299–309
- Ståhlberg K, Goerlandt F, Ehlers S et al (2013) Impact scenario models for probabilistic risk-based design for ship–ship collision. *Mar Struct* 33:238–264
- Szwed P, van Dorp JR, Merrick JRW et al (2006) A Bayesian paired comparison approach for relative accident probability assessment with covariate information. *Eur J Oper Res* 169:157–177
- Tavakoli MT, Amdahl J, Ashrafian A et al (2008) Analytical predictions of oil spill from grounded cargo tankers; In: Abstracts of the 27th international conference on offshore mechanics and arctic engineering (OMAE'08), Estoril, 15–20 June 2008

- Tavakoli MT, Amdahl J, Leira BJ (2010) Analytical and numerical modelling of oil spill from a side damaged tank. In: Ehlers S, Romanoff J (eds) Proceedings of 5th international conference on collision and grounding of ships (ICCGS), Espoo, 2010
- Van LU (2012) Risk analysis methods within offshore wind energy. Dissertation, Norwegian University of Science and Technology
- van de Wiel G, van Dorp JR (2011) An oil outflow model for tanker collisions and groundings. *Ann Oper Res* 187(1):279–304
- van der Tak C (2010) Quantitative risk assessment for offshore wind farms in the North Sea. Report 23601.621/4. In: Nordzeeloket Netherlands information. Available via Nordzeeloket. [https://www.nordzeeloket.nl/images/Quantitative%20risk%20assessment%20for%20offshore%20wind%20farms%20in%20the%20North%20Sea\\_994.pdf](https://www.nordzeeloket.nl/images/Quantitative%20risk%20assessment%20for%20offshore%20wind%20farms%20in%20the%20North%20Sea_994.pdf). Accessed 06 Apr 2016
- Vanem E, Skjong R (2004) Collision and grounding of passenger ships - risk assessment and emergency evacuations. In: Society of Naval Architects of Japan (ed) Proceedings of 3rd international conference on collision and grounding of ships (ICCGS), Izu, 2004
- Wang G, Spencer J, Chen Y (2002) Assessment of a ships performance in accidents. *Mar Struct* 15:313–333
- Xia J (2001) Finite element analysis of ship collisions. Dissertation, Virginia Polytechnic Institute and State University
- Zhang S (1999) The mechanics of ship collisions. Dissertation, Technical University of Denmark
- Zhu L, James P, Zhang S (2002) Statistics and damage assessment of ship grounding. *Mar Struct* 15:515–530
- Zilakos I, Toullos M, Sameulides M et al (2009) Simulation of the response of double bottoms under grounding actions using finite elements. In: Soares G, Das PK (eds) MARSTRUCT'09. 2nd International conference on marine structures, Lisbon, March 2009. Analysis and design of marine structures. CRC Press/Balkema, Leiden, p 305

**Part VII**  
**Offshore Wind Decommissioning**

# Chapter 22

## ODIN-WIND: An Overview of the Decommissioning Process for Offshore Wind Turbines

Johan Finsteen Gjørdvad and Morten Dallov Ibsen

**Abstract** The oldest offshore wind farms in Europe are now well over 2 decades old. Considering this fact, and the technological advancements in wind turbine technology, it is evident that decommissioning of wind farms will soon become a crucial topic of discussion. NIRAS have been at the forefront of offshore wind farm decommissioning, and have developed extensive expertise in the area. Recently, they released a tool—ODIN-WIND—to assist stakeholders with the decommissioning process. The current chapter describes the decommissioning process for wind farms, the inherent challenges that may be faced, and potential solutions. It also provides an overview of ODIN-WIND tool.

### 22.1 Introduction

Decommissioning has previously been seen as simply the reverse procedure of the commissioning of an offshore wind farm (OWF). In recent years the sector has seen a shift from looking at the challenge in this simplified way to viewing it as a more diverse and complex challenge. It is considered prudent to address the future challenge of offshore wind farm decommissioning in a much more detailed manner in order to avoid the situation currently being experienced in the Oil and Gas industry where the failure to consider the potential requirements for decommissioning at an early stage has resulted in significant underestimation of the costs associated with decommissioning.

This chapter presents the processes relevant for decommissioning of offshore windfarms. This is done from a planning/management perspective and a on a high level. It is briefly discusses when it is recommended to make such a decommissioning plan in order to be in due diligence and the obvious results from such an assessment are presented.

---

J.F. Gjørdvad (✉) • M.D. Ibsen  
NIRAS, Sortemosevej 19, 3450 Allerød, Denmark  
e-mail: [jfg@niras.dk](mailto:jfg@niras.dk); [moi@niras.dk](mailto:moi@niras.dk)



Finally the ODIN-WIND tool is presented. ODIN-WIND is a decommissioning management tool that, in large, covers the phases of decommissioning as explained in this chapter.

## 22.2 Decommissioning Management

The planning and management of a decommissioning project must address the issue of decommissioning as a whole, considering the full process and all the associated sub-processes. By addressing and understanding the processes it is also possible to identify where there is a lack of knowledge and where contingencies and assumptions (known unknowns) should be made. Herby it is also possible to address the unknowns as they become known. The typical decommissioning process is explained further in Sect. 22.2.1, and can be seen in Fig. 22.1.

### 22.2.1 *The Decommissioning Assessment*

The assessment of the decommissioning process requires consideration on many levels and of many sub-processes. The typical processes of a OWF decommissioning which should be assessed are shown in Fig. 22.1. The assessment consists of three parts.

At the top, Fig. 22.1 shows the planning process which should asses all the process of decommissioning—i.e.—the decommissioning planning which is the work explained as a whole in this chapter.

Next, Fig. 22.1 illustrates the typical process of decommissioning: preparation, dismantling methods including cutting, lifting and detachment. Also included are considerations such as the used-vessels' capabilities and restraints; these restraints for vessels include weather on the site, challenges with transportation to the port and what the port capabilities are. All in all, this is essentially the offshore operation with an interface of the structure being lifted ashore.

In the middle part of the figure, the onshore operations are addressed, e.g. the treatment of the structural items including decontamination, stripping and waste management.

The bottom part of Fig. 22.1 shows the main components of waste and recourses that are produced. The hierarchy of the four fractions—reuse, recycling, disposal and hazardous waste—is deliberate. The top two fractions are in favour while waste for disposal should be avoided as well as hazardous materials which should be minimised as far as possible.

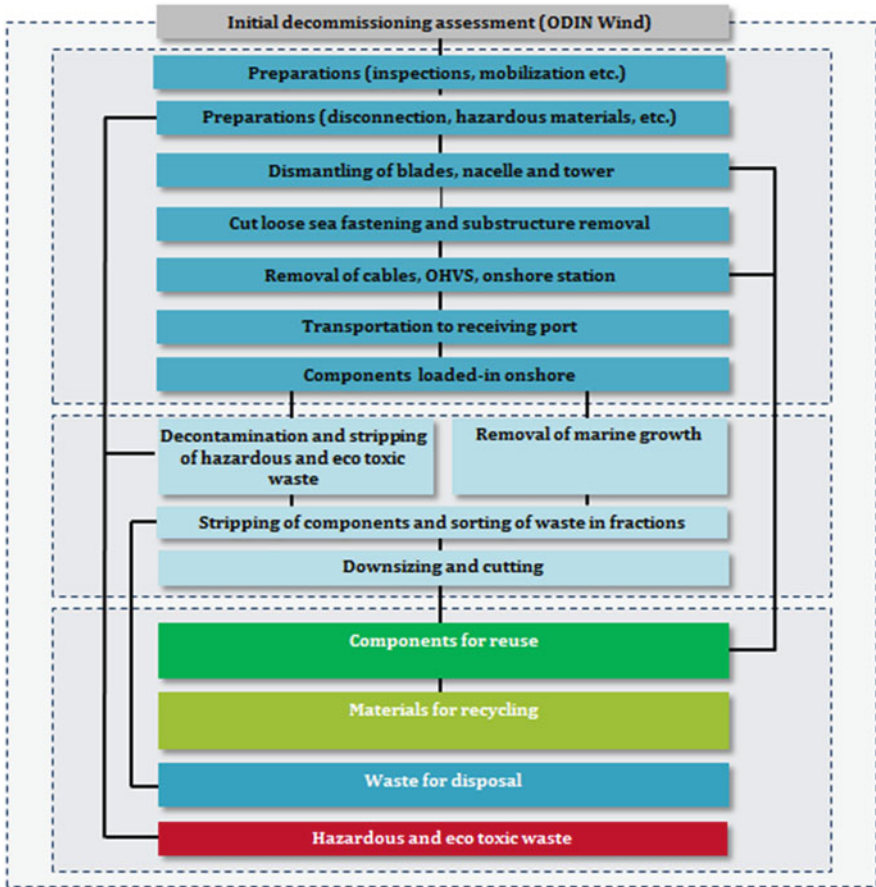


**Fig. 22.1** Typical process decommissioning of an OWF from the ODIN-WIND tool (Gjørdvad 2015)

After assessing the specific decommissioning project, the project should produce project output that can be used by the owner and the stakeholders involved. The focus and details of the output can vary, depending on which state the OWF is in: design, operation, or end of life. Typical outputs from such an assessment can be seen in Fig. 22.2.

It is of course the case that inadequate knowledge on the subject and equally inadequate or insufficient data, when using a tool as ODIN-WIND (Gjørdvad 2015), obviously will result in results of equally poor quality.

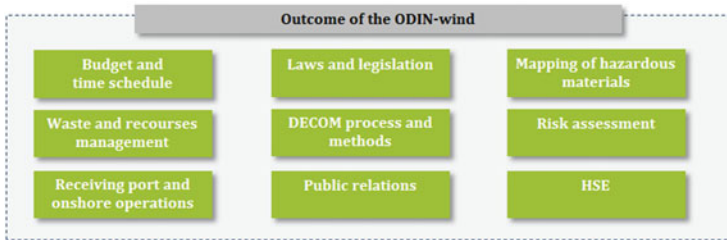


**Fig. 22.2** Typical output from a decommissioning assessment the ODIN-WIND tool (Gjørdvad 2015)

The mentioned method, considerations and other key elements of the decommissioning assessment are described in detail in Sects. 22.3–22.8. Starting with the actual decommissioning process including perpetrations, details on WTG (Wind turbine generator) and tower removal, substructure and OHVS (Offshore High Voltage Station) removal, cables removal, met mast removal followed by the vessel and port, weather and removal sequence, HSE and risk, waste and material management and finally cost estimation including budgeting and time schedule.

Managing an offshore decommissioning project requires involvement at an early state. This means the inclusion of a decommissioning assessment into a given offshore windfarm project as early as possible. The involvement of decommissioning in the different phases of an OWF is described shortly below.

### 22.2.2 *Decommissioning During the Design Phase*

The decommissioning assessments in the design phase can commence early—ideally during the selection of substructures, arrays, location etc. This would mean that a decommissioning analysis is made considering different scenarios with variations of the variables and thereby feedback into the decision of what type of substructure, array type and installation and even location is optimal. Although experience shows that the input from decommissioning is not as important as other considerations—such structure, installation scenarios, etc. . . .—the decommissioning input can still have an important impact on the final decision.

If not included from the beginning the decommissioning analysis can be based on a selected scenario with defined parameters including substructures, arrays, location etc., taken into account. Here the decommissioning assessment feeds back in to the project with cost reductive design adjustments taking the future decommissioning in

to consideration. This means that the existing design can be optimised by including the decommissioning input.

### ***22.2.3 Decommissioning During the Operation Phase***

A decommissioning plan can also be produced during the operation phase of an OWF. Making a plan at this stage can be done regardless of the existence of an decommissioning assessment from the design phase. It is recommended that the assessment should commence half way through the expected life time, typically 12–13 years after commissioning. If a decommissioning plan was made during the initial phases the assessment during the operation phase will naturally be an update. Otherwise the assessment should be made from scratch.

During the operation phase of the OWF, the estimation can be an important tool for the owner to decide what to do after end of operation; this enables the owner to set aside funding and also get a better picture of when the OWF should be taken out of operation. Furthermore the estimate can also be used for the purposes of life-extension and re-powering of the OWF.

The assessments will naturally be more detailed than the one made during the design phase. This is primarily because details of the OWF are actual ‘as-built details’, along with operation and maintenance information.

### ***22.2.4 Decommissioning Prior to the End of Life***

The final decommissioning assessment should be updated in good time prior to the actual decommissioning of the wind farm. The final assessments should be more detailed than the previous assessments, not only with actual details of the OWF in place. The final assessment also includes actual conditions at the time of decommissioning.

Even though such ‘final assessments’ get more precise the closer it is made to the planed time of decommissioning, it should not be left too late—and needs to be made at least 2–4 years ahead, depending on the quality of the previous decommissioning assessments made. As the time of decommission comes closer the assessment can then be used for EIA analysis, permitting and regulatory compliance as well as the actual tendering process.

Not only should the final assessment include details on the actual decommissioning, but also include plans for a post survey and a project close-out report.

### **22.2.5 *The Regulatory Process for Decommissioning***

Depending on which part of its life cycle the OWF is in—design, operation, or end of life—the regulatory process is a little different. Obviously the countries which first established offshore windfarms are most likely to be the ones that are furthest on the matter of decommissioning. This, combined with the level of environmental awareness that the respective countries holds, determines the state of regulations.

For the North Sea and most of the European waters, the regulations and guidelines that need to be fulfilled are international (from organizations such as IMO—International Maritime Organization), regional (from, for instance the OSPAR agreement), and national.

Regulations for the design phase, are at the present, only general rules of design such as Eurocode and environmental rules. Additionally, general rules of vessel operations and such should also be upheld. However, no *actual* rules of assessment of decommissioning of OWF or design input currently exist.

In many cases it is an authority requirement that decommissioning is considered during design, but the actual authority demand and the quality of the required assessment is very variable—and in most cases poor. Regulations for decommissioning assessments during operations are often driven by the fact that most European states require that the owner sets aside funding for the future decommissioning of the offshore structure.

The actual decommissioning for most of the European OWFs is at the present some time away, and therefore only few countries have actually made a fixed set of rules and procedures for decommissioning of offshore windfarms. Existing rules on O&G (oil and gas) are considered as starting points, and of course general regulations on HSE (Health, Safety & Environment) are to be upheld as well as general regulations on vessel operations.

## **22.3 The Decommissioning Process**

For all the assessed methods the process should be considered with regards to HSE (Health Safety and Environment). The considerations of HSE requirements are equally as important as the cost and time consumption. Thus, potential risks related to offshore decommissioning projects must be understood and addressed. The mentioned considerations are as important as managing the project in a cost effective way. Indeed, addressing these matters can actually help to make the project more cost efficient.

### 22.3.1 Preparations

Comprehensive preparations are necessary prior to the commencement of the dismantling and removal operations both onshore and offshore. With regard to vessels, this includes providing sea-fastening, lifting yokes, mobilization of vessel in general, amongst other tasks. An upgrade of the receiving port is also often required—e.g.—reinforcement of quays.

Preparatory work at the site depends on the removal concepts. Prior to the WTG and tower dismantling, preparations usually include jack-up footing assessment of seabed, disconnecting of high voltage system and other installations, securing non-fixed structures, and structural integrity checks.

Preparatory work for substructures, topsides and cable recovery include tasks such as dredging prior to cutting operation, preparing access inside the piles for tool deployment and ROV's (Remotely Operated Vehicles), and removal cables and other equipment.

### 22.3.2 Wind Turbine and Tower Dismantling

The options of removal concepts typically considered are shown in Table 22.1:

These options follow the typical installation options, but in reverse order. Thus, the installation process for a wind farm should be properly documented during the installation stage, and studied closely in the decommissioning planning phase.

Typically WTIVs (Wind Turbine Installation Vessels) and HLVs (Heavy Lift Vessels) are used for installation of wind turbines, and the obvious choice for the dismantling is to use the same or a similar vessels. For minor near shore wind turbines other solutions are possible such as jack-up platforms or barges with a mobile crane.

**Table 22.1** Wind turbine removal concepts

Removal concept	Description of lifts
Bunny ear and tower in 2 pieces	Single blade, nacelle, hub and two of the blades, tower in 2 pieces
Bunny ear and tower in 1 piece	Single blade, nacelle, hub and two of the blades, tower in 1 piece
Rotor and tower in 2 pieces	Hub and three blades, nacelle, tower in 2 pieces
Rotor and tower in 1 piece	Hub and three blades, nacelle, tower in 1 piece
Five pieces separately	All three blades individually, nacelle and hub, tower in one piece
Six pieces separately	All three blades individually, nacelle and hub, tower in two pieces
Removal in 1 piece	Blades, hub, nacelle and tower in one single lift

### 22.3.3 *Transition Piece and Substructure Removal*

The key factor to be considered removing substructures is whether the installation is to be removed entirely or if any parts are to be left behind. The baseline of international law and obligations—e.g.—OSPAR convention and UNCLOS—is complete removal of offshore installations, with exceptions according to the IMO guidelines. The IMO guidelines list 6 key components that should be considered when making decommissioning decisions regarding how much—if any—of a platform or a structure should be left on the seabed.

The substructure design and installation concepts must be taken into consideration when planning the decommissioning. Typical substructure designs include: Monopile, 4 legged jacket, 3 legged jacket, tripod, gravity based. Typical installation and design concepts include: transition piece grouted onto top of pile, driven or drilled (grouted), or suction bucket (monopod).

#### 22.3.3.1 *Monopiles, Jackets and Tripods*

The common practice for removal of monopiles, tripod and jackets at other offshore installations has been to cut piles just under the seabed. Concepts for complete removal are yet to be field tested in full scale. The feasibility of the concepts and methods vary depending on the installation method—namely suction buckets and type of pile installation used. Various decommissioning concepts for monopiles, jackets and tripods are shown in Table 22.2.

**Table 22.2** Decommissioning concepts for Monopiles, Jackets and Tripods

Decommissioning concept	Description
Partial removal	Substructure with TP in one piece cut below seabed level
Partial removal	Substructure and TP in separate pieces cut below seabed level and TP
Complete removal	Removal of monopiles, tripod or jackets with suction buckets by reversing the suction process. Field proven on met mast leaving the seabed unmarked
Complete removal	Removal of the monopile, tripod and jacket piles in its full height using water pressure. Novel concept which not yet have been field tested
Complete removal	Removal of the monopile in its full height by removing sand around the pile. Considerable impact on the benthic ecologic and challenging. The impact and challenge increase proportional with the substructure depth

If the substructure is to be partially removed selecting the correct cutting concepts and methods is crucial for the operation to be successful. There are several cutting methods concepts, including:

- Internal pile cutting tool. The cutting tool is lowered inside the MP after clearance of internal parts and necessary seabed excavation
- External cutting. The cutting tool is installed after dredging soil around piles

The best solution of cutting tool and dredging method depends on the site conditions. In many cases it is preferable to minimize the use of divers which can cause safety risks and long downtimes. Cutting tools include flame cutting (oxy-fuel cutting); wire cutting; abrasive water jet cutting; cutting using linear shaped charge (explosives); blade sawing; and laser cutting. Explosives can be placed and detonated safely in regard to personnel health but are usually wrongly counted out due to environmental concerns.

### 22.3.3.2 Gravity Based Substructures (GBS)

In the Oil & Gas sector partial removal or leave wholly in place (reefing) are conceivable solutions in some case for large concrete GBS situated on deep waters. GBS for wind turbines are in most cases situated at shallow water depths and typically minor constructions than the ones used for oil rigs. GBS' are not piled and therefore they do not have the issue of cutting and leaving the piles partly in the seabed hence most likely complete removal is the only acceptable solution. Decommissioning concepts for GBS are shown in Table 22.3.

The weight of GBS' is substantial by design, and moving the GBS is a challenging operation. Conceivable options are shown in Table 22.4.

### 22.3.4 Substation (Offshore High Voltage Station) Removal

Substructure concepts for substations are the same as for wind turbines and can in general be decommissioned applying the same measures as for wind turbines

**Table 22.3** Decommissioning concepts for GBS

Decommissioning concept	Description
Offshore disposal	Moving the GBS further off shore and dumping it on greater depth
Demolition at other location	Moving the GBS inshore at location with wider and cheaper options for deconstruction
Demolition on site	Demolition on site and removal of debris/pieces
Onshore demolition	Moving the GBS onshore for conventional demolition



**Table 22.4** Options for moving GBS

Options for moving GBS	Description
Single heavy lift in one	The lift requires very large vessels with large draughts for the heavy lift. The feasibility of the solution is dependent on the water depth and the weight
Heavy lift in two pieces	Dividing the GBS by wire cutting or sawing will reduce required lifting capacity significantly and enabling more vessels do carry out the lift. The cutting operation is very sensitive to weather conditions due to underwater operations. Feasibility is dependent on the GBS design
Floating	Floating the GBS supported by salvage pontoons and filling it with ballast on site is usually used for the installation and it is obvious to reuse the method if the design allows pumping out sufficient ballast weight to enable buoyancy.

**Table 22.5** Overview of removal concepts for substation topsides

Removal concept	Description
Single heavy lift	Removal of topsides by heavy lift vessels.
Float-over	Float-over is the removal by lifting the topside of the substructure with semisubmersible heavy lift vessels or dual barges with jack-up systems. No crane lift is required for this method.
Skidding	The method is the reverse of skid-on where the topside is transferred to a vessel by drifting on rails from the substructure.
Modular	Lifted in modules reverse of the installation process.

substructures. The substructures for substations however, are typically bigger than wind turbine substructures. The logical solution for removing the topside is using the same concept as is used for the installation. Self-installing (jack-up) concepts have been used at other offshore installations but most offshore high voltage station (OHVS) topsides have been installed using the single full topside concept. The concepts for removal of substation topsides are shown in Table 22.5.

Independent of the removal concepts, the separation of the topside and substructure requires a cut at stabbing pipe sleeves and all welded connections. A OWF typically only includes one OHVS and therefore opting to use a lifting vessel already at the site is likely to be cost-effective.

### 22.3.5 Cable Removal

The installation concepts for inner array cables and export cables are given in Table 22.6.

At the time of decommissioning seabed conditions may have change dramatically from the installation phase due to current and sand waves. Hence a thorough

**Table 22.6** Installation concepts for offshore cables

Installation concepts	Description
Buried	Typically buried 1–2 m under seabed in a trench and possible partly scour protected
Covered	Typically covered with 0.5–1.0 m of rock boulders

**Table 22.7** Overview removal methods for cables

Recovery	Storing on CLB or CLV
Jetted up on seabed (if buried) and pulled on board	On drums On an on-board turntable Cut in sections
Directly “Brute forced” (if rock covered)—the cable is pulled free first from the J-tube and then from the rock layer	On drums On an on-board turntable Cut in sections

inspection is required prior to decommissioning planning. The decommissioning concepts for cables are:

- Complete removal of all cables
- Leave all in place
- Partial removal.

The solution depends on the regulatory obligations and/or the economical balance between the cost of recovery and the scrap value. In some cases, it the possible repowering and reuse of cables will determine the best solution. An overview of removal methods for cables is given in Table 22.7.

The best solution for storing the cable is interdependent of transport distance and offload facilities and if direct load-in to scrapyard is relevant. The main vessels used are CLV (Cable Laying Vessel) or CLB (Cable Laying barge). For the jetting operation and attaching the cable to the crane hook a ROV can be applied. Divers are often preferred in shallow waters, or used when the ROV is not applicable.

### 22.3.6 *Met Mast*

Wind farms usually have one or more met masts. The design of met masts varies a great deal. Met masts with lattice tower mounted on monopiles are a quite common design. The towers can often be dismantled without crane use. The substructure is more likely to be removed totally—and removing a mono suction bucket substructure totally, by reversing the suction process, has been field proven.

## 22.4 Vessels and Ports

This section describes the challenges that may arise during the decommissioning process due to inadequate vessel technology or port facilities.

### 22.4.1 Vessel Types

Many vessels are used in the process of decommissioning. The main vessel types are listed in Table 22.8.

Beside the main decommissioning vessels a fleet of support vessel is required. This includes work boats, construction support vessels, diver operation vessel, ROV operation vessels, anchor handling tug and crew boats for transit.

### 22.4.2 Vessel Suitability

The vessels used for the wind farm installation will by nature be capable of decommissioning. However the market for installation vessels is constantly developing

**Table 22.8** Main decommissioning vessels

Vessel type	Description
Jack-up barge	Barge or platform equipped with legs and a jacking system allowing the barge to self-elevate when operating. Used for installation of blades, hub, nacelle and tower. The components are transported to the site by a barge.
WTIV	Purpose build jack-up vessel for the installation of blades, hub, nacelle and tower. WTIV is self-elevating similar to a jack-up barge but transport the components on the its own deck.
Heavy lift vessel (HLV)	Designed to lift very large loads and used for installation of topsides and substructures. There are several types and variations of HLV e.g. floating sheerleg cranes, monohull crane vessel, catamaran cranes, semi-submerging vessels lifting with-out the use of cranes.
Semi-submersible crane vessel (SSCV)	Designed with increased stability allowing very large crane capacity. Used for topside installation.
Barge	Capacious flatbottom vessel used for transportation of wind turbines, substructures and OHVS topsides etc.
Cable laying vessel (CLV) and cable laying barge (CLB)	Used for cable recovery by pulling the cable on drums or turntables.

to increasing installation performances—and at the time of decommissioning the original installation vessels could be decommissioned themselves.

The physical character of the structures and the proposed method for removal will result in a number of requirements for the vessels to be used. Parameters to be considered include lift capacity, cargo load capacity, etc. As a key factor in the planning stage the vessels operational limits in regard to environmental loads must be taken into account. Furthermore the logistic planning must take cargo area, transportation/transit speed, length, draft, breadth, and other such factors into account in order to line up port requirements and get realistic cost estimations.

### **22.4.3 Ports**

The receiving port should be able to meet the requirements derived from the load-in and the downsizing activities. Examples of physical requirements for the port include water depth, load capacity, storage facilities, and load-in facilities. The lesser the port restraints, the more vessels are available—leading to increased completion in the tendering process. Other port requirements that should be considered are environmental approvals for emissions, noise, dust, and facilities for the specific hazardous materials. Matching the requirements with vessel performance, port capacity and methodology should be done in an iterative process.

## **22.5 Removal Sequence and Weather Windows**

The removal process must be broken down in a removal sequence to analyse the downtime for the decommissioning operation duration.

The time schedules for offshore operations are based on a weather model or met-ocean data. A common approach to the weather model used for the estimation of operation duration is to combine the planned offshore decommissioning activities (removal sequence)—defined as a combination of duration, required weather windows and weather restrictions specific for selected vessels—with the assumed future weather conditions of wind speed, significant wave heights and peak wave periods. In this manner, the time schedules can include vessel downtime due to weather restrictions.

## **22.6 Waste and Material Management**

The policy for waste treatment is a waste hierarchy, shown in Fig. 22.3.

The EU Waste Framework Directive (EU, 2015) specifies that companies involved in the production of materials, construction, demolition, renovation,

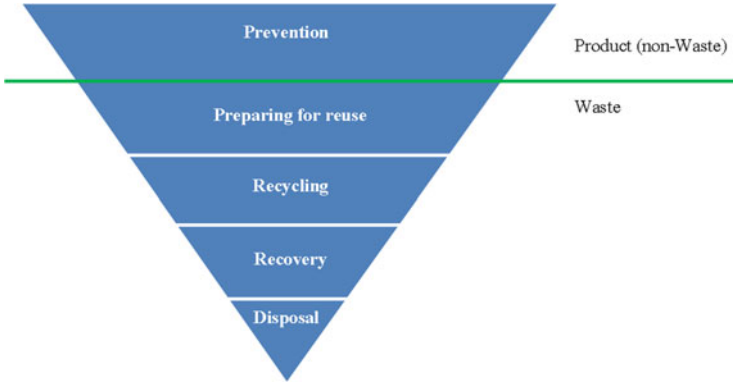


**Fig. 22.3** Waste hierarchy

buildings and public works will improve the sorting and recycling of their waste to achieve performance in terms of material recovery of 70 % in 2020. The material received onshore from the wind farm will, as far as possible, be re-used, alternatively recycled or incinerated for energy recovery. If none of these alternatives are possible, for instance, due to content of environmentally hazardous compounds, the material will be deposited at landfills. The trend of circular economy will also influence the offshore wind industry and the design of the modules will by time be easier to dismantle, refurbish and reuse.

### ***22.6.1 Reuse of Components***

The nacelle with hub and blades can either be reused completely, or be disassembled in major components and sold as spare parts. The reuse of substructures, towers and sea cables is less attractive. This aftermarket business of selling old turbines is developing as the wind industry is coming to a mature state.

### ***22.6.2 Recycling***

The majority of the materials are fit for recycling. All metals, electronics, batteries, gears and motors can be recycled through re-melting. Concrete can be crushed and recycled as secondary construction materials. Oils can be refined and that way upcycled to new oil products. For rubber, plastics and glass fibre, or other composites and epoxy, recycling is possible, but depending on the quality and compositions of the specific products.

Marine growth on the subsea parts will consist of algae, barnacles and mussels. Due to the anti-fouling agent on the substructure they might be contaminated with the active components of the anti-fouling agent. Due to the organic content in the material, it is possible that the material can be used as other types of sludge.

### **22.6.3 Incineration**

If rubber, plastics and glass fibre, or other composites and epoxy, cannot be recycled it is possible they can be incinerated for energy purposes. For glass fibre it is known that a large amount can cause challenges for the incineration plants filtration system, and that the emission of dioxin can rise.

PVC is a problematic compound, because it can contain phthalates or heavy metals—and if incinerated in a waste incineration plant, the amount of slag produced will increase significantly. This slag is classified as hazardous waste and has to be landfilled. Although a method exists for the recycling of mainly hard PVC, it is not feasible for OWFs. In wind turbines, PVC is sometimes used as cores in the blades and has to be split from the glass fibre, before it can be recycled, which currently is quite difficult. It can therefore be expected that PVC in current blades will be incinerated.

### **22.6.4 Deposit**

Currently, the recycling of composites is quite limited. It is a field of innovation, as presently, these materials are mainly incinerated or landfilled depending on their content. If the marine growth on these materials is highly contaminated by anti-fouling agents the composites will have to be deposited.

Some fractions of hazardous waste must be expected. In some cases, this can be treated (through the use chemicals, for instance); otherwise depositing is the only option.

## **22.7 Cost Estimation**

The cost estimate should include the proposed decommissioning measures described earlier in this chapter (Sect. 22.3). The estimation should have a budget covering:

- Planning and engineering
- Decommissioning design
- Offshore removal and transportation

- Clearance of site
- Onshore dismantling
- Waste and recourse handling
- Assumptions and contingencies

The budget should be accompanied by a time schedule which naturally will appear as the methods are assessed. The schedule should show the different phases of the decommissioning work which naturally would be undertaken in the most suitable part of the year in regards to weather, based on the implementation of sequence and removal windows.

## 22.8 ODIN-WIND: The Tool

The ODIN-WIND project is a Danish development program under EUDP (energy technological development and demonstration program) supported project NIRAS has, together with its partners, Vattenfall, TWI (Technical Welding Institute), DTU (Technical University of Denmark) and Maersk Broker, created the ODIN-WIND modelling tool.

The ODIN-Wind modelling tool is based on a standard estimation of decommissioning procedures. This includes an input phase where the user is guided through the process of establishing the model. This aids the user in inputting the initial data after which the modelling tool preselects the next steps based on the provided data. Preselection is based on logical choices from what is possible with the previously given input. The user can also update the model to achieve different end results by improving data input, or making different selections. Finally the end result is computed, and results from each iteration can be saved separately for future use. In other words the user can iterate and justify the built model to retrieve the optimised result.

The model is built up in stages and at any time a user can return to previous stages and make changes. However, it is not possible to move on to a later stage unless the previous stage is completed.

The input function part of the modelling tool includes the steps below:

- Log in
- Initial study
- Mapping of Hazardous materials
- Deconstruction
- Receiving ports
- Supplier selection

The end result is presented to the user as a summary of the model with a listing of estimates and relations linked to: the installation details, selected methods, suppliers, geography etc. The end result is presented to the user as relevant information regarding:

- Cost estimation (budget and time schedule)
- Applicable laws, legislation, regulations and standards
- Mapping of Hazardous materials
- Waste and recourse management
- Decommissioning process and methods
- Risk assessments/analysis
- Receiving ports and onshore operations
- Public relations
- HSE

The ODIN-WIND tool is described in more details in the EWEA paper “Preparing for the future—the full process of decommissioning” (Gjørdvad 2015).

## 22.9 Conclusions

As OWFs become increasingly common, there will—inevitably—be a need to decommission obsolete turbines. Decommissioning is a process that has not been explored or researched widely until now, as the need was not so pressing. NIRAS, being at the forefront of technology have anticipated the needs of the industry and developed a comprehensive tool to address the decommissioning process, as described in this chapter.

It is expected that this tool, and indeed the decommissioning process, will be updated and adapted in the future, as wind turbine technology continues to evolve.

**Open Access** This chapter is distributed under the terms of the Creative Commons Attribution-NonCommercial 4.0 International License (<http://creativecommons.org/licenses/by-nc/4.0/>), which permits any noncommercial use, duplication, adaptation, distribution and reproduction in any medium or format, as long as you give appropriate credit to the original author(s) and the source, provide a link to the Creative Commons license and indicate if changes were made.

The images or other third party material in this chapter are included in the work’s Creative Commons license, unless indicated otherwise in the credit line; if such material is not included in the work’s Creative Commons license and the respective action is not permitted by statutory regulation, users will need to obtain permission from the license holder to duplicate, adapt or reproduce the material.

## Reference

Gjørdvad J (2015) Preparing for the future – the full process of decommissioning. Paper presented at the EWEA Offshore 2015 Conference, Copenhagen, 10–12 March 2015



# Chapter 23

## Wind Turbine Blades: An End of Life Perspective

Justine Beauson and Povl Brøndsted

**Abstract** In 2016, the first offshore windfarm constructed in the world—located in Denmark, near Ravensborg—is turning 25 years old, and will soon be decommissioned. After decommissioning, most of the material of the turbine can be recycled; only the composite materials found in the blades represent a challenge. This part looks at end of life solutions for this material. Wind turbine blade structure and material are described. The ends of life solutions existing and under development are detailed.

### 23.1 Introduction

Wind turbines are designed to have a lifetime of 20 years (Nijssen and Brøndsted 2013). In this period of time, the turbines can be inspected and some components can be replaced or repaired several times. The blades, for example, can be damaged by hostile weather conditions, impacts or other. However, there can be other reasons for decommissioning a windfarm than the age or the damage state of the turbines. A wind farm can also be repowered with newer and bigger turbines.

A wind turbine is basically composed of a rotor, a nacelle, a tower and a foundation. Figure 23.1 shows the weight of each part for an onshore Vestas V82 turbine (Schmidt 2006). The foundation made of concrete and steel represent nearly 80 % of the structure total weight. At the end of life of the turbine, the foundation can be left in situ or destroyed and the site restored. The environmental risk associated with leaving the foundation in situ can in some cases, be considered as relatively low compared to the environmental impact generated with excavation, breaking, processing, and transporting activities needed to remove it (Welstead et al. 2013). The tower is the next largest component in terms of weight and is mainly made of steel. Metals such as steel, aluminum and copper represent 94 % of the turbine weight excluding the foundation and are generally considered as materials that can be recycled (Schleisner 2000). The 6 % remaining corresponds to plastic, rubber,

---

J. Beauson (✉) • P. Brøndsted  
Department of Wind Energy, Technical University of Denmark (DTU), DTU Risø Campus,  
Frederiksborgvej 399, 4000 Roskilde, Denmark  
e-mail: [jube@dtu.dk](mailto:jube@dtu.dk); [pobr@dtu.dk](mailto:pobr@dtu.dk)

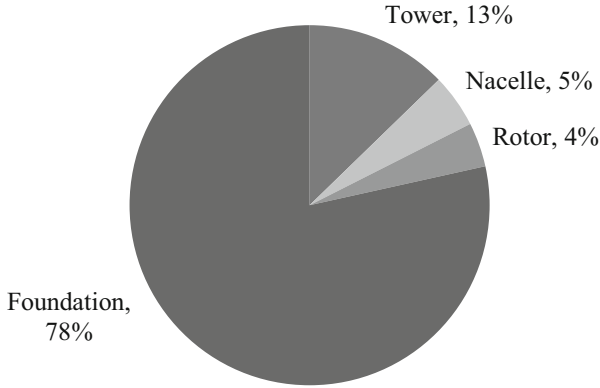


Fig. 23.1 Diagram representing the weight of the part and the corresponding percentage in a Vestas V82 onshore turbine (Schmidt 2006)

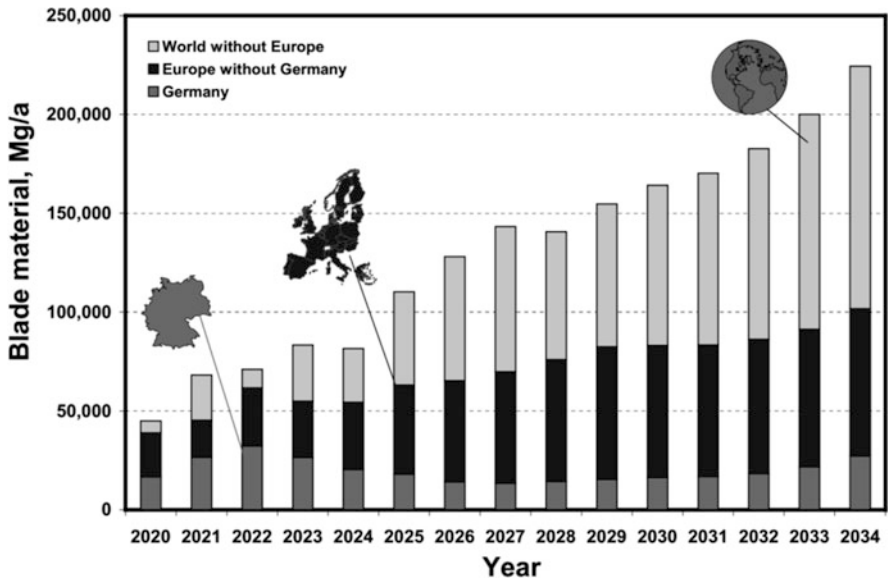


Fig. 23.2 Expected amount of end of life blade material in Germany, in Europe and worldwide from 2020 to 2034 (Albers et al. 2009)

fibre reinforced polymer composites and other. These materials are mostly found in the rotor blades and do not have established recycling solutions.

The amount of wind turbine blade material expected to reach end of life in the coming years is shown in Fig. 23.2. It is estimated to reach 50,000 tons per year in Europe, in 2022.

In Europe, the legislation on the disposal of composite waste is mainly regulated by the waste framework and the landfill directive (Halliwell 2006). The implementations of these directives in the European countries have, for examples, led to higher tax on landfill or a prohibition to landfill in Germany. Recycling solutions for composite waste are therefore needed and research project investigating this issue are ongoing in Europe. In Denmark, the innovation consortium named GenVind (2012–2016), is looking at possible recycling solutions for wind turbine blade and other products made of glass fibre reinforced polymer composite. The project's many partners, from both industry and universities are working to develop suitable technologies and future industrial applications. This section will detail some of the outcomes of the project and other existing solution for end of life rotor blade.

This chapter is organized as follows: the wind turbine blades structure and materials are first presented. Then, the recycling solutions for wind turbine blades are presented, starting with the one implemented on an industrial scale followed by the solutions used occasionally and ending with the solutions on a research stage.

## 23.2 Wind Turbine Blades: Structure and Materials

Two parts can be distinguished in a blade, the root section and the aerodynamic section. The root section is the part of the blade connected to the turbine (Fig. 23.3a). It is tubular with a circular shape, as shown in Fig. 23.3b. The composite material used for this section is a thick unidirectional glass fiber laminate. Metallic T-bolt also named IKEA bolts or treaded bushings are inserted for mounting the blade to the hub. The root section shown in Fig. 23.3 is from a 25.8 m blade. It has a diameter of 1675 mm and a composite thickness of 80 mm.

In the full blade length, the cross section can be designed as shown in Fig. 23.4a, with a girder box on which two aerodynamic shells are bonded, one on the suction or downwind side and one on the pressure or upwind side. The two sides are adhesively bonded to the box and at the leading and the trailing edge. In other designs the girderbox is integrated as beams in the aerodynamic profile and the two shells

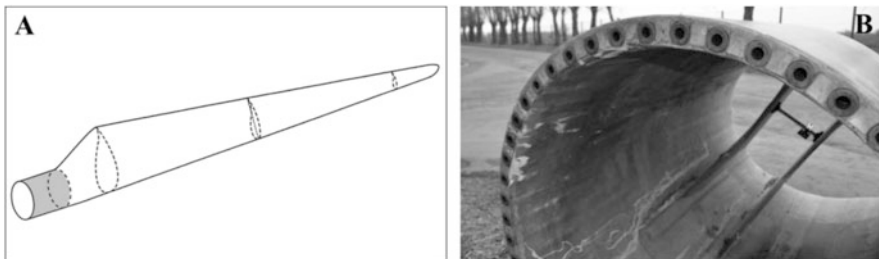


**Fig. 23.3** The root section of a wind turbine blade, (a) Location of the root section, (b) Closer view of the metallic bolt

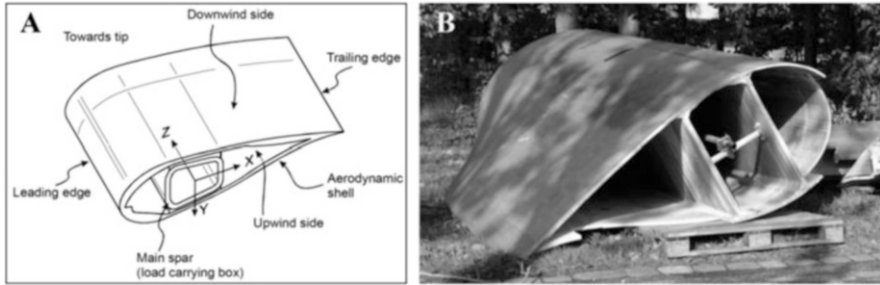


**Fig. 23.4** Cross section of a blade, (a) Design with a load carrying box (Sørensen et al. 2004), (b) Design with two shear webs LM25.8

will be supported in by one or more structural shear webs (Fig. 23.4b). All these structural components are assembled using adhesive bonds.

Regarding the materials, the load carrying beam, the trailing edge and the leading edge are mostly made of unidirectional glass fibre reinforced thermoset matrix. The glass fibres used are E-glass fibres, which are inexpensive and combine high strength from 1500 to 2500 MPa and stiffness, 72 to 76 GPa. As the trend goes towards longer blades, the weight and the stiffness of the blade become an issue. Therefore, reinforcement with a high modulus glass or a hybrid combination made of glass and carbon fibres are introduced in the composites to keep the weight down. The thermoset resins used can be epoxy, polyester or vinylester resins. The shells and the shear webs are made of sandwich structure composites, built as biaxial or multiaxial glass fiber laminates with balsa wood or polyvinyl chloride foam as core material. Surfaces are protected using gel coats, polyurethanes and thermoplastic foils or special paints are used on leading edges (Brøndsted et al. 2005).

As a part of the GenVind project, the residual strength of the composite material from a wind turbine blade after being tested in fatigue was investigated. The aim was to get an idea of the quality of real end of life composite laminate from blades. The results of these measurements demonstrate that the material is keeping its high strength and stiffness. A measurement of the porosity of the materials shows high fiber volume fraction and low porosity content. The microstructural investigation does not reveal any traces of fatigue damages due to the blade testing (Fig. 23.5).

A common size of turbine in 1990 had a power of 600 kW and blades length of 18 m. In year 2015, one of the biggest turbines produced was a 7 MW turbine with about 85 m long blade. The design of blade has also improved throughout the years. To ensure the lifetime of 20 years, the first blades produced were based on conservative design, using more material compared to the blade produced nowadays. Thanks to more optimized design, the blades produced nowadays are lighter (Mølholt Jensen and Branner 2013). This means that, after 20 years, the first blades produced might still be able to last a number of years more.

To summarize, blades are a complex structure made of different parts and materials, which will have different structure depending on the manufacturer and the year



**Fig. 23.5** Microstructure of a unidirectional composite from the load carrying beam

of production. When decommissioned, blades will be found in different condition depending on their design and the reason for decommissioning. Altogether, this will make recycling of blade challenging. The following part looks at solutions for end of life wind turbine blades at an industrial scale.

## 23.3 Industrial Scale Solutions

### 23.3.1 Refurbishment

The first and simplest end of life solutions for wind turbine blades is to be reused after being decommissioned. This way, their service life is extended. As previously explained, after the design lifetime of 20 years, the wind turbine blades may still have high residual capacity. A study conducted in Germany by Sayer et al. (2009) support this statement. Sayer et al. (2009) investigated the effect of service life on wind turbine blades based on the comparison of the performance of the blades after 20 years of use. The study reported no significant damages by visual inspection and no significant lost in stiffness of the blade. Therefore, reusing wind turbine and wind turbine blades is technically possible. In Europe and in Northern America, a number of companies such as Green-Ener-Tech, Repowering Solutions, Enerpower, Windturbines i.e. and Blue Planet Wind have built business on selling refurbished wind turbine. The advantages are among other an access to a wide range of proven small and medium size turbines, a short lead time and a low cost of about half the price per MW (Tucker 2009).

Standardized refurbishment procedures may include visual inspection, ultrasonic inspection, and natural frequency measurements of the blades. The blades can also be repaired, repainted, weighed and balanced (Beauson et al. 2013). Refurbishment seems technically affordable for blades with a rather small size. The companies mentioned previously handle wind turbine in the range of 10 kW to 1 MW. For blades longer than 50 m, which are commonly produced nowadays, the viability of that solution might be challenged, due to transport difficulties.

### 23.3.2 *Incineration*

Blade material can be incinerated for energy recovery. This solution is currently used in Denmark. It has however several drawbacks. Structural composite material, such as the one used in wind turbine blade contain up to 70 wt% of glass fiber. Energy recovery will be difficult, as glass fibers are not combustible and will hinder the incineration (Duflou et al. 2012). It has also been reported that the presence of glass fibre in the flue gas could disturb the gas cleaning system (Schmidt 2006). Finally, the large amounts of fly ashes, which will come from the combustion of large structure such as blade, will remain at the end of the combustion process. This residue also needs to be disposed of or used (Papadakis et al. 2010).

### 23.3.3 *Mechanical Grinding*

Mechanical grinding of composites consists in reducing composite waste down to pieces of a few centimeters or less. The resulting mixture, also called shredded composite, is then used in new applications. A number of companies dedicated to collect and process the composite waste brought mechanical grinding to an industrial scale. However, they all terminated, such as Phoenix Fibreglass Inc. in Canada, which was active from year 1990 to 1996 or ERCOM GmbH in Germany from 1990 to 2004.

More recently and until 2014, the company Zagons in Germany collected and grinded wind turbine blade material to be used in cement production. The procedure implemented by Zagons started by cutting the blades onsite to pieces of 10–12 m. At the factory place, these sections were further reduced to pieces of about 1 m in length. These smaller sections were then transformed to shredded composite material by a series of crushing and shredding steps. The resulting material had a size of 5 cm and was mixed with other wet waste materials. Finally, this mixture was sent to the cement production factory Holcim, which used it as a substitute for fuel, to reduce coal-ash, and as a raw material to replace virgin washed sand (Job 2013). Since 2012, using composite waste in the production of cement is considered as a viable recycling solution by the European Union (European Commission Directorate General Environment 2012; European Composites Industry Association 2013). Unfortunately, Zagons was the only industrial scale factory able to process end of life wind turbine blade for cement production worldwide.

The main challenge of this recycling solution is to find applications for the shredded composite material. Apart from the cement production, reinforcement of concrete and polymer composite have also been investigated. However, published results on concrete reinforced with shredded composite underline the need for a consistent quality of shredded composite to observe improved properties of concrete (Asokan et al. 2009). Reinforcement of polymer composite with shredded composite does not provide better results. Shredded composite is a dry material

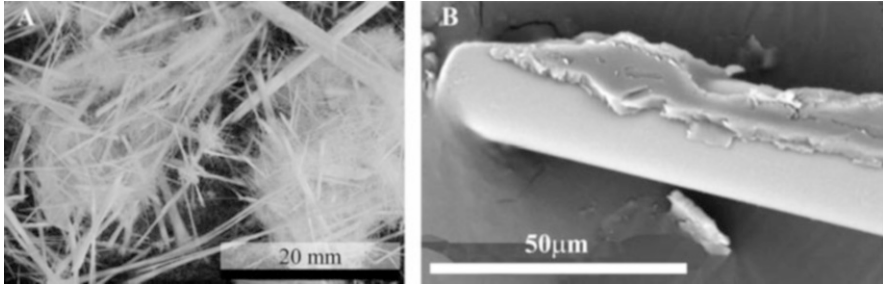


**Fig. 23.6** Shredded composite, (a) Shredded composite from unidirectional glass fiber composite, (b) A glass fiber from shredded composite covered with old matrix material (Toncelli 2014)

which needs a lot of resin to be impregnated properly (Fig. 23.6a). A study conducted under the GenVind project investigated the quality and the performance of composite manufactured with shredded composite. The conclusion is that the shredded composite shows no adherence to the new polymer matrix, because the fibres present in the shredded composite are covered with old matrix material (Fig. 23.6b). The resulting composite tensile strength is very low (Toncelli 2014).

Shredded composite can also be used in sound insulation panel, by using glue to agglomerate it. This is currently under development by a Danish company named Miljøskærm (Friis Farsøe 2013). Mass production is not available yet.

Grinding wind turbine blade material has one considerable drawback; it does not take advantage of the initial structural properties of the composite and reduces considerably the value of the material. The next solutions presented look at reusing the structure and the properties of these composites. These solutions benefit from the capacity of the material, but are difficult to implement on an industrial scale. These solutions are named occasional solutions.

## 23.4 Occasional Solutions

### 23.4.1 Large Sections

Large sections of wind turbine blades can be reused for architectural or other structural purposes. This solution offers the possibility to use the good quality and the structural capacity of the blade material. It also extends the life of the material with little re-processing. On the other hand, the number of possible applications is limited by the complexity of the structure of the blade and a mass production is close to impossible. To industrialize such solution a reliable source of material with given dimension is needed, and this is difficult with end of life wind turbine blade. Examples of occasional applications have been proposed by the SuperUse studio in the Netherlands. These are a playground for children (Fig. 23.7a) or benches on a



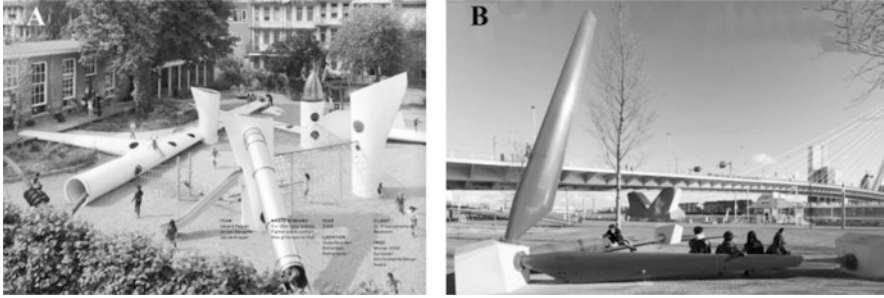


**Fig. 23.7** Examples of applications for large sections of wind turbine blades by the SuperUse studio, (a) Wikado playground in Rotterdam, (b) Benches at Willemsplein in Rotterdam



**Fig. 23.8** Furniture made out of end of life wind turbine blades by Wigh Design, (a) Table and longboard, (b) Prototype of furniture

public place (Fig. 23.7b). Within the GenVind project, a bridge is under planning by the same Dutch architectural studio. The bridge will use two blades from Siemens Wind Power and will be located in Aalborg in Denmark.

### 23.4.2 Construction Element

Construction elements such as beams, plates and curved elements can also be cut out of the blades. This requires heavier reprocessing and the geometries of these elements are also restricted by the blade structure. However, the production of such standard element could diversify the possible applications. The use of such material in furniture has been investigated by Lars Wigh in the GenVind project, as shown in Fig. 23.8. Similar to the use of large section of wind turbine blade, industrialization



of this recycling solution would also require having a reliable source of wind turbine blade material with known dimensions.

### 23.5 Solutions on a Research Stage

The last recycling solutions presented in this chapter are the ones requiring the heaviest re-processing and still mostly exist on a research stage; these solutions do not exist, or have not been trialed, on a commercial scale yet. Research on composite recycling technique has been ongoing for more than 20 years (Job 2013; Pickering 2006). The techniques are usually divided into two categories: the thermal and the chemical recycling processes. The thermal recycling techniques are for example pyrolysis or fluidized bed and allow recovering of the fibers mainly. Pyrolysis is the decomposition of organic molecules to smaller ones in an inert atmosphere with processing temperature ranging from 300 to 700 °C depending on the heating system used and the presence of a catalyst (Allred and Busselle 2000; Åkesson et al. 2012). Pyrolysis was once used on a commercial scale by ReFiber, a Danish company recycling wind turbine blade into glass fiber insulation material. The company stopped its activities in 2007. The fluidised bed is a thermal oxidative process with a processing temperature around 450 °C. The main disadvantage of these thermal recycling techniques is the reduction by a factor two or more of the glass fiber tensile strength (Kennerley et al. 1998; Thomasson et al. 2014).

Regarding the chemical recycling techniques, the most advanced and promising one is probably supercritical fluids, which uses both heat and chemicals. Supercritical fluids are fluids at temperature and pressure just above the critical point, where the fluid presents itself in one single supercritical phase, having combined characteristics: liquid like density, dissolving power, diffusivity and gas like viscosity (Oliveux et al. 2012). With this technique both the resin and the fibers can be recovered. This technique also investigated under the GenVind project has shown that glass fibers can be recovered with most of their initial tensile strength (unpublished work).

These recycling techniques are meant to enable the reuse of recycled glass fibres in new polymer composite. However, the decreased tensile strength of the fibers, the degraded surface properties (loss of the silane coupling agent) and the cost of these fibers, more expensive than pristine fibers, make it difficult.

### 23.6 Conclusion

Wind turbine blades are a complex structure made of different composite materials. They are built according to different design and are produced at different length. In addition, windfarms will be decommissioned at different time and for different reasons. End of life wind turbine blades material is therefore a discontinuous and

inhomogeneous source of material. Altogether, this makes end of life wind turbine blade a material challenging to recycle. This section reviewed recycling solutions which are used or could be potentially be used nowadays.

The potential of these recycling solutions can be compared on: the amount of reprocessing involved, the value of the material produced and the number of possible applications. Ideally, a recycling solution would involve little reprocessing to produce a cheap valuable material, which can be used in many applications.

Considering the amount of reprocessing needed in the different solutions presented, refurbishment is certainly the one requiring the less, compared to a process like mechanical grinding or supercritical fluids. When comparing the value of the material produced, here again, refurbishment, by renewing blades which will produce electricity for a couple of more years is probably of higher value than expensive recovered glass fiber with low mechanical properties. However, when considering the number of possible applications which can be made out of the material produced, the solutions involving heavy reprocessing might be more interesting. All in all, this shows that the recycling solutions presented in this section all have advantages and drawback, which could be attenuated by combining them.

**Acknowledgments** The authors would like to thank the innovation consortium GenVind (“Nationalt initiativ omkring genanvendelse af plastkompositter”): especially Karin Magelund Møller and Jacob Boutrup from LM Wind Power, for providing a wind turbine blade to this study. The research has been supported by The Danish Council for Technology and Innovation under the Ministry of Science, Innovation and Higher Education.

**Open Access** This chapter is distributed under the terms of the Creative Commons Attribution-NonCommercial 4.0 International License (<http://creativecommons.org/licenses/by-nc/4.0/>), which permits any noncommercial use, duplication, adaptation, distribution and reproduction in any medium or format, as long as you give appropriate credit to the original author(s) and the source, provide a link to the Creative Commons license and indicate if changes were made.

The images or other third party material in this chapter are included in the work’s Creative Commons license, unless indicated otherwise in the credit line; if such material is not included in the work’s Creative Commons license and the respective action is not permitted by statutory regulation, users will need to obtain permission from the license holder to duplicate, adapt or reproduce the material.

## References

- Åkesson D, Foltynowicz Z, Christeen J et al (2012) Microwave pyrolysis as a method of recycling glass fibre from used blades of wind turbines. *J Reinf Plast Compos* 31:1136–1142
- Albers H, Greiner S, Seifert H et al (2009) Recycling of wind turbine rotor blades – fact or fiction? *DEWI Mag* 34:32–41
- Allred RE, Busselle LD (2000) Tertiary recycling of automotive plastics and composites. *J Thermoplast Compos Mater* 13:92–101
- Asokan P, Osmani M, Price ADF (2009) Assessing the recycling potential of glass fibre reinforced plastic waste in concrete and cement composites. *J Clean Prod* 17:821–829
- Beauson J, Ilsted Bech J, Brøndsted P (2013) Composite recycling: characterizing end of life wind turbine blade material. In: Van Hoa S, Hubert P (eds) *Proceedings of the 19th international*

- conference on composite materials 2013 (ICCM-19), Montreal, 2013
- Brøndsted P, Lilholt H, Lystrup A (2005) Composite materials for wind power turbine blades. *Annu Rev Mater Res* 35:505–538
- Duflou JR, Deng Y, Van Acker K et al (2012) Do fiber reinforced polymer composites provide environmentally benign alternatives? A life cycle assessment based study. *Mater Res Soc Bull* 37:374–382
- European Commission Directorate General Environment (2012) Guidance on the interpretation of key provisions of Directive 2008/98/EC on waste. In: European Commission, environment, framework Directive on waste. Available via the EC Directorate-General Environment. [http://ec.europa.eu/environment/waste/framework/pdf/guidance\\_doc.pdf](http://ec.europa.eu/environment/waste/framework/pdf/guidance_doc.pdf). Accessed 12 Apr 2016
- European Composites Industry Association (2013) Composite recycling made easy. In: European Composites Industry Association (EuCIA) sustainability. Available via EuCIA. [http://www.avk-tv.de/files/20130212\\_recycling\\_made\\_easy.pdf](http://www.avk-tv.de/files/20130212_recycling_made_easy.pdf). Accessed 12 Apr 2016
- Friis Farsøe L (2013) Gamle vindmøllevinger får nyt liv i støjskærme. <http://www.plast.dk/aktuelt/nyhed/Gamle-vindmoelevinger-faar-nyt-liv-i-stojskaerme>. Accessed 12 Apr 2016
- Halliwell S (2006) End of life options for composite waste: recycle, reuse or dispose? National Composite Network best practice guide. In: End of life options. Available via Composites UK. <https://compositesuk.co.uk/system/files/documents/endoflifeoptions.pdf>. Accessed 12 Apr 2016
- Job S (2013) Recycling glass fibre reinforced composites – history and progress. *Reinf Plast* 57(5):19–23
- Kennerley JR, Kelly RM, Fenwick NJ et al (1998) The characterization and reuse of glass fibres recycled from scrap composites by the action of a fluidized bed process. *Compos Part A* 29A:839–845
- Mølholt Jensen F, Branner K (2013) Introduction to wind turbine blade design. In: Brøndsted P, Nijssen RPL (eds) *Advances in wind turbine blade design and material*. Woodhead Publishing Limited, Cambridge, pp 3–28
- Nijssen RPL, Brøndsted P (2013) Fatigue as a design driver for composite wind turbine blades. In: Brøndsted P, Nijssen RPL (eds) *Advances in wind turbine blade design and material*. Woodhead Publishing Limited, Cambridge, pp 175–209
- Oliveux G, Bailleul JL, Le Gal La Salle E (2012) Chemical recycling of glass fibre reinforced composites using subcritical water. *Compos Part A* 43:1809–1818
- Papadakis N, Ramirez C, Reynolds N (2010) Designing composite wind turbine blades for disposal, recycling or reuse. In: Goodship V (ed) *Management recycling and reuse of waste composites*. Woodhead Publishing Limited, Cambridge, pp 443–457
- Pickering S (2006) Recycling technologies for thermoset composite materials – current status. *Compos Part A* 37:1206–1215
- Sayer F, Bürkner F, Blunk M et al (2009) Influence of Loads and environmental conditions on material properties over the service life of rotor blades. *DEWI Mag* 34:24–31
- Schleisner L (2000) Life cycle assessment of a wind farm and related externalities. *Renew Energ* 20:279–288
- Schmidt A (2006) Life cycle assessment of electricity produced from onshore sited wind power plants based on Vestas V82-1.65 MW turbines. In: Vestas reports. Available via Vestas. <https://www.vestas.com/~media/vestas/about/sustainability/pdfs/lca%20v82165%20mw%20onshore2007.pdf>. Accessed 12 Apr 2016
- Sørensen BF, Jørgensen E, Debel CP et al (2004) Improved design of large wind turbine blade of fibre composites based on studies of scale effects (Phase 1) Summary report Risø-R-1390. In: Research reports, DTU Orbit – The Research Information System. Available via DTU. [http://orbit.dtu.dk/fedora/objects/orbit:90493/datastreams/file\\_7702048/content](http://orbit.dtu.dk/fedora/objects/orbit:90493/datastreams/file_7702048/content). Accessed 12 Apr 2016
- Thomasson JL, Yang L, Meier R (2014) The properties of glass fibres after conditioning at composite recycling temperatures. *Compos Part A* 61:201–208
- Toncelli C (2014) Reuse of shredded composite in new polymer composite. Dissertation, Technical University of Denmark

- Tucker L (2009) Old turbines get a second wind through remanufacturing. <http://green.blogs.nytimes.com/2009/01/26/old-turbines-get-a-second-wind-through-remanufacturing/>. Accessed 17 Mar 2016
- Welstead J, Hirst R, Keogh D et al (2013) Research and guidance on restoration and decommissioning of onshore wind farms. In: Scottish Natural Heritage (SNH) Publications. Available via SNH. [http://www.snh.org.uk/pdfs/publications/commissioned\\_reports/591.pdf](http://www.snh.org.uk/pdfs/publications/commissioned_reports/591.pdf). Accessed 12 Apr 2016